

Lecture Notes in Mechanical Engineering

Mohd Hasnun Arif Hassan *Editor*

Intelligent Manufacturing & Mechatronics

Proceedings of Symposium, 29 January
2018, Pekan, Pahang, Malaysia

 Springer

Lecture Notes in Mechanical Engineering

Lecture Notes in Mechanical Engineering (LNME) publishes the latest developments in Mechanical Engineering—quickly, informally and with high quality. Original research reported in proceedings and post-proceedings represents the core of LNME. Volumes published in LNME embrace all aspects, subfields and new challenges of mechanical engineering. Topics in the series include:

- Engineering Design
- Machinery and Machine Elements
- Mechanical Structures and Stress Analysis
- Automotive Engineering
- Engine Technology
- Aerospace Technology and Astronautics
- Nanotechnology and Microengineering
- Control, Robotics, Mechatronics
- MEMS
- Theoretical and Applied Mechanics
- Dynamical Systems, Control
- Fluid Mechanics
- Engineering Thermodynamics, Heat and Mass Transfer
- Manufacturing
- Precision Engineering, Instrumentation, Measurement
- Materials Engineering
- Tribology and Surface Technology

More information about this series at <http://www.springer.com/series/11236>

Mohd Hasnun Arif Hassan
Editor

Intelligent Manufacturing & Mechatronics

Proceedings of Symposium, 29 January 2018,
Pekan, Pahang, Malaysia

 Springer

Editor
Mohd Hasnun Arif Hassan
Faculty of Manufacturing Engineering
Universiti Malaysia Pahang
Pekan, Pahang
Malaysia

ISSN 2195-4356 ISSN 2195-4364 (electronic)
Lecture Notes in Mechanical Engineering
ISBN 978-981-10-8787-5 ISBN 978-981-10-8788-2 (eBook)
<https://doi.org/10.1007/978-981-10-8788-2>

Library of Congress Control Number: 2018934933

© Springer Nature Singapore Pte Ltd. 2018

This work is subject to copyright. All rights are reserved by the Publisher, whether the whole or part of the material is concerned, specifically the rights of translation, reprinting, reuse of illustrations, recitation, broadcasting, reproduction on microfilms or in any other physical way, and transmission or information storage and retrieval, electronic adaptation, computer software, or by similar or dissimilar methodology now known or hereafter developed.

The use of general descriptive names, registered names, trademarks, service marks, etc. in this publication does not imply, even in the absence of a specific statement, that such names are exempt from the relevant protective laws and regulations and therefore free for general use.

The publisher, the authors and the editors are safe to assume that the advice and information in this book are believed to be true and accurate at the date of publication. Neither the publisher nor the authors or the editors give a warranty, express or implied, with respect to the material contained herein or for any errors or omissions that may have been made. The publisher remains neutral with regard to jurisdictional claims in published maps and institutional affiliations.

Printed on acid-free paper

This Springer imprint is published by the registered company Springer Nature Singapore Pte Ltd. part of Springer Nature
The registered company address is: 152 Beach Road, #21-01/04 Gateway East, Singapore 189721, Singapore

Preface

The Symposium on Intelligent Manufacturing and Mechatronics (SymposIMM) 2018 was held at Universiti Malaysia Pahang in Pekan, Pahang, Malaysia, on 29 January 2018. It was organized by the Faculty of Manufacturing Engineering, Universiti Malaysia Pahang (UMP), in collaboration with the Faculty of Manufacturing Engineering of Universiti Teknikal Malaysia Melaka (UTeM), Melaka. Both parties aimed to provide a platform for deliberating empirical and theoretical research that are foreseen in the context of Industry 4.0. With the theme of “Strengthening Innovations Towards Industry 4.0”, it is the first dedicated symposium to Industry 4.0 hosted by the organizers. The symposium was graced by a vivacious keynote speech entitled “The Ideas of Mechatronics” by Prof. Ir. Dr. Wan Azhar Wan Yusoff.

This symposium enticed 120 submissions from authors nationwide. All submissions underwent a strenuous peer review process from members of the Peer-Reviewing Technical Committee. The reviews were based on the manuscript’s relevance to the tracks, novelty of the findings, the importance and presentation of the studies towards the particularity of Industry 4.0’s current trends. Following the review process, only 65 submissions made it into the symposium, 15 submissions were withdrawn, and 40 submissions were rejected due to various reasons. The accepted submissions were divided into five tracks covering various scopes of manufacturing engineering and mechatronics stream, namely Intelligent Manufacturing, Robotics, Artificial Intelligence, Instrumentation, and Modelling and Simulation. This book was divided into five parts based on the aforementioned tracks.

We would like to express our gratitude to all members of the Organizing Committee, without which the organization of this symposium would never be possible. Special thank goes to the management of the Faculty of Manufacturing Engineering, Universiti Malaysia Pahang, for the support towards the successful organization of the symposium. Further, we would like to extend our thanks to all authors for their participation in the symposium and their valuable contribution to this book. Last but not least, we would like to appreciate the help from the

publisher, especially to Dr. Christoph Baumann and Mr. Arumugam Deivasigamani. We hope that the contents of this book will benefit the readers in embracing the new era of industrial revolution 4.0.

Pekan, Pahang, Malaysia
January 2018

Mohd Hasnun Arif Hassan
Zamzuri Hamedon
Siti Zubaidah Ismail
Ahmad Shahir Jamaludin
Muhammad Aizzat Zakaria
Ahmad Shahrizan Abdul Ghani
Nurul Akmal Che Lah
Nurul Hidayah Razak
Ahmad Fakhri Ab. Nasir
Ahmad Najmuddin Ibrahim
Asrul Adam
Zulhelmi Ismail
Mohd Yazid Abu
Radhiyah Abd. Aziz

Organizing Committee

Chairman of the Organizing Committee

Zamzuri Hamedon, Universiti Malaysia Pahang, Malaysia

Vice Chairman of the Organizing Committee

Mohd Hasnun Arif Hassan, Universiti Malaysia Pahang, Malaysia

Secretary

Siti Zubaidah Ismail, Universiti Malaysia Pahang, Malaysia

Treasurer

Ahmad Shahir Jamaludin, Universiti Malaysia Pahang, Malaysia

Submission and Publication Committee

Muhammad Aizzat Zakaria, Universiti Malaysia Pahang, Malaysia

Asrul Adam, Universiti Malaysia Pahang, Malaysia

Radhiyah Abd. Aziz, Universiti Malaysia Pahang, Malaysia

Zulhelmi Ismail, Universiti Malaysia Pahang, Malaysia

Scientific Reviewing Committee

Ahmad Shahrizan Abdul Ghani, Universiti Malaysia Pahang, Malaysia
Nurul Akmal Che Lah, Universiti Malaysia Pahang, Malaysia
Nurul Hidayah Razak, Universiti Malaysia Pahang, Malaysia
Mohd Yazid Abu, Universiti Malaysia Pahang, Malaysia
Ahmad Yusairi Bani Hashim, Universiti Teknikal Malaysia Melaka, Malaysia
Zamberi Jamaludin, Universiti Teknikal Malaysia Melaka, Malaysia
Muhammad Hafidz Fazli Md Fauadi, Universiti Teknikal Malaysia Melaka

Publicity Committee

Ahmad Fakhri Ab Nasir, Universiti Malaysia Pahang, Malaysia
Azrul Azwan Abdul Rahman, Universiti Teknikal Malaysia Melaka, Malaysia

Venue and Logistics Committee

Ahmad Najmuddin Ibrahim, Universiti Malaysia Pahang, Malaysia
Lokman Abdullah, Universiti Teknikal Malaysia Melaka, Malaysia

Special Tasks Committee

Nurul Hidayah Razak, Universiti Malaysia Pahang, Malaysia
Syamimi Shamsuddin, Universiti Teknikal Malaysia Melaka, Malaysia
Mohd Khairulnazri Saidi, Universiti Malaysia Pahang, Malaysia

Name of Editors

Mohd Hasnun Arif Hassan, Universiti Malaysia Pahang, Malaysia
Zamzuri Hamedon, Universiti Malaysia Pahang, Malaysia
Siti Zubaidah Ismail, Universiti Malaysia Pahang, Malaysia
Ahmad Shahir Jamaludin, Universiti Malaysia Pahang, Malaysia
Muhammad Aizzat Zakaria, Universiti Malaysia Pahang, Malaysia
Ahmad Shahrizan Abdul Ghani, Universiti Malaysia Pahang, Malaysia
Nurul Akmal Che Lah, Universiti Malaysia Pahang, Malaysia
Nurul Hidayah Razak, Universiti Malaysia Pahang, Malaysia
Ahmad Fakhri Ab. Nasir, Universiti Malaysia Pahang, Malaysia
Ahmad Najmuddin Ibrahim, Universiti Malaysia Pahang, Malaysia

Asrul Adam, Universiti Malaysia Pahang, Malaysia

Zulhelmi Ismail, Universiti Malaysia Pahang, Malaysia

Mohd Yazid Abu, Universiti Malaysia Pahang, Malaysia

Radhiyah Abd. Aziz, Universiti Malaysia Pahang, Malaysia

Contents

Part I Intelligent Manufacturing

Mathematical Modelling of Biomechanics Factors for Push Activities in Manufacturing Industry	3
Seri Rahayu Kamat, Mohammad Firdaus Ani, Athira Ghazali, Syamimi Shamsuddin, Momoyo Ito and Minoru Fukumi	
Ergonomics Study of Working Postures in Manual Hand Layup Process	15
Nur Syafiqah Rayme, Seri Rahayu Kamat, Syamimi Shamsuddin, Wan Hasrulnizzam Wan Mahmood and Noor'ain Azizan	
Mismatch in Anthropometric Parameters of Malaysian Manufacturing Workers	27
Nur Syafiqah Rayme, Seri Rahayu Kamat, Syamimi Shamsuddin, Wan Hasrulnizzam Wan Mahmood and Ruzy Haryati Hambali	
Development Tools of an Adaptive Controller	41
Muhammad Azri Othman, Mohamad Minhat, Zamberi Jamaludin and Ahamad Zaki Mohamed Noor	
Innovative Method of Measuring Electrode Wear During EDM Drilling Process Using Vision System	53
Zamzuri Hamedon, I. Razemi, A. R. Abdul Manaf and Nafrizuan Mat Yahya	
Suppression on Effect of Cutting Forces Towards Tracking Performance in Milling Cutting Process Using State Observers	65
Madihah Maharof, Zamberi Jamaludin, Mohamad Minhat, Nur Amira Anang, Tsung Heng Chiew and J. Jamaludin	

Effect of Filler Loading on Tracking and Erosion of Silicone Rubber Based Composites Under DC Voltage 73
 Najwa Kamarudin, Jeefferie Abd Razak, Nurbahirah Norddin, Aminuddin Aman and Nazurah Nazir

Design and Implementation of Cascade NP/PI Controller for Feed Table Ball Screw Driven Milling Machine 85
 Nur Amira Anang, Lokman Abdullah, Zamberi Jamaludin, Madihah Maharof and Tsung Heng Chiew

A Resonant Type AC Magnetometer for Evaluation of Magnetic Nanoparticles 93
 Nazatul Sharreena Suhaimi, Mohd Mawardi Saari, Hamzah Ahmad, Mohd Rusllim Mohamed and Nurul Akmal Che Lah

Optimization of Multi-holes Drilling Path Using Particle Swarm Optimization. 101
 Najwa Wahida Zainal Abidin, Mohd Fadzil Faisae Ab. Rashid and Nik Mohd Zuki Nik Mohamed

Development of 3D Printed Heart Model for Medical Training 109
 Khairul Shah Affendy Yakof, Nor Fazlin Zabudin, Idris Mat Sahat and Mohd Azrul Hisham Mohd Adib

Investigating the Influences of Automated Material Handling System (AMHS) and Effect of Layout Changing in Automotive Assembly Process 117
 Seha Saffar, Zamberi Jamaludin and Fairul Azni Jafar

Systematic Approach for Uncertainty Delta E Data for Composites Panel Coating Analysis. 131
 Elmi Abu Bakar, W. A. F. W. Othman and A. R. Othman

Statistical Analysis of the Machining Parameters in Drilling of Carbon Fibre Reinforced Plastics (CFRP) Composite with Various Drill Types 141
 A. R. Othman, M. H. Hassan, Elmi Abu Bakar and W. A. F. W. Othman

Surface Roughness and Wear Properties of Al–Al₂O₃ Metal Matrix Composites Fabricated Using Friction Stir Processing 155
 N. Fatchurrohman and Azrie Abdullah

A Knowledge-Based Ergonomics Assessment System for WMSD Prevention Using AHP Methodology 161
 Fazilah Abdul Aziz, Zakri Ghazalli, Mohd Jawad Mohd Jamil, Awanis Romli and Nik Mohd Zuki Nik Mohamed

Part II Robotics

The Identification and Control of a Finger Exoskeleton for Grasping Rehabilitation 177
 Zahari Taha, Muhammad Muaz Alim, Anwar P. P. Abdul Majeed, Muhammad Aizzat Zakaria, Mohd Azraai Mohd Razman, Mohd Ali Hanafiah Shaharudin and Mohd Hasnun Arif Hassan

Trajectory Tracking Analysis of Planar End-Effector Upper Limb Rehabilitation Device 183
 H. Y. Lim and Muhammad Aizzat Zakaria

Survey on Animal Robot PARO in Malaysia: Perception and Acceptance 197
 Muhammad Winal Zikril Zulkifli, Syamimi Shamsuddin and Lim Thiam Hwee

Shortest Path Planning for Noncircular Omnidirectional Mobile Robot 209
 Salah Addin Amin Ahmed and M. Juhairi Aziz Safar

Preparation, Field Observation and Survey on STEM Engagement of 5-Axis Pick-and-Place Pneumatic Robotic Arm Remote-Manipulation 219
 Ahmad Anas Yusof, Ihsan Ismail, Syarizal Bakri, Mohd Khairi Mohamed Nor and Rabiah Ahmad

Facing the Autonomous Underwater Vehicle Competition Challenge: The TUAH AUV Experience 231
 Ahmad Anas Yusof, Mohd Khairi Mohamed Nor, Shamsul Anuar Shamsudin, Mohd Rizal Alkahari, Mohd Shahrieel bin Mohd Aras and Mohamad Riduwan Md. Nawawi

Motion Tracker Based Wheeled Mobile Robot System Identification and Controller Design 241
 Dwi Pebrianti, Yong Hooi Hao, Nur Aisyah Syafinaz Suarin, Luhur Bayuaji, Zulkifli Musa, Mohammad Syafrullah and Indra Riyanto

The Development of PANTHER AUV for Autonomous Underwater Vehicle Competition Challenge 2017/2018 259
 Ahmad Anas Yusof, Mohd Khairi Mohamed Nor, Shamsul Anuar Shamsudin, Mohd Rizal Alkahari and Masjuri Musa

Waypoint Navigation of Quad-rotor MAV Using Fuzzy-PID Control 271
 Goh Ming Qian, Dwi Pebrianti, Luhur Bayuaji, Nor Rul Hasma Abdullah, Mahfuzah Mustafa, Mohammad Syafrullah and Indra Riyanto

Development of Pole-Like Tree Spiral Climbing Robot	285
M. A. Mustapa, W. A. F. W. Othman, Elmi Abu Bakar and A. R. Othman	
Data-Driven PID Tuning Based on Safe Experimentation Dynamics for Control of Double-Pendulum-Type Overhead Crane	295
Nor Sakinah Abdul Shukor and Mohd Ashraf Ahmad	
Integral Super Twisting Sliding Mode Control (ISTSMC) Application in 1DOF Internal Mass Autonomous Underwater Glider (AUG)	305
Maziyah Mat-Noh, M. R. Arshad, Rosmiwati Mohd-Mokhtar and Zainah Md Zain	
X4-ROV: The Open Source Underwater Vehicle	327
Zainah Md Zain and Khairil Ashraf Ab. Rahim	
Effect of Assistive Grouser Mechanism on Lightweight Rover Power Consumption Pattern on Steep Soft Sand Inclines	343
Ahmad Najmuddin Ibrahim and Yasuhiro Fukuoka	
Part III Artificial Intelligence	
Development of Ergonomic Vehicle Model and Decision Support System for Driving Fatigue	355
Mohammad Firdaus Ani, Seri Rahayu Kamat, Minoru Fukumi, Momoyo Ito, Mohamad Minhat and Nur Syafiqah Rayme	
Talent Identification of Potential Archers Through Fitness and Motor Ability Performance Variables by Means of Artificial Neural Network	371
Zahari Taha, Rabiuh Muazu Musa, Anwar P. P. Abdul Majeed, Mohamad Razali Abdullah and Mohd Hasnun Arif Hassan	
Classification of High Performance Archers by Means of Bio-physiological Performance Variables via <i>k</i>-Nearest Neighbour Classification Model	377
Zahari Taha, Rabiuh Muazu Musa, Anwar P. P. Abdul Majeed, Mohamad Razali Abdullah, Ahmad Fakhri Ab. Nasir and Mohd Hasnun Arif Hassan	
The Application of Support Vector Machine in Classifying Potential Archers Using Bio-mechanical Indicators	385
Zahari Taha, Rabiuh Muazu Musa, Anwar P. P. Abdul Majeed, Mohamad Razali Abdullah, Muhammad Amirul Abdullah and Mohd Hasnun Arif Hassan	

The Identification of Hunger Behaviour of *Lates Calcarifer* Using *k*-Nearest Neighbour 393
 Zahari Taha, Mohd Azraai Mohd Razman, F. A. Adnan,
 Anwar P. P. Abdul Majeed, Rabi Muazu Musa,
 Ahmad Shahrizan Abdul Ghani, M. F. Sallehudin and Y. Mukai

Decision Making Support System Using Intelligence Tools to Select Best Alternative in Design for Remanufacturing (Economy Indicator) 401
 Ahamad Zaki Mohamed Noor, Muhammad Hafidz Fazli Md Fauadi,
 Fairul Azni Jafar, Nor Rashidah Mohamad,
 Muhammad Winal Zikril Zulkifli, Muhammad Haziq Hasbulah,
 Muhammad Azri Othman, Mahasan Mat Ali, Jee Boon Goh
 and Rajandran Morthui

Towards EEG-Based Brain-Controlled Modular Robots: Preliminary Framework by Interfacing OpenVIBE, Python and V-REP for Simulate Modular Robot Control 415
 Muhammad Haziq Hasbulah, Fairul Azni Jafar, M. Hisham Nordin
 and Kazutaka Yokota

Genetic Algorithm Optimization of PID Controller for Brushed DC Motor 427
 A. A. M. Zahir, S. S. N. Alhady, W. A. F. W. Othman and M. F. Ahmad

SKF-Based Image Template Matching for Distance Measurement by Using Stereo Vision 439
 Nurnajmin Qasrina Ann, Dwi Pebrianti, Luhur Bayuaji,
 Mohd Razali Daud, Rosdiyana Samad, Zuwairie Ibrahim,
 Rosyati Hamid and Mohammad Syafrullah

Butterfly Species Recognition Using Artificial Neural Network 449
 S. S. N. Alhady and Xin Yong Kai

Investigation of Steering Wheel Control of an Electric Buggy Car for Designing Fuzzy Controller 459
 Hafiz Halin, Wan Khairunizam, K. Ikram, Hasri Haris, S. A. Bakar,
 Z. M. Razlan, I. Zunaidi and H. Desa

Statistical Pattern Recognition as an After Service for Statistical Process Control 469
 Norazlin Nasir, A. Y. Bani Hashim, Muhammad Hafidz Fazli Md Fauadi
 and Teruaki Ito

Visual Based Distance Recognition Technique by Using Pixy CMUcam5 479
 M. F. Ahmad, S. S. N. Alhady, Wan Rahiman,
 W. A. F. W. Othman and A. A. M. Zahir

Parallel Guided Image Processing Model for <i>Ficus Deltoidea</i> (Jack) Moraceae Varietal Recognition	487
Ahmad Fakhri Ab. Nasir, Ahmad Shahrizan Abdul Ghani and M. Nordin A. Rahman	
Part IV Instrumentation	
Ontological Framework of Arm Gesture Information for the Human Upper Body	507
Wan Khairunizam, K. Ikram, S. A. Bakar, Z. M. Razlan and I. Zunaidi	
RGB Classification Determination with Different Light Intensity Using Pxy CMUcam5	517
M. F. Ahmad, S. S. N. Alhady, Wan Rahiman, W. A. F. W. Othman and A. A. M. Zahir	
Detection of Metallic Contaminant in Aluminium Soda Can Using TMR Sensor	527
Nurul A'in Nadzri, Mohd Mawardi Saari, Saifuddin Razali, Mohd Rusllim Mohamed and Hamzah Ahmad	
Performance Evaluation of Distributed Gain Offered by Raman Amplifier in WDM and EDFA	537
M. Z. H. Jesmeen, J. Hossen, Thangavel Bhuvaneswari, M. A. Hasnayeem, J. Emerson Raja and K. Tawsif	
Vehicle Detection System Using Tunnel Magnetoresistance Sensor	547
Nurul A'in Nadzri, Chai Kar Hoe, Mohd Mawardi Saari, Saifuddin Razali, Mohd Razali Daud and Hamzah Ahmad	
Ergonomic Study on Wrist Rehabilitation Therapy (WRist-T) Device	557
Nurul Ain Abdul Shukor, Idris Mat Sahat and Mohd Azrul Hisham Mohd Adib	
Pressure Transient Characteristic in Fluid Condition During Opened and Closed Water Line Based on Experimental Method	565
Syarizal Bakri, Ihsan Ismail, Ahmad Anas Yusof and Suhaimi Misha	
Electronic Water Balancing Tool	573
Cheow Kah Chun, Ahmad Shahrizan Abdul Ghani, Ker Shao Jiun, Nur Syazwani Abdul Gani, Muhamad Izdhar Zaki and Ahmad Fakhri Ab. Nasir	
Development of a Soccer Ball Launching Device	591
Mohd Hasnun Arif Hassan, Zahari Taha, Mohd Ali Hanafiah Shaharudin, Lim Kok Wee and Zulfika Anuar	

Part V Modelling and Simulation

A Study on the Exposure of Vertical Vibration Towards the Brain on Seated Human Driver Model 601
 Nurul Afiqah Zainal, Muhammad Aizzat Zakaria and K. Baarath

An Investigation on the Effect of Lateral Motion on Normal Forces Acting on Each Tires for Nonholonomic Vehicle 611
 K. Baarath, Muhammad Aizzat Zakaria and Nurul Afiqah Zainal

Numerical Analysis of Fuzzy Logic Temperature and Humidity Control System in Pharmaceutical Warehouse Using MATLAB Fuzzy Toolbox 623
 Nurainaa Elias, Nafrizuan Mat Yahya and Er Hong Sing

Parameter Properties of a Sliding Mode Controller Design in Friction Compensation 631
 N. A. Rafan, Zamberi Jamaludin, Tsung Heng Chiew and N. A. Mulop

System Interface Design for CAD/CAM-Simulink Data Exchange System Using MATLAB® 639
 N. Mat Seman, Zamberi Jamaludin and Mohamad Minhat

Single-Solution Simulated Kalman Filter Algorithm for Routing in Printed Circuit Board Drilling Process 649
 Nor Hidayati Abdul Aziz, Zuwairie Ibrahim, Nor Azlina Ab Aziz, Zulkifli Md. Yusof and Mohd Saberi Mohamad

Performance Evaluation of Random Search Based Methods on Model-Free Wind Farm Control 657
 Mok Ren Hao, Mohd Ashraf Ahmad, Raja Mohd Taufika Raja Ismail and Ahmad Nor Kasruddin Nasir

The Development of Graphical Overall Equipment Effectiveness Interface 671
 Norazlin Nasir, Teruaki Ito, A. Y. Bani Hashim and Muhammad Hafidz Fazli Md Fauadi

Effect of Length on Pressure Characteristic in the Water Hydraulic Main Line Circuit Using Simulink-Simscape 685
 Ihsan Ismail, Syarizal Bakri, Ahmad Anas Yusof and Suhaimi Misha

An Enhancement in Control Laws of Super Twisting Sliding Mode Servo Drive Controller Using Hyperbolic Tangent Function and Arc Tangent Smoothing Function 695
 Zamberi Jamaludin, Tsung Heng Chiew, A. Y. Bani Hashim, Lokman Abdullah and N. A. Rafan

Finite Element Analysis of Strand Burner 705
M. Hafizi, M. M. Noor, R. Mamat, A. Aziz and A. T. Termizi

**High Precision Estimation on Physical Behavior for Cutting
with Various Tool Rake Angle by Finite Element Method** 715
Ahmad Shahir Jamaludin, Hosokawa Akira, Tatsuaki Furumoto,
Tomohiro Koyano and Yohei Hashimoto

Contributors

M. Nordin A. Rahman Faculty of Informatics and Computing, Universiti Sultan Zainal Abidin, Besut, Terengganu, Malaysia

Nor Azlina Ab Aziz Faculty of Engineering and Technology, Multimedia University, Melaka, Malaysia

Ahmad Fakhri Ab. Nasir Innovative Manufacturing, Mechatronics, and Sports Lab (IMAMS), Faculty of Manufacturing Engineering, Universiti Malaysia Pahang, Gambang, Pahang, Malaysia

Khairil Ashraf Ab. Rahim Robotics and Unmanned Research Group (RUS), Instrument & Control Engineering (ICE) Cluster, Faculty of Electrical and Electronics Engineering, Universiti Malaysia Pahang, Pekan, Pahang, Malaysia

Mohd Fadzil Faisae Ab. Rashid Manufacturing Focus Group, Faculty of Mechanical Engineering, Universiti Malaysia Pahang, Pekan, Malaysia

Jeefferie Abd Razak Advanced Manufacturing Center, Faculty of Manufacturing Engineering, Universiti Teknikal Malaysia Melaka, Durian Tunggal, Melaka, Malaysia

Fazilah Abdul Aziz Faculty of Mechanical Engineering, Universiti Malaysia Pahang, Pekan, Pahang, Malaysia; Faculty of Manufacturing Engineering, Universiti Malaysia Pahang, Pekan, Pahang, Malaysia

Nor Hidayati Abdul Aziz Faculty of Engineering and Technology, Multimedia University, Melaka, Malaysia; Faculty of Electrical and Electronics Engineering, Universiti Malaysia Pahang, Pekan, Malaysia

Nur Syazwani Abdul Gani Faculty of Manufacturing Engineering, Universiti Malaysia Pahang, Gambang, Pahang, Malaysia

Ahmad Shahrizan Abdul Ghani Innovative Manufacturing, Mechatronics, and Sports Lab (IMAMS), Faculty of Manufacturing Engineering, Universiti Malaysia Pahang, Gambang, Pahang, Malaysia

Anwar P. P. Abdul Majeed Innovative Manufacturing, Mechatronics and Sports Laboratory, Faculty of Manufacturing Engineering, Universiti Malaysia Pahang, Pekan, Pahang, Malaysia

A. R. Abdul Manaf Faculty of Manufacturing Engineering, Universiti Malaysia Pahang, Pekan, Pahang, Malaysia

Nurul Ain Abdul Shukor Medical Engineering & Health Intervention Team (MedEHiT), Human Engineering Group, Faculty of Mechanical Engineering, Universiti Malaysia Pahang, Pekan, Pahang, Malaysia

Azrie Abdullah Faculty of Manufacturing Engineering, Universiti Malaysia Pahang, Pekan, Pahang, Malaysia

Lokman Abdullah Faculty of Manufacturing Engineering, Universiti Teknikal Malaysia Melaka, Durian Tunggal, Melaka, Malaysia

Mohamad Razali Abdullah Faculty of Applied Social Sciences, Universiti Sultan Zainal Abidin, Kuala Terengganu, Terengganu, Malaysia

Muhammad Amirul Abdullah Innovative Manufacturing, Mechatronics and Sports Laboratory, Faculty of Manufacturing Engineering, Universiti Malaysia Pahang, Pekan, Pahang, Malaysia

Nor Rul Hasma Abdullah Faculty of Electrical and Electronics Engineering, Universiti Malaysia Pahang, Pekan, Malaysia

Elmi Abu Bakar School of Aerospace Engineering, Universiti Sains Malaysia, Nibong Tebal, Penang, Malaysia

F. A. Adnan Innovative Manufacturing, Mechatronics and Sports Lab (iMAMS), Faculty of Manufacturing Engineering, Universiti Malaysia Pahang, Pekan, Pahang, Malaysia

Hamzah Ahmad Faculty of Electrical & Electronic Engineering, Universiti Malaysia Pahang, Pekan, Pahang, Malaysia

M. F. Ahmad School of Electric and Electronic, Engineering Campus Universiti Sains Malaysia, Nibong Tebal, Penang, Malaysia

Mohd Ashraf Ahmad Instrumentation & Control Engineering Research Group (ICE), Faculty of Electrical Engineering, Universiti Malaysia Pahang, Pekan, Pahang, Malaysia

Rabiah Ahmad Faculty of Information and Communication Technology, Universiti Teknikal Malaysia Melaka, Durian Tunggal, Melaka, Malaysia

Salah Addin Amin Ahmed School of Mechatronic Engineering, Universiti Malaysia Perlis, Arau, Perlis, Malaysia

Hosokawa Akira Institute of Science and Technology, Kanazawa University, Kanazawa, Ishikawa, Japan

S. S. N. Alhady School of Electrical and Electronic Engineering, Universiti Sains Malaysia, Nibong Tebal, Penang, Malaysia

Muhammad Muaz Alim Innovative Manufacturing, Mechatronics and Sports Laboratory, Faculty of Manufacturing Engineering, Universiti Malaysia Pahang, Pekan, Pahang, Malaysia

Mohd Rizal Alkahari Faculty of Mechanical Engineering, Universiti Teknikal Malaysia Melaka, Durian Tunggal, Melaka, Malaysia

Aminuddin Aman Faculty of Electrical Engineering, Universiti Teknikal Malaysia Melaka, Durian Tunggal, Melaka, Malaysia

Nur Amira Anang Faculty of Manufacturing Engineering, Universiti Teknikal Malaysia Melaka, Durian Tunggal, Melaka, Malaysia

Mohammad Firdaus Ani Faculty of Manufacturing Engineering, Universiti Teknikal Malaysia Melaka, Melaka, Malaysia; Tokushima Malaysia Academic Center (TMAC), Tokushima University, Tokushima, Japan; Department of Information Science and Intelligent System, Tokushima University, Tokushima, Japan

Nurnajmin Qasrina Ann Faculty of Electrical and Electronics Engineering, Universiti Malaysia Pahang, Pekan, Malaysia

Zulfika Anuar Faculty of Mechanical Engineering, Universiti Malaysia Pahang, Pekan, Pahang, Malaysia

M. R. Arshad Underwater, Control Robotics Research Group (UCRG), School of Electrical and Electronic Engineering, Engineering Campus, Universiti Sains Malaysia, Nibong Tebal, Pulau Pinang, Malaysia

A. Aziz Faculty of Mechanical Engineering, Universiti Malaysia Pahang, Pekan, Malaysia

Noor'ain Azizan Faculty of Manufacturing Engineering, Universiti Teknikal Malaysia Melaka (UTeM), Durian Tunggal, Malaysia

K. Baarath Faculty of Manufacturing Engineering, Universiti Malaysia Pahang, Pekan, Pahang, Malaysia

S. A. Bakar School of Mechatronic, Universiti Malaysia Perlis, Perlis, Malaysia

Syarizal Bakri Faculty of Mechanical Engineering, Universiti Teknikal Malaysia Melaka, Durian Tunggal, Melaka, Malaysia

A. Y. Bani Hashim Institute of Technology and Science, Tokushima University, Tokushima-shi, Tokushima, Japan; Faculty of Manufacturing Engineering, Universiti Teknikal Malaysia Melaka, Durian Tunggal, Melaka, Malaysia

Luhur Bayuaji Faculty of Computer Science and Software Engineering, Universiti Malaysia Pahang, Gambang, Malaysia; Magister of Computer Science, Universitas Budi Luhur, South Jakarta, Indonesia

Thangavel Bhuvaneshwari Faculty of Engineering and Technology, Multimedia University, Ayer Keroh, Melaka, Malaysia

Nurul Akmal Che Lah Innovative Manufacturing, Mechatronics and Sports Lab (iMAMS), Faculty of Manufacturing Engineering, Universiti Malaysia Pahang, Pekan, Pahang, Malaysia

Tsung Heng Chiew Faculty of Manufacturing Engineering, Universiti Teknikal Malaysia Melaka, Durian Tunggal, Melaka, Malaysia

Cheow Kah Chun Innovative Manufacturing, Mechatronics, and Sports Lab (IMAMS), Faculty of Manufacturing Engineering, Universiti Malaysia Pahang, Gambang, Pahang, Malaysia

Mohd Razali Daud Faculty of Electrical & Electronic Engineering, Universiti Malaysia Pahang, Pekan, Pahang, Malaysia

H. Desa Advanced Computing and Sustainable School of Mechatronic, Universiti Malaysia Perlis, Perlis, Malaysia

Nurainaa Elias Faculty of Manufacturing Engineering, University Malaysia Pahang (UMP), Pekan, Malaysia

J. Emerson Raja Faculty of Engineering and Technology, Multimedia University, Ayer Keroh, Melaka, Malaysia

N. Fatchurrohman Faculty of Manufacturing Engineering, Universiti Malaysia Pahang, Pekan, Pahang, Malaysia

Minoru Fukumi Department of Information Science and Intelligent System, Tokushima University, Tokushima, Japan

Yasuhiro Fukuoka Department of Intelligent Systems Engineering, College of Engineering, Ibaraki University, Hitachi, Japan

Tatsuaki Furumoto Institute of Science and Technology, Kanazawa University, Kanazawa, Ishikawa, Japan

Athira Ghazali Universiti Teknikal Malaysia Melaka (UTeM), Melaka, Malaysia

Zakri Ghazali Faculty of Mechanical Engineering, Universiti Malaysia Pahang, Pekan, Pahang, Malaysia

Jee Boon Goh Faculty of Manufacturing Engineering, Universiti Teknikal Malaysia, Durian Tunggal, Melaka, Malaysia

M. Hafizi Faculty of Mechanical Engineering, Universiti Malaysia Pahang, Pekan, Malaysia

Hafiz Halin Advanced Computing and Sustainable School of Mechatronic, Universiti Malaysia Perlis, Perlis, Malaysia

Ruzy Haryati Hambali Faculty of Manufacturing Engineering, Universiti Teknikal Malaysia Melaka (UTeM), Durian Tunggal, Malaysia

Zamzuri Hamedon Faculty of Manufacturing Engineering, Universiti Malaysia Pahang, Pekan, Pahang, Malaysia

Rosyati Hamid Faculty of Electrical and Electronics Engineering, Universiti Malaysia Pahang, Pekan, Malaysia

Mok Ren Hao Instrumentation & Control Engineering Research Group (ICE), Faculty of Electrical Engineering, Universiti Malaysia Pahang, Pekan, Pahang, Malaysia

Yong Hooi Hao Electrical & Instrument Department, CNI Engineering Construction Sdn. Bhd, Johor, Malaysia

Hasri Haris Advanced Computing and Sustainable School of Mechatronic, Universiti Malaysia Perlis, Perlis, Malaysia

Muhammad Haziq Hasbullah Faculty of Manufacturing Engineering, Universiti Teknikal Malaysia, Durian Tunggal, Melaka, Malaysia

Yohei Hashimoto Institute of Science and Technology, Kanazawa University, Kanazawa, Ishikawa, Japan

M. A. Hasnayeem International Islamic University Chittagong, Chittagong, Bangladesh

M. H. Hassan School of Mechanical Engineering, Universiti Sains Malaysia, Nibong Tebal, Pulau Pinang, Malaysia

Mohd Hasnun Arif Hassan Innovative Manufacturing, Mechatronics and Sports Laboratory, Faculty of Manufacturing Engineering, Universiti Malaysia Pahang, Pekan, Pahang, Malaysia

M. Hisham Nordin Faculty of Manufacturing Engineering, Universiti Teknikal Malaysia Melaka, Durian Tunggal, Melaka, Malaysia

Chai Kar Hoe Faculty of Electrical & Electronic Engineering, Universiti Malaysia Pahang, Pekan, Pahang, Malaysia

J. Hossein Faculty of Engineering and Technology, Multimedia University, Ayer Keroh, Melaka, Malaysia

Lim Thiam Hwee Psychosocial Department, SOCSO Tun Razak Rehabilitation Center, Durian Tunggal, Melaka, Malaysia

Ahmad Najmuddin Ibrahim Faculty of Manufacturing Engineering, Universiti Malaysia Pahang, Pekan, Pahang, Malaysia

Zuwairie Ibrahim Faculty of Electrical and Electronics Engineering, Universiti Malaysia Pahang, Pekan, Malaysia; Faculty of Manufacturing Engineering, Universiti Malaysia Pahang, Pekan, Malaysia

K. Ikram Advanced Computing and Sustainable School of Mechatronic, Universiti Malaysia Perlis, Perlis, Malaysia

Ihsan Ismail Faculty of Mechanical Engineering, Universiti Teknikal Malaysia Melaka, Alor Gajah, Melaka, Malaysia

Momoyo Ito Department of Information Science and Intelligent System, Tokushima University, Tokushima, Japan

Teruaki Ito Faculty of Manufacturing Engineering, Universiti Teknikal Malaysia Melaka, Hang Tuah Jaya, Durian Tunggal, Melaka, Malaysia

Fairul Azni Jafar Faculty of Manufacturing Engineering, Universiti Teknikal Malaysia Melaka, Durian Tunggal, Melaka, Malaysia

Ahmad Shahir Jamaludin Faculty of Manufacturing Engineering, Universiti Malaysia Pahang, Pekan, Pahang, Malaysia

J. Jamaludin Faculty of Engineering, Technology and Built Environment, UCSI University Kuala Lumpur, Taman Taynton View, Kuala Lumpur, Malaysia

Zamberi Jamaludin Faculty of Manufacturing Engineering, Universiti Teknikal Malaysia Melaka, Durian Tunggal, Melaka, Malaysia

M. Z. H. Jesmeen Faculty of Engineering and Technology, Multimedia University, Ayer Keroh, Melaka, Malaysia

Ker Shao Jiun Faculty of Manufacturing Engineering, Universiti Malaysia Pahang, Gambang, Pahang, Malaysia

Xin Yong Kai School of Electrical & Electronic Engineering, Universiti Sains Malaysia, George Town, Malaysia

Najwa Kamarudin Advanced Manufacturing Center, Faculty of Manufacturing Engineering, Universiti Teknikal Malaysia Melaka, Durian Tunggal, Melaka, Malaysia

Seri Rahayu Kamat Faculty of Manufacturing Engineering, Universiti Teknikal Malaysia Melaka (UTeM), Durian Tunggal, Malaysia; Tokushima Malaysia Academic Center (TMAC), Tokushima University, Tokushima, Japan

Wan Khairunizam Advanced Computing and Sustainable School of Mechatronic, Universiti Malaysia Perlis, Perlis, Malaysia

Tomohiro Koyano Institute of Science and Technology, Kanazawa University, Kanazawa, Ishikawa, Japan

H. Y. Lim Innovative Manufacturing, Mechatronics & Sports Laboratory (IMAMS), Faculty of Manufacturing Engineering, Universiti Malaysia Pahang, Pekan, Pahang, Malaysia

Madiah Maharof Faculty of Manufacturing Engineering, Universiti Teknikal Malaysia Melaka, Durian Tunggal, Melaka, Malaysia

R. Mamat Faculty of Mechanical Engineering, Universiti Malaysia Pahang, Pekan, Malaysia

Mahasan Mat Ali Faculty of Manufacturing Engineering, Universiti Teknikal Malaysia, Durian Tunggal, Melaka, Malaysia

Idris Mat Sahat Medical Engineering & Health Intervention Team (MedEHIT), Human Engineering Group, Faculty of Mechanical Engineering, Universiti Malaysia Pahang, Pekan, Malaysia

N. Mat Seman Fakulti Kejuruteraan Pembuatan, Universiti Teknikal Malaysia Melaka, Durian Tunggal, Melaka, Malaysia

Maziyah Mat-Noh Instrumentation and Control Engineering (ICE) Cluster, Faculty of Electrical and Electronics Engineering, Universiti Malaysia Pahang, Pekan, Pahang, Malaysia

Muhammad Hafidz Fazli Md Fauadi Institute of Technology and Science, Tokushima University, Tokushima-shi, Tokushima, Japan; Faculty of Manufacturing Engineering, Universiti Teknikal Malaysia Melaka, Durian Tunggal, Melaka, Malaysia

Zulkiffi Md. Yusof Faculty of Manufacturing Engineering, Universiti Malaysia Pahang, Pekan, Malaysia

Zainah Md Zain Robotics and Unmanned Research Group (RUS), Instrument & Control Engineering (ICE) Cluster, Faculty of Electrical and Electronics Engineering, Universiti Malaysia Pahang, Pekan, Pahang, Malaysia

Mohamad Minhat Faculty of Manufacturing Engineering, Universiti Teknikal Malaysia Melaka, Melaka, Malaysia

Suhaimi Misha Faculty of Mechanical Engineering, Universiti Teknikal Malaysia Melaka, Durian Tunggal, Melaka, Malaysia

Mohd Saberi Mohamad Faculty of Creative Technology and Heritage, Universiti Malaysia Kelantan, Pengkalan Chepa, Malaysia

Nor Rashidah Mohamad Faculty of Manufacturing Engineering, Universiti Teknikal Malaysia, Durian Tunggal, Melaka, Malaysia

Mohd Ruslim Mohamed Faculty of Electrical & Electronic Engineering, Universiti Malaysia Pahang, Pekan, Pahang, Malaysia

Ahamad Zaki Mohamed Noor Faculty of Manufacturing Engineering, Universiti Teknikal Malaysia, Durian Tunggal, Melaka, Malaysia

Mohd Azrul Hisham Mohd Adib Medical Engineering & Health Intervention Team (MedEHiT), Human Engineering Group, Faculty of Mechanical Engineering, Universiti Malaysia Pahang, Pekan, Pahang, Malaysia

Mohd Shahrieel bin Mohd Aras Faculty of Electrical Engineering, Universiti Teknikal Malaysia Melaka, Durian Tunggal, Melaka, Malaysia

Mohd Jawad Mohd Jamil Faculty of Computer Systems and Software Engineering, Universiti Malaysia Pahang, Gambang, Pahang, Malaysia

Rosmiwati Mohd-Mokhtar Underwater, Control Robotics Research Group (UCRG), School of Electrical and Electronic Engineering, Engineering Campus, Universiti Sains Malaysia, Nibong Tebal, Pulau Pinang, Malaysia

Rajandran Morthui Faculty of Manufacturing Engineering, Universiti Teknikal Malaysia, Durian Tunggal, Melaka, Malaysia

Y. Mukai Kulliyah of Science, International Islamic University Malaysia, Jalan Sultan Ahmad Shah, Kuantan, Pahang, Malaysia

N. A. Mulop Faculty of Manufacturing Engineering, Universiti Teknikal Malaysia Melaka, Durian Tunggal, Melaka, Malaysia

Masjuri Musa Faculty of Mechanical Engineering, Universiti Teknikal Malaysia Melaka, Durian Tunggal, Melaka, Malaysia

Rabiu Muazu Musa Innovative Manufacturing, Mechatronics and Sports Laboratory, Faculty of Manufacturing Engineering, Universiti Malaysia Pahang, Pekan, Pahang, Malaysia; Faculty of Applied Social Sciences, Universiti Sultan Zainal Abidin, Kuala Terengganu, Terengganu, Malaysia

Zulkifli Musa Faculty of Electrical and Electronics Engineering, Universiti Malaysia Pahang, Pekan, Malaysia

Mahfuzah Mustafa Faculty of Electrical and Electronics Engineering, Universiti Malaysia Pahang, Pekan, Malaysia

M. A. Mustapa School of Electrical & Electronic Engineering, Universiti Sains Malaysia, Nibong Tebal, Penang, Malaysia

Nurul A'in Nadzri Faculty of Electrical & Electronic Engineering, Universiti Malaysia Pahang, Pekan, Pahang, Malaysia

Ahmad Nor Kasruddin Nasir Instrumentation & Control Engineering Research Group (ICE), Faculty of Electrical Engineering, Universiti Malaysia Pahang, Pekan, Pahang, Malaysia

Norazlin Nasir Institute of Technology and Science, Tokushima University, Tokushima-shi, Tokushima, Japan; Faculty of Manufacturing Engineering, Universiti Teknikal Malaysia Melaka, Hang Tuah Jaya, Durian Tunggal, Melaka, Malaysia

Mohamad Riduwan Md. Nawawi Faculty of Electrical Engineering, Universiti Teknikal Malaysia Melaka, Durian Tunggal, Melaka, Malaysia

Nazurah Nazir Faculty of Electrical Engineering, Universiti Teknikal Malaysia Melaka, Durian Tunggal, Melaka, Malaysia

Nik Mohd Zuki Nik Mohamed Manufacturing Focus Group, Faculty of Mechanical Engineering, Universiti Malaysia Pahang, Pekan, Malaysia

M. M. Noor Faculty of Mechanical Engineering, Universiti Malaysia Pahang, Pekan, Malaysia

Mohd Khairi Mohamed Nor Faculty of Mechanical Engineering, Universiti Teknikal Malaysia Melaka, Durian Tunggal, Melaka, Malaysia

Nurbahirah Norddin Faculty of Engineering Technology, Universiti Teknikal Malaysia Melaka, Durian Tunggal, Melaka, Malaysia

A. R. Othman Mechanical Engineering Department, Universiti Teknologi Petronas, Seri Iskandar, Perak, Malaysia

Muhammad Azri Othman Faculty of Manufacturing Engineering, Universiti Teknikal Malaysia, Durian Tunggal, Melaka, Malaysia

W. A. F. W. Othman School of Electrical & Electronic Engineering, Universiti Sains Malaysia, Nibong Tebal, Penang, Malaysia

Dwi Pebrianti Faculty of Electrical and Electronics Engineering, Universiti Malaysia Pahang, Pekan, Malaysia; Magister of Computer Science, Universitas Budi Luhur, Jakarta, Indonesia

Goh Ming Qian Faculty of Electrical and Electronics Engineering, Universiti Malaysia Pahang, Pekan, Malaysia

N. A. Rafan Faculty of Manufacturing Engineering, Universiti Teknikal Malaysia Melaka, Durian Tunggal, Melaka, Malaysia

Wan Rahiman School of Electrical and Electronic Engineering, Universiti Sains Malaysia, Nibong Tebal, Penang, Malaysia

Raja Mohd Taufika Raja Ismail Instrumentation & Control Engineering Research Group (ICE), Faculty of Electrical Engineering, Universiti Malaysia Pahang, Pekan, Pahang, Malaysia

Nur Syafiqah Rayme Faculty of Manufacturing Engineering, Universiti Teknikal Malaysia Melaka (UTeM), Durian Tunggal, Malaysia

Saifuddin Razali Faculty of Electrical & Electronic Engineering, Universiti Malaysia Pahang, Pekan, Pahang, Malaysia

I. Razemi Faculty of Manufacturing Engineering, Universiti Malaysia Pahang, Pekan, Pahang, Malaysia

Z. M. Razlan Advanced Computing and Sustainable School of Mechatronic, Universiti Malaysia Perlis, Perlis, Malaysia

Mohd Azraai Mohd Razman Innovative Manufacturing, Mechatronics and Sports Laboratory, Faculty of Manufacturing Engineering, Universiti Malaysia Pahang, Pekan, Pahang, Malaysia

Indra Riyanto Department of Electronics Engineering, Faculty of Engineering, Universitas Budi Luhur, Jakarta, Indonesia

Awanis Romli Faculty of Computer Systems and Software Engineering, Universiti Malaysia Pahang, Gambang, Pahang, Malaysia

Mohd Mawardi Saari Faculty of Electrical & Electronic Engineering, Universiti Malaysia Pahang, Pekan, Pahang, Malaysia

M. Juhairi Aziz Safar School of Mechatronic Engineering, Universiti Malaysia Perlis, Arau, Perlis, Malaysia

Seha Saffar Centre of Graduates Studies, Universiti Teknikal Malaysia Melaka, Hang Tuah Jaya, Durian Tunggal, Melaka, Malaysia

M. F. Sallehudin Kulliyyah of Science, International Islamic University Malaysia, Jalan Sultan Ahmad Shah, Kuantan, Pahang, Malaysia

Rosdiyana Samad Faculty of Electrical and Electronics Engineering, Universiti Malaysia Pahang, Pekan, Malaysia

Mohd Ali Hanafiah Shaharudin Innovative Manufacturing, Mechatronics and Sports Lab (iMAMS), Faculty of Manufacturing Engineering, Universiti Malaysia Pahang, Pekan, Pahang, Malaysia

Syamimi Shamsuddin Faculty of Manufacturing Engineering, Universiti Teknikal Malaysia Melaka (UTeM), Durian Tunggal, Malaysia

Shamsul Anuar Shamsudin Faculty of Mechanical Engineering, Universiti Teknikal Malaysia Melaka, Durian Tunggal, Melaka, Malaysia

Nor Sakinah Abdul Shukor Faculty of Electrical & Electronics Engineering (FKEE), Universiti Malaysia Pahang (UMP), Pekan, Pahang, Malaysia

Er Hong Sing Faculty of Manufacturing Engineering, University Malaysia Pahang (UMP), Pekan, Malaysia

Nur Aisyah Syafinaz Suarin Faculty of Electrical and Electronics Engineering, Universiti Malaysia Pahang, Pekan, Malaysia

Nazatul Sharreena Suhaimi Faculty of Electrical & Electronic Engineering, Universiti Malaysia Pahang, Pekan, Pahang, Malaysia

Mohammad Syafrullah Magister of Computer Science, Universitas Budi Luhur, Jakarta, Indonesia

Zahari Taha Innovative Manufacturing, Mechatronics and Sports Laboratory, Faculty of Manufacturing Engineering, Universiti Malaysia Pahang, Pekan, Pahang, Malaysia

K. Tawsif Faculty of Engineering and Technology, Multimedia University, Ayer Keroh, Melaka, Malaysia

A. T. Termizi Faculty of Mechanical Engineering, Universiti Malaysia Pahang, Pekan, Malaysia

Wan Hasrulnizam Wan Mahmood Faculty of Engineering Technology, Universiti Teknikal Malaysia Melaka (UTeM), Durian Tunggal, Malaysia

Lim Kok Wee Innovative Manufacturing, Mechatronics and Sports Lab (iMAMS), Faculty of Manufacturing Engineering, Universiti Malaysia Pahang, Pekan, Pahang, Malaysia

Nafrizuan Mat Yahya Faculty of Manufacturing Engineering, University Malaysia Pahang (UMP), Pekan, Malaysia

Khairul Shah Affendy Yakof Medical Engineering & Health Intervention Team (MedEHiT), Human Engineering Group, Faculty of Mechanical Engineering, Universiti Malaysia Pahang, Pekan, Malaysia

Kazutaka Yokota Research Division of Design and Engineering for Sustainability, Graduate School of Engineering, Utsunomiya University, Utsunomiya-shi, Japan

Ahmad Anas Yusof Faculty of Mechanical Engineering, Universiti Teknikal Malaysia Melaka, Durian Tunggal, Melaka, Malaysia

Nor Fazlin Zabudin Medical Engineering & Health Intervention Team (MedEHiT), Human Engineering Group, Faculty of Mechanical Engineering, Universiti Malaysia Pahang, Pekan, Malaysia

A. A. M. Zahir School of Electrical and Electronic Engineering, Universiti Sains Malaysia, Nibong Tebal, Penang, Malaysia

Najwa Wahida Zainal Abidin Manufacturing Focus Group, Faculty of Mechanical Engineering, Universiti Malaysia Pahang, Pekan, Malaysia

Nurul Afiqah Zainal Faculty of Manufacturing Engineering, Universiti Malaysia Pahang, Pekan, Pahang, Malaysia

Muhammad Aizzat Zakaria Innovative Manufacturing, Mechatronics & Sports Laboratory (IMAMS), Faculty of Manufacturing Engineering, Universiti Malaysia Pahang, Pekan, Pahang, Malaysia

Muhamad Izdhar Zaki Faculty of Manufacturing Engineering, Universiti Malaysia Pahang, Gambang, Pahang, Malaysia

Muhammad Winal Zikril Zulkifli Faculty of Manufacturing Engineering, Universiti Teknikal Malaysia, Durian Tunggal, Melaka, Malaysia

I. Zunaidi Technopreneur at UniMAP Sdn. Bhd., Perlis, Malaysia

Part I
Intelligent Manufacturing

Mathematical Modelling of Biomechanics Factors for Push Activities in Manufacturing Industry



Seri Rahayu Kamat, Mohammad Firdaus Ani, Athira Ghazali,
Syamimi Shamsuddin, Momoyo Ito and Minoru Fukumi

Abstract In manufacturing industries, many working tasks require their workers to perform the works in push-pull activities. The workers need to push or pull the tool or material handling in a long distance into a workplace and performing these activities continuously throughout the working hours, may lead to an early initiation of musculoskeletal disorders (MSDs) symptoms as workers developed muscle fatigue particularly concerning the hand muscles. Grip strength is the force applied by the hand to pull objects and is a part of hand strength. This paper is about the mathematical model of biomechanical factors that contributes to fatigue while worker involved on the push activities in manufacturing industry. The experimental was conducted by using Tekscan system to evaluate the muscle fatigue and hand grip pressure force while workers performing pushing excessive loads. The input parameters were time exposure, hand side and body mass index (BMI); while the output responses are muscle fatigue (voltage), hand grip pressure force (left hand), and hand grip pressure force (right hand). An important parameter that affects the output response is also identified. The finding result from mathematical model for both factors, show that the muscle fatigue was influenced by time exposure, hand side, BMI, and interaction between hand side and BMI; while hand grip pressure force was influenced by time exposure, hand side, BMI, interaction between time exposure and hand side, interaction between time exposure and BMI, and interaction between hand side and BMI.

Keywords Push activity • Hand grip force • Muscle fatigue
Hand size • Body mass index

S. R. Kamat (✉) · M. F. Ani · A. Ghazali · S. Shamsuddin
Universiti Teknikal Malaysia Melaka (UTeM), Melaka, Malaysia
e-mail: seri@utem.edu.my

M. Ito · M. Fukumi
Tokushima University, Tokushima, Japan

© Springer Nature Singapore Pte Ltd. 2018
M. H. A. Hassan (ed.), *Intelligent Manufacturing & Mechatronics*,
Lecture Notes in Mechanical Engineering,
https://doi.org/10.1007/978-981-10-8788-2_1

1 Introduction

Manual material handling such as lifting heavy products, reaching materials, pushing or pulling excessive loads and bending forward their back when doing tasks because those tasks require a large degree of freedom and stable position. Pushing and pulling activities for manual material handling that can increase the risks of back pain problem [1]. The pushing and pulling activities are a continuous activity for a large segment of the workforce, including hospital workers, manufacturing workers, construction workers, forest workers, etc. [2]. Furthermore, all of these activities are associated with the awkward posture. Awkward posture is a posture when joints are not in neutral position either muscle of lumbar in strength position or compress position such as bending forward or backward of the body. When the processes work is not appropriate and impossible to be performed in neutral position, the workers have to bend forward their back during the working hours. The theory of the awkward posture can be understood as a discomfort posture because it is a harmful position for the human body when a joint is not in its neutral range of postures and cause muscles are either less or more than resting length. Awkward posture in the workplace can cause discomfort and muscle fatigue especially in the lower extremities of workers back at the end of the working tasks. The muscles around the joint are stretched or compressed when joints are exposed to postures that involve range of movement near the extreme position. If the exposure to extreme postures is prolonged, the muscles do not immediately revert to their resting length [3]. Other than that, the workers need to bend their neck forward greater than 30° , raise their elbow above their shoulder, bend their wrist downward with palm facing downward greater than 30° , bend their back forward greater than 45° , and squatting [4].

Musculoskeletal disorders can be caused by repetitive usage of hand-held tools due to factors such as awkward hand posture [5]; static loading of the muscle during repetitive gripping of the handle [6]; excessive force exertions [7]; the weight of the tool being supported exposure to hand-arm vibration [8] and etc. To determine the optimal diameter for handle use for the general population an extensive research has been conducted. Tool handle diameter has been identified as the most significant factors that affect grip force production [9]. Grip production, local contact pressure of a handle configuration and the perceived acceptability can be affected by factors such as handle orientation; texture, angle and shape [10]. The Ergonomics Design and Analysis tool of Computer-Aided Three-Dimensional Interactive Application (CATIA) software and Tekscan software are one of the ergonomics analysis tool that have been applied to analyze pushing and pulling activities of workers while performing tasks in awkward posture [11–15].

In aerospace industry, almost workers performed the jobs in standing position and it can lead to muscle fatigue. Most of the task involved performing the job tasks such as pushing and pulling activity, the operators might feel the discomfort and pain in their arms and wrist. The operators are tending to experienced fatigue while performing the job at Layup Station that may take to serious injuries known as

Musculoskeletal Disorders (MSDs). Musculoskeletal disorders (MSDs) are often caused by awkward postures, excessive force and repetition because of the limited work area, standing for prolonged periods and heavy equipment.

This study focus on analysing the activity related with push activity that gives discomfort for workers in layup room by using Tekscan system, Electromyography (EMG) and lastly giving suggestion on proper technique to reduce hand discomfort and muscle fatigue by using an ergonomic approach to overcome all the problems. According to the previous research done [16] most of the problem related to Musculoskeletal disorder (MSD) in Layup department is related with push activities. Workers have discomfort experience with carpal tunnel syndrome and back pain while undertake the activities. The muscle fatigue develops when the workers used the sustained force in a long period of time. Due to muscle fatigue, the muscles will involve with contraction and this condition lead to discomfort. Therefore, this research is proposed to investigate the ergonomic factors and psychophysical experience that contribute to worker's fatigue and discomfort experience in the aerospace industry while performing the jobs involving push activities, analyze the biomechanical factors for worker's fatigue through and actual experiment felt. This paper is prepared to develop and validate the mathematical model using ergonomic approach in studying the relationship of the worker's fatigue and hand grip pressure force.

2 Methodology

2.1 Psychological Study

In this study the information on psychological perception contributes to the significant problem is assessed by using the questionnaire survey. Twenty respondents are involved in this survey. The purpose of this survey was to examine the psychological worker experience performed processes jobs in awkward posture and get involved in the push and pull activities in aerospace industry at demould process. The questionnaire obtains the personal information, particular workers involved, working years, duration of work, working experience, and human body discomfort which related to work and task. Figure 1 shows the part of the questionnaire related on the human body discomfort and the body and hand part while worker's performance the push and pull activities.

Based on observation, the current design of demould workstation, workers required to push the product which is quite heavy with the weight of the tool 35 kg minimum and maximum weight is 72 kg. Figure 2 illustrates workers who are exposed to workstation operation and manual material handling (MMH) at their workstations due to pushing activity. The worker experience is focus on the location of pain and discomfort particularly on the body parts. The respondents being asked to state the location of hand, that feeling discomfort while performing the task.

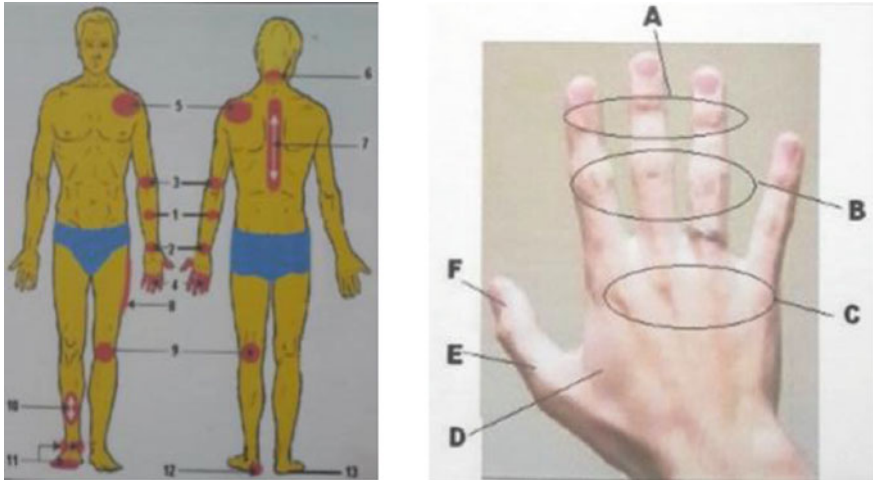


Fig. 1 Human body discomfort [17] and part hand location [18]

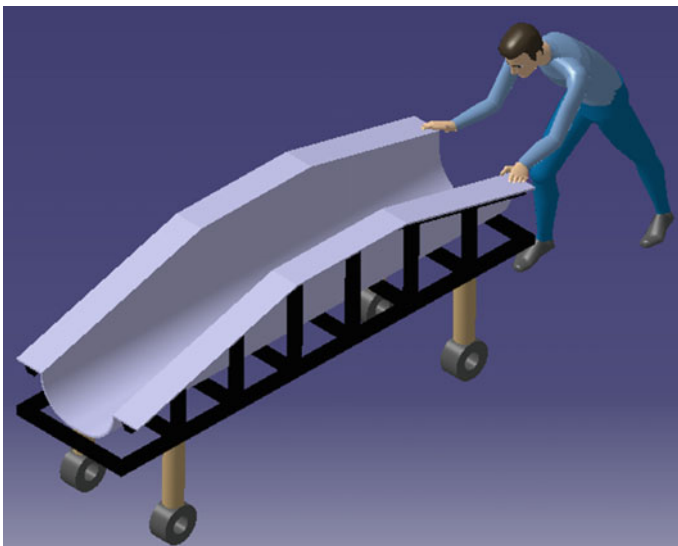


Fig. 2 Worker perform the push activities that produce awkward posture

2.2 Experimental Design

A total of six production workers from the demould process are involved in the study. The workers are selected, only workers who performed processes jobs in awkward posture and get involved in the push and pull activities and allowed to

Fig. 3 Grip sensor built-in with glove



participate in the study. The sEMG system is equipped with electrodes to detect the myoelectric signal of a subjects' muscle while performing jobs in awkward postures. The electrodes are attached conscientiously to the subject's skin to measure the activity in the six muscles: left and right thoracolumbar fascia, left and right middle trapezius, and left and right triceps. The selected muscle is also suggested by the established guidelines (HHS 1992) and recent review article [19]. The setting of sEMG system during the measurement is based on surface EMG for the Non-Invasive Assessment of Muscles (SENIAM) [20]. Tekscan's Grip Pressure Measurement System is devices used to measure and evaluate the static and dynamic pressure and force while the six workers doing pushing activities. This grip sensor can be used on hand or built-in with glove and can instrument both left and right hands. Figure 3 show the subject and outfit the subject with Grip sensor built-in with glove.

2.3 Data Analysis for Mathematical Model

In developing and formulating mathematical model, Design Expert 8.0.6 software was used and Response Surface Methodology (RSM) data analysis was carried out through this study. The RSM includes a collection of mathematical and statistical techniques that can be used for modelling and optimizing of processes. The output responses data for each experimental run were entered into the respective run number matrix. The software recognizes which model chooses for further analysis. The identification and selection is based on the sequential sum of square. This analysis compares the models by viewing the statistical significance of adding model terms to those already in the model. The highest degree model that has a p-value less than 0.10 should be chosen as the model to represent the model. Then,

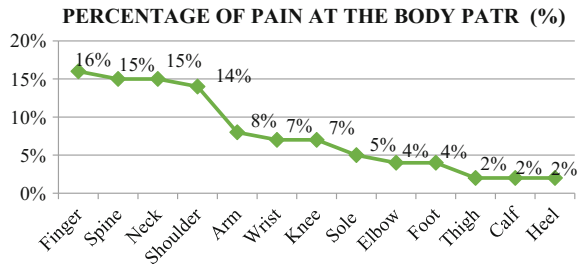
the selected model was analyzed using ANOVA where the significant of the model, significant parameters, and interaction factors were determined. The Prob > F value is small or less than 0.1 indicates that the model or factors has a significant consequence on the output response. Finally, the final equation of the model was generated through the analysis. This final equation of the model then been validated by using quantitative validations to analyzed the results. This validation runs should meet the following two conditions: First to determine if the model can predict the validation run outcome based on specific output parameters within 90% of its predictive interval. Second, the accuracy of a process model can be assessed using residual error method with respect to the validation run [21]. The residual error was calculated based on the percentage difference between the validation run value and predicted value over the predicted value. The percentage value should be less than 10% to represent the accuracy of the model.

3 Results and Discussion

3.1 Psychological Factor Analysis

The questionnaire result is more focus on the human body discomfort while worker’s performance the push and pull activities in lay-up department. Figure 4 shows the location of body parts from the highest percentage to the least percentage. Figure 5 showing the percentage of level of discomfort from the highest to lowest for each of the location of hand provided. The highest level of discomfort lies at location D where it contributes 25.80% of the discomfort experience in the hands, followed by 22.60% at location C, then with 19.35% at the location A, 12.90% at location B and E respectively, and finally 6.45% at location F. Location C and D contributes the highest level of discomfort as it is used to grip the mold holder and pushing the heavy mold while handling the job task daily.

Fig. 4 Percentage of pain at the body parts expressed in percentage (%)



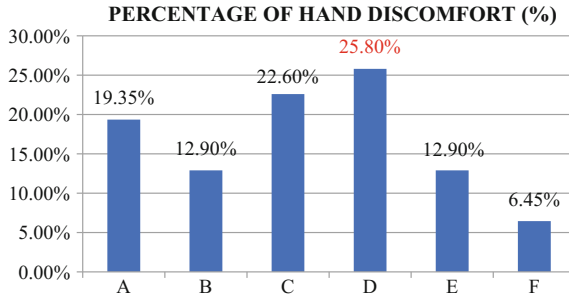


Fig. 5 Level of hand discomfort expressed in percentage (%)

Table 1 Experimental runs and results of hand grip pressure force (N) for the subjects

Std	Run	Factor 1	Factor 2	Factor 3	Response 1
		A: Time exposure (min)	B: Hand side	C: BMI (kg/m ²)	Handgrip force, (N)
1	1	5.00	Right	Underweight	181.31
2	2	10.00	Left	Normal	355.45
3	3	5.00	Right	Normal	361.94
4	4	10.00	Right	Underweight	168.92
5	5	5.00	Left	Normal	343.99
6	6	5.00	Right	Overweight	2421.54
7	7	10.00	Left	Normal	357.14
8	8	10.00	Right	Normal	356.89
9	9	10.00	Right	Overweight	2412.51
10	10	5.00	Left	Overweight	2500.32
11	11	5.00	Left	Overweight	2524.24
12	12	5.00	Left	Normal	345.15
13	13	5.00	Left	Underweight	198.13
14	14	5.00	Right	Normal	359.83
15	15	10.00	Right	Overweight	2403.01
16	16	5.00	Right	Overweight	2413.35
17	17	10.00	Right	Normal	353.21
18	18	5.00	Left	Underweight	201.34
19	19	10.00	Left	Overweight	2403.21
20	20	10.00	Left	Overweight	2418.95
21	21	10.00	Left	Underweight	177.89
22	22	10.00	Left	Underweight	176.64
23	23	5.00	Right	Underweight	183.22
24	24	10.00	Right	Underweight	169.59

3.2 Mathematical Modelling of Biomechanical Factor (Hand Grip Pressure Force, N)

Table 1 shows the experimental runs and results of the hand grip pressure force. Twenty-four experimental runs are carried out as listed. The hand grip pressure force of the both hands for each experimental run is analyzed by using Tekscan tactile force and pressure measurement (grip system). Three factors are studied as the input parameters, which are time exposure, hand side, and BMI, while hand grip pressure force as the output response in this experimental runs. The historical data are used as the design type, which focused on finding the main effect and developed the model relationship between all of the factor.

The appropriate polynomial equation to represent the relationship between the input parameters and the output response (hand grip pressure force), the sequential model sum of squares (SMSS) and lack of fit test are carried out by using Design Expert 8.0.6 software as shown in Table 2 and Table 3 respectively. The results from these two analysis show that the correlation between factors and output response can be modeled using 2FI (factor of interaction).

Table 4 shows the ANOVA for response 2FI surface model. P-value less than 0.1 show that the model is significant. Hence, time exposure, hand side, BMI, interaction between time exposure and hand side, interaction between time

Table 2 Sequential model sum of squares (SMSS) analysis for hand grip pressure force model

Sequential model sum of squares [Type 1]						
Source	Sum of squares	df	Mean square	F value	P-value Prob > F	
Mean versus total	2.358E+007	1	2.358E+007			
Linear versus mean	2.521E+007	4	6.304E+006	10244.62	<0.0001	
2FI versus linear	7956.29	5	1591.26	5.97	0.0037	Suggested
Quadratic versus 2FI	0.000	0				Aliased
Residual	3734.44	14	266.75			
Total	4.880E+007	24	2.033E+006			

Table 3 Lack of fit test for the hand grip pressure force model

Source	Sum of squares	df	Mean square	F value	P-value Prob > F	
Linear	11183.03	7	1597.58	37.76	<0.0001	
2FI	3226.74	2	1613.37	38.13	<0.0001	Suggested
Quadratic	3226.74	2	1613.37	38.13	<0.0001	Aliased
Pure error	507.70	12	42.31			

exposure and BMI, and interaction between hand side and BMI term are the significant influencing factors of the resultant hand grip pressure force

The surface response modelling, the 2FI polynomial equation developed to relate the input parameters to the hand grip pressure force as shown in Table 5. The table shows the equation of the actual factors. The equation of the actual factors can be

Table 4 ANOVA for hand grip pressure force model

ANOVA for response surface 2FI model						
Source	Sum of squares	df	Mean square	F value	P-value Prob > F	
Model	2.522E+007	9	2.802E+006	10506.08	<0.0001	Significant
A-Time exposure	3288.87	1	3288.87	12.33	0.0035	
B-Hand side	1964.39	1	1964.39	7.36	0.0168	
C-BMI	2.521E+007	2	1.260E+007	47252.59	<0.0001	
AB	1159.68	1	1159.68	4.35	0.0559	
AC	3505.63	2	1752.82	6.57	0.0097	
BC	3290.98	2	1645.49	6.17	0.0120	
Residual	3734.44	14	266.75			
Lack of fit	3226.74	2	1613.37	38.13	<0.0001	Significant
Pure error	507.70	12	42.31			
Cor total	2.523E+007	23				

Table 5 Polynomial equation for the hand grip force in terms of actual model

Hand side	Left
BMI	Underweight
Handgrip = +235.96375 – 6.32850 * Time exposure	
Hand side	Left
BMI	Normal
Handgrip = +366.86875 – 2.19150 * Time exposure	
Hand side	Left
BMI	Overweight
Handgrip = +2565.69750 – 13.86900 * Time exposure	
Hand side	Right
BMI	Underweight
Handgrip = +181.51625 – 0.76750 * Time exposure	
Hand side	Right
BMI	Normal
Handgrip = +332.69625 + 3.36950 * Time exposure	
Hand side	Right
BMI	Overweight
Handgrip = +2474.91250 – 8.30800 * Time exposure	

Table 6 Validation data of hand grip pressure fore model

Input parameters			Prediction (N)	90% PI low (N)	90% PI high (N)	Actual (N)	Error (%)
Time exposure	Hand size	BMI					
5.00	Left	Underweight	204.32	170.08	238.56	198.13	3.030
7.50	Left	Underweight	118.50	156.34	220.66	187.50	0.531
10.00	Right	Overweight	2391.83	2357.6	2426.1	2412.5	0.865

used to make predictions about the response for given levels of each factor. The levels should be identified in the original units for each factor.

3.3 Mathematical Biomechanical Model Validation

Table 6 shows the validation results of biomechanical model for three set parameter. The result indicates that the hand grip pressure force of validation runs data fall within the 90% prediction interval and the residual errors are ranging from 0.531 to 3.030% in absolute value which are less than 10%. This model is accurate enough to predict the resultant hand grip pressure force within 90% CI and the residual error relative to predicted values are less than 10%.

4 Conclusion

This paper formulated and mathematical model of biomechanical factor that contributes for Manufacturing workers while performing the push activities. All objectives were successfully achieved through this study. The mathematical model in the form of polynomial equation was successfully developed to biomechanical factor (hand grip pressure force). The developed hand grip pressure force is successfully developed and validated. Table 7 summarized the significant parameters that influenced the output responses This study identified the significant parameters that affected the hand grip pressure force through ANOVA analysis during the development of the model. The model validation found that the hand grip pressure force output of the modelling validation run was within the 90% prediction intervals

Table 7 The significant input parameters and interaction influencing the respective model

Developed models	Significant parameters	Significant interaction factors
Hand grip pressure force	<ul style="list-style-type: none"> • Time exposure • Hand side • BMI 	<ul style="list-style-type: none"> • Time exposure and hand side • Time exposure and BMI • Hand side and BMI

of the developed model and the residual error which compared to the predicted values, was less than 10%.

Acknowledgements The authors would like to acknowledge to Tokushima Malaysia Academic Centre and the funding of this research under Research Acculturation Grant Scheme (RAGS) (Research Acculturation Grant Scheme RAGS/1/2015/SG0/FKP/03/B00107), Centre for Research and Innovation Management (CRIM) UTeM Malacca for providing facilities, laboratories, respondents and assistance throughout this study.

References

1. Kuijer, P.P.F., Hoozemans, M.J., Frings-Dresen, M.H.: A different approach for the ergonomic evaluation of pushing and pulling in practice. *Int. J. Ind. Ergon.* **37**(11), 855–862 (2007). <https://doi.org/10.1016/j.ergon.2007.07.011>
2. Jellad, A., Lajili, H., Boudokhane, S., Migaou, H., Maatallah, S., Frih, Z.B.S.: Musculoskeletal disorders among Tunisian hospital staff prevalence and risk factors. *Egypt. Rheumatol.* **35**(2), 59–63 (2013). <https://doi.org/10.1016/j.ejr.2013.01.002>
3. Hayot, C., Decatoire, A., Bernard, J., Monnet, T., Lacouture, P.: Effects of ‘posture length’ on joint power in cycling. *Procedia Eng.* **34**, 212–217 (2012). <https://doi.org/10.1016/j.proeng.2012.04.037>
4. Burgess-Limerick, R., Steiner, L.J., Torma-Krajewski, J.: Ergonomics processes: implementation guide and tools for the mining industry. US Department of Health and Human Services, Centers for Disease Control and Prevention, National Institute for Occupational Safety and Health, DHHS (NIOSH) (2009). ISBN: 978-1-61583-949-0
5. Bovenzi, M.: Exposure-response relationship in the hand-arm vibration syndrome: an overview of current epidemiology research. *Int. J. Arch. Occup. Environ. Health* **71**, 509–519 (1998). <https://doi.org/10.1007/s004200050316>
6. Granata, K.P., Bennett, B.C.: Low-back biomechanics and static stability during isometric pushing. *J. Human Factors Ergon. Soc.* **47**, 536–549 (2005). <https://doi.org/10.1518/001872005774859962>
7. Lei, L., Dempsey, P.G., Xu, J.G., Ge, L.N., Liang, Y.X.: Risk factors for the prevalence of musculoskeletal disorders among Chinese foundry workers. *Int. J. Ind. Ergon.* **35**, 197–204 (2005). <https://doi.org/10.1016/j.ergon.2004.08.007>
8. Li, K.W., Yu, R.-F., Gao, Y., Maikala, R.V., Tsai, H.: Physiological and perceptual responses in male Chinese workers performing combined manual materials handling tasks. *Int. J. Ind. Ergon.* **39**, 422–427 (2009). <https://doi.org/10.1016/j.ergon.2008.08.004>
9. Sancho-Bru, J.L., Pèrez-González, A., Vergara, M., Giurintano, D.J.: 3D biomechanical model of the hand for power grip. *J. Biomech. Eng.* **125**, 78–83 (2003). <https://doi.org/10.1115/1.1532791>
10. Vieira, E., Kumar, S.: Occupational risks factors identified and interventions suggested by welders and computer numeric control workers to control low back disorders in two steel companies. *Int. J. Ind. Ergon.* **37**, 553–561 (2007). <https://doi.org/10.1016/j.ergon.2007.03.001>
11. Landau, K., Rademacher, H., Meschke, H., Winter, G., Schaub, K., Grasmueck, M., Moelbert, I., Sommer, M., Schulze, J.: Musculoskeletal disorders in assembly jobs in the automotive industry with special reference to age management aspects. *Int. J. Ind. Ergon.* **38**, 561–576 (2008). <https://doi.org/10.1016/j.ergon.2008.01.006>
12. Sheikhzadeh, A., Bakola, H., Zyga, S., Stergioulas: The Perception of Musculoskeletal risk factors (PMRF) for operating room nurses (ORN): translation and cultural adaption of the questionnaire in the Greek language. *Int. J. Caring Sci.* May–August 2017 **10**, 834 (2009)

13. Daraiseh, N.M., Cronin, S.N., Davis, L.S., Shell, R.L., Karwowski, W.: Low back symptoms among hospital nurses, associations to individual factors and pain in multiple body regions. *Int. J. Ind. Ergon.* **40**, 19–24 (2010). <https://doi.org/10.1016/j.ergon.2009.11.004>
14. Govindu, N.K., Babski-Reeves, K.: Effects of personal, psychosocial and occupational factors on low back pain severity in workers. *Int. J. Ind. Ergon.* **44**, 335–341 (2014). <https://doi.org/10.1016/j.ergon.2012.11.007>
15. Kamat, S.R., Yoxall, A.: A kinetikk study: understanding hand and finger motion whilst squeezing bottles. In: Proceedings of the International Conference on Industrial Engineering and Operations Management 2014, pp. 45–52, Bali Indonesia, 7–9 Jan 2014
16. Kuorinka, I., Jonsson, B., Kilbom, A., Viterbreg, H.: Standardised nordic questionnaires for the analysis of musculoskeletal symptoms. *J. Appl. Ergon.* **18**, 233–237 (1987). [https://doi.org/10.1016/0003-6870\(87\)90010-x](https://doi.org/10.1016/0003-6870(87)90010-x)
17. Kamat, S.R.: Strength capabilities and subjective limit of repetitive manual insertion scottish journal of arts. *Soc. Sci. Stud.* **6**, 2047–1278 (2012)
18. Reid, C.R., Bush, P.M., Karwowski, W., Durrani, S.K.: Occupational postural activity and lower extremity discomfort: a review. *Int. J. Ind. Ergon.* **40**, 247–256 (2010). <https://doi.org/10.1016/j.ergon.2010.01.003>
19. Soderberg, G. L., Cook, T. M.: Electromyography in biomechanics. *J. Phys. Ther.* **64**, 1813–1820 (1984)
20. Stegeman, D., Hermens, H.: Standards for surface electromyography: The European project surface EMG for non-invasive assessment of muscles. In: SENIAM 2008. <http://www.med.uni-jena.de/motorik/pdf/stegeman>. Last Accessed 29 Sept 2017
21. Baluch, N.H., Abdullah, C.S., Mohtar, S.: Maintenance management performance—an overview towards evaluating Malaysian palm oil mill. *Asian Malays. J. Human Factors Ergon.* **1**(2), 1–9 (2017)

Ergonomics Study of Working Postures in Manual Hand Layup Process



Nur Syafiqah Rayme , Seri Rahayu Kamat,
Syamimi Shamsuddin , Wan Hasrulnizam Wan Mahmood
and Noor'ain Azizan

Abstract In composite manufacturing, hand layup is of the fabrication methods that is widely used. Composite is the basic material used in the manufacturing of products such as shipbuilding and the process requires manual handling. Currently, there is a significant number of absenteeism that due to low back pain, indicating that workers in manual composite manufacturing have problems related to musculoskeletal disorder (MSD). The objective of this paper is to study the working posture and discomforts experienced by workers in layup process station. A preliminary survey is conducted on 45 workers to obtain their experience of discomforts while working. Survey results show that 83.33% of the workers experience discomforts on the lower back of the body. When rating their level of pain on the lower back on a scale from 1 (lowest) to 5 (highest), 41% of them rated 4 on the level pain. Pain and discomforts lead to lower productivity of workers. Consequently, this can jeopardise the quality of the products. At the layup station, this problem arises due to the design of current workspace and the posture of workers when executing the job tasks. Rapid Upper Limb Analysis in CATIA V5R20 software was used to calculate the RULA scores. All postures had scored more than 6 that need further investigation and immediate change. Ergonomically designed layup workstations and good education on proper working posture will be able to improve the workers' health conditions on the future.

N. S. Rayme · S. R. Kamat (✉) · S. Shamsuddin · N. Azizan
Faculty of Manufacturing Engineering, Universiti Teknikal Malaysia Melaka (UTeM),
Durian Tunggal, Malaysia
e-mail: seri@utem.edu.my

N. S. Rayme
e-mail: syafiqah.rayme@yahoo.com

S. R. Kamat
Tokushima Malaysia Academic Center (TMAC), Tokushima University,
2-1 Minamihosanjima-cho, Tokushima 770-8506, Japan

W. H. Wan Mahmood
Faculty of Engineering Technology, Universiti Teknikal Malaysia Melaka (UTeM),
Durian Tunggal, Malaysia

Keywords Ergonomics • CATIA V5R20 • Musculoskeletal disorder (MSD)
Rapid upper limb assessment (RULA)

1 Introduction

1.1 Ergonomics

Ergonomics is defined by Greek words; “Ergon” which means work and “nomoi” meaning natural laws [7] and is the science of refining the design of products to optimize it for human usage [18]. The word ergonomics are defined in multiple definitions, however, always leads to the similar understanding and improvisation. The academic literature on ergonomics has revealed the emergence of several contrasting definitions. It may, for example, in United States Department of Safety and Health interpreted ergonomics as the study of work [14] thereby draws adaptation in task, workstation, tools and equipment. Such expositions are ensuring that the tasks are fit to a human being because it ease the workloads and providing safer working environment by eliminating risk towards worker’s health.

In summary, it has been shown from the reviews that ergonomics, in short, is the study of the interaction between workers, workstation, environment. Ergonomics also is the study of any evaluation and improving methods towards human safety and health. As explained earlier, it does not only focus on the design of the workstation or working tools but also improvising the human towards better working posture by including the mechanics of human.

1.2 Manual Material Handling (MMH)

Manual material handling (MMH) is a working task that requires worker to complete without the help of automation. Example of MMH is lifting heavy products, reaching materials, bending forward their back when doing tasks, pushing or pulling excessive loads because those tasks require a stable position and large degree of freedom [6]. In composite manufacturing especially aerospace manufacturing, most of the work processes were using manual material handling [9]. In contrast with automotive industries and other manufacturing industries, the fabrication or production method are capable to change from MMH to automation. However, some automation in Malaysian manufacturing industries are semi-automated, thus, workers are still prone to be diagnosed with MSD. In MMH stated by Md. Deros et al. [11] is one of the contributors of MSD in workers.

1.3 Musculoskeletal Disorder (MSD)

Musculoskeletal disorder (MSD) is any injuries that caused human movement or musculoskeletal system of a human being become malfunction [12]. The nearest examples are tendons, ligaments, disks, nerves and tissues of a human. This disorder is either caused by working tasks or working environment that related to human safety and health issues.

Some diseases that relate to MSD are well-known to industries and companies. Low back pain (LBP) is one of the diseases related to MSD [13]. Other related MSD diseases are Carpal Tunnel Syndrome (CTS) and Trigger Finger that are caused by ligaments and tendons around the hand area (wrist, palm and fingers). The risk factors for MSD diseases are correlated to Ergonomic Risk Factor (ERF). ERF is the risk factors that are correlated to working tasks where workers are prone to occupational injuries and in Malaysia, manufacturing industries recorded the high number of occupational injuries [5]. Previous researchers have established that the activities that contribute to ERF are excessive lifting, repetitive movements and awkward postures [3, 5, 9, 11, 16].

1.4 Low Back Pain (LBP)

The term LBP is used here to refer to pain related to the lower part of the body. Specifically, it is defined as pain that is located anywhere from the range between the twelfth rib to inferior gluteal folds, with or without leg pain [10] (refer Fig. 1). One possible implication of LBP is that it became the strongest predictor of absenteeism [13]. This is correlated with the interview session with one of the Safety and Health officers of manufacturing sectors that says most absenteeism are claimed by the cause of a backache [20]. Awkward posture is one of the causes of getting LBP [17]. In previous studies, awkward posture is one of the ERF, hence, most manufacturing industries working tasks are categorized as ERF.

Fig. 1 The figure of 12th rib to inferior gluteal folds.

Source [15]



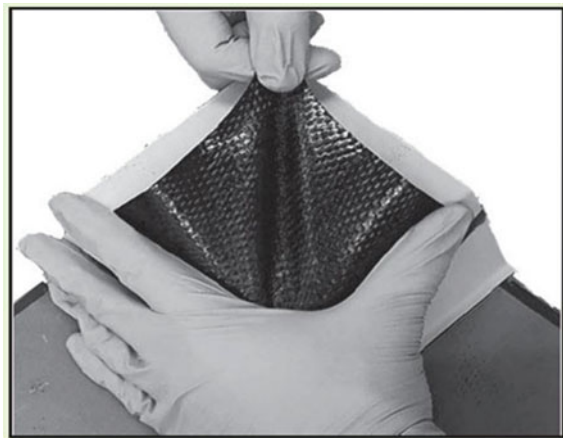
1.5 Composite Manufacturing

Composite manufacturing is on demand nowadays because of the composite characteristics. In the same way, the composite is a cost-effective material when it comes to typical weight-sensitive structure such as aircraft and spacecraft [8] similar with the manufacture of ship parts. In composite manufacturing, especially Malaysia, automation is not adaptable because of the difference in production demands as a large initial investment that are required in automated machinery and the price is up to the degree and complexity of the automated machine and with automation machining contributes a higher cost and requires higher intelligent workers.

1.6 Manual Hand Layup

In layup process, it is known as “hand layup” where manually setting down individual layers of carbon reinforcement composite known as “prepreg” for example the close up layup in Fig. 2. It is layered per the mould shape leaving no air between sheets of composites [2]. Hence, knowing the cruciality of a manufacturing process will help in understanding the process flow and then making the ergonomics study become easier. Elkington et al. [2] also, stated that the layup process had been changing for the past 30 years and this somehow provides a room for improvement in the manual process in terms of ergonomics study. This is due to a limited research study that had been done in this layup process flow in Malaysia. Recent studies conducted by Hashim et al. [6], were based on biomechanical factors

Fig. 2 Hand layup up close-up. Source [2]



of push-pull analysis at the aerospace manufacturing in layup process department. Their studies show that the layup process department does have ergonomic risk factor in pushing activities because after the mould had been completed by layup, the workers must manually push the mould to the autoclave sections. Another study has been done by Malaysian researcher at layup process department was on the MSD risk of workers and it covers the design of the workstation is suited to the anthropometry of the workers [9].

The aim of this study is to investigate the working postures of the layup process department workers by including the anthropometry measurements of the Malaysian manufacturing workers. This is due to a significant number of absenteeism due to a backache [20]. The manual layup workers are observed in their postures while doing the working task. From critical working postures identified in this study, only three awkward postures are taken as sample. Later the postures are evaluated using the Rapid Upper Limb Analysis (RULA) in the virtual environment of Computer-Aided Three-Dimensional Interactive Application (CATIA) V5 software.

2 Methodology

This study embarks quantitative and qualitative methods in obtaining the data. In the first stage of the research, literature studies were done in order to obtain the methodology for the whole process. Similar from studies done by previous researchers, this study will be using software which is CATIA V5 to prove that the awkward posture of the workers was having high risk in getting MSD as hand layup process which is classified as MMH.

In this study, a survey was developed based on conceptual guidelines proposed by Crawford [1]. This survey was validated by using expert evaluation which is the manufacturing company safety officer and head of the department of safety and academician with ergonomics expertise. The next step will be approaching the software procedures to validate survey data obtained.

Apart from that, in CATIA V5 software, the awkward postures were imitated inside a virtual environment in software. RULA analysis features in the Ergonomics section of the CATIA software was used to evaluate whether the awkward postures were having a high risk of getting MSD. This is the validation of the Survey answers regarding the discomforts experience that felt by the subjects.

2.1 Survey Participants

The participants for survey were selected based on working area. Since the study was researching about manual hand layup, the participants were the workers that are working in the layup department in a composite manufacturing industry. In order to

understand the layup process clearly; interviews, observations and literature methods were adopted in this study.

Nonetheless, the study covers only one department of a layup that is occupied by 45 personnel for two working shifts was selected. In an attempt to make the participants feel as comfortable as possible, the survey was explained one on one participants to ensure the participants understood the purpose of the surveys. For this survey, the session took two weeks to be fully completed.

To begin the process, prior to data collection, the participants received an explanation of the project. After the collection, using one on one interview method, the data was transferred to Microsoft Office Excel 2016 for graphical presentation. Once, the data were extracted from surveys, it was first necessary to plot into graphical in order to observe the trend. Following to this data presented, CATIA V5R20 software with RULA analysis features was used to validate the data from the Survey.

2.2 CATIA V5R20 RULA Analysis

Many researchers have utilized CATIA V5 software to analyze ergonomics issues virtually such as Hashim et al. [6] and Kamat et al. [9]. Traditionally, RULA analysis had been assessed by using RULA assessment sheet that needed an evaluation from ergonomics or RULA experts. However, there are certain drawbacks associated with the use of this method. This is because the expertise needed to require some cost in accessing the RULA. The major advantage of using CATIA V5 software compared to traditional assessment method is that cost-saving and simple. Some of the composite manufacturing is very difficult to access because of confidentiality issues and business purposes, hence, it is complicated to invite outsiders that are considered as ergonomics expert into the manufacturing companies. Hence, the RULA analysis was done in order to recognize the risk of these awkward postures towards the workers' health that can lead to MSD.

The initial steps of the analysis were to insert the manikin into the environment of the software. In order to do this, the 50th percentile of Japanese manikin population was chosen according to the similar geography of the Malaysian and Japanese, in which located in the Asian region. After that, the postures were imitated in the virtual environment and RULA analysis was done and the score obtained by each posture (as in Fig. 3) were tabulated according to the left and right side of the human body (refers Table 1).

Finally, the correlation between the survey and the RULA analysis score is obtained as the validation of the existence of ERF in the manual hand layup process. In the postural angle, there is a potential bias and human error in the CATIA V5 software, in future, it is recommended that the angle can be detected using Microsoft Kinect camera in order to obtain the correct angles in the human posture.

Score	Level of MSD Risk
1-2	negligible risk, no action required
3-4	low risk, change may be needed
5-6	medium risk, further investigation, change soon
6+	very high risk, implement change now

Fig. 3 Standard score from NIOSH for the comfort level of RULA analysis. Source [6]

Table 1 RULA analysis by using CATIA V5R20

Posture	Right	Left	RULA score
1			7
2			7
3			6

3 Results and Discussions

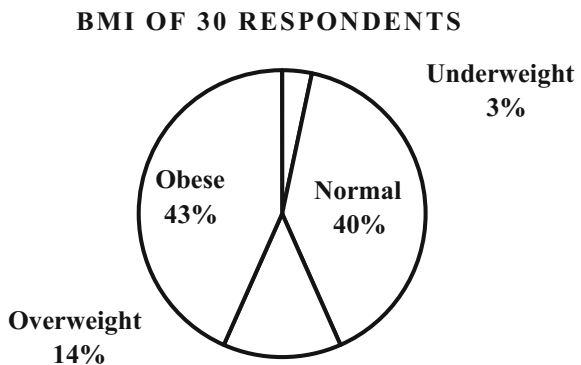
The first set of the questions aimed to identify the percentage of Body Mass Index (BMI) of the overall workers at the current layup department. The second set of questions asked the participants about the body discomforts and the level of pain of body parts whilst working at current layup process. The questions on level of pain are using Borg’s scale; where the 1st level indicates no pain and the 5th level indicates the extreme pain.

In this study, the data presented are selected from the survey focusing on MSD that leads to LBP. Hence, this section will cover on BMI, body discomforts and level of pain in the lower back region.

3.1 RULA Analysis and Body Mass Index (BMI)

As described in the methodology section, the RULA score obtained from the CATIA V5R20 software are using the chosen criteria for human manikin in anthropometry measurement sections that are the 50th percentile human manikin and with restriction population of Japanese. As the most obvious finding was that the CATIA V5R20 software available in R20 (a version of release significant to the year 2014) was not competent in providing Malaysian population itself. Hence, the usage of the Japanese population is significant towards Asian countries population based on the geography. However, the current study also found that there were many restrictions in range of measurement that cannot be avoided since the population between both countries had slight differences in terms of BMI especially in obesity class, where 44% of total respondents were obese by referring to Fig. 4 data extracted from the Survey. In Japan, only 3.6% had BMI more than 30 based on Senauer and Gemma [19]. “Malaysia is ranked sixth in the Asia Pacific region for obesity and tops the list in South-East Asia for both obesity and diabetes,” stated

Fig. 4 The BMI of workers from survey



Prof. Dr. Mohd Ismail Noor, the president of Malaysian Society for the Study of Obesity, during a press interview [4]. This proves that there is a limitation in using software analysis in ergonomics features in CATIA V5R20 software.

3.2 Awkward Postures and RULA Score

Several kinds of literature had stated that awkward posture is one of the classified ERF as in Introduction section and RULA score refers to Fig. 3, shows that the maximum score should be 6 and above. This score indicated the level of risk in getting MSD. One interesting finding is that MSD diseases are too broad to discuss as it is related to a human musculoskeletal system where it stated by Morken et al. [13] that LBP is another form of MSD. In Table 1 illustrated three different type of awkward posture that must be applied during the layup process. From the table, it was shown that the first column is the posture type during layup process, and the two-middle column separated left and right coloured human manikin in CATIA V5R20 software with RULA analysis and the last forth column indicated the score for the RULA score for each posture.

Posture 1, 2 and 3 in Table 1 showed the awkward postures while doing the layup process (imitating the real posture). In Posture 1, the worker needed to bend and twist body in order to reach the specific area of the mould composite product. Similar to, Posture 1, Posture 2 was a little bit different in the tool as the tools are used specifically according to the fixed manual obtained from the manufacturing customers. In posture 1, the worker was actually working without a tool (bare hand with gloves) and needed to apply force to layup the ceramic sheets into the mould and Posture 2 showed that the specific tools were used in order to layup ceramic sheet at the edges of the mould.

In Posture 3, however, it represented the most awkward posture between the three where three main body parts were affected due to squatting position, bending of both lower back and neck. This position had to be bear by the worker in order to layup ceramic sheet into that particular part of the mould. Nonetheless, all three awkward body postures of the workers can lead to lower back pain (one of MSD effects on the body) as stated by Roffey et al. [17]. So far, this study had found that all the RULA scores for both left and right posture in Table 1 indicated the score of more than 6 which in need of further investigation as stated by Hashim et al. [6]. However, in one mould of the composite product, the number of resources had been segregated were up to 4 workers per mould. Thus, one worker was not obligated to one type of body posture for the whole 8–12 h of working time per shift.

Although the risk of MSD is low back pain, MSDs can be triggered by other combination of several ergonomic factors from doing the current workload as mention by Roffey et al. [17]. The risk of getting MSD was reflected from the Survey data that had been distributed throughout the session. Finally, the score 7 is related to the discomforts experience that been felt by the respondent whilst working in manual hand layup that had been considered as MMH.

3.3 Discomfort Experience and Level of Pain

From the graph in Fig. 5., the workers answered on the discomforts experience on the body is coherent with the RULA analysis by CATIA V5R20 software. Closer inspection of the graph shows that the most answered discomforts body part was the waist, 27 out of 45 respondents answered and second was the lower back where 25 out of 45 respondents had experienced discomforts. This proved the statement by Syed Uda Hashim [20] that sick leaves were caused by back ache since waist and lower back can be classified as back of body. Another significant finding obtained from the process at layup process department was the workload were including the excessive lifting of item that weighed approximately 40 kg into a mould. Apparently, from this study, awkward posture and excessive lifting does have influenced the health of the workers. This is because both working tasks fall into ERF classification [5].

Referring the Fig. 6, the level of pain experienced by the workers at the lower back part of the body is rated by using scale 1–5. The study would like to highlight the level of pain experienced by the workers at lower back body part significant to the aim of this study, in which to find the evidence on the manual hand layup of composite against the LBP. From Fig. 6, 41% of the respondent answered 4 as the level of pain, this is because the pain is still bearable by the workers while doing job according to the workers in Survey session, as after the mould had been filled with ceramic sheets, it needed to be compact (vacuum to remove any air in between sheets) that were done in sequence. Thus, the workers still have time to relief the

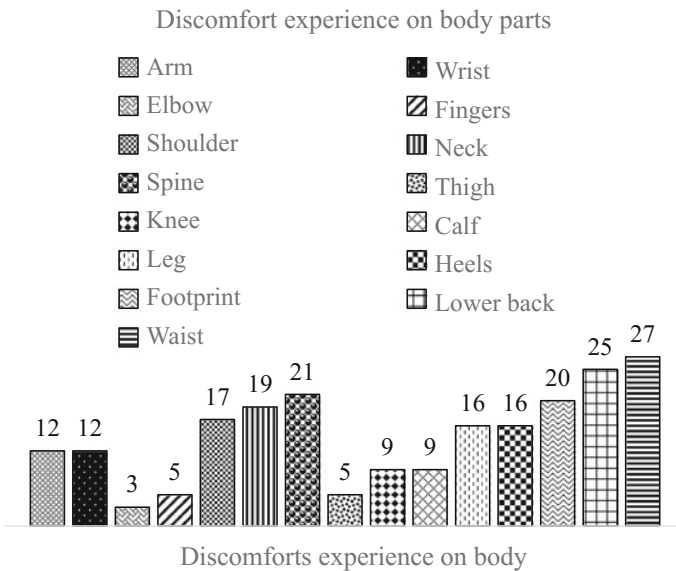
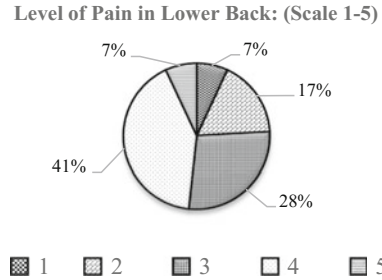


Fig. 5 Discomforts experience on body parts

Fig. 6 Level of pain on lower back part of body



muscle pain on lower back before started working on the next sequence in the Standard of Procedure (SOP). However, from the study, the significant finding was similar to Hashim et al. [6] where it was deduced that the lower back pain is associated with bending forward back in a long period of time and static contraction of muscles on the back part of the body.

4 Conclusion

In shorts, the current study aimed to investigate the working postures of manual hand layup process. This study had shown that manual hand layup process had a significant impact on the human health. Overall, this study strengthens the idea of manual hand layup does have ergonomic risk. The study confirms that there is a need for ergonomics study in composite manufacturing, this is because one the fabrication method of the composite is manual hand layup. In order to reduce the risk of getting MSD, this study suggested that the posture of the workers should be change and reanalyse by making sure the score of RULA is reduce from 7 to at least 5.

Being limited to awkward posture, the study lacks in proving caused of LBP thoroughly. Hence, it would be interesting if the study involved any experimentation on participants that includes the usage of surface electromyograph (EMG) as to detect the time to fatigue when doing the layup process. A further study should access the time where muscles on the lower back start to fatigue and in anthropometry section of CATIA V5R20 software, the next study can embark in creating Malaysian population anthropometry database that can be uploaded by Dassault Systemes in the software produced by the company.

Acknowledgements The authors would like to thank Universiti Teknikal Malaysia Melaka (UTeM) and Ministry of Higher Education (MOHE). This project is funded by RAGS/1/2015/SG01/FKP/03/B00107.

References

1. Crawford, J.O.: The Nordic Musculoskeletal Questionnaire, pp. 300–301. Oxford University Press (2007)
2. Elkington, M., Bloom, D., Ward, C., Chatzimichali, A., Potter, K.: Hand layup: understanding the manual process. *Adv. Manuf.: Polym. Compos. Sci.* **1**(3), 138–151 (2015)
3. Fuller, J.R., Lomond, K.V., Fung, J., Cote, J.N.: Posture-movement changes following repetitive motion-induced shoulder muscle fatigue. *J. Electromyogr. Kinesiol.* **19**, 1043–1052 (2009)
4. Gan, R.: Malaysians: most obese in South East Asia. Are you one of them? Find out here. <http://www.healthworks.my/malaysians-most-obese/> (2014). Accessed 30 Dec 2016
5. Halim, I., Omar, A.R., Saad, N.H.: Ergonomic Design to Improve Occupational Health in Manufacturing Industry. Sabah, Malaysia (2014)
6. Hashim, N., Kamat, S.R., Othman, M.S.: A study on push-pull analysis associated with awkward posture among workers in aerospace industry. In: International Conference on Industrial Engineering and Operations Management, Bali, Indonesia (2014)
7. Helander, M.: A Guide to Human Factors and Ergonomics, 2nd edn. CRC Press Taylor & Francis Group, Boca Raton, New York, London (2006)
8. Jones, R.M.: Preface to the First Edition. *Mechanics of Composite Materials*, 2nd edn., p. xv. Taylor & Francis Inc, New York and London (1999)
9. Kamat, S.R., Hashim, N., Halim, I., Othman, M.S., Ani, M.F.: Reduction of maximum effort level of lumbar muscle among workers in aerospace industry. *Malays. J. Hum. Factors Ergon.* **1**(2), 10–15 (2015)
10. Krimer, M., van Tulder, M.: Low back pain (non-specific). *Best Pract. Res. Clin. Rheumatol.* **21**(1), 77–91 (2007)
11. Md. Deros, B., Daruis, D.D.I., Ismail, A.R., Abdullah Sawal, N., Ghani, J.A.: Work-related musculoskeletal disorders among workers' performing manual material handling work in an automotive manufacturing company. *Am. J. Appl. Sci.* **8**(7), 1087–1092 (2010)
12. Middlesworth, M.: Ergonomics Plus. <http://ergo-plus.com/musculoskeletal-disorders-msd/>. Accessed 17 Oct 2017
13. Morken, T., Riise, T., Moen, B., Hauge, S.H.V., Holien, S., Langedrag, A., Pedersen, S., Saue, I.L.L., Seljebo, G., Thoppil, V.: Low back pain and widespread pain predict sickness absence among industrial workers (2013)
14. OSHA: United States Department of Labor Occupational Safety and Health, OSHA 3125. <https://www.osha.gov/Publications/OSHA3125.pdf> (2000). Accessed 16 Nov 2017
15. PhysioPrescription EFFECTIVE INJURY REHAB. <http://www.physioprescription.com/2016/02/16/ql-muscle-strengthening-beat-low-back-pain/> (2016). Accessed 01 July 2017
16. Punnett, L., Wegman, D.H.: Work-related musculoskeletal disorders: the epidemiologic evidence and the debate. *J. Electromyogr. Kinesiol.* **14**, 13–23 (2004)
17. Roffey, D.M., Wai, E.K., Bishop, P., Kwon, B.K., Dagenais, S.: Causal assessment of occupational sitting and low back pain: results of a systematic review. *Spine J.* **10**(3), 252–261 (2010)
18. Rouse, M.: WhatIs.com. <http://whatis.techtarget.com/definition/ergonomics> (2007). Accessed 16 Nov 2017
19. Senauer, B., Gemma, M.: Why Is the Obesity Rate So Low in Japan and High in the U.S.? Some Possible Economics Explanations. University of Minnesota, Minnesota (2006)
20. Syed Uda Hashim, S.K.: Overview on Safety and Low Back Pain, interviewed on 21 Oct 2016

Mismatch in Anthropometric Parameters of Malaysian Manufacturing Workers



Nur Syafiqah Rayme , Seri Rahayu Kamat,
Syamimi Shamsuddin , Wan Hasrulnizam Wan Mahmood
and Ruzy Haryati Hambali

Abstract The software Digital Enterprise Lean Manufacturing Interactive Application (DELMIA) is a virtual simulation software that was used in digital product manufacturing. In contrast with Computer Aided Three-dimensional Interactive Application (CATIA), DELMIA ergonomics feature is built with Human Task Simulation which can simulate the design workspace virtually. However, population available for the human manikin population are excluding Malaysian population. This study is aiming to investigate the gap and the error of anthropometry data in Malaysian manufacturing workers between the Japanese and American population in DELMIA V5R2016. A sample population of 241 people at manufacturing industries was taken in this study. The total number of anthropometric parameters used for experimentation are 100 parameters obtained from literature studies. The American and Japanese population are chosen to represent the Caucasian and Asian population for comparison of 15 randomly selected parameters of anthropometry. There are several mismatches found in the anthropometry parameter between the three comparisons of the population where the percentage of error and gap in between populations are more than 5%. In conclusion, this study recommended that future research increase the sample size of the anthropometry subjects for database comparison. For future research, it is recommended to use other methods available for measurement such as digital measurement for the anthropometry database to compare the accuracy with the traditional measuring method.

N. S. Rayme · S. R. Kamat (✉) · S. Shamsuddin · R. H. Hambali
Faculty of Manufacturing Engineering, Universiti Teknikal Malaysia Melaka (UTeM),
Durian Tunggal, Malaysia
e-mail: seri@utem.edu.my

N. S. Rayme
e-mail: syafiqah.rayme@yahoo.com

S. R. Kamat
Tokushima Malaysia Academic Center (TMAC), Tokushima University, 2-1
Minamihosanjima-cho, Tokushima 770-8506, Japan

W. H. Wan Mahmood
Faculty of Engineering Technology, Universiti Teknikal Malaysia Melaka (UTeM),
Durian Tunggal, Malaysia

Keywords Ergonomics • Anthropometry • DELMIA • Manufacturing

1 Introduction

Malaysia especially, ergonomics is lacking to the certain extent and it was considered a new field compared to other developed countries such as Japan and United States [23]. In DOSH definition of ergonomics, it is about integrating knowledge derived from the human sciences to match jobs, systems, products and environments to the physical and mental abilities and limitations [23]. Since then, Malaysian researchers mostly from the ergonomics field are struggling in researching this field as the conceptual knowledge and technology implementation are still far behind other well-developed countries especially in manufacturing side. National Institution of Occupational Safety and Health (NIOSH) had established an ergonomics department from 1992 until now and Mustafa et al. [22] research shows that only 35.6% of manufacturing industries has the high awareness of ergonomics. This statement proved that the manufacturing industries are still ongoing and the needs of the software analysis are on demand. Previously, ergonomics analysis is being done using expert evaluation and this is time-consuming and hard to be accomplished. Some manufacturing companies are very restrictive in terms of confidentiality. Outsiders or expert are not welcomed into manufacturing companies unless there are agreements such as Memorandum of Association (MOA) between industries and institutions. Hence, using software analysis is an easy way to obtain good analysis on ergonomics without having the extra additional costs for expert evaluation. This study aims to investigate the accuracy of anthropometry data in Malaysian manufacturing workers to be inserted into DELMIA software.

1.1 Anthropometry Definition

The word “anthropometry” is derived from the Greek words “Anthropos” (man) and “metron” (measure) and means the measurement of the human body [4]. Anthropometry focuses on the measurement of bodily features such as body shape and body composition (“static anthropometry”), the body’s motion and strength capabilities and use of space (“dynamic anthropometry”). Anthropometric measurements are used widely in a variety of scientific and technical fields. Within the field of ergonomics, the application of anthropometric measurements is primarily associated with different aspects of design for human use.

Anthropometry in the definition is the science of measurement and the art of application that establishes the physical geometry, mass properties, and strength capabilities of the human body [6]. From previous research and study, the measurement of anthropometry is crucial to fit the design to the user. The utilization of anthropometric data will enable designers to accommodate a desired portion of the

potential user population in their designs [25]. There is a lack of data in terms of anthropometry in Malaysia as the country has many different ethnicities [13]. Hence, the study in workers posture was inclusive with the study of anthropometry as well as to differentiate the percentile range of the measurement in the Malaysian population.

Anthropometric Data for Malaysian Population. Anthropometric data are the data referred to a group of quantifiable physical dimensions and parts of the human body [2]. There are various fields involved with the use of anthropometric data since quite a long time, then, such as forensics and physical anthropology. Nowadays, the anthropometrics data have been used within the areas of attire sizing and ergonomics workspace design instead of the others. Anthropometry of the Malaysia population database is still not available, hence, to redesign workstation in DELMIA V5R2016, the anthropometry or measurements of manikin must be inserted manually.

Several kinds of literature were presented in this paper to show the importance of incorporating anthropometric concern in designing processes. Anthropometric data on the general population is essential in ergonomics to specify the physical dimensions of workspace, equipment, furniture and clothing to fit the user and to avoid a physical mismatch between the dimensions of products and equipment and corresponding user dimensions [3]. There is a lack of anthropometric data involving major ethnic groups in Malaysia [14]. Population means the group of people that share the same ancestors, same occupations, same geographical locations or age groups. The people of different races or different ethnic groups such as different cultures, customs, language and others, is called as user population. The most important step in designing the workstation is to decide the user population. The good ergonomic design makes provision for the range of variability to be expected in the user population. Variation in user population can also affect design for safety. In many research, the ergonomist uses anthropometric measurements and try to include at least 90% of the population. To achieve this effort, designer attempt to design the workplace by including people dimension between the 5th and 95th percentiles and only one way is by providing adjustable devices.

1.2 DELMIA Software

Definition. The software Digital Enterprise Lean Manufacturing Interactive Application (DELMIA) is a virtual simulation software that was used in digital product manufacturing and one of it is aerospace [7]. The software is enabling the users to plan and test the product, systems or even the whole factory design in a virtual environment without committing the real tasks [5]. In a way, this helps industries to save costing of raw materials in early designing parts or products [5]. In this research, DELMIA V5 provides the part design, assembly, layout simulation and ergonomics analysis applications. The difference between DELMIA V5 and Computer-Aided Three-Dimensional Interactive Application (CATIA) is that it

contains simulation, application of ergonomics and it can interact manikin with the assembly layout or workstation design. In the workstation improvements of the manufacturing process, the virtual environment will be redesigned following the original workstation design and evaluate the current workstation design with the new insert population manikin to compare virtually using the Rapid Upper Limb Assessment (RULA) tool available in DELMIA V5R2016 software. In Figs. 1 and 2 show the features of the manikin and RULA analysis available in CATIA V5 and also DELMIA V5 that had been developed by Dassault Systemes company.

Fig. 1 Example of manufacturing worker's posture



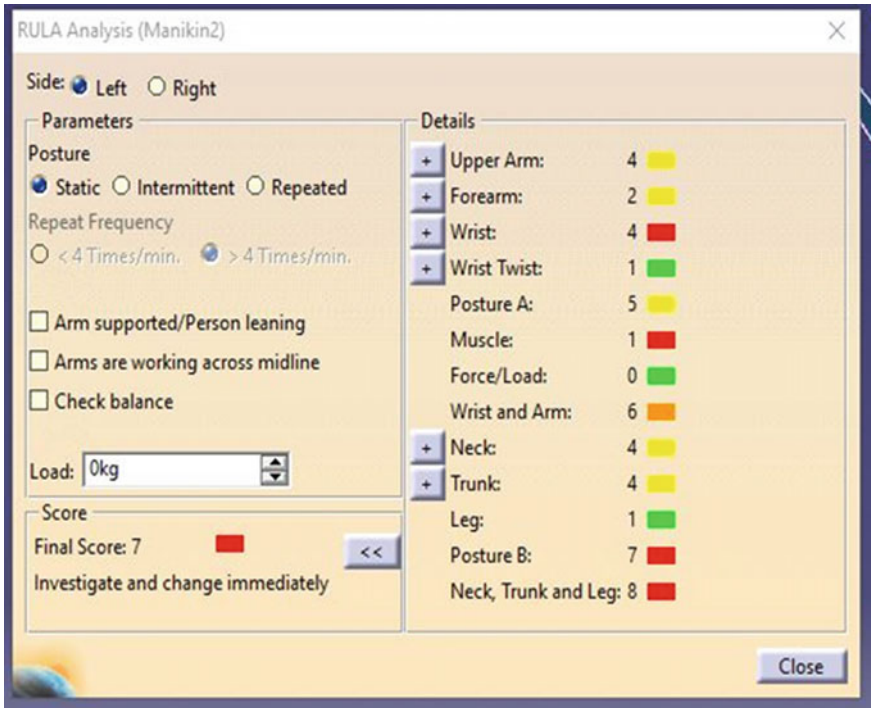


Fig. 2 RULA analysis of posture using software

2 Methodology

One of the most well-known tools for assessing anthropometric measurement is by traditional measuring method. However, the larger the sample size for the data collection, the longer the time taken in completing the task. Hence, most researchers such as Lu and Wang [18] was using 3D scanner where anthropometry measurement was done automatically. Apart from that, the limitation of automated measuring using 3D scanner was that the parameters that can be measured are only 14 parameters. This is not compatible with this study which uses 100 parameters overall.

2.1 Parameters and Sample Size

The parameters available from DELMIA V5R2016 is 103 parameters by Dassault Systemes [5], which includes bispinous breadth, tenth rib height and iliocristale height. These parameters are not available to be measured using traditional

measuring tools. Hence, only 100 parameters are selected from DELMIA V5R2016. From the parameters obtained from software, the comparison of parameters was used by selecting from literature studies. The traditional measuring method is one of the most common procedures for measuring anthropometry with a large number of parameters and sample size in order to validate the population.

In this study, a convenience sample of 241 male workers of layup process. This is the total number of workers available for hand layup process department. The sample was taken overall. Furthermore, it had been discussed by Baharmpour et al. [1] that 30–500 is adequate for this type of research (anthropometry sample), thus, 241 had fallen in the range of 30–500 samples. It is important that the required individuals to have given consent before conducting the collection as the parameters that needed to be measured were specific and required skinship to feel the location of several points. It was quite sensitive issues and measurement of the human body was quite taboo for the Malaysian culture leading to difficulties in data collections. In Malaysia, the largest number of parameter that had been done was 62 parameters done by Mohamad et al. [21], however in this study, it covers 100 parameters and the average duration to measure one sample was 45 min.

2.2 Anthropometry Measurements Tools

In Fig. 3 shows the essential measuring tools used in this study, however, the weighing scale had been changed into digital body weighing scale before the conduction of the collection for accuracy purpose. As for other tools, this study still uses the analogue tools such as large and small anthropometer set and measuring tape. This tools had been calibrated occasionally to ensure the reliability of the measurement. The tools were used for measuring the 100 parameters identified were large and small anthropometer, ruler, measuring tape, human measuring tape (for circumference measurement) and a weighing scale.

To control accuracy, the data collectors need to undergo training before collection. The measurements were carried out by the same person for this set of data to rule out the tolerance of human error in the readings. Method of measurement was studied and implemented according to standards and one of the sources is available in Tolonen et al. [26]. As in Fig. 4, shows the measuring of anthropometry takes place at the manufacturing company. To standardize the measurements units, this study used centimetres unit as the anthropometer scale unit. The measuring activities were done inside the production line; this is because to avoid messing up in the workers' time cycle. The measuring time with the addition of survey answering, took up almost 30 min for each respondent. Hence, the activities must be done near or in the line to reduce any non-value-added time for the workers.



Fig. 3 Anthropometry measuring tools

Fig. 4 Measuring the anthropometry



3 Results and Discussions

For anthropometry parameters identification, the study on literature gap was done. As for percentile calculation, the simple statistical analysis was used to calculate the percentile of the data of human population which in this case the manufacturing workers. Nonetheless, in this paper, only the standard deviation between the parameters was tabulated and discussed in order to see the mismatched between the populations of Malaysian, Japanese and American.

3.1 Literatures Gap in the Anthropometry Parameters Measured

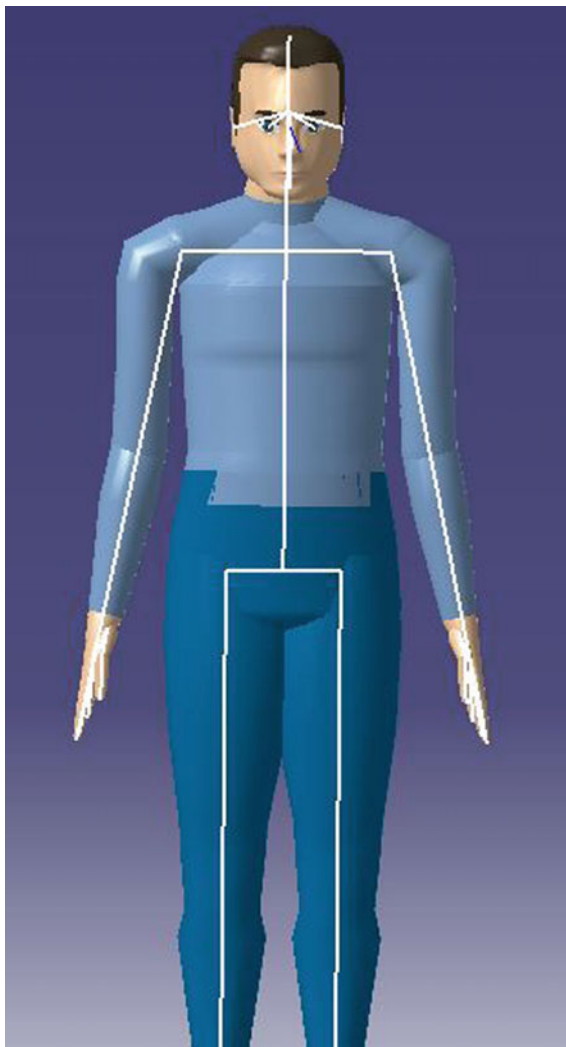
From the comprehensive literature studies, the number of parameters used in studies was different towards each other. The highest number of parameter that had been conducted by Human Systems Information Analysis Center [10]. Surprisingly, the highest number of parameters was done in the United States, not by the Asian countries. As mention in a study done by Klamkay et al. [15], the parameters taken were 39 in total however it was done using the human population of Thailand.

From Table 1, Mohamad et al. [21] had done the anthropometry measurement using the highest number of parameters which was 62 using Malaysian population sample size. This study utilized the number of parameters taken by the previous research and the study found that only small parameters measured were compatible with the range of Japanese population. Concerns were expressed as the human

Table 1 Number of anthropometry parameters based on literature studies

Author(s)	Year	Number of parameters
Lin et al. [17]	2004	33
Human Systems Information Analysis Center [10]	1994	980
Hassan et al. [9]	2015	23
Md. Dawal et al. [20]	2012	21
Karmegam et al. [13]	2011	33
Masson et al. [19]	2015	14
Kothiyal and Tettey [16]	2001	23
Karmegam et al. [14]	2011	34
Klamkay et al. [15]	2008	39
Lu and Wang [18]	2008	14
Simmons and Istook [24]	2003	25
Mohamad et al. [21]	2016	62
Dassault Systemes [5]	2016	103

Fig. 5 Human manikin distortion and unable to be analyze



manikin become distorted or unable to be used when the manual anthropometry measurement is keyed in the software as in Fig. 5.

3.2 Mismatch in Standard Deviation of Anthropometric Data

In this study, refereeing Table 2 is the standard deviation of the 100 parameters when compared with the standard deviations of the Japanese and American

population that are available in the DELMIA software. From the results obtained, it showed that when the insertion of anthropometry data for the human manikin, it is needed to select the population of Malaysia in the software. Furthermore, the unavailability of the Malaysian population, compel researchers to used Japanese or any other default population available in the software. In this study, surprisingly it is found that the data of anthropometry of Malaysian compared to other population are slightly and majorly different for each parameter as in Table 2.

Previously, research done by Hashim et al. [8], Kamat et al. [11] and Kamat et al. [12] were using CATIA V5 software which was also developed by Dassault Systemes company. In CATIA or DELMIA, the software is adequate with Ergonomics features that use manikin of human-related to analysis such as Rapid Upper Limb analysis and Postural analysis.

Nonetheless, this study found that there is a mismatch between the parameters of the anthropometry when the data was key in into the human manikin in software.

Table 2 Standard deviation, minimum and maximum value from 15 randomly selected anthropometry parameters

Anthropometry parameters	Std. Dev	Min	Max	Std. Dev	Min	Max	Std. Dev	Min	Max
	Malaysian			Japanese			American		
Bitracion breadth headboard	0.92	11.7	18.1	0.60	11.9	16.7	0.60	12.9	16.9
Bizigomatic breadth headboard	1.21	11	17.3	0.64	11.5	16.6	0.64	11.7	16.9
Calf circumference	5.16	26.5	73.8	2.24	28.2	46.1	2.54	27.7	48.0
Calf height	3.24	21.5	56.6	1.83	24.8	39.5	2.37	25.9	44.8
Chest circumference below breast	11.36	64.6	120.1	5.43	69.4	112.9	6.54	66.5	118.8
Heel ankle circumference	2.06	23.4	39	1.63	25.7	38.7	1.63	27.4	40.4
Infraorbitale to back of head	0.89	13.6	20.5	0.70	15.0	20.6	0.70	15.3	20.9
Midshoulder height, sitting	3.86	43.7	84.6	2.50	53.3	73.3	2.82	51.8	74.3
Promenton to back of head	1.38	11.1	21.8	1.03	14.5	22.7	1.03	15.3	23.5
Pronasale to top of head	1.53	12	27.6	0.84	12.7	19.4	0.84	11.8	18.6
Span	7.64	153	192	6.90	148.5	203.7	8.19	149.6	215.1
Stomion to top of head	1.23	15.5	22.4	0.78	16.1	22.3	0.78	15.5	21.8
Thumbtip reach	4.54	38.2	83.5	3.00	66.5	90.5	3.92	64.4	95.8
Waist circumference, omphalion	15.11	54.2	144	6.02	58.8	107.0	8.64	51.7	120.8
Waist depth	4.71	10.5	39.9	1.98	12.8	28.7	2.56	12.4	32.9

Prior to this study, it had been noted that the importance of having Malaysian population inside the software such as CATIA and DELMIA because the software analysis eases the ergonomics analysis that been studied here in Malaysia as the sample for the research that will be conducted in future is using Malaysian population. As stated by Mustafa et al. [22], the manufacturing that has a high awareness of ergonomics adaptation is only 35.6% overall in Malaysia. This statement proved that the manufacturing industries are still not fully adopting and integrating ergonomics into the whole manufacturing processes and portray the demand for ergonomics analysis in the future.

Percentage Error and Percentage Gap of Anthropometry Parameter for the Malaysian, Japanese and American Population. From the experimentation done by measuring the anthropometry of 241 samples, the data of percentage error and gap in between the population is calculated and tabulated in Table 3. From Table 3, it can be concluded that there are mismatches in the anthropometry parameters measurements between population. Supposedly, the percentage error data must be zero to be accepted in the human manikin range in software. An error box will rise in the software if the measurement fell over or less than the range of the minimum and maximum values. From the percentage gap between Japanese and American, all randomly selected anthropometry parameters were less than 10% of the gap, however, for two parameters (which were Span and Waist circumference, omphalion) the gap was more than 10% respectively, 10.3% and 21.0%. This also showed that in between American and Japanese population, there are mismatches in anthropometry.

Table 3 Percentage error and gap for 15 randomly selected anthropometry parameters

Anthropometry parameters	% Error			% Gap		
	M-J*	M-A*	J-A*	M-J*	M-A*	J-A*
Bitragion breadth headboard	52.8	52.8	0.0	1.6	1.6	0.0
Bizigomatic breadth headboard	89.5	89.5	0.0	1.18	1.2	0.0
Calf circumference	130.4	103.2	13.4	29.38	27.0	2.4
Calf height	76.9	36.6	29.5	20.46	16.1	4.3
Chest circumference below breast	109.2	73.7	20.4	12.06	3.2	8.9
Heel ankle circumference	26.6	26.6	0.0	2.56	2.6	0.0
Infraorbitale to back of head	27.3	27.3	0.0	1.3	1.3	0.0
Midshoulder height, sitting	54.4	36.9	12.8	20.9	18.3	2.6
Promenton to back of head	34.4	34.4	0.0	2.46	2.5	0.0
Pronasale to top of head	81.8	81.8	0.0	8.88	8.9	0.0
Span	10.8	6.7	18.7	16.2	26.5	10.3
Stomion to top of head	57.8	57.8	0.0	0.66	0.7	0.0
Thumbtip reach	51.2	15.7	30.7	21.3	13.9	7.4
Waist circumference, omphalion	151.0	74.9	43.5	41.64	20.7	21.0
Waist depth	138.0	84.1	29.3	13.56	8.9	4.6

*Where M refers to Malaysian, J refers to Japanese and A refers to American

4 Conclusion

The main goal of the current study was to investigate the accuracy of anthropometry data in Malaysian manufacturing workers. Hence, it had been proven that there is a mismatch in between parameters of the anthropometry and mismatch in the human population. Different populations contribute to different range set of anthropometries parameters. The most obvious finding to emerge from this study is that the need to have a complete database of anthropometry for Malaysian population. Apart from that, this database is mostly required in the software because of the adequacy of the software analysis, so that, the software analysis is accurate and reliable to be concluded for any result of any studies regarding ergonomics analysis. In general, to be compatible with the software, the parameters taken for the measurement must be according to the software requirements which is 103 parameters. However, there are three parameters are unable to be measured which are bispinous breadth, tenth rib height and iliocristale height. Hence, this study was covering 100 parameters of anthropometry.

Therefore, for recommendations for this study, there is in need to be in control with the measuring procedures and also the accuracy of the tools for measuring. This study recommends the use of sample size up to 500 to observe the range standard deviation of parameters is significant or not. Last but not least, there is an encouragement for the Malaysian population feature in the software that can be used for ergonomics analysis apart from Dassault Systemes software.

Acknowledgements The authors would like to thank Universiti Teknikal Malaysia Melaka (UTeM) and Ministry of Higher Education (MOHE). This project is funded by RAGS/1/2015/SG01/FKP/03/B00107.

References

1. Baharampour, S., Nazari, J., Dianat, I., Asgharijafarabadi, M.: Student's body dimensions in relation to classroom furniture. *Health Promot. Perspect.* 165–174 (2013)
2. BenAbdelkader, C., Yacoob, Y.: Statistical body height estimation from a single image. *IEEE* (2008)
3. Bridger, R.S.: *Introduction to Ergonomics*. McGraw-Hill, New York, London (1995)
4. Bridger, R.S.: *Introduction to Ergonomics*, 2nd edn. Taylor & Francis, Boca Raton (2009)
5. Dassault Systemes Homepage. www.3ds.com. Accessed 25 May 2017
6. Del Prado-Lu, J.L.: Anthropometric measurement of Filipino manufacturing workers. *Int. J. Ind. Ergon.* **1**(37), 487–503 (2007)
7. Geng, J., Chen, G., Huo, L., Zhou, D.: Application Research on Motion Capture System Data Reuse in Virtual Reality Environment. *IEEE* (2010)
8. Hashim, N., Kamat, S.R., Othman, M.S.: A study on push-pull analysis associated with awkward posture among workers in aerospace industry. In: *International Conference on Industrial Engineering and Operations Management*. Bali, Indonesia (2014)

9. Hassan, S.N., Mohd Yusuff, R., Md. Zein, R., Hussain, M.R., Tamil Selvan, H.R.: Anthropometric data of Malaysian workers. In: 10th Pan-Pacific Conference on Ergonomics. Tokyo (2015)
10. Human Systems Information Analysis Center. http://mreed.umtri.umich.edu/mreed/downloads/anthro/ansur/ADAS-Dimension_Definitions.pdf (1994). Accessed 02 Sept 2016
11. Kamat, S.R., Hashim, N., Halim, I., Othman, M.S., Ani, M.F.: Reduction of maximum effort level of lumbar muscle among workers in aerospace industry. *Malays. J. Hum. Factors Ergon.* **1**(2), 10–15 (2015)
12. Kamat, S.R., Rayme, N.S., Md. Zula, N.E.N., Shamsuddin, S., Hassan, K.: The ergonomics body posture on repetitive and heavy lifting activities of workers in aerospace manufacturing warehouse. In: IOP Conference Series: Material Science and Engineering. Kuala Lumpur, pp. 1–12 (2017)
13. Karmegam, K., Sapuan, S.M., Ismail, N., Shamsul Bahri, M.T., Shuib, S., Hanapi, M.J.: Anthropometric study among adults of different ethnicity in Malaysia. *Int. J. Phys. Sci.* **6**(4), 777–788 (2011)
14. Karmegam, K., Sapuan, S.M., Ismail, M.Y., Ismail, N., Shamsul Bahri, M.T., Mohana, G.K., Thiyagyu, P.: Anthropometry of Malaysian young adults. *J. Hum. Ergol.* **40**(1), 37–46 (2011)
15. Klankay, J., Sungkhapong, A., Yodpajit, N., Patterson, P.E.: Anthropometry of the southern Thai population. *Int. J. Ind. Ergon.* **38**(1), 111–118 (2008)
16. Kothiyal, K., Tettey, S.: Anthropometry for design for the elderly. *Int. J. Occup. Saf. Ergon.* **7**(1), 15–34 (2001)
17. Lin, Y.C., Wang, M.J.J., Wang, E.M.: The comparisons of anthropometric characteristics among four peoples in East Asia. *Appl. Ergon.* **35**(2), 173–178 (2004)
18. Lu, J.M., Wang, M.-J.J.: Automated anthropometric data collection using 3D whole body scanners. *Expert Syst. Appl.* **35**(1), 407–414 (2008)
19. Masson, A.E., Hignett, S., Gyi, D.E.: Anthropometric study to understand body size and shape for plus size people at work. *Procedia Manuf.* **3**, 5647–5654 (2015)
20. Md. Dawal, S.Z., Zadry, H.R., Syed Azmi, S.N., Rohim, S.R., Sartika, S.J.: Anthropometric database for the learning environment of high school and university student. *Int. J. Occup. Saf. Ergon.* **18**(4), 461–472 (2012)
21. Mohamad, D., Md Deros, B., Daruis, D.D.I., Ramli, N., Sukadarin, E.H.: Comfortable driver's car seat dimensions based on Malaysian anthropometrics data. *Iran. J. Public Health* **45**(1), 106–113 (2016)
22. Mustafa, S.A., Kamaruddin, S., Othman, Z., Mokhtar, M.: Ergonomics awareness and identifying frequently used ergonomics programs in manufacturing industries using quality function deployment. *Am. J. Sci. Res.* **3**(1), 51–66 (2009)
23. New Straits Times: Occupational safety: ergonomics cuts down injuries at workplace. <http://www.dosh.gov.my/index.php/en/archive-news/2012-archive-news/677-occupational-safety-ergonomics-cuts-down-injuries-at-workplace> (2012). Accessed 25 May 2017
24. Simmons, K.P., Istook, C.L.: Body measurement techniques applications. *J. Fashion Mark. Manag.: Int. J.* **7**(3), 306–332 (1996)
25. Tayyari, F., Smith, J.L.: Occupational ergonomics: principles and applications. In: Weight, Height and Selected Body Dimensions of Adults, pp. 41–60. Kluwer Academics Publications, London (2000)
26. Tolonen, H., Kuulasma, K., Laatikainen, T., Wolf, H.: European Health Risk Monitoring (EHRM), http://www.thl.fi/publications/ehrm/product2/part_iii5.html. Accessed 01 Sept 2016

Development Tools of an Adaptive Controller



Muhammad Azri Othman, Mohamad Minhat, Zamberi Jamaludin and Ahamad Zaki Mohamed Noor

Abstract Manufacturing enterprise today crucially needs computer numerical control (CNC) to employ higher level input languages and reducing dependency on proprietary system. In traditional CNC system, most predefined numerical control (NC) commands programmed at early stage were often found to be unsuitable or sometimes unusable especially when the machining process was interrupted by unscheduled event. This will result in additional effort spent for advance process planning and NC code generation. Moreover, readjustment of the program consumes time and requires high skills. To address this issue, considerable efforts are being undertaken to improve CNC system by replacing traditional CNC to a next generation of intelligent CNC. This paper proposes a framework for adaptive controller of an open CNC system by merging established STEP-NC and IEC 61499 standards. This project applies STEP-NC as data input program; taking advantages offered by both standards. IEC 61499 is a layered architecture function that simplifies controller design and enhances the controller performance. As a result, both decision making and control activities are embedded inside the controller architecture whereby optimal machining parameters are issued automatically based on available online machine resources. Hence, a tool-path will be generated just-in-time by the CNC controller. The generated tool path can be directly used to drive the open architecture machine tool without any intermediate.

Keywords STEP-NC · Adaptive controller · Function Block

M. A. Othman · M. Minhat (✉) · Z. Jamaludin · A. Z. Mohamed Noor
Faculty of Manufacturing Engineering, Universiti Teknikal Malaysia Melaka,
Hang Tuah Jaya, 76100 Durian Tunggal, Melaka, Malaysia
e-mail: mohdm@utem.edu.my

© Springer Nature Singapore Pte Ltd. 2018
M. H. A. Hassan (ed.), *Intelligent Manufacturing & Mechatronics*,
Lecture Notes in Mechanical Engineering,
https://doi.org/10.1007/978-981-10-8788-2_4

1 Introduction

Computer Numerical Control (CNC) machining systems have been proved to be economical across various types of production; including mass or flow production, batch production and one-off production. Today, numerous CNC machine brands with multiple capabilities are widely used in manufacturing industry to meet the quality requirement and customer demands. Embedded with multiple capabilities and functionalities, CNCs give the shop floor some alternatives in respect of flexibility. However, in the face of today’s fluctuating shop floor environments, flexibility and interoperability of current CNC system to respond dynamically and adaptively are believed to be inadequate [1–3]. In most situations, the CNC systems are not able to handle unforeseen changes efficiently and effectively. The impediment of existing technologies is illustrated in Fig. 1.

CNC machine tool as a termination mechanism converts inputs into semi-finished or finished outputs based on customer requirements. The way that CNC machines are being programmed remains almost unchanged over the years. Traditionally, machining operations are executed based on predefined NC program that is generated beforehand. This program is mostly rigid in such a way that modifications on any cutting conditions and machining sequences during machining operations are nearly impossible. Simply said, CNC machines are ‘blind slave’ that only followed the input program without fail. In the absent of intelligence element, CNCs disregard whether the program led to inappropriate machine movements, which may result in low productivity or low-quality product.

In the progressive development of next generation CNCs, existing CNC systems still utilising outdated ISO 6983 (also called G&M code) as interface language have

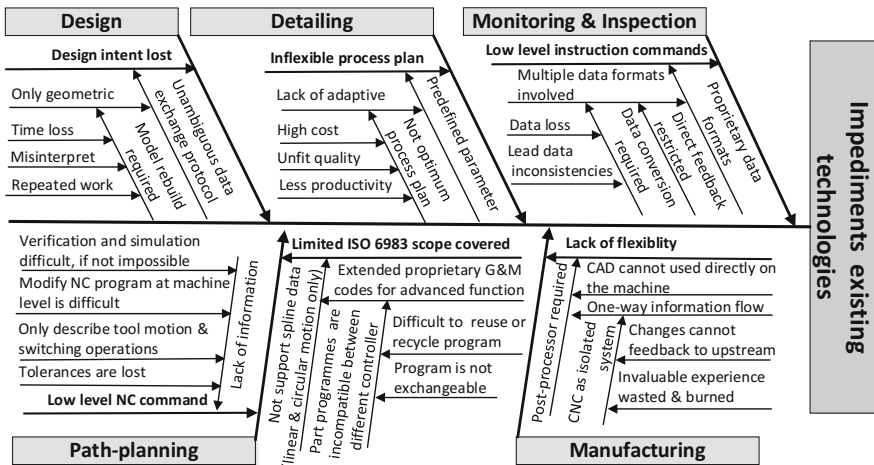


Fig. 1 Key issues in limiting existing technology to create more adaptable and interoperable CNC system

become major issue and must be faced out [4]. G&M code is a collection of low-level codes and has large number of limitations such as delivering limited information to CNC, unsupported bi-directional data flow and vendor dependency. Due to the limited scope of G&M-code, most CNC vendors have extended the ISO 6983 through creation of their own proprietary G&M code dialects. Extended version of G&M code was used to support development of new advanced CNC functions. Consequently, it was realized that interoperability and reusability among the systems become more difficult, if not impossible. These proprietary dialects are not compatible with each other, making it difficult to reuse the program. Thus, the same data must be key-in several times into several systems since every system has its own dialects. This non value added activities have led to redundancy and possible errors [5].

To date, many researchers have reported different approaches to enhance capabilities of CNC controller system toward intelligence or smart machine system. In this paper, a new framework of a novel structure of adaptive controller based on STEP-NC/Function Block technology is proposed. Basically, this research works utilizes advantages of both technologies by bringing high level information into CNC level and layered controller architecture in creating a new breed of intelligent controller that offers new possibilities of adaptive control strategies. With the proposed structure, decision making and control abilities are both embedded inside the controller architecture. A new algorithm will be developed to generate automatically optimal machining parameter at machine tool level based on available online machine resources.

2 Machine Tools Evolution

Machine tools are core apparatus of industrialization. Evolution of machine tools is a continuous and everlasting innovation process. The outcome was the new era of production methods that replaced tedious, hard, repetitive jobs with autonomous and intelligent machine tools in metalworking processes.

2.1 Machine Tools Transition Epoch (1700s–1940s)

The histories of machine tools development were started in the late 1700s up to 1940s, where first industrial revolutionary transformation occurred in the metalworking industry with the conversion from hard production method to machine assisted production method. Most of the machine tool available at this time was manually operated with some form of human assistance and highly depending with the human expertise's and experiences to operates [6].

2.2 Automatization Machine Tools Epoch (1945–1980)

In the 1950s, numerical control (NC) machine tools technology was developed and introduced in metalworking industry. NC is defined as a method of controlling the motions of machine components and other auxiliary functions by directly inserting coded instruction in the form of series alpha-numerical characters into an electronic control system [7]. At this period, machine tools motion actuation and control gradually shifted from mechanical to electronic actuators and was called “Hard-wire NC”. In this system, electrical wiring was used to connect the elements for performing NC functions. In 1960s, machine automation faced significant development with the introduction of direct numerical control (DNC) concept. DNC system permits the programmers to directly send NC program files from central control system to the machine unit [8]. Employment of NC machine tools bring multiple advantages such as reduced manpower, machining time, part rejected and improve product quality.

2.3 High Speed, Adaptive and Flexible Machine Tools Epoch (1980–Present)

Computer numerical control (CNC) was introduced as advanced version of NC machine in the 1970s. The advancement of computer technology was used in assisting NC machines, where most punch cards and electronic hardware were replaced by computers. In CNC technology, the machine control unit (MCU) is a microcomputer that uses to stores machining programs, parse each commands code and execute the sequential controls of machine operation, one command at a time. Typically, the data-processing unit (DPU) and the control-loops unit (CLU) are two main components inside MCU [6]. The function of DPU is to process the command coded data and then deliver the instruction with the required information such as each axis position, motion direction, machining parameters and auxiliary function control signals to the CLU. Whereas, the CLU activates the drive mechanisms of the CNC machine and obtains feedback signals regarding the exact position and speed of each machine axis [6].

Emerging CNC machines enable effective utilization of machine tools towards more automatic and more flexible machining system. Due to their capability to reprogram for a different part in single machine tool, CNC machines have become critical manufacturing resources. The advancement of computer technology together with development of information and communication technology (ICT) infrastructure brought a great improvement to CNC machine capabilities. Today, CNC machine was embedded with the multiple abilities such as multi-axis, multi-tool, and multi-processes manufacture to fulfill customer demands [9].

However, CNC languages still pose an issue at hand that is not fully solved towards development of more intelligent and smart CNC system. Unstable

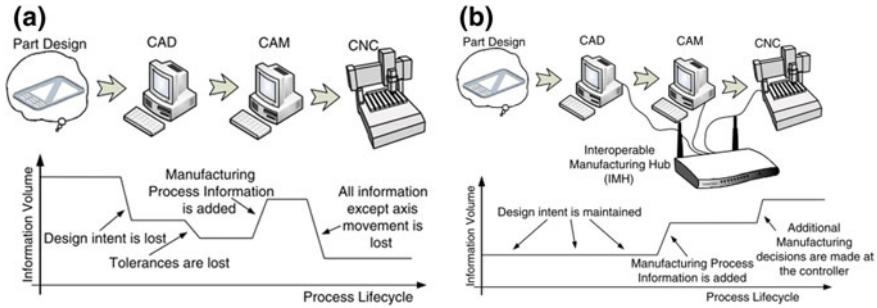


Fig. 2 Information dealt with in current CNC (a) and next-generation CNC (b) [6]

information volume and information lost at each stage of process has become barrier to development of more robust, intelligent, and smart CNC system. Figure 2 presents scenarios of information for current CNC system and next generation of CNC systems.

2.4 Smart and Intelligent Machine Tools Epoch (Next Generation Machine Tools)

Revolutionary shift in paradigm is not easy to be implemented on traditional CNC system when most CNC machines are still predominantly use outdated G&M codes as machine control language. Stringent quality requirements and customer demands are the core behind the development of next generation machine tool that are more intelligent, adaptable and interoperable [10]. In previous developments, tremendous efforts were placed by researchers to create machine tools that are faster, more accurate, more reliable, and safer. Today, the concept of sustainable, economical, resource efficient and multiple function machine tools has sparked interest in researchers and industrial communities. It has encouraged energetic research into supportive areas that are proving very beneficial to existing machine tools. e.g., process planning, jigs and fixturing.

The requirements and the characteristics of next generation of CNC have been described by many authors. Some most commonly accepted characteristics and issues are associated with intelligence and versatility of the system. New CNC machine tools system that are smarter, well connected, widely accessible, more adaptive and more autonomous need to be developed in response to the needs of modern manufacturing challenges and demands [6]. To facilitate such characteristics, CNC system should be designed to have:

- (i) seamless vertically integrated between machine tools and CAx chain by using high level programming language.

- (ii) ability to generate machining parameter and tool path automatically at machine level.
- (iii) ability to react adaptively and automatically in real time for maintain a desired performance.
- (iv) open architecture with software-based modular structure as an implementation technology.

3 STEP-NC and IEC 61499 as Enabler Technology

STEP-NC and function block as two enabler technology for creating interoperable CNC machining system has been discussed in depth by Xu and their co-researcher in [11]. Merging of these two standards believed will bring more beneficial features for next generation CNC machining system. Comprehensive data model provided by STEP-NC combined with distributed control architecture by IEC61499 FBs will enabled extra and autonomy from system to adapts any unscheduled changes without sacrificed their manufacturing objectives.

3.1 STEP-NC: High-Level Data Interface

Since 2002, a new standard called ISO 14649, also recognised as STEP-NC was being developed thru intelligent manufacturing project that involves European Union, Korea, Switzerland and USA [4, 11]. This project objectives to provide a data model for a new breed of intelligent CNCs system. By provides a high level and standardized data model between CAx and CNC systems and is considered as the next generation of CNC programming languages. Commonly, STEP-NC is being developed by the international community with the motivation to formalise the data model interface used at CNC machine level and remedies the shortcoming of the outdated ISO 6983 standard, which yet still dominates the control system of the most existing CNC machines.

Unlike the current standard, STEP-NC does not defines the cutting tool movements as ISO 6983 does, but it treated high level object-oriented information and standardized information such as feature geometry, cutting tool description, operation attributes and work plan from design to CNC system [12]. Though it is possible to develop a new breed of intelligent controller NC controller that have capability to act more intelligently than ever before and with the abilities of decision making as well as control of the machine tool. This can be achieved through STEP-NC by providing generic file as a controller input and the machine-specific decisions to be made at a final stage by a CNC and its controller. As a result, part programs may be written once and reused on multiple CNC machine tool controller [4]. Besides that, STEP-NC also include a data model for inspection, simulation and

optimisation in real time CNC system environment. Implementation of STEP-NC programming approaches will provides new possibilities for adaptive force control and decision making process is migrated from CAM to CNC [12]. As a result, CNC controller now functional as a central element between design and manufacturing chain system.

3.2 IEC 61499 Function Block

IEC 61499 is extends the programmable Function Blocks (FBs) notion from the IEC 61131-3 standard based on an explicit event-driven model. Each FB is functional as a software unit that encapsulates algorithms which can be designed to behave in a similar way as an electronic device or a circuit and this function block can represent a small task in a control plan or can be encapsulate with multiple control unit [5]. The execution of an individual FB in the network is triggered by the event it received, if not, FB will keep remaining in idle condition for the rest of time. There are three standard classes of function blocks defined in IEC 61499:

- (i) Basic function blocks (BFBs): Explicit event-triggered component containing algorithms and has an execution control chart (ECC), together with input and output data set variables.
- (ii) Composite function blocks (CFBs): Encapsulate a network of multiple blocks (combined both basic and composite). It is interconnected by external data sources and the functionality is determined by network of FBs inside.
- (iii) Service interface function blocks (SIFBs); used to provide complete communication interface with its surrounding environment of a FB network.

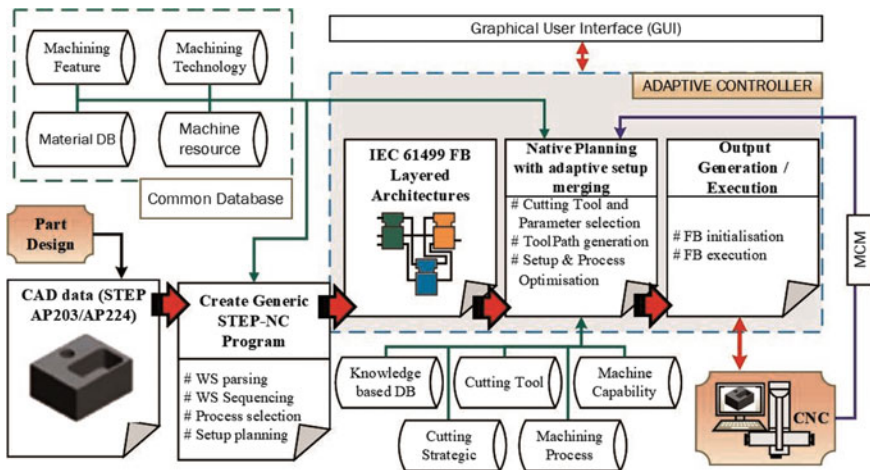


Fig. 3 Proposed adaptive machining systems

In general, all FB types provide an interface that has been represented as “head” and “body” in the block. Head located at upper part listed all the event inputs and outputs for function block. While, data inputs and outputs are connected to the body at lower part of block.

4 Overview on Development of Next-Generation CNC Controller

Open architecture control (OAC) technology is one of the key element on creating next generation CNC to become more flexible and openness system. The OAC offers more beneficial advantages such as interoperability, interchangeability, scalability, portability, etcetera to CNC system [13]. The aims of OAC is to developed CNC system that was independent from any manufactures technology. With OAC, user enable to freely assemble and integrate any software and hardware from different manufacturers. Nowadays, OAC is core of modern controller technology. One of famous research work in OAC field is the development of PC based open controllers that can provide high flexibility and quality at low cost [14, 15]. Major researches on open architecture CNC were carried out in many nations and research organizations, such as open modular architecture controller (OMAC) in USA, open system architecture for control within automation system (OSACA) in Europe and open system environment for controller (OSEC) in Japan.

The introduction of OAC increases the possibility of STEP-NC implementation. Most of the existing STEP-NC controllers have been reviewed by [12, 16–18]. STEP-NC as a new language, it is required to have a new breed of CNC controllers that capable to carrying out various intelligent tasks using this new language as an input. At the research front, multiple efforts are being made not only just to expand CNC automation and flexibility capabilities of the machine tool but also to embed intelligence and reconfigurable functionality into the machine. There are various different approaches were introduced by various scholars based on STEP-NC implementation on CNC system, those approaches can be classified into several level of implementation as follow; Indirect STEP-NC programming (Level 1), Interpreted STEP-NC programming (Level 2), Adaptive STEP-NC programming (Level 3) and Collaborative STEP-NC enabled machining (Level 4). All the approaches that had been carried out by various researchers within the implementation level has discussed by Othman et al. in [18]. His and their co-workers conclude that the development of adaptive STEP-NC programming controller still have not completed. There still have a room and research work need to be done to achieve that aims.

Merging STEP-NC and IEC 61499 FBs technology in machine tool advancement research work is not a new approach. In 2007, Wang et al. in [19] introduced a adaptable CNC system to addresses an issue of feeding STEP-NC data to existing CNC controllers. This prototype system reads data from STEP-NC file and translate

them into machine specific G&M code via FB mapping system. The main advantage of this system is do not need to modify the configuration of the existing CNC machines. Two years later, Minhat and their co-researchers has demonstrated an open layered STEP-NC/FBs architecture controller to simplifying the design of CNC machine controllers [5]. This prototype is no longer required G&M code, STEP-NC programming is totally interpreted by controller for machine execution.

Combined STEP-NC with IEC 61499 FBs provides great opportunity for CNC system to have characteristic such as intelligent, portability, interoperability, flexibility, configurability, and openness. Applying FB to the control of CNC machines means giving them extra intelligence and autonomy to better handle and adapts to changes, for a more successful fulfillment of their manufacturing objectives. However, without using real time information, both of developed controller discussed previously are still lack of flexibility and adaptability functionality when dealing with uncertainty and unpredictable events. Therefore, an advanced STEP-NC/FBs controller CNC system design framework is urgently required to cater the problems discussed in previous. The proposed adaptive controller framework is discussed in next section.

5 Adaptive Controller Framework

The proposed adaptive machining control system model aims at developing the next generation of CNC using STEP-NC as a data model interface (Fig. 3). In this research, STEP-NC is used to provide high level information to the CNC and the IEC61499 function block serves as the controller architecture. As STEP-NC is a passive data model that does contain any intelligent functionality, employment of IEC61499 function block will provides intelligent function onto it. This research focuses on developing adaptive DPU system using FBs for open architecture CNC controller.

For increasing the flexibility and interoperability of the proposed system, instead use of native NC program, CNC controller will only be providing with generic information only. Then, based on online manufacturing resource available, native program will automatically generated including machining parameter and tool path. It starts with the activity where generic STEP-NC is converted to IEC61499 FB structure. Once machine resource is connected to the system, optimization module will trigger and run analysis based on machinability and performance criteria to generate optimal machining parameter. When the calculation is completed, the optimal parameter will be sent to online process planning to create native CNC program automatically. Finally, the tool path generation module interprets that native program to generate machining tool path. Without use of any intermediate file, the generated tool-path can be directly used to drive the machine tools without any intermediate file.

The outcome of this research was a plug and play software based controller called adapSTEP-NC/FB controller. This controller has capability to interpreter

generic STEP-NC (Part 21) program files as data input and able to automatically generates machining tool-path and optimal parameter such as spindle speed and federate based on the online machine resources availability. The benefits of this structure are the execution of a same STEP-NC file on different machine structures that will able to provides different optimal feed rates, spindle speeds, and tool paths. This structure allows the controller to have more capable mechanism, where decision making and control strategic done inside controller level. For easy and user-friendly purpose, the controller will supported with GUI interface to monitoring the process and communicate with user.

6 Conclusion

Dynamic changes in machining environment have created the needs for CNC system with online optimisation and real-time control of machining operations. Use of STEP-NC data model brings comprehensive and high-levels information into the CNC machine levels, allowing CNC controller to perform intelligent control mechanism such as generation and optimization of machining parameters and tool paths. This paper proposed a framework for adaptive controller of an open CNC system by merging established STEP-NC and IEC 61499 standards utilizing advantages offered by both standards. STEP-NC is proposed as the data input program while IEC 61499 is the layered architecture function to simplify the controller design and enhance the controller performance. With the proposed structure, both decision making and control activities are embedded inside the controller architecture. In this system optimal machining parameters will be issued automatically based on available online machine resources. Hence, tool-path will be generated just-in-time within CNC controller. The generated tool path can be directly used to drive the open architecture machine tool without any intermediate.

References

1. Xiao, W., Zheng, L., Huan, J., Lei, P.: A complete CAD/CAM/CNC solution for STEP-compliant manufacturing. *Robot. Comput. Integr. Manuf.* **31**, 1–10 (2015)
2. Xu, X.: A concerted endeavour toward intelligent machining solutions. *Int. J. Mater. Prod. Technol.* **48**, 23–26 (2014)
3. Zinhat, Y., Bai, X.L.: Architecture for a novel STEP-NC-compliant CNC system. *Appl. Mech. Mater.* **681**, 110–114 (2014)
4. Xu, X.W., Newman, S.T.: Making CNC machine tools more open, interoperable and intelligent—a review of the technologies. *Comput. Ind.* **57**(2), 141–152 (2006)
5. Minhat, M., Vyatkin, V., Xu, X., Wong, S., Al-Bayaa, Z.: A novel open CNC architecture based on STEP-NC data model and IEC 61499 function blocks. *Robot. Comput. Integr. Manuf.* **25**(3), 560–569 (2009)
6. Xu, X.: Machine Tool 4.0 for the new era of manufacturing. *Int. J. Adv. Manuf. Technol.* **92** (5), 1893–1900 (2017)

7. Kalpakjian, S., Schmid, S.R.: *Manufacturing Engineering and Technology*, 6th edn. Prentice Hall, Singapore (2010)
8. Ramesh, R., Jyothirmai, S., Lavanya, K.: Intelligent automation of design and manufacturing in machine tools using an open architecture motion controller. *J. Manuf. Syst.* **32**(1), 248–259 (2013)
9. Rosso, R.S.U., Allen, R.D., Newman, S.T.: Future issues for CAD/CAM and intelligent manufacture. In: *The 19th International Manufacturing Conference* (2002)
10. Ridwan, F., Xu, X.: Advanced CNC system with in-process feed-rate optimisation. *Robot. Comput. Integr. Manuf.* **29**(3), 12–20 (2013)
11. Xu, X.W., Wang, L., Rong, Y.: STEP-NC and function blocks for interoperable manufacturing. *IEEE Trans. Autom. Sci. Eng.* **3**(3), 297–308 (2006)
12. Rauch, M., Laguionie, R., Hascoet, J.Y., Suh, S.H.: An advanced STEP-NC controller for intelligent machining processes. *Robot. Comput. Integr. Manuf.* **28**(3), 375–384 (2012)
13. Pritschow, G., Altintas, Y., Jovane, F., Koren, Y., Mitsuishi, M., Takata, S., van Brussel, H., Weck, M., Yamazaki, K.: Open controller architecture—past, present and future. *CIRP Ann.—Manuf. Technol.* **50**(2), 463–470 (2001)
14. Cha, J.-M., Suh, S.-H., Hascoet, J.-Y., Stroud, I.: A roadmap for implementing new manufacturing technology based on STEP-NC. *J. Intell. Manuf.* **27**(5), 959–973 (2016)
15. Ma, X., Han, Z., Wang, Y., Fu, H.: Development of a PC-based open architecture software-CNC system. *Chin. J. Aeronaut.* **20**(3), 272–281 (2007)
16. Xu, X.W., Wang, H., Mao, J., Newman, S.T., Kramer, T.R., Proctor, F.M., Michaloski, J.L.: STEP-compliant NC research: the search for intelligent CAD/CAPP/CAM/CNC integration. *Int. J. Prod. Res.* **43**(17), 3703–3743 (2005)
17. Hu, P., Han, Z., Fu, H., Han, D.: Architecture and implementation of closed-loop machining system based on open STEP-NC controller. *Int. J. Adv. Manuf. Technol.* **83**(5), 1361–1375 (2016)
18. Othman, M.A., Minhat, M., Jamaludin, Z.: An overview on STEP-NC compliant controller development, *IOP Conference Series: Materials Science and Engineering* 257, IOP Publishing, (2017)
19. Wang, H., Xu, X., Des Tedford, J.: An adaptable CNC system based on STEP-NC and function blocks. *Int. J. Prod. Res.* **45**(17), 3809–3829 (2007)

Innovative Method of Measuring Electrode Wear During EDM Drilling Process Using Vision System



Zamzuri Hamedon, I. Razemi, A. R. Abdul Manaf
and Nafrizuan Mat Yahya

Abstract The aim of this project is to develop a fully automated electrode wear detection system in EDM by using machine vision system and apply this system in detecting electrode wear in EDM drilling. Machine vision system was image-based technology used to perform automatic inspection and analysis of the electrode wear for EDM drilling. The high resolution's DSLR camera as monitoring device to capture the image. The brass electrode with the diameter of 3 mm undergo hole making process with a depth of 10, 20, 30, 40, and 50 mm to obtain the level of wear. The images of the electrodes were remotely captured using DSLR camera then read from the laptop and undergo image processing process using Matlab software to calculate and determine the electrode wear. The result showed the wear percentage of the electrode is 4.235% for 10–30 mm in depth and 3.59% for depth of 30–50 mm. This project showed that the developed system was suitable and applicable in monitor an EDM electrode super drill machine.

Keywords Electrode wear · Vision system · DSLR · EDM · Power drill

1 Introduction

Rapid advancements in the image-processing method and machine vision systems have empowered direct electrode wear estimation to be proficient in the field of EDM [9]. Kaneko et al. [5] presented an optical measurement of the electrode

Z. Hamedon (✉) · I. Razemi · A. R. Abdul Manaf · N. M. Yahya
Faculty of Manufacturing Engineering, Universiti Malaysia Pahang,
26600 Pekan, Pahang, Malaysia
e-mail: Zamzuri@ump.edu.my

I. Razemi
e-mail: Nuriqbalrazemi@gmail.com

A. R. Abdul Manaf
e-mail: Arosli@ump.edu.my

N. M. Yahya
e-mail: nafrizuanmy@ump.edu.my

deformation by using a charge-coupled device (CCD) sensor which shortened the time interval of the machining interference from a few minutes to several seconds without reducing the accuracy of the measurement. Guo et al. [2] developed an online electrode measurement module based on a CCD vision system to fabricate microelectrodes. The diameter of the electrode with a relative measurement error of 3% was achieved by the machine vision system when comparing the measured result using a scanning electron microscope.

A standout amongst the most critical component in equipment design is light. Determination of a fitting light source is subject to the interrupt separations needed, lighting amount and also ecological concerns included [7]. As for tool wear monitoring, the primary necessity of the system is to give sufficient complexity between electrode eroded region and the background. Intensity and angle of the light source ought to be acclimated to complement the device for better quality results. The illumination sources that are generally utilized for instrument condition checking are glowing lights and lasers. Notwithstanding the choice of an appropriate source of illumination, are likewise thought tend to the system which can give the best results. Hamedon et al. [3] embedded small CCD camera inside die to observe the deformation of the die with the help of LED light for clarity.

There are two types of video cameras used to monitor tool condition. One's used vidicon cameras that include a light-sensitive surface present within a thermionic vacuum tube. Once an electromagnetic wave scans this surface, analogue voltage proportional to the scene brightness (at that time within the image) is created. However these cameras suffer from geometric distortions and image drift. The emergence of price effective and improved solid state technology over the past decade, has created CCD sensors pronto accessible for numerous machine vision applications. The fundamental structure of the CCD is that of an analogue register consisting of a series of closely spaced capacitors. Typical sensors supply a pixel resolution of 768×493 with imaging rates of 30 images/set. In order to obtain a high-resolution cameras with sensing element sizes up to 2048×2048 pixels, it must come with lower temporal resolution and high price. However the lower the temporal resolution, the higher the spatial resolution is. High speed camera, with imaging rates of up to 1000 images/set, are restricted by a reduced spatial resolution and high price. The CCD cameras have a typical C-mount, which is compatible with a broad type of lenses.

An infinitely variable value (analogue signal) will be converted by image digitization to an integer from 1 to N, where N represent level of Gray scale identified by the system. Broad range of frame grabbers available for the A/D conversion of a standard video signal. A few of latest frame grabbers are implemented with real time of low level image preprocessing.

According to [1] there are advantages in using machine vision in TCM method. Firstly, this technique is relatively a low-cost system. Next, it is a flexible technique as it can be easily setup and mobile. It can also be assembled and dissembled at ease and controlled using remote system. CNC machine tools latest trend is to be influenced by operator, who does not seem to be totally equipped with the mix of coaching and skill necessary to measure a tool's wear. A talented machinist can pay shut attention to cutlery performance significantly once a brand new combination of

tool, material and half of program parameters by trial and error method. The trend approaching unsupervised machining centres equipped with open design controllers has modified the manufacturing surroundings considerably. With the machining conditions ever-changing significantly, the pre-planned tool replacement methods are not any longer suitable [6]. This demonstrate how critical is automatic monitoring system as it can spare the machining time furthermore the expense of manufacturing. Although machine vision features a vital and a lot of accuracy in monitoring tool condition, the method has its own disadvantages. This method inability to provide real dimension of the tool mensuration (i.e. length, width, volume), solely limited info of wear is provided [8]. Although tool breakage is typically related to a modification within the tool shadow, the utilization of model matching of the tool before and after cutting to see breakage would require massive computer storage space and high C.P.U. time, therefore makes the technique computationally preventative. Moreover, an accurate matching of the templates will rely upon the tool and camera individual positions remaining constant in each monitoring. Third, they did not utilize the flexibleness of the computer vision system by not investigating the utilization of different wear land features (e.g. length, width, perimeter and area of the wear region) as attainable indicators of wear severity. Besides that, this method is time-consuming because the tool has to be compelled to stop its operation for tool observation [4]. Hence this research was done to develop a system of an automated tool condition monitoring using machine vision system to detect electrode wear in EDM drilling.

2 Experimental Setup

The machine used was Joemars JM528D EDM super drill machine as shown in Fig. 1. In this project, machine vision system was introduced on this machine to monitor and obtain data of the electrode wear. This machine is used to drill hard materials using brass electrode with the diameter of 3 mm and the workpiece is Pre-harden steel.

The general setup for the devices for experiment are shown in Fig. 2. The camera with the support of the tripod was placed in front of the machine and link to the laptop for data acquisition were. The laptop and the camera are connected through USB cable where the camera will be remotely controlled from the laptop to capture images of the electrode. Green paper was placed at the back of the workpiece for Chroma keying effect. Machining parameters were fixed and set as shown in Table 1.

A camera used for the monitoring system is Canon EOS 600D with specifications as presented in Table 2. Since the diameter of the electrode was small ($\text{Ø}3.0$ mm), a regular lens cannot focus on the electrode to captured a detail image of the wear on the electrode. To solve this, an extension tube was be added to lens mounting which turns the lens into macro lens and this will magnify the image of the wear as the focus of the lens towards electrode become closer. The distance

Fig. 1 EDM super drill machine



between lens to electrode is fix at 500 mm. While the main software used was Matlab version R 2015a with image processing toolbox inclusive of a set of algorithms, functions and apps for image processing which supports wide range image types. Through this toolbox, image processing such as image analysis and enhancement could be done to analyze the wear of the electrode form the image captured from the camera.

The electrodes used was brass material and workpiece was AISI P20 pre-hardened steel. For the purposed of measuring the wear of the electrode. EDM drilling operations were incidentally intruded, and the electrode will be pulled up to a fixed position where the machine vision system worked legitimately for direct sensing. The processing flow of the work in measuring the electrode wear is illustrated in Fig. 3.

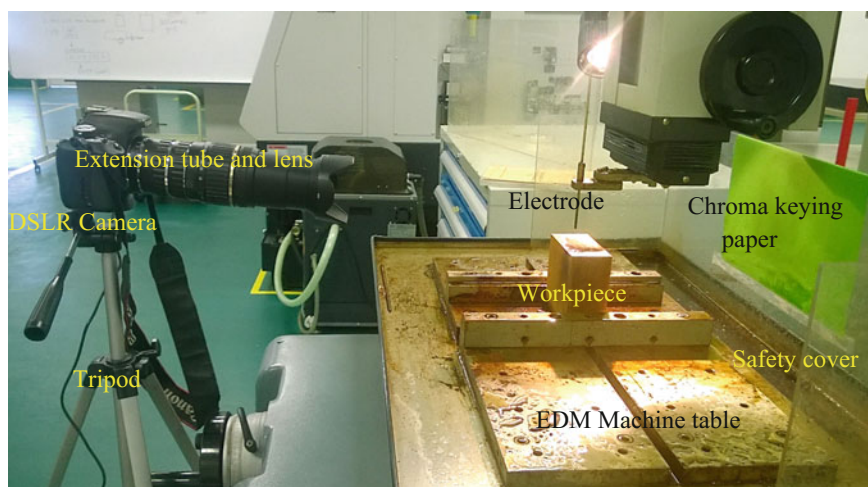


Fig. 2 Experimental setup for obtaining the wear of electrode

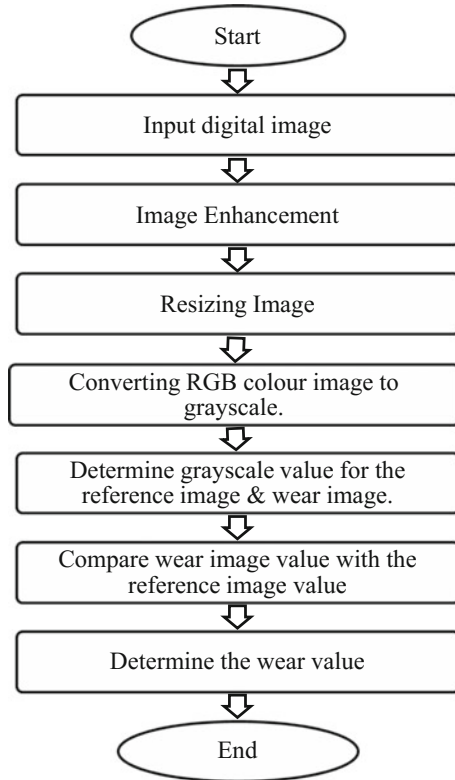
Table 1 Fig. 2. Machining parameters

Parameters	Values
Electrode diameter (mm)	3.0
Current (A)	8
On-time (μ s)	18
Off-time (μ s)	4
Gap	2
Duty factor (%)	10–90
Servo rate (mm/s)	2.5
Water pressure (kg/cm^2)	30
Spindle speed (rpm)	100
Dielectric fluid	Distilled water

Table 2 Specifications of Canon EOS 600D

Parameter	Dimension
Dimension/Weight	133.1 \times 99.5 \times 79.7 mm/570 g
Image sensor	CMOS
Effective pixel/Effective sensor size	18.0 Mp/22.3 \times 14.9 mm
ISO range	100–6400, expandable to ISO 12,800
Autofocus	9 point (1 cross-type)
Shutter speed	1/4000–30 s, bulb
Max. Burst rate	3.7 fps
Max. Image resolution	5184 \times 3456 pixel
Max. Video resolution	1920 \times 1080 @ 24/25/30 fps
A/V Output/USB connection	HDMI/USB 2.0

Fig. 3 Image processing flow chart

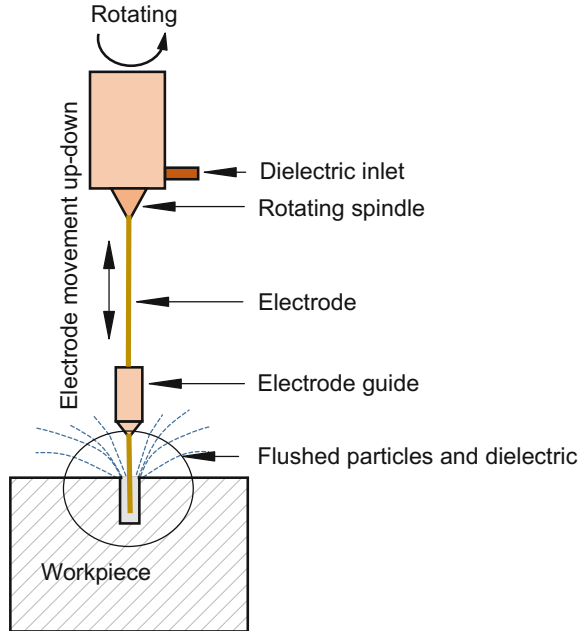


3 Result and Discussion

The process consists of using a precision tubular tool electrode (copper) mounted into the drill chuck located on the “Z” axis and located on top of the workpiece by the ceramic guide. The top of the workpiece was located and the drilling depth was set. The electrode rotation is turned on and the deionized water solution, which is pressurized between 50 and 100 kg/cm², flushed through the tube to remove machining debris.

The power supply parameters are set-which commonly consist of on-time, off-time, peak current and amount of capacitance. At this time, the discharge is turned on to start the drilling cycle. At the top of the drilling cycle, the discharge is turned off and therefore the “Z” axis is retracted on top of the workpiece. NC system allowed large numbers of holes to be precisely located. Figure 4 shown the process of EDM.

Fig. 4 EDM drilling



EDM drilling operations were incidentally intruded and the hole making process was interrupted for a while and the electrode will be pulled up to a fixed position where the machine vision system worked legitimately for direct sensing. For data collections, 3 workpieces were used for each experiment. The images of the wear electrodes were capture, to the laptop for image processing.

Figures 5, 6, 7 and 8 shown the RGB image and the grayscale image of the electrode starting from the initial condition (Fig. 5) to electrode condition after drilling at 50 mm depth (Fig. 8). Same electrodes are used for continuous assessment. It can be seen from the images of electrode listed, how the tip of the electrode change after drilling certain depth. By using image processing tool from Matlab, the percentage of the wear can be calculated and determined. To calculate the wear percentage of the electrode, the RGB image will undergo image enhancement stage by removing the unwanted noise which could causes inaccuracy in the result later on. After removing noises, the RGB images (on the left side in Figs. 5, 6, 7 and 8), were converted to grayscale images (right side Figs. 5, 6, 7 and 8). The pixels data of the grayscale image were counted and calculated using ‘SUM’ function in Matlab and the grayscale value of the images are obtained. The coding for the process explained above are shown in the Fig. 9.

To calculate the wear percentage of the electrode, the formula in Eq. 1 was be used. Note that, the parameter of the original Eq. 1 will be change accordingly using the image parameters (grayscale value). The new equation is:

Fig. 5 Reference image

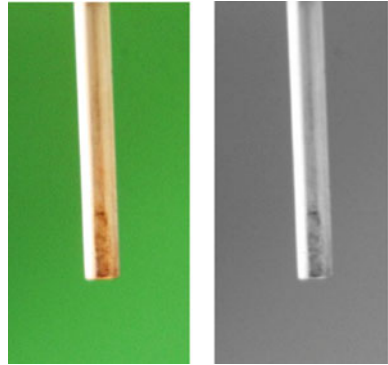


Fig. 6 After 10 mm drilling depth

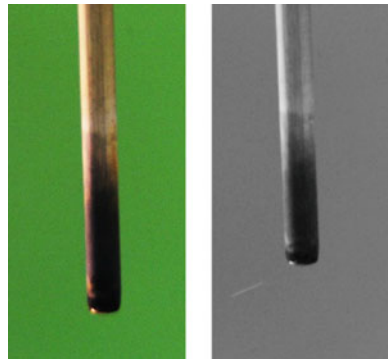


Fig. 7 After 20 mm drilling depth

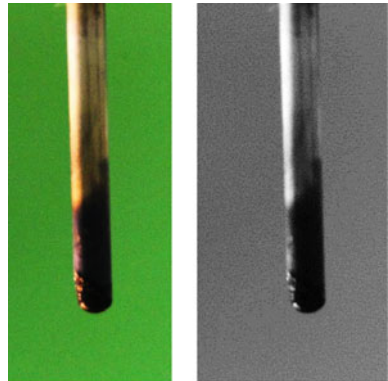
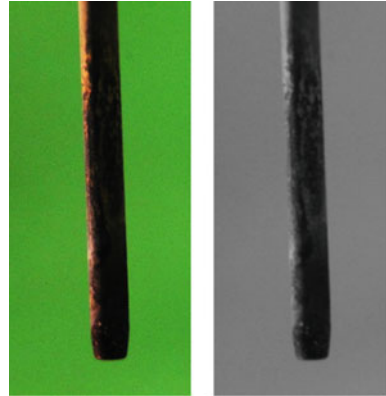


Fig. 8 After 50 mm drilling depth



```
>> clc; clearall;
a=imread('images.jpg');
a1=imresize(a,[100100]); figure,imshow(a1)
a2=rgb2gray(a1); figure,imshow(a2)
K =xlswrite('images.xls',a2);
K1= 'images.xls';
A = xlsread(M)
func = @sum;
B = varfun(func,A)
K1=sum(A1;CV100)/10000;|
```

Fig. 9 Coding for pixels identification

$$Electrode\ wear\ percentage = \frac{|R - W|}{W} \times 100\% \tag{1}$$

where

R reference image grayscale value.

W wear image grayscale value.

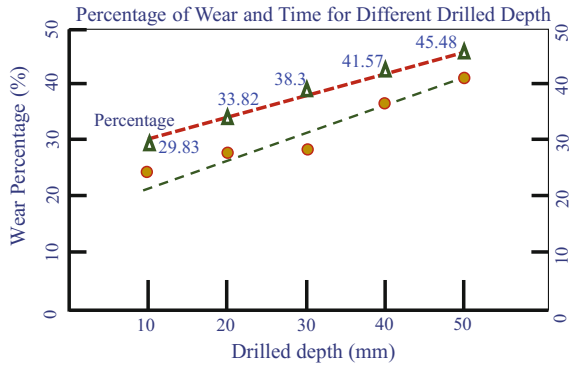
From the above equation, the results can be tabulated in a table.

Table 3 showed the depth of drilling with grayscale value of the images. It showed that as the depth increase, the grayscale value of the wear images decrease compare to reference image and wear percentage of tool increase. Below will show the relation between the depth of drill and wear percentage in a graph so that, the relation between them can be observed clearly.

Table 3 Depth of drilling with grayscale value of the images

Depth of drill (mm)	Reference image gray value (pixel)	Wear tool gray value (pixel)	Wear percentage (%)
10	170.75	119.82	29.83
20	170.75	112.99	33.82
30	170.75	105.35	38.30
40	170.75	99.76	41.57
50	170.75	93.10	45.48

Fig. 10 Relationship between wear percentage and time for different drilled depth



The Fig. 10 show a relationship between wear percentage and time for different drilled depth. As the depth of drill increase, the wear percentage of the electrode increase for depth 10–30 mm is 4.235% in average while for depth of 30–50 mm is 3.59% in average. Drilled depth directly proportional with the time.

4 Conclusions

It can be concluded from this project the machine vision system can be implemented in EDM super drill machine. It is a reliable method to monitor the electrode conditions. Since EDM super drill process required splash coolant, it become difficult to measure in real time. Machine need to be stop in order to capture the images.

Acknowledgements We are grateful to the University Malaysia Pahang for providing grant to run this study. (Grant RDU1703214).

References

1. Davim, J.P.: *Modern Mechanical Engineering: Research, Development and Education*: Springer Science & Business Media (2014)
2. Guo, R., Zhao, W.-S., Li, L., LI, Z.-Y., Zheng, G.J.-M.: Micro electrical discharge machining CNC system based on Linux. *Comput. Integrat. Manufact. Syst. Beijing* **13**(2), 370 (2007)
3. Hamedon, Z., Mori, K., Abe, Y.: In-situ measurement of three-dimensional deformation behaviour of sheet and tools during stamping using borescope. *J. Mater. Process. Technol.* **214**(4), 945–950 (2014)
4. Kalpakjian, S., Schmid, S.: *Manufacturing, Engineering and Technology SI* 6th ed. (2006)
5. Kaneko, T., Tsuchiya, M., Kazama, A.: Improvement of 3D NC contouring EDM using cylindrical electrodes—optical measurement of electrode deformation and machining of free-curves. In: Paper Presented at the Proceedings of 10th International Symposium for Electro Machining (ISEM-10) (1992)
6. Kurada, S., Bradley, C.: A review of machine vision sensors for tool condition monitoring. *Comput. Ind.* **34**(1), 55–72 (1997)
7. Novini, A.R.: Fundamentals of on-line gauging for machine vision. Paper Presented at the Industrial Vision Metrology (1991)
8. Oguamanam, D., Raafat, H., Taboun, S.: A machine vision system for wear monitoring and breakage detection of single-point cutting tools. *Comput. Ind. Eng.* **26**(3), 575–598 (1994)
9. Yan, M.-T., Huang, K.-Y., Lo, C.-Y.: A study on electrode wear sensing and compensation in micro-EDM using machine vision system. *Int. J. Advanc. Manufact. Technol.* **42**(11–12), 1065–1073 (2009)

Suppression on Effect of Cutting Forces Towards Tracking Performance in Milling Cutting Process Using State Observers



Madiah Maharof, Zamberi Jamaludin, Mohamad Minhat,
Nur Amira Anang, Tsung Heng Chiew and J. Jamaludin

Abstract In milling cutting process, tracking performance of the CNC servo drive system is influenced by the characteristics of the cutting forces generated during the milling operation. The undesired frequency harmonics of the cutting force contributes negatively to the positioning accuracy; thus an effective compensation of these harmonics is desired. This paper presents results related to suppression of cutting forces in milling process for minimal impact on tracking performance using controller design approach. A cascade P/PI position controller was designed and numerically analysed in combination with an Inverse Model Based Disturbance Observer (IMBDO) plus Disturbance Force Observer (DFO). The effectiveness of this control approach was validated on the x -axis of the XY feed table of a ball-screw driven milling machine. Results showed that the combined approach of cascade P/PI controller with IMBDO plus DFO produced the best tracking control performance with reduction of 78.8% in magnitude component of the cutting forces using Fast Fourier Transform (FFT) analysis of the tracking errors; compared to individual dedicated approach using IMBDO (62.7%) and DFO (78.2%) respectively.

Keywords Inverse model based disturbance observer (IMBDO)
Disturbance force observer (DFO) • Cutting force • Disturbance compensation

M. Maharof · Z. Jamaludin (✉) · M. Minhat · N. A. Anang · T. H. Chiew
Fakulti Kejuruteraan Pembuatan, Universiti Teknikal Malaysia Melaka, Hang Tuah Jaya,
76100 Durian Tunggal, Melaka, Malaysia
e-mail: zamberi@utem.edu.my

J. Jamaludin
Faculty of Engineering, Technology and Built Environment, UCSI University Kuala Lumpur,
Lot 12734, Jalan Choo Lip Kung, 56000 Taman Taynton View, Kuala Lumpur, Malaysia
e-mail: jailani@ucsiuniversity.edu.my

1 Introduction

In motion control system, disturbance observer is commonly applied to compensate for modeling errors and uncertainties as well as external disturbance. According to [1, 2], observers are effective in estimation of input disturbance force signal for compensation purposes. Observer adds a high gain loop to an existing position control configuration in order to improve the disturbance rejection ability of existing control system. In milling process, since cutting force is a natural outcome of the material removal process and cannot be avoided, a study by [3] have stated that Inverse-Model-based Disturbance Observer (IMBDO) is able to compensate for the negative impact that the cutting forces had on tracking performance of the milling table drives system. Also, in another application, cutting force was compensated using state observer [4]. Another type of observer, known as Disturbance Force Observer (DFO) was introduced in [5] and the experimental results presented had showed the effectiveness of DFO in compensating the cutting force. The paper showed that the magnitude of the high frequency components of the cutting force was significantly reduced thus reducing its effect on the servo drive performance of the feed table. This paper presents analysis on control performances of a cascade P/PI position controller combined with IMBDO plus DFO on the basis of reduction in magnitudes of the tracking errors and harmonics components of the cutting forces. This paper includes details on research methodology applied, controller and observer design, and discussion on results obtained with conclusions on the main findings.

2 Methodology

This section introduces the (i) test setup consisted of an XY milling table ball screw driven unit, (ii) system identification and system modeling, as well as (iii) dynamics analyses on the cutting force characteristics.

2.1 Test Setup

Figure 1a shows the XY milling table ball screw driven system produced by Googol Tech. The XY milling table consists of two positioning axes, each driven by a Panasonic MSMD 022GIU A.C. servo motor. Both axes are equipped with an incremental encoder for positioning measurement with resolution of 0.0005 mm/pulse. Figure 1b shows a schematic diagram of the overall system that consists of four main components, namely; a personal computer with MATLAB/Simulink and ControlDesk software, dSPACE DS1104 Digital Signal Processing (DSP) board, an amplifier and the XY milling table ball screw driven unit. The XY milling table is connected to a servo amplifier linked to a DS1104 DSP board. The personal computer that is connected to the DSP board applies the controller design and managed the data communication and collection.

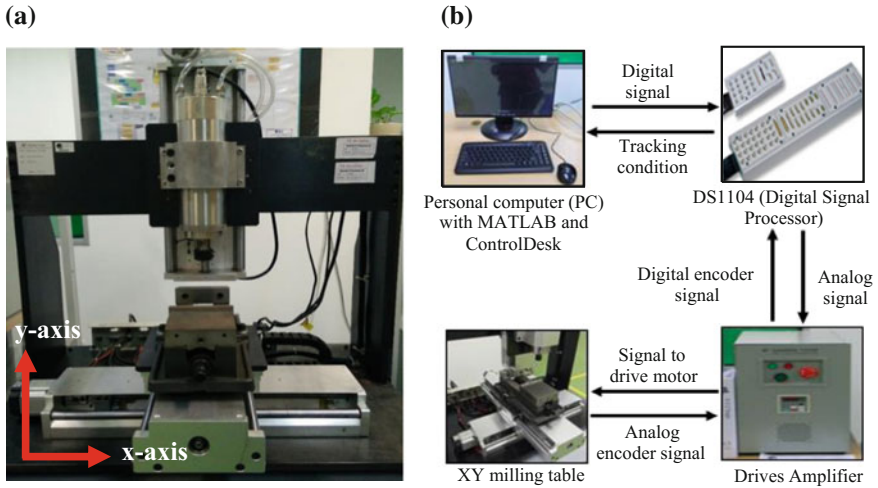


Fig. 1 a XY milling table ball screw driven system, and b Schematic diagram of the overall system setup

2.2 System Identification

The system was first identified and modelled. The system transfer function for the x -axis was identified according to [5]. For a single-input single-output (SISO) system, the frequency response function (FRF) of the system was estimated using H1 estimator [6] based on measured input voltage in volts, $u(t)$ and output position signals, $z(t)$ in mm. Figure 2 shows the Bode diagram of the measured FRF and the

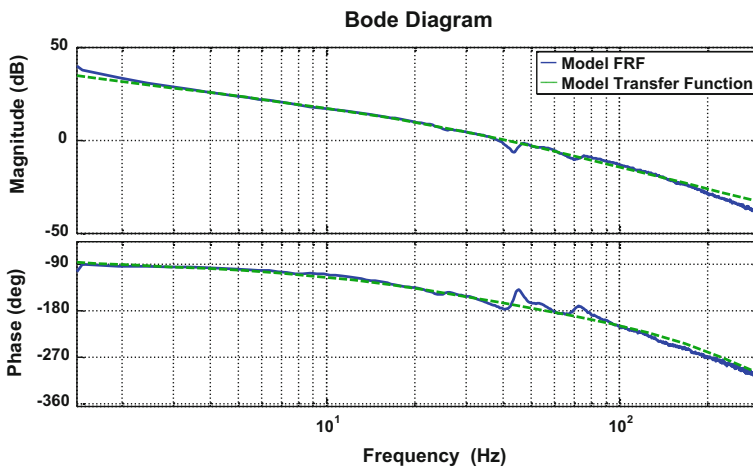


Fig. 2 Measured FRF and fitted second order model with time delay

fitted model transfer function for the x -axis. The parametric model was fitted using Nonlinear Least Square (NLLS) frequency domain identification method [7, 8].

The second order transfer function of the parametric model with time delay of 0.0012 s is:

$$\frac{Z(s)}{U(s)} = \frac{78020}{s^2 + 193.9s + 163} e^{-0.0012s} \quad (1)$$

2.3 Cutting Force Characterization

For the purpose of simulating actual cutting process during controller design analysis, actual milling cutting forces were measured using a Kistler Dynamometer measurement unit. A straight line cut was performed in the direction of the x -axis at spindle speed rotation of 1500 rpm, an end-mill cutter diameter of 10 mm, at the depth of cut of 1.0 mm, and a feed rate of 502 mm/min. The measured cutting force characteristics was then analysed in frequency domain to identify its harmonic frequencies content. Figure 3a show schematic diagram of the system used for the measurement while Fig. 3b shows results of the Fast Fourier Transform (FFT) analysis of the measured cutting forces in the x -axis. The highest harmonic frequency was identified at 26 Hz. The measured cutting forces were applied as input disturbance for numerical validation of the controller.

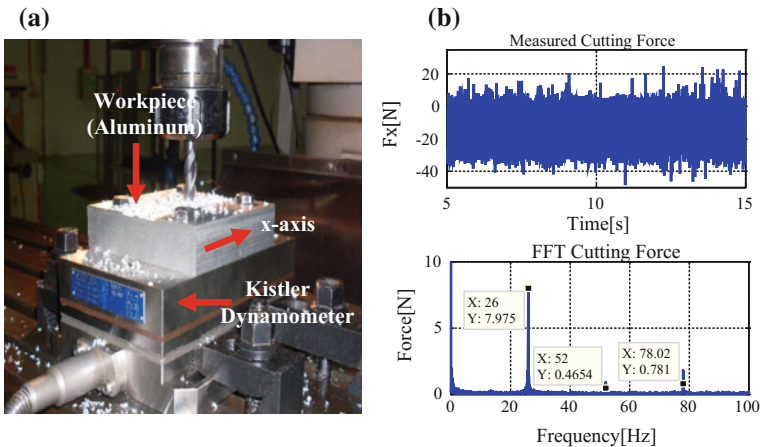


Fig. 3 a Schematic diagram of cutting force characterization, and b FFT analysis of the measured cutting force in the x -axis

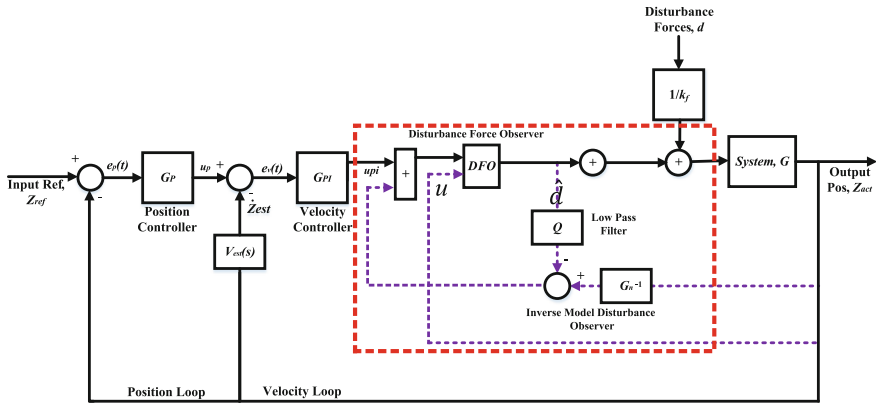


Fig. 4 Schematic diagram of cascade P/PI controller combined with IMBDO plus DFO

3 Controller and Observer Design

The control scheme consists of a cascade P/PI position controller combined with both IMBDO and DFO (indicate in red square) as shown in Fig. 4. This approach utilizes the strengths and advantages of both IMBDO and DFO to compensate for the input cutting forces that act as disturbance to the system. IMBDO compensates for the unmodelled dynamics while DFO uniquely compensates for the harmonics frequencies of the cutting forces. Details design of IMBDO and DFO including the stability analysis are presented in [5].

4 Result and Discussion

Numerical analyses on control performance of the system were performed using four different control configurations, namely; (i) cascade P/PI (ii) cascade P/PI with IMBDO (iii) cascade P/PI with DFO, and (iv) cascade P/PI with IMBDO plus DFO. The system was made to track a sinusoidal signal of amplitude 10 mm and frequency of 0.5 Hz. Figure 5 shows tracking errors and results of FFT on the tracking errors for each control scheme.

FFT analysis focuses on reduction in peak magnitudes at 26 Hz of the force harmonic components. Results showed that maximum reduction in peak values at 26 Hz harmonic frequency was observed in the case of cascade P/PI combined with IMBDO and DFO. An analysis was performed with regard to the effectiveness of DFO in estimating the input disturbance signal. Figure 6 compares the input disturbance $d(t)$ and the estimated disturbance $\hat{d}(t)$ obtained using DFO for input disturbance signal in the form of a sine wave with single harmonic frequency content. A close match between actual disturbance and estimated disturbance signal

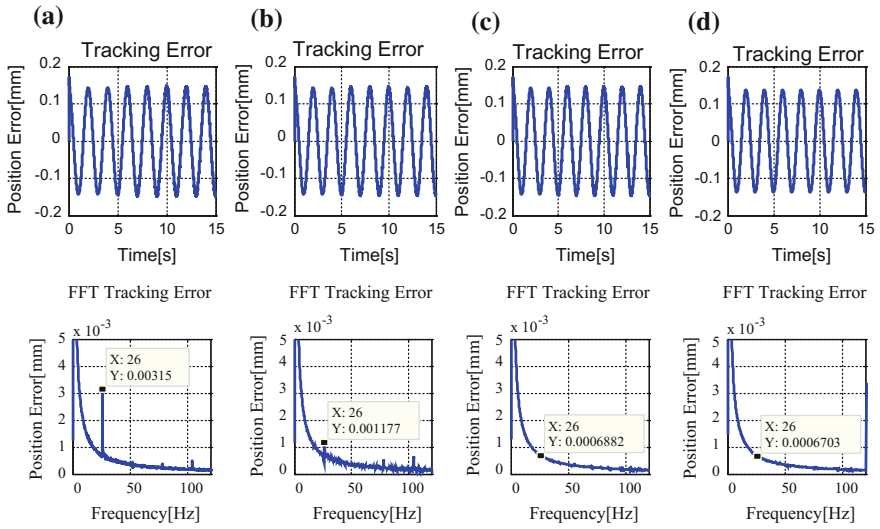


Fig. 5 Tracking errors and results of FFT for **a** cascade P/PI, **b** cascade P/PI with IMBDO, **c** cascade P/PI with DFO and **d** cascade P/PI with IMBDO plus DFO

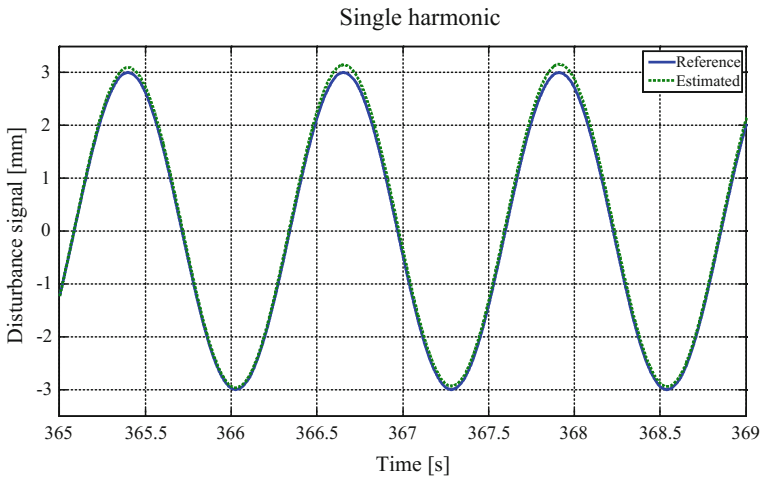


Fig. 6 Comparison between input disturbance $d(t)$, and estimated disturbance $\hat{d}(t)$

was observed indicating successful application of DFO as a component in the control scheme applied. A further improvement is desired to address delay that was observed between actual input and the estimated signal.

5 Conclusion

As conclusion, this paper has presented results on control performance of cascade P/PI position controller combined with observers in the forms of IMBDO and DFO. Results were compared in terms of reduction in the magnitude of the tracking errors and peak values of the harmonics frequencies of the cutting forces. Results showed that cascade P/PI controller combined with IMBDO plus DFO produced the best tracking performance with largest reduction in peak amplitude of the cutting force at frequency of 26 Hz based on the FFT results. Here, the peak value of the harmonic frequency was reduced from 3.1580 μm to 0.6703 μm in comparison to individual dedicated approach using IMBDO and DFO that showed reduction to 1.1770 μm and 0.6882 μm respectively. The combined approach has successfully utilizes the individual strength of IMBDO and DFO resulting in superior control performance. In future, further study on addressing issue of delay in the estimated disturbance signal is desired in order to further improve the overall tracking performance of the system.

Acknowledgements The authors would like to thank the Ministry of Higher Education for the funding of this research with the reference number FRGS/1/2015/TK03/FKP/02/F00281 and the Faculty of Manufacturing Engineering, UTeM for the facilities provided.

References

1. Umeno, T., Hori, Y.: Robust speed control of DC servomotors using modern two degrees-of freedom controller design. *IEEE Trans. Industr. Electron.* **38**(5), 363–368 (1991)
2. Hori, Y., Shimura, K.: Position/force control of multi-axis robot manipulator based on the TDOF robust servo controller for each joint. In: *Proceedings of the American Control Conference ACC/W9*, vol. 1, pp. 753–757 (1992)
3. Ohnishi, K., Murakami, T.: Advanced motion control in robotics. In: *IEEE Association, 15th Annual Conference of IEEE Industrial Electronics Society (IECON 1989)*, Philadelphia USA, pp. 356–359, 6–10 November 1989
4. Huang, S., Tan, K., Hong, G.S., Wong, Y.S.: Cutting force control of milling machine. *Mechatronics* **17**(10), 533–541 (2007)
5. Jamaludin, Z., Jamaludin, J., Chiew, T.H., Abdullah, L., Rafan, N.A., Maharof, M.: Sustainable cutting process for milling operation using disturbance observer. *Procedia CIRP* **40**, 486–491 (2016)
6. Pintelon, R., Schoukens, J.: *System Identification: A Frequency Domain Approach*. Wiley (2012)
7. Pintelon, R., Guillaume, P., Rolain, Y., Schoukens, J., Van hamme, H.: Parametric identification of transfer functions in the frequency domain—a survey. *IEEE Trans. Autom. Control* **39**(11), 2245–2260 (1994)
8. Kollar, I.: *Frequency domain system identification toolbox*. MATLAB Toolbox Manual, Electronic Version (2001)

Effect of Filler Loading on Tracking and Erosion of Silicone Rubber Based Composites Under DC Voltage



Najwa Kamarudin, Jeefferie Abd Razak, Nurbahirah Norddin, Aminuddin Aman and Nazurah Nazir

Abstract Silicone rubber (SiR) is the most common material used nowadays for composite insulators and as a chosen candidate for outdoor high voltage applications, benefited from their excellent electrical performance. However, SiR also suffered from many drawbacks since electrical properties are becoming the major factors to the failure of insulation. Thus, by varying filler loading also is considered as an alternative way to improve the properties of SiR based composite insulator. In this paper presents the results of erosion weight and inclined plane tracking test for SiR based composite prepared by using different types of fillers. The purpose of using different fillers is to improve the properties of silicone rubber as an insulator which is necessary for good outdoor insulation applications. Calcium carbonate, silica and wollastonite were used as fillers in SiR matrix to enhance the resistance to tracking and erosion. The performances of materials also have been compared by conducting inclined plane tracking (IPT) test. Eroded mass and tracking length were examined to support the result. It is found that CaSiO_3 had proved their ability as good fillers to be integrated with SiR for high voltage insulator by having the utmost number of passing sample.

Keywords Silicone rubber · Tracking · Erosion · Wollastonite Insulator

N. Kamarudin (✉) · J. Abd Razak (✉)

Advanced Manufacturing Center, Faculty of Manufacturing Engineering,
Universiti Teknikal Malaysia Melaka, Hang Tuah Jaya,
76100 Durian Tunggal, Melaka, Malaysia
e-mail: kknajwa@gmail.com

J. Abd Razak
e-mail: jeefferie@utem.edu.my

N. Norddin
Faculty of Engineering Technology, Universiti Teknikal Malaysia Melaka,
Hang Tuah Jaya, 76100 Durian Tunggal, Melaka, Malaysia

A. Aman · N. Nazir
Faculty of Electrical Engineering, Universiti Teknikal Malaysia Melaka,
Hang Tuah Jaya, 76100 Durian Tunggal, Melaka, Malaysia

1 Introduction

Polymeric insulators address most of the problems faced by the porcelain insulators. Their advantages include light weight, which allows easier erection and commissioning of the insulators, even in distant areas including places with resistance to vandalisms. Furthermore, polymeric insulators inhibit a hydrophobicity property which is suitable to be used in high pollution areas. These kinds of properties make polymeric insulators good for use, however they also have certain drawbacks. Polymeric insulators are vulnerable to tracking and erosion under electrical stress, and also to degradation under corona and weathering [1].

Polymers have been used to replace an inorganic porcelain and glass for external housings of HV outdoor devices since the 1960s. Polymers offer significant advantages over porcelain and glass, such as light weight, easy installation, reduced breakage, and high impact resistance. In addition, polymers facilitate a greater flexibility in product design, and also can provide improved electrical performance especially under contaminated conditions. These advantages have been possible, mainly because polymers can be conveyed suitably to make them more resilient to damage from the several elements in nature, such as temperature extremes, ultra-violet radiation in sunlight, chemicals, corona and electrical arc discharge activity. Today, there are standard test in the ASTM for evaluating the resistance of materials to these elements [2].

Over the past few years, composite insulator has been found to be capable and reliable choice as near-future advanced dielectric insulation based on its outstanding properties [3]. Among their benefits, composite designs compromise lighter weight, less breakage, improved seismic performance and more flexibility in design than ceramic insulators. These features can give a lower installation cost, better durability and more aesthetically pleasing line design. Integrating silicone rubber with fillers is a growing demand among researchers and common industrial practitioners. Basically, reinforcements material or fillers are regularly used to enhance the polymeric composite properties and also to reduce the cost of materials [4, 5]. The common fillers that often been used for electrical insulation application are silica, calcium carbonate and wollastonite.

1.1 Silica from Waste Glass

Silica glass has been the chosen materials to be used as a filler to manufacture electrical insulators for HV transmission lines [6]. Glass is a very solid material that has an amorphous or non-crystalline material [4]. It is generally accepted that the first manufactured glass was in the form of a glaze on ceramic vessels, about 3000 B.C. The first glass vessels were produced about 1500 B.C. in Egypt and Mesopotamia. The glass industry was extremely successful for the next 300 years

and then declined. It was revived in Mesopotamia in the 700 B.C. and in Egypt in the 500 B.C. [7].

Glass is typically brittle and optically transparent. It is normally made of silica-SiO₂ and by adding several minor additives for the purpose of chemical stability. The commercial glass or named as soda-lime glass has chemical composition of 75% silica (SiO₂) and 25% composition of sodium carbonate (Na₂CO₃), calcium oxide (CaO) and some magnesium oxide (MgO) [4]. Besides that, waste glass also is a large component of household and industry for example, containers for beverage and food as well as the commodity item [8]. However, glasses are not ceramics, but they are used for similar type of things as ceramics and have some properties that are typical for ceramics. The most common property of ceramics and glasses is brittleness [7].

1.2 Calcium Carbonate from Cockle Shell

Calcium carbonate is recognized as an efficient carbon dioxide (CO₂) adsorbent and separation of CO₂ from gas stream using CaO based adsorbent is widely applied in gas purification process especially at high temperature reaction. CaO is normally been produced via thermal decomposition of calcium carbonate (Ca₂O₃) sources such a limestone which is attained over mining and quarrying limestone hill [9].

1.3 Tracking and Erosion

Polymeric insulators are known with degradation as their main drawbacks due to environmental and operating conditions. Thus, the lifetime of an insulator is difficult to determine because of the variability of these conditions from one place to another. Thereto, an inspection should be done in order to detect the degradation at early stages [10].

Furthermore, tracking has been the well-known reason of insulation failure [11]. Tracking and erosion are considered as important aspects to be looked into since it leads to better strength of insulator. The evaluation of tracking and erosion resistance of polymeric insulator is a necessary testing performed on outdoor insulators. Tracking can be defined as a formation of a surface carbonaceous path while erosion is a weight loss of the material [12]. The development of tracking starts from continuous dry band arcing due to the flow of leakage current on the insulator surface under wet contaminated conditions [11].

Whilst, tracking resistance is a measure of its ability to withstand the intense leakage currents combined with dry band arcing. This test is evaluated in terms of number of cycles or time to failure. The degradation of polymer by erosion and tracking is due to the heat generated by leakage currents and dry band arcing.

The ability of an insulating material to withstand with the electrical discharges on the surface is similar to those occur in service under the influence of dirt, moisture and conducting salts condensed from the atmosphere [13].

2 Preparation of Sample

2.1 Preparation of Fillers

Fillers consist of silica from waste glass which is collected from recycle waste company, calcium carbonate from cockle shells and wollastonite are used in this research work. The natural cockle shell which is collected from domestic waste in local restaurant is then washed to remove the dirt and dried in an oven (Venticell). The cockle shell is placed in a container and the oven is operated at 80 °C for 24 h. Next, crusher machine is used to break the waste glass material and the cockle shell is changed into refine form. The following process is to ensure the waste glass and cockle shell samples can be transformed into powder form. In this step, Horizontal Mill Machine is used with two opposing cycle. The machine is carried out at 30 min for each cycle at 400 rpm, with 15 min resting time in between. All the parameter is chosen by referring to the study by [4].

2.2 Preparation of Wollastonite

To produce the wollastonite there are two main constituents involved which are Calcium Oxide (CaO) and Silica (SiO₂). The preparation is done by weighing both calcium carbonate and silica using ratio 48.3%: 51.7% and undergo ball milling process at 20 rpm for 45 min. The purpose of this process is to ensure the combination of the calcium carbonate and silica powder turn into homogeneous form. Then, the mixture is calcined in a furnace (Nabertherm) to heat up with a heating rate of 10 °C/min, up to 1000 °C in 3.5 h and heating rate of 10 °C/min also is used for the purpose of cooling process. Next, X-ray diffraction (X-RD) technique is conducted to verify the chemical composition of composite of glass and cockle shell after calcination process.

2.3 Mixing the Silicone Rubber with Fillers

The silicone rubber is obtained from Immortal Green Industrial Sdn Bhd. The type of SiR used is Elastosil R401/60S and it is bought together with an Aux Heat Stabilizer H3. Silicone rubber is mixed together with heat stabilizer and Dicumyl

Peroxide (Aldrich) along with the fillers. To ensure the mixture of the composite is homogeneously dispersed according to the right formulations, internal mixer (Barabender) is utilized at roller rotor speed of 70 rpm for 7 min. The values of the settings are decided according to the previous studies done for natural rubber by [14, 15]. For each composition, the amount of composite is fixed to approximately 50 g per run. The composites with the dimension of $l \times w \times t$ (50 mm \times 120 mm \times 6 mm) according to the standard method of ASTM 60587 then is compressed using hot press machine (Gotech) with setting 15 min compression period with a pressure 70 kg/cm³ and temperature of 185 °C. The composite sheet is compressed by this machine with internal water flow for 12 min. The flat sheet sample specimens are produced with 6 mm thickness.

3 Experimental Setup

3.1 Inclined Plane Tracking Test Process

Figure 1 shows the schematic diagram of the experimental setup and the electrode configuration used in the present study. The tracking resistance test on the silicone rubber based composite material was carried out following the IEC-60587 inclined plan test method.

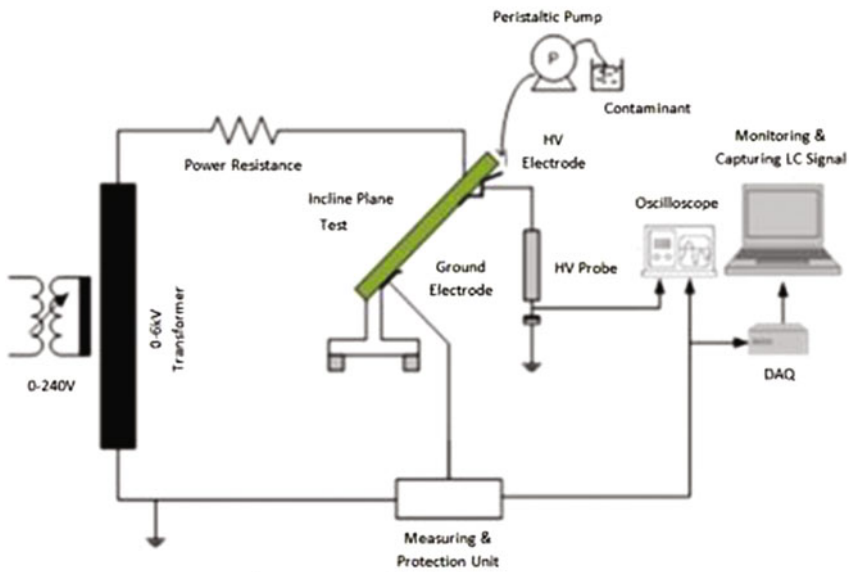


Fig. 1 Inclined plane tracking test setup

Based on the standard method of AC (BS EN 60587:2007), the specimen is put through a test voltage for six hours. The specimen was mounted at an angle of 45° and the contaminant was allowed to flow from high voltage to ground electrode over the surface of the plate specimen. As for this experiment, the voltage proposed was 3.04 kV, with contaminant flow rate from the pump of 0.3 ml/minute and power resistance of 22 k Ω . By referring to the standard test method of BS EN 62039-2007-Selection Guide for Polymeric Materials for Outdoor Use Under HV Stress, the common voltage used for polymeric material for AC voltage is 3.5 kV. Since there is no standard test method for DC voltage, thus a research conducted by Cherney et al. [16] had proved that 1.0 kV of voltage for AC is equivalent to 87% of -ve DC. Thus, 3.5 kV of AC is equivalent to 3.04 -ve DC. While the flow rate and resistance is chosen according to the standard test method of AC [17]. This is because in the standard test method of AC has already been stated the constant value of flow rate and resistance for each voltage applied. A contaminant liquid is made from 0.1% by mass ammonium chloride (NH_4Cl) in distilled water. To ensure the specimen wets out easily and promptly to the specimen surface, a non-ionic wetting agent Triton X-100 (isooctylphenoxy polyethanol) with a concentration of 0.02% by mass is applied in the solution. The conductivity testing meter is used to measure the conductivity of the liquid. All the parameter is chosen according to BS EN 60587:2007 and BS EN 62039:2007. A measurement system consisted of measuring and protection units which act as a sensor and a protection circuit was set up to monitor and capture the leakage current data.

4 Results and Discussion

4.1 Tracking Failure

This paper is only focusing on the physical performance and appearance of the resulted composite materials. The mechanism of tracking failure starts when an insulator gets wet due to the presence of a small leakage current on the surface of the specimen. The rising of atmospheric temperature caused the evaporation of water and a dry band is formed around an insulator as shown in Fig. 2. The phenomenon of dry band resulted an interruption in current flow and a voltage gradient appears across the dry band. As the test progressed, erosion and tracking appeared a channel, starting at the lower electrode and extending towards the upper electrode. The heat from the sparks discharges between the two electrodes causes the formation of carbon on the specimen surface as shown in Fig. 3. Hence, the degradation caused by tracking and erosion appeared on the surface of the sample as shown in Fig. 4.

Length of the tracked path is one of the methods to obtain information about the surface tracking resistance of the polymeric material. After completing the tracking

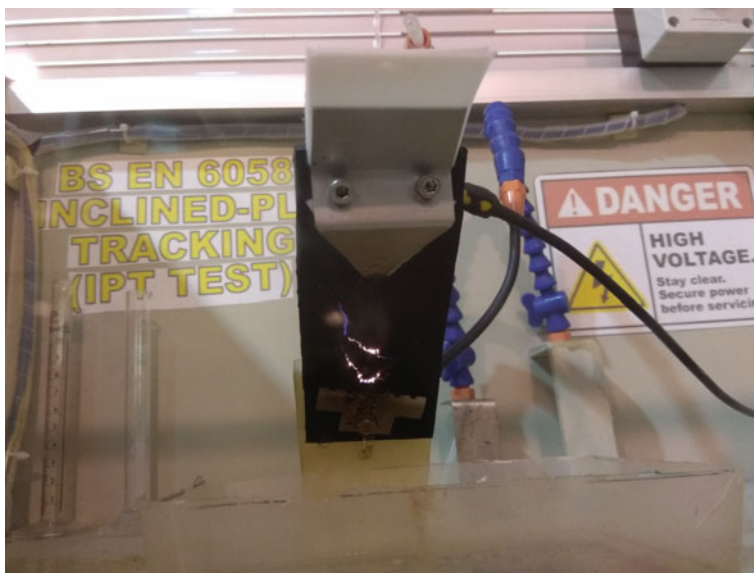


Fig. 2 Arcing on insulator sample



Fig. 3 Carbon formed on the specimen surface

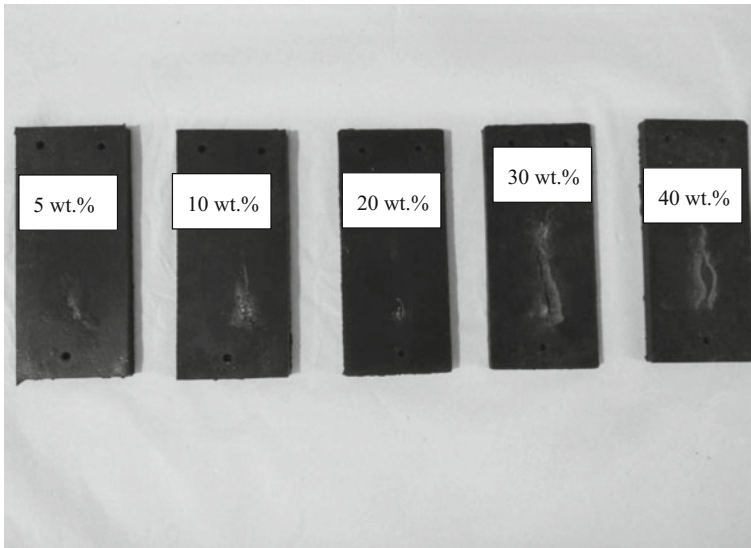


Fig. 4 Insulator samples of SiR/SiO₂ after test showing degradation caused by tracking and erosion

test, the length of the tracking path of each specimen was measured and the average value of the tracking length is shown in the Fig. 5.

Figure 5 shows the result of the tracking length of silicone rubber filled with different fillers. It was observed that SiR/CaSiO₃ passed the tracking failure with the highest number of samples followed by SiR/CaCO₃, and SiR/SiO₂.

It can be clearly seen that for SiR/CaSiO₃, all the samples pass the tracking failure except for the sample with 20 wt% filler loading. This sample is considered failed by having tracking length more than 2.5 cm. This is might be due to an agglomeration occurs during the dispersion of the composite to achieve a balance matrix absorption as mentioned by Yaacob et al. [18] in their studies. However, in order to enhance the dispersion, previous researcher found the usage of silane coupling agent to be added into the materials mixture [19]. Overall, most of the SiR/CaSiO₃ samples are accepted and is concluded potential to be used as insulator.

However, SiR/SiO₂ shows poor performance by having 3 out of 5 samples failed since its tracking length is more than 2.5 cm. It shows that SiR/SiO₂ with filler loading more than 20 wt% failed by having tracking length more than 2.5 cm due to an increase of filler loading. This result indicate that the maximum filler loading for silica to withstand the voltage is only at 5 and 10 wt%. SiR/CaCO₃ samples on the other hand failed two samples, whereas the other three samples stayed below than the pass limit according to the standard.

Thus, it is proposed that SiR/CaSiO₃ has a better tracking performance compared to the other two materials. The value of the weight percentage of filler loading

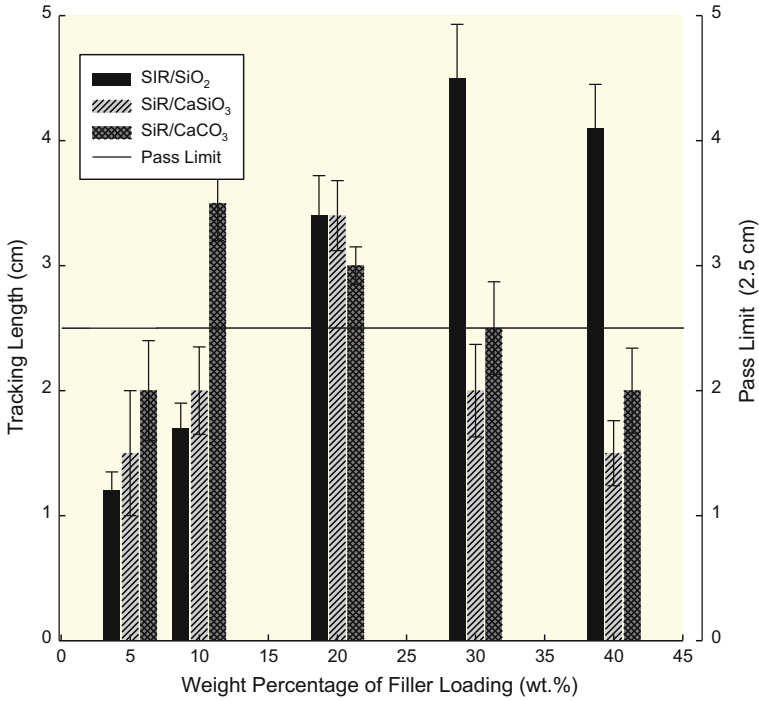


Fig. 5 Tracking length of silicone rubber based composites

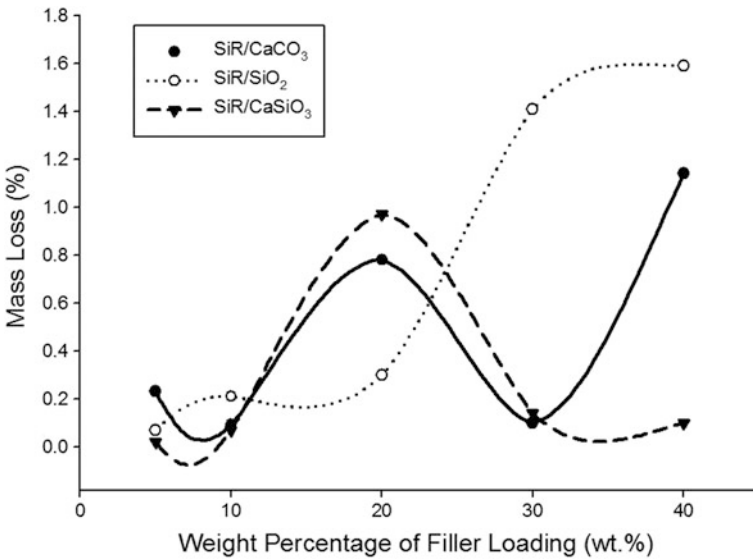


Fig. 6 Mass loss of silicone rubber based composite after tracking test

that passed the test was 5, 10, 30 and 40 wt%, while sample with 20 wt% of filler loading failed. From these results, show the beneficial effect of CaSiO_3 as mineral filler to be incorporated with SiR for high voltage insulator. In order to understand the eroded mass of the material due to tracking test, the weight of the samples before and after tracking test were measured.

Figure 6 reveals the comparison of the weight loss of the silicone rubber based composite material due to tracking test at different weight percentage of filler loading. For SiR/ CaSiO_3 , it is observed that as the weight percentage of filler loading increase above 20 wt%, then significant reduction in eroded mass of the material is detected and this is quite related with the earlier reported tracking resistance results.

While focusing on SiR/ SiO_2 , the percentage of eroded mass keep increasing as the filler loading increase. It is contradict with the result studied by Loganathan and Chandrasekar [20] which they stated in their research paper that the mass loss would reduce when the filler loading increases. The phenomenon occurred on SiR/ SiO_2 might cause by the particle size of SiO_2 which might affect the insulator behavior as mentioned by Vas et al. [1]. In their work, they state that by adding nano fillers into polymer matrix could produce better dispersion as an agglomeration of nano particles can be avoided. Thus, further investigation on particle size would be a good choice to study for SiO_2 material in order to identify whether SiO_2 can be as good as other materials. However, the pattern of the mass loss graph is closely related to the tracking graph where it's tracking length keep on increasing as the filler loading increase. Other than that, by comparing with all the fillers, it was clear that SiR/ CaSiO_3 has the lowest mass loss compared to the other two fillers. Furthermore, this result also shows that the sample which has less mass loss has high potential to be good insulators as indicated by Vas et al. [21].

5 Conclusion

As a conclusion, experimental results on tracking and erosion resistance characteristics of silicone rubber material filled with different fillers at various weight percentages of filler loading under DC voltages have been presented in this paper. Influence of type of filler on the performance of tracking and erosion for high voltage insulator is studied. From the obtained results, it can be stated that the SiR/ CaSiO_3 samples show less tracking resistance compared to SiR/ CaCO_2 and SiR/ SiO_2 by measuring the tracking length. It is found that SiR/ CaSiO_3 has the utmost number of pass sample by having only 1 sample failed the pass limit. While the eroded mass between three fillers proved that there is a relation to the previously recorded tracking resistance. In comparison with two fillers, it is proved that SiR/ CaSiO_3 had the better tracking resistance compared to the other two fillers.

References

1. Vas, J.V., Venkatesulu, B., Thomas, M.J.: Tracking and erosion of silicone rubber nanocomposites under DC voltages of both polarities. *IEEE Trans. Dielectr. Electr. Insul.* **19**(1), 91–98 (2012)
2. Gorur, R.S., et al.: A laboratory test for tracking and erosion resistance of HV outdoor insulation. *IEEE Trans. Dielectr. Electr. Insul.* **4**(6), 767–774 (1997)
3. Momen, G., Farzaneh, M.: Survey of micro/nano filler use to improve silicone rubber for outdoor insulators. *Rev. Adv. Mater. Sci.* **27**, 6–7 (2011)
4. Aman, A. et al.: Polymeric composite based on waste material for high voltage outdoor application. *Int. J. Electric. Power Energy Syst.* **45**(1), 346–352. Available at: <http://dx.doi.org/10.1016/j.ijepes.2012> (2013)
5. Ansoorge, S., et al.: Improved performance of silicone rubbers for the use in composite insulators. *Cigre* **19**(1), 1–10 (2012)
6. Fanderlik, I.: *Silica Glass and Its Application*, Elsevier (1991)
7. Axinte, E.: Glasses as engineering materials: a review. *Mater. Des.* **32**(4), 1717–1732 (2011). <https://doi.org/10.1016/j.matdes.2010.11.057>
8. Thoo, V.W.F. et al.: Studies on the Potential of Waste Soda Lime Silica Glass in Glass Ionomer Cement Production (2013)
9. Mohamed, M., Yousuf, S., Maitra, S.: Decomposition study of calcium carbonate in cockle shell. *J. Eng. Sci. Technol.* **7**(1), 1–10 (2012)
10. Ramirez-vazquez, I., Hernandez-corona, R.: Tracking and Erosion Requirements for High Voltage Silicone Rubber Insulators., pp. 4–7 (2016)
11. Vasudev, N. et al.: Effect of ATH filler content on the performance of silicone rubber by inclined plane tracking and erosion test method. In: *Proceedings of the IEEE International Conference on Properties and Applications of Dielectric Materials* (2012)
12. Ghunem, R.A.: Using the inclined-plane test to evaluate the resistance of outdoor polymer. *IEEE Electr. Insul. Mag.* **31**(5), 16–22 (2015)
13. Allen Bernstorf, R., Niedermier, R.K., David, S., Winkler: *Polymer Compounds Used In High Voltage Insulators*. Hubbell Power Systems the Ohio Brass Company, p. 12. Available at: <http://linemansafestart.com/literature/insulators/EU1407.pdf> (2000)
14. Mohamad, N., et al.: Effects of epoxidized natural rubber (ENR-50) and processing parameters on the properties of NR/ EPDM blends using response surface. *Methodology* **40713**, 1–8 (2014)
15. Razak, J.A. et al.: NR/EPDM elastomeric rubber blend miscibility evaluation by two-level fractional factorial design of experiment. In: *AIP Conference Proceedings*, 1614 October, pp. 82–89. Available at: <http://scitation.aip.org/content/aip/proceeding/aipcp/10.1063/1.4895176> (2014)
16. Cherney, E., et al.: DC inclined-plane tracking and erosion test of insulating materials. *IEEE Trans. Dielectr. Electr. Insul.* **22**(1), 211–217 (2015)
17. Code, P.: *International Standard* (2007)
18. Yaacob, M.M., et al.: Jurnal Teknologi Full paper Electrical Characteristics of Polyvinyl Chloride with Wollastonite Filler for High Voltage Outdoor Insulation Material **4**, 1–7 (2013)
19. Datashvili, Brostow, Tea, W.: Chemical modification and characterization of Boehmite particles. *Chemist. Chem. Technol.* **2**(1), 27–32 (2008)
20. Loganathan, N., Chandrasekar, S.: Analysis of surface tracking of micro and nano size alumina filled silicone rubber for high voltage AC transmission. *J. Electric. Eng. Technol.* **8** (2), 345–353 (2013)
21. Vas, J.V., Venkatesulu, B., Thomas, M.J.: Tracking and erosion resistance of silicone rubber nanocomposites under positive and negative DC voltages. *Annual Report—Conference on Electrical Insulation and Dielectric Phenomena, CEIDP*, pp. 0–3 (2010)

Design and Implementation of Cascade NP/PI Controller for Feed Table Ball Screw Driven Milling Machine



Nur Amira Anang, Lokman Abdullah, Zamberi Jamaludin,
Madiah Maharof and Tsung Heng Chiew

Abstract This paper presents improvements on conventional cascade P/PI position control structure with implementation of nonlinear function onto the existing control structure resulting in cascade NP/PI controller. The controller design process involved three main steps, namely; (i) design of PI controller for the speed loop, (ii) design of P controller for the position loop, and (iii) design of the nonlinear function. The speed and position controllers were designed based on gain margin and phase margin considerations. There were three main elements involved in the design of the nonlinear function, namely; rate of variation of nonlinear gain (KO), maximum value of error, (e_{\max}) and sampling frequency, (δ). Results obtained from implementation on the x -axis of a milling machine feed table shows that the proposed cascade NP/PI controller generated an improvement of 1.3% in tracking performance in term of RMS error values compared to the classical cascade P/PI controller.

Keywords Cascade NP/PI · Cascade P/PI · Tracking performance
Ball screw driven system

1 Introduction

The developments in control system technologies have resulted in stark increment in areas related to process efficiency, cost effectiveness [1] and energy saving [2]. Over the last decades, overwhelming efforts have been made by researchers in the field of machine tools control strategy, especially in precision machining [3–5]. Precise machining is characterized by astute tracking performance of the machine tools drive system. Therefore, tremendous research have been done to improve tracking performances of various control systems [6–8]. Examples of control

N. A. Anang · L. Abdullah (✉) · Z. Jamaludin · M. Maharof · T. H. Chiew
Faculty of Manufacturing Engineering, Universiti Teknikal Malaysia Melaka,
Hang Tuah Jaya, 76100 Durian Tunggal, Melaka, Malaysia
e-mail: lokman@utem.edu.my

strategies that are based on classical P + I+D controllers are PID itself, cascade P/PI and nonlinear PID (NPID) controllers [9–11]. Recently, Rafan [12] has published an improvement for the conventional cascade P/PI controller utilizing two friction compensation techniques; namely, Generalized Maxwell Slip (GMS) and Sigmoid like Curve function (SLCF). This has proven that cascade P/PI controller is capable to be implemented for friction compensation and cutting force compensation; two elements that often affect tracking performance in machine tools. A further enhancement is desired especially for the purpose of improving the controller robustness and ability to address non-linear issues during application. The addition of nonlinear function within the structure of a linear controller has been proposed and developed in literature. However, most of these approaches are performed in combination with PID controller. The collaboration between nonlinear function and classical cascade P/PI needs further investigation and analysis. This paper presents design analyses and experimental results relating to the implementation of combined nonlinear function and cascade P/PI controller; where the nonlinear function was embedded at the position loop of the control structure.

2 Methodology

2.1 Experimental Setup

The experimental setup consisted of four important components; such as, (i) a computer, (ii) a Digital Signal Processing (DSP) board, (iii) an amplifier, and (iv) a ball screw driven XY milling machine feed table. The computer was installed with MATLAB and dSPACE software for interaction with the DSP board. DS1104 board was interfaced with the servo amplifier connected to the XY ball screw system. Figure 1 shows the experimental setup applied for this research.

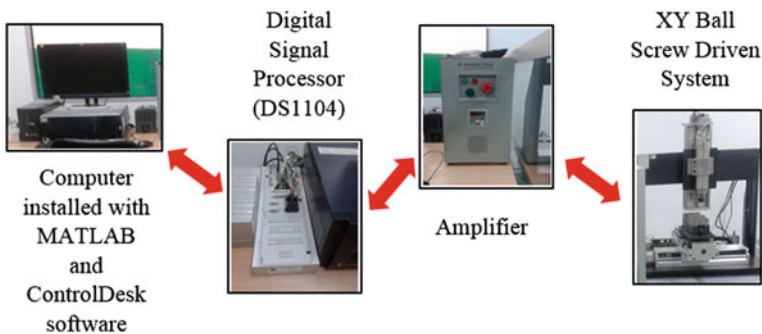


Fig. 1 Experimental setup

2.2 System Identification

System identification is initial and important step in any controller design process. This process helps to identify the dynamic behaviour of the electro-mechanical system using single-input single-output (SISO) model in frequency domain. The dynamics characteristics of the system were captured based on the measured and synthesized Frequency Response Function (FRF).

The FRF plot was generated based on measured input voltage to the drive system, $u(t)$ and the output positions, $z(t)$ of the ball screw table [13]. The FRF was then estimated using H1 estimator [14]. The system was modelled using Matlab toolbox 'fdident' yielding a second order model with time delay [15]:

$$G_m = \frac{Z(s)}{U(s)} = \frac{78020}{s^2 + 163s + 193.3} e^{-s0.0012} \tag{1}$$

3 Controller Design

3.1 Design of PI Controller (Speed Loop)

The first step in designing the controller was to design the speed PI controller. As shown in Fig. 2, the PI controller was represented in terms of controller parameters k_p and k_i . The controller was designed in frequency domain based on gain margin and phase margin consideration. This method was used to maintain the stability margin and improved the system transient response [16]. As a rule of thumb, the gain margin and the phase margin are advised to be within the range of 4–10 dB and 30° to 70° respectively. Equation (2) shows the speed open loop transfer function that generated 9.37 dB and 56.4° of gain margin and phase margin. The tuned parameters of k_p and k_i were 0.006607 and 0.12075 respectively.

$$V_{openloop}(s) = \frac{\dot{Z}_{est}(s)}{E_v(s)} = PI \cdot G(s) \cdot V_{est}(s) \tag{2}$$

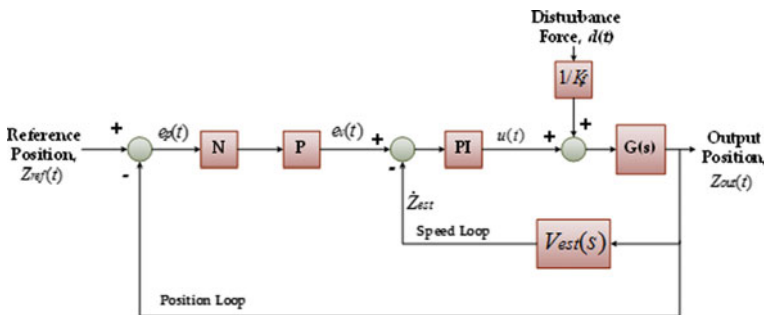


Fig. 2 Schematic diagram of cascade P/PI

3.2 Design of P Controller (Position Loop)

The position loop consisted of a proportional gain, k_v . The controller was designed over the speed controller loop whereby the gain margin and the phase margin obtained for k_v equals 225 s^{-1} were 9.1 dB and 67.1° respectively. The position open loop transfer function is represented in Eq. (3).

$$P_{openloop}(s) = \frac{Z(s)}{E_p(s)} = \frac{P \cdot PI \cdot G(s)}{1 + PI \cdot G(s) \cdot V_{est}(s)} \quad (3)$$

3.3 Design of Nonlinear Function

This section discusses design of the nonlinear function that is embedded on the position loop of the cascade P/PI controller. The design process involved tuning of three control parameters, namely; sampling frequency (δ) which is set at 0.0005, maximum value of error (e_{\max}) of 0.5 and rate of variation of the nonlinear gain (KO). The values of KO1 and KO2 were set at 3.5 and 4.0 respectively. The related equations of the nonlinear function parameters are shown below:

$$KO = \begin{cases} 3.5 & \text{if } |e| \leq e_{\max} \\ 4.0 & \text{else } |e| < e_{\max} \end{cases} \quad (4)$$

$$\text{Nonlinear gain, } K_e = \frac{\exp(KO \times e) + \exp(-KO \times e)}{2} \quad (5)$$

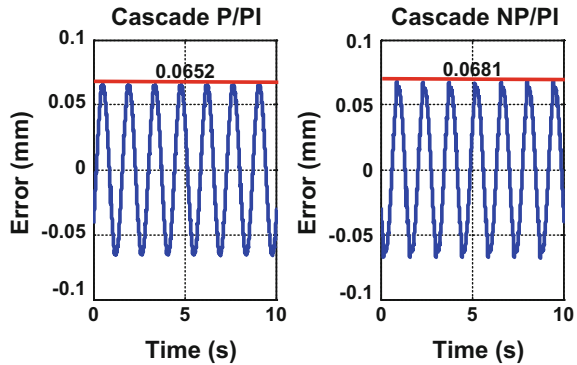
$$\text{Switching function, sigmoid } (e) = \frac{e}{|e| + \delta} \quad (6)$$

$$\text{Maximum Nonlinear Gain, } K(e_{\max}) = - \frac{1}{R_e + [G(j\omega)] + \omega^* I_m [G(j\omega)]} \quad (7)$$

4 Result and Discussion

For validation purposes and controller performances analyses, the designed controller was subjected to a sinusoidal input reference signal of amplitude 10 mm at 0.7 Hz. Figure 3 shows results of tracking errors for cascade P/PI controller and cascade NP/PI controller. The maximum tracking errors recorded by cascade P/PI and cascade NP/PI controller were 0.0652 mm and 0.0681 mm respectively. Cascade NP/PI controller shows greater maximum tracking error compared to cascade P/PI controller; suggesting a negative influence of the nonlinear function on the

Fig. 3 Tracking errors for cascade P/PI and cascade NP/PI controllers



controller performance. A closer analysis on the tracking errors of cascade NP/PI as shown in Fig. 4 reveals the existence of spikes at near maximum position, commonly associated with the presence of nonlinear friction at near zero velocity. This phenomenon then led to significant positioning error [17]. The magnitude of the spike was identified at 0.01 mm. Therefore, in-fact, the real maximum tracking error for the proposed cascade NP/PI controller was 0.0581 mm instead of 0.0681 mm.

A root mean square of the errors (RMS) produced a more balance conclusion regarding the controller tracking performance when compared to maximum tracking errors measurement. Here, the proposed cascade NP/PI produced an RMS errors value of 0.0453 mm compared to conventional cascade P/PI controller that produced an RMS error value of 0.0459 mm. The error reduction between the two controllers was 1.31%. Therefore, the experimental results have showed that the nonlinear function embedded on the position controller of cascade P/PI has managed to improve the tracking performance of the control system.

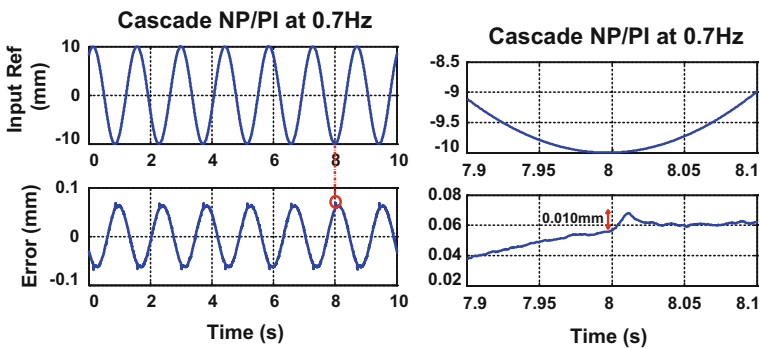


Fig. 4 Formation of significant spike

5 Conclusion

The paper presents design and validation of proposed cascade NP/PI controller for the x-axis of a XY table ball screw driven system. The controllers' parameters were tuned and designed in frequency domain based on open loop characteristics such as gain margin and phase margin. Meanwhile, the nonlinear function was designed based on three components that are KO , e_{\max} and δ . The tracking performances for both controllers were compared based on sinusoidal input reference signal of amplitude 10 mm at 0.7 Hz. Based on maximum tracking error, cascade P/PI controller has lower error compared to proposed cascade NP/PI controller that is 0.0652 mm and 0.0681 mm respectively. This is because the proposed controller was affected by friction produced during maximum position. However, the proposed cascade NP/PI controller produced an RMS error value that is 1.31% lower compared to the cascade P/PI controller. This proved that the nonlinear function of cascade NP/PI controller managed to produce an improvement in overall tracking performance of the control system.

Acknowledgements The authors would like to acknowledge the financial support by Universiti Teknikal Malaysia Melaka (UTeM) under the scholarship of 'Skim Zamalah UTeM' and Ministry of Higher Education of FRGS grant with reference number FRGS/1/2016/TK03/FKP-AMC/F00320.

References

1. Götze, U., Koriath, H.J., Kolesnikov, A., Lindner, R., Paetzold, J.: Integrated methodology for the evaluation of the energy and cost effectiveness of machine tools. *CIRP J. Manuf. Sci. Technol.* **5**(3), 151–163 (2012)
2. Albertelli, P.: Energy saving opportunities in direct drive machine tool spindles. *J. Clean. Prod.* **165**, 855–873 (2017)
3. Villegas, F.J., Hecker, R.L., Peña, M.E., Vicente, D.A., Flores, G.M.: Modeling of a linear motor feed drive including pre-rolling friction and aperiodic cogging and ripple. *Int. J. Adv. Manuf. Technol.* **73**(1), 267–277 (2014)
4. Strakos, P., Karasek, T.: Adaptive model predictive control as a prospect for control of machine tools with significant flexibility. In: *Proceedings of the International Conference of Numerical Analysis and Applied Mathematics 2014*, p. 830006 (2015)
5. He, Z., Fu, J., Zhang, X., Shen, H.: A uniform expression model for volumetric errors of machine tools. *Int. J. Mach. Tools Manuf.* **100**, 93–104 (2016)
6. Armstrong, B., Neevel, D., Kusik, T.: New results in NPID control-tracking, integral control, friction compensation and experimental results. *IEEE Trans. Control Syst. Technol.* **9**(2), 399–406 (2001)
7. Retas, Z., Abdullah, L., Salim, S.N.S., Jamaludin, Z., Anang, N.A.: Tracking error compensation of XY table ball screw driven system using cascade fuzzy P + PI. *Int. Rev. Autom. Control* **9**(5), 324–329 (2016)
8. Zhang, C., Chen, Y.: Adaptive tracking control of ball screw drives with load mass variations. *Proc. Inst. Mech. Eng. Part I J. Syst. Control Eng.* **231**(9), 693–701 (2017)
9. Fan, Y.H., Chen, C.E., Liao, H.W.: Design of an optimal PID controller by genetic algorithms for a pantograph type XY platform. *Key Eng. Mater.* **625**, 417–422 (2014)

10. Ibrahim, M., Salim, S.N.S., Kamarudin, M.N., Noordin, A.: Real time cascade PI control for position monitoring of DC brushed motor. *World Acad. Sci. Eng. Technol.* **60**, 983–987 (2009)
11. Abdullah, L., Jamaludin, Z., Jamaludin, J., Salleh, M.R., Bakar, B.Abu, Maslan, M.N., Chiew, T.H., Rafan, N.A.: Design and analysis of self-tuned nonlinear PID controller for XY Table ballscrew drive system. In: 2nd International Symposium on Computer, Communication, Control and Automation, vol. 845, pp. 419–422 (2013)
12. Rafan, N.A., Jamaludin, Z., Chiew, T.H.: Investigation on Tracking Performance of Adaptive Friction Compensation Using Cascade P/PI Controller at Low Velocity (2016)
13. Abdullah, L.: A New Control Strategy for Cutting Force Disturbance Compensation for XY Table Ball Screw Driven System. Universiti Teknikal Malaysia Melaka (2014)
14. Pintelon, R., Schoukens, J.: *System Identification: A Frequency Domain Approach*, 2nd Edn. Wiley (2012)
15. Abdullah, L., Jamaludin, Z., Maslan, M.N., Jamaludin, J., Halim, L., Rafan, N.A., Chiew, T. H.: Assessment on tracking performance of cascade P/PI, NPID and NCasFF controller for precise positioning of XY table ballscrew drive system. *Proc. CIRP* **26**, 212–216 (2015)
16. Abdullah, L., Jamaludin, Z., Chiew, T.H., Rafan, N.A., Yuhazri, M.Y.: Extensive tracking performance analysis of classical feedback control for XY stage ballscrew drive system. *Appl. Mech. Mater.* **229–231**, 750–755 (2012)
17. Rafan, N.A., Jamaludin, Z., Abdullah, L., Chiew, T.H., Mat Ali, M.: Review on friction compensation approach for machine tools application. In: International Conference on Design and Concurrent Engineering, Oct 2012

A Resonant Type AC Magnetometer for Evaluation of Magnetic Nanoparticles



Nazatul Sharreena Suhaimi, Mohd Mawardi Saari, Hamzah Ahmad, Mohd Rusllim Mohamed and Nurul Akmal Che Lah

Abstract Characterization of magnetic nanoparticles is crucial in order to optimize them for different applications requiring specific characteristics. In this article, we report a characterization system using AC susceptibility method. An AC magnetometer system which is composed of the induction coil and resonant capacitors is developed to evaluate the performance of the magnetic nanoparticles. The induction coil consists of excitation and detection coil. The excitation coil is designed with solenoid coils and fabricated with a Litz wire which is composed of 60 strands of copper wire with 0.1 mm diameter to reduce the increase of AC resistance at high frequency. The detection coil is designed to be a first-order differential coil which is used to reduce the environmental noise and cancel the excitation magnetic field. The detection coil is fabricated with a copper wire and it is placed at the center of the excitation coil. The excitation coil is connected to the resonant capacitors to cancel the reactant component and to permit the high magnetic field in the high-frequency region. The resonant capacitors are fabricated with multiple values of capacitors. When the developed system is in the resonant mode, the current flow is constant up to the frequency of 32.5 kHz. The developed system can evaluate the magnetic nanoparticles at different frequency responses. Using the developed system, it is shown that the Neel particles exist inside the solution of magnetic nanoparticles used in this study.

Keywords AC magnetometer • Magnetic nanoparticles • Coil

N. S. Suhaimi · M. M. Saari (✉) · H. Ahmad · M. R. Mohamed
Faculty of Electrical & Electronic Engineering, Universiti Malaysia Pahang,
Pekan Campus, 26600 Pekan, Pahang, Malaysia
e-mail: mmawardi@ump.edu.my

N. A. Che Lah
Innovative Manufacturing, Mechatronics and Sports Lab (iMAMS),
Faculty of Manufacturing Engineering, Universiti Malaysia Pahang,
Pekan Campus, 26600 Pekan, Pahang, Malaysia

© Springer Nature Singapore Pte Ltd. 2018
M. H. A. Hassan (ed.), *Intelligent Manufacturing & Mechatronics*,
Lecture Notes in Mechanical Engineering,
https://doi.org/10.1007/978-981-10-8788-2_9

1 Introduction

Magnetic nanoparticles are mostly applied in the biomedical areas such as *in vivo* imaging [1], magnetic hyperthermia [2], and magnetic immunoassay. There are different applications of magnetic nanoparticles requiring different characteristics of the magnetic nanoparticles. Therefore, the characterization of the magnetic nanoparticles is important. The characterization of the magnetic nanoparticles can be done by AC susceptibility [3], magnetic relaxation [4], and remanence measurement. In this paper, the AC susceptibility is used to characterize the magnetic properties of the magnetic nanoparticles. The AC susceptibility measurement can provide the information of size distribution, harmonics and magnetic anisotropy with a fast response to the measurement. Moreover, the use of a phase sensitive detector can permit a higher sensitivity. In this method, the excitation coil will apply an AC field to a sample and the detection coil will detect the AC response that produced by the sample [5]. During this process, magnetic relaxations such as Neel and Brownian relaxations can be observed. Neel relaxation occurs when the rotation of magnetic moment occurs within the nanocrystals while Brownian relaxation occurs when the particles are physically rotated and the magnetic moment is blocked at a certain direction [6].

For that purpose, an AC magnetometer system is developed to evaluate the performance of the magnetic nanoparticles. There are a few systems, that have been developed such Imego AC susceptometry using an ordinary induction coil technique [7]. This system is possible to measure the dynamic magnetic properties from 1 Hz until 10 MHz at a low excitation field of $H = 24$ A/m. There is also another system was reported that measure hysteresis loop in a high frequency region using an air-cooled Litz wire coil [8]. Since the magnetic nanoparticles are applied in different frequencies and excitation fields, an AC magnetometer that is able to characterize them in a wide region of frequency and excitation field is highly desired. This AC magnetometer can also serve as a standardization technique for magnetic nanoparticles.

In this article, to fulfill the aforementioned system, we have developed an AC magnetometer system using an induction coil technique for the characterization of the magnetic nanoparticles [9]. The induction coil is composed of an excitation and detection coils. The excitation coil is designed as a Helmholtz coil which has two solenoid coils aligned to be co-axial in a series configuration, separated with a 4 mm gap. The radius of the excitation coil is 15 mm. The detection coil is designed as a first-order differential coil. In order to achieve high homogeneity and sufficient amplitude of the excitation magnetic field, the excitation coil with resonant capacitors is developed [10]. The resonant capacitor is developed with the multiple values of the capacitors in order to achieve a resonant frequency up to 82.32 kHz. The capacitors are constructed in the series and/or parallel configuration. For this study, film capacitors such as polypropylene capacitors are used where they are capable to withstand high current and voltage.

2 Methodology

2.1 System Configuration

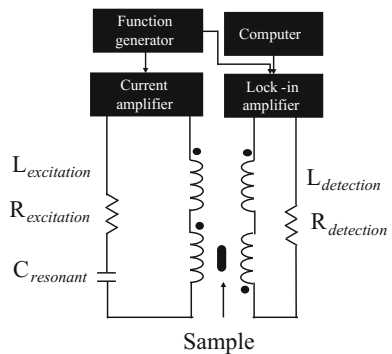
Figure 1 shows the system configuration of AC magnetometer with the resonant capacitor. The detection coil is inserted into the center of the excitation coil. The excitation coil is connected to a current amplifier (TS 250, Accel Instruments). The current amplifier will provide a high current to the excitation coil. The high current from the current amplifier is based on the reference signal that is supplied by the function generator of the lock-in amplifier (LI 5640, NF Corporation). The lock-in amplifier is used as a Phase Sensitive Detection (PSD) to detect the signal. When the high current flows through the excitation coil, the sample is magnetized. The magnetization of the sample can cause the sample to produce a magnetic field. The magnetic field of the sample is detected by the detection coil. The detection coil will send the signal to the lock-in amplifier and lock-in amplifier will send the signal to a computer.

2.2 The Design of Excitation Coil

The excitation coil is designed based on the Helmholtz coil configuration with two solenoid coils. The design of the excitation coil is referred to the Biot-Savart's law based on a multi-layer surface current model and can be expressed as;

$$\mathbf{B}(\mathbf{r}') = \frac{\mu_0}{4\pi} \sum_{n=1}^N \sum_{i=1}^S \frac{\mathbf{J}_n S_{i,n} \times (\mathbf{r}' - \mathbf{r}_n)}{|\mathbf{r}' - \mathbf{r}_n|^3}, \tag{1}$$

Fig. 1 The schematic diagram of the developed AC magnetometer system with resonant capacitors



where μ_0 is referred to the vacuum magnetic permeability, \mathbf{J}_n is the surface current density vector at n layer, $s_{i,n}$ is the surface unit area, \mathbf{r}_n is the position of the surface current and \mathbf{r}' is the position of the point observation. From the Eq. (1), it shows that the strength of the magnetic field can be high if the distance between the current element to the observation point is reduced and this is equal to the radius minimization of the excitation coil. The radius of the excitation coil should not be designed too big or small because it will give an effect to the reduction of the magnetic field uniformity area. However, the radius of the excitation coil must fit the diameter of the detection coil.

The excitation coil was fabricated of two solenoid coils which are connected in series and both solenoid coils are separated by a 4 mm gap. The excitation coil is fabricated from a Litz wire which is composed of 60 strands of the copper wire. The number of turn for each side of the coil is 150 turns. The length and radius of the coil are 26 mm and 15 mm. The resistance and inductance of the excitation coil were measured to be 1.3516 Ω and 1.5176 mH at 1 V and 1 kHz by a LCR meter (GW INSTEK LCR-816).

Then, the excitation coil will be connected to the resonant capacitor in a series connection and it will form an RLC circuit. The resonant capacitor is designed with the multiple values of capacitors. In the resonance mode, the capacitance can be calculated as;

$$C = \frac{1}{(2\pi f)^2 \times L}, \quad (2)$$

where f is the frequency and L is the inductance of excitation coil. From the RLC circuit, the resonant frequency can be calculated by manually selecting the values of capacitors. The range of the resonant frequency was set from 581 Hz to 82.32 kHz.

2.3 The Design of Detection Coil

The detection coil is designed as a first-order differential coil. The first-order differential coil is chosen because it can minimize the environmental magnetic noise and external magnetic field. The detection coil is composed of a copper wire with the diameter of 0.25 mm. The length and the radius of the detection coil are 19 mm and 7 mm. The number of turn for each side of the coil is 1000 turns and the detection coil was wound in the opposite direction for both sides of the coil [9]. The resistance and inductance of the detection coil were measured to be 41.456 Ω and 16.755 mH.

2.4 The Preparation of the Iron Oxide Nanoparticles as a Sample

The iron oxide nanoparticles (Nanomag-D102, Micromod Partikeltechnologie GmbH) with a median diameter 100 nm was used in the experiment. The iron oxide nanoparticles of D102 were prepared in two different environments such as liquid and dry states to evaluate their frequency response. The solution was filled inside a tube whose diameter is 7 mm and it will be placed at the center of one detection coil. For this experiment, the sample of D102 was prepared in 200 μl .

3 Result and Discussion

3.1 The Characteristic of the Excitation Coil

The distribution of magnetic field was determined by using a teslameter. The rod of the teslameter was moved through the excitation coil from 0 mm to 92 mm with the interval of 2 mm. Figure 2a shows the distribution line of the excitation magnetic field at the excitation coil with respect to the different positions of the teslameter. The magnetic field was uniform from the region of 30 mm to 60 mm which was from the center of one coil to the center of another coil and the magnetic field produced at the center was 5.22 mT/A. The result of measurement was compared to the result of the simulation. The simulation result showed the same value with the measurement result. The inhomogeneity in this region has been calculated to be 7%.

The small sample coil with 30 turns was fabricated to detect the magnetic signal at the detection coil. The small sample coil was moved along the detection coil from 0 mm to 72 mm with 2 mm interval. Figure 2b shows the magnetic signal of the

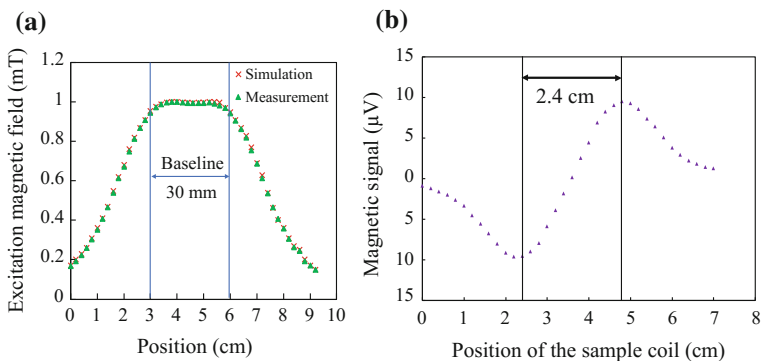
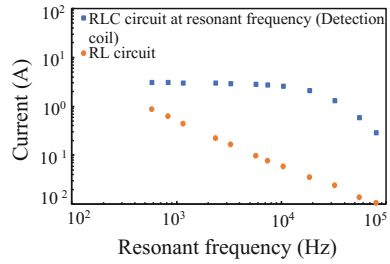


Fig. 2 **a** The distribution line of excitation magnetic field at the excitation coil with respect to the position of rod teslameter. **b** The magnetic signal of the detection coil with respect to the position of the small sample coil

Fig. 3 The intensity of current flow through the excitation coil with respect to the frequency



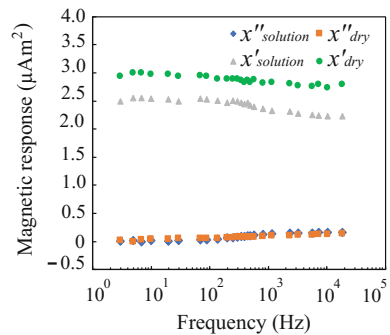
detection coil by moving the small sample coil along the detection coil. The highest magnetic signal was produced from the center of each coil. The distance between the first peak to the second peak was 24 mm which was the distance between the centers of each coil. The negative and positive magnetic signal produced by the detection coil was referred to the turn direction of each coil.

Figure 3 shows the result of the intensity of current flow through the excitation coil at different resonant frequencies. Before the resonant capacitor was connected to the excitation coil, the current flow through the excitation coil was decreased when the frequency was increased. Then, when the resonant capacitor was connected to the excitation coil, the current flow through the excitation was constant at 3 A until 32.5 kHz.

3.2 The Frequency Response of the Magnetic Nanoparticles in Dry and Solution State

Figure 4 shows the magnetic response produced by the D102 at different frequencies. In this experiment, two components such as χ' (in-phase magnetization) and χ'' (out-of-phase magnetization) were measured. For χ' , the magnetic response of the D102 in the solution state showed a same characteristic of the magnetic response that produced in the dry state, which it was constant over the frequency

Fig. 4 The magnetic response of the D102 with respect to the frequency



region. This was because the sample of D102 did not being affected by Brownian relaxation. For the χ'' , the magnetic response of the D102 is started to increase when the frequency is increased. This could be thought that D102 has undergone Neel relaxation.

4 Conclusion

In this work, an AC magnetometer system with resonant capacitors is developed. The AC magnetometer system is able to measure the magnetic response of the magnetic nanoparticles in the range of 3 Hz–32.5 kHz with the amplitude magnetic field per unit current at the center of 5.2 mT/A. The resonant capacitor with the multiple values of capacitance was developed to maintain the flow of current through the resonant circuit until the frequency reached 32.5 kHz. The developed AC magnetometer system was capable to evaluate the magnetic response of the magnetic nanoparticles based on the frequency response. The mechanism of Neel relaxation was observed for D102.

Acknowledgements This work was supported by Ministry of Higher Education of Malaysia under grant number of RDU 160115 and Research Management Center of Universiti Malaysia Pahang under grant number of RDU 170377.

References

1. Enpuku, K., et al.: Magnetic nanoparticle imaging using cooled pickup coil and harmonic signal detection. *Jpn. J. Appl. Phys.* **52**, 87001 (2013)
2. Sadiq, A.A., Othman, N.B., Jamil, M.M.A.: Magnetic Particle Imaging System For Cancer Diagnosis : An Overview, vol. 10, no. 19, pp. 8556–8561 (2015)
3. Ludwig, F., Balceris, C., Jonasson, C., Johansson, C.: Analysis of ac susceptibility spectra for the characterization of magnetic nanoparticles, vol. 9464, no. 3 (2017)
4. Ludwig, F., Heim, E., Schilling, M.: Characterization of superparamagnetic nanoparticles by analyzing the magnetization and relaxation dynamics using fluxgate magnetometers. *J. Appl. Phys.* **101**(11), 113909 (2007)
5. Youssif, M.I., Bahgat, A.A., Ali, I.A.: AC Magnetic Susceptibility Technique for the Characterization of High Temperature Superconductors, vol. 23, pp. 231–250 (2000)
6. Bogren, S., et al.: Classification of magnetic nanoparticle systems—synthesis, standardization and analysis methods in the nanomag project. *Int. J. Mol. Sci.* **16**(9), 20308–20325 (2015)
7. Ahrentorp, F., et al.: Sensitive high frequency AC susceptometry in magnetic nanoparticle applications. *AIP Conf. Proc.* **1311**, 213–223 (2010)
8. Connord, V., Mehdaoui, B., Tan, R.P., Carrey, J., Respaud, M.: An air-cooled Litz wire coil for measuring the high frequency hysteresis loops of magnetic samples—a useful setup for magnetic hyperthermia applications. *Rev. Sci. Instrum.* **85**(9) (2014)
9. Tumanski, S.: Induction coil sensors—a review. *Meas. Sci. Technol.* **18**(3), R31–R46 (2007)
10. Yang, T.Q., Enpuku, K.: SQUID magnetometer utilizing normal pickup coil and resonant-type coupling circuit. *Phys. C Supercond.* **392–396**, 1396–1400 (2003)

Optimization of Multi-holes Drilling Path Using Particle Swarm Optimization



Najwa Wahida Zainal Abidin, Mohd Fadzil Faisae Ab. Rashid
and Nik Mohd Zuki Nik Mohamed

Abstract In multi-holes drilling process, the tool movement and tool switching consumed on average 70% of the total machining time. Tool path optimization is able to reduce the time taken in machining process. This paper is focus on the modeling and optimization of multi-holes drilling path. The problem is modeled as traveling salesman problem (TSP) and optimized using Particle Swarm Optimization (PSO). To test the PSO performance, 15 test problems were created with different range of holes numbers. The optimization results from PSO were compared with other top algorithms such Genetic Algorithm and Ant Colony Optimization algorithm. PSO is also compared with another algorithm like Whale Optimization Algorithm, Ant Lion Optimizer, Dragonfly Algorithm, Grasshopper Optimization Algorithm, Moth-flame Optimization and Sine Cosine Algorithm. The result indicates that PSO algorithm is performed better than comparison algorithms. PSO algorithm gives the minimum value of fitness path and their CPU time compared to other algorithms. Hence, the smaller their value, the algorithm is better and more efficient. In future, researchers should more focus on environmental issues and energy consumption for sustainable manufacturing. Besides, need to explore other potential of new meta-heuristics algorithms to increase the hole drilling operation efficiencies.

Keywords Multi-holes drilling • Tool path • Particle swarm

1 Introduction

Multi-holes drilling is one of machining modes in Computer Numerical Control (CNC) milling for metal removal process [1]. Multi-holes drilling process takes a long time for manufactured part. Tool movement and tool switching time take 70%

N. W. Zainal Abidin · M. F. F. Ab. Rashid (✉) · N. M. Z. Nik Mohamed
Manufacturing Focus Group, Faculty of Mechanical Engineering, Universiti Malaysia
Pahang, 26600 Pekan, Malaysia
e-mail: ffaisae@ump.edu.my

© Springer Nature Singapore Pte Ltd. 2018
M. H. A. Hassan (ed.), *Intelligent Manufacturing & Mechatronics*,
Lecture Notes in Mechanical Engineering,
https://doi.org/10.1007/978-981-10-8788-2_10

of machining time in hole-making operation, on average [2]. Tool path optimization can lead to improve productivity and reduce non-productive machining time [3].

Tool path optimization is vital for improving and maintaining includes both aspect of manufacturing such productivity and quality in drilling process [4]. Tool switch scheduling and tool movement is the main issues in tool path optimization during hole-making process [5]. There are examples that applied in industrial products such as dies, molds, engine block with different size of holes, surface finishing and depth [6]. Besides, tool path optimization also can be used in milling, turret punching and laser cutting. As an example the tool path optimization is applied for printed circuit board (PCB) drilling based on previous research [7].

Travelling Salesman Problem (TSP) concept is the most widely used than precedence sequence and traveling cutting tool problem (TCP) [6]. Based on review paper, the optimization objectives is consists of minimize the travel distance, cutting time operation, cutting cost project, improve their efficiency, quality, productivity and different size of holes for drilling process [6]. To optimize the problem, the Particle Swarm Optimization that simulates the social behavior of bird flocking and fish schooling is used. The PSO is compared with different relatively new optimization algorithms including Whale Optimization Algorithm (WOA), Ant Lion Optimizer (ALO), Dragonfly Algorithm (DA), Grasshopper Optimization Algorithm (GOA), Moth-flame Optimization (MFO) and Sine Cosine Algorithm (SCA).

WOA for instance implements three mechanisms to mimic the search, encircling, and bubble-net foraging prey behaviour of humpback whales. The DA algorithm meanwhile simulates the static and dynamic swarming behaviours for the dragonfly insect. GOA on the other hand, models the grasshopper swarms in nature which considered the different phases in their life. The MFO utilized a transverse orientation mechanism for navigation by maintaining a fixed angle with respect to the light source to search for optimum solution. Meanwhile in the ALO five main steps of hunting prey; random walk, building traps, entrapment of ants, catching preys, and re-building traps are implemented.

This research is proposed to optimize the tool path in multi-holes drilling. In different with existing research that mainly focus to optimize uniform holes arrangement, this research will focus on irregular holes arrangement. In order to model the problem, TSP model will be implemented. TSP is a problem to find the shortest possible route that visits each city exactly once and returns to the origin city. In this work, a standard Particle Swarm Optimization algorithm will be implemented to minimize the non-machining time for the process.

2 Problem Modeling

The problem of multi-holes drilling path is modelled as a travelling salesman problem (TSP). TSP is implemented to find the shortest route of drilling paths. To solve the problem, the final path must be returned to the initial path. For example in

Fig. 1 Example of TSP problem

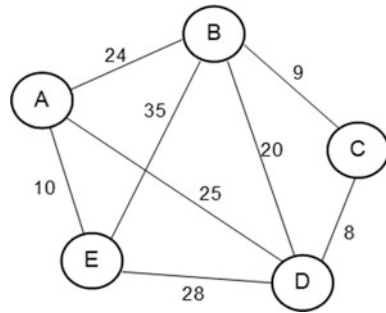


Fig. 1, the salesman begins their journey from point A to B, C, D, E and return to A. So the total distance is 79 km. For the same starting point, if the salesman moves to point A, D, C, B, E and return to A, the total distance is 87 km. In this case, the shortcut path is better in term of the journey distance. To model the problem, the following objective function is used.

$$F(x) = \sum_i^n \sum_j^n X_{ij} D_{ij} \tag{1}$$

$$\sum_{i=1}^n X_{ij} = 1, j = 1, \dots, n \tag{2}$$

$$\sum_{j=1}^n X_{ij} = 1, i = 1, \dots, n \tag{3}$$

$$D_{ij} = D_{ji} = \sqrt{(x_i - x_j)^2 + (y_i - y_j)^2} \tag{4}$$

where;

n , number of holes; D_{ij} , distance from point i to j ; $X_{ij} \in \{0, 1\}$; $X_{ij} = 1$, travel distance from point i to point j as part of the path that through on all the holes in the matrix;

$X_{ij} = 0$, the path does not travel from point i to point j as part of the tool path. Meanwhile, x and y are the Cartesian coordinates;

x_i , coordinate location of point i along the x -axis;

x_j , coordinate location of point j along the x -axis;

y_i , coordinate location of point i along the y -axis;

y_j , coordinate location of point j along the y -axis.

Equation (1) is the summation for all distances, between holes and chosen travel tool path. Equation (2) shows the set of constraints ensure that each hole j is only visited once in the path defined by X_{ij} . While Eq. (3), ensure the path coming out of every hole i move to one other hole, j . Equation (4) described the distance matrix as in-plane distance between node centres.

3 Particle Swarm Optimization

PSO is an algorithm to optimize a problem iteratively. PSO is trying to improve a candidate solution with regard to a given measure of quality. In this study, PSO algorithm is proposed for TSP model. PSO optimizes a problem by having a population of particles, and move these particles around in the search-space based on simple mathematical formulae over the position of particle and velocity.

In the beginning, the initial parameters are determined. The initial parameters are the particle number (n_p) and the maximum iteration ($iter_{max}$). Then, the initial position (X) consist of random number within 0 and 10 is created. At the same time, the random velocity (V) is also generated. As an example, Table 1 shows one of the particles from origin population is, $x_1 = [4.24 \ 2.15 \ 9.29 \ 3.44 \ 4.52 \ 6.51]$ and $v_1 = [2.00 \ 7.10 \ 2.30 \ 0.50 \ 4.08 \ 8.40]$.

The sequence of holes is sorted according to the x_1 value in descending order. For example, the largest x_1 value is belong to hole 3. Then it is followed by 6, 5, 1, 4 and 2. In the end, the tool path will return to the starting hole position. For this example, the path that being decoded from this approach is [3 6 5 1 4 2 3].

The function of predefined objective is to evaluate the feasible route. Then, the total summation of travelling time is defined as $t_{36}, t_{65}, t_{51}, t_{14}, t_{42}$ and t_{23} for $fr_1 = [3 \ 6 \ 5 \ 1 \ 4 \ 2 \ 3]$. The last one is to update the swarm position and velocity. The function is to establish new swarm set which is followed by the current best personal particle solution, P_{best} and best solution among all particles, G_{best} that appear in every iteration. The position and velocity is updated in PSO. As an example, the position and velocity is formulated as:

$$V_i(k + 1) = wV_i(k) + c_1(P_{best} - X_i(k)) + c_2(G_{best} - X_i(k)) \tag{5}$$

$$X_i(k + 1) = X_i(k) + V_i(k + 1) \tag{6}$$

$X_i(k)$ is the i th position at k th iteration, while $V_i(k)$ represents the i th velocity at k th iteration. The w on the other hand is the inertia coefficient, while c_1 and c_2 the cognitive and social coefficients.

Table 1 Position value of cities

Cities	1	2	3	4	5	6
x_1	4.24	2.15	9.29	3.44	4.52	6.51
v_1	2.00	7.10	2.30	0.50	4.08	8.40

4 Results and Discussions

A computational experiment was conducted to measure the performance of PSO to optimize making sequence. From our review, the range number of holes for drilling path is 50–150 approximately. Thus, the problems were classed into small ($n = 1–50$), medium ($n = 51–100$) and large ($n = 101–150$). The population size for all algorithms is set to 20 with maximum iteration is 300. Then, the optimization is repeat for 15 times with different pseudo-random seeds. The computational results of PSO algorithm is compared to other meta-heuristic algorithms as mention in Sect. 1.

Table 2 presents the average of the optimization results obtained from 15 runs. The number in bold shows the best value for the average fitness for a particular problem. Based on the observation from Table 2, the ACO algorithm performed better in small size problem. But when the size of problem increased to medium, the PSO algorithm have shown better performance in four out of five problems in term of average fitness. The best PSO performance is observed in the large size problem, with the best average fitness in all problems. Overall, the proposed PSO came out with the majority of the best minimum and average fitness. This is followed by the ACO and GA algorithms.

PSO performance is also compared with other algorithms such MFO, WOA, ALO, DA and SCA algorithms. Between the five other algorithms, MFO shows the better performance in small and medium size problems after ACO and GA algorithms. Meanwhile, for large size problem, WOA have shown better performance in three out of five problems in term of average fitness after ACO and GA algorithms. Then, this is followed by ALO, DA and SCA algorithms for all problems.

Table 2 Computational experiment results

Problem	GA	PSO	ACO	WOA	ALO	DA	MFO	SCA
1	1277	1214	1047	1196	1248	1332	1128	1146
2	189	180	131	188	192	227	173	211
3	2772	2720	2007	3096	3110	3449	2516	3516
4	3683	3510	3063	3908	3928	4642	3412	4840
5	4280	4244	4815	4948	4978	5861	4306	6146
6	5683	4990	6101	6069	6001	7148	5374	7364
7	7097	6038	6773	6888	7028	8202	6211	8641
8	10198	6755	8242	8249	8489	9765	7387	10395
9	7737	7797	10353	8872	10221	11123	8971	11767
10	12330	8681	11563	10423	10820	12329	9890	13118
11	11762	9324	14082	11634	11967	13670	10782	14505
12	12064	11290	15223	12387	14021	14771	11820	15369
13	15266	11368	15602	12952	14436	16310	13258	16932
14	17998	13954	18474	14143	16296	18170	14910	19007
15	18841	13393	18365	14843	16436	18225	15079	19352

This result indicated that the new algorithms were not suitable for the discrete combinatorial optimization problem. For the further investigation, the focus should be given to the well-established algorithms.

5 Conclusions

This paper aims to optimize multi-holes drilling path using Particle Swarm Optimization (PSO). The problem is modeled as a Travelling Salesman Problem (TSP). TSP is classified as NP-hard combinatorial optimization problem, which cannot be solved in polynomial time. PSO is developed to optimize the hole making sequence. PSO as meta-heuristic algorithm which capable to search for real optimum solution in shortest computational time. 15 test problems consisted of different number of holes, n had been used to measure the performance of algorithms. PSO is compared with seven algorithms including Genetic Algorithm (GA) and Ant Colony Optimization (ACO). The optimization results indicated that the proposed PSO approach had outperformed the best performance in all problems.

This finding is related to the simple mechanism in PSO that make this algorithm converge faster towards the optimal solution. Besides, the divergence of the search direction in PSO also contributed to the promising performance. Later, a machining experiment will be conducted to validate the optimization results. As suggestion, continuous effort to explore more new meta-heuristics algorithms to improve their efficiencies. Besides, researchers also need to consider environmental issues and energy consumption for sustainable manufacturing.

Acknowledgements This research is funded by Universiti Malaysia Pahang under grant number RDU160356.

References

1. Tamta, N., Jadoun, R.S.: Parametric optimization of drilling machining process for surface roughness on aluminium alloy 6082 using Taguchi method. *J. Mater. Environ. Sci.* **2**(7), 49–55 (2015)
2. Lim, W.C.E., Kanagaraj, G., Ponnambalam, S.G.: A hybrid cuckoo search-genetic algorithm for hole-making sequence optimization. *J. Intell. Manuf.* (2014)
3. Setiawan, K., Tambunan, S.T.B., Yuliana, P.E.: Adjustment of mill CNC parameters to optimize cutting operation and surface quality on acrylic sheet machining. *Appl. Mech. Mater.* **377**, 117–122 (2013)
4. Tufail, P.M.S.: A review on optimization of drilling process parameters of AISI 304 austenite stainless steel by using response surface methodology. *Procedia Eng.* **4**(2), 402–405 (2016)
5. Dalavi, A.M., Pawar, P.J., Singh, T.P., Warke, A.S., Paliwal, P.D.: Review on optimization of hole-making operations for injection mould using non-traditional algorithms. *Int. J. Ind. Eng. Manag.* **7**(1), 9–14 (2016)

6. Zainal Abidin, N.W., Ab Rashid M.F.F., Nik Mohamed N.M.Z.: A review of multi-holes drilling path optimization using soft computing approaches. *Arch. Comput. Methods Eng.* **0**(0), 0 (2017)
7. Dalavi A.M.: Optimal sequence of hole-making operations using particle swarm optimisation and shuffled frog leaping algorithm. In: 8th International Conference on Intelligent Systems Design Application, vol. 36, no. 2, pp. 187–196 (2016)

Development of 3D Printed Heart Model for Medical Training



Khairul Shah Affendy Yakof, Nor Fazlin Zabudin, Idris Mat Sahat and Mohd Azrul Hisham Mohd Adib

Abstract Three-Dimensional (3D) printing is emerging as an enabling technology for a wide range of new applications. This study focuses on the medical application of 3D printer using basic fundamental 3D printing mechanisms. The objective of this study is to develop a heart model with specific requirements for medical training using Flyingbear P902 3D printer and Flex Thermoplastic Polyurethane (TPU) filaments as the depositing materials. The study involved two trials with the same operation procedure and 3D printer specifications. The first trial utilized non-transparent TPU filament and the second trial utilized transparent TPU filament. The application of this technology in developing a heart model was evaluated based on the requirements fulfilled by both printed heart models in both trials. The problems (such as inflexibility and less transparency), limitations and proposed solutions are discussed. The emergence of cardiovascular diseases such as congenital heart disease, coronary artery disease, surgical and catheter-based structural disease make 3D printing a new tool to design, plan and carry out challenging cardiovascular interventions.

Keywords 3D printing · Coronary artery · Heart model · Transparent filament · Thermoplastic polyurethane (TPU)

1 Introduction

3D printing technology, also known as rapid prototyping (RP) is the technique used to build structures of arbitrary geometries by depositing printing material in successive layers on the basis of digital design under the computer control [4].

K. S. A. Yakof · N. F. Zabudin · I. Mat Sahat · M. A. H. Mohd Adib (✉)
Medical Engineering & Health Intervention Team (MedEHiT), Human Engineering Group,
Faculty of Mechanical Engineering, Universiti Malaysia Pahang, Pekan, Malaysia
e-mail: azrul@ump.edu.my

© Springer Nature Singapore Pte Ltd. 2018
M. H. A. Hassan (ed.), *Intelligent Manufacturing & Mechatronics*,
Lecture Notes in Mechanical Engineering,
https://doi.org/10.1007/978-981-10-8788-2_11

Development in rapid prototyping technology has opened up new opportunities in the advancement of medicine when combined with medical imaging [1]. This technique has been applied in dentistry, plastic surgery, orthopaedics [5] and cardiovascular diseases such as congenital heart disease, coronary arteries disease and mitral valve disease [2, 6]. Although the use of 3D printing in cardiovascular treatment is still relatively new, advancement in this discipline is occurring at a rapid rate that a contemporary review is warranted. In medical industry, 3D printing provides touchable structures to be used by trainee doctors prior to treating real patients and allows procedures to be planned without having to directly inspect the patient [2].

Realizing on its huge potentials in medicine, 3D printing technology is applied in this study to develop a heart model for medical training. Hollow, transparent and flexible are the specific requirements set for the heart model. Other than that, it was also designed to have coronary arteries surrounding its surface. Coronary arteries study is vital since it contributes to the highest percentage of the overall heart disease known as coronary artery disease (CAD). Atherosclerosis is the most common CAD that involves blood blockage due to the plaque deposit in the arteries [3]. For that matter, catheter insertion procedure through the narrow arteries is the medical training intended from the heart model development. The training is beneficial for familiarizing with coronary arteries intricacy before conducting real surgery. It thus reduces the risk of treatment failure significantly.

1.1 3D Printer Technology

Fused Diffusion Modelling (FDM) 3D Flyingbear P902 printer was used in this study. The printer specification is shown in Table 1.

Fabrication speed, resolution, quality, cost, build volume, surface finish and part strength are the parameters involved in additive manufacturing (AM) process of 3D printer. Among these parameters, fabrication speed and resolution are the most critical properties.

1.2 Transparent Flexible Filament

The Magma Flex TPU Transparent Filament (thermoplastic elastomer) is used in this study to create a flexible and transparent heart model. This is a family of plastics that can be melted and shaped via FDM process and has similar characteristics to rubber. This type of filament is chosen to fulfill the flexibility (high strength, high elongation at break and high elasticity) and transparency requirement of the heart model. Table 2 shows the specification of the material used.

Table 1 Specification of flyingbear P902 3D printer

Brand	Flyingbear P902
Print size	220 × 220 × 280 mm
Layer thickness	0.05 mm
MAX printing speed	150 mm/s
Material type	PLA, ABS, PETG, Wood, PVA, Flexible Filament
Material specification	1.75 mm in diameter
Positioning accuracy	Z 0.004 mm, XY 0.012 mm
Nozzle diameter	0.4 mm
Recommended extruder temperature	210 °C (the maximum 260 °C)
Hot bed temperature	60–110 °C
Best ambient temperature	≥ 25 °C
Power requirements	110 V/220 V, 250 W, 50 Hz, 0.89 A
Connection	SD card or USB
File print format	STL, G-Code
Compatibility	Windows, Mac
Slicing software	Cura, Repetier-host
Machine weight	10 kg

Table 2 Specification of magma flex TPU filament transparent material

Material type	Flex TPU/transparent
Print temperature	200–230 °C
Heated bed temperature	50–60 °C
Length	335 mm
Diameter	1.75 mm ± 0.03 mm
Recommended printing speed	20/60 mm/s

Flexible filaments however, are inherently harder to print than rigid filaments since they are easily tangled into the extruder, having a harder time to be pushed and pulled by the motors and to be retracted during the printing process.

2 Procedure

The flowchart in operating 3D printer is shown in Fig. 1. 3D heart model was firstly designed using computer-aided design (CAD) software called Solidworks 2013 × 64 Edition as shown in Fig. 2a.

The file of the complete 3D model design from CAD software was converted to Stereolithography (STL) format. Upon conversion, the STL file was transferred to Ultimaker Cura 3.0.4 to create the tool path on the build platform. This process allowed support structure to be formed and the model scale to be changed

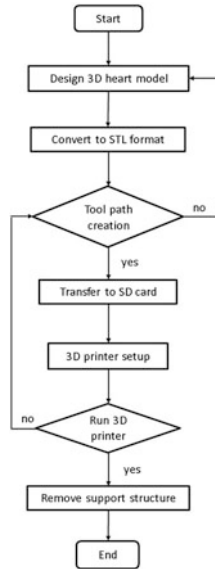


Fig. 1 Flowchart of the 3D printer operation

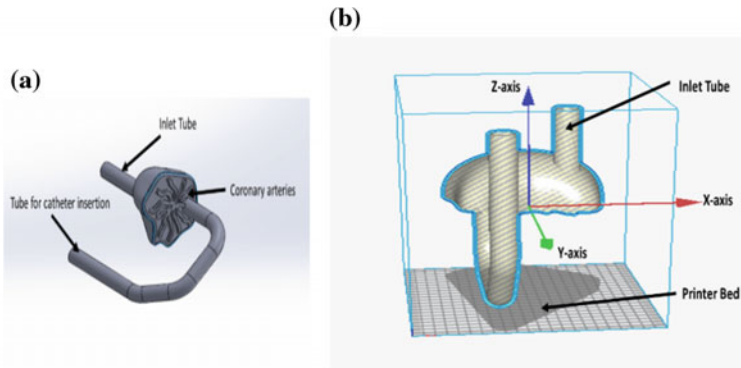


Fig. 2 a Development of heart model using solidworks. b Tool path creation using Ultimaker Cura 3.0.4

accordingly as shown in Fig. 2b. The output was then saved in the Secure Digital (SD) memory card to be transferred to the 3D printer. The specifications shown in Tables 1 and 2 were set to the 3D printer.

After the specifications were properly set and the filament was inserted into the extruder, the machine was run automatically as shown in Fig. 3b. Each layer was laid successively until the heart model including the support structure was completed. Each layer printed was about 0.3 mm in thickness (the thickness is

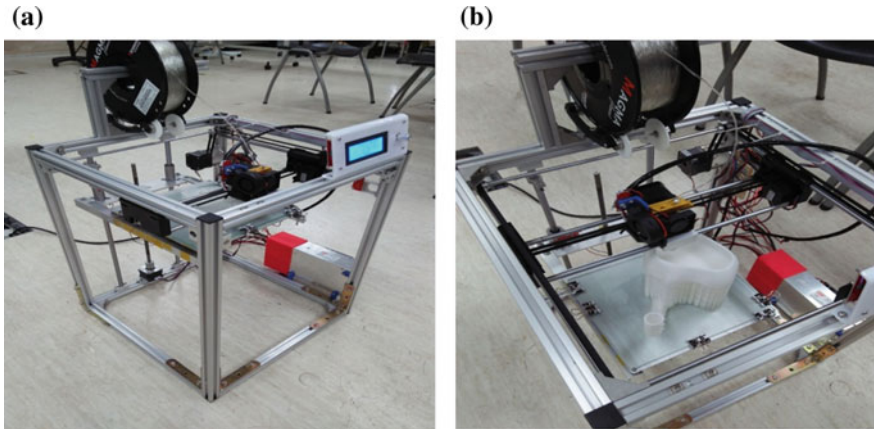


Fig. 3 a The setup of 3D printer. b 3D printing in progress

adjustable) for both heart models. The machine in progress was monitored from time to time to ensure no errors were made.

The printed object was removed from the platform after the printing was complete and was allowed to properly set before removing the support structure.

3 Result and Discussion

The attainment extent of 3D printing technique in developing a heart model was evaluated based on the number of specific requirements fulfilled by the heart models. The purpose of having flexibility and elasticity are to allow the heart structure to beat rhythmically at a specific rate range. The chamber and coronary arteries are required to be hollowed to allow air flow, fluid flow and catheter insertion practice. Transparency is compulsory for observing fluid flow structure formed inside the heart chamber and also for catheter insertion practice. This study was conducted in two trials. The first trial used non-transparent flexible filament as the printing material. Transparency and coronary arteries features were not yet considered at this stage. The second trial was the improved version of the first trial using a more flexible and transparent material.

3.1 Heart Model Using Non-transparent Flexible Filament

The first heart model was successfully printed without any disturbance during the printing process. The product is shown in Fig. 4. The model however had defect in term of flexibility or elasticity despite of the flexible material used. As a result, the

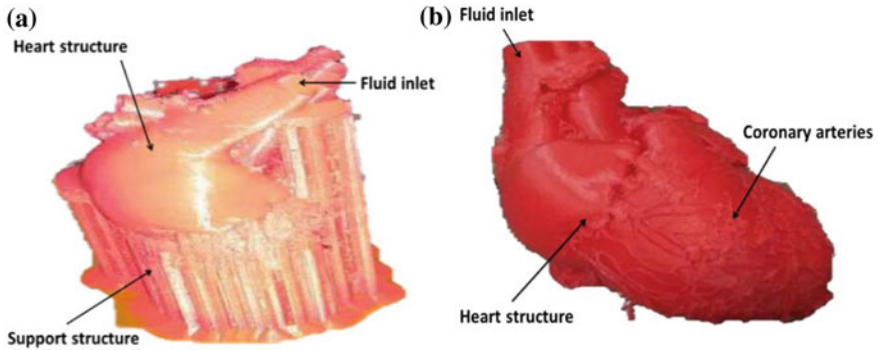


Fig. 4 a Printed heart model with support. b Printed heart model without support

heart model was unable to beat and act as a pump. In addition, the size formed was insufficient for use in medical training and the heart chamber was fully filled with the support structure instead of being hollowed. Leakage was another unexpected problem because of the thin heart wall. In other words, all of the requirements set above were not yet fulfilled in the first trial. Inflexibility was due to the less suitable material used while size insufficiency and support structure formation inside the heart chamber were due to the wrong setting at the tool path creation stage. These problems were improved by designing a new heart model using CAD software (Solidworks), replacing previous printing material with a more flexible and transparent material and obtaining the right size and support structure formation from the tool path creation program.

3.2 Heart Model Using Transparent Flexible Filament

The next model was designed to include a new feature: hollowed coronary arteries. Magma Flex TPU Flexible Filament Transparent (with a more flexible and transparent features) was used instead, to replace the previous material. The Tool Path creation setting using Ultimaker Cura 3.0.4 was properly set to obtain the right size product and to avoid unnecessary support system formation. Based on the improvements done above, the second version of the printed heart model had improved in term of size and had successfully fulfilled hollowed chamber and hollowed coronary arteries requirements.

The second version of the heart model nevertheless, was still less flexible and less transparent. The tiny holes formed as labelled in Fig. 5a are due to the small gap formed between the artery plane and the main curve on the surface fill as a result of the defect from the designing phase. This small defect however led to a serious leakage problem. The leakage would cause the pressure applied to be disturbed. Without the right pressure, the heart model was unable to beat

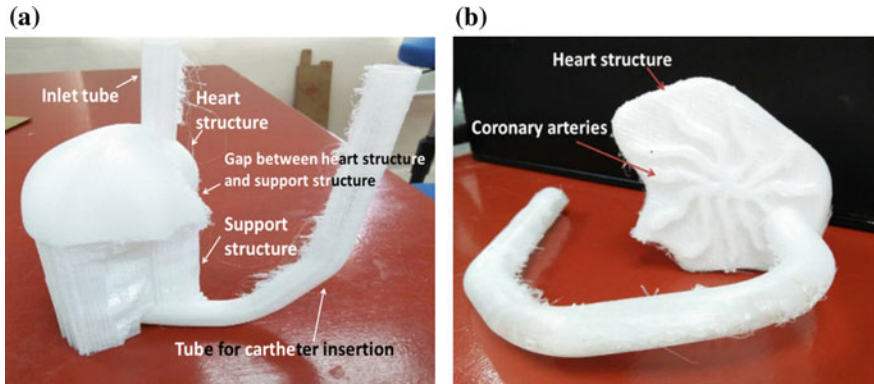


Fig. 5 a Transparent heart model with support. b Transparent heart model without support

rhythmically. Another new problem faced in the second trial was in the support structure removal. Coronary arteries structures were situated in between the heart surface and the support structures. Removing the support mechanically needed to be done carefully and delicately, to avoid damaging the arteries structure. Support structure is essential for creating certain geometries with overhangs in FDM since the melted thermoplastic was unable to be deposited in thin air. Surfaces printed on the support structure usually have low surface quality than the rest of the model. This can be observed in Fig. 5b.

The analysis of the problems shows that, printing three-dimensional heart model was challenging and would require multiple steps of improvements before the desired model could be achieved. Unlike other objects, medical objects usually have complex geometries and materials. There are a few suggestions for further improvements in the future. The stiffness and opaqueness were planned to be reduced by reducing the thickness of the model or by using a much more flexible material such as silicon. The serious leakage problem will be sealed by fixing the heart model design. The support structure issue will try to be resolved by using water-soluble support or the model is designed in such a way to minimize the need for supports. The usage of better versions of 3D printer or moulding techniques are also considered for future improvements.

4 Conclusion

This study investigates the application of 3D modelling and printing technology in the context of heart model. Based on the investigation, various factors need to be properly considered when printing complex medical objects especially the type of the materials used (for both model and support structure), the model design, the specifications, setting and also the type of 3D printer used. Other than technical

issues, the application has limitations in term of commercialization. 3D printing is not competitive due to the high printing costs per part and counter to common perception, 3D printing involves considerable pre- and post-processing, which incur non-trivial labor costs. Furthermore, the process involves certain printable 3D files such as STL. An electronic CAD drawing only is not sufficient. Currently, there is no way to automatically convert the CAD drawing into a 3D file. Lastly, creating printable files involves two tacit steps: creating a three-dimensional volume model that can be printed and ‘slicing’ the model volume in the best possible way to avoid material wastage and prevent printing errors. However, it is suggested that, with further advances in 3D printing, it may serve as a useful clinical tool with the potential to benefit both engineers and medical doctors.

References

1. Banoriya, D., Purohit, R., Dwivedi, R.K.: Modern trends in rapid prototyping for biomedical applications. *Mater. Today Proc.* **2**, 3409–3418 (2015). <https://doi.org/10.1016/j.matpr.2015.07.316>
2. Birbara, N.S., Otton, J.M., Pather, N.: 3D modelling and printing technology to produce patient-specific 3D models. *Heart, Lung Circ.* 1–12 (2017). <https://doi.org/10.1016/j.hlc.2017.10.017>
3. Ceponiene, I., Nakanishi, R., Osawa, K., Kanisawa, M., Nezarat, N., Rahmani, S., Kissel, K., Kim, M., Jayawardena, E., Broersen, A., Kitslaar, P., Budoff, M.J.: Coronary artery calcium progression is associated with coronary plaque volume progression: Results from a quantitative semiautomated coronary artery plaque analysis. *JACC Cardiovasc. Imaging* (2017) (In Press, Corrected Proof)
4. Martelli, N., Serrano, C., Brink, H.V.D., Pineau, J., Prognon, P., Borget, I., El Batti, S.: Advantages and disadvantages of 3-dimensional printing in surgery: a systematic review. *Surgery* **159**, 1485–1500 (2016). <https://doi.org/10.1016/j.surg.2015.12.017>
5. Vukicevic, M., Mosadegh, B., Min, J.K., Little, S.H.: Cardiac 3D printing and its future directions. *JACC Cardiovasc. Imaging* **10**, 171–184 (2017). <https://doi.org/10.1016/j.jcmg.2016.12.001>
6. Wang, J.Z., Li, Z.Y., Zhang, J.P., Guo, X.H.: Could personalized bio-3D printing rescue the cardiovascular system? *Int. J. Cardiol.* **223**, 561–563 (2016). <https://doi.org/10.1016/j.ijcard.2016.08.208>

Investigating the Influences of Automated Material Handling System (AMHS) and Effect of Layout Changing in Automotive Assembly Process



Seha Saffar, Zamberi Jamaludin and Fairul Azni Jafar

Abstract The material handling equipment adds utilization to the performance level of the manufacturing process. Thus, by investigating the influences of AMHS and at the same time seeing the effect of changing its layout in automotive assembly process help the research in improvising the system easier and guaranteed to be success. A case study focus at the material flow of warehouse to assembly shop is done and the result show the work is done manually and has a lot of time are wasted. From the case study, an approach tool are used to simulate the system by using Delmia Quest simulation software. 4 models are simulated which consist of AGV and tigger train as transportation system, 2 layouts which are the current used layout in case study and new layout, and the supply order system which are picking list and pick-to-light system. The result shows the number of part deliveries highly increase by the changed of layout in the system in model 4. The deliveries able to achieve 3 times value from the current old system in the factory. As the system improves with the change of supply order system and layout in model 3 and 4, the idle time reduce to below 0.5 h and maintain linearly in the system. Lastly, it can be summarized that the improvement shows the influences of automated material handling system and facility layout in increasing the performance of the automotive assembly factory.

Keywords AMHS • Factory layout • Delmia quest

S. Saffar

Centre of Graduates Studies, Universiti Teknikal Malaysia Melaka,
76100 Hang Tuah Jaya, Durian Tunggal, Melaka, Malaysia
e-mail: M051420004@student.utem.edu.my

Z. Jamaludin (✉) • F. A. Jafar

Faculty of Manufacturing Engineering, Universiti Teknikal Malaysia Melaka,
76100 Hang Tuah Jaya, Durian Tunggal, Melaka, Malaysia
e-mail: zamberi@utem.edu.my

F. A. Jafar

e-mail: fairul@utem.edu.my

© Springer Nature Singapore Pte Ltd. 2018

M. H. A. Hassan (ed.), *Intelligent Manufacturing & Mechatronics*,
Lecture Notes in Mechanical Engineering,
https://doi.org/10.1007/978-981-10-8788-2_12

1 Introduction

The Material Handling Industry of America (MHIA) define Material handling involves the movement, storage, control and protection of material throughout the process of manufacturing which covers the consumption, disposal, and distribution [1]. Material handling can affect 80% of production activity by which 50% of the company operation costs are material handling costs [2, 3]. By having the right quality of material at the right moment and the right place, production effectiveness can be increased [4]. In addition, the direct cost of material handling cannot be measured where it does not directly add to the finished product [5]. The most important part of manufacturing and distribution is the effectiveness of material handling in order to turn the product into profit.

Aim to have income in product make technology and automated system in high demand and the trend to optimize the material handling system is arising. Current topic such as insufficient material handling [5], old technology implementation [6], separation of production system and material handling system can cause various problems in term of cost and time consuming [7]. Thus, the gap of problem is research in between the tolls or the platform that integrates between method of material supplies in production line and the inventory system in warehouse.

Based on case study observation done in automotive factory, the production background is begin from logistic warehouse to body shop, paint shop and lastly is assembly shop where the painted body is assemble in three main stations which are trim line, chassis line and final assembly line. The process during assembly is done by semi-auto processes that involve manual and auto system. The current layout of assembly line is called old layout as show at Fig. 1 state the transportation track from warehouse to assembly line which are called trim line and chassis line. This research work only focus on chassis line which consist of 10 stations with different process and part supplies. In addition, Fig. 2 shows the distance travelled from warehouse to assembly line. In assembly line, each process have their own stations and each station is not fixed with only one process. It involves assembles of 3–4 types of different parts for each stations. Basically, the distance travelled is according movement of transportation from pick-up point at warehouse and return back to its starting point in order to have a total distance travelled in 1 cycle of working hour.

Studies at the assembly shop showed that the process flow of material from warehouse to assembly line is done fully manually. Based on the case study, the current transport equipment that is used to transfer parts is manually driven ‘tugger’ truck called easy-go truck. The truck function is to pull mother trolley and transfer part from warehouse to every station in assembly process. In order to see the improvement that can be made by automated material handling, this research work recommended to change the manual drive truck into automated guided vehicle, AGV. The automated transport equipment is chosen based on the suitable demand to bring the mother trolley to assembly line.

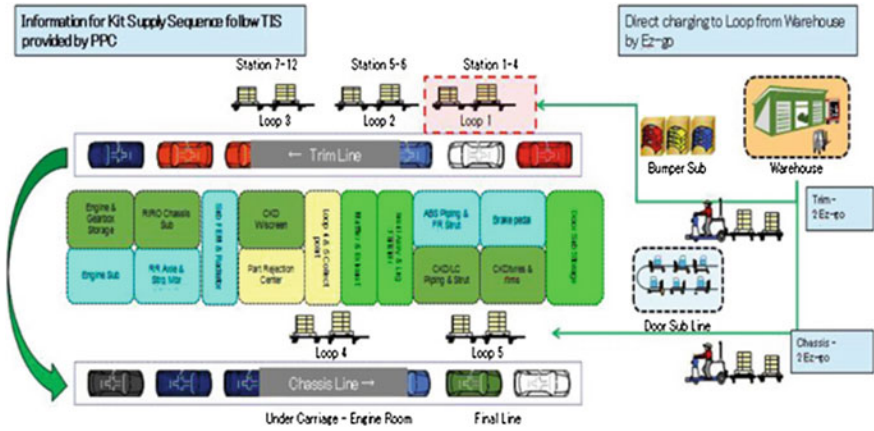


Fig. 1 Old layout of case study factory

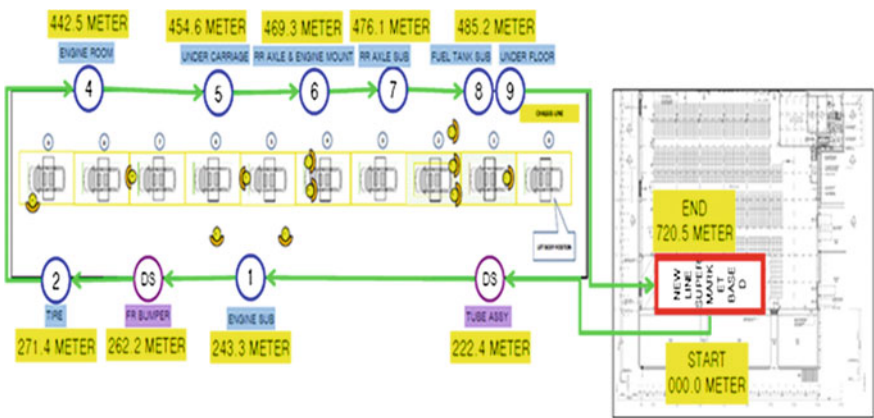


Fig. 2 Measurement of old layout in chassis line

The case study storage equipment that’s currently used is storage bin and rack in warehouse. Meanwhile storage for part handling during distribution process is called kit supply and was put inside mother trolley which was pulled by tugger truck. The picking list method is applied, where so called ‘Maruka’ concept in Japanese is implemented by workers to pick component and place in the kit. Its purpose is to simplify the operators work and easy for unskilled operators to do their work. But, this method took a lot of time to order and transfer the material.

All the parts in the kit need to be placed inside the cart and into mother trolley as shown in Fig. 3 and brought directly to the assembly line through easy-go cart which drive by workers. Thus it took time in trafficking the material and high risk of damage (either human or material) when transfer the material. The pick-to-light



Fig. 3 Mother trolley carry carts in plant layout of actual automation factory

system is recommended to replace the old picking list system from the case study. Pick-to-light system guided worker to pick specific parts for different variances. The necessary picking information is show on small display boards. Each variants has individual identification displays, acknowledgement button with digital display for indicating quantity.

The main purpose of this study is to assess the influences of automated material handling system and at the same time seeing the effect of changing its layout in automotive assembly process. A design on the integration system that is comparable with current system of material handling system in the automotive industry will be done through simulation and analysis of the influences of the new system with the conventional system will be done in order to achieve the main objective.

2 Materials and Methodology

This section explained the process flow of this research as shown in Fig. 4, starting from phase 1 which consist of literature review and preliminary data gathering. This phase is meant to understand the research problem and assess data from case study in real automotive manufacturing environment. Phase 2 is to design and propose a new material handling system.

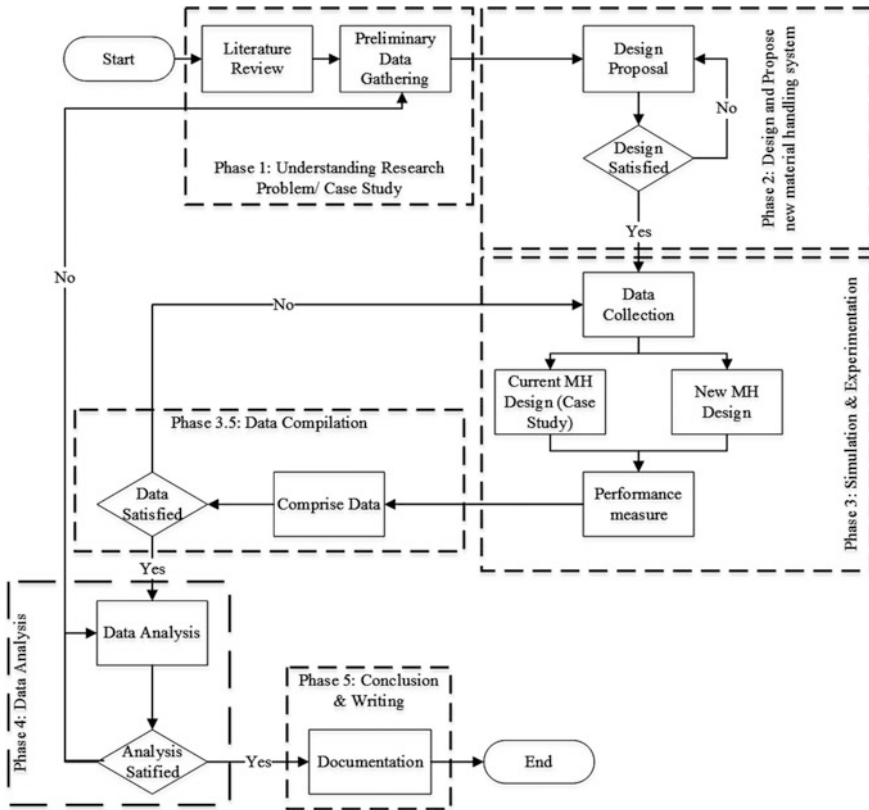


Fig. 4 Overall research process flow [9, 10]

The design process flow is using a stand product design and development where it involves the process of creating a concept too concept selection and concept proposal. In this phase, a decision block is put in order to have satisfaction design so that the process can only be proceed to the next phase. After that, phase 3 is where the experiments is conducted and phase 3.5 and 4 is where the result is compiled and analyse. Lastly, the documentation phase where the process of writing is done.

In order to see the result of the system, the material handling system and the layout need to be replaced from the current system. Thus, by doing so a simulation is a suitable method to avoid wasting the resource and consume a lot of time. Simulation modelling is an effective tools used in addressing and challenging issues to become more flexible, feasible and provide infinite integration of various simulation method [8].

Delmia Quest software is the selected software to use in this research. Its aim to prepare, setup and perform the simulation for this research. Delmia Quest simulation software able to conduct the design system without destroying in a factory of disturbing the system and enable the users to experience the process of the target equipment.

2.1 Variation of Factors and List of Models

The preliminary data gathering shows the collection of data from case study of real industry situation. The data involves plant layout from warehouse too assembly line, travel distance, distance between each station, parts involved in the process and their material handling equipment used during the transfer process. The current layout used in the factory shows the transportation track from warehouse to assembly line which consist of few workstations. Certain models contains same and different material handling system and layout.

The factors focused in this research experiments are type of layout, transport equipment, and storage equipment. Table 1 describe the variation of factors used for the experiments. Noted, that model 1 is similar process used in the case study factory. Model 2 aims to study the influence of automated guided vehicle replacing the tugger train transportation.

Meanwhile, model 3 purpose is to observe the influences of new supply order system which is pick-to-light replacing the old current picking list system. Lastly, model 4 hold the purpose of studying the new layout effect together with the improved material handling system to the whole system performance. The comparison between all models is to show the significant effect of the improved AMHS and layout too the system. The validation of all models is when all the system are capable to function similarly to the real case study factory.

Table 1 The list of models and variation of factors used in experiments

Models	MHS configuration		
	Layout	Transport equipment	Storage equipment
Model 1	Old layout	Tugger train	Picking list system
Model 2	Old layout	AGV	Picking list system
Model 3	Old layout	AGV	Pick-to-light
Model 4	New layout	AGV	Pick-to-light

2.2 Simulation Decision Point for Each Models

In Quest, transport and labor elements loading and unloading parts at decision point where the parts from other elements may enter and exit the path system only through the decision points. In addition, traffic management of AGVs' and trains' stopping point is also at decision point. Process logic defined the behavior of the decision point and the decision point able to make their own decision making logics acting as local controller. Basically, if there is no local decision making involved, the decision making is passed to the AGV and labor controller.

AGV and tugger train

In this research work, the decision point for AGV and train will divided into 2 sections covers 4 models used in the experiment. Section 1 consist of model 1 and 2, where their path system and decision point is created similar with case study's transportation path system. For model 4, the path system is a bit different due to the different layout and application of pick-to-light system in their warehouse. In Table 2, show the list of decision point for model 1 and 2. It consist of 10 decision points at assembly line and function as the parts drop-off point and 1 decision point at warehouse and function as the parts pick up point.

All the decision point were located on the path system at every assembly and warehouse part entry point. As illustrates in Fig. 5, the red-cross mark is the decision point location in model 1 and 2.

The list of decision point for model 3 is shown in Table 3 and model 4 in Table 4. It consist of decision point at assembly line as much as 8 drop off points and 7 pickup points at warehouse. Also as illustrates at Figs. 6 and 7, the location of decision point for model 3 and 4 is much differ from model 1 and 2. Due to the different layout and storage system applied in both sections make the path and behavior of the AGV and train a bit different.

Table 2 List of AGV and train decision points for model 1 and 2

Position	Decision points	Name of stations
Assembly line	AGV_Dec_Pt2	Station 1: Engine Sub 1
	AGV_Dec_Pt3	Station 2: Engine Sub 2
	AGV_Dec_Pt4	Station 3: FR Bumber and Axle Sub
	AGV_Dec_Pt5	Station 4: RR Bumper
	AGV_Dec_Pt6	Station 5: Engine Room
	AGV_Dec_Pt7	Station 6: Under Carriage
	AGV_Dec_Pt8	Station 7: RR Axle and Engine Mount
	AGV_Dec_Pt9	Station 8: RR Axle Sub
	AGV_Dec_Pt10	Station 9: Fuel Tank Sub
	AGV_Dec_Pt11	Station 10: Under Floor
Warehouse	AGV_Dec_Pt1	Warehouse pick up point

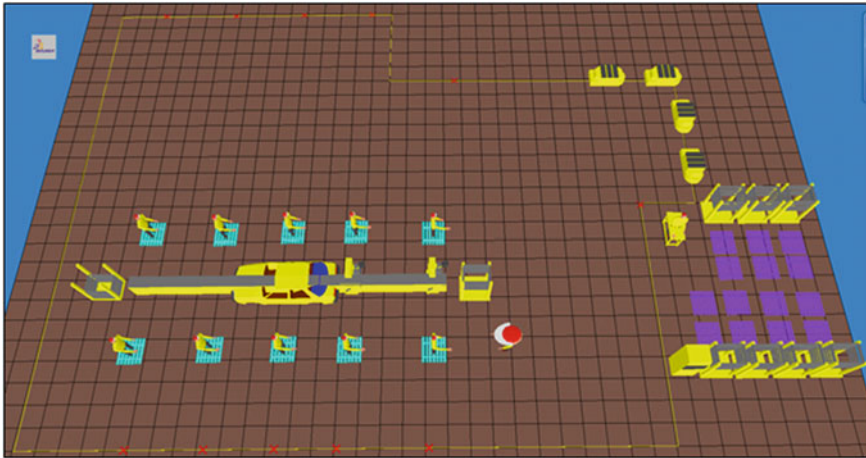


Fig. 5 The location of AGV and train decision point for model 1 and 2

Table 3 List of decision points for model 3

Position	Decision points	Name of stations
Assembly line	AGV_Dec_Pt1	Station 1: Engine Sub 1
	AGV_Dec_Pt2	Station 2: Engine Sub 2
	AGV_Dec_Pt3	Station 3: FR Bumber & Axle Sub
	AGV_Dec_Pt4	Station 4: RR Bumper
	AGV_Dec_Pt5	Station 5: Engine Room
	AGV_Dec_Pt6	Station 6: Under Carriage
	AGV_Dec_Pt7	Station 7: RR Axle and Engine Mount
	AGV_Dec_Pt8	Station 8: RR Axle Sub
	AGV_Dec_Pt9	Station 9: Fuel Tank Sub
	AGV_Dec_Pt10	Station 10: Under Floor
Warehouse	AGV_Warehouse_1	OPT1
	AGV_Warehouse_2	OPT2
	AGV_Warehouse_3	OPT3
	AGV_Warehouse_4	OPT4
	AGV_Warehouse_5	RC Bin
	AGV_Warehouse_6	Dash Insul
	AGV_Warehouse_7	RR Centre Bracket

Table 4 List of decision point for model 4

Position	Decision points	Name of stations
Assembly line	AGV_Line_1	Station 1: Engine Sub 1
	AGV_Line_2	Station 2: FR and RR Bumper and Axle Sub
	AGV_Line_3	Station 3: Engine Room
	AGV_Line_4	Station 4: Under Carriage
	AGV_Line_5	Station 5: RR Axle and Engine Mount
	AGV_Line_6	Station 6: RR Axle Sub
	AGV_Line_7	Station 7: Fuel Tank Sub
	AGV_Line_8	Station 8: Under Floor
Warehouse	AGV_Warehouse_1	OPT1
	AGV_Warehouse_2	OPT2
	AGV_Warehouse_3	OPT3
	AGV_Warehouse_4	OPT4
	AGV_Warehouse_5	RC Bin
	AGV_Warehouse_6	Dash Insul
	AGV_Warehouse_7	RR Centre Bracket

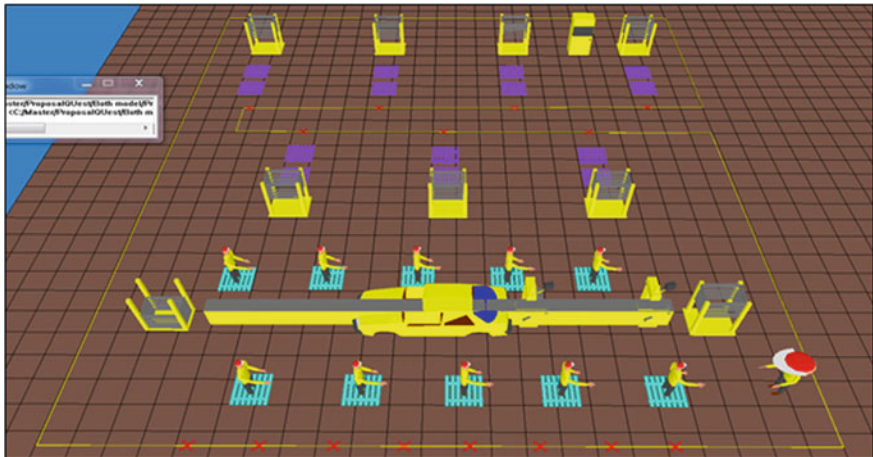


Fig. 6 The location of decision point for model 3

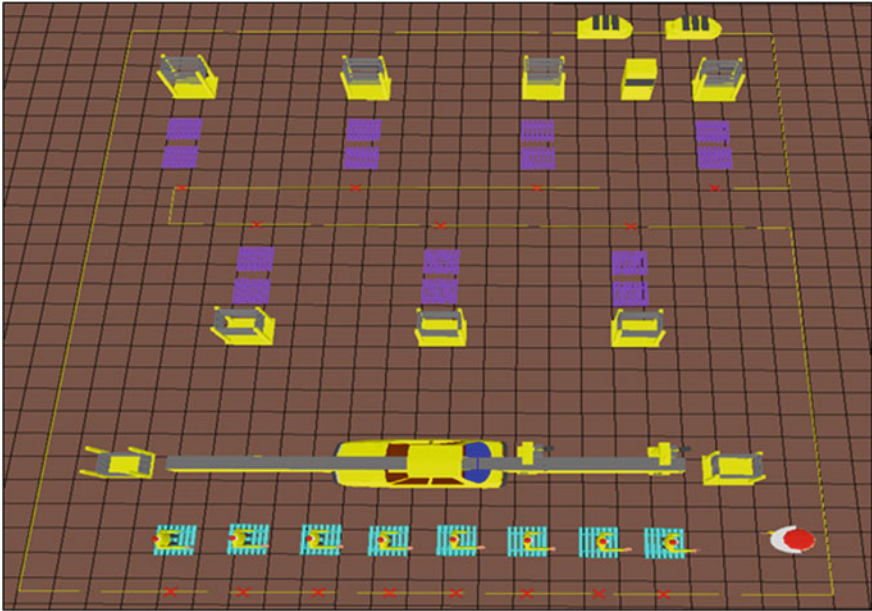


Fig. 7 The location of decision point for model 4

3 Result and Discussion

The result is compiled and presented in the statistical charts that focus on a few elements such as the element class statistics where the result show the number of total part created are showed, the idle time of drop off stations and the utilization of transportation.

As illustrates at Fig. 8, the pie chart show the total number of parts delivered between every models. The chart area increase through every models especially at model 3 where the number of parts delivered increase tremendously from 14 parts to 36 parts per simulation. Its show the changed of AGV and pick-to-light system to the system are effective. Nonetheless, the number highly increase by the changed of layout in the system in model 4. The deliveries able to achieve 3 times value from the current old system in the factory.

Figure 9 shows a line graph for comparison of idle time in assembly line supply buffer. It is observe at stations *Assem_Line_Buffer_1*, the supply time reduce sharply through *Assem_Line_Bufer_2* for model 1. That is due to the layout configuration where the distance between both stations is not too far from each other. Therefore, transportation able to transfer parts faster, thus avoiding time wasted. But, it does not seem a problem for model 2 where the changes of transportation too AGV covers the large difference of idle time between stations. The result at model 2 reduce the idle time and the trend is more linear compared to

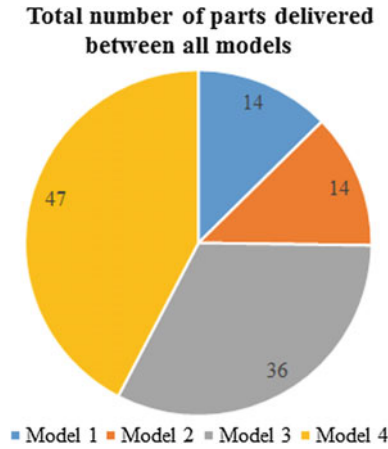


Fig. 8 The pie chart of total number of parts delivered between all models

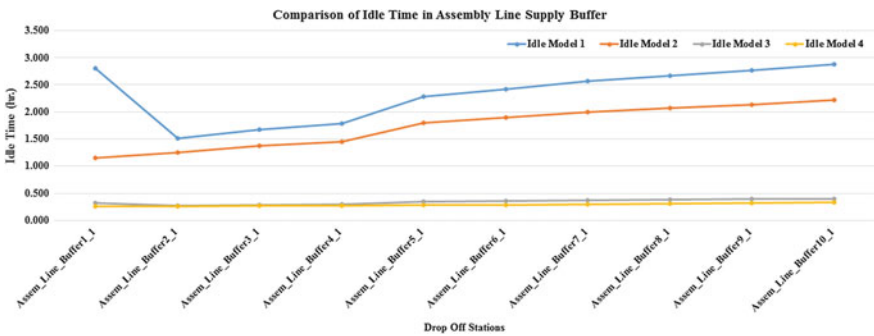


Fig. 9 The line graph of comparison of idle time in assembly line supply buffer

model 1. As the system improves with the change of supply order system and layout in model 3 and 4, the idle time reduce to below 0.5 h and maintain linearly in the system.

The radar chart illustrates at Fig. 10 shows the comparison of transport utilization. Number of transport claimed with no wait shows the utilization of the transport in the system during simulation. No wait means the AGV are claimed by station continuously. The increase the AGV shows the higher its productivity. A small increment can be seen from model 1 to model 2. The changes of transport to automated material handling give a slight increment to the utilization of the transportation. But as supply order system are changed into semi-automated pick-to-light system, the utilization of transport largely increase. From current system in model 1, the transport claimed with no wait only maximum of 13 unit transports during working hour. Thus, the transport are claimed for at least 1 h per

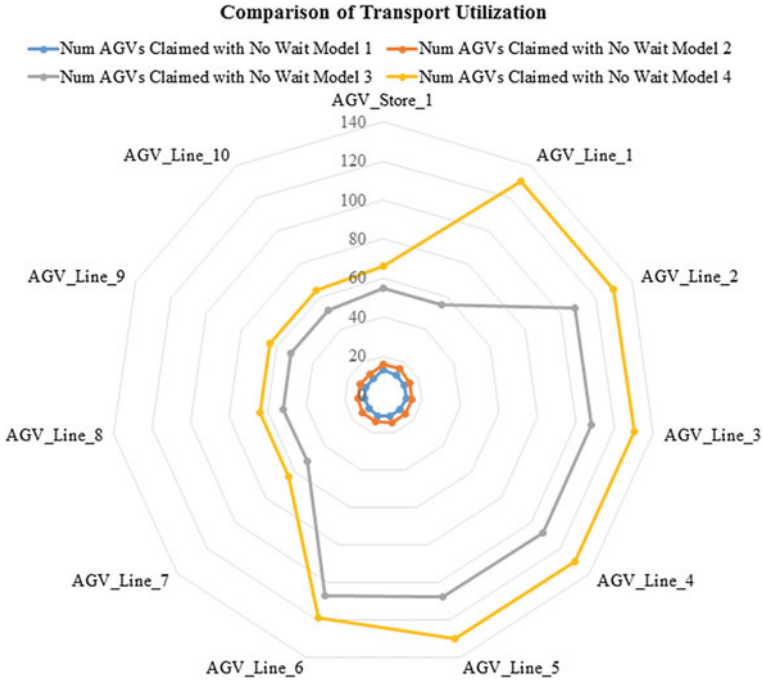


Fig. 10 The radar chart of comparison of transport utilization

cycle. Meanwhile, in model 4 the least claimed transport with no wait is 64 unit of transport during working hour. Therefore, it shows the system able to cover the demands of the stations more than the current old system.

4 Conclusion and Recommendation

This research aim to shows the influences of automated material handling system at the same time observe the effect of layout changing in the system of automotive assembly process. Based on manufacturing strategy and constraint, this research work field covers the improvement of integration between material handling and facility layout from the current case study factory.

Delmia Quest software gave ability for researcher to simulated the manufacturing line and optimize the system without disturbing the real life element. Furthermore, the result can be used to study the influences of the changes made to the system. From the result, 3 elements are discuss to show every influences and effect happen to the system.

Based on the result, the application of AGV and pick-to-light system gave high significant effect into the system. Not to mention, the changes of layout give a large

effect to the system where the productivity, time management and transportation become more effective and efficient. Hence, it can be summarized that the improvement shows the influences of automated material handling system and facility layout in increasing the performance of the automotive assembly factory.

A few features in this research study are not covered such as the flexibility of the system and the industrial engineering aspects. Hence, the constraints is likely the manufacturing towards flexibilities and leans.

Acknowledgements First of all, thanks to Allah for allowing us to finish this paper. We would like to thank Universiti Teknikal Malaysia Melaka for giving us the opportunity to develop this study. Special thanks to research grant FRGS/1/2015/TK03/FKP/02/F00277 for funding the research. We also want to thank engineers from Mawea Industries Sdn. Bhd. for support and guide us to conduct a simulation in Delmia Quest software.

References

1. Material Handling Industry: Annual Report. Charlotte, NC (2017)
2. Apple, J.M.: Plant Layout and Material Handling, 3rd edn. Wiley, New York (1977)
3. Meyer, F.E.: Plant Layout and Material Handling. Prentice Hall, Englewood Cliffs (1993)
4. Amstead, B.H., et al.: Manufacturing Processes, 7th edn. Wiley, New York (1979)
5. Thomas, D.: Material Handling Solutions: A Look into Automated Robotics. Material Handling Price, Wunsch (2010)
6. Ioannou, P., Jula, H., Liu, C.: Advanced Material Handling: Automated Guided Vehicles in Agile Ports. Centre for Advance. <http://www.ccdott.org/transfer/projresults/1998/task1261/task1.2.6.1.pdf>. Accessed 10 Oct 2015
7. Zhou, Z., et al.: IEEE Trans. Syst. Man Cybern. Syst. **44**(8), 1067–1076 (2014)
8. Boteanu, E., Zapciu, M.: Improving layout and workload of manufacturing system using Delmia quest simulation and inventory approach. Int. J. Innov. Res. Adv. Eng. **6**, 52–61 (2014)
9. Seha, S., Zamberi, J., Fairul, AJ.: Improving material handling system performance in automotive assembly line using Delmia quest simulation. In: Mohamed Ali, M.S. et al. (eds.), AsiaSim 2017, Part 1, CCIS 751, pp. 468–482. Springer, Singapore (2017)
10. Seha, S., Fairul, AJ., Zamberi, J.: Methodology on investigating the influences of automated material handling system in automotive assembly process. In: IOP Conference Series: Material Science and Engineering, pp. 1–10 (2016)

Systematic Approach for Uncertainty Delta E Data for Composites Panel Coating Analysis



Elmi Abu Bakar, W. A. F. W. Othman and A. R. Othman

Abstract In general, Aerospace industry has been developing significantly throughout the economy as demands on technology in advanced transportation is increasing. Furthermore, as a multi-billion dollar industry, the efforts is needed to sustain high quality of products for safety, minimizing waste during process and increase in a pace of manufacturing. Therefore, Six Sigma tool which is DMAIC approach is chosen to presents a case of an efficient and systematic method of improvement cycle ‘Define, Measure, Analyze, Improve and Control’ to define and analysis defect, hence to improve the quality of production in aerospace industry. In this study, the focus is done by studying how the implementation of Six Sigma on an aerospace company especially to solve the problem of uncertainty condition of Delta-E for Panel Coating. By using the DMAIC approaches, defects and problems that arise in the production line of the company are being sorted out and solved. Trials and experiments were also conducted on the company’s production line and the data is being collected for analysis and study purpose. Through observation and data taken from above problem, analyzed results perform remarkable solution to be applied by Aerospace Industry.

Keywords DMAIC • Defects • Production line

E. Abu Bakar (✉)
School of Aerospace Engineering, Nibong Tebal, Malaysia
e-mail: meelmi@usm.my

W. A. F. W. Othman
School of Electric and Electronics Engineering, Engineering Campus,
Universiti Sains Malaysia, 14300 Nibong Tebal, Penang, Malaysia

A. R. Othman
Mechanical Engineering Department, Universiti Teknologi PETRONAS,
32610 Seri Iskandar, Perak, Malaysia

1 Introduction

Nowadays, in growing competitive market environment, customers or stakeholders are always demanding on a quality products and services. Therefore, quality is considered as one of the most remarkable performance that measures and influences the manufacturer's competitiveness. In this circumstances, quality improvement activities have become a part of the business culture and the way of life. A multi-billion dollar business industry need to sustain low expenditure with good quality products and minimizing the waste. Furthermore, industry also need a to increase the pace of manufacturing in order to accomplish and also maintain the competition in the market.

Throughout the past few decades, Six Sigma is defined as a practice to improve business processes by not only restraining oneself to quality control purposes. Moreover, it's have been enormously implemented by global industries and achieved remarkable enhancements in their stakeholders' satisfaction, consistency and performance of products or services. Moreover, the Six Sigma is a collegiate assortment of many well-established tools and techniques. One of the main advantage from a Six Sigma program is the removal of partiality in decision-making by creating a scheme where everyone in the organization collects, analyses, and displays data in working area as reference.

DMAIC approach has been widely used in manufacturing areas and industries but not regularly has been applied in aerospace manufacturing line process. An experiment has been conducted in Aerospace Company located in Selangor. In manufacturing line process, in order to improve the current process problem, the first stage of DMAIC by defining a problem, measure important data, analysis the problem, suggest improvements and control the improvements for their future success. The early stage of defining a problems and measuring data from manufacturing line process is very important for defects' validation purpose. From the data measured, analysis can be made and the root cause can be obtained. Hence, steps for improvement can be built and controlled later.

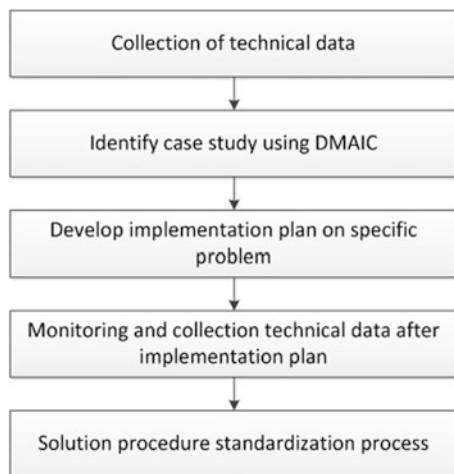
Six Sigma is a business performance improvement strategy that aims to reduce the number of mistakes/defects to as low as 3.4 occasions per million opportunities. Sigma is a measure of "variation about the average" in a process which could be in manufacturing or service industry [1]. Linderman et al. defined Sig Sigma as an organized and systematic method for strategic process enhancement and new product and service development that relies on statistical methods and the scientific method to make dramatic reductions in through the standard has been provided by main Aerospace industry customer [2]. Six Sigma was accepted as an effective quality management tool for driving and achieving changes within an organization and it is a continuous improvement process focusing on the customer requirements, process design, planning and association together with demanding, analytical and statistical tools [3]. Based on the nature of the process, the selection of tools may be varied. Different tools can be used in different phases of the implementation process. The five steps of DMAIC method often called as process improvement

methodology is designed to allow for flexibility and iterative work. Assumption or hypotheses as to the root cause of the problem may be invalidated, requiring the project team to revisit them and change or to discover alternative possibilities. Over the years, elevated safety principles are pursued by the aerospace industry to improve the composite products in order to develop the processes involved. Furthermore, the developments of the method in order to shape up intricate products to the great safety standards are led by the aerospace industries. The utilization of the tools that are currently being practiced by the modern enterprises of business such as Total Quality Management (TQM) and Six Sigma have currently been tested as well as espoused predominantly in the aerospace industry. There are plenty of case studies that have been provided on the implementation of Six Sigma principles in the aerospace industries [4]. Six Sigma is used widely in the aerospace companies for the enhancement of design, business, supply chain procedures and also manufacturing. This paper discuss on the implementation of DMAIC approach in Aerospace industries.

2 Methodology

This study is conducted at one of Aerospace Industry located in Selangor, Malaysia. The Aerospace Company in Malaysia that focused on manufacturing and responsible for Sub-Assembly of Wing's panels before shipping to main industry that assembly the overall aircraft component. One of the general issues that arise in manufacturing line process is focused and studied to apply the DMAIC approach. The flow of manufacturing line process is deliberate before the main issue is being focused. The methodology of this research is illustrated in Fig. 1.

Fig. 1 The methodology illustration



2.1 Case Study of Delta E for Panel Coating Analysis

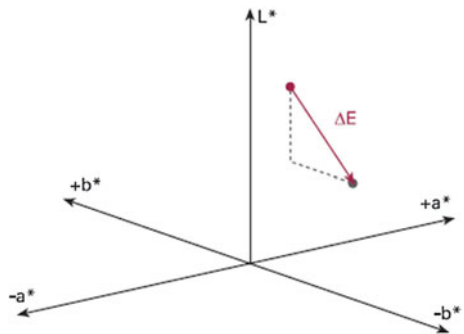
Delta E is defined as the difference between two colors in the format of “L*a*b*” color space. As the values determined are based on a mathematical formula, it is important that the type of color formula is taken into account when comparing the values. In Color Verifier alone, there are three different formulas to choose from, each producing different results. The CIE L*a*b* formula used in the proofing market calculates the Euclidian distance, the distance between two points in a three-dimensional color space. The actual position of the points themselves is irrelevant. Figure 2 shows the color space of related Delta E information and related equation in Eq. (1) below.

However, the human eye is more sensitive to some areas of color and less sensitive to others, a fact that the formula does not take into account. To avoid the uncertainty judgement reading from the human eye, further color formulas have been developed. Colors in a highly saturated area are assigned less importance during the evaluation than colors along the grey axis, which is where the human eye is most sensitive.

$$\Delta E_{ab}^* = \sqrt{(\Delta L^*)^2 + (\Delta a^*)^2 + (\Delta b^*)^2} \quad (1)$$

To say that a Delta E value of 1 is visible to the untrained eye is, therefore, true for the grey axis which not apply for the highly saturated area. Nevertheless, the CIE L*a*b* color formula is still used by the proofing market. However, it is perfectly acceptable to use, for example, CMC or CIE 94 in the production market to check the stability of the output device [5].

Fig. 2 Delta E



2.2 Identify Case Study Using DMAIC

Specific problems that arise in the company are focused to implement through this approach as the case studies to be done. Frequent issues and problems that arise are focused and studied. General process flow and work break structure (WBS) flow of the process is taken into account. Each process of sub-assembly process need to be monitored and observed before process of collecting data can be conducted. Then, the DMAIC approach can be applied. The general flow of DMAIC should be brainstorm as Fig. 3 shown.

2.3 Solution Procedure Standardization Process

The next step is proceed once the solution has been decided, the procedure must be standardized and control of the implement plan for sustainability to achieve the targets. Such new procedure must be carried out as standard and usual procedure by the operators. In Fig. 4 represent the overall flow of stages of process.

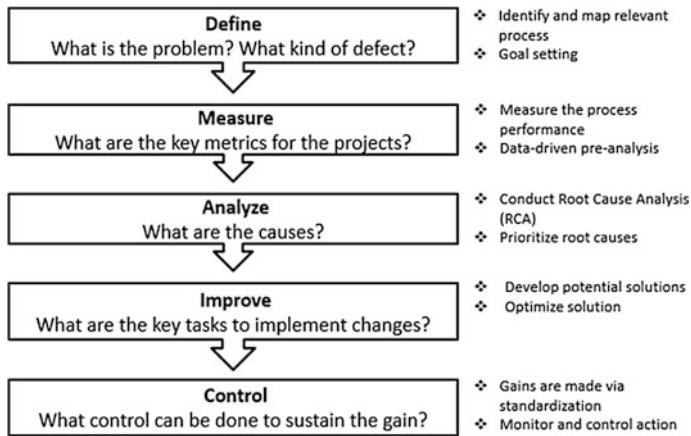


Fig. 3 Illustration of DMAIC approach

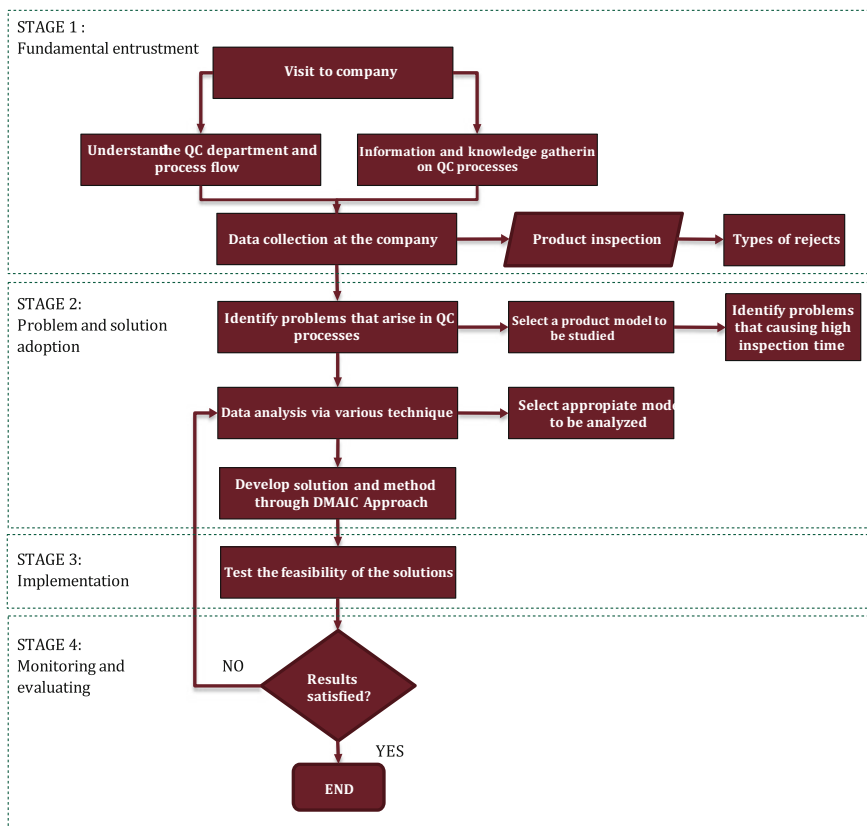


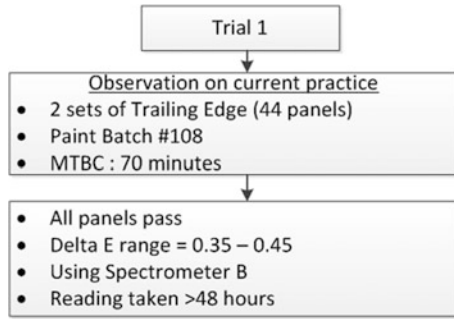
Fig. 4 Overall process flow

3 Results and Discussion

3.1 Trial One: Identify Current Observation on Paint Batch #108

Trial one with flow chart as shown in Fig. 5. The trial one is an observation on current activity of painter or Paint Shop’s operator. The trial is conducted on two sets of Trailing Edge panels which sum up to 44 panels as each set of Trailing Edge have 22 parts (11 parts for PORT and 11 parts for STBD). Paint that was used for the Top Coat of the panels is from the new Paint Batch #108. Maximum Time between Coating (MTBC) is flash off time for the panels. During, paint coating process or surface coating, the panels will be left for several periods before the painter begin to do the second coating, this is because to maintain the paint consistency and coating quality. Hence, we want to study whether the MTBC will affect the reading of Delta E values and results. For trial one, the MTBC is 70 min.

Fig. 5 Illustration of trial 1



Based on the current trial activity, all panels passed the requirement of the Airbus which is to maintain the Delta E values less than 0.50. The reading of Delta E values is taken after 48 h when the Top Coat of the panels are done. 3 panels in the range 0.30–0.39 and 16 panels in the range 0.40–0.49 but the highest Delta E value obtained is 0.45. From the trial, the current practice shows positive results, but MTBC of 70 min is quite time consuming as Paint Shop has limited quantity of Paint Booth to do the surface coating. The result as shows in Fig. 6.

3.2 Trial 2: Identify Current Observation on Paint Batch #65

The second trial is done by using the suspected problem Paint Batch #65 with MTBC of 30 min. The second trial is conducted on one set of Trailing Edge panels, which contain 22 parts. The flow as shown in Fig. 7.

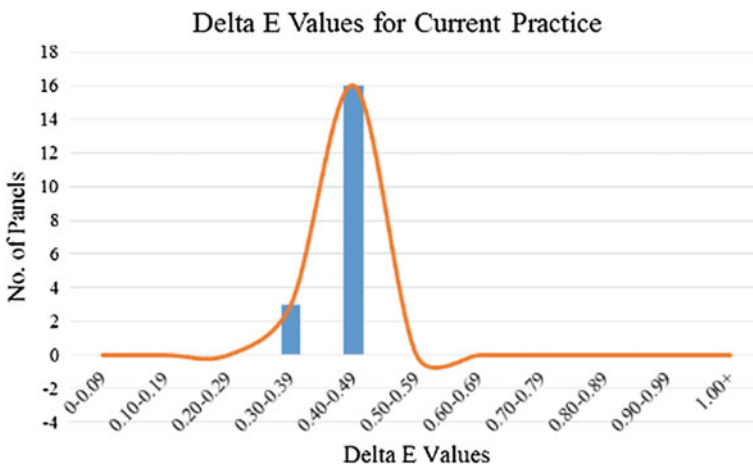
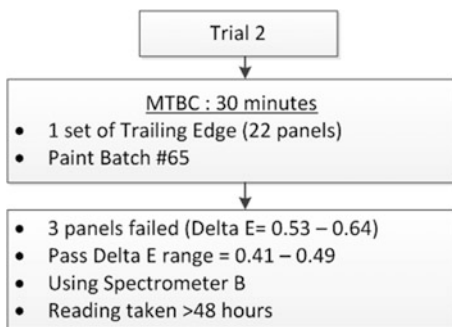


Fig. 6 Graph of Delta E values for current practice

Fig. 7 Illustration of trial 2



Based on the second trial, 19 panels passed and the other 3 panels failed. The 3 panels are in a range of 0.53–0.64. The Delta E readings are taken 48 h later after the Top Coat of the panels by using Spectrometer from Paint Shop which labelled as Spectrometer B. The result shows in Fig. 8.

As result is shows in Fig. 9, for Paint Batch #65, panels are majorly in a range of 0.40–0.48, 1 panel in a range of 0.30–0.39 and the other two panels in a range of 0.50–0.59 for the Delta E values. However, 1 panel in the range of 0.50–0.59 is passed the Delta E requirement with a reading of 0.50, hence only 1 panel is failed with a reading of 0.52. While as for Paint Batch #108, all the panel passed the Delta E requirement with range of 0.17–0.38; most of the panels in a range of 0.20–0.29, 4 panels in a range of 0.30–0.39 while the other 2 panels are in a range 0.10–0.19 and 0.40–0.49 each. In conclusion, as from the results analysis of the forth trial, the Spectrometer A and Spectrometer B gave inconsistent reading as shown in the graphs above.

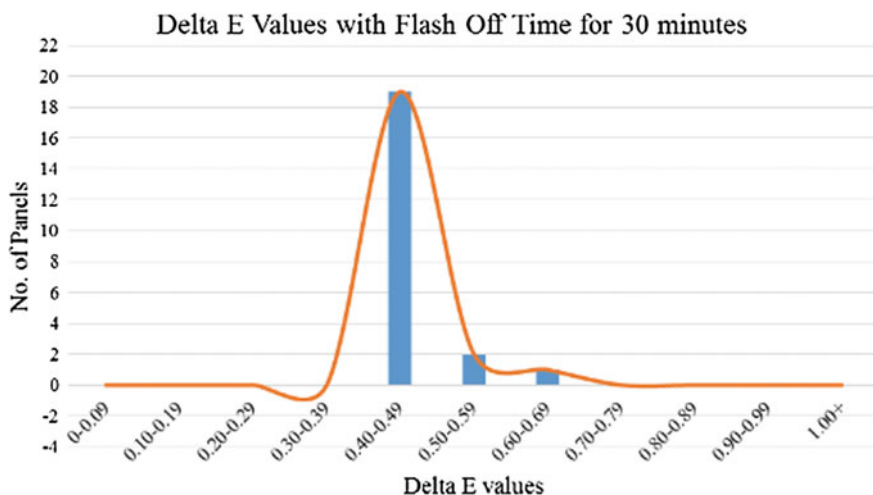


Fig. 8 Graph of Delta E values with flash off time of 30 min

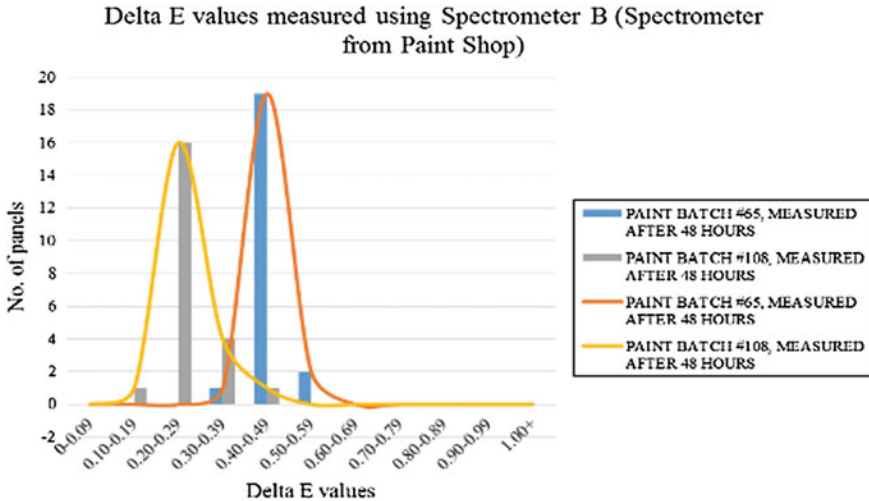


Fig. 9 Graph of Delta E values measured by using spectrometer B

The validation process is conducted through each trial by comparing the current practicing method and DMAIC approach method that has been mentioned in the above figure in the content.

4 Conclusion

This paper proves the practicality of using the DMAIC approach in solving a problem that usually arises in a production line, which affects time consumption and production of products. This study has been carried out in two departments of the company, the Paint Shop department and the Final Assembly department, in consonance with the Quality Control of the departments. The problem of uncertainty in data reading of Delta E values for the panels does not meet the requirement, which exceeds the maximum value of Delta E. As a result, the panels cannot be sent to the Outbound (Logistics) and cannot be sent to the customer, which failed to fulfill the demand per week of production. By introducing the defining problem root cause using the DMAIC tool and applying a trial of 48 hours for two batches, #108 and #65, we can further understand that the reading of Delta E values can be improved.

Hence, the general process of the panels is being studied, and the Paint Shop department is the second department that is being focused on. The manufacturing line process in the Paint Shop department is being analyzed, and several processes that affect Delta E values are being highlighted. Using the correct method in problem solving is also vital. This was demonstrated in this paper, where this project was carried out in proper steps so that the root cause can be figured out. A detailed

process flow was developed in advance and phases were created to make sure that the project can be carried out chronologically. Detailed planning of the project will aid in problem identifying and problem solving tasks.

References

1. Srinivasan, K., et al.: Enhancing effectiveness of shell and tube heat exchanger through six sigma DMAIC phases. *Procedia Eng.* **97**, 2064–2071 (2014)
2. de Mast, J., Lokkerbol, J.: An analysis of the six sigma DMAIC method from the perspective of problem solving. *Int. J. Prod. Econ.* **139**(2), 604–614 (2012)
3. Chattinnawat, W.: Methodology of DMAIC with Why-Why Analysis in a Hierarchical Decision, p. 438 (2008)
4. Khaled, M.M.: Analysis of six sigma in the aerospace industry. *Int. J. Soc. Behav. Edu. Econ. Bus. Ind. Eng.* **7**(12), 4 (2013)
5. Mokrzycki, W.S., Tatol, M.: Color difference Delta E machine graphic and vision (2012)
6. Sokovic, M., Kern Pipan, D.P.: Quality improvement methodologies—PDCA cycle, RADAR matrix, DMAIC and DFSS. *J. Achieve. Mat. Manuf. Eng.* **43**(1), 8 (2010)
7. Ramamoorthy, S.: Lean Six-Sigma Applications in Aircraft Assembly, p. 62 (2007)
8. Ang, B.S.: A study of knowledge creation in six sigma Dmaic project success and its impact on organizational performance. Ph.D. Thesis, Universiti Sains Malaysia (2015)

Statistical Analysis of the Machining Parameters in Drilling of Carbon Fibre Reinforced Plastics (CFRP) Composite with Various Drill Types



A. R. Othman, M. H. Hassan, Elmi Abu Bakar
and W. A. F. W. Othman

Abstract In contrast to the machining of metallic materials, drilling of the fiber reinforced composite materials presented unique challenges as its cutting behavior differs in several aspects. This work presents an analysis to determine the drilling characteristics in carbon fiber reinforced plastics (CFRP) composite using HSS twist drill, HSS brad drill and carbide dagger drill. The study is based on Taguchi's method and analysis of variance (ANOVA). The experiments were conducted to quantify the statistical contributions of the spindle speed and feed rate for those three drills. The results indicated that the feed rate is recognized to make the most significant contribution to the thrust force, which reflects the hole quality and tool wear. In overall, brad drill promoted better hole quality at the exit side. A low thrust force, insignificant hole defect and hence, better drill condition was obtained with this drill at a cutting speed of 800 rpm and feed rate of 0.04 mm/rev.

Keywords Composite drilling • Carbon fibre reinforced plastics
Hole quality

A. R. Othman (✉)

Mechanical Engineering Department, Universiti Teknologi PETRONAS, 32610 Seri Iskandar, Perak, Malaysia
e-mail: rahim.othman@utp.edu.my

M. H. Hassan

School of Mechanical Engineering, Universiti Sains Malaysia, 14300 Nibong Tebal, Pulau Pinang, Malaysia

E. Abu Bakar

School of Aerospace Engineering, Universiti Sains Malaysia, 14300 Nibong Tebal, Pulau Pinang, Malaysia

W. A. F. W. Othman

School of Electrical and Electronic Engineering, Universiti Sains Malaysia, 14300 Nibong Tebal, Pulau Pinang, Malaysia

© Springer Nature Singapore Pte Ltd. 2018

M. H. A. Hassan (ed.), *Intelligent Manufacturing & Mechatronics*,

Lecture Notes in Mechanical Engineering,

https://doi.org/10.1007/978-981-10-8788-2_14

1 Introduction

The superior properties of composite materials in comparison to those of conventional counterparts have generated a rising interest in utilizing the materials in various applications. Although composite structures are usually made to near-net shape products, more intricate components require secondary machining processes for the required accuracy in assembly. For that, drilling provides the most significant machining to allow the application of screw and rivets in the assembly of parts. The drilling of the fiber reinforced composite materials presented unique challenges as its machining behavior differs in various aspects. Koplev [1] was the first to declare that chip formation in composite removal is a process of serial material fractures. The material is not only inhomogeneous and anisotropic, but the behavior is also dependent on the constituents' properties, fiber orientation and fabric constructions [2]. Inappropriate choice of cutting parameters or drill bits could cause different type of damages such as delamination, pull out of the fibers, fiber-matrix debonding, splintering, thermal alterations and geometrical defects [3–5]. Drilling-induced delamination occurs both at the entrance and the exit planes of the workpiece. Davim and Reis [6] has clearly distinguished two different mechanisms of delamination, referring as peel-up and push-down, with both are primarily influenced by the thrust force developed during drilling [5].

The influences of cutting parameters and the drill geometry on the holes quality have been comprehensively discussed. Grilo et al. [7] has examined the influence of cutting parameters for three distinct drills on the delamination, assessed through two delamination factors using processed images analyses. In a great detail, Davim and Reis [6] has characteristically computed the physical and statistical influence of the cutting speed and the feed rate on the delamination at entrance as well as at exit holes for both tested drill types. Interestingly, by combining the low feed rates and high spindle speeds, a much lower thrust force could be generated, and hence reducing the delamination [9]. It was established that different designs of the drill produced different extent of delamination and holes quality. Piquet et al. [10] has highlighted that the use of helical drill and a special geometry drill leads to damage at the entrance and the exit of the hole, in which the latter caused significant reduction in the final damage. A similar work in the drilling of CFRP with helical flute carbide drill produced lesser delamination in comparison to the drilling using a four-flute carbide drill [11]. In addition, the use of a spur drill could produce higher rate of production without the occurrence of delamination, obtained with a feed rate of 2025 mm/min and a spindle speed of 6750 rpm [7]. To some extent, the drilling of composite laminates involves complex interaction between various parameters with regards to the hole quality [12]. Hence, more recent publications [13–17] have reported the use of various statistical and experimental design approaches to analyze the effect of specific parameters on the hole quality [2, 8–10]. For an instant, Palanikumar et al. [14] has developed empirical models to analyze the interaction of cutting parameters on the delamination factor in drilling GRP composites with four-flute cutter and HSS twist drill. While, Davim and Reis [11] presented an

approach using Taguchi's method and ANOVA to establish a correlation between cutting speed and feed rate on the delamination in a composite laminate. Using a similar method, Tsao and Hocheng [13] has evaluated the specific contribution of the feed rate, spindle speed and drill diameter for various drill bits.

In this particular work, an analysis on the effect of the machining parameters using high speed steel (HSS) twist drill, HSS brad drill and carbide dagger drill on the quality of hole geometry and tool wear is presented. The work focuses on the drilling process of carbon fiber reinforced plastic (CFRP) composites for the use in the assembly of wing section of civil aircraft. Although several researchers have decisively reported on the composite drilling using the twist drill, the performance of the brad and dagger tools in the drilling of aircraft composite panel particularly, is not conclusively presented elsewhere. Nonetheless, the study includes detailed analysis using the Taguchi method and analysis of variance (ANOVA) to quantify the specific contribution of individual parameters as well as the interaction of the combined parameters during the drilling.

2 Methodology

2.1 *Experimental Materials and Drilling Tests*

The composite panels used in this study were fabricated from the unidirectional tape prepreg of Fiber dux 914C-T300 carbon fiber with epoxy matrix using an autoclave molding process. The laminate was prepared out of 20 alternating layers of CFRP with the stacking sequence of $[0/90]_{10}$, resulting in 3.5 mm thick. Drilling tests were conducted on a 15 kW DMU 40 monoBLOCK[®] CNC machine as shown in Fig. 1. The workpiece was mounted on Kistler dynamometer which was fixed on the bed of the drilling machine. A backing plate was used to support the laminate, which was firmly held in between the workpiece and dynamometer. The drilling trials were carried out using 6.35 mm diameter drill bits of three different types: a HSS twist drill with a point angle of 120° , HSS brad drill and a carbide dagger drill (30° -point angle) as shown in Fig. 2.

2.2 *Design of Experiment*

Figure 3 summarized the framework of the methodology. The method of Taguchi for two factors at three levels was considered to observe the degree of influence of the control factors in drilling is shown in Table 1. Experiments for three different drill bits were conducted using full factorial L_9 (3^2) arrays corresponding to the number of trials with two columns at three levels was assigned to feed rate (f) and cutting speed (V). The basis for the selection of the cutting parameters relies on the recommendations of the main OEM of aircraft part. For each cutting condition,

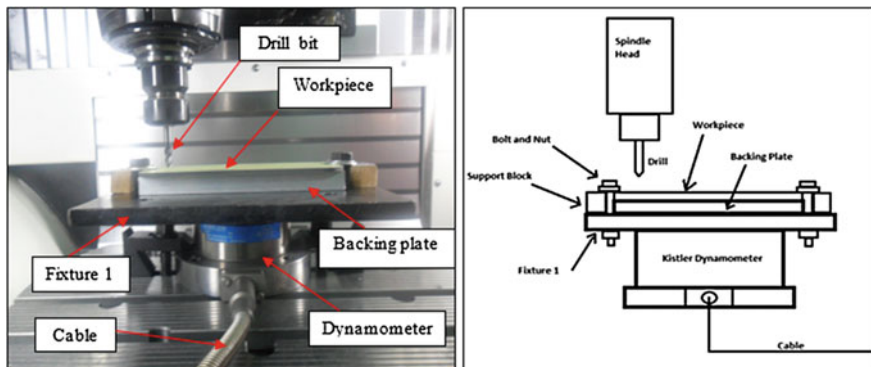


Fig. 1 Experimental setup of the drilling test on CFRP composite



Fig. 2 Drill bits used in the experiments: a dagger drill, b twist drill and c brad drill

twenty holes at approximately 6.35 mm in diameter were produced and the thrust force values were recorded using the dynamometer. It is anticipated that the occurrence of the damages on the holes is significant at this total number of holes. The output from the dynamometer was visualized in the graph form using IMC Device software to analyze the force fluctuations, where the positive value represents the thrust force applied by the drill bit, whilst the negative value represents the reaction force from the panels. Subsequently, the experimental results were analyzed based on the analysis of variance (ANOVA), to determine the contribution percentage and interaction of the machining parameters.

Hole quality in composite material was evaluated with regards to the severity of damages after the drilling. The drilled holes were scanned using a flatbed Canon MP145 scanner with a resolution of 600 dpi. In addition, the condition of the tools was examined using an Infinite Focus Alicona Microscope at the cutting edge of the drill bits to determine the influence of the spindle speed and feed rate on the tool condition. At the 20th holes, the tool was analyzed under 20x lens magnification ratio to evaluate the surface profiles of the tool's cutting edge in comparison to those of the unused tool.

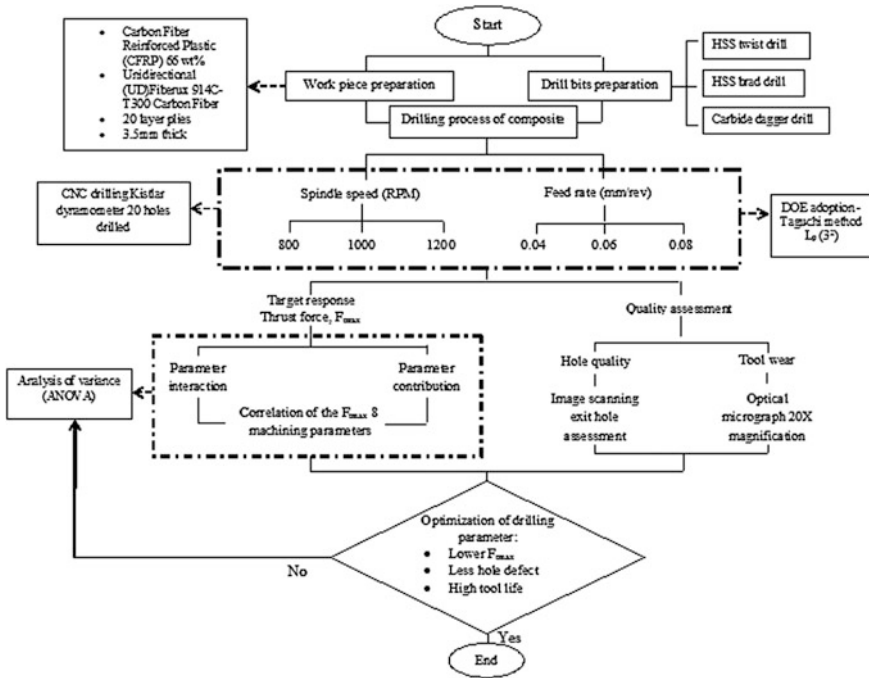


Fig. 3 Methodological framework of the study

Table 1 Levels of drill test factors

Control factor	Level 1	Level 2	Level 3
Feed rate, f (mm/rev)	0.04	0.06	0.08
Spindle speed, V (rpm)	800	1000	1200

3 Results and Discussion

3.1 Effect of Cutting Parameters on Thrust Force

Figure 4 shows the influence of feed rate and cutting speed on thrust force when drilling CFRP using three different cutting tools. It can be seen that the maximum thrust force increased with the feed rate due to the fact that a greater shearing effect has occurred during the drilling. As the feed rate increased from the lowest to the maximum value, the recorded maximum thrust force for brad drill was more than two-fold of its initial values. In this case, it has been observed that the geometrical shape of the drill plays a significant role to the difference of thrust force recorded between the rates discrepancy. Within the range tested, lower thrust force values were obtained for the dagger drill, with the brad drill indicated more superior performance than the twist drill in lower and intermediate ranges. However, at

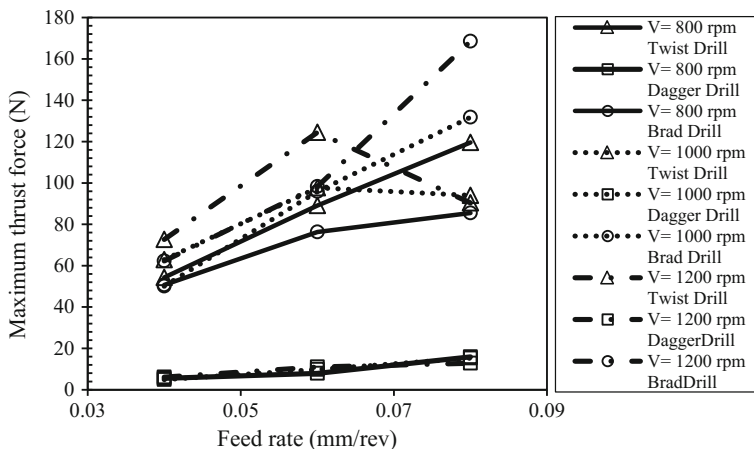


Fig. 4 Effect of feed rate and spindle speed on thrust force when drilling CFRP composites using three different drills

higher cutting range brad drill produced the worst results. The reason why the dagger drill presented the lowest thrust force may subsist in the fact that its geometry allows an ‘efficient’ cutting action to take place. The sharp tip of dagger drill helps much in decreasing the thrust force by indenting through the plies as the feed rate was increased. The drill possesses a point angle of 30° and this small angle may contribute in reducing the indentation effect.

Due to its particular geometry, dagger drill represented a smaller difference in maximum thrust force compared to those other drills. A similar case was also observed at different cutting speeds, in which the changes in the speeds did not have much influence on the maximum thrust force. The smaller increase in thrust force with regards to the change in feed rate has indicated a good effect for specified types of drill. An increased in the cutting speed does not contribute much on wear at the cutting edge as low maximum thrust force was observed. As a result, a low maximum thrust force can be maintained at higher cutting speed condition. However, for the brad and twist drills with considerable blunt tips, the increase in the feed rate causes the elevation of the thrust force. Similarly, higher cutting speed has also increased the value of the thrust force. The brad drill has a specific point geometry causing the fiber tensioning prior to cut, with the twists drill possesses a high point angle of 120°. As the particular drill geometry is rather different, an increase in the cutting speed created more heat due to friction in the cutting zone, leading to increased tool wear. In addition, the brad and twist drill was made from high speed steel, with a low hardness value compared to carbide material (i.e. dagger drill). This inferior hardness value has caused an increased in the tool wear with the cutting speed as well as the feed rate, which lead to an increased in the tool wears and leading to rise in the maximum thrust force.

Table 2 L9 (3²) Orthogonal array and values of trust force (F_t)

Trial	Parameter		Trust force (F_t)		
	Feed rate (mm/rev)	Cutting speed (RPM)	Twist drill (N)	Brad drill (N)	Dagger (N)
1	0.04	800	54.32	50.66	5.49
2	0.04	1000	62.87	50.05	4.88
3	0.04	1200	72.64	64.46	6.10
4	0.06	800	89.12	76.30	7.94
5	0.06	1000	97.66	95.83	9.77
6	0.06	1200	124.50	98.27	10.99
7	0.08	800	119.60	85.45	15.87
8	0.08	1000	94.00	131.80	15.26
9	0.08	1200	90.34	168.50	12.82

3.2 Analysis of Variance

Results of the thrust force, F_{max} for three drill bits were computed for each of the 9 trials, and the values are reported in Table 2. The drilling using the twist and brad drills have experienced a comparable maximum F_{max} between them, yielding a range of between 54.32 N–124.5 N and 50.05 N–168.5 N, respectively. Surprisingly, those trials using the dagger drill would provide a significantly low F_{max} , with the value ranged from 4.88 N to only 15.87 N. In addition, Tables 3, 4 and 5 illustrate the results of the ANOVA with the maximum trust force in CFRP laminate for those three drill bits, accordingly.

In Table 3, it was observed that the feed rate played the most important role that contributes to the F_{max} for the twist drill, contributing to 89.57% and followed by the spindle speed (9.72%). On the other hand, for the brad drill, the analysis in Table 4 has shown that the feed rate and cutting speed have statistical significance of 69.14% and 20.06%, respectively on the F_{max} obtained. Moreover, a combined factor that describes the interaction between in the feed rate and spindle speed was also observed, where it has contributed 10.22% to the development of F_{max} .

In the use of ANOVA in the analysis, the correlation between F_{max} and cutting parameters in the drilling of CRFP laminates for different types of the drill was obtained. The equation can be expressed as follows with f is the feed rate in mm/rev and N is the spindle speed in rpm:

(a) Twist drill

$$F_{max} = -28.215 + 1266.083(f) + 0.0417(N) \tag{1}$$

Table 3 ANOVA for trust force (F_t) of twist drill

Source	Sum of squares	Mean square	F-value	p-value > F	% infl
Model	4264.454	2132.227	69.0534	<0.0001	
A-feed rate	3847.121	3847.121	124.591	<0.0001	89.57
B-cutting speed	417.3336	417.3336	13.5156	0.0104	9.72
Residual (error)	185.2676	30.87793			0.72
Cor total	4449.722				
Std. dev.	5.556791	R-Squared		0.958364	
Mean	89.45	Adj R-Squared		0.944486	
C.V. (%)	6.212176	Pred R-Squared		0.896197	
PRESS	461.8944	Adeq Precision		20.98467	

Table 4 ANOVA for trust force (F_t) of twist drill

Source	Sum of squares	Mean square	F-value	p-value > F	% infl
Model	11661.18	3887.06	57.03227	0.0003	
A-feed rate	8109.256	8109.256	118.9818	0.0001	69.14
B-cutting speed	2353.032	2353.032	34.52449	0.0020	20.06
AB	1198.891	1198.891	17.59053	0.0085	10.22
Residual (error)	340.7772	68.15544			0.58
Cor total	12001.96				
Std. dev.	8.255631	R-Squared		0.97161	
Mean	91.25778	Adj R-Squared		0.95457	
C.V. (%)	9.046496	Pred R-Squared		0.87435	
PRESS	1508.044	Adeq Precision		20.55567	

Table 5 ANOVA for trust force (F_t) of twist drill

Source	Sum of squares	Mean square	F-value	p-value > F	% infl
Model	125.8584	125.8584	78.84767	<0.0001	
A-feed rate	125.8584	125.8584	78.84767	<0.0001	98.75
Residual (error)	11.17356	1.596222			1.25
Cor total	137.032				
Std. dev.	1.263417	R-Squared		0.91846	
Mean	9.902222	Adj R-Squared		0.906812	
C.V. (%)	12.75892	Pred R-Squared		0.867691	
PRESS	18.13055	Adeq Precision		15.37995	

(b) Brad drill

$$F_{max} = 141.6386 - 2489.96(f) - 0.16067(N) + 4.3288125(f \times N) \quad (2)$$

(c) Dagger drill

$$F_{max} = 9.9022 + 4.58(f) \quad (3)$$

Whilst in Table 5, only the feed rate recorded the statistical significance of 98.75% on the F_{max} obtained for the dagger drill. As a result, the feed rate is seen to make the largest contribution to the value of F_{max} . The increase in feed rate will directly affect the reaction force at the interface between workpiece and tools, causing higher force due to friction in the cutting zone. This emphasizes that the particular parameter should be given more consideration for all type of tool during drilling. Figure 5 further summarizes the source of contribution for each drill tool. It was clearly shown that the residuals value for each drill bit was found to be less than 2% indicating an insignificant error in the analysis.

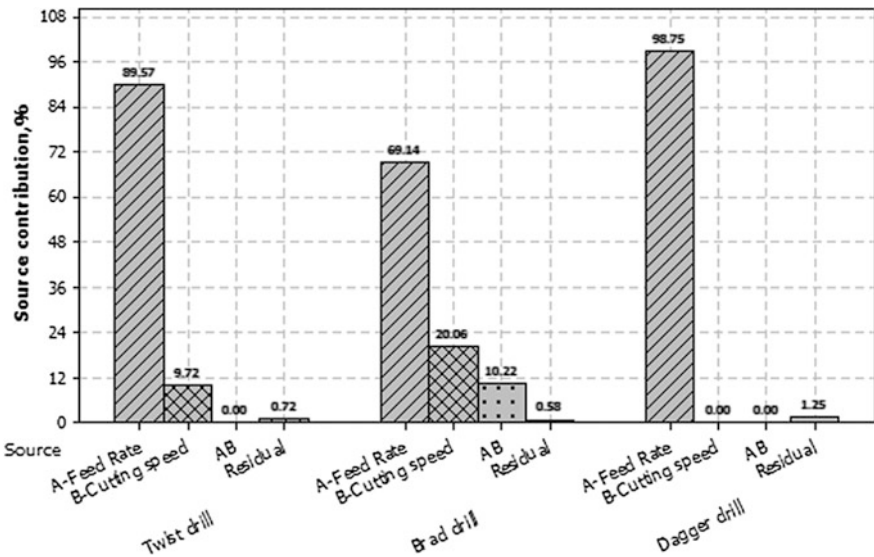


Fig. 5 Parameters contribution for twist, brad and dagger drill

3.3 Effect of Cutting Parameters on Hole Quality and Tool Condition

From Fig. 6, the damage observed on the drilled hole is more pronounced with the blunt drill of the 120° twist drill. The hole drilled using the twist drill was found to produce rather worse hole quality compared to those of other drill types. The particular holes suffered from high delamination and long burr formation at the exit side. It was agreed that the extent of the damages, i.e. delamination and burr formation, at the exit side could be reduced by the use of a drill with sharp tip angle such as dagger drill. The hole drilled by the dagger drill presented a better hole quality than those of the twist drill, since its sharp tip angle enable the tool to punch through the last plies over a smaller area. As a result, a smaller width of the laminates was subjected to only a small bending force from the tip, thus reducing

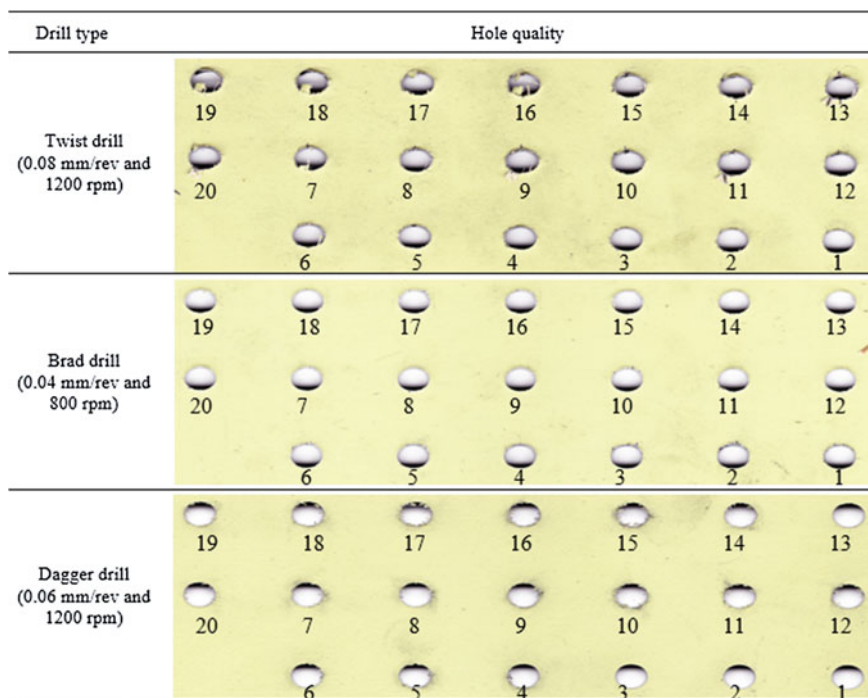


Fig. 6 Hole quality of the 20th drilled holes using the twist, brad and dagger drills

the effect of exit delamination. It has been observed that most of the hole drilled using the brad drill suffered from minor exit delamination except for cutting condition at feed rate 0.06 mm/rev and cutting speed 800 rpm. This cutting parameter produced holes with edge fracture on the surface even though the recorded thrust force values were at the smallest.

In overall, the best hole quality was attained from the drilling using the brad drill. The hole only suffered a minor delamination at the exit side. In the case of brad drill, the drill geometry allowed the cutting action to take place from the outer to the inner diameter. Consequently, the drill acts as a trepanning tool, which helps to prevent severe plastic deformation at the center of the drill, where the cutting speed is null.

The tool condition was characterized by the profile of cutting edge at the flank faces. Figure 7 shows the worn section of the drill as well as the hole characteristics at 20th drilled hole. From the observation, all the twist drill was suffered from the flank wear after twentieth drilled holes. In addition, the dagger drill contained a groove on the cutting edge which indicates the tool had suffered from wear. The tool condition for the dagger drill was evaluated in terms of the loss of sharpness at the cutting edge of the tool. It has been observed that at the constant feed rate, the tool condition was degraded as the cutting speed decreased. Slow cutting speed increased the engagement time between the tool and the hole wall. This resulted in longer times of fibers rubbing on the tool which reduced the sharpness of the cutting edge and wore out the tool. At this stage, an insignificant sharpness loss was observed at the cutting edge and less delamination on the drilled hole. The surface profiles at the cutting edges remain similar to those of the new drill, which could indicate the optimal cutting condition which promotes longer tool life and good hole quality.

At the lowest feed rate, it has been observed that after the 20th drilling, the used cutting tool still remained in good condition in comparison to those at other feed rates. Similarly, the quality of the drilled holes was comparatively better at the lower feed rate. However, an increase in the cutting speed has not significantly affecting the two results. Based on Fig. 7, the best drilling output was observed at the combination of lower feed rate at various cutting speeds. However, if the thrust force and tool life needs to be considered, the optimal cutting parameters were achieved at the low feed rate and low cutting speed (0.04 mm/rev and 800 rpm). This finding agreed well with Abrao et al. [18], who highlighted that the best hole quality was obtained at lower feed rates when drilling glass fiber composites using brad drill.

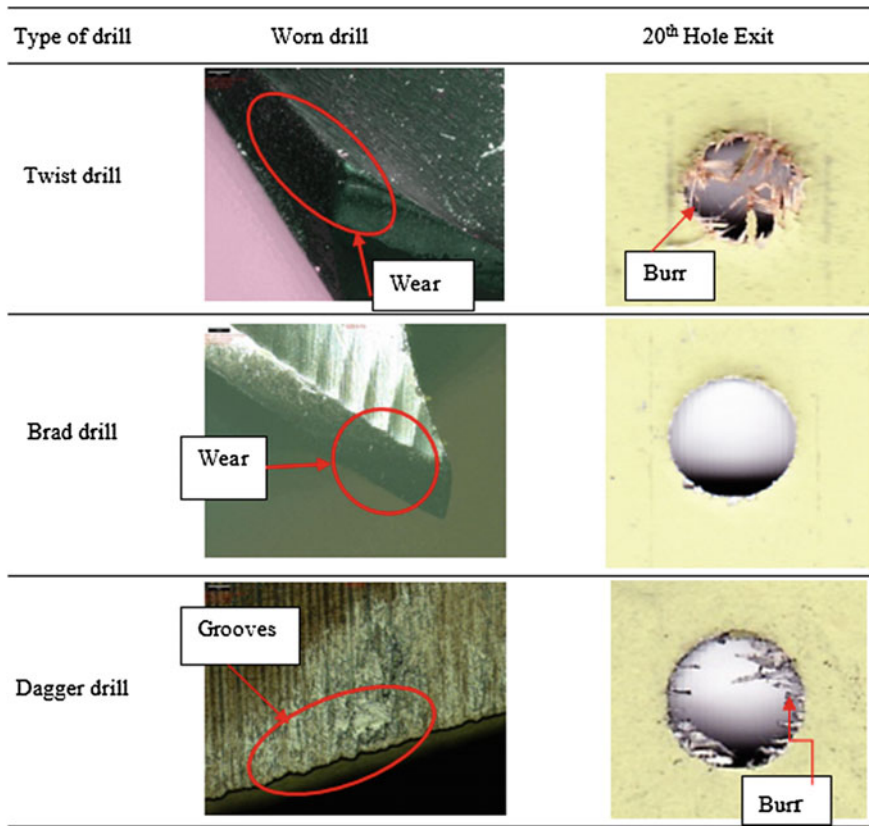


Fig. 7 Worn section at the cutting edge of the drill and the hole quality at 20th drill at 0.04 rev/mm and 800 rpm

4 Conclusion

The experimental study of the drilling process of CFRP composite laminates using HSS twist drill, HSS brad drill and carbide dagger drill has been presented. The effect of cutting speed and feed rate on the thrust force, hole quality and tool wear has been analyzed using the Taguchi method and analysis of variance (ANOVA). Followings are the summaries of this investigation:

- Feed rate has a greater influence on thrust force during drilling, contributing to 98.75% for the dagger drill, 89.57% (twist drill) and 69.14% (brad drill). While the spindle speed provided statistical influence of 20.06% for the drilling using brad drill, 9.72% (twist drill), but none for the dagger drill.
- In addition, for the brad drill, an interaction between the feed rate and spindle speed existed and contributed 10.22% to the thrust force.

- Using the twist drill, drilling at the highest cutting speed (1200 rpm) and feed rate (0.08 mm/rev) has resulted in the decrease in thrust force value, smaller hole defects and hence, longer drill life.
- Drilling using the brad drill at the lowest cutting speed (800 rpm) and feed rate (0.04 mm/rev) has contributed to the decrease in maximum thrust force value, smaller hole defects and longer drill life.
- On the hand, using the dagger drill has provided insignificant hole damages and longer tool life when drilling at the highest cutting speed (1200 rpm) and intermediate feed rate (0.06 mm/rev).

Acknowledgements The authors would like to thank Universiti Teknologi PETRONAS and the Ministry of Higher Education, Malaysia for the financial support through the Fundamental Research Grant Scheme (FRGS) [0153AB-K74] for this research.

References

1. Koplev, A.: Cutting of CFRP with single edge tool. In: Proceedings of the 3rd ICCM, pp. 1597–1605. Paris, France (1980)
2. Koenig, W., Wulf, C., Grass, P.: Machining of fibre reinforced plastics. *CIRP Annals—Manuf. Technol.* **34**(2), 537–548 (1985)
3. Wern, C.W., Ramulu, M., Schukla, A.: Investigation of stresses in the orthogonal cutting of fiber-reinforced plastics. *Exp. Mech.* **36**, 33–41 (1994)
4. Hocheng, H., Tsao, C.C.: Effects of special drill bits on drilling-induced delamination of composite materials. *Int. J. Mach. Tools Manuf* **46**(12–13), 1403–1416 (2006)
5. Krishnaraj, V., Prabukarthi, A., Ramanathan, A., Elanghovan, N., Zitoune, R., Davim, J.P.: Optimization of machining parameters at high speed drilling of carbon fiber re-inforced plastic (CFRP) laminates. *Compos. B* **43**, 1791–1799 (2012)
6. Davim, J.P., Reis, P.: Drilling carbon fiber reinforced plastics manufactured by auto-clave-experimental and statistical study. *Mat. Design* **24**, 315–324 (2003)
7. Grilo, T.J., Paulo, R.M.F., Silva, C.R.M., Davim, J.P.: Experimental delamination analyses of CFRPs using different drill geometries. *Comp. Part B: Eng.* **45**(1), 1344–1350 (2013)
8. Ramulu, M., Young, P., et al.: Drilling of graphite/bismaleimide composite material. *J. Mater. Eng. Perform.* **8**(3), 330–338 (1999)
9. Lin, S.C., Chen, I.K.: Drilling carbon fiber-reinforced composite material at high speed. *Wear* **194**(1–2), 156–162 (1996)
10. Chen, W.-C.: Some experimental investigations in the drilling of carbon fiber-reinforced plastic (CFRP) composite laminates. *Int. J. Mach. Tools Manuf* **37**(8), 1097–1108 (1997)
11. Davim, J.P., Reis, P.: Study of delamination in drilling carbon fiber reinforced plastics (CFRP) using design experiments. *Compos. Struct.* **59**(4), 481–487 (2003)
12. Venkateshwaran, N., ElayaPerumal, A.: Hole quality evaluation of natural fiber composite using image analysis technique. *J. Reinf. Plast. Compos.* **32**(16), 1188–1197 (2013)
13. Tsao, C.C., Hocheng, H.: Taguchi analysis of delamination associated with various drill bits in drilling of composite material. *Int. J. Mach. Tools Manuf* **44**(10), 1085–1090 (2004)

14. Palanikumar, K., Prakash, S., et al.: Evaluation of delamination in drilling GFRP compo-sites. *Mater. Manuf. Process.* **23**(8), 858–864 (2008)
15. Tsao, C.C., Hocheng, H.: Evaluation of thrust force and surface roughness in drilling composite material using Taguchi analysis and neural network. *J. Mat. Process. Technol.* **203** (1–3), 342–348 (2008)
16. Enemuoh, E.U., El-Gizawy, A.S., et al.: An approach for development of damage-free drilling of carbon fiber reinforced thermosets. *Int. J. Mach. Tools Manuf* **41**(12), 1795–1814 (2001)
17. Park, K.H., Beal, A., Kwon, P., Lantrip, J.A.: Comparative study of carbide tools in drilling of CFRP and CFRP-Ti stacks. *J. Manuf. Sci. Eng.* **136**(1), 014501 (2014)
18. Abrão, A.M., Rubio, J.C.C., et al.: The effect of cutting tool geometry on thrust force and delamination when drilling glass fibre reinforced plastic composite. *Mater. Des.* **29**(2), 508–513 (2008)

Surface Roughness and Wear Properties of Al–Al₂O₃ Metal Matrix Composites Fabricated Using Friction Stir Processing



N. Fatchurrohman and Azrie Abdullah

Abstract Friction stir processing (FSP) involves the mixing reinforcement particles on metal surface and the control of its dispersion is more difficult to attain with conventional techniques such as casting. The objective of present work was to perform tribology characterization of Al alloys Al-6061 and Al-6061 with 5 weight % Al₂O₃ produced using FSP. The parameters involved were rotation speed 1000, 1200 and 1400 rpm and traversed speed constant at 25 mm/min. The results show that the surface roughness with the presence of the reinforcement demonstrated better surface roughness compared to specimens with no reinforcement. Furthermore, high increment of the tool rotation speed indicates the declined value of the coefficient of friction of the specimen material.

Keywords Metal matrix composites • Friction stir processing
Tribology • Al-6061 alloy • Al₂O₃ particles

1 Introduction

Friction stir processing (FSP) is a technique of changing the properties of metal through inserting a suitable reinforce particles into the work piece in order to achieved surface modifications of the work piece. It was known that this is a solid-state modification process formerly established for aluminum alloys by evolving technique of metalworking that involved localized heat treatment. This technique also controlled the microstructure of the near-surface layers of metallic modules [1].

FSP was used to improve of surface metal matrix composites properties including abrasion resistance, hardness, strength, ductility, corrosion resistance, fatigue life and formability. This can be done while unchanging the bulk properties

N. Fatchurrohman (✉) · A. Abdullah
Faculty of Manufacturing Engineering, Universiti Malaysia Pahang,
26600 Pekan, Pahang, Malaysia
e-mail: fatchurrohman@ump.edu.my

© Springer Nature Singapore Pte Ltd. 2018
M. H. A. Hassan (ed.), *Intelligent Manufacturing & Mechatronics*,
Lecture Notes in Mechanical Engineering,
https://doi.org/10.1007/978-981-10-8788-2_15

of the matrix material. Besides that, friction stir processing is an ideal process for producing low cost and high performance surface modification. Surface composites exhibit enhanced characteristics of composites on-the surface while retaining properties of the base material. FSP effectively eliminates casting defect, break up or dissolves second phase particles and lead to the considerable improvement in properties [2].

In recent investigations, FSP has been introduced to modify the upper surface of metallic materials [3]. FSP has been developed for the application with aluminium alloys, with the goal of high-strain-rate processing [4]. FSP is a fast technique with simple processing and low cost to in situ synthesizes particulate-reinforced composites especially in aluminium alloy [5, 6]. FSP improved the distribution of the reinforced particles which resulting more homogeneous and thermodynamically more stable in metallurgical properties as the matrices and reinforcement have a strong interfacial bonding [7]. FSP or friction stir welding (FSW) was initially applied to Al alloys [7] and extended to other metals such as Cu alloys [8], Mg alloys [9], or Ti alloys [10]. Until now, Al alloys are the most commonly used materials in FSP applications. Research have been dedicated to the effect of FSP parameters on the affected zone such as by Karthikeyan et al. [11, 12]. They studied the friction stir performance of the Al alloys in order to examine effect of feed rate and rotational speed on microstructure and properties. They informed the increased tensile, yield strengths ductility and grain size reduction because of FSP.

The objective of this preliminary study was to investigate the surface roughness and wear properties of Al, Al₂O₃ metal matrix composites fabricated using FSP.

2 Materials and Methodology

2.1 Material Selection

The materials used were Al alloy Al-6061 and reinforcement Al₂O₃ particles. The size of Al-6061 with dimension of (100 mm × 120 mm × 10 mm). The average particle size of Al₂O₃ was 30 microns and reinforce up to 5 weight %. The physical properties of the materials are shown in Table 1.

Table 1 Material properties of Al-6061 and Al₂O₃

Properties	Al-6061	Al ₂ O ₃
Density (g/cm ³)	2.70	3.95
Molecular weight (g/mol)	26.98	101.96
Melting point (°C)	580	2072

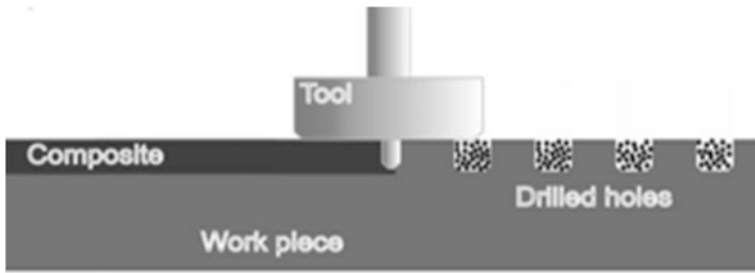


Fig. 1 Schematic process of FSP [2]

2.2 Sample Preparation

The specimens were prepared using FSP process with three different parameters. The rotation speeds of 1000, 1200, 1400 rpm and traverse speed of constant at 25 mm/min. The schematic of the process is as in Fig. 1.

The surface roughness of the samples was then measured using a calibrated Mahr-Perthometer surface roughness tester. Surface roughness is generally described using two methods: arithmetic mean value and root-mean-square average. The arithmetic mean value (Ra, formerly identified as AA for arithmetic average or CLA for center-line average) is based on the schematic illustration of a rough surface, which in figure the arithmetic value, Ra is defined as follow.

$$Ra = \frac{a + b + c + d + \dots}{n} \tag{1}$$

The wear test was conducted using calibrated Tribology Test Rig in order to gain the coefficient of friction (COF). The COF of wear sample was calculated from the friction force and load applied through Eq. 2.

$$\mu_k = F_k / N \tag{2}$$

where μ_k is the COF, F_k is the friction force and N is the load applied from the wear test machine.

3 Result and Discussion

The surface roughness of the substrate was determined from the value of arithmetic average roughness, Ra shown in Fig. 2. Based on the overall result for the average roughness-rpm curve, the properties of the average roughness decreases if the parameter of the tool rotation increase. The blue line shows the average roughness without reinforce and the orange shows the average roughness with reinforcement.

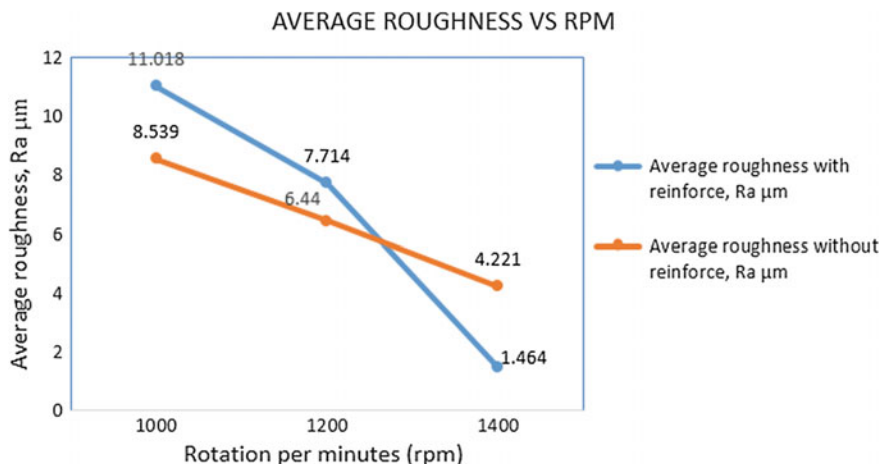


Fig. 2 The surface roughness using different tool rotational speeds

At rpm 1400 the average roughness with reinforce is lower compare to the without reinforce. Average roughness with reinforce was 1.464 μm and average roughness without reinforce 4.221 μm . The small size addition of particles contributed on the effectiveness for FSP process to produce higher surface roughness. The higher rpm makes the surface smoother because the particle mixture of the composite was well distributed using FSP process.

By reviewing on the graph in Fig. 3, it clearly shows that the average of coefficient of friction (COF) was inversely proportionally to the rpm of the tools. This was because the surface became smoother as the tool speed was increased.

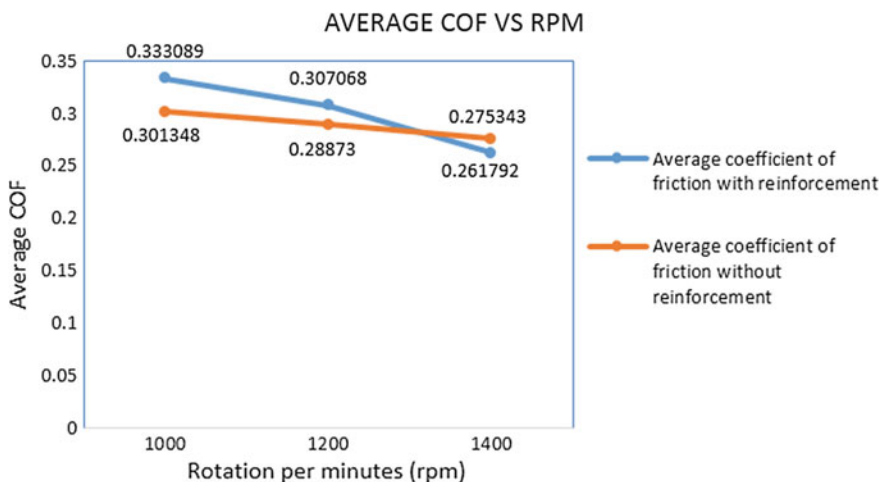


Fig. 3 The COF using different tool rotational speeds

The COF with reinforcement was higher than the average COF without reinforcement for rotation speeds 1000 and 1200 rpm. This means, by adding Al_2O_3 reinforcements it increased the hardness of the material and hence it can improve wear performance. This was due to the properties of Al_2O_3 which is a hard ceramic material. FSP caused in a significant disintegration and well distribution of Al_2O_3 particles in the Al matrix as well as elimination of porosity. This contributes to the reduction of COF the stir zone of the FSP sample.

4 Conclusion

Through this preliminary study, it can be concluded that the roughness and COF of modified surface composites were influenced by the addition of reinforcement and the rotation speed of the FSP tool. This was achieved by the formation of smaller grain in the matrix Al-6061 as the rotation speed was increased. Also the distribution of reinforcement Al_2O_3 influence the composite microstructure and in turn influenced the roughness and the COF of the material. FSP can be used as a tool to locally modify the microstructures in regions experiencing high frictional loading and significantly improve the overall performance of Al alloy matrix.

Acknowledgements The authors would like to gratefully acknowledge University Malaysia Pahang for the financial support through Internal Research Grant RDU 150371.

References

1. Ma, Z.Y.: Friction stir processing technology: a review. *Metall. Mater. Trans. A* **39**(3), 642–658 (2008)
2. Sharma, V., Prakash, U., Kumar, B.M.: Surface composites by friction stir processing: a review. *J. Mater. Process. Technol.* **224**, 117–134 (2015)
3. Wang, W., Shi, Q.Y., Liu, P., Li, H.K., Li, T.: A novel way to produce bulk SiCp reinforced aluminum metal matrix composites by friction stir processing. *J. Mater. Process. Technol.* **209**(4), 2099–2103 (2009)
4. Morishige, T., Hirata, T., Tsujikawa, M., Higashi, K.: Comprehensive analysis of minimum grain size in pure aluminum using friction stir processing. *Mater. Lett.* **64**(17), 1905–1908 (2010)
5. Abdollahi, S.H., Karimzadeh, F., Enayati, M.H.: Development of surface composite based on Mg–Al–Ni system on AZ31 magnesium alloy and evaluation of formation mechanism. *J. Alloy. Compd.* **623**, 335–341 (2015)
6. Qian, J., Li, J., Xiong, J., Zhang, F., Lin, X.: In situ synthesizing Al_3Ni for fabrication of intermetallic-reinforced aluminum alloy composites by friction stir processing. *Mater. Sci. Eng. A* **550**, 279–285 (2012)
7. Hsu, C.J., Kao, P.W., Ho, N.J.: Intermetallic-reinforced aluminum matrix composites produced in situ by friction stir processing. *Mater. Lett.* **61**(6), 1315–1318 (2007)

8. Menon, S.K., Pierce, F.A., Rosemark, B.P., Oh-Ishi, K., Swaminathan, S., McNelley, T.R.: Strengthening mechanisms in NiAl Bronze: hot deformation by rolling and friction-stir processing. *Metall. Mater. Trans. A* **43**(10), 3687–3702 (2012)
9. Darras, B.M., Khraisheh, M.K., Abu-Farha, F.K., Omar, M.A.: Friction stir processing of commercial AZ31 magnesium alloy. *J. Mater. Process. Technol.* **191**(1), 77–81 (2007)
10. Buffa, G., Ducato, A., Fratini, L.: FEM based prediction of phase transformations during friction stir welding of Ti6Al4V titanium alloy. *Mater. Sci. Eng. A* **581**, 56–65 (2013)
11. Karthikeyan, L., Senthilkumar, V.S., Balasubramanian, V., Natarajan, S.: Mechanical property and microstructural changes during friction stir processing of cast aluminum 2285 alloy. *Mater. Des.* **30**(6), 2237–2242 (2009)
12. Karthikeyan, L., Senthilkumar, V.S., Balasubramanian, V., Arul, S.: Analysis of first mode metal transfer in A413 cast aluminum alloy during friction stir processing. *Mater. Lett.* **64**(3), 301–304 (2010)

A Knowledge-Based Ergonomics Assessment System for WMSD Prevention Using AHP Methodology



Fazilah Abdul Aziz, Zakri Ghazalli, Mohd Jawad Mohd Jamil,
Awanis Romli and Nik Mohd Zuki Nik Mohamed

Abstract This research develops a knowledge-based ergonomics assessment system (KBEAS) that measure and predicts the degree of criticality of risk factors related to work-related musculoskeletal disorders (WMSD). Predicting WMSD individual risk level provides critical decision support information to occupational safety and health (OSH) practitioners in the ergonomic analysis. The KBEAS is based on the analytic hierarchy process (AHP) methodology. The current study integrates AHP method with real workplace ergonomics risk data and design web-based system assisting a sensible multi-criteria WMSD related risk factors. The objectives involve knowledge acquisition performed through preliminary study, MSD symptom study, literature analysis, and tacit knowledge analysis and practitioner survey to identify the ergonomics risk factors that include individual, organizational, physical and psychosocial. The application of this system shows that the design of the proposed KBEAS for WMSD risk factors has been validated and gets each risk factors weight easily by using AHP. The study findings showed that ‘organizational ergonomics risk factors’ is more critical than other factors. The overall prioritization revealed that ‘exposure to physical demands’ had a priority vector of 26.33%, and it was perceived as the item with the most critical factor. The KBEAS could help the user to make an objective judgement on the subjective description and get the correct result of the ergonomics risk factors.

Keywords Knowledge-based ergonomics assessment system • WMSD
AHP • Web-based system

F. Abdul Aziz (✉) · Z. Ghazalli · N. M. Z. Nik Mohamed
Faculty of Mechanical Engineering, Universiti Malaysia Pahang,
26600 Pekan, Pahang, Malaysia
e-mail: fazilahaa@ump.edu.my

M. J. Mohd Jamil · A. Romli
Faculty of Computer Systems and Software Engineering,
Universiti Malaysia Pahang, 26300 Gambang, Pahang, Malaysia

F. Abdul Aziz
Faculty of Manufacturing Engineering, Universiti Malaysia Pahang,
26600 Pekan, Pahang, Malaysia

1 Introduction

Industry workers performing manual operations are subjected to musculoskeletal disorders (MSD) [1, 2]. The high prevalence of MSD symptoms as a significant problem among Malaysia automotive workers [3–5]. The occupational health and safety management system (OHSMS) has been known to play an essential role in controlling the safety conditions of workplaces and health of the employees in the companies [6, 7]. However, occupational safety and health (OSH) practitioners appear to focus on checking the safety and health aspects rather than zooming in on getting to the human factors or ergonomics issues.

Most of the companies had no information with regards to the health, safety and ergonomics performance [8]. Thus, WMSDs consistently continues as one of the occupational safety and health (OSH) related problems due to OSH and ergonomic intervention have not been wholly implemented [9]. In particular, with regards to the OHSMS, the focus should not be only on the development of healthy and safe working conditions, but also equally to the workplace comfort and wellness, and employee's well-being. Thus, a practical approach to predict workplace ergonomics risk exposure can be beneficial to occupational health and safety practitioners and production managers to prevent WMSD symptom among production workers. Therefore, this research is an effort to develop a knowledge-based ergonomics assessment system (KBEAS) that assists in evaluating the potential of WMSD risk factors at an automotive component manufacturer.

The proposed algorithm of the system is based on AHP method (T. L. Saaty 1980) for the rules and inference system. The AHP was used for multi-criteria decision-making process and provides reasonable support [10] and flexible approach to risk analysis [11]. Since decision maker can unbiasedly get numerical pair-wise comparisons by choosing proper numerical scale to quantify linguistic pair-wise comparisons [12]. The web-based system was set up as ergonomics assessment tool since it was fundamental for such a medium to be open efficiently and auspicious [13]. Web-based system application has upgraded the effect of a decision support system when the choice available is considered by an expansion in the quantity of other options to assess [14].

The final experiment results show that KBEAS could use to predict a particular risk factors level to obtain several appropriate measures proposed by OSH practitioners in engineering and administration controls. Consequently, a smart and practical tool can be developed to identify WMSD risk related to a variety of factors.

2 Knowledge Acquisition Process

The required information and knowledge to construct the knowledge base are obtained through knowledge acquisition process (KAP). KAP consists of a mixture of knowledge acquisition methods. The preliminary knowledge acquisition gains an overview of the workplace ergonomics problem. The WMSD symptom knowledge acquisition finds about the body pain complaint among production workers.

Initially, the potential risk factors are obtained from literature associated to back, neck, shoulder, and arm pain. The literatures contain a wealth of information about the possible causes of MSD [15–18]. Based upon the expertise, experience, and accessibility the group of subject matter experts (SME) consists of a managing director and general manager, as well as department managers from production, engineering, and safety health and environment are selected for tacit knowledge analysis. The recognized risk factors and common characteristics are acquired from the literature that represents the categories individual-related, organizational-related, physical-related and psychosocial-related risk factors.

To validate the risk factors related to WMSDs, the survey is considered useful in identifying the dominant risk factors. The questionnaire was distributed to practitioners at three automotive production plants. The consequences of the knowledge acquisition lead to the generation of various risk factors. The final risk factors thus acquired are summarised to formulate the AHP hierarchy, as shown in Fig. 1.

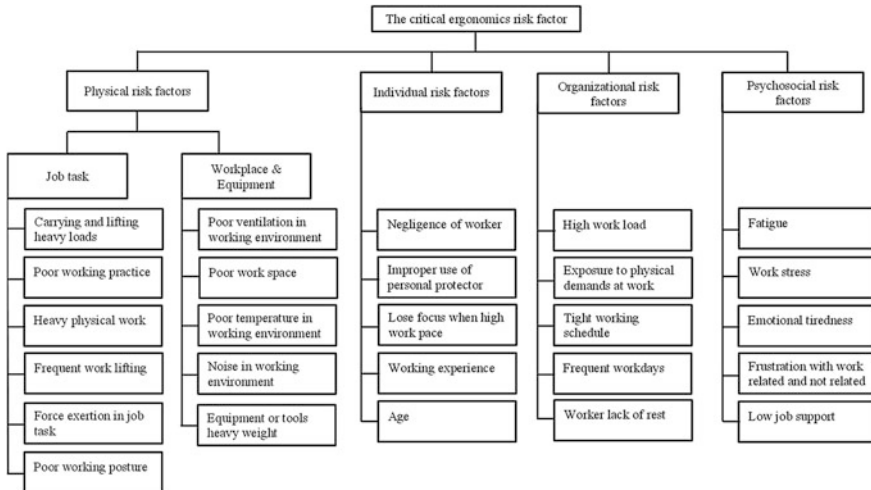


Fig. 1 AHP hierarchy structure of ergonomics risks factors

3 AHP Methodologies

The risk factors related to WMSD are diversity, various, and dynamic. Based on that, to achieve intelligence and dynamic in early detection and meantime facilitate employees to make an objective descriptive of subjective judgments, the current study applies AHP methodology. The pair-wise comparison is the relative importance of one criterion over another in meeting a specific goal [13, 19]. Given those, current study set up ergonomics assessment model of WMSD risk factors to do the quantitative analysis. The AHP-based method involves the following significant steps:

1st Step: Develop a hierarchy of factors based on KAP results (refer Fig. 1).

2nd Step: Construct judgement matrix and make pair-wise comparisons: Practitioners are asked to evaluate the relative importance of risk factors within and among the leading ergonomics factors. A matrix of element evaluation, denoted as A , will be formed using the comparisons. Each entry a_{ij} of the matrix, in the position (i, j) is obtained comparing the row element A_i with the column element A_j ; Means of pair-wise comparison administered the survey questionnaire. A numerical scale is then assigned to each pair of alternatives (A_i, A_j) by the experts (refer Table 1).

3rd Step: Synthesize judgments: The process is to calculate a vector of local weights or priorities of each risk factor in term of its contribution to the overall goal. It includes the following steps.

Step 3.1 Once the overall expert judgments are created and calculated using the geometric mean [refer Eq. (1)],

Table 1 Pair-wise comparison scale used with AHP adapted from [3]

Intensity of importance	Score	Definition	Explanation
1	1	Equal importance	Two elements contribute equally to the property
2	3	Moderate importance of one over another	Experience and judgment slightly favor one over the other
3	5	Essential or strong importance	Experience and judgment strongly favor one over another
4	7	Very strong importance	An element is strongly favored and its dominance is demonstrated in practice
5	9	Extreme importance	The evidence favoring one element over another is one of the highest possible orders of affirmation
Reciprocals	When activity I compared to j assigned one of the above numbers, the activity j compared to i is assigned its reciprocal		
Rational	Ratios arising from forcing consistency of judgments		

$$\text{Geometric mean, } GM_i = \sum_{i=1}^n n\sqrt{a_{ij}} = \sqrt[n]{a_{ij1} \times a_{ij2} \times \dots \times a_{ijn}} \quad (1)$$

where n = number of participants

Step 3.2 The next step is to calculate a vector of local weights or priorities of elements [refer Eq. (3)]. The principal eigenvector w of the matrix can be calculated using the Eq. (2).

$$\text{Eigenvector} = w_i \frac{GM_i}{\sum_{i=1}^n GM_i} \quad (2)$$

$$\text{Eigenvalues} = \text{local weight} = \frac{\sum_{i=1}^n w_i}{n} \quad (3)$$

where n = number of elements

Step 3.3 The synthesized weight or global priority vector for elements can be presented as in the Eq. (4):

Global priority vector, W_i :

$$W_i = (\text{Criteria local weight})(\text{Sub} - \text{criteria local weight}) \quad (4)$$

4th Step: Upon having the local priority vector determined, it is then necessary to evaluate the consistency of the pairwise comparison matrix. The consistency index and consistency ratio can be seen in the Eqs. (5) and (7).

$$\text{Consistency index (CI)} = \frac{\lambda_{\max} - n}{n - 1} \quad (5)$$

$$\lambda_{\max} = \sum_{i=1}^n \left[\left(\sum_{i=1}^n GM_i \right) (w_j) \right] \quad (6)$$

where, λ_{\max} = maximum eigenvalue and n is the number of elements

$$\text{Consistency ratio (CR)} = \frac{\text{Consistency index (CI)}}{\text{Random index (RI)}} \leq 0.10 \quad (7)$$

If the value of consistency ratio (CR) is smaller or equal to 0.1 the inconsistency is acceptable. If the CR is greater than 0.1 then the subjective judgment need to be revised.

4 KBEAS Development

In the present convenience working environment, it is fundamental to propose and set up a reasonable system which will consolidate the power of web-based systems, AHP analysis, and empirical data and therefore advance the efficiency of prioritizing processes. The KBEAS was designed as a web-based system since it was planned to accessible anytime and anyplace inside the organization.

4.1 Structure of System

The basic structure of the web-based system includes the user interface, a knowledge base, and an AHP inference engine. The proposed system is implemented by using XAMPP and MySQL server is used as a database. XAMPP is a free and open source cross-platform web server solution stake package. XAMPP consists mainly of the Apache HTTP Server, Maria DB database, and interpreters for scripts written in the PHP and Perl programming languages. The structure of the developed web-based system for ergonomics assessment purpose is given in Fig. 2.

Component of the system. Figure 3 demonstrates the system components and their corresponding functions. The system has four major components. First one is a database component in which all factors information are stored. Users would retrieval be able to the risk factors record by time and embed new record.

The second component is data input part. Concerning user's determination comparing data is recovered from the database. The third component is a data processing part which allows the server to use AHP method to calculate each criterion and sub-criteria weights. The consistency test for data input also performed. This component can retrieve the corresponding numerical values regarding the submitted specific condition about those criteria and sub-criteria mentioned previously. The fourth component is data output part. This component is to prioritize for criteria and sub-criteria of risk factors. Also, rank all the criteria and sub-criteria within the group and all groups of factor.

Section of a web-based system. The system is divided into two sections. One of them is administrator side and the other one is user side. Administrator or user can

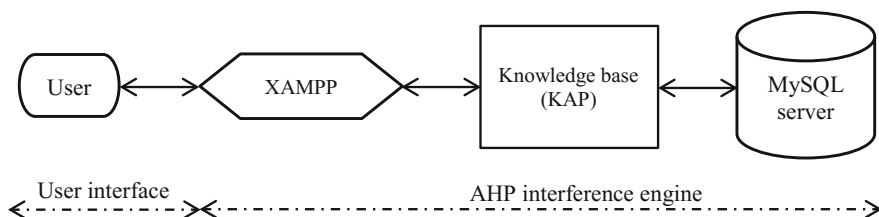


Fig. 2 Web-based of knowledge-based ergonomics assessment system structure

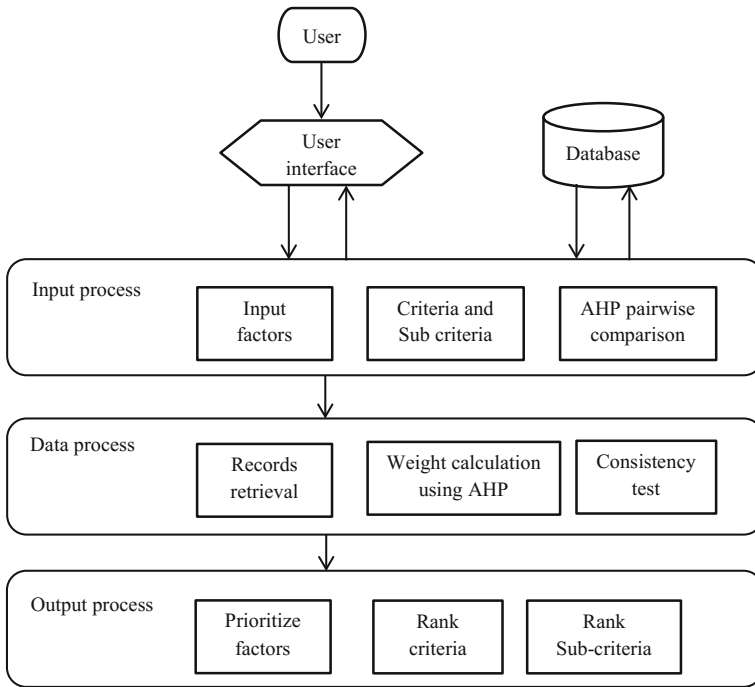


Fig. 3 Components of the KBEAS and their corresponding functions

access the system wherever he/she needs. The flow diagram of the system is illustrated in Fig. 4. Under administrator section, administrator of the system makes some definitions on the purpose of use. These definitions are as follows: remove a record, remove a user, modify risk factors, modify questions, and adding a legend.

Company’s Safety Health Officer (SHO) User: Safety Health Officer User has primary responsibility for ergonomics risk report for the production plant. Safety Health Officer can login both administrator and user. Other Users: system’s other defined users, registered user who is employee representative from the related department and had authority over the ergonomics assessment.

4.2 System Application

To validate the proposed KBEAS, an application in a local automotive component manufacturer has been done. The evaluation group was made up of fifteen practitioners from several departments under production plant, whose expertise was different. All practitioners that participated had at least 5 years of working experience in the company. The practitioners were selected according to their job tasks, roles and influences on OHSM system practices.

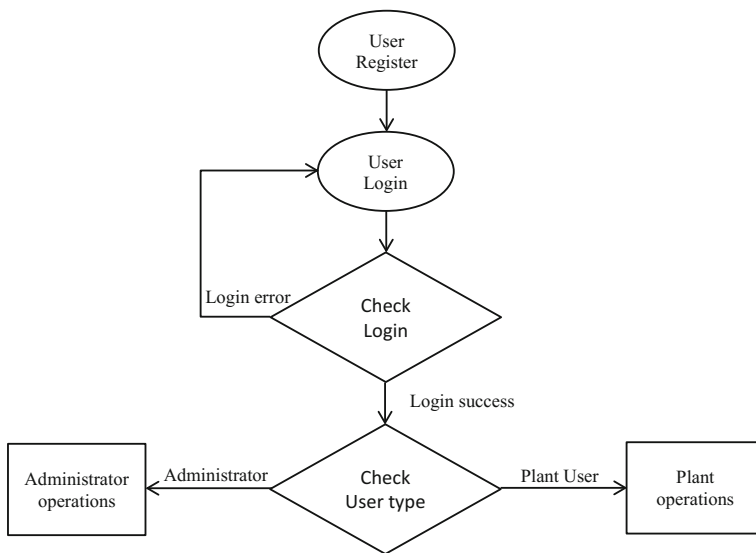
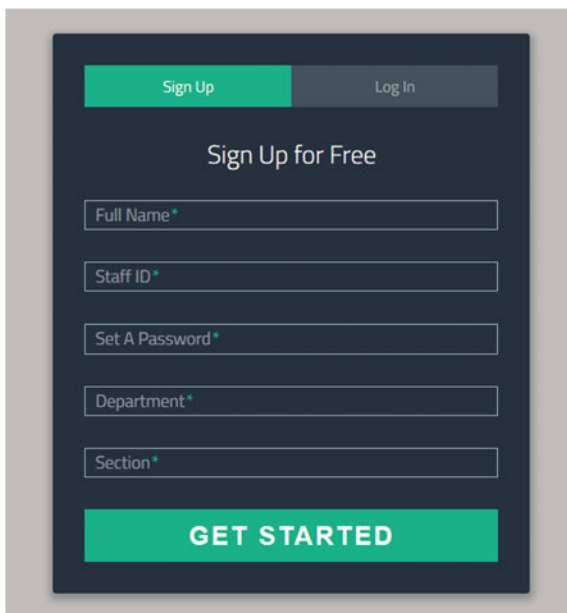


Fig. 4 Flow diagram of the system

The system works as follows, after registering to the system (refer Fig. 5), the user can log into the system for data input purpose.

Then, once the user logs into the system the comparison module page of the system appears. Figure 6 displays one out of seven comparison modules. Each question defined under different potential risks is answered and scale is selected. After the comparison module is completed, user click button “Next questions” and

Fig. 5 User interface: registration page of the web-based system



When you are considering the ergonomics job task risk factors in the early phase of project, which one do you think is more important to make improvement and how many times more important than others?

No.	First Pair	Values									Second Pair
		5	4	3	2	1	2	3	4	5	
1.	Carrying and lifting heavy loads	<input type="radio"/>	<input type="radio"/>	<input type="radio"/>	<input type="radio"/>	<input type="radio"/>	<input type="radio"/>	<input type="radio"/>	<input type="radio"/>	<input type="radio"/>	Poor working practice
2.	Carrying and lifting heavy loads	<input type="radio"/>	<input type="radio"/>	<input type="radio"/>	<input type="radio"/>	<input type="radio"/>	<input type="radio"/>	<input type="radio"/>	<input type="radio"/>	<input type="radio"/>	Heavy physical work
3.	Carrying and lifting heavy loads	<input type="radio"/>	<input type="radio"/>	<input type="radio"/>	<input type="radio"/>	<input type="radio"/>	<input type="radio"/>	<input type="radio"/>	<input type="radio"/>	<input type="radio"/>	Frequent work lifting
4.	Carrying and lifting heavy loads	<input type="radio"/>	<input type="radio"/>	<input type="radio"/>	<input type="radio"/>	<input type="radio"/>	<input type="radio"/>	<input type="radio"/>	<input type="radio"/>	<input type="radio"/>	Force exertion in job task
5.	Carrying and lifting heavy loads	<input type="radio"/>	<input type="radio"/>	<input type="radio"/>	<input type="radio"/>	<input type="radio"/>	<input type="radio"/>	<input type="radio"/>	<input type="radio"/>	<input type="radio"/>	Poor working posture
6.	Poor working practice	<input type="radio"/>	<input type="radio"/>	<input type="radio"/>	<input type="radio"/>	<input type="radio"/>	<input type="radio"/>	<input type="radio"/>	<input type="radio"/>	<input type="radio"/>	Heavy physical work
7.	Poor working practice	<input type="radio"/>	<input type="radio"/>	<input type="radio"/>	<input type="radio"/>	<input type="radio"/>	<input type="radio"/>	<input type="radio"/>	<input type="radio"/>	<input type="radio"/>	Frequent work lifting
8.	Poor working practice	<input type="radio"/>	<input type="radio"/>	<input type="radio"/>	<input type="radio"/>	<input type="radio"/>	<input type="radio"/>	<input type="radio"/>	<input type="radio"/>	<input type="radio"/>	Force exertion in job task
9.	Poor working practice	<input type="radio"/>	<input type="radio"/>	<input type="radio"/>	<input type="radio"/>	<input type="radio"/>	<input type="radio"/>	<input type="radio"/>	<input type="radio"/>	<input type="radio"/>	Poor working posture
10.	Heavy physical work	<input type="radio"/>	<input type="radio"/>	<input type="radio"/>	<input type="radio"/>	<input type="radio"/>	<input type="radio"/>	<input type="radio"/>	<input type="radio"/>	<input type="radio"/>	Frequent work lifting
11.	Heavy physical work	<input type="radio"/>	<input type="radio"/>	<input type="radio"/>	<input type="radio"/>	<input type="radio"/>	<input type="radio"/>	<input type="radio"/>	<input type="radio"/>	<input type="radio"/>	Force exertion in job task
12.	Heavy physical work	<input type="radio"/>	<input type="radio"/>	<input type="radio"/>	<input type="radio"/>	<input type="radio"/>	<input type="radio"/>	<input type="radio"/>	<input type="radio"/>	<input type="radio"/>	Poor working posture
13.	Frequent work lifting	<input type="radio"/>	<input type="radio"/>	<input type="radio"/>	<input type="radio"/>	<input type="radio"/>	<input type="radio"/>	<input type="radio"/>	<input type="radio"/>	<input type="radio"/>	Force exertion in job task
14.	Frequent work lifting	<input type="radio"/>	<input type="radio"/>	<input type="radio"/>	<input type="radio"/>	<input type="radio"/>	<input type="radio"/>	<input type="radio"/>	<input type="radio"/>	<input type="radio"/>	Poor working posture
15.	Force exertion in job task	<input type="radio"/>	<input type="radio"/>	<input type="radio"/>	<input type="radio"/>	<input type="radio"/>	<input type="radio"/>	<input type="radio"/>	<input type="radio"/>	<input type="radio"/>	Poor working posture
Next Question >											

Legends	
Value	Weightage
1	Equally Important
2	Weakly important
3	Strongly important
4	Very strong important
5	Absolutely important

Fig. 6 User interface: comparison module for job task risk factors

system allows the user to pass on to the next page. Afterward, the user clicks the button “submit and finish” (see Fig. 7), the end of questions and data input process.

The registration page (refer Fig. 5) will appear for next data input. Once completing the comparison modules, the system calculates the risk factors weight. After the prioritization process, the system provides the user with intermediate results consisting of the priority factors and the consistency of the pairwise comparison module.

When you are considering the psychosocial risk factors in the early phase of project, which one do you think is more important and how many times more important than the others?

No.	First Pair	Values										Second Pair
		5	4	3	2	1	2	3	4	5		
1.	Fatigue	<input type="radio"/>	<input type="radio"/>	<input type="radio"/>	<input type="radio"/>	<input type="radio"/>	<input type="radio"/>	<input type="radio"/>	<input type="radio"/>	<input type="radio"/>	<input type="radio"/>	Work stress
2.	Fatigue	<input type="radio"/>	<input type="radio"/>	<input type="radio"/>	<input type="radio"/>	<input type="radio"/>	<input type="radio"/>	<input type="radio"/>	<input type="radio"/>	<input type="radio"/>	<input type="radio"/>	Emotional tiredness
3.	Fatigue	<input type="radio"/>	<input type="radio"/>	<input type="radio"/>	<input type="radio"/>	<input type="radio"/>	<input type="radio"/>	<input type="radio"/>	<input type="radio"/>	<input type="radio"/>	<input type="radio"/>	Frustration with work related and not related
4.	Fatigue	<input type="radio"/>	<input type="radio"/>	<input type="radio"/>	<input type="radio"/>	<input type="radio"/>	<input type="radio"/>	<input type="radio"/>	<input type="radio"/>	<input type="radio"/>	<input type="radio"/>	Low job support
5.	Work stress	<input type="radio"/>	<input type="radio"/>	<input type="radio"/>	<input type="radio"/>	<input type="radio"/>	<input type="radio"/>	<input type="radio"/>	<input type="radio"/>	<input type="radio"/>	<input type="radio"/>	Emotional tiredness
6.	Work stress	<input type="radio"/>	<input type="radio"/>	<input type="radio"/>	<input type="radio"/>	<input type="radio"/>	<input type="radio"/>	<input type="radio"/>	<input type="radio"/>	<input type="radio"/>	<input type="radio"/>	Frustration with work related and not related
7.	Work stress	<input type="radio"/>	<input type="radio"/>	<input type="radio"/>	<input type="radio"/>	<input type="radio"/>	<input type="radio"/>	<input type="radio"/>	<input type="radio"/>	<input type="radio"/>	<input type="radio"/>	Low job support
8.	Emotional tiredness	<input type="radio"/>	<input type="radio"/>	<input type="radio"/>	<input type="radio"/>	<input type="radio"/>	<input type="radio"/>	<input type="radio"/>	<input type="radio"/>	<input type="radio"/>	<input type="radio"/>	Frustration with work related and not related
9.	Emotional tiredness	<input type="radio"/>	<input type="radio"/>	<input type="radio"/>	<input type="radio"/>	<input type="radio"/>	<input type="radio"/>	<input type="radio"/>	<input type="radio"/>	<input type="radio"/>	<input type="radio"/>	Low job support
10.	Frustration with work related and not related	<input type="radio"/>	<input type="radio"/>	<input type="radio"/>	<input type="radio"/>	<input type="radio"/>	<input type="radio"/>	<input type="radio"/>	<input type="radio"/>	<input type="radio"/>	<input type="radio"/>	Low job support
<input type="button" value="Submit & Finish"/>												

Legends	
Value	Weightage
1	Equally Important
2	Weakly important
3	Strongly important
4	Very strong important
5	Absolutely important

Fig. 7 User interface: comparison module for psychosocial risk factors

4.3 Results

In this study, the experience with the system and ergonomics risk factors data obtained from the company resulted in a priority vector as illustrated in Table 2.

Based on the results acquired in the AHP analysis, the following statements can, therefore, be made:

- i. Organizational risk factors are more critical than physical risk factors.
- ii. Physical risk factors are more critical than psychosocial risk factors.
- iii. Psychosocial risk factors are more critical than individual risk factors.
- iv. Individual risk factors are less significant than organizational risk factors.

The weights for each of the factors in the hierarchy were calculated in line with their perceived contribution to the risky situation to the workers in automotive component production plant (refer Table 3).

Table 2 Priority results for ergonomics risk factors related to WMSD

Criteria	Priority
Individual ergonomics risk factors	0.0845
Organizational ergonomics risk factors	0.5440
Physical ergonomics risk factors	0.2036
Psychosocial risk factors	0.1679

Table 3 Ranking of risk factors associated with WMSD

Ergonomics risk factors	Global priority (%)	Rank
<i>Exposure to physical demands</i>	26.33	1st
<i>Higher work load</i>	10.29	2nd
Tight working schedules	6.41	3rd
Equipment or tools heavy weight	6.10	4th
Frequent work days	5.99	5th
Low job support	5.79	6th
Lack of rest	5.38	7th
Poor work space	4.26	8th
Fatigue	3.51	9th
Frustration with work related and not related	3.48	10th
Lose focus when higher work load	3.46	11th
Emotional tiredness	2.39	12th
Noise in working environment	2.20	13th
Poor temperature in working environment	2.12	14th
Poor ventilation in working environment	1.72	15th
Work stress	1.62	16th
Working experience	1.60	17th
Negligence of worker	1.60	17th
Improper use of personal protector equipment	1.34	19th
Force exertion in job task	1.06	20th
Poor working posture	1.01	21st
<i>Poor working practice</i>	0.53	22nd
<i>Heavy physical work</i>	0.51	23rd
<i>Carrying and lifting heavy loads</i>	0.47	24th
<i>Age</i>	0.44	25th
<i>Frequent work lifting</i>	0.37	26th

The overall prioritization revealed that ‘exposure to physical demands’ had a priority vector of 26.33%, and it was perceived as the item with the most critical factor. It is compulsory to execute a consistency validation for each hierarchy and the model as a whole for every comparison module form. In this regard, Table 4

Table 4 Consistency validation

Comparison modules	CR
Criteria of occupational ergonomics risk factors	0.0517
Sub-criteria of Individual risk factors	0.0923
Sub-criteria of organizational risk factors	0.0295
Sub-criteria of physical risk factors	0.0000
Sub-criteria of physical (job task) risk factors	0.0712
Sub-criteria of physical (workplace and equipment) risk factors	0.0596
Sub-criteria of psychosocial risk factors	0.0074

shows consistency ratio (CR) value consistency check. Since the CR for all comparison modules is less than 0.1, the hierarchy has therefore passed consistency validation.

Acknowledgements We thank University Malaysia Pahang (UMP) for grant support RDU160390, the Ministry of Higher Education Malaysia (MoHE) of the scholarship SLAI (Sijil latihan akademik IPTA).

References

1. Sylla, N., Bonnet, V., Colledani, F., Fraisse, P.: Ergonomic contribution of ABLE exoskeleton in automotive industry. *Int. J. Ind. Ergon.* **44**, 475–481 (2014). <https://doi.org/10.1016/j.ergon.2014.03.008>
2. Yoon, S.-Y., Ko, J., Jung, M.-C.: A model for developing job rotation schedules that eliminate sequential high workloads and minimize between-worker variability in cumulative daily workloads: application to automotive assembly lines. *Appl. Ergon.* **55**, 8–15 (2016). <https://doi.org/10.1016/j.apergo.2016.01.011>
3. Anita, A.R., Yazdani, A., Hayati, K.S., Adon, M.Y.: Association between Awkward posture and Musculoskeletal disorders (MSD) among assembly line workers in an automotive industry. *Malays. J. Med. Heal. Sci.* **10**, 23–28 (2014)
4. Aziz, F.A., Ghazalli, Z., Mohamed, N.M.Z., Isfar, A.: Investigation on musculoskeletal discomfort and ergonomics risk factors among production team members at an automotive component assembly plant. In: *IOP Conference Series: Materials Science and Engineering*, p. 12040. IOP Publishing (2017)
5. Nur, N.M., Dawal, S.Z., Dahari, M.: The prevalence of work related musculoskeletal disorders among workers performing industrial repetitive tasks in the automotive manufacturing companies, pp. 1–8. *Int. Conf. Ind. Eng. Oper. Manag. Bali, Indones* (2014)
6. İnan, U.H., Gül, S., Yılmaz, H.: A multiple attribute decision model to compare the firms' occupational health and safety management perspectives. *Saf. Sci.* **91**, 221–231 (2017). <https://doi.org/10.1016/j.ssci.2016.08.018>
7. Mohammadfam, I., Kamalinia, M., Momeni, M., Golmohammadi, R., Hamidi, Y., Soltanian, A.: Evaluation of the quality of occupational health and safety management systems based on key performance indicators in certified organizations. *Saf. Health Work.* **8**, 156–161 (2017). <https://doi.org/10.1016/j.shaw.2016.09.001>
8. Khandan, M., Aligol, M.H., Shamsi, M., Poursadeghiyan, M., Biglari, H., Koohpaei, A.: Occupational health, safety, and ergonomics challenges and opportunities based on the organizational structure analysis: a case study in the selected manufacturing industries in Qom Province, Iran, 2015. *Ann. Trop. Med. Public Heal.* **10**, 606–611 (2017). https://doi.org/10.4103/ATMPH.ATMPH_110_17
9. Oakman, J., Rothmore, P., Tappin, D.: Intervention development to reduce musculoskeletal disorders: Is the process on target? *Appl. Ergon.* **56**, 179–186 (2016). <https://doi.org/10.1016/j.apergo.2016.03.019>
10. Karaca, F.: An AHP-based indoor air pollution risk index method for cultural heritage collections. *J. Cult. Herit.* **16**, 352–360 (2015). <https://doi.org/10.1016/j.culher.2014.06.012>
11. Lam, H.Y., Choy, K.L., Ho, G.T.S., Cheng, S.W.Y., Lee, C.K.M.: A knowledge-based logistics operations planning system for mitigating risk in warehouse order fulfillment. *Int. J. Prod. Econ.* 1–17 (2015). <https://doi.org/10.1016/j.ijpe.2015.01.005>
12. Saaty, T.L.: Decision making with the analytic hierarchy process. *Int. J. Serv. Sci.* **1**, 83 (2008). <https://doi.org/10.1504/IJSSCI.2008.017590>

13. Xiong, D., Chen, J.: A web-based automatic warning system for citrus bacteria canker disease using AHP methodology. In: Proceedings of the 2011 International Conferences Information Technology Computer Engineering and Management Sciences ICM 2011 vol. 1, pp. 324–327 (2011). <https://doi.org/10.1109/icm.2011.200>
14. Sundarraj, R.P.: A web-based AHP approach to standardize the process of managing service-contracts. *Decis. Support Syst.* **37**, 343–365 (2004). [https://doi.org/10.1016/S0167-9236\(03\)00033-2](https://doi.org/10.1016/S0167-9236(03)00033-2)
15. Rafeemanesh, E., Kashani, F.O., Parvaneh, R., Ahmadi, F.: A Survey on low back pain risk factors in steel industry workers in 2015. *Asian Spine J.* **11**, 44–49 (2017)
16. Biswas, G., Bhattacharya, A., Bhattacharya, R.: Occupational health status of construction workers: a review. *Int. J. Med. Sci. Public Heal.* **6**, 1 (2017). <https://doi.org/10.5455/ijmsph.2017.0745302112016>
17. de Cássia Pereira Fernandes, R., da Silva Pataro, S.M., de Carvalho, R.B., Burdorf, A.: The concurrence of musculoskeletal pain and associated work-related factors: a cross sectional study. *BMC Public Health* **16**, 628 (2016). <https://doi.org/10.1186/s12889-016-3306-4>
18. Bodin, J., Garlantézec, R., Costet, N., Descatha, A., Fouquet, N., Caroly, S., Roquelaure, Y.: Forms of work organization and associations with shoulder disorders: results from a French working population. *Appl. Ergon.* **59**, 1–10 (2017). <https://doi.org/10.1016/j.apergo.2016.07.019>
19. Cakir, O., Canbolat, M.S.: A web-based decision support system for multi-criteria inventory classification using fuzzy AHP methodology. *Expert Syst. Appl.* **35**, 1367–1378 (2008). <https://doi.org/10.1016/j.eswa.2007.08.041>
20. Saaty, T.L.: The analytic hierarchy process. *Decis. Anal.* 1–17 (1980)
21. Saaty, R.W.: The analytic hierarchy process-what it is and how it is used. *Math. Model.* **9**, 161–176 (1987). [https://doi.org/10.1016/0270-0255\(87\)90473-8](https://doi.org/10.1016/0270-0255(87)90473-8)
22. Saaty, T.L.: How to make a decision: the analytic hierarchy process. *Interfaces (Providence)*. **24**, 19–43 (1994). <https://doi.org/10.1287/inte.24.6.19>

Part II

Robotics

The Identification and Control of a Finger Exoskeleton for Grasping Rehabilitation



Zahari Taha, Muhammad Muaz Alim, Anwar P. P. Abdul Majeed, Muhammad Azzat Zakaria, Mohd Azraai Mohd Razman, Mohd Ali Hanafiah Shaharudin and Mohd Hasnun Arif Hassan

Abstract This paper evaluates the efficacy of different classical control architectures in performing grasping motion. The exoskeleton system was obtained via system identification method in which the input and output data was measured by means of current sensor (ACS712) and encoder attached to a DC geared motor (SPG30e-270k). The data obtained is split with a ratio of 70:30 for estimation and validation, respectively. The transfer function of the system is evaluated by varying the number of poles and zeros that are able to fit well with validation data. The performance of the classical P, PI, PD and PID control techniques were then evaluated in its ability to track the desired trajectory. It was demonstrated from the study that the PID controller provides the least steady state error as well as a reasonably fast settling time.

Keywords Grasping exoskeleton • PID • Rehabilitation

1 Introduction

The inability to perform grasping motion is often caused by stroke and spinal cord injury amongst others [1, 2]. This inability somewhat affects their capability to carry out activities of daily living (ADL). Studies have shown that continuous passive motion (CPM) may regain their basic hand and finger functions [3–9]. Conventional rehabilitation therapy is often deemed too laborious to the physiotherapist and in turn, limits the duration of the therapy sessions as well as the number of patients that could be catered. Rehabilitation robotics, in particular, exoskeletons, appear to be a plausible candidate in addressing the aforementioned problems.

Z. Taha · M. M. Alim (✉) · A. P. P. Abdul Majeed · M. A. Zakaria · M. A. M. Razman
M. A. H. Shaharudin · M. H. A. Hassan
Innovative Manufacturing, Mechatronics and Sports Laboratory, Faculty of Manufacturing
Engineering, Universiti Malaysia Pahang, 26600 Pekan, Pahang, Malaysia
e-mail: aqumuz@gmail.com

© Springer Nature Singapore Pte Ltd. 2018
M. H. A. Hassan (ed.), *Intelligent Manufacturing & Mechatronics*,
Lecture Notes in Mechanical Engineering,
https://doi.org/10.1007/978-981-10-8788-2_17

To date, there has been a number of hand exoskeletons that have been developed to carry out either CPM or assistive modes [2, 10–15]. Different types of actuation mechanisms, as well as control strategies, have been investigated. Nonetheless, it is worth mentioning that for the initial phase of rehabilitation CPM has been demonstrated to be sufficient as the primary aim of the aforesaid rehabilitation phase is merely to allow the unresponsive limbs to regain its mobility. The present study aims at evaluating different classical PID control configurations on a grasping exoskeleton developed that will assist patients that require CPM.

2 Identification and Control

The developed exoskeleton system is shown in Fig. 1. System identification technique was utilised in order to attain the plant model of the system [16]. A sinusoidal signal (typical rehabilitation motion for grasping) with an amplitude of 45° and a frequency of 0.5 rad/s for a period of 30 s is supplied to the system. The angular displacement or the output measurement of the 12 V DC motor (SPG30e-270k) was measured by using the motor's encoder. Conversely, the input measurement, i.e., the current value is measured via a current sensor (BB-ACS756) (as shown in Fig. 2). The transfer function of the system derived from the input-output data is obtained through the MATLAB system identification toolbox. Arduino Mega 2560 is used as the data acquisition (DAQ) device. MATLAB Simulink Arduino Support Package was used to calibrate the sensors as well as recording the data. Figure 3 depicts the Simulink blocks used to acquire the input-output data.

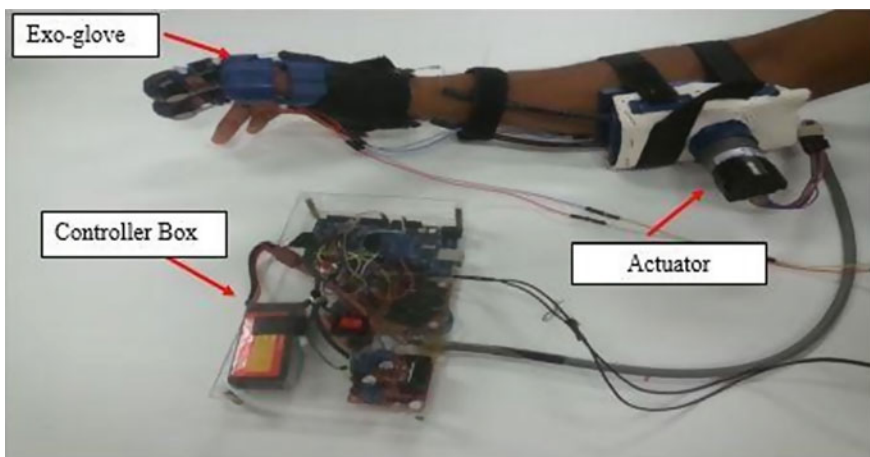


Fig. 1 Experimental setup

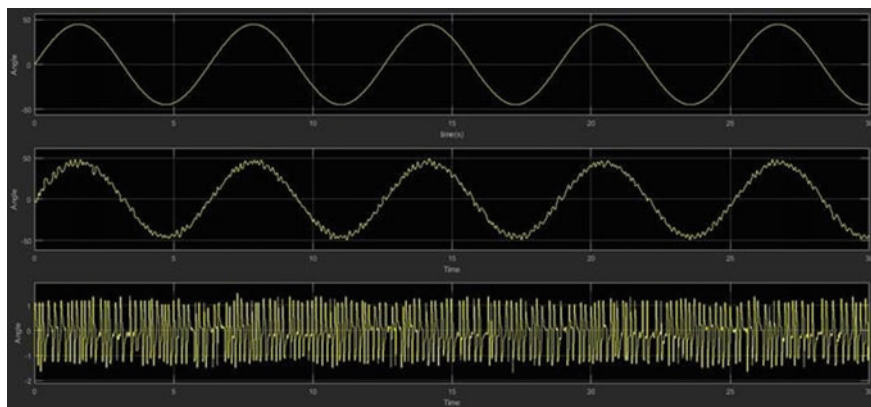


Fig. 2 Desired angle (top), actual angle (middle) and current (bottom) readings

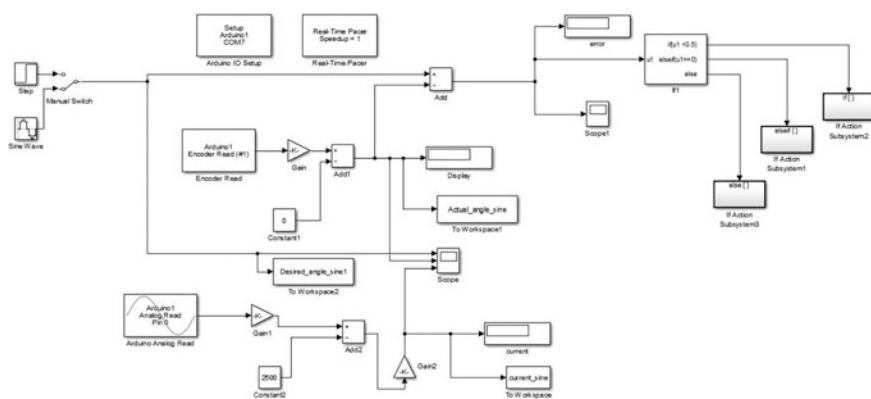


Fig. 3 Input-output data acquisition via Simulink

Approximately 70% of the data is used for the estimation process, and 30% of the data is utilised for the validation process. A number of continuous transfer function (ctf) were estimated by varying the number of zeros and poles of the system. $AzBp$, where A corresponds to the number of zeros, z whilst B the number of poles, p . All the estimation and validation fit of the estimated models are evaluated. Once the transfer function is attained, the PID variation gains are heuristically tuned through hardware-in-the-loop (HIL) simulation and the gains are implemented to the system for experimental evaluation.

Table 1 Controller gains

Controller	Gains		
	P	I	D
PI	5.4478	0.0078	
PD	5.4478		0.33860
PID	5.4478	0.0078	0.33860

Table 2 Time response analysis

Controller	Settling time (s)	Steady state error (°)
PI	0.77	±7
PD	0.45	±8
PID	0.53	±3

3 Result and Discussion

Upon extensive testing on the variation of the number of poles and zeros as described previously, the following transfer function yields the best estimation (92.74%), and validation (93.52%) fits, respectively against the measured input-output data.

$$G(s) = \frac{18.07}{s^2 + 0.004908s + 3.979} \tag{1}$$

It was observed from the zero-pole mapping that the plant is marginally stable as both poles lie in the imaginary axis at the intersection of the real axis, suggesting that the plant should be controlled to ensure the stability of the system.

The classical PID variation gains are acquired through the MATLAB’s PID tune application on the identified plant. This process is essentially the HIL process as mentioned earlier. The heuristical controller gains obtained are listed in Table 1. Table 2 on the other hand, tabulates the time response performance of the controllers.

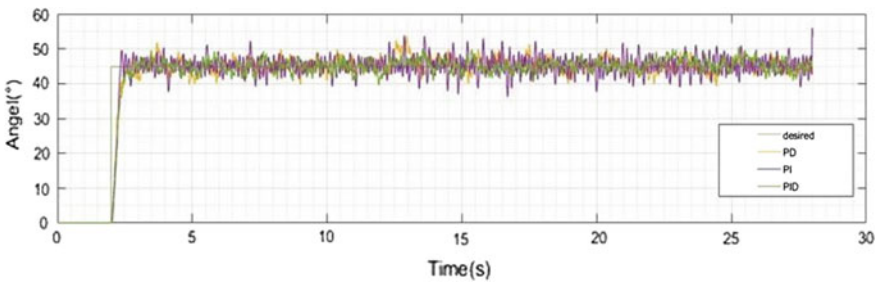


Fig. 4 Time response behaviour of the controllers

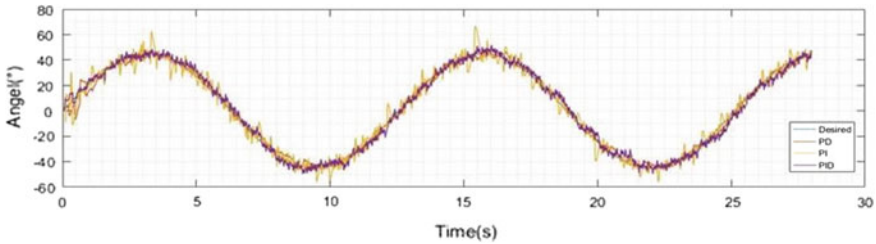


Fig. 5 Trajectory tracking performance

It is evident from the table that the PID controller works best as it provides the least steady state error and a reasonable settling time. Figure 4 illustrates the controllers' performance with respect to a step input. Conversely, Fig. 5 depicts the trajectory performance of the controllers evaluated upon providing a sinusoidal input with a magnitude of 45° that imitates the grasping motion.

4 Conclusion

The study examines the identification and control of a finger exoskeleton that performs the grasping motion. It was demonstrated that the transfer function of the system was successfully identified as the estimation as well as the validation fits provides reasonable accuracy. The identified plant was then used to evaluate the performance of the classical PI, PD, and PID and it was established that the PID control provides the least steady state error as well as reasonably fast settling time that is non-trivial for grasping rehabilitation. Future works will include the incorporation of active force control to the existing controller to investigate its effectiveness in attenuating disturbances.

References

1. Hansen, T.B., Carstensen, O.: Hand injuries in agricultural accidents. *J. Hand Surg. Am.* **24**, 190–192 (1999)
2. Hasegawa, Y., Mikami, Y., Watanabe, K., Firouzimehr, Z., Sankai, Y.: Wearable handling support system for paralyzed patient. In: 2008 IEEE/RSJ International Conference on Intelligent Robots and Systems IROS, pp. 741–746 (2008)
3. Zhang, J.F., Yang, C.J., Chen, Y., Zhang, Y., Dong, Y.M.: Modeling and control of a curved pneumatic muscle actuator for wearable elbow exoskeleton. *Mechatronics* **18**, 448–457 (2008)
4. Loureiro, R., Amirabdollahian, F., Topping, M., Driessen, B., Harwin, W.: Upper limb robot mediated stroke therapy—GENTLE/s approach. *Auton. Robots.* **15**, 35–51 (2003)
5. Murphy, T.H., Corbett, D.: Plasticity during stroke recovery: from synapse to behaviour. *Nat. Rev. Neurosci.* **10**, 861–872 (2009)

6. Masiero, S., Armani, M., Rosati, G.: Upper-limb robot-assisted therapy in rehabilitation of acute stroke patients: Focused review and results of new randomized controlled trial. *J. Rehabil. Res. Dev.* **48**, 355–366 (2011)
7. Rey, G., Donnan, A., Fisher, M., Macleod, M., Davis, S.M.: Stroke. *Lancet* **371**, 1612–1623 (2008)
8. Basteris, A., Nijenhuis, S.M., Stienen, A.H., Buurke, J.H., Prange, G.B., Amirabdollahian, F.: Training modalities in robot-mediated upper limb rehabilitation in stroke: a framework for classification based on a systematic review. *J. Neuroeng. Rehabil.* **11**, 111 (2014)
9. Teasell, R.W., Kalra, L.: What's new in stroke rehabilitation: back to basics. *Stroke* **36**, 215–217 (2005)
10. Lucas, L., Dicicco, M., Matsuoka, Y.: An EMG-controlled hand exoskeleton for natural pinching. *J. Robot. Mechatron.* **16**, 1–7 (2004)
11. Heo, P., Gu, G.M., Lee, S., Rhee, K., Kim, J.: Current hand exoskeleton technologies rehabilitation and assistive engineering. *Int. J. Precis. Eng. Manuf.* **13**, 807–824 (2012)
12. Mulas, M., Folgheraiter, M., Gini, G.: An EMG-controlled exoskeleton for hand rehabilitation. In: *Proceedings of the 9th International Conference on Rehabilitation Robotics*, pp. 371–374 (2005)
13. Wege, A., Kondak, K., Hommel, G.: Development and Control of a Hand Exoskeleton for Rehabilitation Construction of the Exoskeleton, pp. 149–157 (2006)
14. Dicicco, M., Lucas, L., Matsuoka, Y., Engineering, M.: Comparison of control strategies for an EMG controlled orthotic exoskeleton for the hand. In: *International Conference on Robotics and Automation*, pp. 1622–1627 (2004)
15. Chiri, A., Vitiello, N., Giovacchini, F., Roccella, S., Vecchi, F., Carrozza, M.C.: Mechatronic design and characterization of the index finger module of a hand exoskeleton for post-stroke rehabilitation. *IEEE/ASME Trans. Mechatron.* **17**, 884–894 (2012)
16. Ljung, L., Singh, R.: Version 8 of the system identification toolbox. IFAC (2012)

Trajectory Tracking Analysis of Planar End-Effector Upper Limb Rehabilitation Device



H. Y. Lim and Muhammad Aizzat Zakaria

Abstract Rehabilitation devices have become one of the more sought-after focus areas among researchers in the robotics field, where it could be used to assist patients in the process of stroke recovery. Therefore, the motivation of this thesis is to further investigate the planar end-effector upper limb rehabilitation device as a viable solution for patients with movement disorders, instead of the more expensive alternative of exoskeleton robots. This paper illustrates the mathematical modelling and simulation of a planar end-effector rehabilitation device for the upper limb. The rehabilitation device is of two degrees of freedom, and is used in this research due to its cost effectiveness and practicality. The derivation of the forward and inverse kinematics of the robotic system is established by using the Denavit-Hartenberg algorithm, which is proceeded to be used in the trajectory tracking of the end-effector of the device, as well as the programming of the feedback control system to control the actuators used in the system. The results of the simulation suggest that the mathematical modelling of the system is able to predict the behaviour of the system, which is to be implemented in this robotic device for upper limb rehabilitation.

Keywords End-effector · Planar · Upper-limb rehabilitation

1 Introduction

The number of patient population with movement disorders are on the rise in this fast-paced world, and there are many causes of the disorders, such as sports-related injuries or accidents, chronic diseases like arthritis, children with special needs, muscle sprains, stroke, and more. Physical rehabilitation is one of the main solution

H. Y. Lim · M. A. Zakaria (✉)

Innovative Manufacturing, Mechatronics & Sports Laboratory (IMAMS),
Faculty of Manufacturing Engineering, Universiti Malaysia Pahang,
26600 Pekan, Pahang, Malaysia
e-mail: maizzat@ump.edu.my

© Springer Nature Singapore Pte Ltd. 2018

M. H. A. Hassan (ed.), *Intelligent Manufacturing & Mechatronics*,
Lecture Notes in Mechanical Engineering,
https://doi.org/10.1007/978-981-10-8788-2_18

183

to these problems [1]. During the rehabilitations, physical therapists are required to repeat intensive coordinated motor movements which could be quite laborious if done for a long period of time. The process would take quite some time depending on the patients' severity in the movement disorder, and these therapies are costly to some. It is because of these reasons and the advancement in technology that people are turning to robotics as a rehabilitation alternative.

There is a wide range of research studies conducted on the devices that could assist physical rehabilitation [1–3]. The robotic devices which are technically advanced are those with the ability to perform repetitive tasks on patients are currently being developed. Upper limb rehabilitation alone has garnered much attention in the studies that are conducted on them and also the solutions provided. Many of these devices of clinical setting are targeted at different parts of the upper limb and are tailored for different patients.

Rehabilitation devices are getting more commercialized and their effectiveness in treating movements compared to conventional therapy is still arguable but the same cannot be said for end-effector robots. The patients' hand is fixed at one point on the end-effector robot and forces are generated at the interface. These rehabilitation robots are less complicated and easier to build. The results from an extensive clinical testing of this rehabilitation device proves to be promising for those who have undergone this robotic therapy [4].

According to a survey done by Paweł Maciejasz and the team [5], the efficiency of the upper limb rehabilitation devices has room for improvement, and the cost reduction for home-based therapy and assistance are still possible. To minimize cost for rehabilitation robots in this project, the end-effector planar device could be taken as an advantage. Previous similar works have been done such as ARM Guide [6], MEMOS [7], and ARC-MIME [8], where they used planar end-effector robotic devices to save up on cost yet help stroke patients in the rehabilitation process. A feedback control system is also incorporated to better control the trajectory of the device, similar to what was done in PLEMO [9].

A common design for a simpler version of an upper limb rehabilitation device would be a planar robotic system. A planar upper rehabilitation devices offer a simple mechanical configuration, and the exercise treatments are relatively straightforward. In a study [10], a few planar upper limb rehabilitation robots were compared, which were SCARA robots (MIT-Manus) [11], Cartesian robots (CBM-Motus) [12], and wire-based robots (Sophia-4) [10]. The study [10] compared the force exertion capabilities on the devices and the inertial properties as well. Cable-driven devices fared better in maximum mass perceived in at the end-effectors, having the lowest values because of their lightweight and simple design. However, the Cartesian device was proven to have the highest isotropicity in terms of inertial properties [10], which means that the inertia that the user may feel at the end-effector is constant throughout the whole device due to its construction. The upper rehabilitation device in this study will be using the Cartesian configuration, with two motors as actuators controlling the movement of the end-effector.

The contribution of this paper is in the development of the forward and inverse kinematics of a Cartesian end-effector upper limb rehabilitation device as this has not been done in previous studies. Furthermore, the practicality of the PID controller is also investigated when implemented on this robotic device.

This project aims to provide an effective upper limb rehabilitation device which could be built with a minimal budget so that robotic therapy could be more accessible to patients with movement disorder.

2 Methodology

This project is carried out beginning with a derivation of the forward and kinematics of the proposed system using the Denavit-Hartenberg algorithm, then the system modelling is done in MATLAB along with its validation of the kinematics and feedback control system using PID to prove that the proposed device is practical.

2.1 Mathematical Modelling

The Denavit-Hartenberg (D-H) method of kinematics derivation is utilized so that the position and orientation of each link of joint in the robotic device with reference to the chain or link preceding it can be predicted [13]. To derive the forward kinematics of an end-effector robotic device using the D-H convention, we first have to locate and label the joints of the system along with its axes. Next, the base frame of the system is identified, followed by the connecting joint and the common normal of this joint with the previous joint. This step is continued until the frame of the end-effector and all the degree of rotation and length of links are determined. Finally, a table with the link parameters is tabulated and then the transformation matrix of the system is established. As for inverse kinematics, a geometric approach is used as the lesser the degree of freedom the simpler the derivation. The geometric approach utilizes the forward kinematics previously formed, and the angles of rotation are compared within the matrix to obtain the end-effector position value relative to the origin of joint 0. This method may seem complicated with systems constituent of many degrees of freedom (DoF), but in this project, only a simple, 2-DoF planar (x-, y-axis) device is to be used. Therefore, using the D-H algorithm would be more systematic, and the assignment of link and joints are accurate and precise.

The labelled points with number 1 and 2 in the concept design of Fig. 1 are where the DC geared motors will be placed. The DC motors will move the loads using a belting system, so the motions of the blocks are seen as translational movements by the motor. The first DC motor (at the front right of the device) will be moving the block with the second DC motor, and the second motor will be

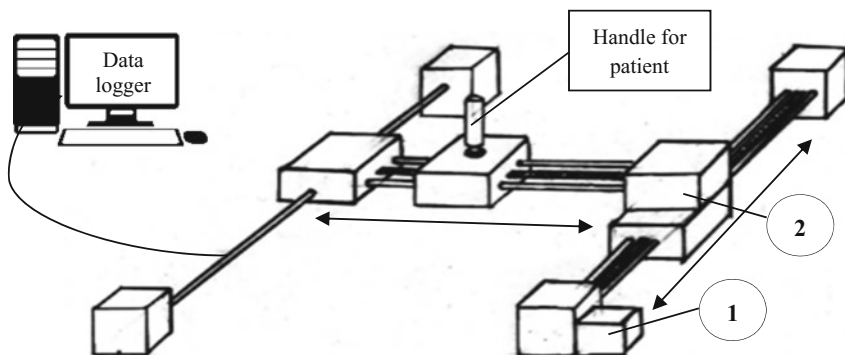


Fig. 1 Conceptual design of device

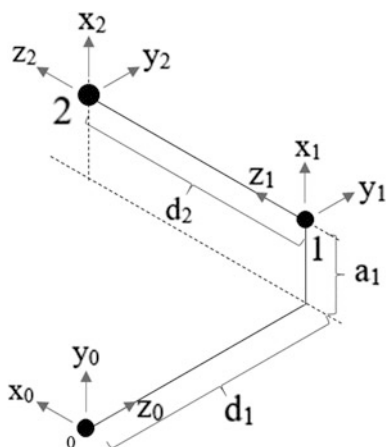


Fig. 2 Simplified diagram of kinematics model of device with links, joints, and axes labelled

moving the end effector at the middle of the device, where the patient will grip the handle (Fig. 2).

After assigning the x -, y -, z -axis of the different joints and end-effector, the D-H parameter table is tabulated as shown below (Table 1).

From the D-H parameters that we have identified, the forward kinematics equation derived to show the position of the end-effector with reference to the first joint of the system, which is the block on the front right.

Table 1 D-H parameters table

Joint	Joint angle, θ_i	Twist angle, α_i	Link length, a_i	Link length, d_i
1	90°	90°	a_1	d_1
2	0	0	0	d_2

$$A_1 = \begin{bmatrix} 0 & 0 & 1 & 0 \\ 1 & 0 & 0 & a_1 \\ 0 & 1 & 0 & d_1 \\ 0 & 0 & 0 & 1 \end{bmatrix} \quad (1)$$

$$A_1 = \begin{bmatrix} 0 & 0 & 1 & 0 \\ 1 & 0 & 0 & a_1 \\ 0 & 1 & 0 & d_1 \\ 0 & 0 & 0 & 1 \end{bmatrix} \quad (2)$$

$${}^0T_2 = A_1 \times A_2 \quad (3)$$

$${}^0T_2 = \begin{bmatrix} 0 & 0 & 1 & d_2 \\ 1 & 0 & 0 & a_1 \\ 0 & 1 & 0 & d_1 \\ 0 & 0 & 0 & 1 \end{bmatrix} \quad (4)$$

After the derivation of the forward kinematics, the distanced travelled by the block is known in proportion with the degree rotated by the motor, given by the Eq. (5) below, where d is the position of the block, θ is the degree of rotation of motor, and K is the ratio of the distance travelled by end-effector to the degree of rotation of motor. From there, the inverse kinematics is developed by rearranging Eq. (5) to know how many degrees of motor rotation translates to the distance covered by the block, shown in Eq. (6).

$$d_{(x,y)} = \theta_{(m1,m2)} K_{(m1,m2)} \quad (5)$$

$$\theta_{(m1,m2)} = \frac{K_{(m1,m2)}}{d_{(x,y)}} \quad (6)$$

These forward and inverse kinematic equations are then used in MATLAB for the system modelling which includes the PID feedback control, firstly to validate the forward and inverse kinematic equations, then to control the trajectory of the end-effector.

PID feedback control is used due to its simplicity and robustness in nature, and it is considered one of the simplest feedback controllers to be used.

2.2 Motor Modelling

Two DC geared motors are used in this system to drive the end-effector. The state-space modelling of the motor is derived from two equations, a DC motor dynamics Eq. (7), and the system equation when load is being driven by the

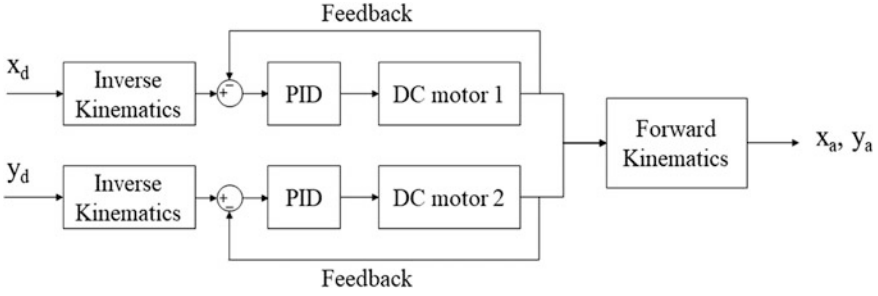


Fig. 3 Simplified block diagram of system modelled in MATLAB Simulink

motor (8). From these equations, the output of the motor angle will be known given the values of different parameters.

$$\frac{d\omega}{dt} = \frac{K_{\phi}i}{J} - \frac{B\omega}{J} - \frac{T_L}{J} \quad (7)$$

$$\frac{di_a}{dt} = \frac{V}{L_a} - \frac{i_a R_a}{L_a} - \frac{K\omega}{L_a} \quad (8)$$

The purpose of these two equations is to simulate the model of a DC geared motor in MATLAB Simulink so that we can predict the behavior of the end-effector with the PID feedback control given the desired input of the system. ω represents the angular speed of the motor, K_{ϕ} refers to the E.M.F. constant, B is the viscous friction, i is the supplied current into the motor, V is the voltage supplied, R_a represents the resistance in the windings, K is the motor constant, while J is the moment of inertia of the load, and finally L_a is the inductance in the motor windings. These parameters are determined beforehand according to the datasheet of the motors, and then substituted in the MATLAB simulated model for validation. We can observe from Eqs. (7) and (8) that the load torque, T_L has an effect on the speed of the motor, ω . There are other factors which could influence the motor speed can also be found in the equations but the focus is on the load torque, which signifies the force exerted by the patient in the actual device.

After the system of the motors are derived, the system is modelled in Simulink with the PID feedback control system incorporated. The block diagram of the system is shown below (Fig. 3).

Table 2 Simulation parameters

Symbol	Value	Unit
d_1	10.0	cm
d_2	10.0	cm
K_P	80.0	–
K_I	20.0	–
K_D	70.0	–
J	10.0	kg m ²
B	0.01	pa s
L_α	10.0	H
R_α	2.00	Ω
K_φ	0.30	–

3 Results

Simulation is performed to validate the forward and inverse kinematics of the upper limb rehabilitation device based on the designed concept. At the same time, the PID feedback control system is tested based on the system modelling and the best PID values are set for the predetermined range of load torque applied to the system.

To set the PID values, first and foremost all gains are set to zero. Then, the P gain is increased gradually until there is a steady oscillation. Next, the D gain is increased until the system is critically damped. The two P and D gains are increased until the D gain does not stop the oscillations, and those values are the values that are chosen. Finally, the I gain is increased until it brings the step response to the desired setpoint.

The variable in this experiment is the load torque, which represents the force exerted by the patients at the end effector. However, both models of DC motor are tested, and the desired distance is set at 10 cm for each motor model in this simulation (Table 2).

The values of the load torque tested are chosen based on the force that is able to be exerted by a person, which is measured using a load sensor. A stroke patient is assumed to be unable to exert a force of more than 2.0 Nm, therefore the values smaller than 2.0 Nm are plugged into the simulation.

The results are shown in Fig. 4, and the percentage overshoot of each condition is measured. The percentage overshoot when load torque is at 0.5 Nm, (a) and 1.0 Nm, (b) is approximately 20%, while at 1.5 Nm, (c) it is 30%, and this proves that the PID values set are acceptable as the end-effector is able to reach the targeted position within 16 s. However, when the load torque is given to be 2.0 Nm as shown in (d), the graph shows a negative gradient because the loaded torque exceeds the maximum torque of the motors, and with that, the motors are unable to rotate in the correct rotation so the end-effector travels in the opposite direction.

In the second simulation, the desired trajectory of the is set to follow the motion of a sine wave with amplitude of 5 cm. From the graphs above in Fig. 5, the motor movements all begin from 0 because that is the initial position of the end-effector.

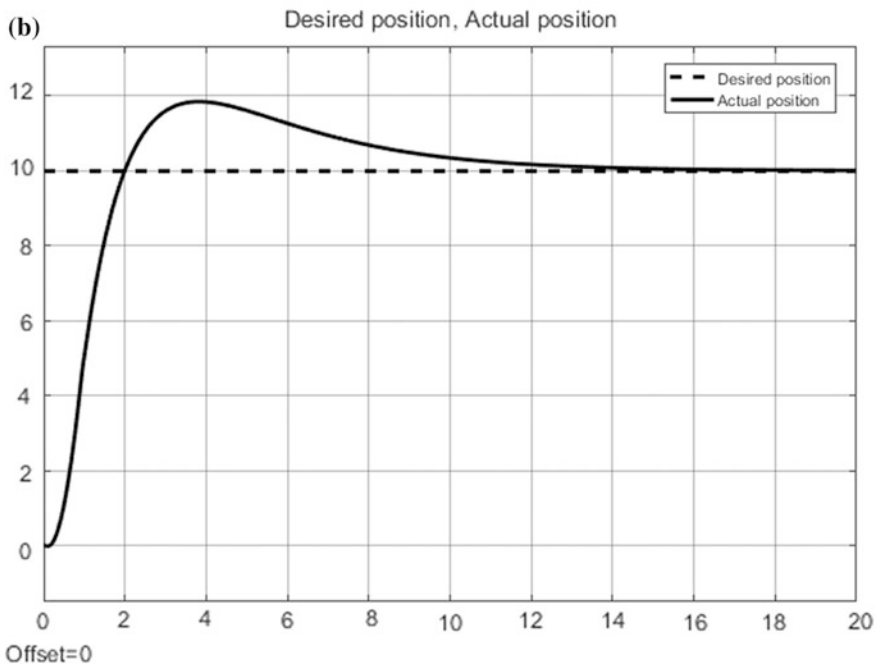
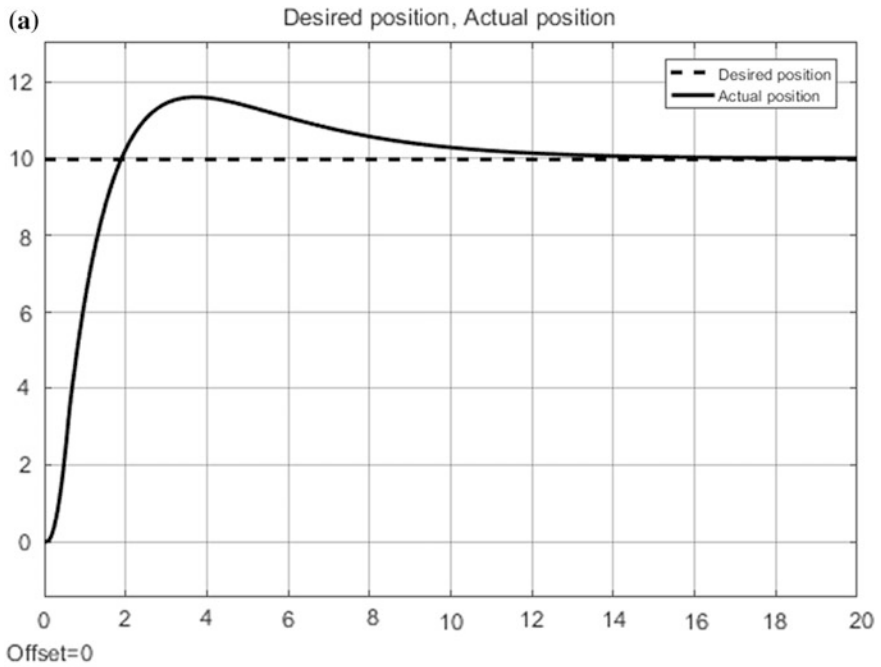


Fig. 4 **a** When load torque = 0.5 Nm, **b** When load torque = 1.0 Nm, **c** When load torque = 1.5 Nm, **d** When load torque = 2.0 Nm

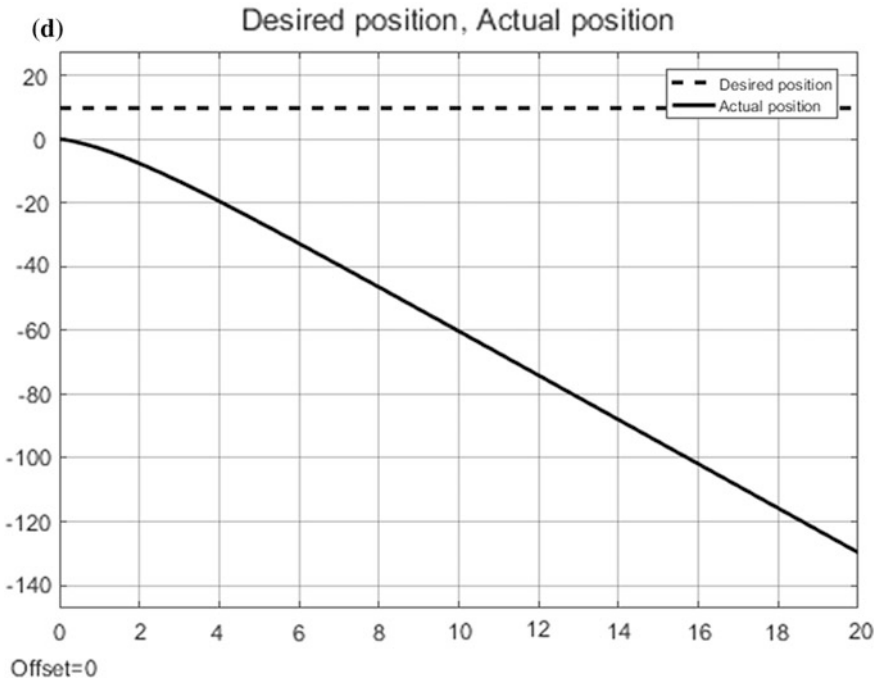
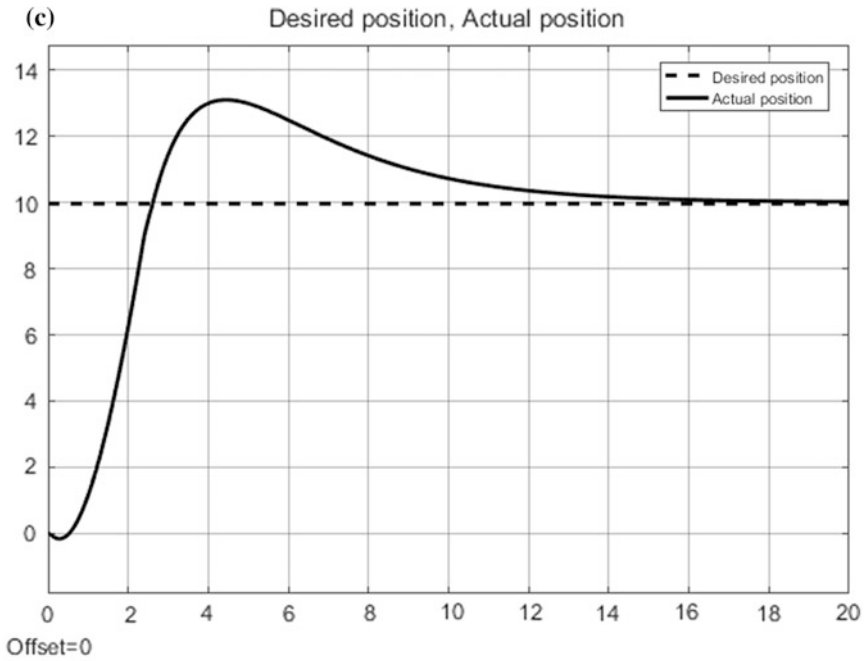


Fig. 4 (continued)

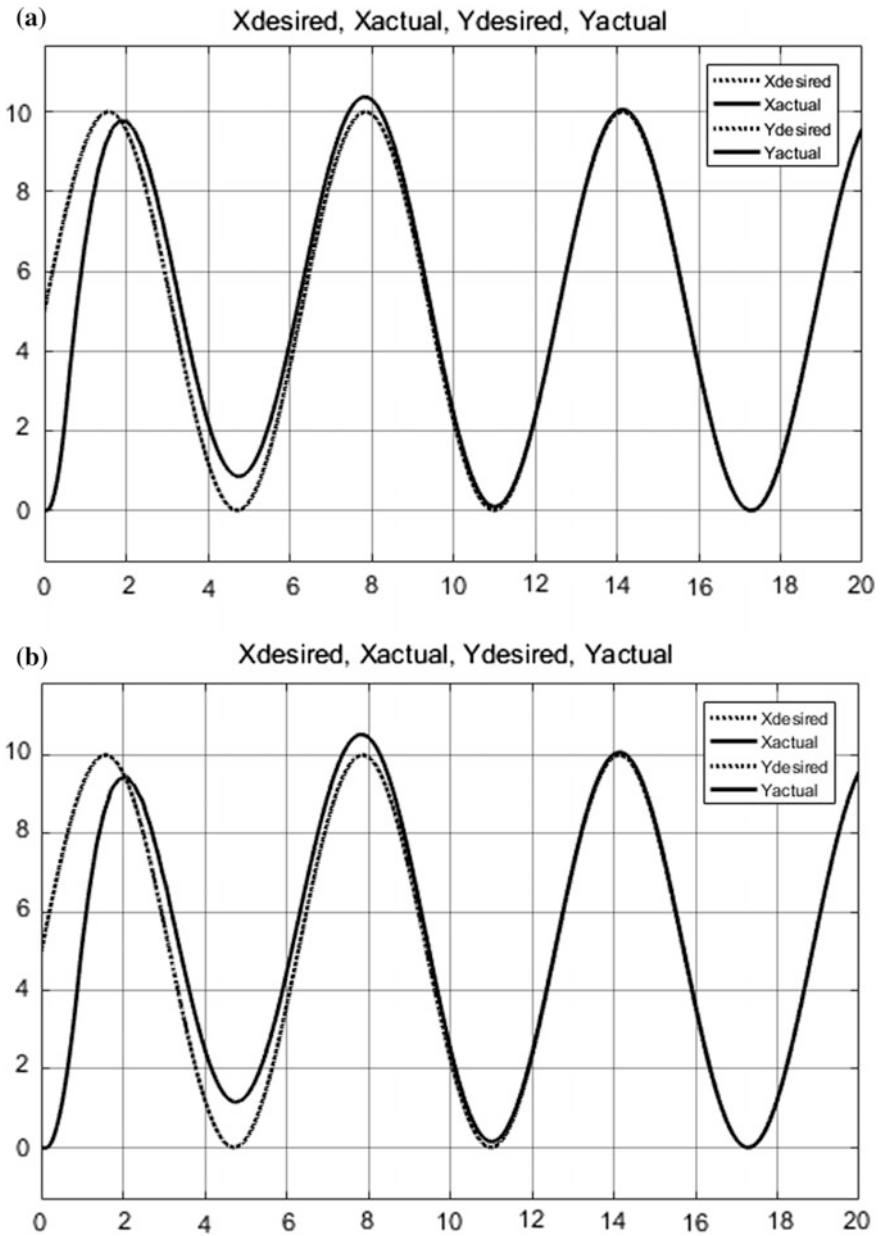


Fig. 5 **a** When load torque = 0.5 Nm, **b** When load torque = 1.0 Nm, **c** When load torque = 1.5 Nm, **d** When load torque = 2.0 Nm

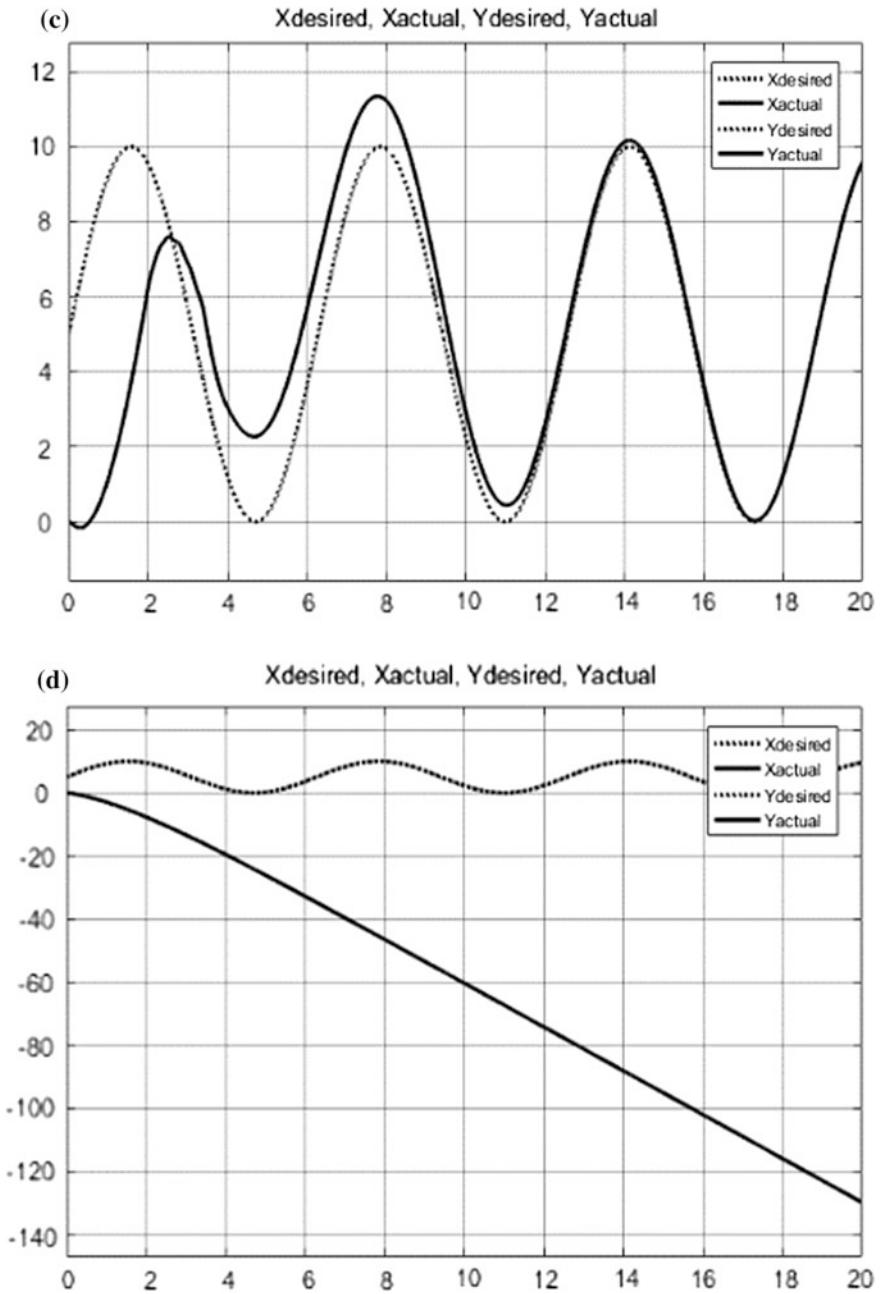


Fig. 5 (continued)

In graphs (a) and (b), the percentage overshoot of the actual position is low and the response time is less than 10 s, while in graph (c) the percentage overshoot is higher and the response time is around 12 s. This trend is similar to the trend as the previous experiment, which indicates that the PID values set have the same effect whether the end-effector movement is fixed or in moving motion. In graph (d), exactly as the experiment before, is the loaded torque is 2.0 Nm, the motors are unable to reach the desired position due to the higher load torque with respect to the motors' torque, therefore the motors are unable to move.

4 Conclusion and Future Works

The forward and inverse kinematics derived are correct as the actual position is able to arrive at the desired position. The defined PID values will be implemented in the fabrication of the rehabilitation device through a National Instruments MyRIO controller. Along with the programming of the system, the PID values will be embedded into the FPGA of the controller in order for it to have a faster processing time. However, from the results of the simulation, the PID values should be redefined as the trajectory of the end-effector is not suitable for the end-user even though the desired position of the end-effector is able to be reached, a more accurate method of acquiring PID values is suggested, such as the Ziegler-Nichols method. Furthermore, only a limited range of load torque can be used with the PID feedback control method because it is impractical to change the PID values every time the patient is different, but the force that is able to be exerted by a stroke patient is assumed to be not higher than 2.0 Nm as they are still recovering from their disorder. Therefore, even though PID feedback control is the simplest form of a controller, there are better controllers available which would better contribute to the performance of a planar end-effector upper limb rehabilitation device. In future works, it is recommended that more advanced control systems be used, such as active force control, adaptive PID control, fuzzy logic, gain scheduling control, and model predictive control. Last but not least, the dynamics of the rehabilitation device is not analyzed, and this paper only studies the spatial movements of the robot. If the dynamics of the system is investigated, the torque of the system can be estimated.

Acknowledgements The authors would like to express their utmost appreciation towards Universiti Malaysia Pahang (UMP) for the financial aid of their research under grant number RDU170371.

References

1. Proietti, T., Crocher, V., Roby-Brami, A., Jarrasse, N.: Upper-limb robotic exoskeletons for neurorehabilitation: a review on control strategies. *IEEE Rev. Biomed. Eng.* **9**, 4–14 (2016)
2. Bertani, R., Melegari, C., De Cola, M.C., Bramanti, A., Bramanti, P., Calabrò, R.S.: Effects of robot-assisted upper limb rehabilitation in stroke patients: a systematic review with meta-analysis. *Neurol. Sci.* **38**(9), 1561–1569 (2017)
3. Loureiro, R.C.V., Harwin, W.S., Nagai, K., Johnson, M.: Advances in upper limb stroke rehabilitation: a technology push. *Med. Biol. Eng. Compu.* **49**(10), 1103–1118 (2011)
4. Lo, H.S., Xie, S.Q.: Exoskeleton robots for upper-limb rehabilitation: state of the art and future prospects. *Med. Eng. Phys.* **34**(3), 261–268 (2012)
5. Maciejasz, P., Eschweiler, J., Gerlach-Hahn, K., Jansen-Troy, A., Leonhardt, S.: A survey on robotic devices for upper limb rehabilitation. *J. Neuroeng. Rehabil.* **11**(1), 3 (2014)
6. Reinkensmeyer, D.J., Kahn, L.E., Averbuch, M., McKenna-Cole, A., Schmit, B.D., Rymer, W.Z.: Understanding and treating arm movement impairment after chronic brain injury: progress with the ARM guide. *J. Rehabil. Res. Dev.* **37**(6), 653–662 (2000)
7. Micera, S., et al.: A simple robotic system for neurorehabilitation. *Auton. Robots* **19**(3), 271–284 (2005)
8. Colombo, R., et al.: Robotic techniques for upper limb evaluation and rehabilitation of stroke patients. *IEEE Trans. Neural Syst. Rehabil. Eng.* **13**(3), 311–324 (2005)
9. Kikuchi, T., Hu, X., Fukushima, K., Oda, K., Furusho, J., Irioue, A.: Quasi-3-DOF rehabilitation system for upper limbs: its force-feedback mechanism and software for rehabilitation. In: 2007 IEEE 10th International Conference on Rehabilitation Robotics, ICORR'07, pp. 24–27 (2007)
10. Rosati, G., Secoli, R., Zanutto, D., Rossi, A., Boschetti, G.: Planar robotic systems for upper-limb post-stroke rehabilitation. In: *Biomedical and Biotechnology Engineering*, vol. 2, pp. 115–124 (2008)
11. Hogan, A., Krebs, N., Charnnarong, H.I., Srikrishna, P., Sharon, J.: MIT—MANUS : A Workstation for Manual Therapy and Training I, pp. 161–165. MIT (1992)
12. Zollo, L., Accoto, D., Torchiani, F., Formica, D., Guglielmelli, E.: Design of a planar robotic machine for neuro-rehabilitation. In: *Proceedings—IEEE International Conference on Robotics and Automation*, pp. 2031–2036 (2008)
13. Bouteraa, Y., Ben Abdallah, I.: Exoskeleton robots for upper-limb rehabilitation. In: *13th International Multi-Conference on Systems, Signals and Devices, SSD 2016* (2016)

Survey on Animal Robot PARO in Malaysia: Perception and Acceptance



Muhammad Winal Zikril Zulkiffi, Syamimi Shamsuddin
and Lim Thiam Hwee

Abstract Researchers having same interest in field of human-robot interaction (HRI) have made large investments in robots for the purpose of interacting with human. However, there is still sparse evidence regarding response of person between animal robots and animals are different. Animal-robot PARO is classified as Class II medical device by Food and Drug Administration (FDA). PARO has a potential to be used as assistive device for treatment of mental illness specially dementia and depression. PARO is helpful through improving mood and help patients to be calm. The aim of this study is to explore the difference among evaluation of the animal-robot by the people in Malaysia. The constructed questions were focused to find out respondent's background such as age and gender, direct effect interaction with PARO, and preferable duration of interact session. Subjective evaluation of animal-robot PARO was conducted during Science, Technology, Engineering and Math education (STEM) exhibitions that were held in Negeri Sembilan and Melaka. Statistical analysis was conducted with total of 120 respondent using dataset. 95.8% responds agree that PARO able to make them calm. Both adult and children dislike PARO with the percentage less than 5%. Half an hour was chosen as the best time so spend with PARO. In future, PARO will be used as a device in rehabilitation center to assists in depression therapy.

Keywords Human-robot interaction • Animal robot PARO • Depression

M. W. Z. Zulkiffi · S. Shamsuddin (✉)

Faculty of Manufacturing Engineering, Universiti Teknikal Malaysia Melaka,
Hang Tuah Jaya, 76100 Durian Tunggal, Melaka, Malaysia
e-mail: syamimi@ieee.org

L. T. Hwee

Psychosocial Department, SOCSO Tun Razak Rehabilitation Center, Bandar Hijau,
Hang Tuah Jaya, Durian Tunggal, Melaka, Malaysia

© Springer Nature Singapore Pte Ltd. 2018

M. H. A. Hassan (ed.), *Intelligent Manufacturing & Mechatronics*,
Lecture Notes in Mechanical Engineering,
https://doi.org/10.1007/978-981-10-8788-2_19

1 Introduction

Robotics is one of the elements of current era which are part of engineering. Robotics is a science-based technology and the term “robot” comes from Czech word, “robota” which means “labor doing compulsory manual works without receiving any remuneration” or “to make things manually” [1]. The definition from Oxford dictionary stated that “Robot” as “a machine resembling a human being and able to replicate certain human movements and functions automatically”. Furthermore, robot can be shaped into a different form for example humanoid, arm robot, mobile, animal and so forth. A robot is developed in form of a replication of something that uses robotic technology with the end goal of mirroring something else in accomplishing a task. The robot also may be controlled by using a device or the device is probably put within the robot.

Not to mention that robots are more and more being advance, in the same way, it is developed for real-world applications, such as robots for rehabilitation, eldercare, and at the same time as household appliances. Moreover, robots can be seen regularly not only in factories but also hospitals, schools, residences and many more. This leads to human-robot interaction (HRI) which is an emerging field of study committed to design, understand and examines the framework of robotics for use by humans [2]. As robots turn to be more and more accessible and inexpensive, their utilization can be seen in scenarios such as robots as assistants, partners and even pets [2]. In general, there are numerous sorts of robot used in HRI with a different application such as a mobile robot, humanoid robot and animal robot. Significantly, this robot has been used in military, services, hospitality and industries. The goal is to make the human more comfortable while interacting with the robot.

1.1 *Motivation and Related Works*

The motivation of this study is based on the functionality of robots in treating a depression. The term Depression is actually a type of mental illness. It is fast becoming a global issue as World Health Organization (WHO) estimates that 350 million people are affected by it. Apart of that, among stroke patients, 25–30% has been diagnosed with depression [3]. Somehow, the prevalence of mental health among adults expanded starting with 10.7% in 1996, followed with 11.2% in 2006, and 29.2% in 2015, showing a significant growth of depression patients. Kuala Lumpur poses high prevalence, which is 39.8%, however, not many investigators were keen on treatment-related studies. Until 2007, only twelve studies covered on the treatment outcomes of depression in Malaysia. One significant milestone was when the Clinical Practice Guideline (CPG) for Management of Major Depressive Disorder (MDD) was introduced by Ministry of Health Malaysia to provide evidence-based guidance in the management of MDD. In the CPG, recommended treatments can be divided into pharmacological treatment (i.e. antidepressants,

antipsychotic drug), electroconvulsive therapy, psychological interventions and computerized cognitive behaviour therapy.

As robots can offer an efficient way to motivate and adapt according to individual needs [4], it is correlates to utilize its function in this field of treating depression. Significantly, robots with facial expression were introduced in the field of robotics [5]. These robots have adapted to clinical settings and care facilities for people with special needs [6]. Some of the robots are created to resemble real animal [7]. This robot widely uses in therapy [8]. One of them is PARO which is created based on baby harp seal. In addition, PARO a seal robot has successfully increase mood, make people happy and encourage human-to-human interaction. Furthermore, animal-robot PARO is considered as Class II medical device by Food and Drug Administration (FDA). Thus, PARO has a potential to be used as an assisted device for depression treatment.

1.2 *Animal-Robot PARO*

Occasionally robots used in mental healthcare are design based on an animal. Nonetheless, PARO is a therapeutic robot designed based on the shape of a baby seal (Fig. 1). The existence of PARO is recognized in 1993 when it was developed by Professor Takanori Shibata. Moreover, the U.S. Food and Drug Administration (FDA) considers PARO as a Class II medical device. The physical characteristics of PARO is that, it weighs around 2.8 kg and equipped with several sensors and actuators, also features with a soft furry coat with built-in intelligence providing psychological and social effects through physical interaction with humans. In robotics characteristics or systems, it reacts to petting and stroking by blinking its eyes and moving its flipper, cries out when handled roughly, but it reacts positively to soft petting. This system acts as a surrogate for a real pet to help reduce stress levels and improve social skills of patients [9]. Furthermore, PARO has high aesthetic value as it is very cute and can give facial expressions to the movement of its

Fig. 1 Animal-robot PARO



eyelids [10]. PARO remembers the situation in which it is petted and tends to repeat the behaviour that led to the petting to the patient's liking. PARO is beneficial to patients in the same ways therapy animals. PARO use in therapies which give the same effects as animal therapy and it also gives a positive feedback. With PARO, patients don't have to worry about the possibility of being bitten or scratched or not being able to use this form of therapy due to allergies. Also, unlike therapy animals, PARO does not require as much care and can be near the patients all the time.

Before this, PARO has been used to treat patients with dementia [11–13] hence, it has been proven that Part is evaluated in the context of multi-sensory behavioural therapy. Generally speaking, PARO provides indirect benefits for users by increasing their activity in particular modalities of social interaction, including visual, verbal, and physical interaction, which vary between primary and non-primary interactors. Secondly, PARO's positive effects on older adults' activity levels show steady growth over the duration.

2 Survey Methodology

This study uses survey as the main methodology as this study aims to explore the differences in people's perception and acceptance of animal robot PARO in Malaysia. The survey was taken place in Melaka and Negeri Sembilan through Science, Technology, Engineering and Math education (STEM) exhibitions. Statistical analysis was conducted in the dataset obtained from over 120 respondents. Table 1 shows the total of the respondent from Melaka (UTeM) is about 43.34% from 120 respondents and the rest of 56.66% are from Negeri Sembilan (USIM). These evaluations were carried out with the help animal robot PARO. The respondent involved primarily forms the exhibition visitors. Multiple questions about PARO were asked in the questionnaires. This paper reports on the results of survey questions from Malaysian people. In this study, PARO will be used as a device for mental commit robot. To prove that PARO able elevate mood changes, this study used survey distribution method.

2.1 Layout Experimentation

The exhibition was set up using the proper layout as in Fig. 2. The layout was established to collect information from survey results. The layout area covers in

Table 1 The total of respondents

Exhibition location	Gender		
	Male (%)	Female (%)	Total (120 respondents) (%)
Universiti Teknikal Malaysia Melaka (UTeM)	14.17	29.17	43.34
Universiti Sains Islam Malaysia (USIM)	22.50	34.16	56.66

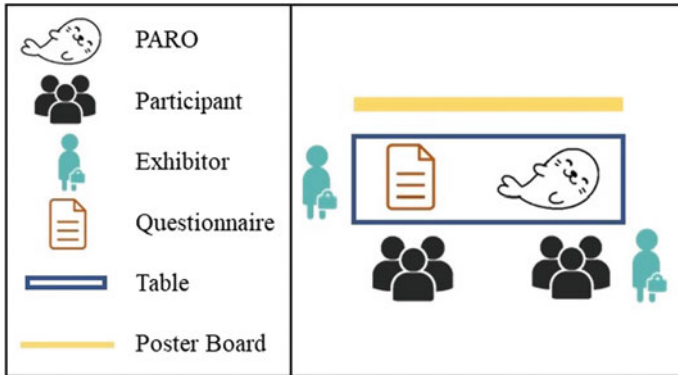


Fig. 2 Exhibition layout

3.5-m². The setup consists of animal-robot PARO, poster boards to display information about animal-robot PARO, the table use animal-robot PARO and questionnaire purposes, and area reserve for exhibitor and participant. The design layout target for consistency. The layout only covers a small area because survey process only can cover the small crowd with the limited robot. At most, it covered 12 people per area. During the presentation the crowd in control to divide into two group, half for demonstration and another half to answer the survey question. It is divided into two group because this setup anticipates the best overall outcome from demonstration and answering survey question are delivered perceptively.

2.2 Survey Distribution Setup

Firstly, PARO was placed on a table to allow visitors to interact with it. The demonstration cycle was set to 10 min per group to permit as many people as possible to experience the interaction in turns. This is because the maximum operating time for PARO was limited to 5 h per full battery. The exhibitor explained the purpose and function of the mental commits robots for about 2 min before distribution of the survey. This session was divided into two sessions; morning and evening respectively 8.30 a.m. to 12.00 p.m. and 2.00 p.m. to 5.00 p.m. PARO was recharged during 1-h break time in order to make it perform for the second session. As in Fig. 3 showed the participants were interacting with PARO. The exhibitor was responsible to introduce PARO and encourage participants to answer the survey question. Most of the participants were at shock the first time when they see PARO can move. Their curiosity leads them to perform more interaction with PARO. The interaction with PARO offers them comfort and

enjoyable moment. There are only a few cases that participant refuses to interact with PARO. The reason behind it because they don't feel comfortable interacting with the hairy animal.



Fig. 3 Exhibitor introduce PARO to participant

2.3 *Survey Participants*

In this study, the target group of participants was in the age from 9 to 50 years old. The other requirements of participants are the interaction between participants and PARO must occur before answer the survey. The sample size for this study was 120 respondents as stated by technical academician for the purpose of having reliable data.

2.4 *Survey Questions*

The survey was designed to extract information from participants regarding their perception and evaluation of animal-robot PARO and divided into two sections (Fig. 4). The validation of the survey was done using expert evaluation by technical academician and psychologist. The survey classifies participants into categories such as gender, age and education level. The next section contained 6 questions about subjective evaluation of animal-robot PARO. Duration of this survey was 5–8 min due to time constraint. For the purpose of robot acceptance in Malaysia gender was asked to determine which gender score more likes to PARO. The age of participant is divided into two categories which is young (9–19 years old) and adult (20–50 years old).

The following section was starting with the first question to ask about the cuteness of the robot. This question was asked to evaluate the physical appearance of the robot. The appearance is important if the appearance was found out very disturbing. Under those circumstances, it may not suitable to be used for depression patients in the study. The second question followed by asking the preferable to stroke the robot. A study had been done and suggested that a facilitate therapy by direct interaction with animal such touching able to treat patient with mild to moderate depression [14]. Given those points, a third question are asked about the compatibility with petting PARO. A study from [15] shows that pet attachment is related to enhanced emotional status. Therefore, is important to find out either PARO would a suitable to substitute as pet for Malaysian people as they like to interact with the robot-animal. Equally important, the fourth question were asked their enjoyment to play with PARO. Of course, playing is fun, but can it treat depression? This question prove the study [16], where the depression patients were exposed f to play with an animal. The therapy succeeds in improving depressive symptoms and cognitive function. The fifth question continues by asking the comfortability when they interact with PARO. Not to mention appearance is important, but comfortability during interaction has equally important. Unfavorable comfort can come from the material used for the fur, the loudness of the voice and the mechanical movement of the robots. The sixth question was looking on the calming effect of PARO. Study on [17] says that a person who experiences relaxation and calm able to reduce their depression. The final question was asked

STEM Kajian Awal Interaksi Robot Haiwan PARO
Projek Interaksi Robot dan Manusia
Faculty of Manufacturing Engineering, UTeM

UTeM
اوتيم
UNIVERSITI TEKNIKAL MALAYSIA MELAKA

Kajian awal ini dijalankan untuk mendapatkan maklum balas awal tentang robot haiwan PARO

Seksyen A: Maklumat

Umur	
Jantina	• Lelaki / Perempuan
Pendidikan	• Sekolah Rendah/PTS/UPSR/PMR/SPM/STPM/SiCIL/DIPLOMA/UNIVERSITI

Robot Haiwan PARO

Seksyen B: Soalan

Tandakan (V) pada jawapan anda mengenai PARO.

1. Anda mendapati PARO comel?
Do you think PARO is cute?
YA TIDAK
2. Anda suka membelai PARO?
Do you like to stroke PARO?
YA TIDAK
3. Anda selesa menyentuh PARO?
Do you like to pet PARO?
YA TIDAK
4. Anda gembira bermain bersama PARO?
Do you happy to play with PARO?
YA TIDAK
5. PARO memberikan keselesaan ketika interaksi?
PARO gave comfort while interacting?
YA TIDAK
6. Anda berasa tenang selepas berinteraksi bersama PARO?
Do you feel calm after interacting with PARO?
YA TIDAK
7. Berapakah jumlah masa anda mahu diluangkan bersama PARO?
How much time do you want to spend with PARO?
5-30MIN 1-4 JAM SEPANJANG HARI

Terima kasih atas kerjasama anda

Penyelidik : Muhammad Winal Zikril b. Zulkifli
Penyelia : Dr. Syamimi Shamsuddin
Lim Thiam Hwee

Fig. 4 Survey question

about the duration that respondent want to spend with PARO. With the attention to design experiment with depression patients, most favorable duration need to be investigate through this question.

3 Results and Discussion

Results and discussions of this study show the 8 questions that were analysed and discussed. This question are selected because it evaluated PARO as mental commits robot.

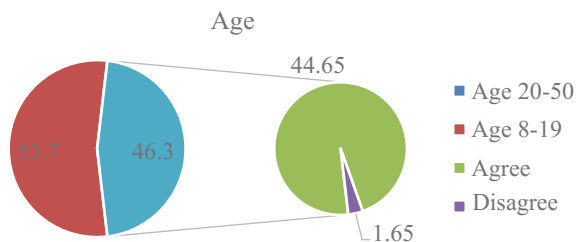
3.1 Results on Respondent Background

The first chart presents the answer to question 6 (refers Fig. 5) with the respective age group. The total number of participants were divided into a range of age. From the highest percentage of participants was in the age range 8–19 years old is 53.7%. Apart from that, 46.3% age range was between 20 and 50 years old. This study focusing on participants age range 20–50 years old only. This is because this group have the highest potential to be affected by depression [18]. From 46.3% participants, 44.65% agreed that they felt calmer aft interacted with PARO. This concluded that PARO is an appropriate helping device in elevating the mood because the calm sensation the participant felt.

3.2 Results on Acceptance of Animal-Robot PARO

Survey results for question 1–5 are presented in radar charts (Fig. 6). From the charts, 111 out of 120 people agree that PARO is a cute animal robot. Furthermore, 96% agree that they like to stroke PARO over and over while 100% agree that petting PARO makes them feel good. This proves that interaction with an animal robot will give satisfaction feelings to the user. From question 4, 117 out of 120 participants enjoy playing with PARO as the part of interaction. On the final question, 95.8% experience calming effect after interacting with PARO. The results showed percentages more than 95.8%, which can be concluded that PARO is favourable as an animal robot.

Fig. 5 Participant response to question #6 distribution by age



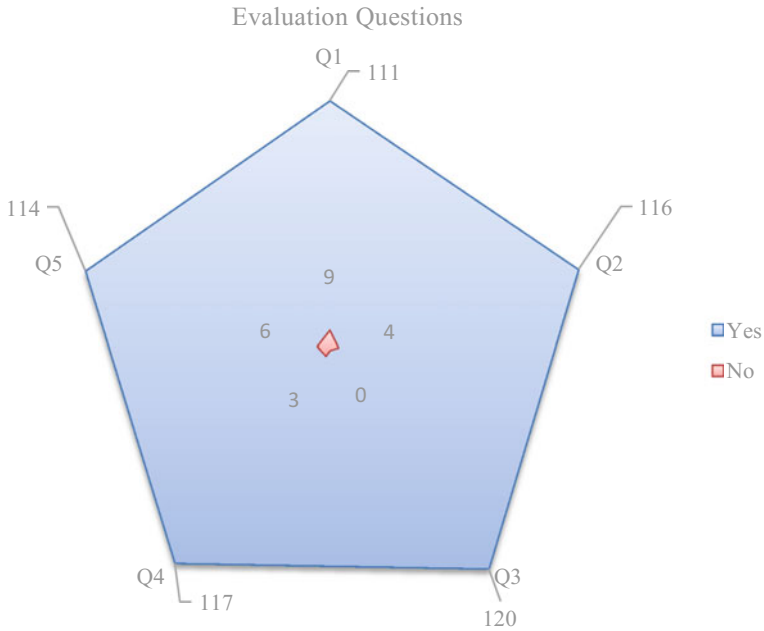
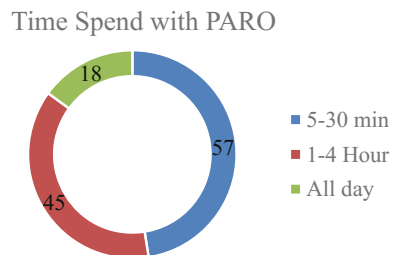


Fig. 6 Response of participants to the PARO evaluation questions

3.3 Results on Duration that Respondents Want to Spend with PARO

The doughnut chart referring to Fig. 7 showed the results for question 7 in the 2nd section of the survey which was the duration to spend with PARO. From the results obtained, the highest percentage of participants answer was 57 over 120 participants in which duration of 5–30 min. The other significant percentage was 45 participants that answer 1–4 h. The last one was 18 participants wanted the whole day to spend time with PARO. Nonetheless, it is significant that the duration to spend time with PARO 30 min at most because PARO is used for the study in major depressive disorder and based on [19], depression people get tired easily. Based on the

Fig. 7 Preferable time to interact with PARO



preferable duration to pent with PARO on the survey, it was suitable for PARO to be used in an interaction or therapy for about 30 min. Apart from that, PARO has a maximum operating time which is 3 h, hence, it is not suitable to be operated for all day long.

4 Conclusion

In conclusion, the results of evaluation provide high scores and important factors that will become key points in robot evaluation were extracted from the results of the principle analysis. The results show that Malaysian people like to interact with animal-robot PARO because of its cuteness and compatibility. Given this point, therapeutic robot such as PARO are suitable to be used in this region. As much as respondent like to interact with PARO, the time they choose are about 30 min per session. On the contrary, the design experiment can use such time. Then again, the results show even an adult is likely to interact with PARO. Seeing that, the experiment with depression patients can be focused into an adult within the age of 20–50 years old. For future recommendation, the results of the perceptions and acceptance obtained in the questionnaire will be used in the study of post-stroke depression with animal-robot PARO.

Acknowledgements The authors gratefully acknowledge the Ministry of Higher Education Malaysia, Universiti Teknikal Malaysia Melaka and Tun Razak Rehabilitation Center Melaka for their support. This project is funded under the Fundamental Research Grants Scheme (FRGS) [FRGS/1/2016/SKK06/FKP-AMC/F00321].

References

1. Xie, M.: *Fundamentals of Robotics: Linking Perception to Action*, vol. 54. World Scientific Publishing Co Inc. (2003)
2. Shamsuddin, S., Yussof, H., Mohamed, S., Hanapiah, F.A., Ainudin, H.A.: Telerehabilitation service with a robot for autism intervention. *Procedia Comput. Sci.* **76**, 349–354 (2015)
3. Tiller, J.W.G.: Post-stroke depression. *Psychopharmacology* **106**(S1), S130–S133 (1992)
4. Shamsuddin, S., Yussof, H., Mohamed, S., Hanapiah, F.A., Ainudin, H.A.: Telerehabilitation service with a robot for autism intervention. *Procedia—Procedia Comput. Sci.* **76**, 349–354 (2015)
5. Fukuda, T., Taguri, J., Arai, F., Nakashima, M., Tachibana, D., Hasegawa, Y.: Facial expression of robot face for human-robot mutual communication. In: *Proceedings of 2002 IEEE International Conference on Robotics and Automation (Cat. No. 02CH37292)*, vol. 1, May, pp. 46–51 (2002)
6. Igo Krebs, H., Hogan, N., Aisen, M.L., Volpe, B.T.: Robot-aided neurorehabilitation. *IEEE Trans. Rehabil. Eng.* **6**(1), 75–87 (1998)
7. Jolly, L., et al.: Animal-to-robot social attachment: initial requisites in a gallinaceous bird. *Bioinspir. Biomim.* **11**(1) (2016)

8. Shibata, T., Wada, K.: Robot therapy: a new approach for mental healthcare of the elderly—a mini-review. *Gerontology* **57**(4), 378–386 (2011)
9. Shamsuddin, S., Abdul Malik, N., Hashim, H., Yussof, H., Hanapiah, F.A., Mohamed, S.: Robots as adjunct therapy: reflections and suggestions in rehabilitation for people with cognitive impairments. In: *Communications in Computer and Information Science, CCIS*, vol. 376, pp. 390–404 (2013)
10. Shamsuddin, S., Yussof, H., Ismail, L.I., Mohamed, S., Hanapiah, F.A., Zahari, N.I.: Humanoid robot NAO interacting with autistic children of moderately impaired intelligence to augment communication skills. *Procedia Eng.* **41**, 1533–1538 (2012)
11. Moyle, W., et al.: Effect of an interactive therapeutic robotic animal on engagement, mood states, agitation and psychotropic drug use in people with dementia: a cluster-randomised controlled trial protocol. *BMJ Open* **5**(8), e009097 (2015)
12. Chang, W., Selma, Š., Coding, A.B.: Use of Seal-like Robot PARO in Sensory Group Therapy for Older Adults with Dementia, pp. 101–102 (2013)
13. Motomura, N., Yagi, T., Ohyama, H.: Animal assisted therapy for people with dementia. *Off. J. Japan. Psychogeriatr. Soc.* **4**(2), 40–42 (2004)
14. Antonioli, C.: Randomised controlled trial of animal facilitated therapy with dolphins in the treatment of depression. *BMJ* **331**(7527), 1231 (2005)
15. Garrity, T.F., Stallones, L.F., Marx, M.B., Johnson, T.P.: Pet ownership and attachment as supportive factors in the health of the elderly. *Anthrozoos* **3**(1), 35–44 (1989)
16. Moretti, F., et al.: Pet therapy in elderly patients with mental illness. *Psychogeriatrics* **11**(2), 125–129 (2011)
17. Mason, O., Hargreaves, I.: A qualitative study of mindfulness-based cognitive therapy for depression. *Br. J. Med. Psychol.* **74**(2), 197–212 (2001)
18. Brodaty, H., et al.: Age and depression. *J. Affect. Disord.* **23**(3), 137–149 (1991)
19. Behrens, M., Kiliarnta, S.: Sick and tired: depression in the margins of academic philosophy. *Topoi* **36**(2), 355–364 (2017)

Shortest Path Planning for Noncircular Omnidirectional Mobile Robot



Salah Addin Amin Ahmed and M. Juhairi Aziz Safar

Abstract This paper introduces the shortest path planning for a noncircular omnidirectional mobile robot. A* and Dijkstra algorithms are evaluated for the shortest path problems in terms of efficiency and time complexity. The Dijkstra algorithm is selected due to its efficiency in the greedy searching and it is integrated to occupancy grid map with the consideration of the vehicle body constraint. Simulation via MATLAB is conducted to verify the effectiveness of the proposed system.

Keywords Shortest path • Noncircular omnidirectional • A* algorithm
Dijkstra algorithm

1 Introduction

Nowadays, the robots play an important role in human life and not anymore limited to the industrial applications. The number of service robots is increased rapidly in recent years and is expected to keep growing. Although most of the service robots adapt the differential drives mechanism, the omnidirectional mobile platforms [1] are more desirable especially dealing with crowded places due to its ability to maneuver in 3 degrees of freedom (3DOF) motion. The omnidirectional mobile robots such shown in [2, 3] have rectangular shaped body which in most cases are considered as circular objects during the path planning [4]. In this paper, the body constraint of the omnidirectional mobile robots is taken into consideration in the shortest path planning solutions. There are several existing algorithms [5–7] that can be applied to determine the shortest path. In this study, A* and Dijkstra

S. A. A. Ahmed · M. J. A. Safar (✉)
School of Mechatronic Engineering, Universiti Malaysia Perlis, 02600 Arau,
Perlis, Malaysia
e-mail: juhairi@unimap.edu.my

S. A. A. Ahmed
e-mail: salahaddin2017@gmail.com

algorithms are chosen and examined for the sake of simplicity where the best algorithm among them is integrated with the proposed shortest path planning. Simulations via MATLAB are conducted to verify the effectiveness of the proposed shortest path planning.

The paper is organized as follows. Section 2 explains the methodology of the study which includes the comparison of shortest path algorithms, image interpolation, occupancy grid mapping, and trajectory planning. In Sect. 3, the results of the simulation is presented and discussed. The study is summarized in Sect. 4.

2 Methodology

2.1 Shortest Path Algorithms

In this section, the A* and Dijkstra algorithms are discussed. The A* algorithm [8] is represents by a cost function, $f(x)$:

$$f(x) = G(x) + H(x) \quad (1)$$

where, $G(x)$ is the path cost and $H(x)$ is the heuristic cost. The path cost is the total cost of the path to reach the current point from the starting point, meanwhile, the heuristic cost is the estimated cost of the path from the current point to the ending point. A* algorithm is guaranteed to provide the shortest path if there is at least one exists [9]. The A* algorithm pseudo code is:

```

 $d(v) \leftarrow \begin{cases} \infty & \text{if } v \neq s \\ 0 & \text{if } v = s \end{cases}$ 
 $Q := \text{the set of nodes in } v, \text{ stored by } d(v) + h(v)$ 
while  $Q$  not empty do;  $v \leftarrow Q.pp()$ 
  for all neighbors  $u$  of  $v$  do
    if  $d(v) + e(v, u) \leq d(u)$  then;
       $d(u) \leftarrow d(v) + e(v, u)$ 
    end if ;
  end for;
end while;
```

Dijkstra search algorithm is solving the single-source shortest path problem to plan the shortest paths from a single source node to all other nodes in the network. The algorithm starts by giving initial values to the distances from the initial node to all nodes in the network. After that it operates in certain steps, and at every step it improves the distance values between the nodes. In all steps, the shortest distance from every node to another is being computed [10]. The Dijkstra algorithm pseudo code is:

```

function Dijkstra(Graph, source):
for each vertex v in Graph:
    dist[v] := infinity;
    previous[v] := undefined;
dist[source] := 0
Q := the set of all nodes in Graph
while Q is not empty:
    u := node in Q with smallest dist[ ];
    remove u from Q;
    for each neighbor v of u:
        alt := dist[u] + dist_between(u, v);
        if alt < dist[v]
            dist[v] := alt; previous[v] := u; return previous[ ];

```

2.2 Image Edge Interpolation

The obstacles in the captured image is enlarged to ensure that the free space is enough for the robot to pass through and this is the integration of the constraint of the robot into the occupancy grid map. For bilinear interpolation, the block uses the weighted average of two translated pixel values for each output pixel value.

2.3 Occupancy Grid Mapping

Occupancy grids are used to represent a robot workspace as a discrete grid. A binary occupancy grid uses true values to represent the occupied workspace (obstacles) and false values to represent the free workspace. This grid shows where obstacles are and whether a robot can move through that space.

2.4 Trajectory Planning

The shortest path is planned by selecting a starting point and ending point in the output image. The shortest path is planned using the best shortest path algorithm obtained from Sect. 2.1. After the trajectories are planned, next is plotting a non-circular omnidirectional robot to follow the shortest from the starting point to the ending point, the velocities profiles are obtained using the following formulas:

$$V_x = r \cos(\theta) \quad (2)$$

$$V_y = r \sin(\theta) \quad (3)$$

where, V_x is the velocity in the X axis, V_y is the velocity in the Y axis, r represents the horizontal and vertical coordinates, and θ represent the angle of rotation.

3 Result and Discussion

3.1 Comparison of A* and Dijkstra Algorithms

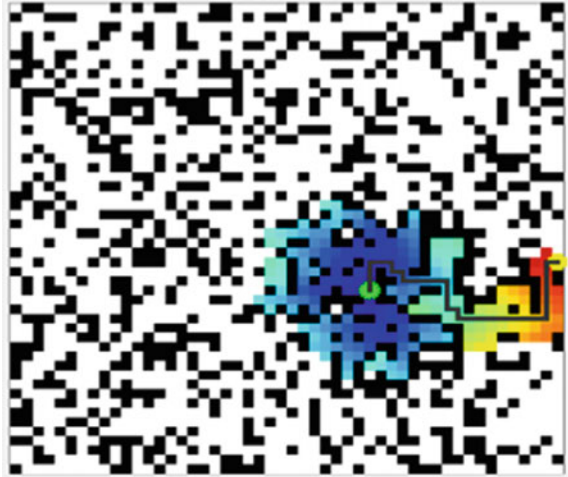
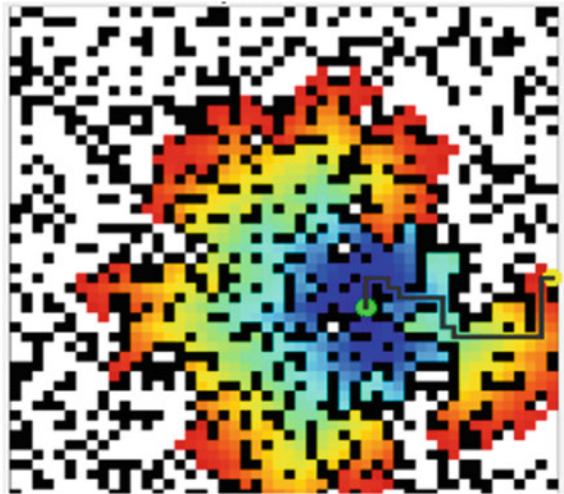
The simulation result for both A* and Dijkstra algorithms is shown in Table 1. A* algorithm is found to consume lesser time than the Dijkstra algorithm for the shortest path problem although with the same cost value. The time consumed for A* and Dijkstra algorithms are 0.75 s and 1.45 s, respectively. As shown in Figs. 1 and 2, both algorithms resulted the same shortest path for the given parameters. However, it is observed that the A* algorithm visited lesser neighbors in comparison with Dijkstra algorithm. The A* algorithm ignores the expensive paths and go through the lower cost path until it reach the target. Meanwhile, the Dijkstra algorithm which has only one cost function (real cost value) from the initial point to each node, finds the shortest path from the source to every other nodes by considering only on the real cost. Thus, the Dijkstra algorithm is slower than the A* algorithm for finding the shortest path solution. On the contrary, the Dijkstra algorithm is observed better than the A* algorithm in term of greedy searching. In this study, the Dijkstra algorithm is chosen as the shortest path planner due to the ability of the greedy searching although the A* algorithm is more superior in term of the time consumed. The difference in the time consumed is not really significant for our project.

3.2 Image Edge Interpolation and Occupancy Grid Mapping

Bilinear method has been used to enlarge the size of the obstacles to ensure enough space for the robot to pass through, and this is the integration of the constraint of the

Table 1 Comparison of A* and Dijkstra algorithms

	A* algorithm	Dijkstra algorithm
Cost value	68.05	68.05
Time consumed (s)	0.75	1.45
Greedy searching	Less visited nodes	More visited nodes

Fig. 1 A* Algorithm search**Fig. 2** Dijkstra algorithm search

robot into the occupancy grid. The enlarging is an amount of 20 pixels from each side of the obstacle, since the length of the front of the robot is 40 pixels in work area of 500×500 pixels. Figure 3 shows the binary image after enlarging the obstacles through the edge interpolation process. The black and grey color show the actual obstacles and the enlarged parts, respectively. Figure 4 shows the result after incorporate with the occupancy grid mapping.

Fig. 3 Image edge interpolation



Fig. 4 Occupancy grid mapping



Fig. 5 The shortest path with image edge interpolation



3.3 Trajectories Planning

Figure 5 shows the shortest path which is planned using the Dijkstra algorithm. The grey area is the same obstacles shown in Fig. 4. The shortest path is successfully generated based on the consideration of the vehicles body length. Figure 6 shows the actual working area with the removal of edge interpolation area.

Fig. 6 The shortest path without image edge interpolation (actual working area)

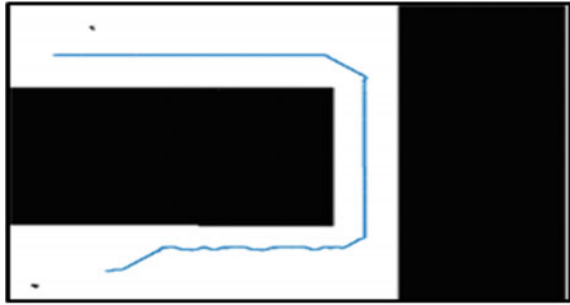


Fig. 7 The velocities plot over time, V_x cm/s, V_y cm/s, and W_z rad/s

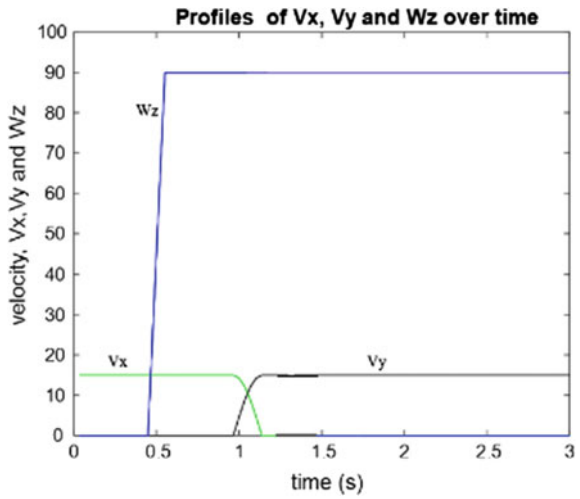
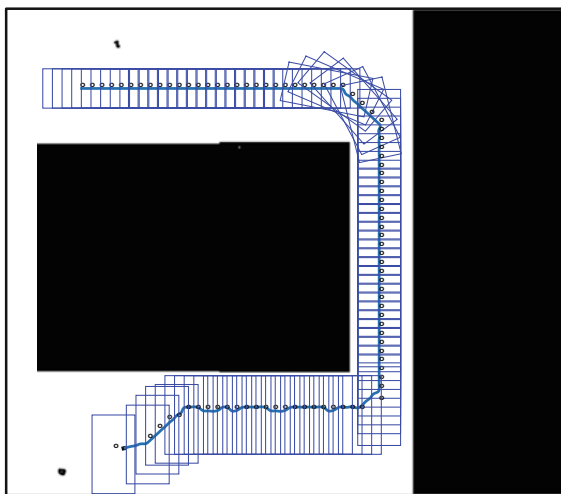


Fig. 8 The movement of the robot along the shortest path



3.4 Motion Planning Along the Generated Shortest Path

Figure 7 shows the velocity profiles generated for the omnidirectional mobile robot based on the shortest path. V_x represents the velocity of the robot in the X axis, V_y represents the velocity of the robot in the Y axis, while W_z represents the angle of rotation of the mobile robot. Meanwhile, Fig. 8 shows the predicted motion of the omnidirectional mobile robot based on the given velocity profiles. Based on this figure, it is verified that the omnidirectional mobile robot is successfully maneuvered in 3 DOF motion and capable to utilize the sideways body to move in narrow spaces.

4 Conclusion

The evaluation of A* and Dijkstra pathfinding algorithms in term of efficiency and time complexity results as A* is the best in term of time complexity and Dijkstra is the best in term of greedy searching. The Dijkstra algorithm is selected due to the greedy search advantage where the difference of time consumption between both algorithms is acceptable. Based on the conducted simulations, it is verified that the non-circular omnidirectional mobile robots can be efficiently planned to move in narrow spaces by utilizing the shortest side of their body.

References

1. Safar, M.J.A.: Omnidirectional locomotion systems for wheeled mobile robots. A Review. *Jurnal Teknologi* **77**(28), 91–97 (2015)
2. Yamada, N., Komura, H., Endo, G., Nabae, H., Suzumori, K.: Spiral mecanum wheel achieving omnidirectional locomotion in step-climbing. In: *Proceeding of 2017 IEEE International Conference on Advanced Intelligent Mechatronics*, pp. 1285–1290 (2017)
3. Safar, M.J.A., Watanabe, K., Maeyama, S., Nagai, I.: Tip-over stability control for a holonomic omnidirectional mobile robot with active dual-wheel caster assemblies using SGCMG. In: *Proceeding of 2013 IEEE/RSJ International Conference on Intelligent Robots and Systems*, pp. 4866–4871 (2013)
4. Jan, G.E., Chang, K.Y., Parberry, I.: Optimal path planning for mobile robot navigation. *IEEE/ASME Trans. Mechatron.* **13**, 451 (2008)
5. Khantanapoka K., Chinnasarn, K.: Pathfinding of 2D & 3D game real-time strategy with depth direction A* Algorithm for multi-layer. *IEEE Oct* 2009
6. Botea, A., Muller, J., Schaeffer, J.: Near optimal hierarchical path-finding. *J. Game Dev.* 7–28 (2004)
7. Hart, P.E., Nilsson, N.J., Raphael, B.: A formal basis for the heuristic determination of minimum cost paths. *IEEE Trans. Syst. Sci. Cybern.* 100–107 (1968)

8. Kito, T., Ota, J., Katsuki, R., Mizuta, T., Arai, T., Ueyama, T.: Smooth path planning by using visibility graph-like method. In: 2003 IEEE International Conference on Robotics and Automation, Proceedings ICRA '03. vol. 3, pp. 3770–3775, Sept 2003
9. Holte, R.C, Perez, M.B., Zimmer, R.M., MacDonald, A.J.: Hierarchical A*: searching abstraction hierarchies efficiently. In: Proceedings AAAI-96, pp. 530–535 (1996)
10. Choset, H., Lynch, K.M., Hutchinson, S., Kantor, G.A., Burgard, W., Avraki, L.E., Thrun, S.: Principles of Robot Motion: Theory, Algorithms, and Implementations. MIT Press, Cambridge, MA (2005)

Preparation, Field Observation and Survey on STEM Engagement of 5-Axis Pick-and-Place Pneumatic Robotic Arm Remote-Manipulation



Ahmad Anas Yusof, Ihsan Ismail, Syarizal Bakri,
Mohd Khairi Mohamed Nor and Rabiah Ahmad

Abstract This paper presents a first account of a public interaction with a remote-manipulation of a pneumatic pick and place robot during a public STEM engagement. A team of mobile STEM workshop group has participated in a STEM Carnival in Universiti Sains Islam Malaysia, Negeri Sembilan and Universiti Teknikal Malaysia Melaka. The aim of the engagement is to build public and student awareness of the advancement of remote-manipulation technology, and to observe their acceptance and interest of the system. The history of STEM education and remote-manipulation of robotic system are provided in the first part of the paper. The second and third part of this paper is dedicated to the preparation and implementation of the proposed system in the field. The last section is dedicated to the survey results and conclusion of the project.

Keywords Remote-manipulation • Remote controlled manipulator
Pneumatic pick and place robot • STEM education

1 STEM Education and Robotic Remote-Manipulation

1.1 *The History Behind STEM Education*

The term “STEM education” refers to teaching and learning in the fields of science, technology, engineering, and mathematics [1]. STEM education typically includes educational activities across all grade levels from pre-school to post-doctorate in

A. A. Yusof (✉) · I. Ismail · S. Bakri · M. K. M. Nor
Faculty of Mechanical Engineering, Universiti Teknikal Malaysia Melaka,
Hang Tuah Jaya, 76100 Durian Tunggal, Melaka, Malaysia
e-mail: anas@utem.edu.my

R. Ahmad
Faculty of Information and Communication Technology, Universiti Teknikal Malaysia
Melaka, Hang Tuah Jaya, 76100 Durian Tunggal, Melaka, Malaysia

both formal and informal approach. Formal education normally delivered by trained teachers in a systematic approach within a school, higher education or university. On the other hand, informal learning generally takes place as part of some other activity, which includes everything else, such as sports instruction provided by non-trained educators without a formal curriculum.

The Ministry of Education has set the roadmap for strengthening delivery of STEM across the education system. In the Malaysia Education Blueprint 2013–2025 for preschool to post-secondary education, [2], three measures have been undertaken which involve raising student interest through new learning approaches and an enhanced curriculum, sharpening skills and abilities of teachers and building public and student awareness. The roadmap focused on strengthening the foundations of existing knowledge and encouraging upper secondary and post-secondary school students to enroll into the Science stream. The blueprint is generally welcomed and supported by the public and private sectors. STEM-related initiatives were run by governmental agencies, institutions of higher education, non-governmental organizations (NGOs) and social communities, with various knowledge and contents. Hence, the aim of the project is to educate the public on the advanced concept of remote-manipulation of advanced machinery.

Thus, Universiti Teknikal Malaysia Melaka has organized STEM-related initiatives and engagements for the surrounding communities focusing on strengthening the foundations of existing knowledge and encouraging upper secondary and post-secondary school students to enroll into the Science stream. This paper explains the preparation of a team that promotes the concept of remote-manipulation in pneumatic pick and place robotic. During the STEM engagement, the public will be asked to learn how to manipulate the system, and to try to pick and place a workpiece from certain distance, within visual range. A survey was also conducted after the public participation of remote-manipulating the robotic system.

1.2 Robotic Remote-Manipulation

Remote-manipulation refers to the control of a mechanical arm or hand to move or manipulate hazardous materials for reasons of safety, due to extreme environment, where direct human involvement can very be counterproductive and extremely dangerous [3, 4]. Robotic remote-manipulation has seen actions in the military and security services [5–7]. In the Second World War, the German Army had remotely manipulated the Goliath robot to send explosive devices to destroy the Allied tanks. Nowadays, remote manipulation has been used for variety of purposes. The most common usage of remote manipulation was in bomb disposal task. One of the first bomb disposal robots created was the Wheelbarrow Mark 1. Invented in 1972 by Lieutenant-Colonel Peter Miller of the British Army, he came up with the idea of using the chassis of an electrically-powered wheelbarrow to tow suspect devices, such as car bombs, so they could be safely detonated without harming anyone.

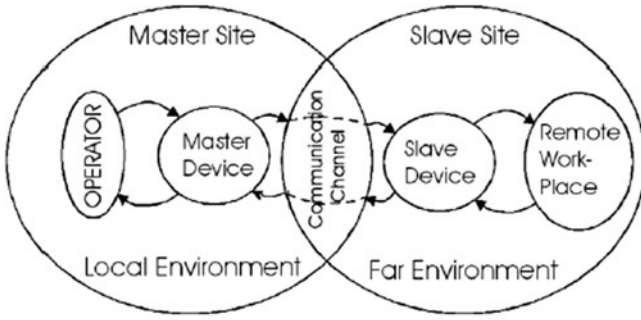


Fig. 1 The interaction of the operator, a bomb squad officer with the remote robotic system, while investigating a suspected explosive device [9]

These initial “Wheelbarrow’s” have been through dozens of generations over the decades and have evolved into modern machines equipped with pincers, disruptors and jammers capable of taking on most improvised explosive devices and even some of the expert-made ones. The STEM education in remote-manipulation involves the learning of the master and slave concept in remote-manipulation. As shown in Fig. 1, the human operator will control the machine in a local environment, with a master device at a master site. A remote robotic system will be controlled through a communication channel, which is received by a slave device, in the far environment of slave site. Master device is defined as the command transmitter, while the slave device is the command receiver [8].

2 Preparation of Robotic Remote-Manipulation for STEM Engagement

For the STEM engagement activity, a pneumatic robotic arm system has been designed so that it can be remotely manipulated by the operator from a distance, as shown in Fig. 2. A programming is written and downloaded into microcontroller Arduino Uno, while a wireless PS2 transmitter and receiver unit is used as the master and slave device. Arduino software is an open source tool that can sense, monitor, store and control algorithm provided to the microcontroller.

The programming is developed by using Arduino integrated development environment (IDE) programming software, where wiring-based language (syntax and libraries) is used. Arduino code is based on the Java and C++ libraries. The programming enables researchers to upgrade the capability of the remote-manipulation system. In addition, signal transferring of the command is done by using wireless PS2 controller starter kit, or SKPSW transmitter where its command library is included in the Arduino ide.

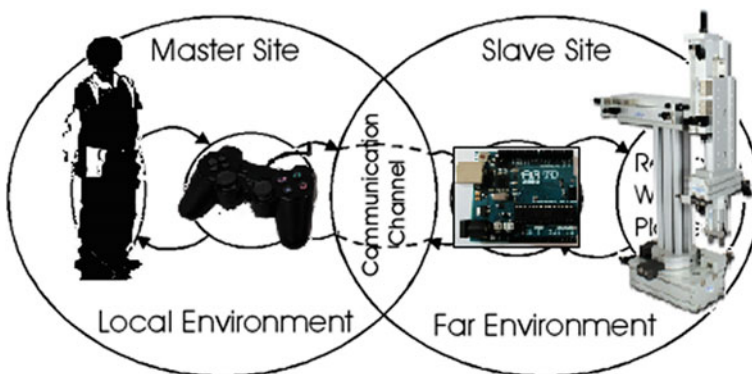


Fig. 2 Remote-manipulation of pneumatic robotic arm

Fig. 3 Test bed for the STEM engagement



The robotic arm is actuated with three pneumatic linear actuators for the gripper, horizontal and vertical movement. Two rotary actuators are used for body and gripper swing movements. All actuators are controlled by five 4/2-way double pneumatic valves. The overall dimension for the pneumatic arm is 464 mm × 88.5 mm × 200 mm (base × width × height). The wireless control has been developed by using 2.4 GHz radio control system. The control of robotic arm is also developed by using PS2 Arduino remote control system software, which provides the command platform that will produce the signals to the actuation of Cartesian robotic arm, and hence the movement of the arm. Figure 3 shows the test bed for the STEM engagement.

3 Field Observation

3.1 Public STEM Engagement

The rule of the remote-manipulation for the public is to be able to transfer the workpiece perfectly, and the operators must start at the beginning of the process, if

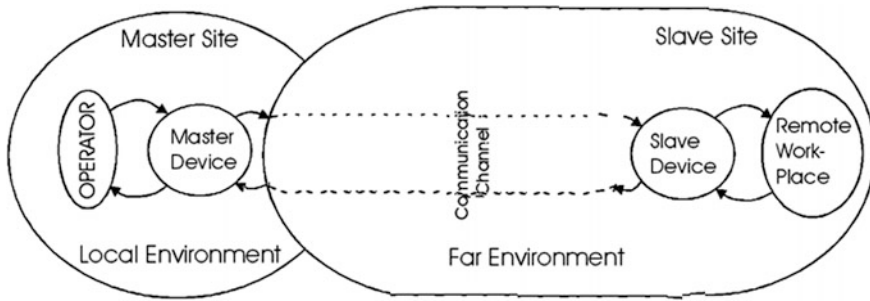


Fig. 4 Learning how to remote-manipulation a robotic arm at an increased distance

they make a mistake in their action. After sometimes, the operators usually will be able to track the movement of the pick and place system, and finish the task in a quicker pace. From the observation, it is also noted that gender difference among the operators does not influence the performance during the remote-manipulation. Figure 4 illustrate the manipulation procedure for the public STEM engagement.

The STEM engagement with pick and place robotic remote-manipulation was conducted at Universiti Sains Islam Malaysia, during the N9 STEM Carnival on July 15th, 2017, as depicted in Fig. 5. The public was asked to participate in the manipulation of the robotic system. The operators from the public will be asked to learn how to manipulate the system, and to try to pick and place a workpiece from certain distance, within visual range. The very first approach in remote-manipulation is the understanding of the public/operator on the function of each control buttons. It is noted that from observations, the person who has the experience in operating PS2 Joypad understands the functions in a quicker pace. The longer it takes for the operators to master the function of the buttons, the more likely that the operators will fail in grasping and transferring the object to its required location. The observation also shows that the manipulation error usually occurred when the operators are standing farther from the robotic system during the remote manipulation.

4 Survey

The STEM engagement with pick and place robotic remote-manipulation was conducted at Universiti Teknikal Malaysia Melaka, during the Melaka STEM Carnival on September 20th, 2017. The public were asked to participate in the remote manipulation of the robotic system. They were asked to learn on how to manipulate the system, to pick and place a workpiece from certain distance and to answer a survey, as shown in Table 1 (Fig. 6).



Fig. 5 Participation by the public in USIM STEM Carnival

5 Results and Discussions

Figures 7, 8, 9, 10, 11, 12, 13 and 14 show that 57 participants have responded to the survey while engaging the pick and place robotic remote-manipulation at the booth. This constitutes of 44 male students and 13 female students from secondary and primary schools. 93% of the participants are secondary school students, ages between 13 and 21 years old, while the rest is from the primary school students.

Table 1 List of questions during the survey

Survey questions on the introduction to pneumatic/air power and robotic remote-control systems	
1	Sex (Male/female)
2	Age (7–21 and above)
3	Do you know about ‘Pneumatic’/air power? (Yes/No)
4	Do you know how ‘Pneumatic’/air power system works? (Yes/No)
5	Do you understand how the remote-control system works? (Yes/No)
6	Are you interested in learning more about robotics after seeing this exhibit? (Yes/No)
7	Do you understand clearly the explanation of the instructor? (Yes/No)
8	After attending this exhibit, what interests you most? (Robotic/technology/engineering/mathematics/pilot/education/science)

Note Visitor can choose more than one



Fig. 6 Participation by the public in UTeM STEM carnival

Fig. 7 Sex

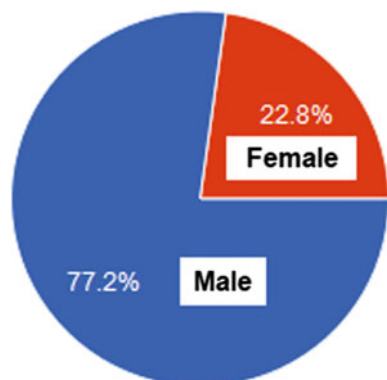


Fig. 8 Age

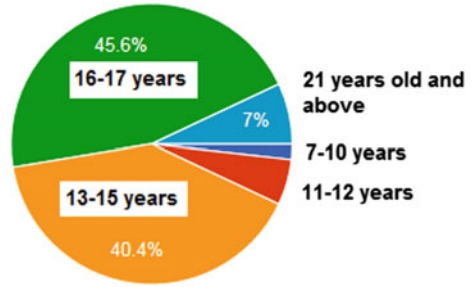


Fig. 9 Knowledge on what is pneumatics?

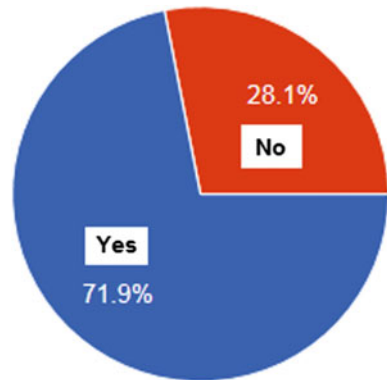
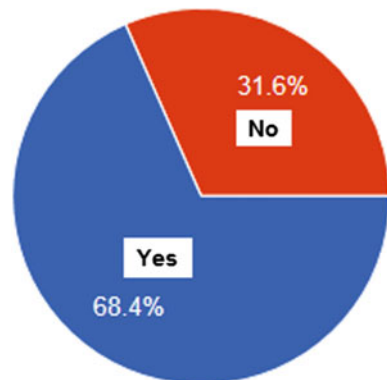


Fig. 10 Knowledge on how pneumatic works?



This shows that secondary students are more attracted to the pneumatic pick and place robot manipulation, rather than their younger counterparts. Figures 10 and 11 show that about 68 and 82.5% have the knowledge on how pneumatics and remote-manipulation works. Most of the participants also says that they are interested in the robotics system. Figure 14 illustrates that robotics attracts the most participant that visited the booth. This is followed by Technology, Engineering and

Fig. 11 Understanding on how remote control system work?

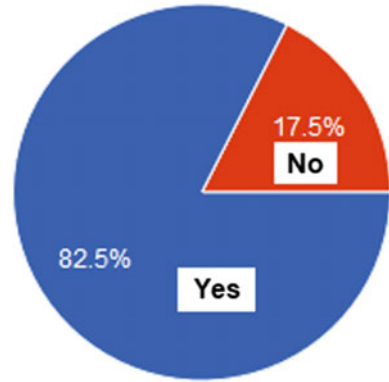


Fig. 12 Interest on robotics

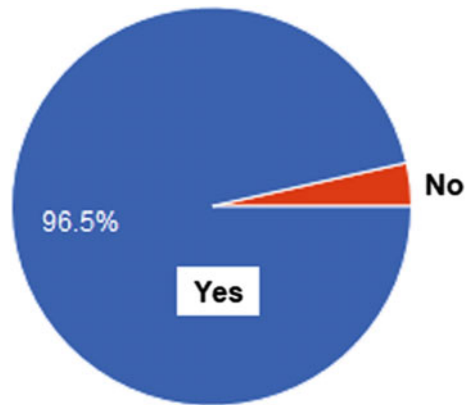
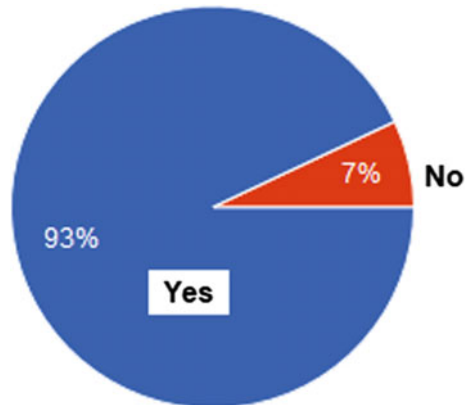


Fig. 13 Instruction understanding



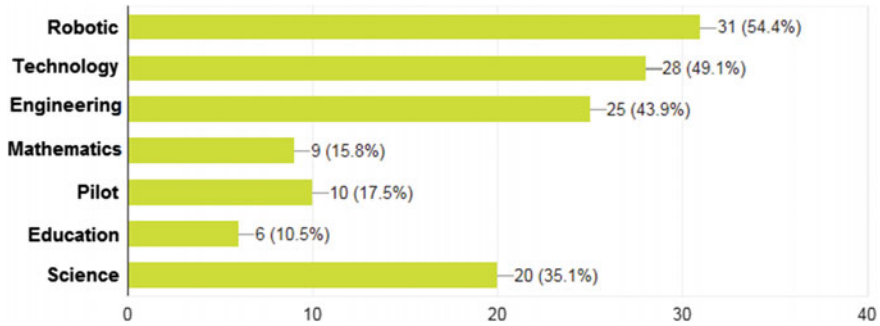


Fig. 14 What's interest the participant after the STEM exhibition

Science. It is also noted that in the STEM elements, interest on Mathematics is at the lowest level, with 15.8%. A more detail result shows that about 25 students that choose robotics as one of their preferences are male, while only 5 female students have opted for the same field. More detail analysis shows that 7 students choose robotics as their only interest, whereby 5 of them are male students.

6 Conclusion

STEM engagement of 5-axis Pick-and-Place Pneumatic Robotic Arm has been conducted during a STEM Carnival in order to build public and student awareness for latest concept of remote-manipulation in STEM education. In a field observation, it is noted that the learning process in remote-manipulation among the public spectators is incremental, since operators can conduct the tasks with more confidence after several trials. Such system can be utilized in STEM education for students and can positively influence the quality of remote education on both teacher's and student's sides. A survey on STEM engagement on robotic remote-manipulation has also been conducted during a STEM Carnival to build public and student awareness STEM education. From the 57 participants, 44 of them are male students and 13 are female students. 93% of the participants are secondary school students, ages between 13 and 21 years old. Secondary students are noted to be more attracted to the pneumatic pick and place robot manipulation, rather than their younger counterparts. A more detail result shows that about 25 students choose robotics as one of their preferences are male, while only 5 female students opted for the same field. More detail analysis shows that 7 students choose robotics as their only interest, whereby 5 of them are male students. The questionnaire shows that Robotics is the most chosen interest. This is followed by Technology, Engineering and Science. It is also noted that in the STEM elements, interest on Mathematics is at the lowest level, with 15.8%.

Acknowledgements The authors wish to thank Ministry of Higher Education and the Universiti Teknikal Malaysia Melaka for their support. This publication was funded by Ministry of Higher Education (MOHE) of Malaysia, under the Fundamental Research Grant Scheme (FRGS). **FRGS/1/2016/TK03/FKM-CARE-F00317.**

References

1. Science, Technology, Engineering and Math: Education for Global Leadership. U.S. Department of Education. <https://www.ed.gov/Stem>. Accessed 8 Dec 2017
2. Malaysia Education Blueprint 2013–2025: Preschool to Post-Secondary Education. Pelan Pembangunan Pendidikan. <https://www.moe.gov.my/index.php/en/dasar/pelan-pembangunan-pendidikan-malaysia> 2013–2025. Accessed 8 Dec 2017
3. Yusof, A.A., Kawamura, T., Yamada, H.: Evaluation of construction robot telegrasping force perception using visual, auditory and force feedback integration. *J. Robot. Mechatron.* **24**(6), 949–957 (2012)
4. Yamada, H., Xinxing, T., Tao, N., Dingxuan, Z., Yusof, A.A.: Tele-operation construction robot control system with virtual reality. *IFAC Proc.* **42**(16), 639–644 (2009)
5. Burks, B.L., Killough, S.M., Thompson, D.H.: Telerobotic excavation system for unexploded ordnance retrieval. In: 26th DOD Explosives Safety Seminar, Miami, Florida (1994)
6. Cry Havoc and Let Slip the Bots of War. *Qwik Connect.* Glenair. vol. 17, no 3 (2013)
7. Kanwal, M.: Sindh Bomb Disposal Squad to get 5 robots and other advanced gadgets. *TechJuice.News.* <https://www.techjuice.pk/sindh-bomb-disposal-squad-to-get-5-robots-and-other-advanced-gadgets/>. Accessed 8 Dec 2017
8. Kawashima, K., Sasaki, T., Miyata, T., Nakamura, N., Sekiguchi, M., Kagawa, T.: Remote control of ordinary backhoe using pneumatic robot system. In: Proceedings of the 6th JFPS International Symposium on Fluid Power, Tsukuba, Japan (2005)
9. German Researchers are Developing a Bomb Squad Robot that Sees Inside Suitcases. *Popular Science.* <https://www.popsci.com/german-researchers-want-bomb-squad-robots-to-see-inside-suitcases>. Accessed 8 Dec 2017

Facing the Autonomous Underwater Vehicle Competition Challenge: The TUAH AUV Experience



Ahmad Anas Yusof, Mohd Khairi Mohamed Nor,
Shamsul Anuar Shamsudin, Mohd Rizal Alkahari,
Mohd Shahrieel bin Mohd Aras and Mohamad Riduwan Md. Nawawi

Abstract This paper describes the experience of UTeM AUV team during an autonomous underwater vehicle international competition. The competition provides the participants with the opportunity to experience the engineering challenges during the development of the autonomous underwater vehicle (AUV) systems. The competition focuses on underwater vehicle technology development that emphasizes on the autonomous operations of the vehicle in a swimming pool.

Keywords Autonomous underwater vehicle • Remotely operated underwater vehicle • Unmanned underwater vehicle • AUV competition

1 Introduction

A total of eight undergraduate students from the Faculty of Electrical Engineering, Faculty of Engineering Technology and the Faculty of Mechanical Engineering take part in the international competition to build underwater robot based on tasks and desirable applications. The autonomous underwater challenge is a competition that gives participants the opportunity to experience the engineering challenges and develop skills in autonomous underwater vehicle (AUV) technology. The competition focuses on the autonomous operations in a swimming pool, with four tasks to be completed. The tasks involve four challenges such as autonomous navigation, visual identification, acoustic localization and robotic manipulation.

The objective of the project is to increase students' participation in international competitions, to develop understanding and skills in AUV technology, with interest

A. A. Yusof (✉) · M. K. M. Nor · S. A. Shamsudin · M. R. Alkahari
Faculty of Mechanical Engineering, Universiti Teknikal Malaysia Melaka,
Hang Tuah Jaya, 76100 Durian Tunggal, Melaka, Malaysia
e-mail: anas@utem.edu.my

M. S. bin Mohd Aras · M. R. Md. Nawawi
Faculty of Electrical Engineering, Universiti Teknikal Malaysia Melaka,
Hang Tuah Jaya, 76100 Durian Tunggal, Melaka, Malaysia

and awareness in related to marine robotics. The competition will give exposure to Universiti Teknikal Malaysia Melaka's students with off-campus activities involvement and by competing with other university students at the international level. The competition was held in March 2017, at the Singapore Polytechnic [1].

2 The Development of TUAH

Underwater robotics is a branch of robotics which can be autonomous or remotely operated. The emerging science of underwater robotics has been used in scientific exploration, military, and even as hobbies [2–7]. An autonomous underwater vehicle (AUV) is a robot that travels without requiring input from an operator. In contrast, a non-autonomous remotely operated underwater vehicles (ROVs) are controlled and powered from the surface by an operator/pilot via an umbilical or teetered. Both AUVs and ROVs constitute part of a larger group of undersea systems known as unmanned underwater vehicles, (UUVs). Figure 1 shows two UUVs, the American SCORPIO (Submersible Craft for Ocean Repair, Positioning, Inspection and Observation) and the Norwegian SNURRE 1 [8].

An AUVs rely on various parameters of sensors, navigation, propulsion and power to navigate autonomously deep in the ocean. Typical sensors include compasses, depth sensors, magnetometers, thermistors and conductivity probes. Since radio waves cannot penetrate deep into the water, AUVs navigate by using dead reckoning. Navigation can however be improved by using an underwater acoustic positioning system. For propulsion, the AUVs use brushed or brushless electric

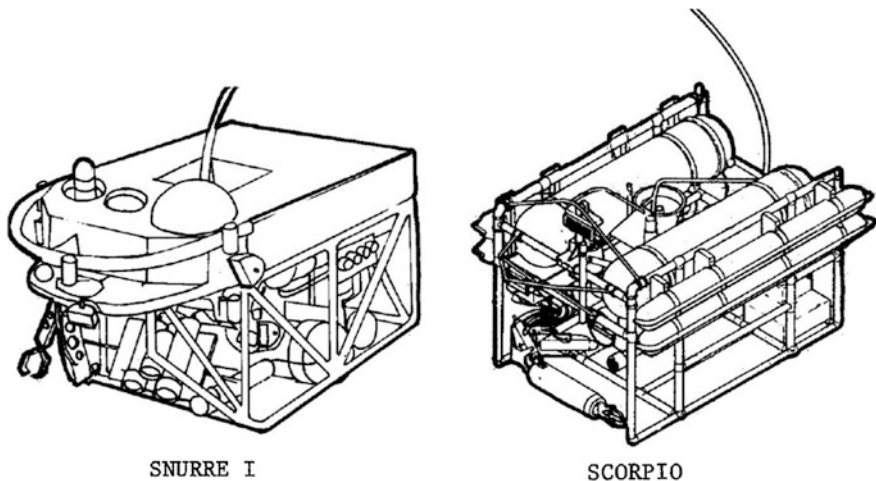


Fig. 1 Unmanned underwater vehicle (UUV)

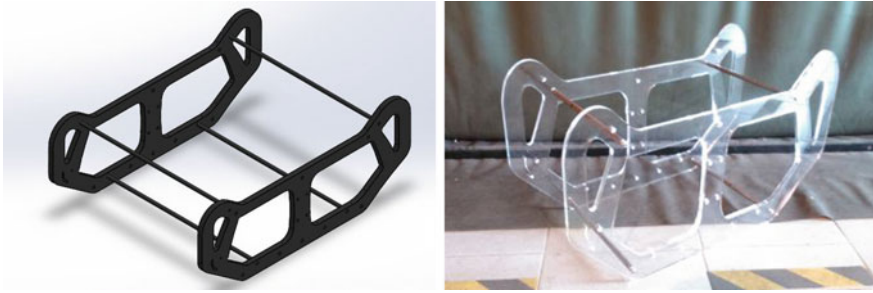


Fig. 2 Design and fabrication of AUV open body frame

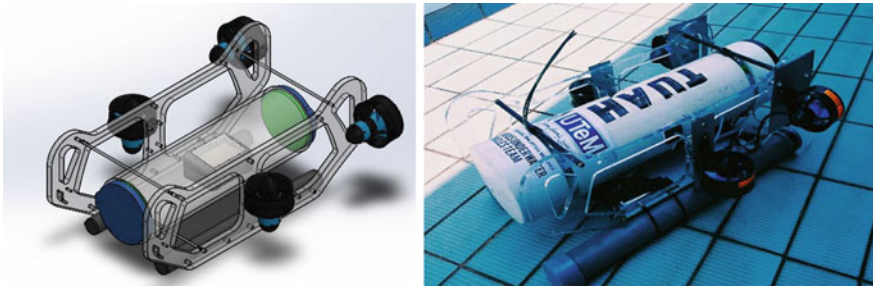


Fig. 3 TUAH UTeM autonomous underwater vehicle (AUVs)

motor, gearbox and a propeller or thruster. Most AUVs in use today are powered by rechargeable lithium ion batteries.

The TUAH autonomous underwater vehicle is designed so that it can navigate independently of human intervention. A programming is written and downloaded into microcontroller Arduino MEGA. Arduino software is an open source tool that can sense, monitor, store and control algorithm provided to the microcontroller. The programming is developed by using Arduino integrated development environment (IDE) programing software, where wiring-based language (syntax and libraries) is used. Arduino code are based on the Java and C++libraries. Figure 2 shows the AUV frame design using Acrylic due to its light weight specification and struggle erosion from the sea water and chemical materials. Four skid rods are used in between the frames for improving stiffness (Figs. 3 and 4).

Figure 5 shows the control architecture of TUAH AUV. The AUV is designed so that it can navigate with the help of inertia measurement unit or IMU that measures and reports a body's specific force and angular rate, by using a combination of accelerometers and gyroscopes. The sensors are equipped with depth sensor for vertical movement control and Pixy (CMUcam5) camera for target recognition. Thrusters are used for forward, reverse, upward and downward movement. The AUV is powered by 14.8 V Lithium-ion batteries. Detail specifications of TUAH AUV specification are tabulated in Table 1.

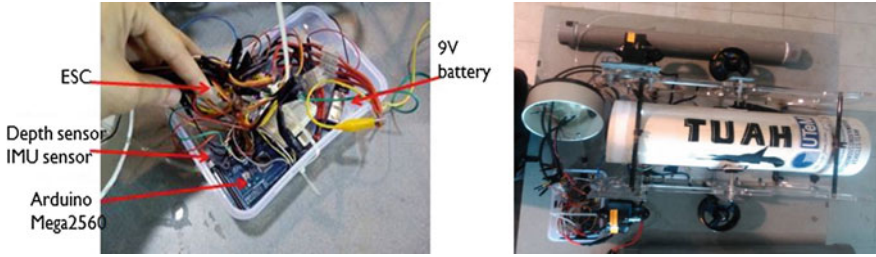


Fig. 4 AUV assembly and electronic parts

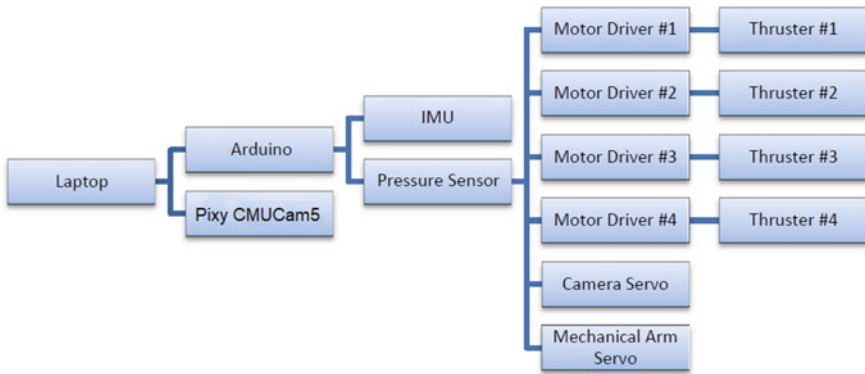


Fig. 5 TUAH AUV control architecture

Table 1 TUAH AUV Technical specifications

Name	TUAH
Dimension	70 cm × 50 cm × 30 cm
Weight	18 kg
Speed	0.4 m/s (25% of full speed)
Depth	3 m (Limitation of swimming pool depth)
Mechanical parts	Acrylic frame, PVC hull, Waterproof box, BlueRobotics Thruster T-200, iron steel weight
Electronics parts	Battery, Arduino MEGA, 10 DOF IMU, MPX5700AP, Afro ESC 30A

Fig. 6 Discussion with AUVs professors



3 Learning Through Experience

3.1 Day 1—Registration and Troubleshooting (10th March 2017)

Upon arriving and registration, the team make preparation in the System Engineering Laboratory. A technical discussion was also held with Professor William Kirkwood, the main speaker for the competition, as shown in Fig. 6. In the evening, the team tested the AUV in the pool, to troubleshoot technical problem regarding buoyancy and stability. This is depicted in Fig. 7.

3.2 Day 2—Qualifying Rounds (11th March 2017)

The qualifying rounds were held on the second day. The team's AUV passed the round with the third fastest speed. The AUV took 25 s to pass the first task. At the same time, the team had to improve technical problem during the game. The first

Fig. 7 Indoor troubleshooting



Fig. 8 Tuah's buoyancy and stability test

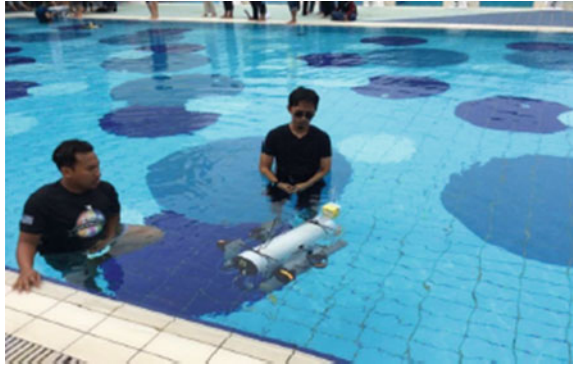


Fig. 9 Outdoor troubleshooting



technical problem involved the kill switch, which was used to switch on/off the AUV, had caused water leakages. Although small in volume, the leakages still affected the stability of the AUV body. It also affected the voltage on the thrusters, causing them not to function properly, which is indicated in Fig. 8.

The Pixy (CMUcam5) camera cannot be used for object recognition. This was due to an underwater casing which was experiencing serious leakage. Adding to that, the gripper cannot work since the Pixy (CMUcam5) camera cannot be used on the AUV. To compensate for all the weaknesses, the robot gripper had been modified to respond to the given task, as shown in Fig. 9. Programming was also modified to address the problem of thruster.

3.3 Day 3—Competition Day (12th March 2017)

Figures 10 and 11 indicates the activities during the competition. Despite all the problems and technical difficulty, the TUAH managed to conduct 9 trials

Fig. 10 Pre-competition preparation



Fig. 11 TUAH in action



throughout the competition. Since all sensors malfunctioned, TUAH was basically a blind AUV, navigating and propelling blindly toward the goal.

As a result, it missed the first task of the competition, which was to navigate through a goal post 3 m by 3 m ahead from the starting line. A dead reckoning method is used, where the current position is calculated by using a previously determined position, or fix position based upon known or estimated speeds over elapsed time and course. But without Pixy (CMUcam5) camera and malfunctioned IMU unit, the error is too large for a victory. The TUAH lost to other AUVs, but maintain the third fastest AUV during the qualifying rounds.

3.4 Day 4—Presentation Day (13th March 2017)

Figures 12 and 13 shows the last day of the competition. In the presentation, each team share the development of their AUVs. Such event provides a very good platform for the students to communicate with other people around them, and share their experience with other university students at the international level.

Fig. 12 Pre-presentation preparation



Fig. 13 Final presentation day



4 Conclusion

A group of student team up in the development of an autonomous underwater vehicle (AUV) for a competition that gives them the opportunity to experience the engineering challenges and develop skills in underwater technology. An AUV is an underwater robot that travels without requiring input from an operator. The vehicle has been designed to provide satisfactory hydrodynamic performance. This design minimizes the overall costs of the vehicle. The implementation of Arduino MEGA microcontroller, inertial measurement unit, depth sensor and Pixy (CMUcam5) camera provide a successful navigation control and propulsion. Minor problems that occurred such as leakages and short circuitry suggest the use of a standardized seal and wiring compartment for the vehicle's future development.

Acknowledgements The authors wish to thank Ministry of Higher Education and the Universiti Teknikal Malaysia Melaka for their support. This publication was funded by Ministry of Higher Education (MOHE) of Malaysia, under the Fundamental Research Grant Scheme (FRGS). **FRGS/1/2016/TK03/FKM-CARE-F00317.**

References

1. Singapore Autonomous Underwater Vehicle Challenge (2017). <https://sauvc.org/>. Accessed 10 Mar 2017
2. Lam, B.: A Mini Sub Made from Cheap Parts Could Change Underwater Exploration. The New York Times: Bits. <https://bits.blogs.nytimes.com/2012/05/28/a-mini-sub-made-from-cheap-parts-could-change-underwater-exploration/last>. Accessed 28 Oct 2017
3. Buhr, S.: OpenROV wants to get to bottom of underwater mystery. USA Today: Tech. <https://makezine.com/2012/02/09/openrov-testing-at-hall-city-cave/>. Accessed 24 Nov 2017
4. Hassan, S.N.H., Yusof, A.A., Tuan, T.B., Saadun, M.N.A., Ibrahim, M.Q., Wan, N.W.M.N.: Underwater manipulator's kinematic analysis for sustainable and energy efficient water hydraulics system. AIP Conf. Proc. **1660**, 070112 (2015)
5. Aras, M.S.M., Iktisyam Z., Abdullah S.S., Kassim A.M., Jaafar. H.I.: Development of an unmanned underwater remotely operated crawler (ROC) for monitoring application. J. Mech. Eng. Technol. **7**(2) (2015)
6. Gomáriz, S., González, J., Arbos, A., Masmitja, I., Masmitja, G., Prat, J.: Design and Construction of the GUANAY-II Autonomous Underwater Vehicle. OCEANS, Spain (2011)
7. Tadahiro, H.: Design of autonomous underwater vehicle. Int. J. Adv. Robot. Syst. Intech Open. (2011)
8. General Purpose Underwater Manipulating System. <http://cyberneticzoo.com/tag/general-purpose-underwater-manipulating-system/page/2/>. Accessed 20 Nov 2017

Motion Tracker Based Wheeled Mobile Robot System Identification and Controller Design



**Dwi Pebrianti, Yong Hooi Hao, Nur Aisyah Syaflnaz Suarin,
Luhur Bayuaji, Zulkifli Musa, Mohammad Syafrullah
and Indra Riyanto**

Abstract This project deals with the mathematical modelling and controller design for autonomous Wheeled Mobile Robot (WMR) by using motion tracking system. The mobile robot vehicle has two driving wheels and the angular speed of the two wheels is the controlled variable. Three reflected markers are attached on a robot to form a 3D rigid body. Motion tracker will track the 3D rigid body in terms of x , y position and orientation θ . Mathematical modelling which is a set of Multi Input Single Output model is done by using System Identification Toolbox in Matlab. Three different controller namely Proportional (P), Proportional Differential (PD) and Proportional Integral Differential (PID) controller are designed for this WMR. The mathematical model obtained from the System Identification has about 95% accuracy. In controller performance, the result shows that P, PD and PID controller have no overshoot for the forward movement. However, the percent overshoot of P, PD and PID controller when the robot is turning on side direction are around 51%, 63% and 48%, respectively. Additionally, the steady state error for all controllers is 0%.

D. Pebrianti (✉) · N. A. S. Suarin · Z. Musa
Faculty of Electrical and Electronics Engineering,
Universiti Malaysia Pahang, Pekan, Malaysia
e-mail: dwipebrianti@ump.edu.my

Y. H. Hao
Electrical & Instrument Department, CNI Engineering Construction Sdn. Bhd,
Johor, Malaysia

L. Bayuaji
Faculty of Computer Science and Software Engineering, Universiti Malaysia Pahang,
Gambang, Malaysia

D. Pebrianti · L. Bayuaji · M. Syafrullah
Magister of Computer Science, Universitas Budi Luhur, Jakarta, Indonesia

I. Riyanto
Department of Electronics Engineering, Faculty of Engineering, Universitas Budi Luhur,
Jakarta, Indonesia

Keywords PID controller • Wheel mobile robot • Motion tracker
Mathematical modelling

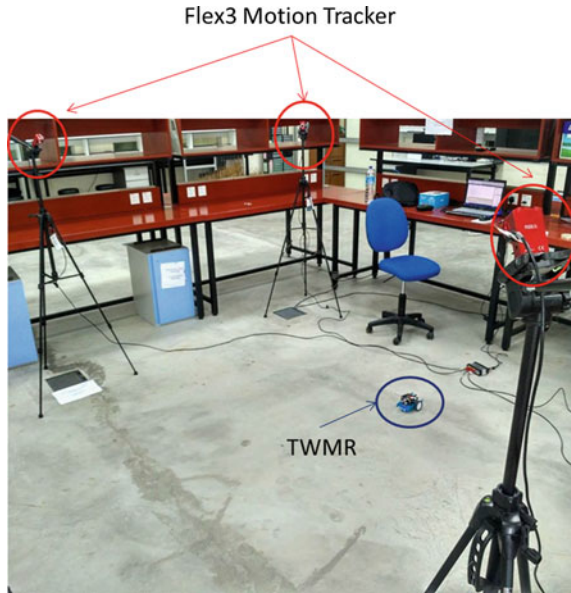
1 Introduction

Nowadays, mobile robot control has attracted attention of researchers in the field of robotics and autonomous systems. Mobile robot in the field of robotics with the purpose to implement the robustness operating in indoor or outdoor environment will offer several services to human. Basically, autonomous mobile robots with appropriate sensor such as ultrasonic sensor, IR sensor and others can achieve a certain target. A mobile robot is an automatic machine which competent to move in given environment that is not definite to one physical location only. Motion tracking is a system that can record the movement of people or objects. It is a method that can be used to figure out the changes between a target object and its surrounding or environment. Nowadays, motion tracker is involved in many sectors such as medical, entertainment, computer vision and sports. In addition, motion tracker is also commonly involved in dynamic hand gesture recognition and body gesture to compute the total angle movement of the body. Moreover, motion tracking system also can be applied to the robotics field. It is used to detect or sense the movement of the robot and collect the data of the robot's gesture.

Shon et al. was using Vicon motion capture for humanoid robot research [1]. In their work, motion tracking system was used for capturing human movement in order to teach humanoid robot in conducting certain task. Jonas et al. in [2] presents a system that enables humanoid robots to imitate complex whole-body motions of humans in real time. In their approach, they use a compact human model and consider the positions of the end effectors as well as the center of mass as the most important aspects to imitate. Stanton et al. in [3] presents and evaluates a novel method for teleoperating a humanoid robot via a full-body motion capture suit. Their method does not use any a priori analytical or mathematical modeling (e.g. forward or inverse kinematics) of the robot, and thus their approach could be applied to the calibration of any human-robot pairing, regardless of differences in physical embodiment. A feed-forward neural network for each DOF on the robot is used in the research. The aim is to learn a mapping between sensor data from the motion capture suit and the angular position of the robot actuator to which each neural network is allocated.

In this project a Wheeled Mobile Robot (WMR) is controlled by using information from motion tracker. There are a lot of methods to control the movement of the mobile robot such as stable tracking control, line tracking control and Linear Quadratic Regulator (LQR) control [4–8]. However, in this project a motion tracker (OptiTrack) is used to control a WMR with non-linear velocity constraints. It is a constraint on the feasible velocities of a body which can move forward and backward direction. In order to measure the position and orientation of the WMR, a motion tracker (OptiTrack) is used to capture the movement of the mobile robot.

Fig. 1 Experimental setup of the Flex 3 cameras and mobile robot



OptiTrack is a device that tracks moving targets by using a set of Infrared Camera (Flex 3 camera). The Flex 3 camera provides whole image capture, processing, and tracking the motion of a project in formidable and compact package [9]. The mathematical model of the WMR needs to be derived by using System Identification. After the mathematical modelling is defined, a PID controller will be designed for autonomous navigation using the motion tracker. The motion tracker will measure the position of x , y position and the orientation θ of the mobile robot. These data are needed for modelling the system. The experimental setup used in this study is shown in Fig. 1.

The paper is divided as follows: Sect. 1 is the introduction of the study. The mathematical model of the mobile robot will be given in Sect. 2. In Sect. 3, the control algorithms are discussed. The simulation result and discussion are presented in Sect. 4. Section 5 will be the conclusion of the project.

2 Mathematical Model of Two Wheel Mobile Robot

In this section, two different models will be introduced. First is the kinematic model that is commonly used for Wheeled Mobile Robot (WMR). This model will be used as a benchmark for the model obtained by using System Identification method. Second one is a model for the WMR obtained from System Identification process. The model will be presented in a state space form.

2.1 Kinematic Model

The configuration of mobile robot is indicated by the three generalized coordinates as written in Eq. (1).

$$Q = (x, y, \theta) \quad (1)$$

where x and y is the position of robot and θ is robot's orientation angle. In order to analyze the data collected form motion tracking system, a mathematical model is derived as follow:

$$\dot{x} = \frac{r}{2}(\omega_r + \omega_l)\cos\theta \quad (2)$$

$$\dot{y} = \frac{r}{2}(\omega_r + \omega_l)\sin\theta \quad (3)$$

$$\dot{\theta} = \frac{r}{D}(\omega_r - \omega_l) \quad (4)$$

where r is the radius of the robot's wheel, ω_r is the right wheel angular velocity, ω_l is the left wheel angular velocity and D is the distance between the robot's wheels. In order to develop a kinematic model a single upright wheel on the plane is given as [5, 6]:

$$\dot{x} = v \cos\theta \quad (5)$$

$$\dot{y} = v \sin\theta \quad (6)$$

$$\dot{\theta} = \omega \quad (7)$$

where \dot{x} , \dot{y} are velocity on x - and y -direction, respectively. θ is the angular rate, v and ω are translational and rotational speed of robot, respectively.

By rearranging the inputs Eqs. (2)–(7), we get:

$$\omega_r = \frac{2v + \omega D}{2r} \quad (8)$$

$$\omega_l = \frac{2v - \omega D}{2r} \quad (9)$$

where ω_r and ω_l are the right and left wheel velocity of the robot, respectively.

The output of ω_r and ω_l are formed from the inputs of v and ω . A constant number 0.113 m is used in the model. This constant number is the distance between two robot's wheels and R refers to the radius of the robot's wheel which is 0.03 m.

2.2 State-Space Model

The next model is generated by using the data obtained from the motion tracking system. The robot was controlled manually. The right and left wheel speed are recorded concurrently with the data of x position, y position and attitude, θ , obtained from the motion tracker.

The recorded samples data will be inspected by using the state space model. In this project three different Multiple Input and Single Output (MISO) models are constructed. The inputs of the system are left (ω_l) and right (ω_r) angular velocity. Meanwhile, the first output is x -position, second output is y -position and third output is θ as attitude angle. The general form of MISO system used in this study is shown in Eq. (10).

$$\begin{aligned} \frac{dx}{dt} &= Ax + Bu \\ y &= Cx + Du \end{aligned} \tag{10}$$

where $u = [u_1 \ u_2] = [\omega_l \ \omega_r]$, while y refers to output x -position, y -position or θ attitude angle.

The aim of system identification is to find the appropriate matrix A, B, C and D so that the output from the model will have same or close values with the measurement values. The process is conducted using System Identification Toolbox in Matlab.

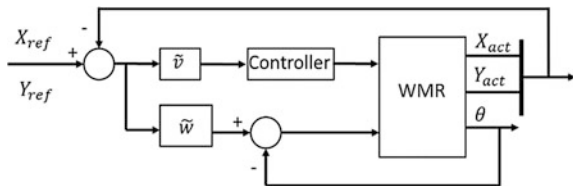
3 Control Algorithm

In this study, three different controllers; Proportional (P), Proportional Differential (PD) and Proportional Integral Differential (PID) controller are analyzed. Figure 2 shows the block diagram of the complete system.

The performances of the controllers will be analyzed in terms of settling time, overshoot percentage and the steady state error. Apart from that, the path kinematics model and state space model are also discussed.

Since there are two inputs for the system, which are velocity and angular speed, then there will be two different controllers, velocity control and angular speed

Fig. 2 Block diagram of TWMR with controller



control. However, in this study, as the preliminary study, the one that will be manipulated is the velocity control, while the angular speed will remain the same.

The velocity of WMR contains velocity along x -axis and y -axis as shown in Eq. (11).

$$v = \sqrt{v_x^2 + v_y^2} \quad (11)$$

where v_x and v_y are velocity along x - and y -axis, respectively.

The path x and path y are set with a certain desired input values. These values will be compared with the actual values to generate an error signal. However, since the input to the system is velocity and angular speed, there is a need to construct the error so that it will be acceptable to the system. Two different functions are designed to transform these error values into the two inputs of WMR system, as shown in Eqs. (12) and (13).

$$\tilde{v} = \sqrt{(x_{desire} - x_{actual})^2 + (y_{desire} - y_{actual})^2} \quad (12)$$

$$\tilde{\omega} = \text{atan2}((y_{desire} - y_{actual}), (x_{desire} - x_{actual})) \quad (13)$$

where \tilde{v} is modified error signal for velocity controller, $\tilde{\omega}$ is modified error signal for angular speed controller, x_{desire} is target of x position, y_{desire} is target of y position, x_{actual} is actual value of x position, y_{actual} is actual value of y position, and atan2 is four-quadrant inverse tangent, where it will return values in the closed interval $[-\pi, \pi]$.

The block diagram of WMR and its controller is shown in Fig. 2.

Control input for the controller used in this study is shown in Eq. (14).

$$v = K_p \tilde{v} + K_i \int \tilde{v} dt + K_d \frac{d\tilde{v}}{dt} \quad (14)$$

where K_p , K_i and K_d are proportional, integral and differential gain, respectively.

By giving values of K_i and K_d are equal to zero (0), then the system is using Proportional (P) controller. PD controller means that only K_i has zero value. And finally, PID controller will use all of the gain in the controller.

4 Simulation Result

This section will discuss the result and analysis of the samples data collected from Flex 3 cameras. There are several samples data with different angular velocity and constant time was collected in this experiment. The samples data will be analyzed by using the kinematic model designed in Simulink and state-space model by using system identification toolbox. The comparison between both methods will be also

discussed. Lastly, an appropriate controller is designed and the performance of each controller will be analyzed in this section.

The angular velocity of left motor and right motor are set to 100 for first five seconds and -100 for another five seconds. As the result, robot will move forward for five seconds and then move backward 100 for another five seconds. The data collected from motion tracker for each frame includes position x , y and z ; orientation yaw, roll and pitch. From 6 different data collected, only the data x , y and θ will be used for analysis. The total number of frames generated from the experiment is 1000 frames. Between frame 10 to frame 500, the speed of the robot is 100. And between frame 510 to frame 1000, the speed is also 100 but to the reverse direction.

4.1 Kinematic Model

From Fig. 3, it can be noticed that the distance for x position is increasing along the frames 0–500 and then decreasing from frames 510–1000. The dashed line is values from the kinematic model and the solid line is the position of robot measured by using Optitrack motion tracking system.

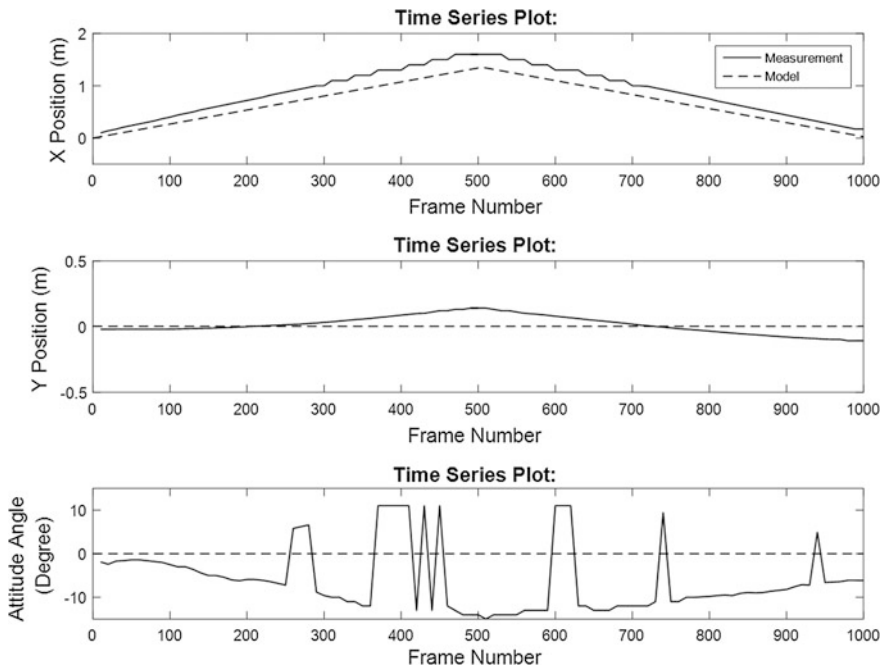


Fig. 3 Kinematic model verification for robot with angular speed 100

Table 1 Percentage error of X position—kinematic model verification

Frames	250	500	750
X Position—model (m)	0.7247	1.429	0.7538
X Position—Measured (m)	0.8800	1.600	0.900
Error (m)	-0.1553	-0.171	-0.1462
Percentage error (%)	21	12	19
Frame Number	250	500	750

Table 2 Percentage error of Y position—kinematic model verification

Frames	250	500	750
Y Position—Model (m)	0	0	0
Y Position—Measured (m)	0.012	0.14	-0.011
Error (m)	-0.012	-0.14	0.011
Percentage error (%)	1.2	14	1.1
Frame Number	250	500	750

From Table 1, it can be deduced that the peak values for reference x -position is 1.429 m, while the peak values for actual x position is 1.6 m. There are three frames to be taken for comparison of the distance. The result shows that the maximum error is ± 0.1553 m and the minimum error is ± 0.099 m.

Apart from that, it can be noticed that the distance for y position is increasing from -0.023 to 0.14 m and then decreasing to -0.11 m. The percentage error of the system is listed in Table 2. From Table 2, it can be deduced that the reference y -position is 0 without any changes, while the peak values for y measured is 0.14 m. As the result, the maximum error obtained is ± 0.14 m and the minimum error is ± 0.023 m.

In case of the orientation, it can be seen that the maximum angle of the robot is $\pm 15^\circ$ and the minimum angle is $\pm 1.4^\circ$. However, in theoretical, since the robot is only moving forward and backward, the orientation of yaw is 0° all the time. Hence, the kinematic model is not quite appropriate to be used in this study. The parameter that gives effect to the orientation of the robot is the surface of the ground. Unsmooth surface will affect the robot to move with some changes on the orientation angle.

Furthermore, in order to analyze the accuracy of the kinematics model, measured values are compared with the output from kinematic model. By considering that 100% accuracy is perfect match between measurement data and model, the accuracy of the system model can be calculated by using Eq. (15).

$$Accuracy = 100\% - average_absolute_error \quad (15)$$

where *average_absolute_error* is obtained by comparing the value of measurement using motion tracker and the output of the kinematics model.

Figure 4 shows the graph of absolute error between measurement data and the output from kinematics model. As seen from the graph, the average error is about 20% for x -position and 6% for y -position. In case of attitude angle θ , the result is

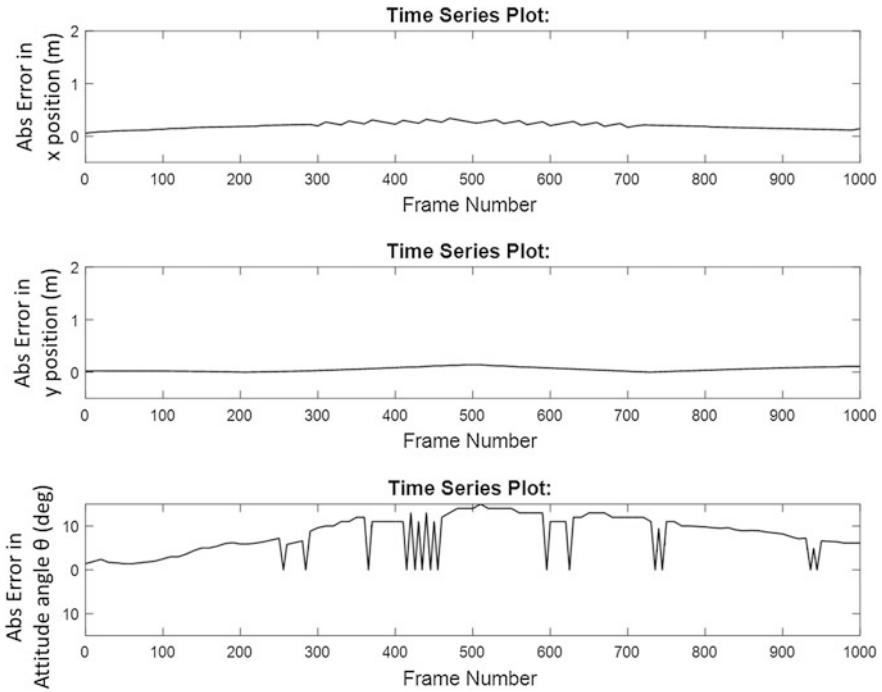


Fig. 4 Absolute error for kinematic model

fluctuating. Therefore the accuracy of the kinematic model is 80% and 94% for x -position and y -position, respectively.

4.2 State-Space Model

By using System Identification toolbox, the obtained MISO model for sub-system x position, y position and orientation, θ is shown in Eqs. (16), (17) and (18), respectively.

$$\frac{dx}{dt} = \begin{bmatrix} -0.004957 & -0.0895 \\ -0.0895 & -1.616 \end{bmatrix} x + \begin{bmatrix} 1.139 & 0.181 \\ 0.4274 & 0.6575 \end{bmatrix} u \tag{16}$$

$$y = [0.5842 \quad -1.616] x + [0.5842 \quad -1.616] u$$

$$\frac{dx}{dt} = \begin{bmatrix} -1.043 & 1.047 \\ 1.047 & -1.051 \end{bmatrix} x + \begin{bmatrix} -0.4599 & 0 \\ 0 & 0 \end{bmatrix} u \tag{17}$$

$$y = [-1.002 \quad -0.5557] x + [-1.352 \quad 0] u$$

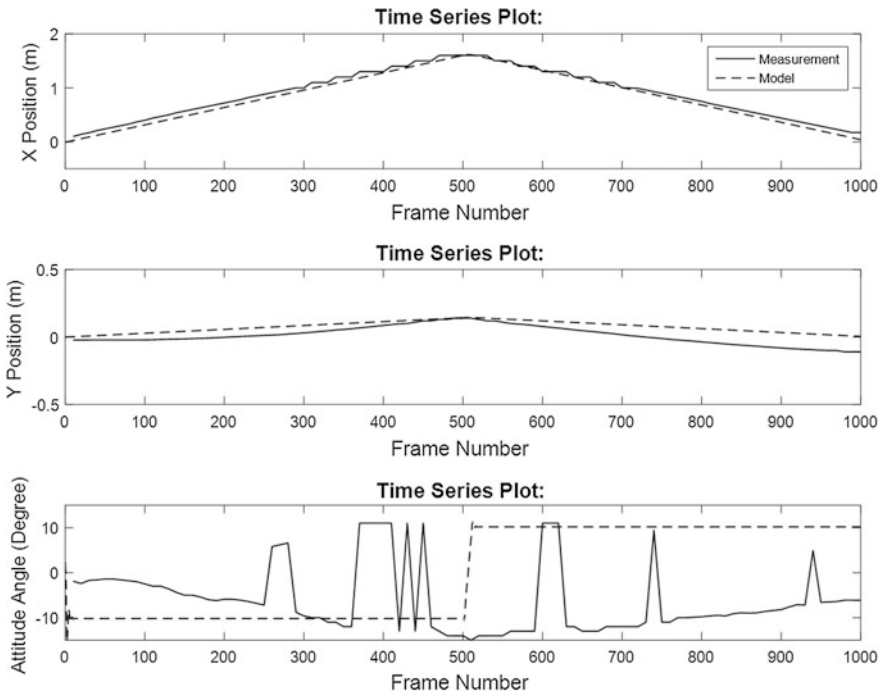


Fig. 5 State space model verification for robot with angular speed 100

$$\frac{dx}{dt} = \begin{bmatrix} -0.4489 & -1.542 \\ 1.542 & -0.4489 \end{bmatrix} x + \begin{bmatrix} 0.09622 & -0.37 \\ -0.7108 & 0.8974 \end{bmatrix} u \tag{18}$$

$$y = [0 \quad 0.511] x + [0 \quad 0] u$$

Figure 5 shows the comparison between measurement data from motion tracker and model. Figure 6 shows the absolute error between these two values.

The verification result is summarized in Table 3. By referring to Table 3, the maximum error for x position model is ± 0.08 m and minimum error is ± 0.002 m. It can be deduced that the peak value for x -model is 1.598 m and x -measured is 1.6 m. The percent error of this point is 0.12%.

Additionally, it can be noticed that the y -model is no more constant with 0 m as compared to the kinematic model in Fig. 3. The accuracy of state space model is about 94% and 95% for x -position and y -position, respectively.

From Table 4, it can be inferred that the position y model is increasing frame 500 and then decreasing up to frame 1000, while the peak values for y model is 0.1428 m and y measured is 0.14 m. The percent error for the peak point is 8.7%.

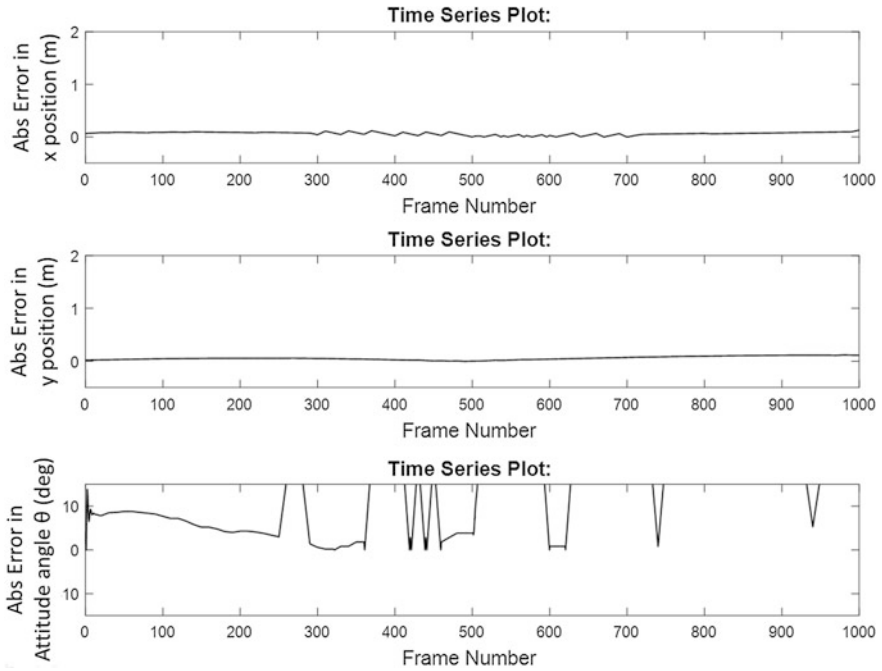


Fig. 6 Absolute error for state space model

Table 3 Percentage error of x position—model obtained from system identification

Frame Number	250	500	750
X Position—Model (m)	0.800	1.598	0.8429
X Position—Measured (m)	0.8800	1.600	0.900
Error (m)	0.08	0.002	0.0571
Percentage error (%)	10	0.12	6.8

Table 4 Percentage error of y position—model obtained from system identification

Frame Number	250	500	750
Y Position—Model (m)	0.071	0.14	0.076
Y Position—Measured (m)	0.012	0.14	-0.011
Error (m)	0.059	0	0.087
Percentage error (%)	5.9	0	8.7

In case of the orientation, it can be noticed that the maximum angle of the robot is $\pm 15^\circ$ and the minimum angle is $\pm 1.4^\circ$. In theoretical, the orientation of yaw angle is $\pm 15^\circ$.

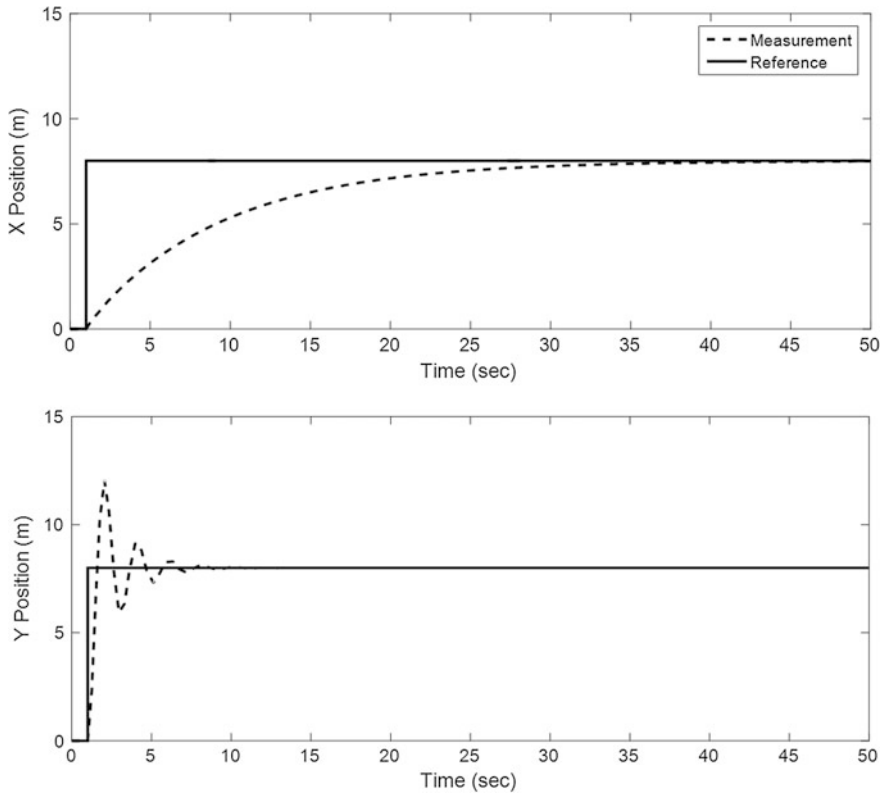


Fig. 7 Time response for $K_p = 10$

4.3 P Controller

Figure 7 illustrates the system time response by using P controller with the gain K_p is equal to 10. By referring to the x position, it can be seen that the overshoot is 0%, the settling time is 34.08 s and the rise time is 18.62 s without any steady state error. However, in y position, the overshoot is 50.76%, settling time is 7.24 s, the rise time is 0.42 s and steady state error is 0%.

4.4 PD Controller

Figure 8 illustrates the time response of the system when running using PD controller. The proportional gain, K_p is 40 and integral gain, K_i is -1 . By referring to the x position, it can be inferred that the overshoot is 0%, settling time is 8.9 s; rise time is 4.2 s and without any steady state error. Apart from that, in y position,

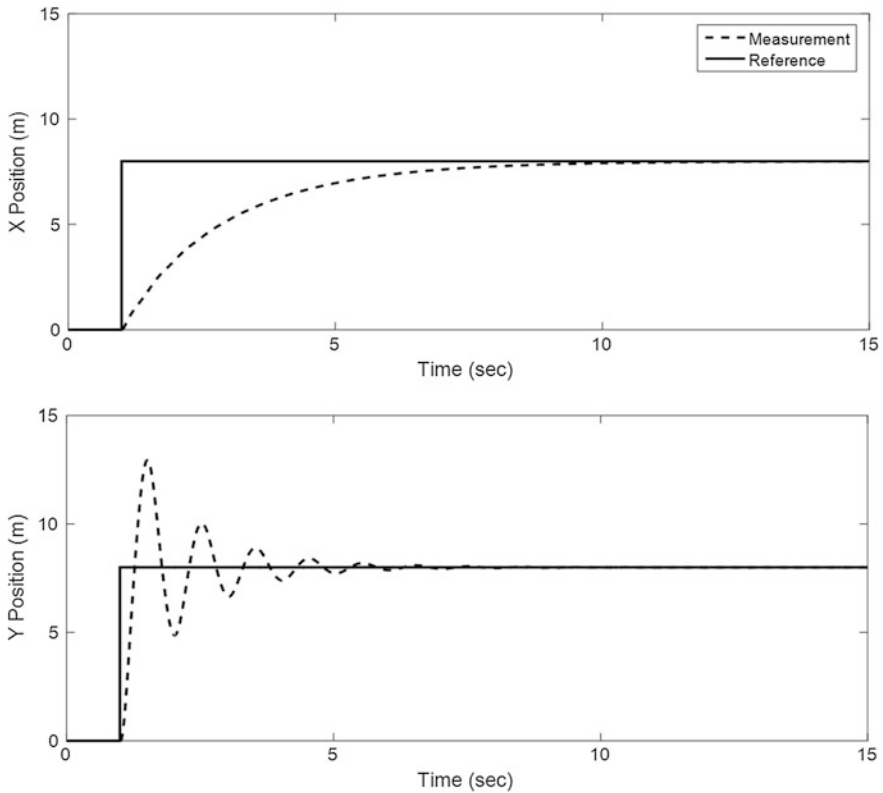


Fig. 8 Time response for $K_p = 40$ and $K_d = -1$

overshoot is 63%, settling time is 5.65 s, rise time is 0.18 s and also without any steady state error.

4.5 PID Controller

Figure 9 illustrates the output of the PID controller with K_p is 9, K_i is 0.001 and K_d is 0.001. In case of x position, the overshoot is 0%, settling time is 37.65 s, rise time is 20.63 s and without any steady state error. Additionally, in y position, the overshoot is 48.5%, settling time is 7.66 s, the rise time is 0.43 s and also without any steady state error.

Based on the result of the three different controllers, it can be concluded that the PID controller is most suitable for the system. This is seen from the percent overshoot obtained in the simulation, where for P, PD and PID controllers are 50.76%, 63% and 48.5%, respectively.

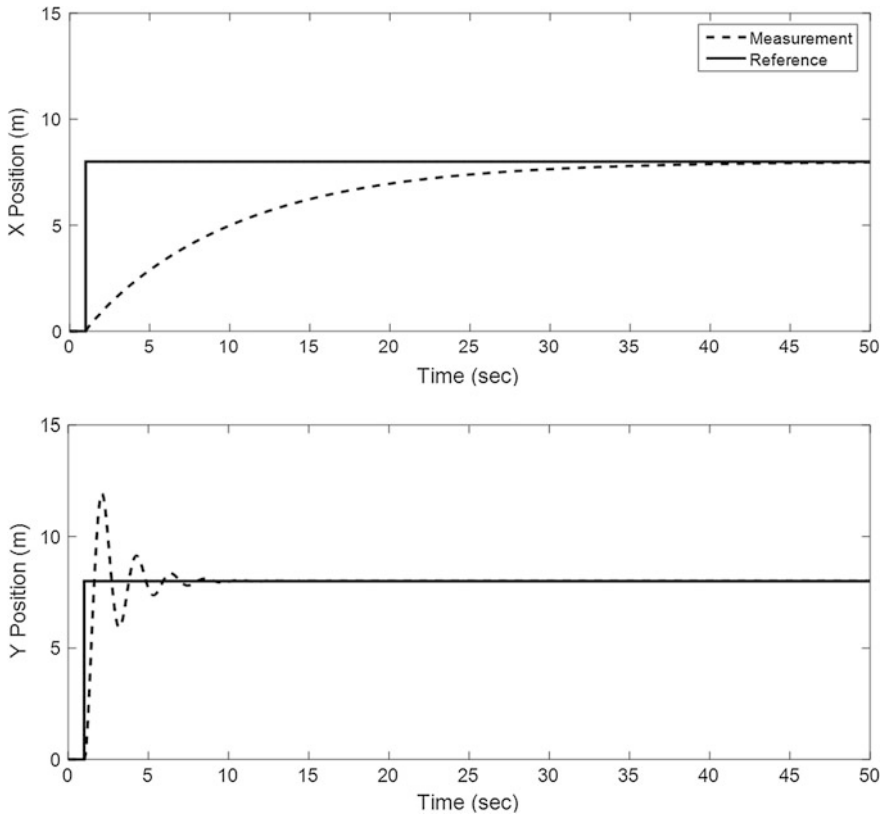


Fig. 9 Time response for K_P is 9, K_i is 0.001 and K_d is 0.001

4.6 Path Following Using PID Controller

The next simulation is the path following by using the controller designed in the previous section. In this simulation, the path is generated first, and then this path will be the reference for the system. The simulation is conducted for both model, kinematics model and model obtained from System Identification.

The result of the kinematic model is shown in Fig. 10 and the summary is listed in Tables 5 and 6. While, the result of the model obtained from System Identification is shown in Fig. 11 and the summary is listed in Tables 7 and 8.

As seen in Fig. 10 and also reported in Table 5, it can be noticed that the output of the reference x and measured x have a maximum percentage error of 14.5% and a minimum percentage error of 0.46%. In case of y position, the both signals, reference and also the system output is very closed. By zooming the graph, it is obtained that the maximum percentage error of the y position is 0.38% and the minimum percentage error is 0.088%.

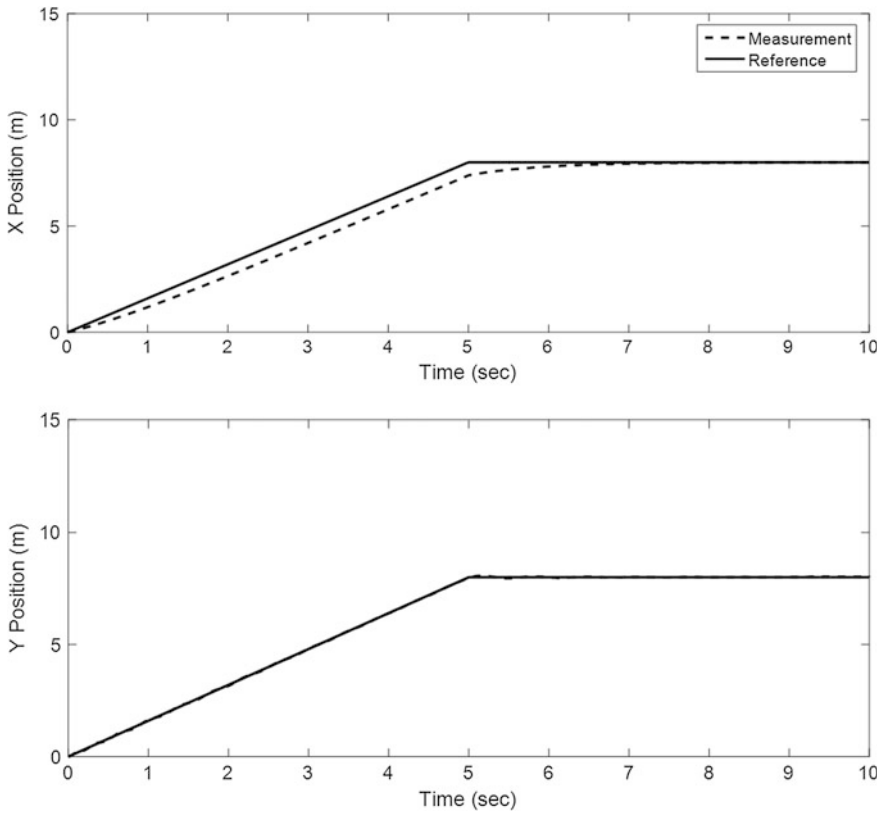


Fig. 10 Path following simulation using kinematic model

Table 5 Percentage error of X position—path following using kinematic model

Time (s)	2.5	5.0	7.5
Reference x (m)	4.000	7.981	8.000
Measured x (m)	3.420	7.382	7.963
Error (m)	0.580	0.599	0.037
Percentage error (%)	14.5	7.5	0.46

Table 6 Percentage error of y-position-path following using kinematic model

Time (s)	2.5	5.0	7.5
Reference y (m)	4.000	7.981	8.000
Measured y (m)	3.985	7.984	7.993
Error (m)	0.015	-0.003	0.0073
Percentage error (%)	0.38	0.038	0.088

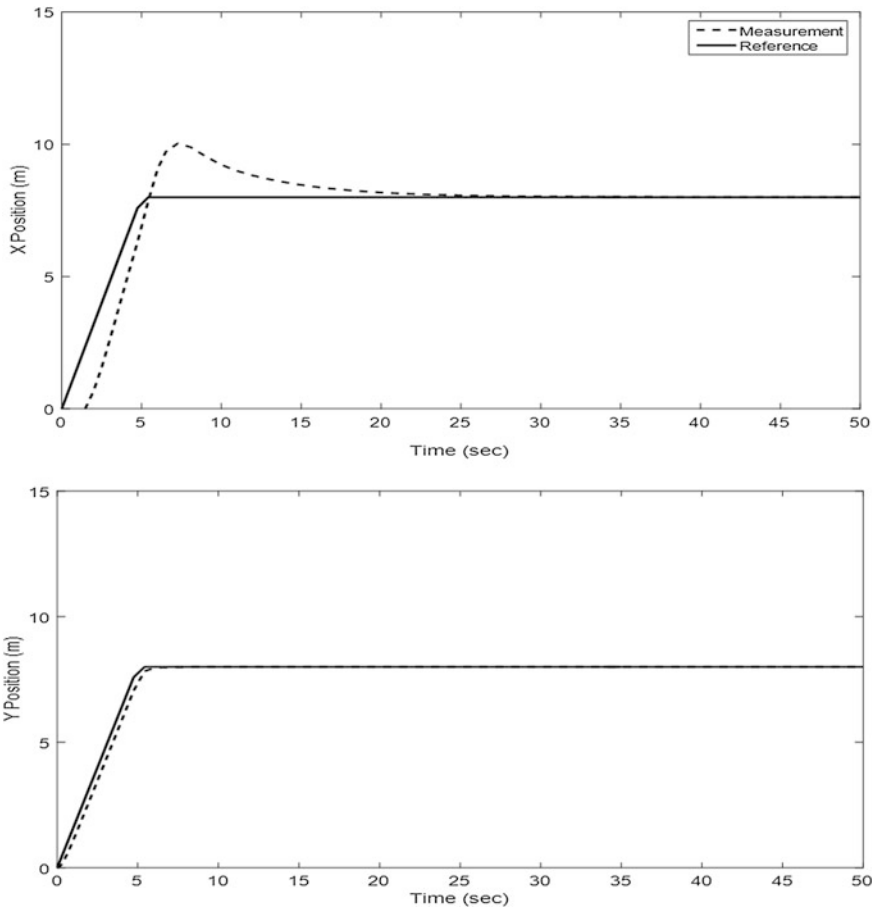


Fig. 11 Path following simulation using model obtained from system identification

Table 7 Percentage error of *x* position—path following using model obtained from SI

Time (s)	2.5	5.0	7.5
Reference <i>x</i> (m)	4.000	7.981	8.000
Measured <i>x</i> (m)	3.261	7.685	7.286
Error (m)	0.739	0.296	0.714
Percentage error (%)	18	3.7	8.9

Table 8 Percentage error of *y* position—path following using model obtained from SI

Time (s)	2.5	5.0	7.5
Reference <i>y</i> (m)	4.000	7.981	8.000
Measured <i>y</i> (m)	2.526	6.115	7.584
Error (m)	1.474	1.866	0.416
Percentage error (%)	36.8	23.4	5.2

By observing the result in Table 5, Tables 6, 7 and 8, it can be seen that the kinematic model has the maximum percentage error of x position is 14.5% and minimum percentage error is 0.46%, while for the state space model, the maximum percentage error is 18% and the minimum error is 3.7%. This result shows that by using kinematics model, the result is better than by using the model obtained from System Identification.

In case of y position, the maximum percentage error of kinematic model is 0.38% and the minimum percentage error is 0.088%, whereas the maximum and minimum percentage error of state-space model is 36.8% and 5.2%, respectively. Therefore, it can be concluded kinematic model is more precise to achieve the desired point.

5 Conclusion

OptiTrack Flex 3 cameras has been implemented successfully in Microsoft Visual Studio 2015 to link the mobile robot and created the assets of rigid body. From the rigid body all the required data has been tracked by Flex 3 cameras and exported in text file. Based on the results, the system is evaluated in kinematic model and state-space model. Afterwards, the PID controller has been developed to analyse the model performances.

In conclusion, the outcomes of this project have been obtained. The programmed of the Visual Studio with Flex 3 OptiTrack and Wheeled Mobile Robot have been executed. The position and orientation of the mobile robot have been tracked by using the motion system. Apart from these, the mathematical model is defined using the system identification of MATLAB the result performance of mobile robot has been analysed. A suitable PID controller has been proposed and the performance of the system has been analyzed. In future, the system can be improved by using the motion tracker to send the appropriate position to the mobile robot.

Acknowledgements This work is supported by Universiti Malaysia Pahang (UMP), under Universiti Malaysia Pahang Research Grant RDU 170378.

References

1. Shon, A.P., Storz, J.J., Rao, R.P.N.: Towards a real-time bayesian imitation system for a humanoid robot. In: 2007 IEEE International Conference on Robotics and Automation, pp. 2847–2852, 10–14 Apr 2007
2. Koenemann, J., Burget, F., Benezewitz, M.: Real-time imitation of human whole-body motions by humanoids. In: 2014 IEEE International Conference on Robotics and Automation (ICRA), pp. 2806–2812, 31 May–7 June 2014

3. Stanton, C., Bogdanovych, A., Ratanasen, E.: Teleoperation of a humanoid robot using full-body motion capture, example movements, and machine learning. In: Proceedings of the Australasian Conference on Robotics and Automation (ACRA) (2012)
4. Sontag, E.D.: *Mathematical Control Theory : Deterministic Finite Dimensional Systems*. Springer (1998)
5. Kwakernaak, H., Sivan, R.: *Linear Optimal Control Systems*. Wiley Interscience (1972)
6. Chow, G.C., Krieger, R.E.: *Analysis and control of dynamic economic systems* (1986)
7. Armah: Implementation of autonomous navigation algorithms on two-wheeled ground mobile robot. *Am. J. Eng. Appl. Sci.* **7**(1), 149–164 (2014)
8. Tsuchiya, K., Urakubo, T., Tsujita, K.: A motion control of a two-wheeled mobile robot. *IEEE Int. Conf. Syst. Man Cybern.* **5**, 690–696 (1999)
9. OptiTrack-motion capture systems. <https://www.optitrack.com/>

The Development of PANTHER AUV for Autonomous Underwater Vehicle Competition Challenge 2017/2018



Ahmad Anas Yusof, Mohd Khairi Mohamed Nor,
Shamsul Anuar Shamsudin, Mohd Rizal Alkahari and Masjuri Musa

Abstract This paper describes the development of an autonomous underwater vehicle for a competition that gives participants the opportunity to experience the engineering challenges of autonomous underwater vehicle (AUV) systems and develop skills in underwater technology. The competition focuses on the autonomous operations in the pool, with four tasks to be completed. The inertial measurement unit, depth sensor and Pixy (CMUcam5) camera are used in AUV navigation, while Arduino Uno is used for the overall controls. Field test has been conducted during the Malaysian Autonomous Underwater Vehicle Challenge (MAUVC) during the IEEE 7th International Conference on Underwater System Technology USYS in Kuala Lumpur. The outcome of the test will be studied for the preparation of the next Autonomous Underwater Vehicle Challenge, which will be held in Singapore.

Keywords Autonomous underwater vehicle · Remotely operated underwater vehicle · Unmanned underwater vehicle

1 Introduction

A total of eight undergraduate students from the Faculty of Mechanical Engineering, Universiti Teknikal Malaysia Melaka take part in the international competition to build underwater robot based on tasks and desirable applications. The autonomous underwater challenge is a competition that gives participants the opportunity to experience the engineering challenges of the autonomous underwater vehicle (AUV) systems and develop skills in underwater technology. An AUV is a robot that travels without requiring input from an operator [1–3]. The competition focuses on autonomous operations in a swimming pool, with four tasks to be

A. A. Yusof (✉) · M. K. M. Nor · S. A. Shamsudin · M. R. Alkahari · M. Musa
Faculty of Mechanical Engineering, Universiti Teknikal Malaysia Melaka,
Hang Tuah Jaya, 76100 Durian Tunggal, Melaka, Malaysia
e-mail: anas@utem.edu.my

completed. The tasks involve four challenges such as autonomous navigation, visual identification, acoustic localization and robotic manipulation. The implementation of Arduino Uno microcontroller, inertial measurement unit, depth sensor and Pixy (CMUcam5) camera are planned to provide a successful navigation control and propulsion.

2 The Underwater Challenge

Navigational accuracy is very important for autonomous underwater vehicles (AUVs). Typically, underwater vehicles use multisensory systems with the intention of estimating their position and determining the location of objects in their workspace.

Usually, inertial measurement units (IMUs), pressure sensors, compasses, and global positioning systems (GPS) are commonly used [4]. Vision-based systems are a good choice because they provide high resolution images with high speed acquisition at low cost [5]. However, underwater environments may provide color attenuation due to the poor visibility when the distance increases. These problems provide navigation and localization challenges for the PANTHER team. Figures 1 and 2 depict the challenges for the team in both Malaysian and Singapore AUVs challenge for 2017 and 2018.

3 The Development of PANTHER AUV

Previously, in 2017, an AUV known as TUAH has being built for Singapore Autonomous Underwater Vehicle Challenge 2017 (SAUVC 2017). During the competition, the AUV, as illustrated in Fig. 3, took 25 s to pass the first task during

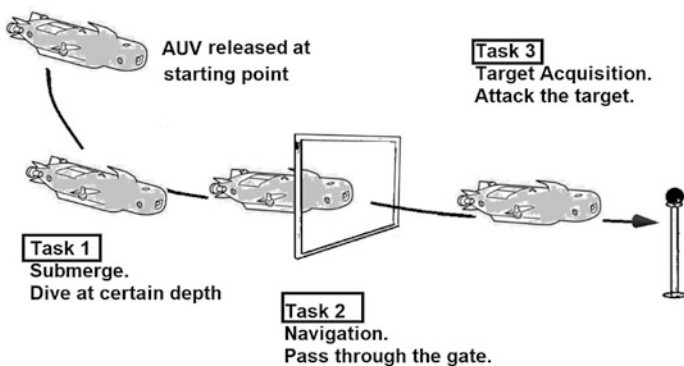


Fig. 1 Basic AUV navigation challenge

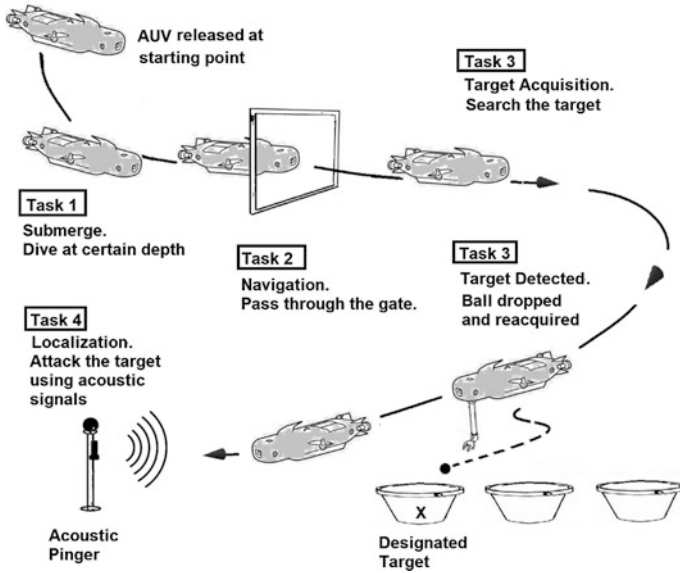
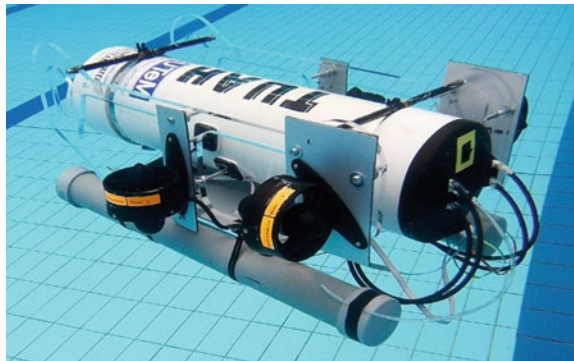


Fig. 2 AUV navigation and localization challenge

Fig. 3 TUAH UTeM autonomous underwater vehicle (AUVs)



the qualifying round. Unfortunately, with all the problems and technical difficulty, the TUAH lost to other AUVs, before bravely conduct 9 trials throughout the competition.

In 2018, the team has designed a new AUV, called PANTHER AUV. The team AUV is an interdisciplinary senior design project team that focuses on building an AUV for competition and research based aspects. The AUV team will be competing in both the Malaysian and Singapore Autonomous Underwater Vehicle Challenge that will be on December 20th, 2017 and March, 9th, 2018 respectively [6, 7].

The PANTHER AUV is designed so that it can navigate with the help of Inertia Measurement Unit or IMU which measures and reports a body's specific force and

Fig. 4 UTeM
PANTHER AUV conceptual
design

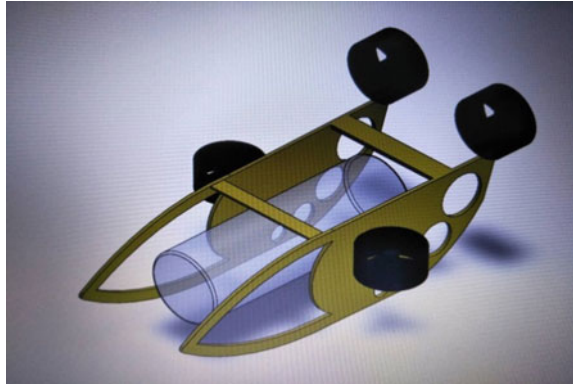
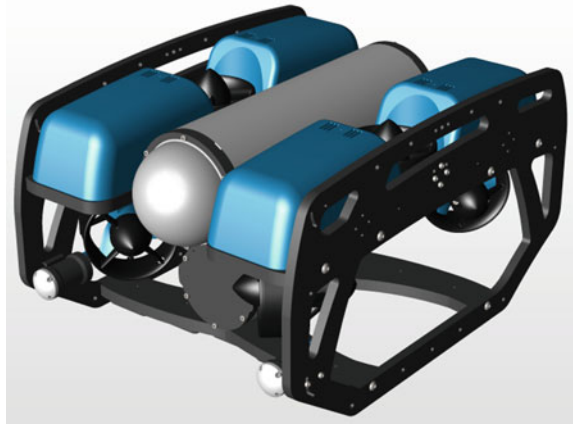


Fig. 5 UTeM
PANTHER AUV based on
BlueROV 2 design



angular rate, by using a combination of accelerometers and gyroscopes. There are 4 thrusters used for forward, reverse, upward and downward movement. Arduino UNO microcontroller is used for control while the IMU/depth sensor is used for surrounding measurements. Pixy (CMUCam5) camera is used for target detection. The vehicle is powered by 14.8 V lithium-ion batteries. Figures 4, 5 and 6 shows the design and control architecture of the PANTHER AUV.

3.1 Arduino Microcontroller

The PANTHER AUV is designed so that it can navigate independently of human intervention. The Arduino microcontroller, as illustrated in Figs. 7 and 8, is used for relaying motor commands to individual thrusters and collecting sensor data to be sent back to the user. All the Arduino code is written in C++ using the Arduino libraries.

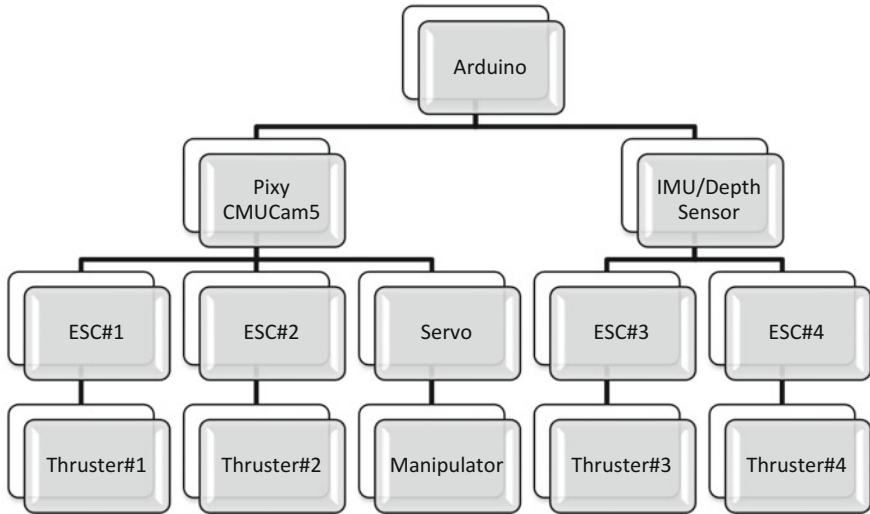


Fig. 6 UTeM PANTHER AUV control architecture

Fig. 7 Arduino UNO microcontroller



Fig. 8 Arduino UNO microcontroller in the control module



3.2 *Inertia Measurement Unit*

The IMU is used for measuring the AUV roll, pitch, yaw rate and depth. It can also be used to monitor the battery voltage of the AUV. In PANTHER AUV, openROV IMU/depth sensor is used [8, 9]. It has a single-axis rate gyro to measure the yaw rate and a 2-Axis accelerometer to measure the roll and the pitch. Analog signals from these sensors and from the depth sensor and the battery monitor are converted into digital form by a 16-bit A/D converter.

3.3 *Vision Sensors*

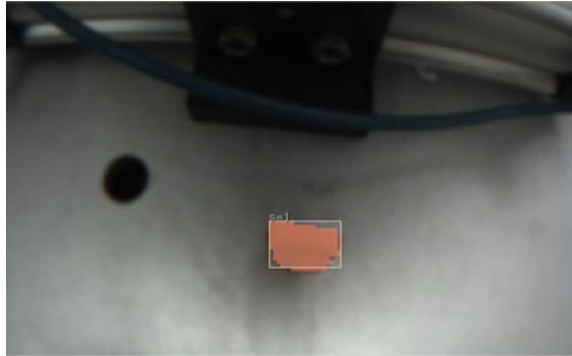
The sensors are provided with depth sensor for vertical movement control and Pixy (CMUCam5) camera for target recognition. The camera processes images from the image sensor and only sends the useful information to Arduino microcontroller. Hence, the microcontroller can communicate easily with the Pixy and still have plenty of CPU available for other tasks.

Pixy camera uses open source software that can be acquired easily from the internet. The camera is small, affordable and easy to use. It learns the object's color and saves it in the memory and can distinguish around 7 different unique colors in 50 frames per second. It is compatible with Arduino through SPI, USB, I2C, UART or analog/digital output interfaces. For the autonomous movement of the AUV, a coding that communicates with the sensor must be created, in order to give instructions for completing the task. As illustrated in Figs. 9 and 10, an object follower has been created by using the camera as the vision sensor. The figures show the movement of the camera that is attached to a servo, and rotates left and right by following the orange colored object. When the camera detects the object, the servo will position the camera to the center position of the object relative to the camera's view. If the position of the object is not at the center of the camera's view, the servo will turn to correct the position of the object, which is set to be always at

Fig. 9 Pixy (CMUCam5) camera is positioned above an object



Fig. 10 Pixy (CMUCam5) camera detects the object



the center of the camera's view. The process continues to loop. PixyMon is a software used in the Pixy camera, which allows the user to see what the camera see in raw and processed video. PixyMon also provides a panel for input parameter detection, such as contrast and saturation.

3.4 Thrusters

The four thrusters installed on the AUV are each connected to their own pin on the Arduino microcontroller. All thrusters are capable of forward and backward thrust at various speeds. The speeds of the motors are set in between 0 and 255. The T200 thrusters from BlueROV are used in the AUV.

The input signals to the ESC produced by the Microcontroller are what are called Pulse-Width-Modulated (PWM) waveforms. The voltage levels of this signal vary in time between the common voltage and the microcontroller input voltage. The PWM signal consists of square pulses separated in time where the width of the pulse corresponds to the commanded position of a servo. A short pulse would drive a servo to its minimum range and a long pulse to the maximum range. When the PWM signal is fed into an ESC the short pulses would signify low throttle (or no throttle) and long pulse to high throttle. The use of throttle here is related to the original use of a servo to literally close and open an air fuel mixture carburetor on a gas engine. For brushless motors, low throttle is used for low RPMs and high throttle for high RPMs. Figures 11, 12 and 13 show the setup of T-200 thruster with the ESC and the current and efficiency of the thruster.

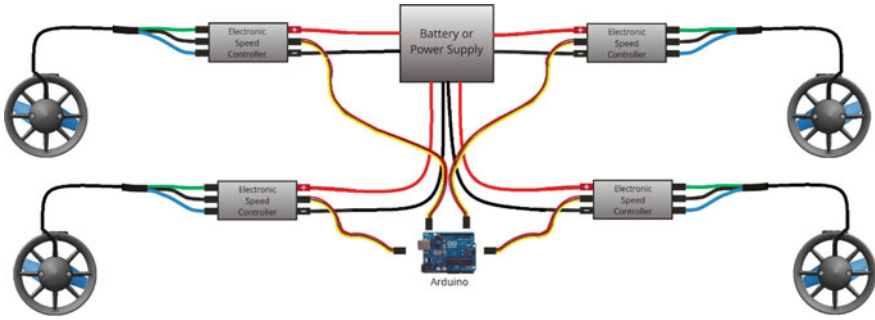


Fig. 11 T-200 thruster setup with ESC and Arduino

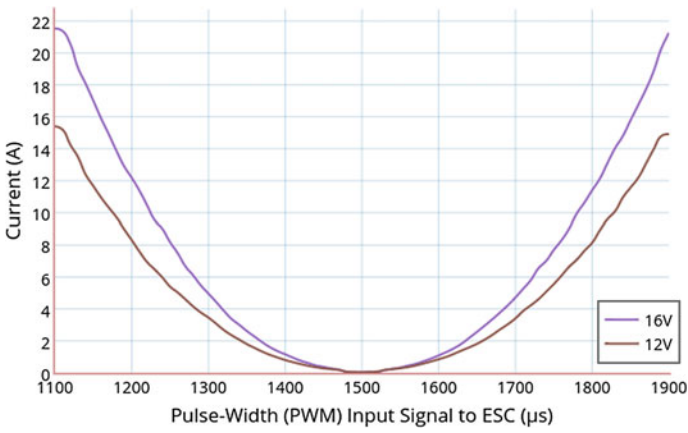


Fig. 12 Current versus PWM input signal to ESC

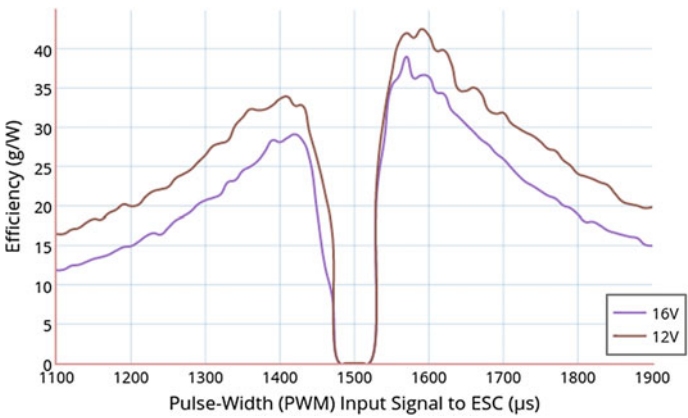


Fig. 13 Efficiency versus PWM input signal to ESC

4 Field Testing

During the Malaysia Autonomous Underwater Vehicle Challenge on December 20th, a test had been conducted on the PANTHER AUV System. The first technical problem involved the kill switch, which was used to switch on/off the AUV, had caused water leakages. Although small in volume, the leakages still affected the stability of the AUV body. However, it does not affect the voltage on the thrusters, since the switch is isolated in a switch module. Lesson learnt during the previous SAUVC 2017 competition proved vital during the field test at the MAUVC 2017 in Kuala Lumpur.

At the same time, the PANTHER AUV ESC had to be recalibrated in many occasions, by changing the coding for the system. As a result, the control module had to be meticulously opened and closed, every time the students enter the new instruction. This prompted for a new design for the next competition. Figures 14 and 15 illustrate the scenario during the field test.

Fig. 14 Troubleshooting the kill switch problem



Fig. 15 Troubleshooting the control module programming problem



5 Conclusion

A group of student team up in the development of an autonomous underwater vehicle (AUV) for a competition that gives them the opportunity to experience the engineering challenges and develop skills in underwater technology. An AUV is a robot that travels without requiring input from an operator. This design minimizes the overall costs of the vehicle. The implementation of Arduino Uno microcontroller, inertial measurement unit, depth sensor and Pixy (CMUcam5) camera are planned to provide a successful navigation and propulsion control. Minor problems that occurred such as leakages and short circuitry during the previous challenges are improved, with provision made in the use of a standardized seal and wiring compartment for the development of PANTHER AUV.

Acknowledgements The authors wish to thank Ministry of Higher Education and the Universiti Teknikal Malaysia Melaka for their support. This publication was funded by Ministry of Higher Education (MOHE) of Malaysia, under the Fundamental Research Grant Scheme (FRGS). **FRGS/1/2016/TK03/FKM-CARE-F00317.**

References

1. Hassan, S.N.H., Yusof, A.A., Tuan, T.B., Saadun, M.N.A., Ibrahim, M.Q., Wan, N.W.M.N.: Underwater manipulator's kinematic analysis for sustainable and energy efficient water hydraulics system. *AIP Conf. Proc.* **1660**, 070112 (2015)
2. Tadahiro, H.: Design of autonomous underwater vehicle. *Int. J. Adv. Robot. Syst.* (2011)
3. General Purpose Underwater Manipulating System. <http://cyberneticzoo.com/tag/general-purpose-underwater-manipulating-system/page/2/>. Accessed 20 Nov 2017
4. Antonelli, G.: Underwater Robots-Motion and Force Control of Vehicle-Manipulator System, 2nd edn. Springer, New York, NY, USA (2006)
5. Bonin-Font, F., Oliver, G., Wirth, S., Massot, M., Negre, P.L., Beltran, J.-P.: Visual sensing for autonomous underwater exploration and intervention tasks. *Ocean Eng.* **93**, 25–44 (2015)

6. Singapore Autonomous Underwater Vehicle Challenge 2018. <https://sauvc.org/>. Accessed 10 Dec 2017
7. Malaysia Autonomous Underwater Vehicle Challenge 2018. <http://oes.ieeemy.org/>. Accessed 10 Dec 2017
8. Buhr, S.: OpenROV wants to get to bottom of underwater mystery. USA Today: Tech. <https://makezine.com/2012/02/09/openrov-testing-at-hall-city-cave/>. Accessed 24 Nov 2017
9. Lam, B.: A Mini Sub Made from Cheap Parts Could Change Underwater Exploration. The New York Times: Bits. <https://bits.blogs.nytimes.com/2012/05/28/a-mini-sub-made-from-cheap-parts-could-change-underwater-exploration/last>. Accessed 28 Oct 2017

Waypoint Navigation of Quad-rotor MAV Using Fuzzy-PID Control



**Goh Ming Qian, Dwi Pebrianti, Luhur Bayuaji,
Nor Rul Hasma Abdullah, Mahfuzah Mustafa,
Mohammad Syafrullah and Indra Riyanto**

Abstract Quad-rotor Micro Aerial Vehicle (MAV) is a multi-rotor MAV with four propellers which propel the MAV up to the air and move around. It has high maneuverability to move around, such as roll, pitch and yaw movements. However, line of sight and radio control effective range are the major limitation for the MAVs which significantly shorten the travel distance. Therefore, we proposed a waypoint navigation quad-rotor MAV based on Fuzzy-PID controller in this paper. User can set mission with multiple waypoint and the Fuzzy-PID controller will control MAV autonomously moving along the waypoint to the desired position without remotely controlled by radio control and guidance of pilot. The results show Fuzzy-PID controller is capable to control MAV to move to the desired position with high accuracy. As the conclusion, Fuzzy-PID controller is successfully designed for waypoint navigation in quad-rotor MAV. The result shows that the overshoot percentage (%OS) of the designed Fuzzy-PID controller for x position is 2.17% while y position is 0.93%. Additionally, the steady-state error for x position and y position are 0.54% and 0.56% respectively. Therefore, the performance of Fuzzy-PID controller is better than PID controller.

G. M. Qian (✉) · D. Pebrianti (✉) · N. R. H. Abdullah · M. Mustafa
Faculty of Electrical and Electronics Engineering, Universiti Malaysia Pahang,
Pekan, Malaysia
e-mail: gohmingqian@gmail.com

D. Pebrianti
e-mail: dwipebrianti@ump.edu.my

L. Bayuaji
Faculty of Computer Science & Software Engineering, Universiti Malaysia Pahang,
Gambang, Malaysia

D. Pebrianti · L. Bayuaji · M. Syafrullah
Magister of Computer Science, Universitas Budi Luhur, South Jakarta, Indonesia

I. Riyanto
Faculty of Engineering, Department of Electronics Engineering, Universitas Budi Luhur,
South Jakarta, Indonesia

Keywords Waypoint navigation · Quad-rotor MAV · Fuzzy-PID (Proportional integral derivation) controller

1 Introduction

Unmanned Aerial Vehicles (UAV) is becoming more and more popular. Most of these UAV are used in military but since the early 1980s, UAVs have been introduced in commercial or domestic use as well. UAV is a flying vehicle with no pilot onboard and remotely controlled by a pilot or a ground station. UAVs were known by many different names such as robot plane, drone, remotely piloted vehicle (RPV) and pilotless aircraft. There are a few types of multi propeller UAV such as tri-copter (3), quad-copter (4), hexa-copter (6) and octo-copter (8). The number of propeller determines the ability to lift where is more propeller can lift heavier load. Quad-rotor MAV is the most researched among the multi propeller UAV due to its maneuverability.

The last decades, various control systems of quadrotor MAV have been reviewed by many researchers and applied successfully for controlling quadrotor MAV in commercial, scientific, recreational, agricultural applications such as policing and surveillance, aerial photography, cargo transport and drone racing [1–4].

The quadrotor MAV flight controllers can be classified into four main categories of controller which are linear flight controllers, model-based nonlinear flight controllers, learning-based control methods and hybrid controllers [5]. In linear controller includes PID [6], LQR [7], and H_∞ [8]. Among these three algorithms, PID controller is widely used and mostly successful in controlling Unmanned Aerial Vehicle (UAV) such as DJI, 3D Robotics and industry [9]. However, PID is a fixed gain algorithm. Therefore, it is not adaptive to physical changes.

In other hand, there are researches on learning based flight controller which includes Fuzzy Logic (FL) controller [10], Artificial Neural Network (ANN) controller [11], Iterative Learning (IL) based controller [12] and Brain Emotional Learning based Intelligent controller (BELBIC) [13]. Among these algorithms FL is simple in application which consumes less time and effort to develop. Unlike ANN that requires significant amount of learning data and layers of neuron in order to develop an efficient controller.

Moreover, there are researchers handle this problem by combining two or more algorithms which is known as hybrid controller. In [14], PID controller using fuzzy logic controller to present a self-tuning method to control the attitude of the quadrotor. Hence, we proposed fuzzy-PID controller for controlling the position of quad-rotor MAV to complete waypoint navigation task in this paper.

The organization of this paper is described as follows. The experimental setup of quad-rotor MAV and its modelling are described in Sect. 2. Section 3 clarifies the development of controller in quad-rotor MAV. In Sect. 4, the validation of results

of simulation between PID controller and Fuzzy-PID controller are discussed. Finally, Sect. 5 provides some concluding remarks and future works.

2 Experimental Setup

Here, the methodology of the experiment is described. First, we build the quad-rotor MAV hardware. Next, a ground control station (GCS) software is used to calibrate the quad-rotor MAV hardware. Lastly, hardware modelling is done in order to be implemented in our simulation.

2.1 Quad-rotor MAV Hardware

The quad-rotor MAV is constructed accordingly as follows. Figure 1 shows the general layout of components that included Ardu-pilot Mega APM 2.6 flight controller, Global Positioning System (GPS), propellers, brushless DC motors, Electronic Speed Controller, mission planner, telemetry, radio transmitter and battery. These components are mounted to a quad-rotor MAV frame as shown in Fig. 2.

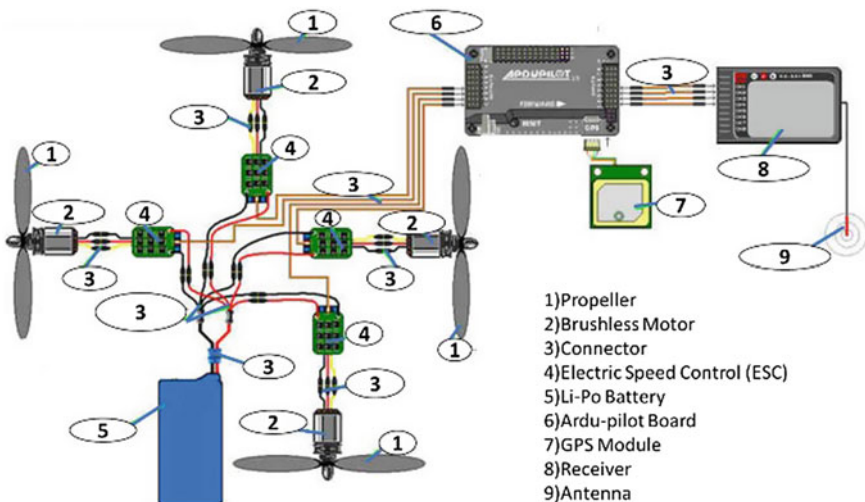


Fig. 1 Circuit connection layout



Fig. 2 Quad-rotor MAV frame

2.2 Ground Control Station Software

The mission planner is a Ground Control Station (GCS) for APM series. The readings of telemetry can be read and the controller parameters can be adjusted through the GCS. All the calibration such as radio transmitter calibration, compass calibration and others sensor calibration can be calibrated by using mission planner as shown in Fig. 3.



Fig. 3 Mission planner GCS software

2.3 Quad-rotor Modelling

The mathematical model of quadcopter is presented before designing the controller. The model contains rotor force and torque, gyroscopic effect and derived force model of “x” configuration. The plant system consists of the physical dynamics of quadrotor as shown in Fig. 4.

A quad-rotor MAV consists of two basic axes, which is translational and rotational axis. The translational axes fall on x, y and z axes; rotational axes on the other hand falls on roll (θ), pitch (ϕ), and yaw (ψ). This happens when the quad-rotor state is being rigid and ungrounded. Figure 5 shows the quad-rotor MAV system.

The modelling of quadrotor system is developed based on the study done by previous study [7, 15]. The dynamic model is equivalent to the real quad-rotor MAV. Dynamic quadrotor can be described by 12 states, divided into 3 categories. The first category is position (P) in x, y and z axes; second category is rotational angles (Ω) of roll (θ), pitch (ϕ), and yaw (ψ); third category is the angular velocities (ω) of p, q and r [16]. The output of quad-rotor includes linear motion

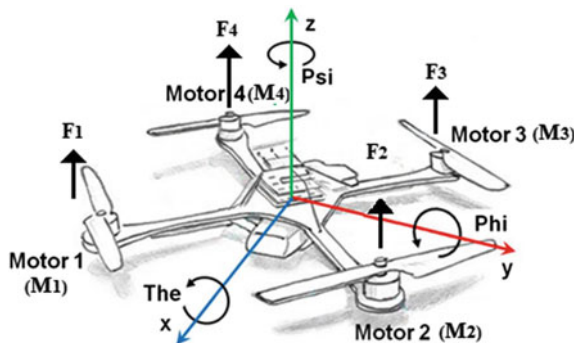


Fig. 4 “x” configuration quad-rotor MAV

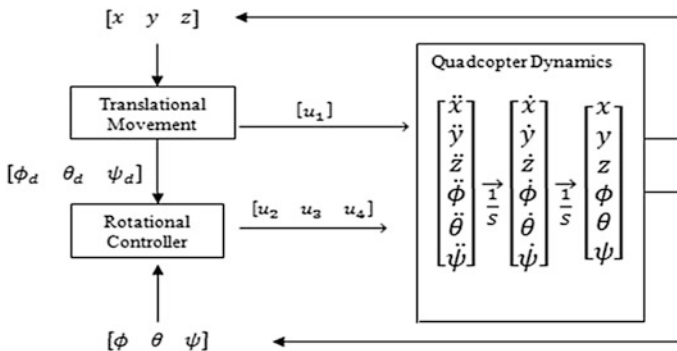


Fig. 5 The quad-rotor MAV System

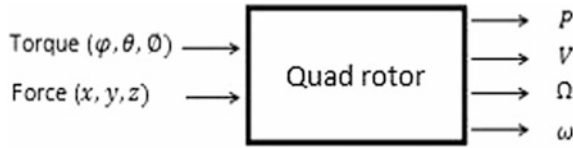


Fig. 6 Quad-rotor input/output

(P), rotational angles (Ω), linear velocities (V) and angular velocities (ω) are the outputs as illustrated in Fig. 6.

Attitude model dynamic can be derived from Newton’s law. The rotating pairs will automatically eliminate coupling between dynamic roll and pitch, hence caused each rotor rotation to be cancelled out. Using a small sized propeller will reduce the torque and increase the motor efficiency. It is easier to drive the blades to a higher velocity without additional mechanical vibration. The stress on mechanical parts will inevitably be reduced if we decrease the vibration and torque [8]. A few assumptions are assigned to simplify the dynamics of the system. The assumptions made was quadrotor and propeller are rigid and symmetric systems, plus ground effect is ignored.

3 Controller Development

In the general of real time operation, the model based cascaded controllers is used to apply on the quadrotor system. The control system is mainly focused on the x and y position which is directly controlled by the roll (θ) and pitch (ϕ) angles respectively. Figure 7 shows the overall system controller in quad-rotor MAV by using Fuzzy-PID controller.

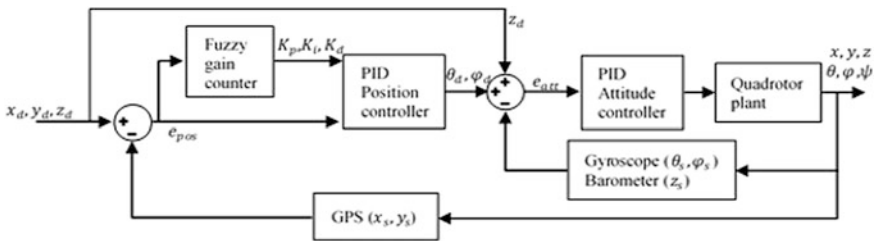


Fig. 7 Overall system control block diagram

3.1 PID Controller

The PID controller is designed in MATLAB Simulink based on Eqs. (1), (2) and (3). The PID controller includes the state and desired value of position of x, y and z and attitude of roll angle (θ), pitch angle (ϕ), and yaw angle (ψ) [6].

$$U_1 = \frac{m}{\cos \phi_d \cos \theta_d} (g + e_z) \quad (1)$$

$$\Phi_d = \sin^{-1} \left(\frac{m}{U_1} (e_y) \right) \quad (2)$$

$$\theta_d = \sin^{-1} \left(\frac{m}{\cos \left(\sin^{-1} \left(\frac{m}{U_1} (e_y) \right) \right) U_1} e_x \right) \quad (3)$$

where, e_z , e_y and e_x are the error of z position, y position and x position, respectively. Meanwhile, U_1 , ϕ_d and θ_d is the control input of altitude, desired angle of pitch and desired angle of roll, respectively. Lastly, g is the gravitation acceleration constant and m is the mass of quad-rotor MAV.

3.2 Fuzzy Logic Controller

The main idea of fuzzy control is to translate the information and knowledge that is used by human pilots into fuzzy rules, which can be used by fuzzy controllers. It has strong robustness, good adaptability and fault tolerance. But the weakness is low steady state accuracy due to lack of integral link [17]. Figure 8 shows the fuzzy system. It is implemented in PID position controller to tune the parameters of PID gains (K_p, K_i, K_d) with the inputs are error (e) and error of rate (\dot{e}). There inputs are obtained from evaluating the feedback of GPS sensor and the reference position given by the user. The system has three output variables which are *alpha* (α), *beta* (β) and *gamma* (γ) as shown in Fig. 9. In first stage of fuzzification, the inputs (e, \dot{e}) are divided into three subsets of fuzzy with trapezoidal membership function between the range from -1 until 1 as shown in Fig. 10. For the outputs, trapezoidal membership function with two subsets of fuzzy is also used in *alpha* (α) and *beta* (β) between the range from 0 until 1 while triangle membership function with four subsets of fuzzy used in *gamma* (γ) between the range from 1 until 6 as shown in Fig. 11. The Fuzzy Inference System (FIS) has 9 rules. The method of Mamdani with Min-Max was chosen for conducting the combination of fuzzy. In last stage defuzzification, the value of K_p, K_i, K_d are obtained by using Eqs. (4), (5) and (6) with *alpha* (α), *gamma* (γ) and *beta* (β) respectively.

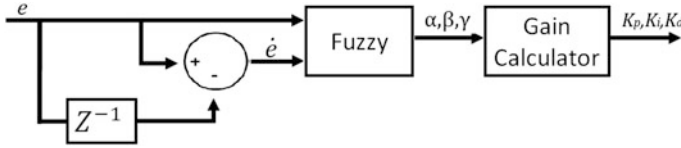


Fig. 8 Fuzzy-PID controller of block diagram

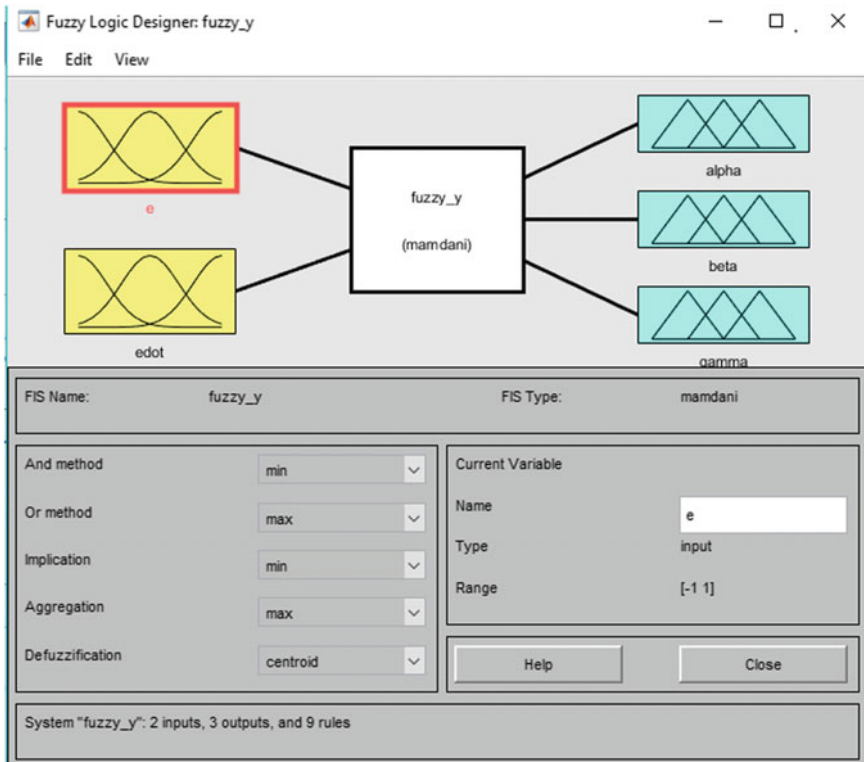


Fig. 9 Fuzzy logic system

$$K_p = K_{p_{min}} + (K_{p_{max}} - K_{p_{min}}) \times \alpha \tag{4}$$

$$K_i = \frac{K_p^2}{K_d \times \gamma} \tag{5}$$

$$K_d = K_{d_{min}} + (K_{d_{max}} - K_{d_{min}}) \times \beta \tag{6}$$

Table 1, Table 2 and Table 3 show 9 rules used in Fuzzy Inference System (FIS) for K_p , K_d and K_i respectively to determine the PID gains parameters. In these

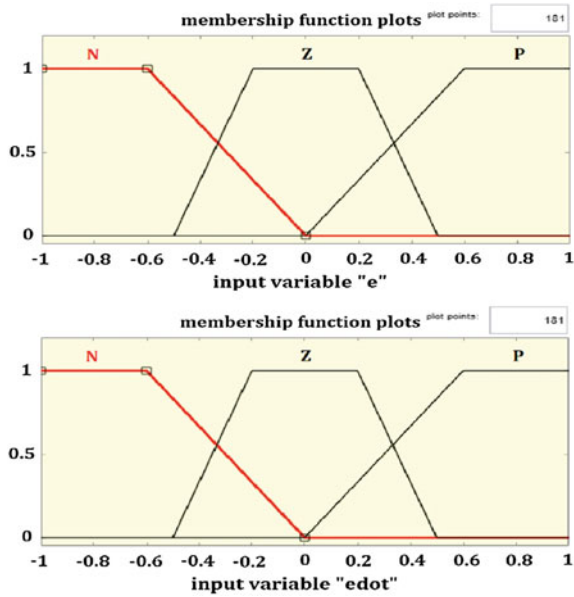


Fig. 10 Membership function of error (e) and rate error (\dot{e})

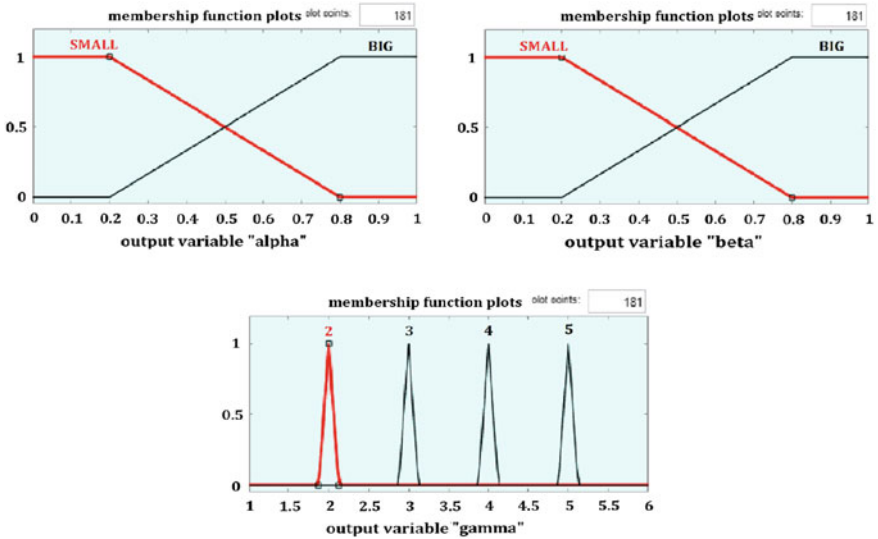


Fig. 11 Membership function of α (α), β (β) and γ (γ)

tables, N, Z, P, S and B represents Negative, Zero, Positive, Small and Big respectively however 2–5 represent from low to high.

Table 1 Fuzzy rules for Fuzzy-PID controller for K_p

			\dot{e}	
		N	Z	P
e	N	B	B	B
	Z	S	S	S
	P	B	B	B

Table 2 Fuzzy rules for Fuzzy-PID controller for K_i

			\dot{e}	
		N	Z	P
e	N	B	S	B
	Z	B	S	B
	P	B	S	B

Table 3 Fuzzy rules for Fuzzy-PID controller for K_d

			\dot{e}	
		N	Z	P
e	N	5	4	5
	Z	3	2	3
	P	5	4	3

4 Discussion and Results

In this paper, we set a flight path in terms of distance as shown in Table 4. The result is simulated in Matlab Simulink software. The proposed controller Fuzzy-PID controller is then compared with PID controller.

This part shows the simulation results of PID controller with optimum gain in term of k_p, k_i and k_d on the x and y position control accuracy. Here, the controllers are set with optimum PID gain as shown in Table 5.

Figures 12 and 13 show the x -position control performance of Fuzzy-PID controller and PID controller with optimum gains of x position control as shown in Table 5 is applied. The performance is acceptable since the percentage overshoot (%OS) in PID controller is 13.9% while in Fuzzy-PID controller is 2.17%. The Fuzzy-PID controller decrease 11.73% of percentage overshoot (%OS) from PID controller. In term of steady state error, PID and Fuzzy-PID have steady-state error about 0.65 and 0.54%.

Table 4 Flight path

Axis	Distance (m)							
	0	0	0	23	23	23	0	0
x	0	0	27	27	27	0	0	0
y	0	7	7	7	7	7	0	0
z	0	7	7	7	7	7	0	0

Table 5 Optimum gains for PID controller of x position and y position

Gain	Position	
	x	y
k_p	1.578	1.758
k_i	0.065	0.076
k_d	8.490	9.036

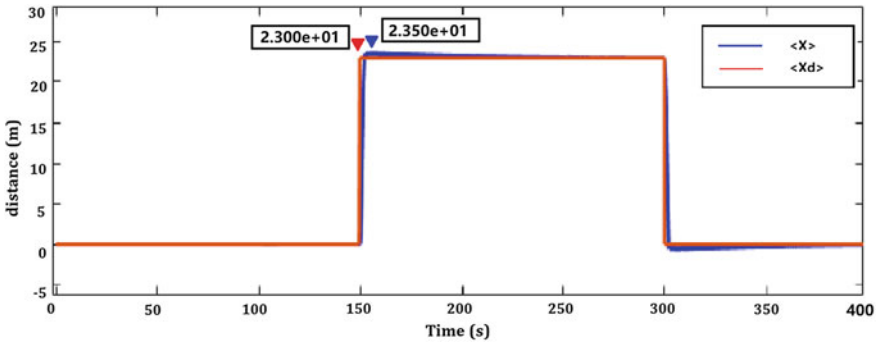


Fig. 12 x position using Fuzzy-PID controller

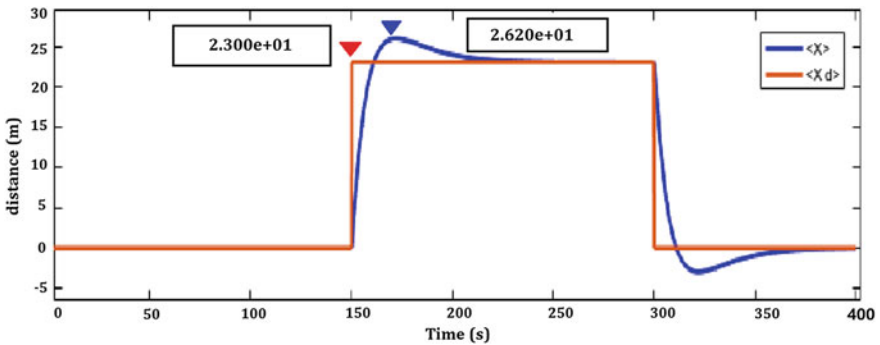


Fig. 13 x position using PID controller with optimum gains, $k_p = 1.578$, $k_i = 0.065$ and $k_d = 8.490$

Figure 14 and Fig. 15 show the y -position control performance of Fuzzy-PID controller and PID controller respectively when optimum gains of y position control as shown in Table 5 is applied. The performance is acceptable since the percentage overshoot (%OS) in PID controller is 11.9% while in Fuzzy-PID controller is 0.93%. The Fuzzy-PID controller decrease 10.97% of percentage overshoot (%OS) compare with PID controller. In term of steady state error, PID and Fuzzy-PID have steady-state error about 0.7% and 0.56% respectively.

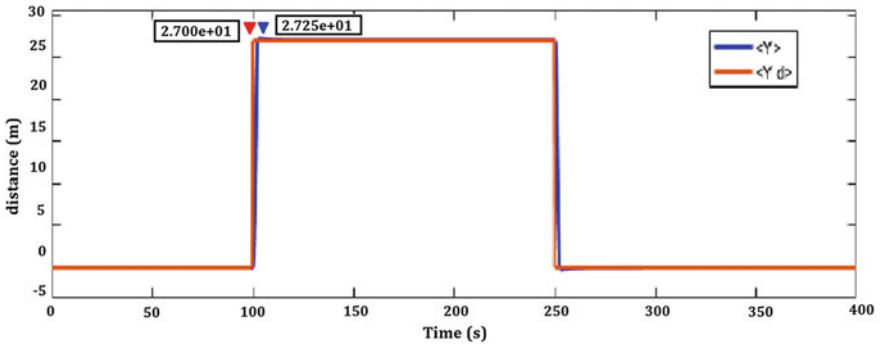


Fig. 14 y position using Fuzzy-PID controller

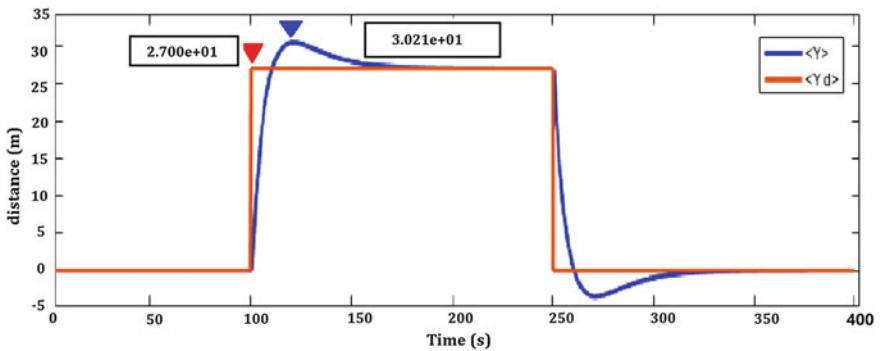


Fig. 15 y position using PID controller with optimum gains, $k_p = 1.758$, $k_i = 0.076$ and $k_d = 9.036$

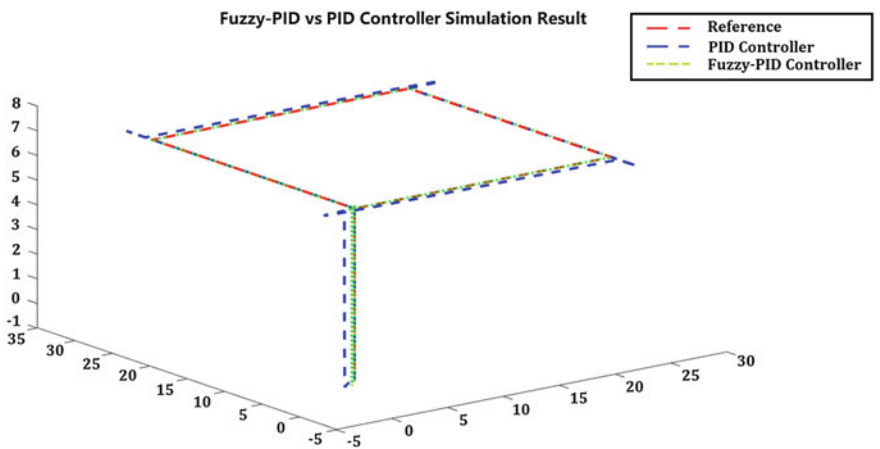


Fig. 16 Waypoint navigation of reference, PID controller and Fuzzy-PID controller

Figure 16 shows 3 dimensional (3D) of waypoint navigation in simulation result to view clearly. Red line is the reference of flight pattern for both controllers, while blue line is the PID controller result and green line is the Fuzzy-PID controller of quad-rotor MAV. Based on Fig. 16, the simulation result of Fuzzy-PID controller is closed with the flight path reference to compare with PID controller's simulation result. As conclusion, Fuzzy-PID controller is high accuracy compare PID controller on positioning of quad-rotor MAV.

5 Conclusion

Fuzzy-PID controller of waypoint navigation on quad-rotor MAV is presented. The result shows that the proposed controller is more accurate compared to PID controller for performing waypoint navigation task. On the other hand, the value of PID gains (k_p, k_i, k_d) must be determined and fine-tuned to increase the stability of controller. Otherwise, the MAV will behave vigorously. Meanwhile, the proposed controller can be applied in autonomous aerial vehicle where minimum guidance of pilot is required.

As the conclusion, Fuzzy-PID controller is successfully designed for waypoint navigation in quad-rotor MAV. The result of shows that the overshoot percentage (%OS) of the designed Fuzzy-PID controller for x position is 2.17% while y position is 0.93%. Additionally, the steady-state error for x position and y position are 0.54% and 0.56% respectively. Therefore, the performance of Fuzzy-PID controller is better than PID controller.

Future work, we can work PID controller using the Interval Type-2 Fuzzy Logic controller on waypoint navigation of quad-rotor MAV and validate the simulation results of positioning with PID controller and Fuzzy-PID controller.

References

1. Franke, U.E.: Drones, drone strikes, and US policy: the politics of unmanned aerial vehicles. *Parameters* **44**(1), 121 (2014)
2. Birk, A., Wiggerich, B., Bülow, H., Pflingsthorn, M., Schwertfeger, S.: Safety, security, and rescue missions with an unmanned aerial vehicle (UAV). *J. Intell. Robot. Syst.* **64**(1), 57–76 (2011)
3. Nex, F., Remondino, F.: UAV for 3D mapping applications: a review. *Appl. Geomatics* **6**(1), 1–15 (2013)
4. Bendig, J., Bolten, A., Bareth, G.: UAV-based imaging for multi-temporal, very high resolution crop surface models to monitor crop growth variability. *Photogramm. - Fernerkundung - Geoinf.* **6**, 551–562 (2013)
5. Kendoul, F.: Survey of advances in guidance, navigation, and control of unmanned rotorcraft systems. *J. Field Robot.* **29**(2), 315–378 (2012)

6. Qian, G.M., Pebrianti, D., Chun, Y.W., Hao, Y.H., Bayuaji, L.: Waypoint navigation of quad-rotor MAV. In: 2017 7th IEEE International Conference on System Engineering and Technology (ICSET), pp. 38–42 (2017)
7. Ismail, N.A., Othman, N.L., Zain, Z.M., Pebrianti, D., Bayuaji, L.: Attitude control of quadrotor. *ARPN J. Eng. Appl. Sci.* **10**, 6 (2015)
8. Raffo, G.V., Ortega, M.G., Rubio, F.R.: Nonlinear H_∞ controller for the quad-rotor helicopter with input coupling. In: *IFAC Proceedings Volumes (IFAC-PapersOnline)*, vol. 18, no. PART 1, pp. 13834–13839 (2011)
9. John, S.: Artificial intelligent-based feedforward optimized PID wheel slip controller. In: *IEEE AFRICON Conference* (2013)
10. Zulu, A., John, S.: A review of control algorithms for autonomous quadrotors. *Open J. Appl. Sci.* **4**(14), 547–556 (2014)
11. Jing, C.S., Pebrianti, D.: Fault detection and identification in Quadrotor system (Quadrotor robot). In: *Proceedings—2016 IEEE International Conference on Automatic Control and Intelligent Systems, I2CACIS 2016*, pp. 11–16 (2017)
12. Schoellig, A.P., Mueller, F.L., D’Andrea, R.: Optimization-based iterative learning for precise quadcopter trajectory tracking. *Auton. Robots* **33**(1–2), 103–127 (2012)
13. Mei, Y., Tan, G., Liu, Z.: An improved brain-inspired emotional learning algorithm for fast classification. *Algorithms* **10**(2) (2017)
14. Fahmizal, Surriani, A., Budiyanto, M., Arrofiq, M.: Altitude control of quadrotor using fuzzy self tuning PID controller. In: 2017 5th International Conference on Instrumentation, Control, and Automation (ICA), pp. 67–72 (2017)
15. Bouabdallah, S., Siegwart, R.: Full control of a quadrotor. In: 2007 IEEE/RSJ International Conference on Intelligent Robots and Systems, pp. 153–158 (2007)
16. Shatat, D., Tutunji, T.A.: UAV quadrotor implementation: a case study. In: 2014 IEEE 11th International Multi-Conference on Systems, Signals and Devices, SSD 2014 (2014)
17. Li, L., Sun, L., Jin, J.: Survey of advances in control algorithms of quadrotor unmanned aerial vehicle. In: *International Conference on Communication Technology Proceedings, ICCT, 2016*, vol. 2016, pp. 107–111

Development of Pole-Like Tree Spiral Climbing Robot



M. A. Mustapa, W. A. F. W. Othman, Elmi Abu Bakar
and A. R. Othman

Abstract This paper presents a tree climbing robot which moves spirally around a pole-like tree of having a circumference of around 40 cm. The aim of this work is to ease the work of inducing *Aquilaria* trees. The designed robot is able to climb with overall weight of the robot can carry is limit to 10 kg. The robot utilizes the wheel mechanism as the locomotion of the robot. Driving module uses two DC motors, and the robot also uses a set of springs and castor balls as a supporting mechanism. To achieve the robot spiral climbing morphology, two DC motors are used as the steering module. At the current stage of development, the angle of climbing is controlled manually by DIP-switches. The advantages of this robot are low cost, uses simple mechanism, easy to control and fabricate. The robot has been built and successfully tested on a tree trunk and PVC tube. Experiment has been carried out to evaluate the speed performances of the prototype. Results indicate that the robot is able to climb in spiral motion with largest error recorded at 13.9%.

Keywords Tree climbing robot • Wheel mechanism • Spiral climbing morphology

M. A. Mustapa · W. A. F. W. Othman (✉)
School of Electrical & Electronic Engineering, Universiti Sains Malaysia,
14300 Nibong Tebal, Penang, Malaysia
e-mail: wafw_othman@usm.my

E. Abu Bakar
School of Aerospace Engineering, Universiti Sains Malaysia,
14300 Nibong Tebal, Penang, Malaysia

A. R. Othman
Mechanical Engineering Department, Universiti Teknologi Petronas,
32610 Seri Iskandar, Perak, Malaysia

© Springer Nature Singapore Pte Ltd. 2018
M. H. A. Hassan (ed.), *Intelligent Manufacturing & Mechatronics*,
Lecture Notes in Mechanical Engineering,
https://doi.org/10.1007/978-981-10-8788-2_26

1 Motivation

Aquilaria cultivation (Fig. 1a) in Malaysia is believed to be started in 2000, but cultivation has been very slow due to many planters are still cautious due to the failure of the previous forestry plantation projects [1]. By 2005, cultivation of Aquilaria began to grow and the support of government agencies such as the *Jabatan Perhutanan Semenanjung Malaysia* (Forestry Department of Peninsular Malaysia) and the private sectors, including government linked companies and individuals [2].

A common method in artificial forestry is to inoculate (agarwood inducement) all the trees with the fungus. The existing artificial agarwood inducement methods include bark removal as well as axe and nail wounding methods, the burning method, and the fungi infection method [3–6]. These methods require a long time for agarwood formation, and produce a low agarwood yield.

To date, some comparatively new and efficient methods have been developed such as the cultivated agarwood kits (CA-Kits) by Blanchette from the University of Minnesota [7] and the whole-tree agarwood-inducing technique (Agar-Wit) by the Chinese Academy of Medical Sciences and Peking Union Medical College [8].

In these techniques [7, 8], (Fig. 1b, c) several small holes will be drilled in spiral at the trunk and apply agarwood inducer into the xylem part of Aquilaria tree through these holes. Due to water transportation, the inducer is transported to the whole trunk, thus forming an overall wound in the tree, and as a result, agarwood is finally formed in the Aquilaria trees in a short period of time.

Currently, climbing and drilling work on Aquilaria tree is mainly conducted by human using hand tools as shown in Fig. 1b. Effective and safe ways are needed to replace such labor work. Automatic systems such as tree climbing and drilling robot have the great potential in sustainable forestry plantation management. For any tree climbing robot, the climbing mechanism plays an important role that determines how the robot climbs the tree trunk safely, stably and quickly.

Aquilaria tree, as shown in Fig. 1a is a tree of medium-sized and grow vertically with a maximum height of 10 m, it has a few branches at the top of the tree



Fig. 1 a 3-year old Aquilaria trees; b Several holes are drilled manually to apply agarwood inducer into the xylem part of the tree; c Spiral holes inducement techniques in [7, 8]

which can be categorized as a pole-like tree. There are several climbing robot that have been introduced recently. The developments of climbing robots were emphasized on two types of mechanism; i.e., continuous and step-by-step based climbing mechanism [9]. Continuous motion robot utilizes the wheel mechanism [10], piston mechanism [11], and slider-crank mechanism [12] for gripping and climbing.

Furthermore, various mechanisms and approaches had been applied on step-by-step based climbing robot, which includes rolling self-locking [13], serial mechanism, modular mechanism [14] etc. The wheel mechanism robots are lighter and quicker than other robots due to less components used and simple mechanism (ease of control and build) [15].

2 Robot Design and Testing

2.1 Conceptual Design

In this work, main material used for the frame of the robot is ready made mild steel. It is selected due to its strength and rigidity. The locomotion of the robot uses wheel mechanism as it is simpler and easier to implement as compare to other mechanisms. Figure 2d shows the conceptual design of the robot using SolidWorks (version 2015), and Fig. 2e depicts the actual physical robot prototype presented in this paper. The robot has 3 modules attached to its frame; namely steering module (Fig. 2a), driving module (Fig. 2b), and support module (Fig. 2c).

To achieve the robot spiral climbing morphology, two DC motors are used as the steering module. At the steering module (Fig. 2a), DC motor is used to rotate the angle of the wheel by steering the driving module at a particular direction. The wheel will be in 0° or move vertically at the tree; 30° to the right, or 60° to the right of the tree. If the steering wheel is not at 0° , the robot will climb spirally around the tree trunk.

The driving module utilizes the wheel mechanism for the ascending and descending motion. At the driving module (Fig. 2b), there is a wheel with diameter of 8 cm, driven by a DC motor to drive the robot upward and downward of the tree. Spring is also added inside the shaft, between the frame and the wheel to push the wheel onto the tree, such that the wheel will be in contact with the tree during climbing.

For the support module (Fig. 2c), ball castors with diameter of 2.5 cm are used to deliver the force from the spring and when the robot is climbing, the ball castors will rotate to ease the movement of the robot.

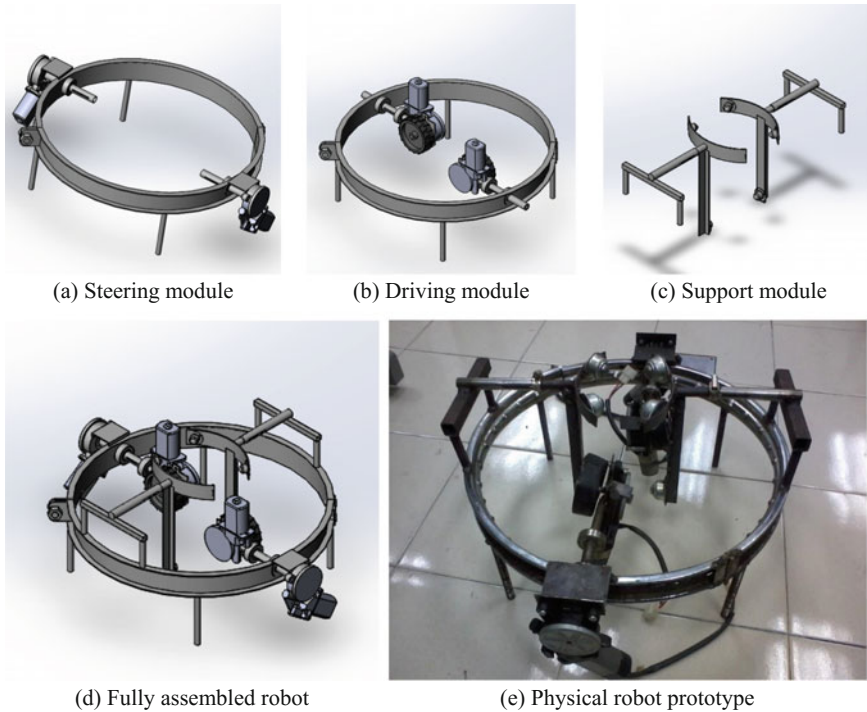


Fig. 2 Conceptual design and prototype of climbing robot consists of three modules; namely steering module, driving module and support module

2.2 Hardware Selection

The selection of appropriate hardware and software are important in the development process. A good selection will assist and make the robot runs smoothly. DC motor plays an important role in determining the successful of the climbing operation as wheel mechanism is powered by the DC motor.

The torque generated by the DC motor is not used solely on climbing operation, but also in overcoming the friction force and the resistance force caused by the spring with the tree, therefore, it must have a high torque.

After a few trial and errors with some DC motors that are available in the market, the power window DC motor is chosen as it can provide sufficient torque (rated at 30 kg cm (2.9 N m)) and power to overcome the resistance forces while having adequate speed rotation (rated at 0.465 rev/s).

Furthermore, the power window DC motor also has a stall self-locking characteristic (rated at 100 ± 15 kg cm (~ 10 N m)). This is to prevent the motor from rotating when the motor is idle or inactive.

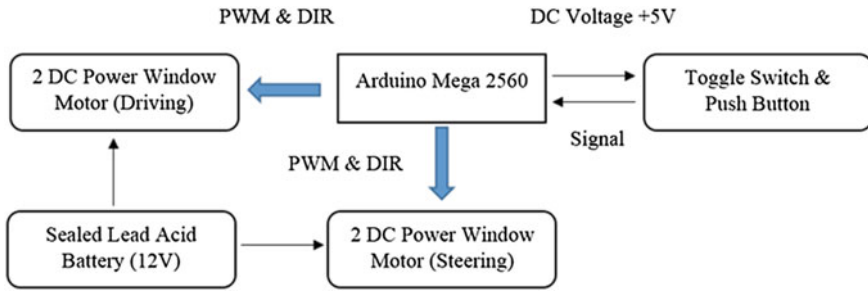


Fig. 3 Tree climbing robot system architecture

2.3 System Architecture

Figure 3 depicts the system architecture for the proposed robot. The main processing unit used in this climbing robot is Arduino Mega 2650 microcontroller. This microcontroller is chosen for its small size and low cost. Although the capacity of memory is only 256 KB, it is more than enough as the developed robot requires only simple control process and minimal programming code.

The power supply of the proposed system is 12 V DC voltage which is supplied by a Lead-Acid (12 V 7AH) rechargeable battery. The voltage of 12 V is supplied directly to the DC motors and the regulated 5 V voltage supply is used to power up the control board. The microcontroller is used to control 4 DC motors, while receiving signal from DIP switches. H-bridge circuit and relay are also connected between microcontroller and the motor to protect the microcontroller from the current surge from the motor lead wires.

2.4 Software Description

Programming code was developed by using Arduino IDE to test the functionality of the robot. The main functionalities include the synchronization of all the components used and the confirmation of the sequences of operation for the robot is in a correct manner.

Figure 4 depicts the flowchart of overall program. The program started by selecting the input from the Dip Switch. SW0 logic 0 is idle; logic 1 is in active mode. The robot will then read SW1 to determine the steering angle. Once the steering angle has been acquired from SW1, the DC motor will turn the steering angle accordingly.

Next, the robot will read SW2 to determine the direction it has to move, either upwards or downwards. The driving motor will rotate according to the direction from SW2 and only stops whenever the limit switch is activated.

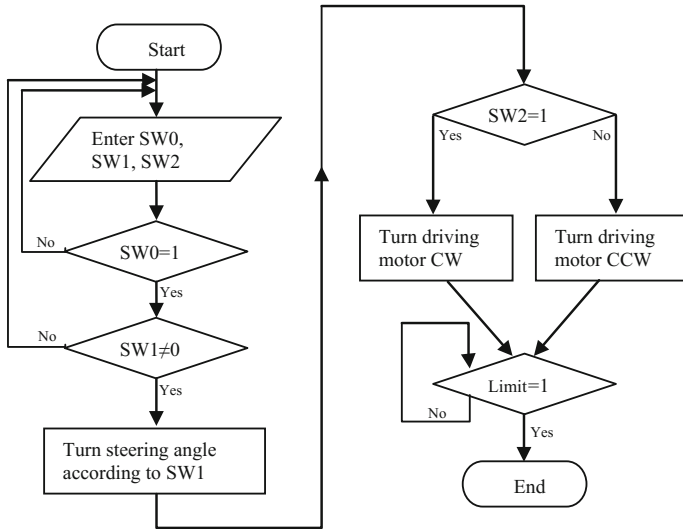


Fig. 4 Pole-like tree climbing robot overall flowchart

2.5 Experimental Method

Once the robot has been fully assembled and software is uploaded, it was then tested on a smooth pole and tree trunk as shows in Fig. 5. The steering angle was set to 0°, 30°, and 60°. The robot is then programmed to climb up 1 m on both poles, 6 times for each steering angle. Time taken to reach 1 m is recorded and the average is calculated.

As previously mentioned, the diameter of the driving wheel is 8 cm; and the circumference is calculated at 25.13 cm. Hence, the distance travelled for one complete revolution of the wheel will be 25.13 cm. The speed of the DC motor is



(a) Robot climbing on a smooth pole

(b) Robot climbing on a tree trunk

Fig. 5 Pole-like tree climbing robot experimental setup

rated at 0.465 revolutions per second. By calculating the angular velocity of the wheel, the distance travelled for 1 m can be determined. Hence, the time taken for 100 cm linear displacement of the robot is 8.55 s. Theoretical result and physical experimental result were then compared and conclusion is drawn in the next section.

3 Results and Discussion

The pole-like tree climbing robot is tested for the actual climbing; six trials on two different poles and three different steering angles have been conducted. Table 1 shows the overall results.

The results show that for vertical climbing, average time taken for the robot to climb up on a rough surface is quicker compared to the smooth pole. This is because the surface of the tree gives a more frictional force for the robot to climb. From the experiment and observation, the robot was slipping during climbing at the smooth pole and this situation takes longer time for the robot to complete the task of climbing up for 1 m. The error for the robot to climb the tree for 1 m is small at 1.4%.

For 30° climbing, average time taken for the robot to climb rough pole is longer than the smooth surface. This happened because the driving wheel was not well touching the surface of the tree due to the irregular size of the tree. The contact surface is reducing and makes the wheel slipping or rotating without touching the tree trunk.

Table 1 Actual climbing time (s) to climb vertically 1 m for various climbing angle on rough-pole (tree trunk) and smooth-pole (PVC pipe)

Test run	Time taken (s), to climb 1 m vertically					
	0° rough pole	0° smooth pole	30° rough pole	30° smooth pole	60° rough pole	60° smooth pole
1	9	10	14	12	–	23
2	9	9	13	12	–	22
3	8	9	14	13	–	22
4	8	9	13	12	–	22
5	9	10	14	13	–	23
6	9	9	14	12	–	22
Average	8.67	9.33	13.7	12.33	NA	22.33
Theoretical result	8.55		12.03		25.00	
Error	1.4%	9.1%	13.9%	2.5%	–	10.7%

For 60° climbing on the rough pole, the robot keeps sliding and not able to climb up the tree due to the same reason as above. For the smooth pole, the error is recorded at 10.7%.

4 Conclusion

Based on the results, current design of the robot is acceptable with the largest error recorded was at 13.9% for 30° spiral tree climbing. The main difficulty for the robot to smoothly climb the tree was that the irregular shape of the tree. This will open up a new challenge for designer to design a suitable gripper such that the robot will not slip during climbing.

For future recommendations, the robot should use wider driving wheel such that the wheel will always in contact with the surface of the irregular diameter of the tree. The driving wheel also can be wrapped with soft rubber to avoid the robot from slipping during climbing a smooth surface.

References

1. Ismail, M., Mohd Zin, J.: *Gaharu Komoditi Khazanah*. Kuala Lumpur, Malaysia. ISBN 9789670101019 (2011)
2. Ismail M.: *Cabaran dan Halatuju Perladangan Karas di Malaysia*. Bengkel Gaharu Sesi I-2014, Fakulti Perhutanan, Universiti Putra Malaysia, Malaysia, 10 Mar 2014
3. CITES: Amendments to Appendices I and II of CITES. In: *Proceedings of Thirteenth Meeting of the Conference of the Parties*. Bangkok, Thailand, 2 Oct 2004
4. Pojanagaroon, S., Kaewrak, C.: Mechanical methods to stimulate aloes wood formation in *Aquilaria crassna* Pierre ex H Lee (kraitsana) trees. *ISHS Acta Hort.* **676**, 161–166 (2006)
5. Barden, A., Anak, N.A., Mulliken, T., Song, M.: *Heart of the Matter: Agarwood Use and Trade and CITES Implementation for Aquilaria malaccensis*. TRAFFIC Southeast Asia. Petaling Jaya, Selangor, Malaysia, pp. 60–87 (2007)
6. IUCN 2009: 2008 IUCN red list of threatened species. <http://www.iucnredlist.org>. Accessed 30 Oct 2017
7. Blanchette, R., Heuveling, V.B.H.: *Cultivated Agarwood*. US 7638145B2 (2009)
8. Liu, Y.Y., Chen, H.Q., Yang, Y., Zhang, Z., Wei, J.H., Meng, H., Chen, W.P., Feng, J.D., Gan, B.C., Chen, X.Y., Gao, Z.H., Huang, J.Q., Chen, B., Chen, H.J.: Whole-tree agarwood-inducing technique: an efficient novel technique for producing high-quality agarwood in cultivated *Aquilaria sinensis* trees. *Molecules* **18**, 3086–3106 (2013)
9. Tavakoli, M., Marjovi A., Marques, L., De Almeida, A.T.: 3D CLIMBER: a climbing robot for inspection of 3D human made structures. In: *IROS 2008. IEEE/RSJ International Conference on Intelligent Robots and Systems* (2008)
10. Sadeghi, A., Moradi, H., Ahmadabadi, M.N.: Analysis, simulation, and implementation of a human-inspired pole climbing robot. In: *Robotica FirstView*, pp. 1–9 (2011)
11. Koo, Y.C., Abu Bakar, E., Wajdi, W.A.F.: Piston mechanism based rope climbing robot. *Procedia Eng.* **41**, 547–553 (2012)

12. Lau, S.C., Othman, W.A.F.W., Abu Bakar, E.: Development of slider-crank based pole climbing robot. In: 2013 IEEE International Conference on Control System, Computing and Engineering, 29 Nov–1 Dec, Malaysia, pp. 471–476 (2013)
13. Fauroux, J., Morillon, J.: Design of a climbing robot for cylindro-conic poles based on rolling self-locking. *Ind. Robot: Int. J.* **37**(3), 287–292 (2010)
14. Nor Faizal, M.I., Othman, W.A.F.W., Syed Hassan, S.S.N.A.: Development of pole-like tree climbing robot. In: 2015 IEEE International Conference on Control System, Computing and Engineering, 27 Nov–29 Nov, Malaysia, pp. 224–229 (2015)
15. Gui, P., Tang, L., Mukhopadhyay, S.: Anti-falling tree climbing mechanism optimization. In: 2nd Asia-Pacific Conference on Intelligent Robot Systems, pp. 284–288 (2017)

Data-Driven PID Tuning Based on Safe Experimentation Dynamics for Control of Double-Pendulum-Type Overhead Crane



Nor Sakinah Abdul Shukor and Mohd Ashraf Ahmad

Abstract This paper reports an investigation of Data-Driven PID tuning based on Safe Experimentation Dynamics (SED) for control of the Double-Pendulum-Type Overhead Crane (DPTOC) system. The SED algorithm is used to find the optimal PID parameters such that the hook and load swing angles are minimized. Performance comparison between the SED based method and Simultaneous Perturbation Stochastic Approximation (SPSA) based method for data-driven PID tuning is observed and discussed. The performance is evaluated by numerical example in terms of trolley trajectory tracking, hook and load swings reduction and control input energy. The findings demonstrated that the SED based data-driven PID is capable to reduce the hook and load swing angles while maintain the desired trolley trajectory position. In addition, faster settling time for control input energy is obtained.

Keywords Safe experimentation dynamics · Data-driven PID tuning
Double-pendulum-type overhead crane

1 Introduction

An overhead crane is a type of crane systems used in various type of industrial environment such as, automotive, manufacturing, chemicals and warehouse. Overhead crane commonly assists in transporting large, heavy and hazardous loads. However, the movement of the trolley with load along the bridge girder lead to undesirable load and hook swing angles (double-pendulum effect) that can affect the system dynamics and performance. Besides, an overhead crane control system

N. S. A. Shukor (✉) · M. A. Ahmad (✉)
Faculty of Electrical & Electronics Engineering (FKEE),
Universiti Malaysia Pahang (UMP), 26600 Pekan, Pahang, Malaysia
e-mail: sakinah_shukor@yahoo.com

M. A. Ahmad
e-mail: mashraf@ump.edu.my

is a class of the underactuated mechanical systems. This class of system is well-known for the very challenging problem of the controller design due to the small number of input space dimension compared to its controlled variable.

In recent decades, various of control designs have been developed by control researchers to minimize the loads swing angle and control input while reaching the desired trolley position of the crane system designed based on the model of the systems [1–5]. However, the controller designs normally impose a huge disparity between the real applications and control theory due to the unmodeled dynamics problem. To vanish this gap, control researchers are now diverting to data-driven control approach, since its controller design is only based on the input and output data measurement of actual process plants which any parts or the whole of plant models not explicitly include and make its control performance independence of the plant model accuracy. Particularly, a data-driven proportional-integral-derivative (PID) tuning is one of the promising strategies for data-driven control due to its simplicity, understandable and more reliable to the industrial usage [6].

On the other hand, it is necessary to design a PID tuning scheme that perform lesser computation time. For example, the simultaneous perturbation stochastic approximation (SPSA) approach has been widely implemented in the data-driven controller tuning due to its effectiveness in using only two objective functions to update the controller parameters [7–9]. Nevertheless, there is a probability that the design parameters in SPSA changed to huge values and abruptly trapped in an impractical region. To solve this weakness, SPSA algorithm has been modified [10], where the saturation function is used to avoid the unstable solution during the optimization [7]. However, there are additional parameters to be determined in advanced, which may require a lot of effort. Moreover, the saturation function will also limit the searching capability of the algorithm. To overcome these problems, a safe experimentation dynamics (SED) based method [11, 12] is seen as a promising tool for this view point. It is because the SED algorithm produces stable convergence due to its memory based structure. Moreover, it requires less pre-defined parameters compared to SPSA. So far, there are few works to discuss the application of the SED to data-driven PID tuning problems. Therefore, it would be beneficial to investigate the proposed method competency in tuning the PID controller for DPTOC system.

In this research, an SED algorithm is applied in a data-driven PID tuning for DPTOC control system. The effectiveness of the proposed controller is validated by numerical model of DPTOC system. The efficiency of the tuning scheme is evaluated based on the trolley trajectory tracking, hook and load swing angles, and control input energy. Besides, a comparative assessment between the SED based method and SPSA based method is presented.

The remainder of this paper is structured as follows; the data-driven PID controller problem formulation for DPTOC control tuning is expressed in Sect. 2. While in Sect. 3, the safe experimentation dynamics implementation is explained. Section 4 presents the simulation results and discussion. Finally, a conclusion of findings is presented in Sect. 5.

2 Problem Formulation

The PID control system for the DPTOC plant is illustrated as in Fig. 1. The DPTOC system is represented by plant G . The $r(t)$, $u(t)$, $x(t)$, $\theta_1(t)$ and $\theta_2(t)$ denotes the reference, control input, trolley position, hook swing angle and load swing angle for the system, respectively. Moreover, $K_i(s)$ ($i = 1, 2, 3$) is the PID controller given by

$$K_i(s) := P_i \left(1 + \frac{1}{I_i s} + \frac{D_i s}{1 + (D_i/N_i)s} \right), \tag{1}$$

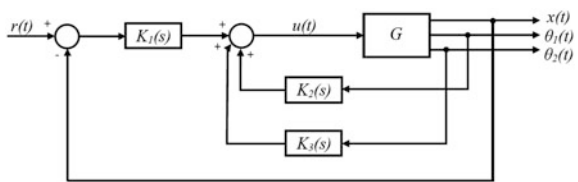
where $P_i \in \mathbb{R}$, $I_i \in \mathbb{R}$, $D_i \in \mathbb{R}$ and $N_i \in \mathbb{R}$ is the proportional gain, integral time, derivative time and filter coefficient, respectively. Next, let the performance index given as

$$J(\mathbf{P}, \mathbf{I}, \mathbf{D}, \mathbf{N}) = w_1 \int_{t_0}^{t_f} |r(t) - x(t)|^2 dt + w_2 \int_{t_0}^{t_f} |\theta_1(t)|^2 dt + w_3 \int_{t_0}^{t_f} |\theta_2(t)|^2 dt + w_4 \int_{t_0}^{t_f} |u(t)|^2 dt, \tag{2}$$

where the $[t_0, t_f]$ is corresponded to the time interval of the performance evaluation, $t_0 \in \{0\} \cup \mathbb{R}_+$ and $t_f \in \mathbb{R}_+$. The $\mathbf{P} := [P_1 P_2 P_3]$, $\mathbf{I} := [I_1 I_2 I_3]$, $\mathbf{D} := [D_1 D_2 D_3]$ and $\mathbf{N} := [N_1 N_2 N_3]$ are defined as matrices of \mathbf{P} , \mathbf{I} , \mathbf{D} and \mathbf{N} . The $w_1 \in \mathbb{R}$, $w_2 \in \mathbb{R}$, $w_3 \in \mathbb{R}$ and $w_4 \in \mathbb{R}$ are the designated weighting coefficients and the values are chosen with the same method of the standard Linear Quadratic Regulator (LQR) problem. Note that in Eq. (2), the first, second and third terms are corresponded to the tracking error while the fourth is the control input energy. Thus, the optimization problem for data-driven PID controller of the DPTOC system can be stated as follows:

Problem: Find the PID controller $K_i(s)$ ($i = 1, 2, 3$), such that the control objective $J(\mathbf{P}, \mathbf{I}, \mathbf{D}, \mathbf{N})$ with respect to \mathbf{P} , \mathbf{I} , \mathbf{D} and \mathbf{N} is minimized based on the measurement data $(u(t), x(t), \theta_1(t), \theta_2(t))$ for the PID control system in Fig. 1.

Fig. 1 PID control system for DPTOC



3 Data-Driven PID Controller Design Based on SED

3.1 Safe Experimentation Dynamics

In this section, a step by step procedure of SED algorithm is explained. A general problem for the optimization is considered as

$$\min_{\mathbf{p} \in \mathbb{R}^n} f(\mathbf{p}), \quad (3)$$

where the objective function is represented by $f: \mathbb{R}^n \rightarrow \mathbb{R}$ and $\mathbf{p} \in \mathbb{R}^n$ is the design parameter. The optimal solution of optimization problem in Eq. (3), $\mathbf{p}^* \in \mathbb{R}^n$ is obtained by repetitively updating the design parameter by using the SED algorithm. The updated design parameter of SED algorithm is based on the action selection given by

$$p_i(k+1) = \begin{cases} \bar{p}_i, & r_1 > E \\ h(\bar{p}_i - K_g r_2), & r_1 < E \end{cases} \quad (4)$$

where $k = 0, 1, \dots$, is the number of iteration, $p_i \in \mathbb{R}$ is the i th element of \mathbf{p} , \bar{p} is used to store the current best value of the design parameter and $\bar{p}_i \in \mathbb{R}$ is the i th element of $\bar{\mathbf{p}} \in \mathbb{R}^n$. The symbol K_g is a scalar that defined the interval size to decide on the random steps on p_i and $r_2 \in \mathbb{R}$ is a random value. The function h in Eq. (4) is defined as follows:

$$h(\cdot) = \begin{cases} p_{\max}, & \bar{p}_i - K_g r_2 > p_{\max} \\ \bar{p}_i - K_g r_2, & p_{\min} \leq \bar{p}_i - K_g r_2 \leq p_{\max} \\ p_{\min}, & \bar{p}_i - K_g r_2 < p_{\min} \end{cases} \quad (5)$$

where p_{\max} and p_{\min} are the pre-defined maximum and minimum values of the design parameter respectively. The step-by-step procedures of SED algorithm are as follows:

Step 1: Determine the value for p_{\min} , p_{\max} , K_g and E . Then, set $k = 0$ and the initial condition for design parameter is set as $\mathbf{p}(0)$ and the objective function be $f(\mathbf{p}(0))$. Therefore, as default $\bar{\mathbf{p}} = \mathbf{p}(0)$ and $\bar{f} = f(\mathbf{p}(0))$.

Note that E is a scalar that define the probability to use a new random setting for \mathbf{p} . Variable \bar{f} is used to store the current best value of the objective function.

Step 2: If the value of $f(\mathbf{p}(k)) < \bar{f}$, execute $\bar{\mathbf{p}} = \mathbf{p}(k)$ and $\bar{f} = f(\mathbf{p}(k))$. Otherwise, proceed to step 3.

Step 3: Generate a random number r_1 . If $r_1 < E$, generate second random number r_2 and obtain the value for $p_i(k + 1)$ by using the update law in Eq. (5). Otherwise, $p_i(k + 1) = \bar{p}_i$.

Note that, $r_1 \in \mathbb{R}$ is value of random number which is chosen by uniformly distribute between 0 and 1, while for r_2 is between p_{min} and p_{max} .

Step 4: Obtain the objective function $f(p_i(k + 1))$.

Step 5: If the pre-stated termination condition is fulfilled, the algorithm terminates with the solution $p^* := \arg \min_{p \in \{p(0), p(1), \dots, p(k+1)\}} f(p)$. Otherwise, set $k = k + 1$ and continue to step 2.

The pre-stated termination condition is based on the designated maximum number of iteration, k_{max} .

3.2 Data-Driven PID Control Design

For this section, the data-driven PID controller design is presented where the design parameter is expressed as

$$\boldsymbol{\psi} = [P_1 \ P_2 \ P_3 \ I_1 \ I_2 \ I_3 \ D_1 \ D_2 \ D_3 \ N_1 \ N_2 \ N_3]^T \in \mathbb{R}^{12}. \quad (6)$$

In this study, the logarithmic scale is employed to $\boldsymbol{\psi}$ for accelerating the exploration of the design parameter. We set $\psi_i = 10^{p_i}$ ($i = 1, 2, \dots, 12$) and the objective function is expressed as $J = [10^{p_1} \ 10^{p_2} \ \dots \ 10^{p_{12}}]$. Then, the data-driven PID procedures can be described as follows:

Step 1: Let $f(\boldsymbol{p}) := J(\boldsymbol{P}, \boldsymbol{I}, \boldsymbol{D}, \boldsymbol{N})$ and $p_i = \log \psi_i$. Then, determine the maximum iteration number, k_{max} .

Step 2: Perform the SED algorithm in Sect. 3.1 for the objective function in Eq. (2).

Step 3: After reaching k_{max} , attain the optimal output $\boldsymbol{p}^* = \bar{\boldsymbol{p}}(k_{max})$. Then, apply the $\boldsymbol{\psi}^* = [10^{p_1^*} \ 10^{p_2^*} \ \dots \ 10^{p_{12}^*}]$ to the $K_i(s)$ in the PID control system in Fig. 1.

4 Simulation Results

4.1 Model of DPTOC

The model of DPTOC system used in this study is adopted from [5, 13]. The hook mass is considered in this system, which caused the present of double-pendulum

effect in the system dynamics. The system's dynamics equations, which is produced by the Euler-Lagrange equations is expressed as described in [5, 13]:

$$M(\dot{y})\dot{y} + C(y, \dot{y})\dot{y} + G(y) = u. \quad (7)$$

Then, the state vector, y and the control vector, u are expressed as in Eqs. (8) and (9).

$$y = [x \quad \theta_1 \quad \theta_2]^T, \quad (8)$$

$$u = [F \quad 0 \quad 0]^T, \quad (9)$$

where F is a force that is applied to move the trolley of the crane. Note that the control input of the above model is simplified to a rectilinear force while one might consider an actuator model to generate the same force. However, since the complexity and underactuated nature of DPTOC are remained, it is enough to validate the proposed data-driven PID controller.

4.2 Numerical Example

The parameters used for the DPTOC system can be referred in [13]. The reference position for the trolley is applied as shown in Eq. (10).

$$r(t) = \begin{cases} 0, & 0 \leq t \leq 1 \\ 5, & 1 < t \leq 40 \end{cases}. \quad (10)$$

Next, the pre-defined parameters for SED algorithm are set as, $p_{max} = 3.0$, $p_{min} = -3.0$ and $k_{max} = 300$. Then, for $w_1 = 5$, $w_2 = 15$, $w_3 = 15$, $w_4 = 1$, $t_0 = 0$ and $t_f = 40$. The probability, $E = 0.59$ and the $K_g = 0.08$ are used.

For fair comparative assessment with SED, we set the maximum iteration for SPSA as $k_{max} = 150$. Since SED algorithm only requires one objective function evaluation per iteration, it requires 300 iterations to obtain equivalent number of objective function evaluations compared with SPSA approach which requires two objective function evaluations per iteration. Next, the initial condition for $\mathbf{p}(0)$ and the optimal design parameters, \mathbf{p}^* for both SED and SPSA are depicted in Table 1. While, the control performances, in terms of the objective function, norm of error, and norm of input are depicted in Table 2. The statistical results are obtained after 30 trials for each of algorithms. Based on the results in Table 2, it is proved that the SED based method produces better mean values of objective function and norm of error as compared to the SPSA based method.

Table 1 Design parameters for SPSA and SED for DPTOC system

ψ	PID Gain	$p(0)$	ψ corresponded to $p(0) \times 10^3$	p^*		ψ corresponded to $p(0) \times 10^3$	
				SPSA	SED	SPSA	SED
ψ_1	P_1	-1.0000	0.0001	-1.3842	-1.3184	0.0000	0.0000
ψ_2	P_2	2.0000	0.1000	2.0593	2.0657	0.1146	0.1163
ψ_3	P_3	2.0000	0.1000	1.9537	1.8898	0.0899	0.0776
ψ_4	I_1	2.0000	0.1000	1.7392	1.6736	0.0549	0.0472
ψ_5	I_2	0.0000	0.0010	0.0981	0.0985	0.0012	0.0013
ψ_6	I_3	0.0000	0.0010	0.0591	0.0519	0.0011	0.0011
ψ_7	D_1	0.0000	0.0010	0.2142	0.2335	0.0016	0.0017
ψ_8	D_2	2.0000	0.1000	2.0302	2.0678	0.1072	0.1169
ψ_9	D_3	0.0000	0.0010	-0.1966	-0.1708	0.0006	0.0007
ψ_{10}	N_1	0.0000	0.0010	0.1959	-0.0198	0.0016	0.0010
ψ_{11}	N_2	0.0000	0.0010	0.0573	0.0739	0.0011	0.0012
ψ_{12}	N_3	2.0000	0.1000	2.2668	1.9923	0.1848	0.0982

Table 2 Statistical result

Algorithm		SPSA	SED
$J(\mathbf{P}, \mathbf{I}, \mathbf{D}, \mathbf{N})$	Mean	406.9245	406.6954
	Best	406.4590	406.5021
	Worst	407.8143	407.0465
	Std	0.3165	0.1328
Total Norm of Error ($\hat{e} + \theta_1 + \theta_2$)	Mean	60.9020	60.7977
	Best	60.7103	60.3986
	Worst	61.1877	61.2874
	Std	0.1229	0.2269
Total Norm of Input (\ddot{u})	Mean	101.89990	102.2802
	Best	101.0129	99.8581
	Worst	102.7171	104.4129
	Std	0.5106	1.1186

Table 3 shows the time response specifications of the trolley position. Based on the results, the settling time for the trolley to achieve the desired position of the SED based approach is lesser than the SPSA based approach. In terms of the hook and load swing angles response, SED based approach is efficiently minimized the hook and load swing angles magnitude compared to the SPSA approach with the settling time for θ_1 and θ_2 by the SED based approach are **39.7597** s and **39.7875** s, respectively and by the SPSA based approach are 39.9612 s and 39.9750 s, respectively. Besides, the settling time for control input is faster by using the SED based approach than the SPSA based approach.

Table 3 Time response for trolley position

Algorithm	Trolley position			Control input
	Rise time (s)	Settling time (s)	Overshoot (%)	Settling time (s)
SPSA	5.4555	15.5364	7.0848	15.5364
SED	5.4605	14.9332	5.2119	14.9330

5 Conclusion

An investigation on data-driven PID tuning based on SED algorithm for DPTOC system has been presented in this paper. The performance of the SED based approach is compared with the SPSA based approach in terms of trajectory tracking of the trolley, hook and load swings reduction and control input energy. In the simulation results, it is demonstrated that the data-driven PID tuning based on SED is capable to reduce the hook and load swing angles magnitude compared to SPSA based method while the trolley maintains the desired position. Moreover, the settling time of SED based approach for the control input is faster than the SPSA based approach. Therefore, it can be concluded that the data-driven PID based on SED algorithm is capable to reduce the hook and swing angles while maintains the desired trolley position of DPTOC system.

Acknowledgements The work was partly supported by Research Grant PGRS1703104 from the Research and Innovation Department, Universiti Malaysia Pahang.

References

1. Liu, D.T., Guo, W.P., Yi, J.Q., Zhao, D.B.: Double-pendulum-type overhead crane dynamics and its adaptive sliding mode fuzzy control. In: 3rd International Conference on Machine Learning and Cybernetics, pp. 26–29. IEEE, Shanghai (2004)
2. Adeli, M., Zarabadipour, H., Zarabadi, S.H., Shoorehdeli, M.A.: Anti-swing control for a double-pendulum-type overhead crane via parallel distributed fuzzy LQR controller combined with genetic fuzzy rule set selection. In: IEEE International Conference on Control System, Computing and Engineering 2011, ICCSCE, pp. 306–311. IEEE, Penang (2011)
3. Raja, I.R.M.T., That, N.D., Ha, Q.P.: Adaptive fuzzy sliding mode control for uncertain nonlinear underactuated mechanical systems. In: International Conference on Control, Automation and Information Sciences 2013, ICCAIS, pp. 212–217. IEEE (2013)
4. He, C., Yongchun, F., Ning, S., Yuzhe, Q.: Pseudospectral method based time optimal trajectory planning for double pendulum cranes. In: 34th Chinese Control Conference 2015, CCC, pp. 4302–4307. IEEE, Hangzhou (2015)
5. Liu, D.T., Guo, W.P., Yi, J.Q.: Dynamics and stable control for a class of underactuated mechanical systems. *Acta Automatica Sinica* **3**(32), 422–427 (2006)
6. Jaafar, H.I., Mohamed, Z., Abidin, A.F.Z., Ghani, Z.A.: PSO-tuned PID controller for a nonlinear gantry crane system. In: IEEE International Conference on Control System, Computing and Engineering 2012, ICCSCE, pp. 515–519. IEEE, Penang (2012)

7. Ahmad, M.A., Rohani, M.A., Raja, I.R.M.T., Jusof, M.F.M., Suid, M.H., Nasir, A.N.K.: A model-free PID tuning to slosh control using simultaneous perturbation stochastic approximation. In: 5th IEEE International Conference on Control System, Computing and Engineering 2015, ICCSCE, pp. 331–335. IEEE, Penang (2015)
8. Ahmad, M.A., Azuma, S.I., Sugie, T.: Performance analysis of model-free PID tuning of MIMO systems based on simultaneous perturbation stochastic approximation. *Expert Syst. Appl.* **14**(41), 6361–6370 (2014)
9. Ahmad, M.A., Azuma, S.I., Sugie, T.: A model-free approach for maximizing power production of wind farm using multi-resolution simultaneous perturbation stochastic approximation. *Energies* **9**(7), 5624–5646 (2014)
10. Baba, I., Azuma, S., Sugie, T.: Controller design for optimizing fuel consumption of hybrid electric vehicles—a model-free approach based on simultaneous perturbation stochastic approximation. *Pap. Meas. Autom. Control Soc.* **9**(49), 887–894 (2013)
11. Marden, J.R., Ruben, S.D., Pao, L.Y.: A model-free approach to wind farm control using game theoretic methods. *IEEE Trans. Control Syst. Technol.* **4**(21), 1207–1214 (2013)
12. Gebraad, P.M.O., van Dam, F.C., van Wingerden, J.W.: A model-free distributed approach for wind plant control. In: American Control Conference 2013, ACC, pp. 628–633. ACC, Washington, DC (2013)
13. Ahmad, M.A., Raja Ismail, R.M.T., Ramli, M.S., Nasir, A.N.K., Abd Ghani, N.M., Noordin, N.H.: Techniques for sway control of a double-pendulum-type overhead crane. *Int. J. Simul. Syst. Sci. Technol.* **2**(11), 1–8 (2010)

Integral Super Twisting Sliding Mode Control (ISTSMC) Application in 1DOF Internal Mass Autonomous Underwater Glider (AUG)



Maziyah Mat-Noh, M. R. Arshad, Rosmiwati Mohd-Mokhtar
and Zainah Md Zain

Abstract This paper presents the design and implementation of the integral super twisting sliding mode control for the tracking control of a linearized model of longitudinal plane autonomous underwater glider. The performance of the proposed controller is evaluated in terms of chattering reduction in control input for the nominal system as well as the system in the presence of external disturbance. The controller is designed for the gliding path from 45° to 30° downward and upward. The performance of the proposed controller is compared with the quasi sliding mode control (boundary layer), integral sliding control, and super twisting sliding mode control. The simulation results have shown that the proposed controller is able to eliminate the undesired chattering in control inputs.

Keywords Autonomous underwater glider (AUG) • Super twisting sliding mode control (STSMC) • Integral sliding mode control (ISMC)

1 Introduction

Underwater offers a wide range of research opportunities. Autonomous underwater vehicles (AUVs) are amongst the popular of underwater vehicles used in underwater for data gathering. While autonomous underwater gliders (AUGs) are considered as a new class of AUVs where the idea was initiated by Henry Stommel in 1989 [1]. However the real operational AUGs are realized more than a decade later

M. Mat-Noh (✉) · Z. Md Zain

Instrumentation and Control Engineering (ICE) Cluster, Faculty of Electrical and Electronics Engineering, Universiti Malaysia Pahang, 26600 Pekan, Pahang, Malaysia
e-mail: maziyah@ump.edu.my

M. R. Arshad · R. Mohd-Mokhtar

Underwater, Control Robotics Research Group (UCRG), School of Electrical and Electronic Engineering, Engineering Campus, Universiti Sains Malaysia, 14300 Nibong Tebal, Pulau Pinang, Malaysia

© Springer Nature Singapore Pte Ltd. 2018

M. H. A. Hassan (ed.), *Intelligent Manufacturing & Mechatronics*,
Lecture Notes in Mechanical Engineering,
https://doi.org/10.1007/978-981-10-8788-2_28

when Slocum AUG, Seaglider AUG and Spray AUG were successfully designed, developed, and tested in 2001. The ideal AUG slides the internal movable mass translational and/or rotational and the ballast is pumped back and forth for controlling its position and attitude.

The maneuverability of AUG in underwater is very much depending on the underwater environment. Many control techniques are reported being employed to control the motion of AUG in underwater. The classical control proportional-integral-derivative (PID) controller have been proposed in [2, 3] is based on the single-input-single-output system. The optimal control known as linear quadratic regulator (LQR) was proposed in [4–6]. The LQR offers very simple design that involves two tuning parameters Q and R to obtain the optimal performance in which minimizing the cost function (J) and become the solution for the Ricatti's equation. In [4–6], the LQR was designed for the system without perturbation. The nonlinear control approach such as model predictive control (MPC) is proposed in [7, 8] and sliding mode control is proposed in [9]. The MPC is also known as Receding Horizon Control and Moving Horizon Optimal Control. In [7] the MPC is designed for controlling the attitude of the Slocum glider where the control architecture is divided into inner and outer loops. The inner loop is responsible for internal glider configuration and outer loop to control the attitude of the glider. Ian Abraham and Jingang Yi in [8] developed the MPC to control the horizontal plane of the glider. The MPC is integrated with the time suspension technique to enable online tuning capability. The sliding mode control (SMC) is employed by Hai Yang and Jie Ma as in [9] to control the pitch angle and the net buoyancy of the glider. The SMC is formulated for the nonlinear longitudinal plane of the glider. The intelligent method is proposed in [10, 11]. In [10] the homeostatic method is formulated to control the motion of the USM hybrid-driven underwater glider. The algorithm is based on emergent approach which combining the property of artificial neural network (ANN), artificial endocrine system (AES) and artificial immune system (AIS). The neural network (NN) is employed in [11] also to control the motion of the USM hybrid-driven underwater glider. The predictive control is designed based on neural network multilayer (three layer) perceptron with six input nodes, six hidden layer nodes and fourteen output nodes.

In this paper the integral super twisting sliding mode control (ISTSMC) is proposed for the linearized model of the AUG longitudinal plane. The model is linearized using Taylor's series expansion method as proposed by J. Graver in 2005 [12]. The proposed controller is considered as a new approach in regards to linearized model of the AUG application and will be the contribution for this paper. The paper is organized as follows. The glider system is explained in Sect. 2. In Sect. 3, the controller design procedures are presented. The result and discussion are explained in Sect. 4 and finally the paper is summarized in Sect. 5.

2 Glider System

The glider model is discussed in this section. The model is restricted to longitudinal plane dynamics where the internal only move along the x -axis. The detail derivation is shown in [13].

The linearized model of a longitudinal plane is computed using Taylor's series expansion method. The linearization is performed for the gliding equilibrium as computed by J. Graver in [12]. Consider the following general nonlinear equations.

$$\begin{aligned} \dot{x}_1 &= f_1(x_1, \dots, x_n, u_1, \dots, u_m) \\ &\vdots \\ \dot{x}_n &= f_n(x_1, \dots, x_n, u_1, \dots, u_m) \end{aligned} \quad (1)$$

The approximation of nonlinear equations in (1) is performed by computing the gradient of the nonlinear equations with respect to the state vectors and input vectors respectively. The general linear system is defined in Eq. (2).

$$\delta\dot{x} = A\delta x + B\delta u + Bh(x, t) \quad (2)$$

where

$\delta x = x - x_d$, $\delta u = u - u_d$ and $h(x, t)$ is the disturbance. u_d is set to zero then Eq. (2) become

$$\delta\dot{x} = A\delta x + Bu + Bh(x, t) \quad (3)$$

The system matrix A and input matrix B are obtained using Eq. (4).

$$\begin{aligned} A &= \left. \frac{\partial f}{\partial x} \right|_{x_e, u_e} \in \mathfrak{R}^{n \times n} \\ B &= \left. \frac{\partial f}{\partial u} \right|_{x_e, u_e} \in \mathfrak{R}^{m \times n} \end{aligned} \quad (4)$$

The matrices A and B for AUG longitudinal plane for downward and upward glides are given in Eq. (5) and (6) respectively.

$$\begin{aligned}
 A_d &= \begin{bmatrix} 0 & 1.0000 & 0 & 0 & 0 & 0 & 0 \\ -7.1379 & 0.0079 & -6.5792 & 0 & -174.4810 & 0 & -0.1708 \\ -0.1709 & -0.0531 & -0.6366 & 1.1003 & 0.8959 & 0 & 0.2537 \\ 0.0439 & 0.1638 & -0.3524 & -3.4850 & -0.0335 & 0 & 0.3251 \\ 0 & 0 & 0 & 0 & 0 & 1.0000 & 0 \\ 0 & 0 & 0 & 0 & 0 & 0 & 0 \\ 0 & 0 & 0 & 0 & 0 & 0 & 0 \end{bmatrix} \\
 B_d &= \begin{bmatrix} 0 & 0 \\ -0.6782 & 0 \\ -0.1249 & 0 \\ -0.0002 & 0 \\ 0 & 0 \\ 1.0000 & 0 \\ 0 & 1.0000 \end{bmatrix}
 \end{aligned} \tag{5}$$

$$\begin{aligned}
 A_u &= \begin{bmatrix} 0 & 1.0000 & 0 & 0 & 0 & 0 & 0 \\ -9.9372 & 0.0797 & 7.1377 & 0 & -162.7320 & 0 & -0.0617 \\ 0.2732 & 0.0538 & -0.7413 & -0.4095 & 0.8761 & 0 & -0.2556 \\ 0.0810 & 0.1602 & 0.3386 & -3.3597 & 0.9299 & 0 & 0.3376 \\ 0 & 0 & 0 & 0 & 0 & 1.0000 & 0 \\ 0 & 0 & 0 & 0 & 0 & 0 & 0 \\ 0 & 0 & 0 & 0 & 0 & 0 & 0 \end{bmatrix} \\
 B_u &= \begin{bmatrix} 0 & 0 \\ -0.6548 & 0 \\ -0.1311 & 0 \\ 0.0020 & 0 \\ 0 & 0 \\ 1.0000 & 0 \\ 0 & 1.0000 \end{bmatrix}
 \end{aligned} \tag{6}$$

The AUG has seven states ($\theta, \omega_2, v_1, v_3, r_{p1}, \dot{r}_{p1}, m_b$) and two inputs (u_1, u_2) as defined in Table 1. The eigenvalues of the open loop system for downward and upward glides are depicted in Table 2. The controllability and observability are full rank. The open loop system is stable since all the eigenvalues are laid on left-hand plane (LHP) except three zero eigenvalues indicate marginally stable.

Table 1 Parameter definition

Parameter	Definition
θ	Pitching angle
ω_2	Pitching rate
v_1	Surge velocity
v_3	Heave velocity
r_{p1}	Internal mass position in x-axis
\dot{r}_{p1}	Internal mass velocity
m_b	Ballast mass

Table 2 The eigenvalues, controllability and observability of AUG open loop system

Glide	Eigenvalue	Controllability	Observability
Downward	$-0.0315 + 2.6339i$ $-0.0315 - 2.6339i$ -3.4160 -0.6347 $0, 0, 0$	7/7	7/7
Upward	$-0.0324 + 3.0843i$ $-0.0324 - 3.0843i$ -3.3304 -0.6260 $0, 0, 0$	7/7	7/7

3 Controller Design

The controllers are designed for the gliding path from 45° to 30° downward and upward. A glide path is specified by a desired gliding angle, ζ_d and desired speed V_d .

$$\zeta_d = \theta - \alpha \tag{7}$$

where θ = pitching angle, α = angle of attack.

$$V_d = \sqrt{v_1^2 + v_3^2} \tag{8}$$

The conventional SMC is suffered from chattering phenomena due to high frequency oscillations induced by signum function where in practical, actuators unable to cope with high frequency oscillations. Therefore in this section all the controllers are designed to reduce the chattering and improve the system performance.

Consider the linear time invariant in Eq. (9)

$$\delta\dot{x} = A\delta x + Bu + Bh(x, t) \tag{9}$$

where $x \in R^n$, and $u \in R^m$, are the state vectors, and input vectors which satisfies the following assumptions

1. The pair (A, B) is controllable.
2. $h(x, t)$ is assumed known and in the range of input distribution B . $h(x, t)$ is a bounded matched perturbation that is a bounded with a known upper bound as defined in Eq. (10)

$$|h(x, t)| \leq d \tag{10}$$

Section 3.1 explains the controller design for the boundary layer sliding mode control which is also called quasi sliding mode control (QSMC) control design. Section 3.2 and Sect. 3.3 explain the design methodology for integral sliding mode control (ISM) and super twisting sliding mode control (STSMC) respectively. Finally the proposed controller, integral super twisting (ISTSMC) is explained in Sect. 3.4.

The block diagram of the proposed controller is shown in Fig. 1. Two basic steps are involved in designing SMC based controllers. Firstly, the stable sliding manifold is designed so that the dynamic of the system is confined to the sliding manifold in which output responses converged to the desired values. Secondly control law is designed such that the system trajectory moves towards the sliding manifold, reach the sliding manifold and remain there.

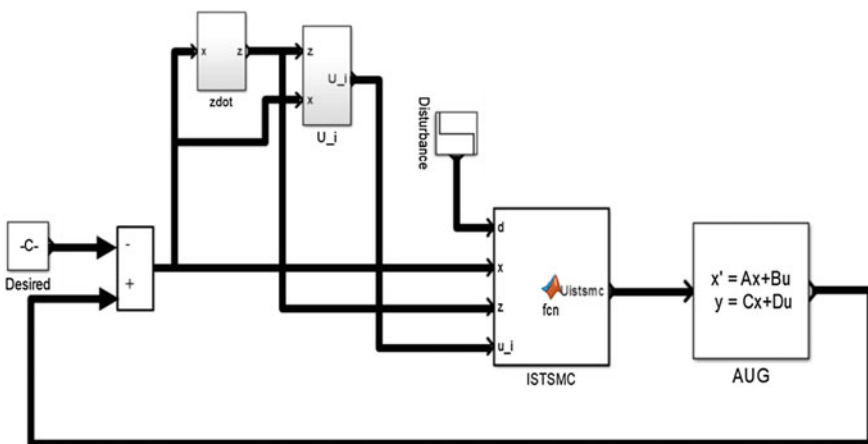


Fig. 1 The block diagram of the integral super twisting sliding mode control (ISTSMC)

3.1 Quasi Sliding Mode Control (QSMC)

The quasi sliding mode control (QSMC) is another name for boundary layer approach. In this method a boundary layer is used to approximate the discontinuous function, signum. This approach is one of the approaches that can be used to reduce chattering phenomena induced by the discontinuous function.

The QSMC sliding manifold and control law are defined in Eqs. (11) and (12) respectively

$$\sigma_{QSMC} = S\delta x(t) \quad (11)$$

$$u_{QSMC} = u_{eq} + u_{dis} \quad (12)$$

where $S \in R^{m \times n}$, u_{eq} and u_{dis} are the sliding gain, equivalent control and discontinuous control respectively. The S is chosen such that $SB \in R^{m \times n}$ is non-singular. From the underwater glider state-space system $m = 2$ and $n = 8$, therefore the sliding gain has 2×8 matrix structure.

The Lyapunov function and its derivative are defined in Eqs. (13) and (14).

$$V(\sigma_{QSMC}) = \frac{1}{2} \sigma_{QSMC}^2 \quad (13)$$

$$\dot{V}(\sigma_{QSMC}) = \sigma_{QSMC} \dot{\sigma}_{QSMC} = \sigma_{QSMC} (S(A\delta(x) + Bu + Bh(x, t))) \quad (14)$$

The equivalent control is defined as $\dot{\sigma}_{QSMC} = 0$ as written in Eq. (15)

$$u_{eq} = -(SB)^{-1}(SA\delta(x) + SBh(x, t)) \quad (15)$$

The reachability condition is chosen as in Eq. (16)

$$u_{dis} = -M \frac{\sigma}{|\sigma| + \varepsilon} \quad (16)$$

where M and ε are the design parameter and boundary layer thickness and both are positive constants.

3.2 Integral Sliding Mode Control (ISMC)

The integral sliding mode control (ISMC) is known as a sliding mode control without reaching phase. The method was proposed by V. Utkin and J. Shi in 1996 [14]. The sliding and control law of the ISMC are defined in Eqs. (17) and (18).

$$\sigma_{ISMC}(t) = S\delta x(t) + z(t) \quad (17)$$

$$u_{ISMC} = u_0 + u_1 \quad (18)$$

where u_0 is the control law for system without perturbations and u_1 is the nonlinear control law for rejecting the perturbations. $S \in R^{m \times n}$ is the sliding gain and $z(t)$ is the integral term.

u_0 is designed using linear feedback control, linear quadratic regulator (LQR) and is defined as in Eq. (19).

$$u_0 = -F\delta x(t) \quad (19)$$

The Lyapunov function and its derivative are defined in Eqs. (20) and (21).

$$V(\sigma_{ISMC}) = \frac{1}{2} \sigma_{ISMC}^2 \quad (20)$$

$$\dot{V}(\sigma_{ISMC}) = \sigma_{ISMC} \dot{\sigma}_{ISMC} = \sigma_{ISMC} (S(A\delta(x) + B(u_0 + u_1) + Bh(x, t)) + \dot{z}(t)) \quad (21)$$

and $\dot{z}(t)$ is chosen as in Eq. (22)

$$\dot{z}(t) = -S(A\delta x(t) + Bu_0), z(0) = -S\delta x(0) \quad (22)$$

Substitute Eq. (22) into Eq. (21), then u_1 which consists of equivalent control and discontinuous control is defined as in Eq. (23).

$$u_1 = -(SB)^{-1}(SBh(x, t)) - M\text{sign}(\sigma_{ISMC}) \quad (23)$$

Finally, the overall control law of ISMC is written in Eq. (24)

$$u_{ISMC} = -F\delta x(t) - (SB)^{-1}(SBh(x, t)) - M\text{sign}(\sigma_{ISMC}) \quad (24)$$

3.3 Super Twisting Sliding Mode Control (STSMC)

The super twisting sliding control (STSMC) was proposed by A. Levant in 1993 [15]. The sliding manifold and control law of STSMC are defined in Eqs. (25) and (26).

$$\sigma_{STW} = S\delta x(t) \quad (25)$$

$$u_{STW} = u_1 + u_2 \quad (26)$$

where $S \in R^{m \times n}$, u_1 and u_2 are the sliding gain, continuous control and discontinuous time derivative control, respectively.

The Lyapunov function is defined in Eqs. (27).

$$V(\sigma_{STW}) = \frac{1}{2} \sigma_{STW}^2 \quad (27)$$

The STSMC control law is written in Eq. (28)

$$u_{STW} = -h(x, t) - \left(\beta_1 |\sigma_{STW}|^{\frac{1}{2}} \text{sign}(\sigma_{STW}) + \beta_2 \int_0^t \text{sign}(\sigma_{STW}) d\tau \right) \quad (28)$$

3.4 Integral Super Twisting Sliding Mode Control (ISTSMC)

The integral super twisting sliding mode control (ISTSMC) is an integration of the integral SMC and super twisting SMC. The sliding manifold and control law are defined based on ISMC as written in Eqs. (29) and (30)

$$\sigma_{ISTW}(t) = S\delta x(t) + z(t) \quad (29)$$

$$u_{ISTW} = u_0 + u_1 \quad (30)$$

where u_0 is the control law for system without perturbations and u_1 is the nonlinear control law for rejecting the perturbations. $S \in R^{m \times n}$ is the sliding gain and $z(t)$ is the integral term.

u_0 was designed using linear feedback control, linear quadratic regulator (LQR) and is defined as in Eq. (31).

$$u_0 = -F\delta x(t) \quad (31)$$

The Lyapunov function and its derivative are defined in Eqs. (32) and (33).

$$V(\sigma_{ISTW}) = \frac{1}{2} \sigma_{ISTW}^2 \quad (32)$$

$$\begin{aligned} \dot{V}(\sigma_{ISTW}) &= \sigma_{ISTW} \dot{\sigma}_{ISTW} = \sigma_{ISTW} (S(A\delta(x) + Bu_{ISTW} + Bh(x, t)) + \dot{z}(t)) \\ &= \sigma_{ISTW} (S(A\delta(x) + B(u_0 + u_1) + Bh(x, t)) + \dot{z}(t)) \end{aligned} \quad (33)$$

and $\dot{z}(t)$ is chosen as in Eq. (34)

$$\dot{z}(t) = -S(A\delta x(t) + Bu_0), z(0) = -S\delta x(0) \quad (34)$$

Substitute Eq. (34) into Eq. (33), then time derivative of sliding manifold is reduced to Eq. (35)

$$\dot{\sigma}_{ISTW}(t) = S(Bu_1 + Bh(x, t)) \quad (35)$$

u_1 was defined based on super twisting algorithm is given in Eq. (36)

$$u_1 = -(SB)^{-1}(Bh(x, t)) + u_{dis} \quad (36)$$

where

$$u_{dis} = u_{dis1} + u_{dis2} = -\beta_1 |\sigma_{ISTW}|^{\frac{1}{2}} \text{sign}(\sigma_{ISTW}) - \beta_2 \int_0^t \text{sign}(\sigma_{ISTW}) d\tau \quad (37)$$

and

$$u_{dis1} = \begin{cases} -\beta_1 |\sigma_0|^{1/2} \text{sign}(\sigma_{ISTW}) & |\sigma_{ISTW}| > \sigma_0 \\ -\beta_1 |\sigma_{ISTW}|^{1/2} \text{sign}(\sigma_{ISTW}) & |\sigma_{ISTW}| \leq \sigma_0 \end{cases} \quad (38)$$

$$\dot{u}_{dis2} = \begin{cases} -u_{dis2} & |u_{dis2}| > 1 \\ -\beta_2 \text{sign}(\sigma_{ISTW}) & |u_{dis2}| \leq 1 \end{cases} \quad (39)$$

Finally the control law for ISTSMC is written in Eq. (40).

$$u_{ISTW} = -F\delta x(t) - (SB)^{-1}(SBh(x, t)) - \left(\beta_1 |\sigma|^{\frac{1}{2}} \text{sign}(\sigma) + \beta_2 \int_0^t \text{sign}(\sigma) d\tau \right) \quad (40)$$

The closed loop error dynamic is computed by substituting back Eq. (36) into Eq. (35) gives the time derivative of Lyapunov function

$$\dot{V}(\sigma_{ISTW}) = \sigma_{ISTW} \dot{\sigma}_{ISTW} = \sigma_{ISTW} \left(-\beta_1 |\sigma|^{\frac{1}{2}} \text{sign}(\sigma) - \beta_2 \int_0^t \text{sign}(\sigma) d\tau \right) \quad (41)$$

To ensure the sufficient conditions for finite time convergence, the conditions in Eq. (42a, 42b) must be satisfied [16].

$$\beta_1^2 \geq \frac{4C_0K_M(\beta_2 + C_0)}{K_m^2K_m(\beta_2 - C_0)} \tag{42a}$$

$$\beta_2 > \frac{C_0}{K_m} \tag{42b}$$

4 Result and Discussion

This section presents the simulation results and discussions. The simulation is done using the parameters adopted from Graver (2005) [12]. The controllers are simulated for the gliding from 45° to 30° downward and upward using MATLAB/SIMULINK software. The simulations are performed for the nominal system and also for the system with induced external disturbance. The desired values of the observed parameters are shown in Table 3.

The sliding gain, *S* is chosen to be the same for all controllers. The same sliding gain and linear feedback gain are used for the nominal system and system with external disturbance. The linear feedback gain, *F* and sliding gain, *S* for the downward and upward glides are written in Eqs. (43–46). No tunings are performed for the sliding gain and feedback gain. The tunings are performed for other controllers’ parameters only. All the controllers’ parameters for nominal system and system with external disturbance are depicted in Table 4 and Table 5, respectively.

$$S_d = \begin{bmatrix} -197.223 & -107.5742 & 24.8201 & 0.5956 & 647.5100 & 8.1147 & 0.7552 \\ -0.6370 & 0.0269 & 56.3215 & 15.0971 & 33.0080 & 7.8103 & 6.5436 \end{bmatrix} \tag{43}$$

$$S_u = \begin{bmatrix} -75.0704 & -73.9775 & -18.0774 & 0.1523 & 409.6529 & 5.9687 & 0.2550 \\ -0.3635 & -0.0023 & -13.1394 & 1.9503 & 7.1941 & -1.4724 & 4.2390 \end{bmatrix} \tag{44}$$

Table 3 Desired parameters’ values

Parameter	Desired value	
	Downward	Upward
Glide (ξ) (°)	-30	30
θ (°)	-23.7	23.7
m_b (kg)	1.36	0.64
m_{em} (kg)	0.36	-0.36

Table 4 Controllers’ parameters (without disturbance)

Controller	Parameter	
	Downward	Upward
QSMC	$M_1 = 3, M_2 = 3, \epsilon_1 = 0.5, \epsilon_2 = 0.5$	$M_1 = 3, M_2 = 3, \epsilon_1 = 0.5, \epsilon_2 = 0.5$
ISMC	$M_1 = 0.5, M_2 = 0.3$	$M_1 = 0.3, M_2 = 0.1$
STSMC	$\beta_{11} = 2.3, \beta_{12} = 0.0001$ $\beta_{21} = 0.3, \beta_{22} = 0.0001$	$\beta_{11} = 1.8, \beta_{12} = 0.0005$ $\beta_{21} = 0.5, \beta_{22} = 0.0001$
ISTSMC	$\beta_{11} = 0.2, \beta_{12} = 0.0001$ $\beta_{21} = 0.5, \beta_{22} = 0.0001$	$\beta_{11} = 0.1, \beta_{12} = 1, \beta_{21} = 0.3, \beta_{22} = 1$

Table 5 Controllers’ parameters (with disturbance)

Controller	Parameter	
	Downward	Upward
QSMC	$M_1 = 5, M_2 = 5, \epsilon_1 = 0.5, \epsilon_2 = 0.5$	$M_1 = 3, M_2 = 3, \epsilon_1 = 0.05, \epsilon_2 = 0.05$
ISMC	$M_1 = 1.5, M_2 = 1.2$	$M_1 = 1.5, M_2 = 1$
STSMC	$\beta_{11} = 3, \beta_{12} = 0.0001$ $\beta_{21} = 3, \beta_{22} = 0.0001$	$\beta_{11} = 3, \beta_{12} = 0.3$ $\beta_{21} = 3, \beta_{22} = 0.3$
ISTSMC	$\beta_{11} = 0.2, \beta_{12} = 0.0001$ $\beta_{21} = 0.5, \beta_{22} = 0.0001$	$\beta_{11} = 0.3, \beta_{12} = 1, \beta_{21} = 0.5, \beta_{22} = 1$

$$F_d = \begin{bmatrix} -107.3832 & -74.4613 & 29.8753 & 312.7714 & 827.4601 & 15.8377 & 3.5445 \\ 4.9429 & -1.1047 & 58.5956 & 51.8619 & 122.73000 & 10.2141 & 7.4767 \end{bmatrix} \tag{45}$$

$$F_u = \begin{bmatrix} -44.0298 & -33.8326 & -25.1949 & 225.0394 & 623.4317 & 16.4489 & 2.3837 \\ 4.3815 & 2.6488 & -21.5701 & 18.9855 & 48.1683 & 1.3245 & 5.4174 \end{bmatrix} \tag{46}$$

The simulation results for the nominal system and system with induced external disturbance are shown in Figs. 2, 3, 4, 5, 6, 7, 8 and 9 and Figs. 10, 11, 12, 13, 14,

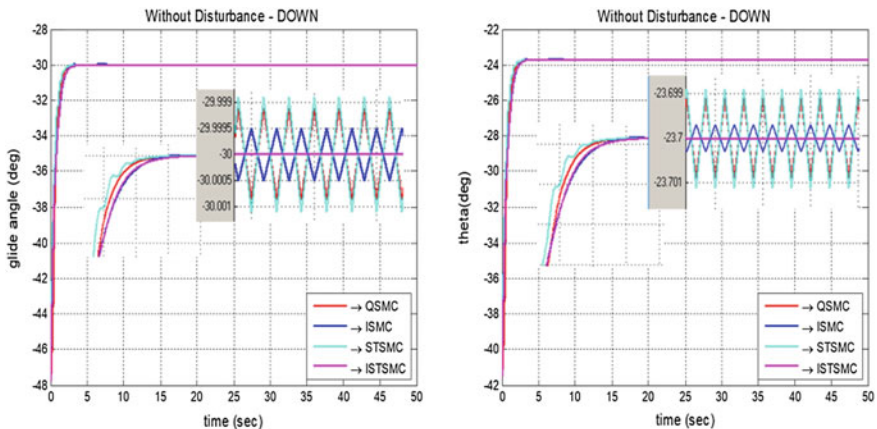


Fig. 2 DOWNWARD—Glide angle (ξ) and pitch angle (θ)—Without disturbance

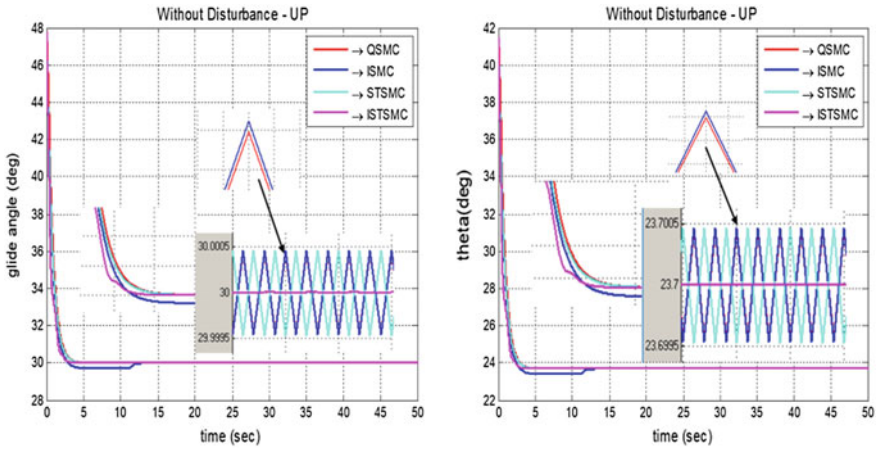


Fig. 3 UPWARD—Glide angle (ξ) and pitch angle (θ)—Without disturbance

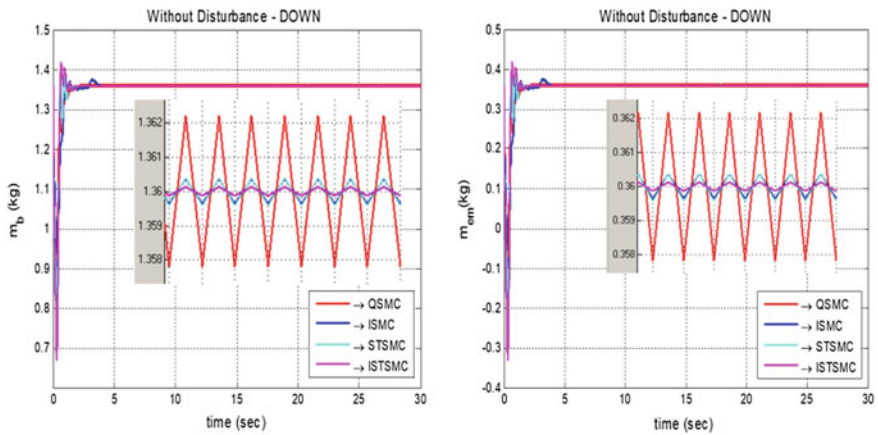


Fig. 4 DOWNWARD—Ballast mass, m_b and net buoyancy, m_{em} —Without disturbance

15, 16 and 17 respectively. Figures 2, 3, 4 and 5 show that all the designed controllers are able to converge to the vicinity of the desired values with proposed controller shows the smallest steady-state error for all the observed outputs. The STSMC provides the highest steady error for the glide and pitch angles, however smaller errors show in ballast mass and net buoyancy. The ISMC provides

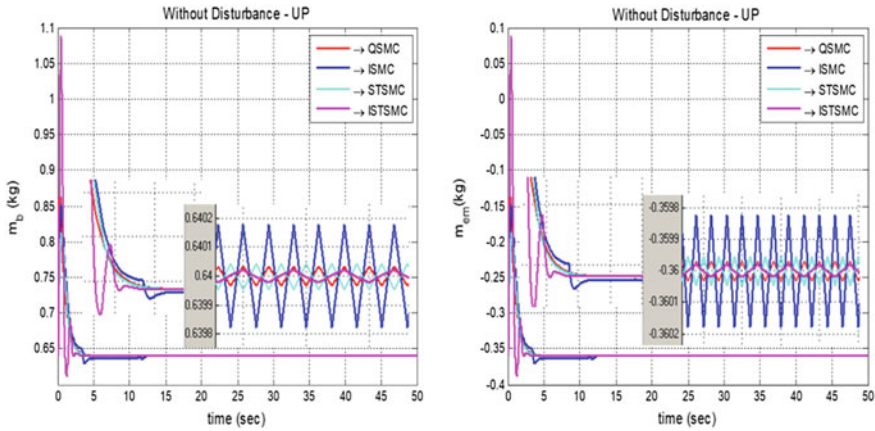


Fig. 5 UPWARD—Ballast mass, m_b and net buoyancy, m_{em} —Without disturbance

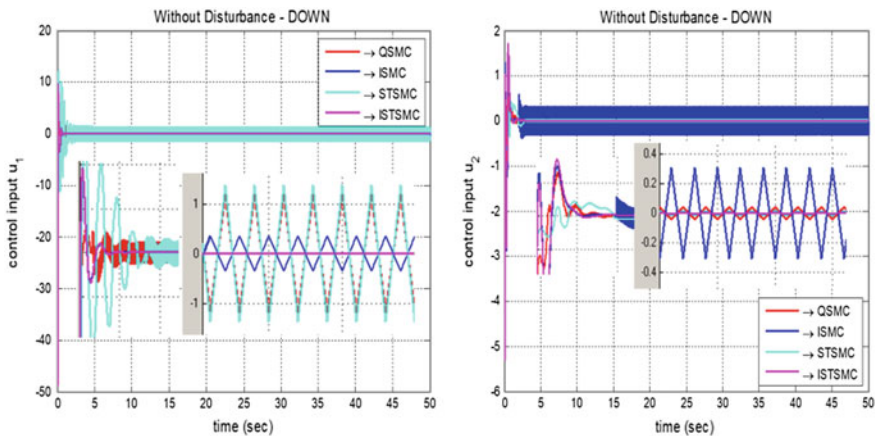


Fig. 6 DOWNWARD—Control inputs u_1 and u_2 —Without disturbance

second highest accuracy in glide and pitching angles, however the worst performance is shown in ballast mass and net buoyancy for the upward glide. The QSMC produce slightly better performance than the STSMC in glide and pitch angles and the worst performance shown in ballast mass and net buoyancy for the downward glide. However, the proposed controller provides slower response (i.e. higher convergence time), in some cases.

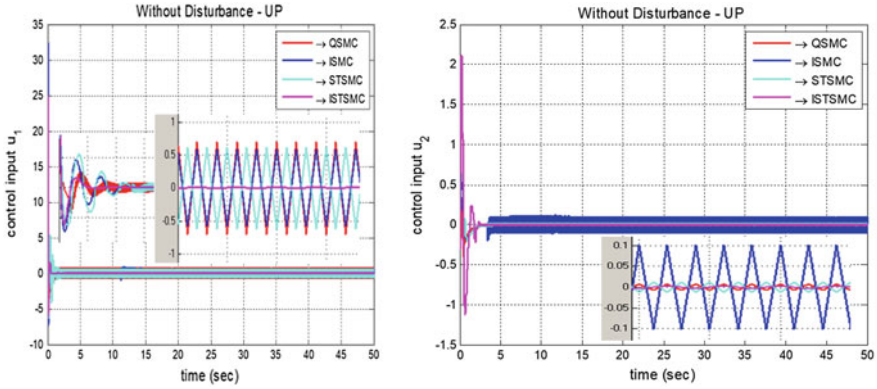


Fig. 7 UPWARD—Control inputs u_1 and u_2 —Without disturbance

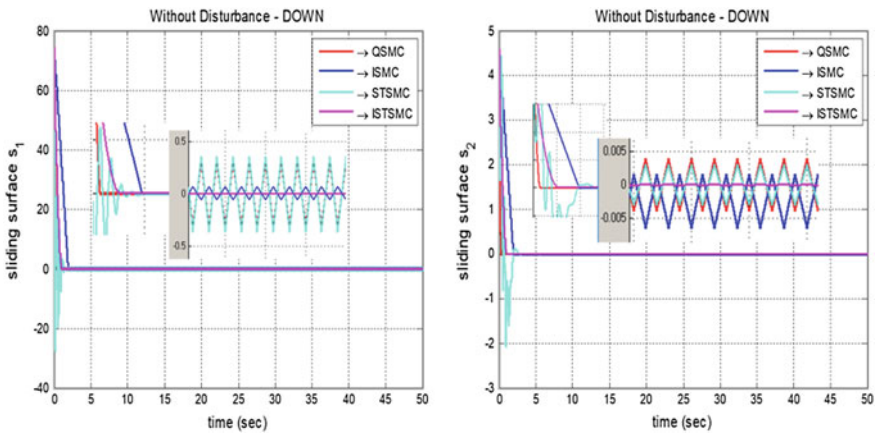


Fig. 8 DOWNWARD—Sliding surfaces s_1 and s_2 —Without disturbance

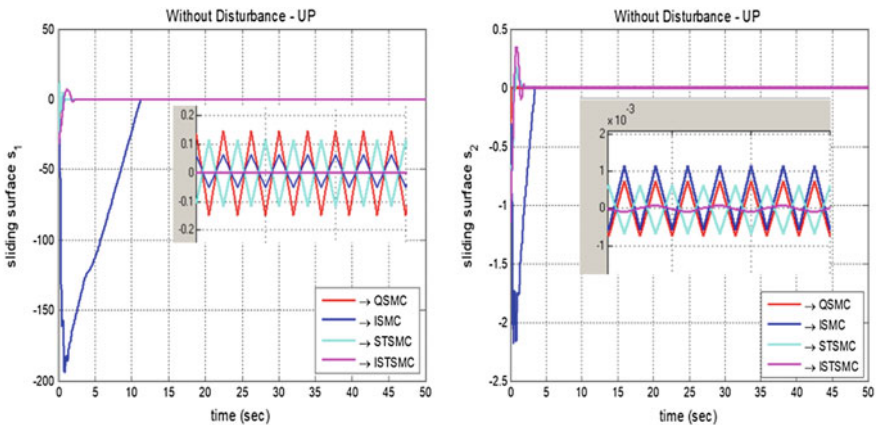


Fig. 9 UPWARD—Sliding surfaces s_1 and s_2 —Without disturbance

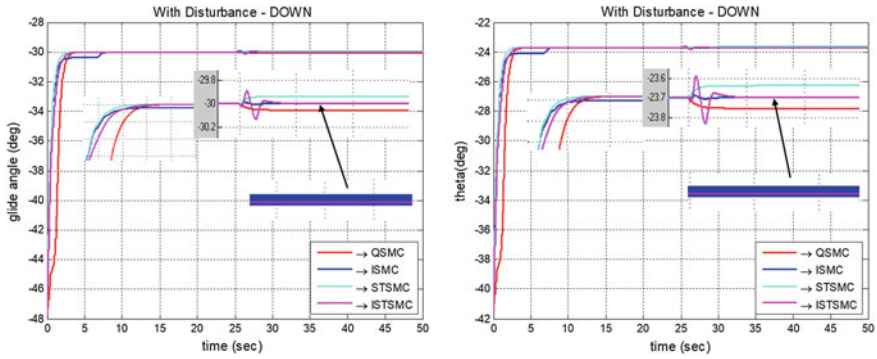


Fig. 10 DOWNWARD—Glide angle (ξ) and pitch angle (θ)—With disturbance

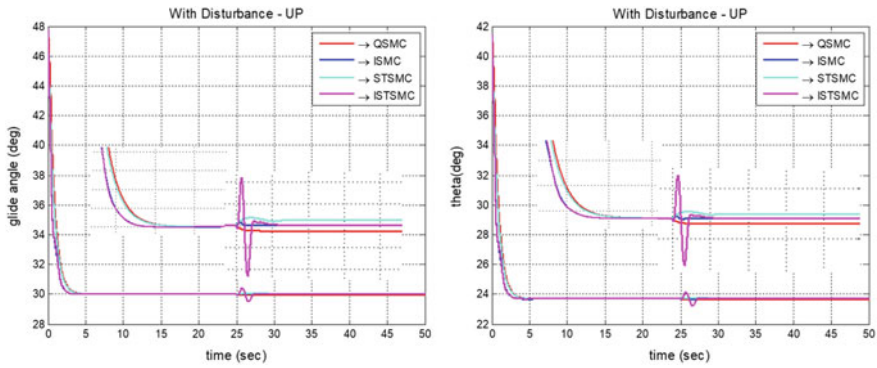


Fig. 11 UPWARD—Glide angle (ξ) and pitch angle (θ)—With disturbance

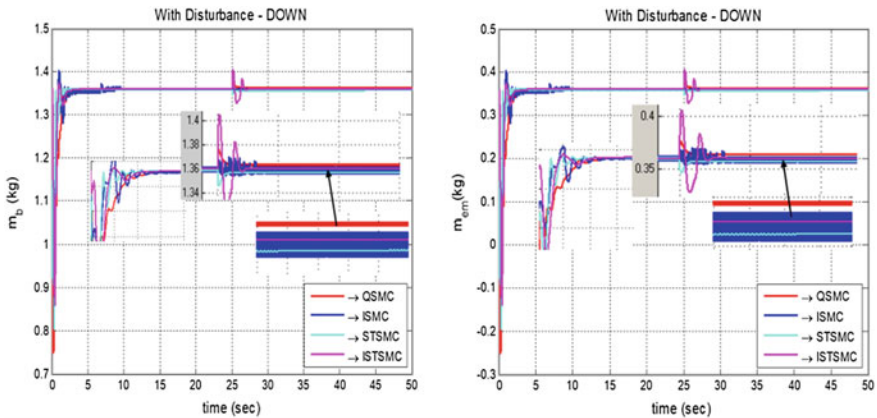


Fig. 12 DOWNWARD—Ballast mass, m_b and net buoyancy, m_{em} —With disturbance

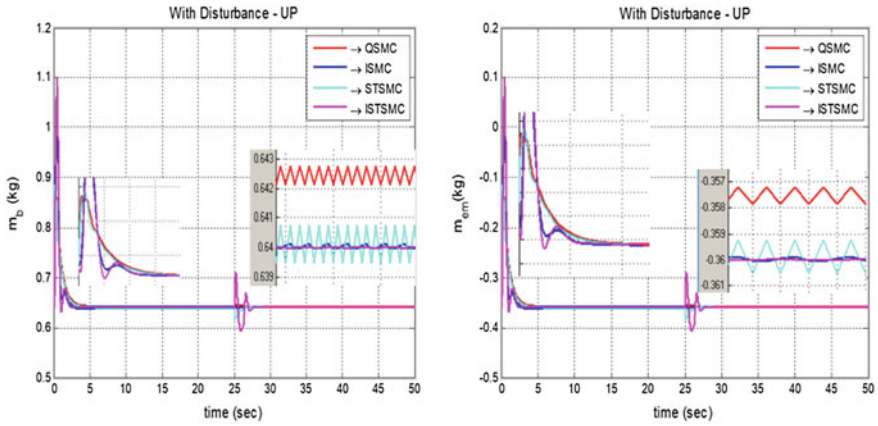


Fig. 13 UPWARD—Ballast mass, m_b and net buoyancy, m_{em} —With disturbance

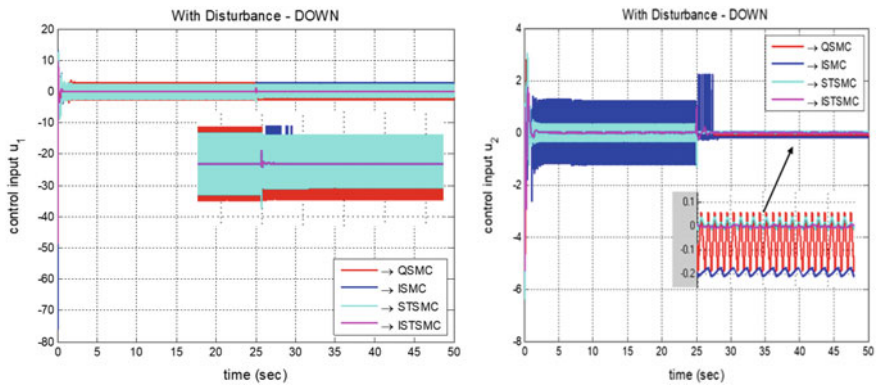


Fig. 14 DOWNWARD—Control inputs u_1 and u_2 —With disturbance

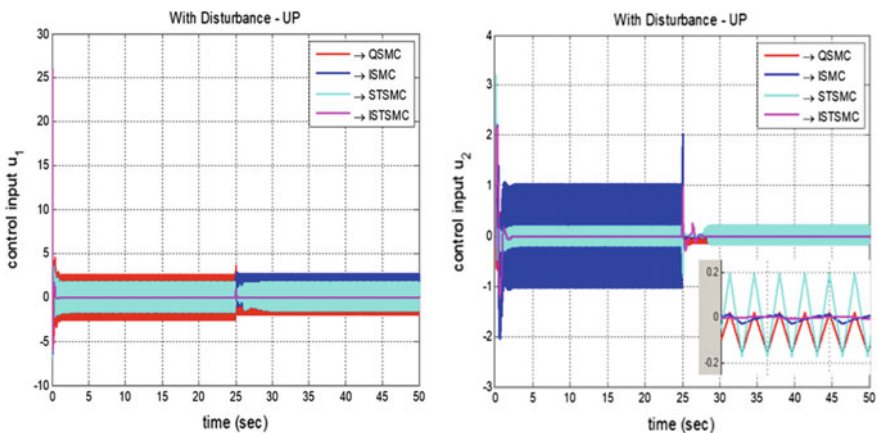


Fig. 15 UPWARD—Control inputs u_1 and u_2 —With disturbance

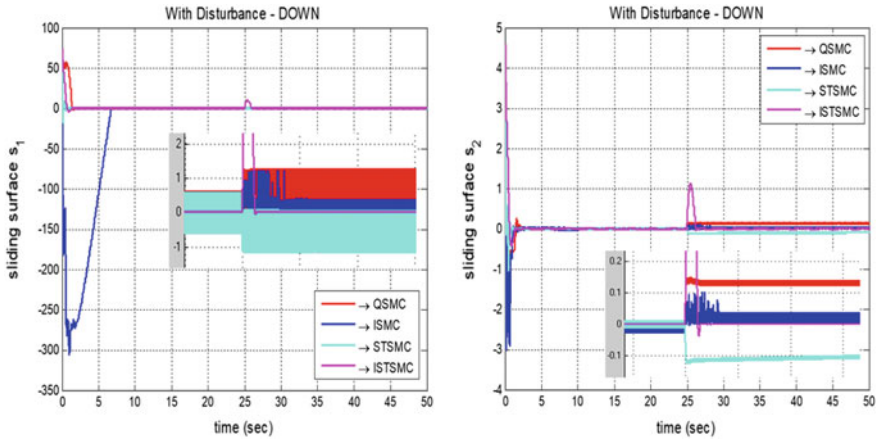


Fig. 16 DOWNWARD—Sliding surfaces s_1 and s_2 —With disturbance

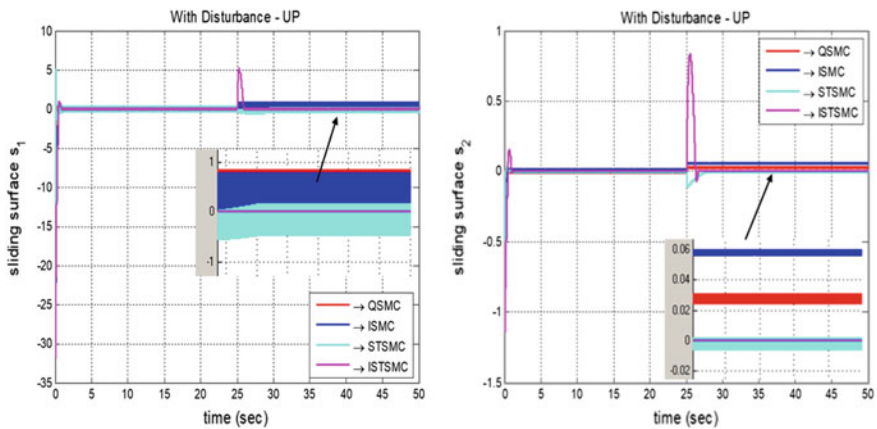


Fig. 17 UPWARD—Sliding surfaces s_1 and s_2 —With disturbance

From Figs. 6 and 7, all the controllers are able to stabilize in the vicinity of origin. The highest control effort in u_2 for both glides is seen in ISMC, the STSMC shows the highest control effort in u_1 for downward glide and the QSMC provides the highest control effort in u_1 for upward glide, whereas the proposed controller demonstrates the lowest control effort in both input channels for both downward and upward glides with no undesired chattering. The sliding surface responses of all

Table 6 Comparative analysis of the controller

Controller	QSMC	ISMC	STSMC	ISTSMC
Robustness	Reject disturbance with highest error	Reject disturbance with small error	Reject disturbance with large error	Reject disturbance with the smallest error
Chattering	High chattering	Small chattering and high in certain case	High chattering	No chattering
Oscillation	Highest frequency oscillation	Smaller frequency oscillation	High frequency oscillation	Very small frequency oscillation
Tracking control	Converged to the desired value with very large error	Converged to the desired value with small error	Converged to the desired value with large error	Converged to the desired value with very small error
Control effort	Very large control efforts	Small control efforts	Large control efforts	Very small control effort
Sliding surface convergence	Did not converge to origin for disturbance case	Did not converge to origin for disturbance case	Converged to origin with chattering	Converged to origin with no chattering

controllers in Figs. 8 and 9 are also stabilized in the vicinity of origin with the proposed controller provides no undesired chattering in its sliding surface responses.

The step input disturbance with magnitude of 1 is induced to both control input channels begins from $t = 25$ s. From Figs. 10, 11, 12 and 13, all the controllers are able to reject the induced disturbance with errors. The QSMC and STSMC show all the observed outputs are deviated from the desired values whereas the ISMC and the proposed controller are able to stabilize within the desired values with proposed controller gives the smallest steady-state error. The control effort of both channels for QSMC, ISMC and STSMC are not stabilized in the vicinity of origin as shown in Figs. 14 and 15 and the undesired chattering is also clearly can be observed. The proposed controller is able to stabilize to origin with no undesired chattering. The sliding surface responses in Figs. 16 and 17 have shown that the QSMC, ISMC and STSMC unable to stabilize within the origin with QSMC shows the highest deviation from origin for s_1 and ISMC for s_2 . Therefore, it can be concluded that the QSMC, ISMC and STSMC have lost their sliding mode. The sliding surfaces of the proposed controller are able to converge to zero and remain there and no undesired chattering is observed. The comparative analysis of all controllers is summarized Table 6.

5 Conclusion

In this paper the integral super twisting (ISTSMC) is proposed for robust tracking for a linearized model of longitudinal plane of AUG. The performance of the proposed controller is compared with three other SMC controllers. Since the performance of the proposed controller is evaluated in terms of chattering reduction, therefore only controllers in SMC family are chosen for this work. The simulation results have shown that the proposed controller demonstrates the smallest steady-error and lowest control effort. The undesired chattering is also eliminated. The inconsistency performance is shown in QSMC, ISMC and STSMC may due to manual tuning and also the performance of the controllers only depend on the controllers' gains. Therefore, in the future, the optimization method can be used to optimize the controllers' gains, linear feedback gain and sliding gain and thus improve the performance of the controllers.

Acknowledgements This research is supported by Universiti Malaysia Pahang (UMP) research grant Vot: RDU1703134, Development of Controller for an Underactuated Autonomous Underwater Vehicle (AUV).

References

1. Stommel, H.: The slocum mission. *Oceanography* **2**, 22–25 (1989)
2. Mahmoudian, N., Woolsey, C.: Underwater glider motion control. In: 47th IEEE Conference on Decision and Control, 2008. CDC 2008, pp. 552–557 (2008)
3. Noh, M.M., Arshad, M.R., Mokhtar, R.M.: Depth and pitch control of USM underwater glider: performance comparison PID vs. LQR. *Indian J. Geo-Marine Sci.* **40**(2), 200–206 (2011)
4. Leonard, N.E., Graver, J.: Model-based feedback control of autonomous underwater gliders. *IEEE J. Ocean. Eng.* **26**(4), 633–645 (2001)
5. Joo, M.G., Qu, Z.: An autonomous underwater vehicle as an underwater glider and its depth control. *Int. J. Control Autom. Syst.* **13**(5), 1212–1220 (2015)
6. Wang, Y., Zhang, H., Wang, S.: Trajectory control strategies for the underwater glider. In: International Conference on Measuring Technology and Mechatronics Automation, Hunan, China, pp. 918–921, 11–12 Apr 2009
7. Tatone, F., Vaccarini, M., Longhi, S.: Modeling and attitude control of an autonomous underwater glider. In: 8th IFAC Conference on Manoeuvring and Control of Marine Craft, vol. 42, No. 18, pp. 217–222 (2009)
8. Abraham, I., Yi, J.: Model predictive control of buoyancy propelled autonomous underwater glider. In: 2015 American Control Conference, pp. 1181–1186 (2015)
9. Yang, H., Ma, J.: Sliding mode tracking control of an autonomous underwater glider. In: 2010 International Conference on Computer Application and System Modeling (ICCAS), 2010, Taiyuan China, vol. 4, pp. V4-555–V4-558, 22–24 Oct 2010
10. Isa, K., Arshad, M.R.: An analysis of homeostatic motion control system for a hybrid-driven underwater glider. In: 2013 IEEE/ASME International Conference on Advanced Intelligent Mechatronics, pp. 1570–1575, July 2013
11. Isa, K., Arshad, M.R.: Neural networks control of hybrid-driven underwater glider. In: OCEANS, 2012—Yeosu, 21–24 May, South Korea, pp. 1–7 (2012)

12. Graver, J.G.: Underwater Gliders: Dynamics, Control and Design. Ph.D. Thesis, Princeton University (2005)
13. Mat Noh, M., Arshad, M.R., Mohd-Mokhtar, R.: Modeling of USM underwater glider (USMUG). In: International Conference on Electrical, Control and Computer Engineering Pahang, Malaysia, June 21–22, 2011, pp. 429–433 (2011)
14. Utkin, V., Shi, J.: Integral sliding mode in systems operating under uncertainty conditions. In: Proceedings of the 35th IEEE Conference on Decision Control, vol. 4, pp. 1–6 (1996)
15. Levant, A.: Sliding order and sliding accuracy in sliding mode control. *Int. J. Control* **58**(6), 1247–1263 (1993)
16. Bartolini, G., Ferrara, A., Levant, A., Usai, E.: On second order sliding mode controllers. In: Young, K.D., Ozgiine, U. (eds.) *Variable Structure Systems, Sliding Mode and Nonlinear Control*. Gt. Britain Springer-Verlag London, vol. 247, pp. 329–350 (1999)

X4-ROV: The Open Source Underwater Vehicle



Zainah Md Zain and Khairil Ashraf Ab. Rahim

Abstract The biggest bottleneck of currently available Remotely Operated Vehicles (ROVs) is the cost of the systems. Therefore, to reduce operational costs and system complexity, the development of micro or handheld inspection ROVs has been increasing lately. An open-source underwater vehicle startup has contributed to the community by producing cheap ROVs, encouraging users to develop their own underwater vehicle. In this project, a low-cost ROV prototype, called X4-ROV using open-source OpenROV computer hardware and software is developed. This new design includes hardware, firmware, software and control architectures.

Keywords OpenROV · X4-ROV · Open-source

1 Introduction

Underwater vehicle is classified into two basic categories which is manned vehicles and unmanned vehicles. These vehicles are divided into a group and subgroup depending on their class/characteristics as shown in Fig. 1.

ROV is the common accepted name for tethered underwater robots. Different from AUVs, ROVs are tele-operated robots, highly maneuverable and operated from a command center. They are linked to command center by a tether which is a group of cables that can carry electrical power, video and data signals back and forth between the operator and vehicle. Most of ROVs are equipped with at least a video camera and lights. Additional equipment is commonly added to the vehicle to expand its capabilities.

Nowadays, several underwater vehicles and robotic platforms have been developed with low cost components, for instance, control platforms that use

Z. Md Zain (✉) · K. A. Ab. Rahim

Robotics and Unmanned Research Group (RUS), Instrument & Control Engineering (ICE) Cluster, Faculty of Electrical and Electronics Engineering, Universiti Malaysia Pahang, 26600 Pekan, Pahang, Malaysia
e-mail: zainah@ump.edu.my

© Springer Nature Singapore Pte Ltd. 2018

M. H. A. Hassan (ed.), *Intelligent Manufacturing & Mechatronics*,
Lecture Notes in Mechanical Engineering,
https://doi.org/10.1007/978-981-10-8788-2_29

327

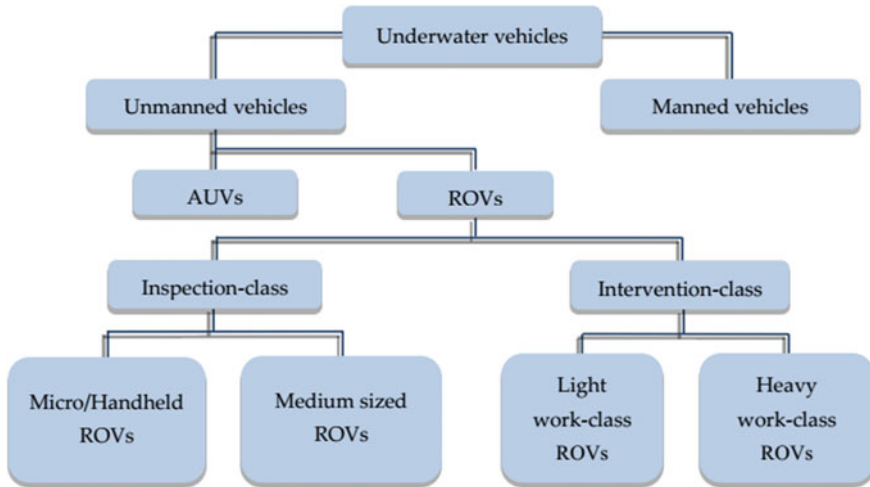


Fig. 1 Outline of underwater vehicle [1]

Arduino[®]-based hardware [2, 3]. These open-hardware platforms can be used in ROVs that are intended for inspection tasks which are performed at low depths, and that do not require high performance real-time computations. Typically, Arduino[®]-based hardware is used to perform low-level tasks, such as data acquisition and communication with sensors and actuators, while the implementation of control algorithms and surface communication systems is done with open source single-board computers such as Beaglebone[®] or Raspberry PI[®] [4]. Arduino platforms simplify the process of developing firmware by using a high level programming language, which implies a trade-off when trying to optimize code.

Recent open hardware designs developed by companies such as OpenROV and BlueRobotics have helped to introduce underwater robotics to the hobbyist and research markets. The design of these robots are adequate for simple exploration and surveying tasks, however they lack either the maneuverability, computational power, sensors or autonomous capabilities necessary for a research platform [5].

A key design goal of X4-ROV is to develop a ROV using open-source OpenROV with a new hull shape to reduce the drag and improve the maneuvering by implement X-configuration thrusters using four thrusters. In this paper, an overview of the X4-ROV hardware and software is presented.

2 Review of OpenROV

OpenROV is an open-source ROV that is available for public use and is designed to be a “do it yourself” ROV. The user can assemble themselves and modify the control software to their needs [6]. It may be the smallest observational ROV on the market with the dimensions of 11.8 × 7.8 × 5.9 in and it weighs only 5.5 lbs.

2.1 OpenROV Design

OpenROV as shown in Fig. 2 is a low cost open source ROV platform that makes it easy to implement tools, as a positioning or docking system, and to develop its control system. The ROV can go 100 m deep. It has three thrusters, one for heave motion and two for surge and yaw, allowing a maximum speed of two knots. This ROV has 4-DOF motion capabilities. The OpenROV is neutrally buoyant since it uses its vertical propeller to move vertically.

It is equipped with a HD Webcam, lights, two red lasers, a compass, and a pressure sensor for control of the depth and heading. The power is supplied with help of batteries contained within the ROV (so no external power supply is required), and the electronics comprise a BeagleBone black computer together with a microcontroller board Arduino Mega that connect all the equipment and enable communication with the operator through Ethernet connection. The software is coded in node.js, a language that allows to use both JavaScript programming for the user interface and camera streaming, and C++ for the Arduino code. The maximum thrust that each individual propeller can reach is 1 kg for horizontal forward motion. With two propellers the total forward thrust should theoretically be approximately 2 kg. It is also said that the four levels of power correspond to respectively 12%, 25%, 40%, and 75% of the total thrust in the OpenROV. The Fig. 2 shows the elements described above onto the vehicle. The vehicle can be used with any computer having a Google Chrome browser installed. The computer

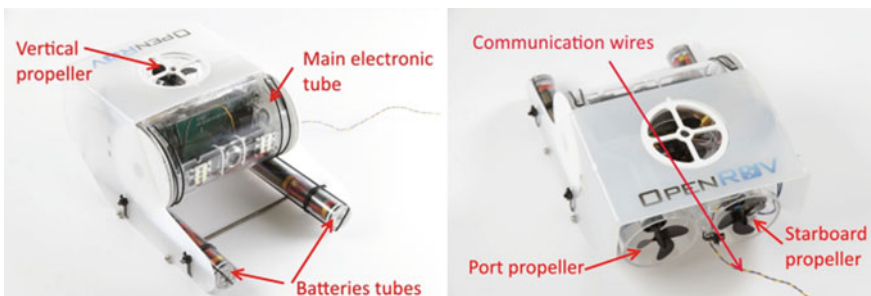


Fig. 2 OpenROV: front and back views [6]

is connected to a little box that allow to use only two wires, that serve as tethers for the Ethernet communication [6].

2.2 Weakness in OpenROV Design

Weaknesses in the OpenROV design according to [7] based on the testing are:

- Hydrodynamic inefficient design.
- Inefficient thrusters build leading to substantial thruster loss, especially in vertical direction.
- Undesired pitch motion when moving in the surge or heave direction. This was concluded due to the placement of the thrusters. Resultantly hard to maintain constant depth when moving.
- Unstable communication. This was concluded to be caused by the HomePlug adapters and the umbilical.
- Sub-optimal umbilical attachment point. It was speculated that this contributed to the undesired pitch motion.
- Water leakage during sea trials.
- Occasional video dropout during rapid change in thrust command. It was speculated that this was due to transient voltage drop.

Therefore, the main goal of this project is to design a new ROV called X4-ROV with the following contributions to the X4-ROV; design and construction of a new hull for better hydrodynamic efficiency and new thruster configuration to improve the vehicle maneuverability.

3 X4-ROV System

The complete block diagram to illustrate the X4-ROV system is shown in Fig. 3. This system has two main parts: control panel on the surface and vehicle in the water which is communicate via tether cable.

3.1 Control Panel

In this project, OpenROV cockpit is modified as an X4-ROV control panel. OpenROV cockpit comes with fully extensible plugin based architecture, built in configurations for many ROV motor configurations, can connect the cockpit on mobile, dekstops and tablets with no installation required and more interesting features that can be used. Cockpit user interface (UI) in web-based application,

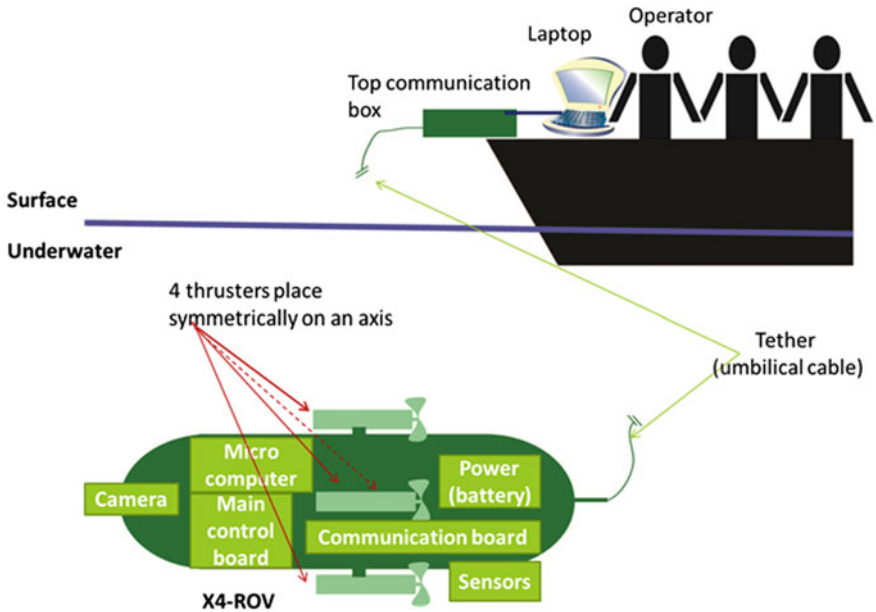


Fig. 3 X4-ROV system diagram

therefore can be used with any device having a Google Chrome browser installed. Cockpit is loaded into a browser and shows live video, sensor feedback, and provides driving controls. The cockpit UI is shown in Fig. 4.

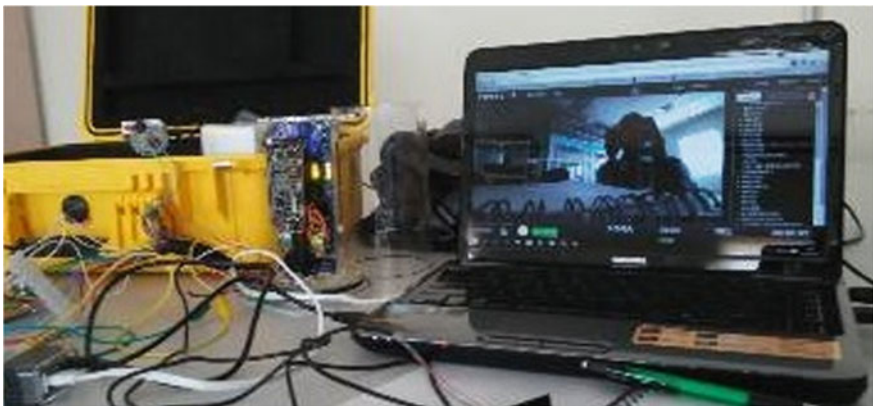


Fig. 4 X4-ROV cockpit (control panel) using laptop

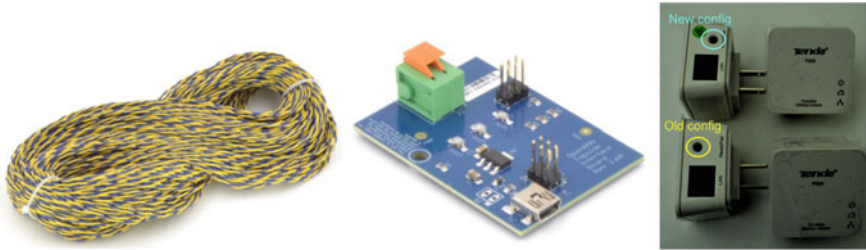


Fig. 5 Ethernet cable, topside interface board and Tenda P200 adapter

3.2 *Tether*

The vehicle is tethered to a computer with a 100 m Ethernet cable, allowing real-time communication and feedback. The topside interface board is used to connect a laptop or desktop to X4-ROV with an Ethernet cable. This interface board is designed to plug in directly to the Tenda Homeplug board (Tenda P200). The twisted pair tether plugs in directly to this board, and with the Tenda pair, enables communication between ROV and computer (Fig. 5).

3.3 *X4-Rov*

X4-ROV is an open-source ROV based-on OpenROV hardware and software. In order to overcome the limitation of OpenROV, X4-ROV is developed with a cylinder hull shape to reduce the drag force and equipped with four thrusters which has 6-DOF of motion. It has the same hardware uses for OpenROV such as HD camera, a 9-DOF inertial measurement unit (IMU) with a depth and temperature sensor. The X4-ROV is controlled over an interface running on the robot itself which is accessible over an internet browser, with no need for additional software. The developed X4-ROV is shown in Fig. 6.

3.4 *Hardware Architecture*

The computer and the vehicle are connected with a twisted pair through the water. The communication between them is done using the Ethernet protocol but the signal must be converted to pass through a single twisted pair, at both ends. The X4-ROV controller board (ATMEGA2650-16AU microcontroller) connected to various input and output as motors, IMU and depth sensor communicate with BeagleBone black through a serial communication. The BeagleBone has most of the computing power for the ROV and allow the connection between the ROV and

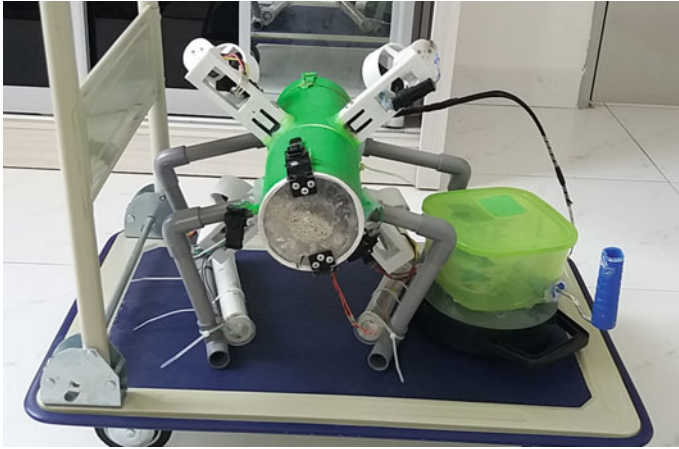


Fig. 6 X4-ROV prototype

the PC that controls it. This board embedded an AM335x 1 GHz ARM Cortex-A8 microcontroller. Unlike the other devices, the camera is connected to this board instead of the ROV controller board. The block diagram of the X4-ROV's electronic is shown in Fig. 7.

The BeagleBone black is connected by a twisted pairs cable to a circuit, called Ethernet converter 2 (which is a part of a Tenda P200 powerline adapter). This circuit converts communication signal to a single twisted pair. At the surface, this 2 wires communication is converted back to a standard twisted pair cable that can be connected to the computer from which the ROV is driven. This conversion is made by two circuits, called Ethernet converter 1 in the Fig. 7, which are a Tenda P200 circuit and topside interface board.

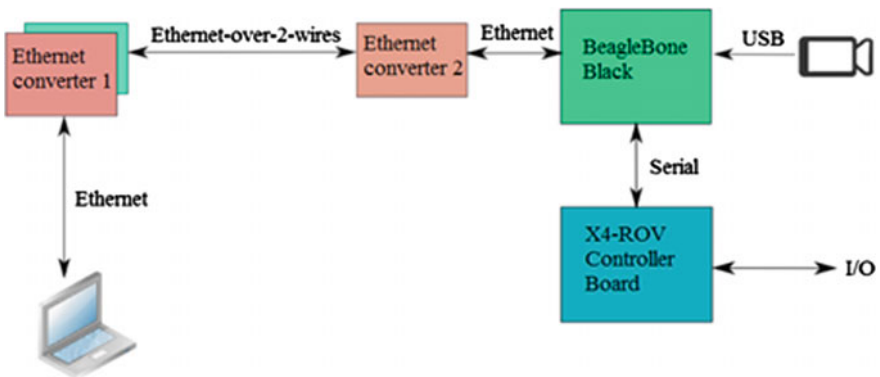


Fig. 7 Block diagram of the X4-ROV's electronic

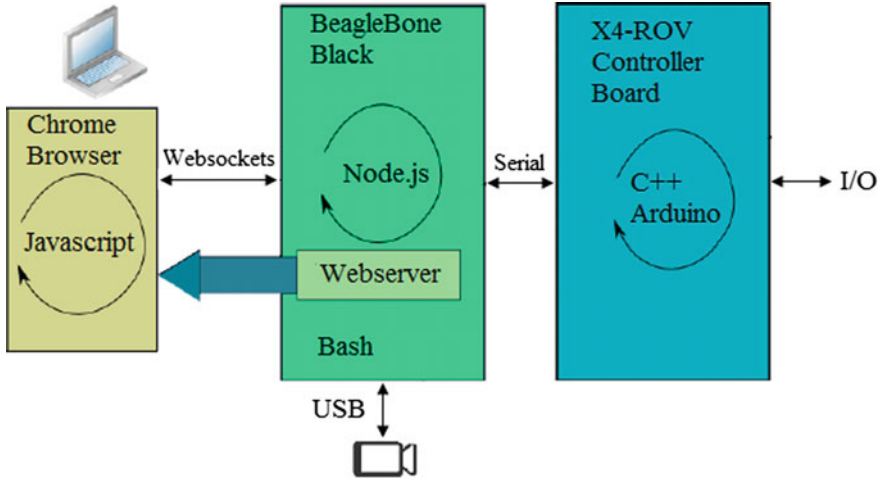


Fig. 8 X4-ROV global architecture

3.4.1 Software Architecture

The software on the X4-ROV Controller Board is a C++ code using an Arduino library. This code controls the sensors and actuators at a low level. The software on the BeagleBone Black is a Node.js code and is charged to control the ROV. It also implements the web server that provides the web pages (accessed through a Chrome browser) allowing to control the vehicle. Those pages are written using Javascript and can communicate with the Node.js code on the rover through web-sockets. Although the compiled code is dispatched between the BeagleBone black and the X4-ROV Controller Board as shown in Fig. 8, all the source files are located on the Beaglebone black and bash scripts on it allow to compile the C++ files and send them into the X4-ROV Controller board. The software is working through 3 loops: the JavaScript global event loop for the browser, the JavaScript global event loop for the BeagleBone Black and the micro-controller loop for the OpenROV Controller Board.

4 X4-ROV Mechanical and Electrical Design

4.1 X4-ROV Mechanical Design

The main consideration in the proposed design is to minimize the effects of drag and enhancing maneuverability to ensure the ROV can freely move. Drag can be reduced primarily by minimizing the surface area normal to the direction of travel.

Maneuverability can be increased by having multiple thrusters located throughout the design with positioning contributing to rotational and translational movement.

4.1.1 New Hull Design

The drag force exerted on a ROV body moving through a fluid is quadratically proportional to the velocity of the body as shown in Eq. 1.

$$F_{drag} = \frac{1}{2} \rho v^2 C_d S \quad (1)$$

where ρ is a density of the water (kg/m^3), v is a velocity of the vehicle (m/s), C_d is a drag coefficient (unitless) and S is a surface area of the body normal to the moving direction (m^2).

It is a fundamental relation of fluid dynamics, giving several important insights for efficient design of a submersible [8]. Drag force is also affected by the density of the fluid, and more importantly by the geometry of the body. Surface area of the body, normal to the moving direction, also proportionally affects drag force applied. Thus, it can be concluded that drag can be reduced by simply designing the surface area of the vehicle normal to the travel direction to be as small as possible.

C_d is a coefficient that expresses how the shape of the body that is moving in the fluid, affects the drag force. The drag coefficients for different shapes are shown on Fig. 9. The arrow shows the direction of the flow relative to the cross-section of the shape. It can be seen that the drag coefficient can substantially vary for different shapes.

Therefore, it can be concluded, that hydrodynamic design of the submersible can give tangible and measurable results in terms of reduced drag force. The less drag the vehicle experience, the less propulsive power is needed, ultimately resulting in improved efficiency, higher speed, more sea-current resistance and longer run-times [8].

The streamline shaped structural parts might prove difficult to produce. Hence, cylinders are the most used shape for pressure compartments among all submersible vehicles, mainly because they can be made from standard parts, such as cylindrical tubing. Many hobbyists use off-the-shelf parts such as PVC piping for their cylindrical dry compartments. For the previously described reasons, cylindrical pressure containers will be most suitable for the X4-ROV.

Figure 10 shows the development of the X4-ROV prototype with cylinder hull design. With this new design, it can overcome the drag issues of OpenROV with box hull shape.







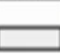



Shape		C_d
Sphere		0.47
Halfsphere		0.42
Cone		0.50
Cube		1.05
Angled Cube		0.80
Long Cylinder		0.82
Short Cylinder		1.15
Streamlined Body		0.04
Streamlined Halfbody		0.09

Fig. 9 Drag coefficients of different shapes [8]

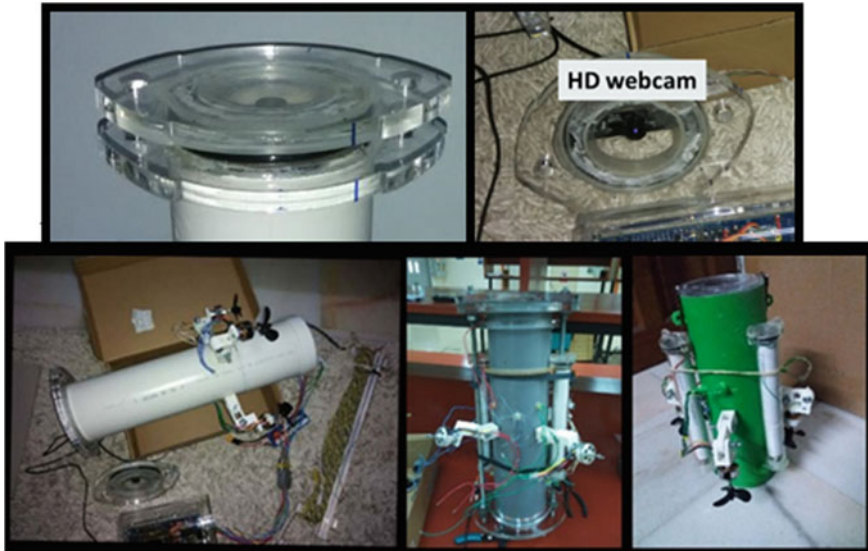


Fig. 10 Development of X4-ROV prototype

4.2 New Thruster Configuration

The propulsion system is a critical design consideration for any ROV as without sufficient thrust, the vehicle can become overwhelmed by environmental conditions and thus unable to perform the desired tasks.

The propulsion system for an X4-ROV is very well modelled with four thrusters in a cross configuration, by applying conventional quadrotor design concepts. The control of the X4-ROV motion can be achieved by varying the speed of each thruster to change the thrust and torque produced by them. Each thruster produces both thrust and torque about its center of rotation, as well as a drag force opposite to the vehicle’s direction of travel.

Longitudinal rotation is achieved by creating an angular speed difference between the two pairs of thrusters. Increasing or decreasing the speed of the four thrusters simultaneously permits forward acceleration. Rotation about the vertical and the lateral axis and consequently horizontal or vertical motion is achieved by tilting the vehicle. This is possible by conversely changing the thruster speed of one pair of thrusters as described in Fig. 11. This design enabled X4-ROV with 6-DOFs of motion using only four thrusters. By implementing the thrusters in this manner many capabilities of the ROV are still preserved and thruster requirements are reduced.

Turnigy aerodrive DST 700 is a brushless DC motor used for X4-ROV locomotion. These motor are electrically isolated and are safe for underwater usage. Propeller Graupner 2310.60 and Graupner 2310.60L are compatible choice for this motor as shown in Fig. 12. This propulsion system work well for both high and low

Fig. 11 X4-ROV thrusters (back view)

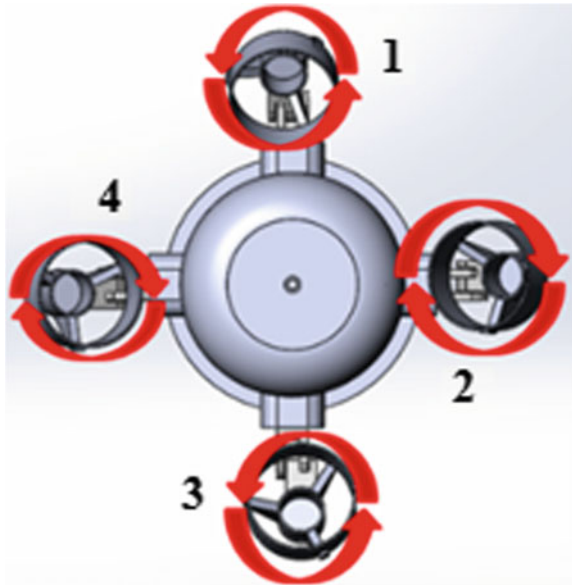




Fig. 12 DST 700 Brushless dc motor and propellers

speed for best control of ROV. The use of different propeller is necessary to prevent an effect called ‘torque steering’ where it would cause the vehicle to roll unnecessarily. Four brushless DC motor (or thrusters) which is attached on the hull by few 3D printed parts as shown in Fig. 13. This part is configurable to mount the thrusters in certain angle.

4.3 X4-ROV Electronic Design

X4-ROV electronic system is adapted from open source ROV platform so called OpenROV. Their main electronic systems consist of two electronic boards as shown in Fig. 14. The microcomputer, Beaglebone black handles higher level tasks, such as running the webserver that hosts the cockpit page/software, acquiring the video stream from the webcam over USB, and more. The controller board however is a hosts and linked to many different electronics, such as sensors, power circuitry, and the electronic stability control (ESC).

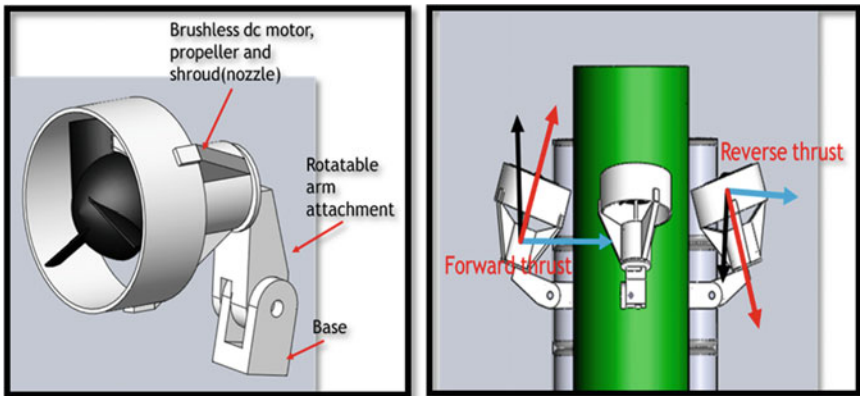


Fig. 13 X4-ROV thrusters mounting design



Fig. 14 X4-ROV thrusters mounting design

The default system is using 3 thrusters, in 2X1 configuration (2 horizontal and 1 vertical thruster). Since we are using different thruster configuration (X4 configuration), an extra ESC is added to the electronic system as shown in Fig. 15 to control the 4th thruster.

The vehicle is equipped with a high definition (HD) web camera for real time image used by the pilot of the ROV and the sensors (IMU and pressure sensor) are also used for helping the pilot maneuver the unit. All the electronic components in the robot are mounted in a watertight acrylic enclosure that can withstand depths up to 100 m (Fig. 16).

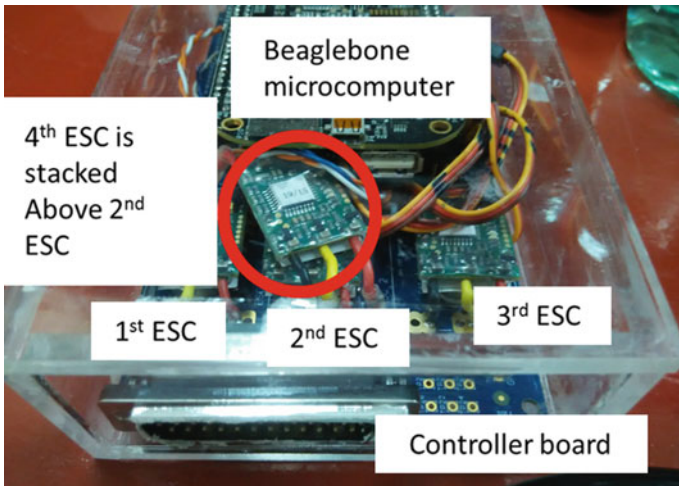


Fig. 15 Modification to the controller board



Fig. 16 Camera and sensors equipped to X4-ROV

5 Preliminary Results

Telemetry is the automated transmission of measured data sent from a remote location (ROV) to a receiver (Operator) for monitoring and storage. Initial experiment of X4-ROV is a testing of the telemetry data/sensors in short dive. The results from IMU and the telemetry data are shown in Fig. 17 and Fig. 18 respectively.

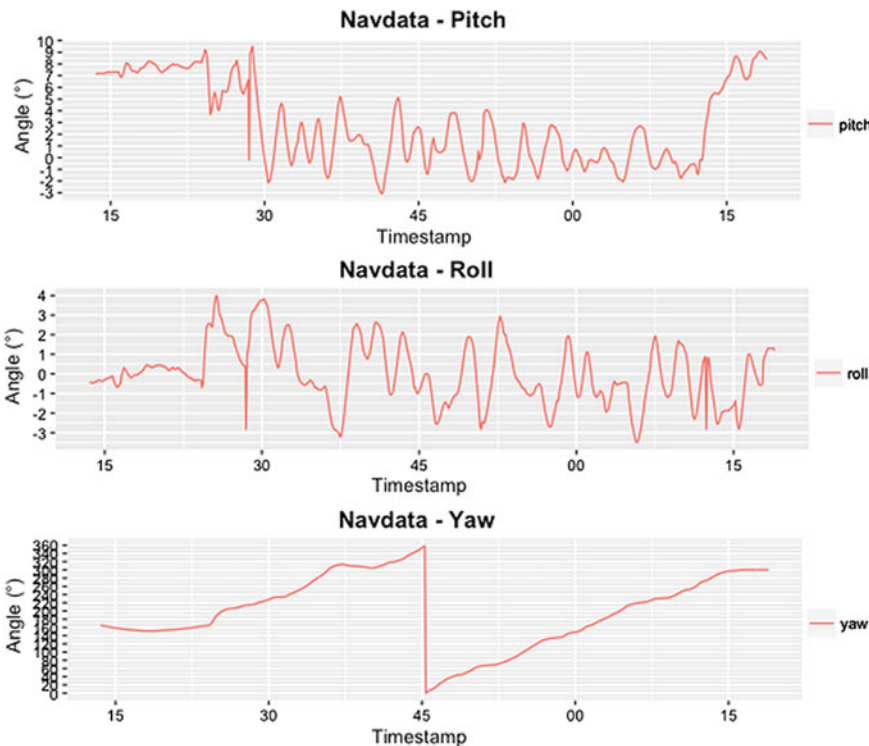


Fig. 17 Navigation data for pitch, roll and yaw

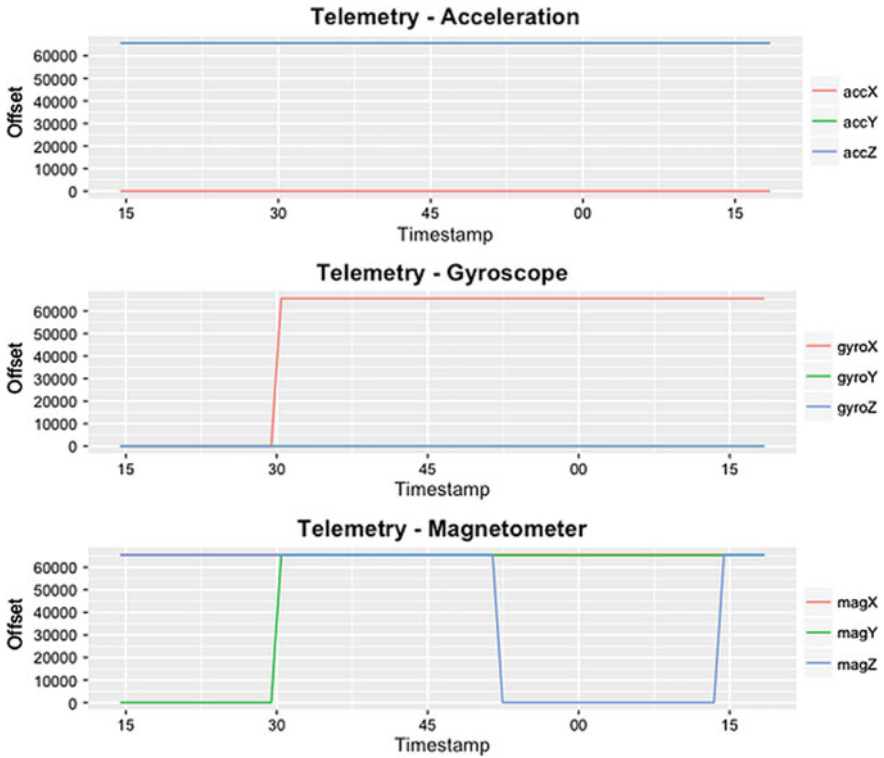


Fig. 18 Telemetry data for accelerometer, gyroscope and magnetometer

This additional telemetry will greatly help with navigation, gathering relevant scientific data, and allows for closed-loop control commands that will make the X4-ROV much easier to dive.

6 Conclusion

This paper addressed the overview of X4-ROV system. The hardware and software architecture of the system based-on OpenROV is discussed. Using OpenROV platform, a low cost X4-ROV prototype is developed. Next, experimental testing will be conducted to test the vehicle in real field.

Acknowledgements The authors would like to thank for the support given to this research by Universiti Malaysia Pahang (UMP) under grant RDU170366.

References

1. Capocci, R., Dooly, G., Omerdić, E., Coleman, J., Newe, T., Toal, D.: Inspection-class remotely operated vehicles—A review. *J. Marine Sci. Eng.* **5**(13) (2017)
2. Busquets, J., Busquets, J.V., Tudela, D., Perez, F., Busquets-Carbonell, J., Barbera, A., Rodriguez, C., Garcia, A.J., Gilabert, J.: Low-cost AUV based on Arduino open source microcontroller board for oceanographic research applications in a collaborative long term deployment missions and suitable for combining with an USV as autonomous automatic recharging platform. In: *Autonomous Underwater Vehicles (AUV)*, 2012 IEEE/OES, pp. 1–10 (2012). <https://doi.org/10.1109/auv.2012.6380720>
3. Johansson, P., Bernhard, J.: Advanced control of a remotely operated underwater vehicle. Technical Report, Department of Electrical Engineering, Linköpings universitet, Sweden (2012). <http://urn.kb.se/resolve?urn=urn:nbn:se:liu:diva-79364>
4. Grimmett, R.: *Mastering Beagle Bone Robotics*. Packt Publishing (2014)
5. Codd-Downey, R., Jenkin, M., Allison, K.: Milton: An open hardware underwater autonomous vehicle. In: *Proceedings of the 2017 IEEE International Conference on Information and Automation (ICIA) Macau SAR, China, July 2017*, pp. 30–34
6. Stackpole, E.: Open ROV—The open source underwater robot by OpenROV. Kickstarter. <http://www.kickstarter.com/projects/openrov/openrov-the-open-source-underwater-robot>. Accessed 7 Dec 2017
7. Follestad, J., Sandved, F., Valle, E.: *Low cost ROV design, based on testing, simulations and analysis of OpenROV* (2014)
8. Christ, R.D., Wernli, R.L.: *The ROV Manual: A User Guide for Observation Class Remotely Operated Vehicles*, 2nd edn. Elsevier Ltd. (2014)

Effect of Assistive Grouser Mechanism on Lightweight Rover Power Consumption Pattern on Steep Soft Sand Inclines



Ahmad Najmuddin Ibrahim  and Yasuhiro Fukuoka

Abstract Lightweight wheeled rover locomotion has been the focus of research due to their reliability and simplicity of use. Soft sand inclines remain a challenge for wheeled rovers due to the high slippage and also a high risk for the wheels to dig into the sand and get stuck, due to the flowing nature of soft sand. During our previous work, we had proposed an assistive grouser mechanism that is attached to the sides of a conventional wheel, which had shown promising performance on soft sand inclines up to 30°. Power consumption pattern is important to lightweight rovers powered by onboard batteries traversing over terrain with high wheel rolling resistance such as soft sand. Therefore, this paper investigates the current consumption of a rover when using conventional wheels with fixed grousers compared to a rover using our proposed assistive grousers. The results show that on steep inclines, the assistive grousers are able to provide a relatively stable and lower current consumption when compared to when using a conventional wheel with fixed grousers.

Keywords Rover locomotion • Soft terrain • Mobile robots

1 Introduction

Lightweight wheeled rovers are widely used in various environments, such as in agriculture automation, scientific exploration, search and rescue, and also monitoring in hazardous areas. Wheels possess a large advantage in control simplicity and robustness in irregular terrain when compared to other mechanisms such as

A. N. Ibrahim ()

Faculty of Manufacturing Engineering, Universiti Malaysia Pahang, 26600 Pekan, Pahang, Malaysia
e-mail: anajmuddin@ump.edu.my

Y. Fukuoka

Department of Intelligent Systems Engineering, College of Engineering, Ibaraki University, 316-8511 Hitachi, Japan

© Springer Nature Singapore Pte Ltd. 2018

M. H. A. Hassan (ed.), *Intelligent Manufacturing & Mechatronics*,
Lecture Notes in Mechanical Engineering,
https://doi.org/10.1007/978-981-10-8788-2_30

tracks and multi legged systems [1, 2]. One of the most challenging terrains for wheeled rovers is the soft sand incline, where high slippage and the tendency for the wheel to get stuck in the freely flowing sand surface might cause mobility problems for the rover [3, 4]. This is an especially significant problem for unmanned wheeled rovers such as the Mars planetary rovers, where human help is not possible when the rover is immobilized. Mars rovers “Spirit” and “Opportunity” both experienced difficulty traversing soft sand and was immobilized after the wheels were embedded inside the sand surface [5, 6].

Wheels that are used on soft terrain are often fixed with grousers (also known as cleats or lugs) on the surface of the wheel to improve traction. The fixed arrangement of the grousers means that the grousers will rotate together with the wheel, resulting in a half-circular motion under the soft terrain subsurface. The rotating motion of the grousers produces two different effects depending on the stage of the wheel rotation. During the grouser entry until the grouser is situated directly under the wheel (from OM until OP in Fig. 1a), the grouser will generate a net forward and upwards force, providing the wheel with forward thrust. However, when the wheel continues to rotate and the grouser continues moving backward from directly under the wheel until it exits the sand surface (from OP until ON in Fig. 1a), the grouser will generate a downwards net force which will work against the forward thrust and drive the wheel into the sand. Moreover, in a high slippage situation such as on a steep incline, the latter half movement of the grouser will excavate sand from under the wheel, causing an increase in the wheel sinkage which will contribute towards the wheel becoming stuck inside the sand surface [7].

To improve wheeled rover performance on soft sand inclines, we had developed an assistive grouser mechanism that is able to control the angle of the grousers independent of the wheel rotation [7]. By maintaining a constant angle of attack when the grouser is moving under the terrain subsurface, the wheel is able to maintain a constant positive net force (B in Fig. 1b) throughout the wheel rotation, while also not digging the sand from under the wheel. This results in a reduced tendency for the wheel to get stuck in the sand. The mechanism attached to the

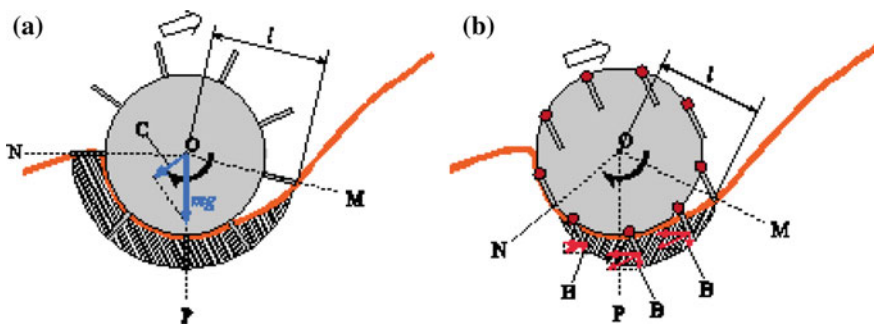


Fig. 1 a A wheel with conventional fixed grousers, b a wheel with assistive grousers with variable grouser angle on a steep incline of soft terrain

wheels of a rover is as shown in Fig. 2. In our previous work, we had compared the performances of a rover when using our proposed assistive grouser mechanism and when using conventional fixed grousers, using wheel sinkage angle, sand displacement volume, and average current consumption as the performance evaluation criterion. We had proven that the use of assistive grousers had resulted in the rover being able to climb soft sand inclines of 0° , 10° , 20° and 30° with a lower amount of sinkage when compared to when using conventional wheels with fixed grousers.

For this paper, we are interested in investigating in more detail the effect of assistive grouser on the overall rover power consumption pattern when the rover is traversing on a steep slope of soft sand. By comparing the current consumption trend for the rover when using the assistive grousers and when it is not as the rover climbs the inclines, the effects of the assistive grouser mechanism could be confirmed.

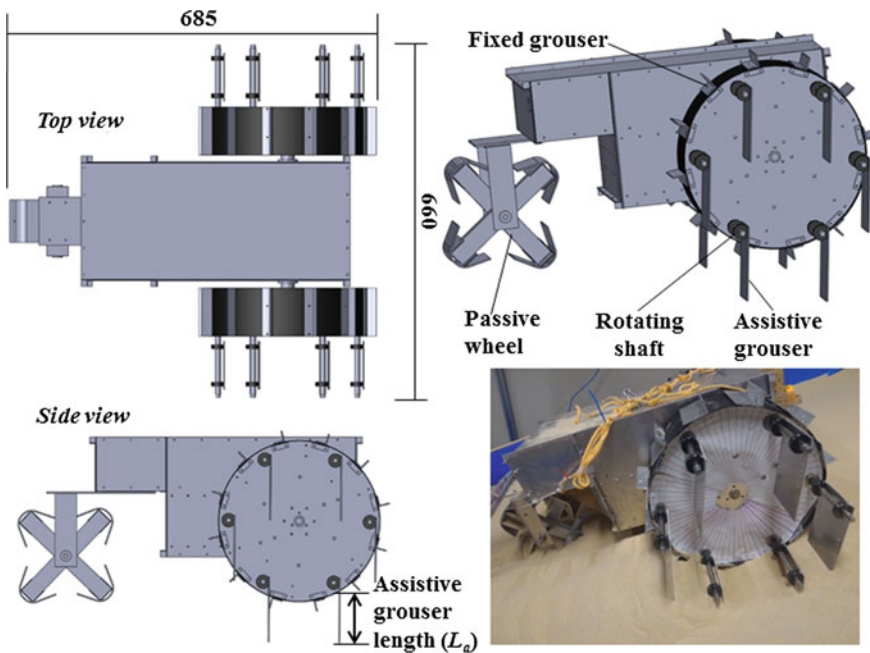


Fig. 2 CAD design of the rover used in the experiment with assistive grouser attached, and a picture of the rover on a sand test bed [5]. Assistive grouser length L_a is measured distance from the surface of the wheel until the tip of the grouser. Fixed grouser length is measured from the surface of the wheel to the tip of the grouser

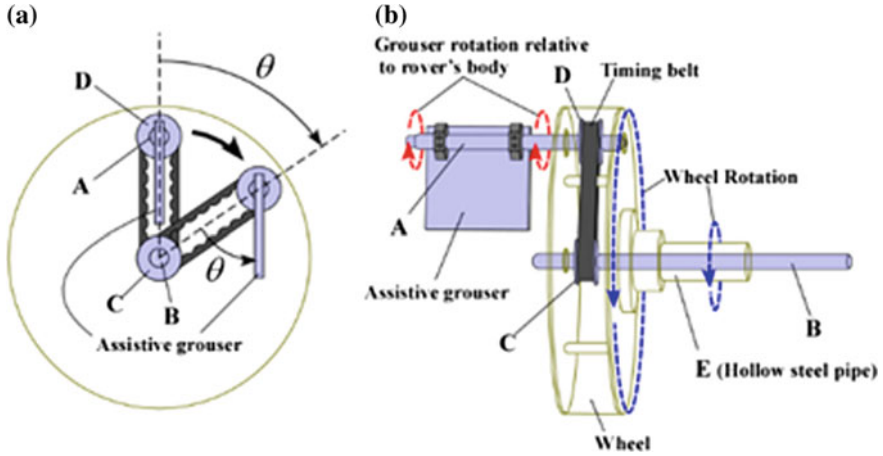


Fig. 3 **a** Assistive grouser maintains a constant angle independent of wheel rotation because it is locked in place by timing belts and pulleys, **b** the angle of the wheel and the assistive grousers were controlled using dedicated motors that are connected to a hollow steel pipe for the wheels and a central shaft B for the assistive grousers

2 Assistive Grouser Mechanism

The assistive grousers are able to maintain a constant angle independent of the wheel rotation because the grousers are fixed to a shaft which angle is controlled using timing belts and pulleys as shown in Fig. 3a. The assistive grouser mechanism consists of a dedicated motor that controls the angle of the assistive grousers through a system of belts and pulleys that is connected to a central shaft as shown in Fig. 3b.

3 Experiment

Experiment was carried out using an indoor rover locomotion test sand bed that is capable of producing inclines of 0° , 10° , 20° and 30° . The sand used in this experiment is Toyoura sand, which has an angle of repose of 29.71° [8], which means that the sand will crumble on its own when placed on an angle higher than approximately 30° .

Before each of the test run, the rover is placed at the foot of the incline and then the rover is allowed to independently climb the incline for a length of 1900 mm along the incline. The test run, however, was halted if the current consumption reaches 20 A as we deem the rover as stuck and unable to recover. The parameters for grouser lengths and assistive grouser angles used for the test were based on our previous work. During our previous work, we had concluded that for the

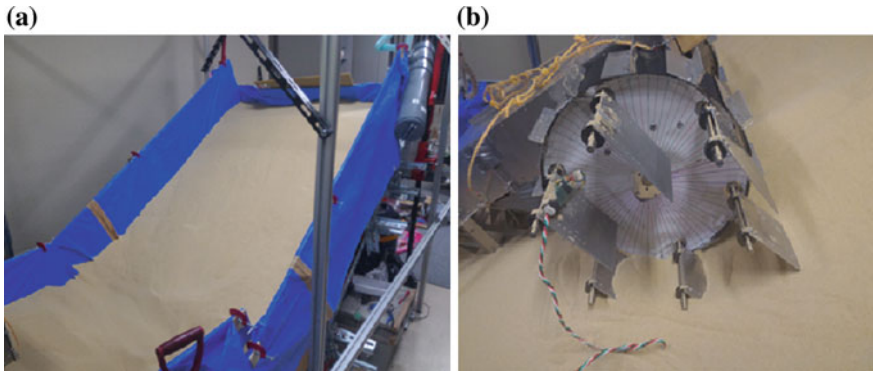


Fig. 4 **a** The test sand bed filled with Toyoura sand at 30° incline, **b** the rover with assistive grousers attached when climbing a 20° incline

conventional wheel with fixed grousers, the grouser length (measured from the wheel surface to the tip of the grouser) that produced the most optimal performance is 80 mm, while for the modified wheel with assistive grouser mechanism attached, the best performance was produced when the assistive grouser length L_a (refer to Fig. 2) was 90 cm with the grouser angled 20° forward from gravity vertical direction for inclines of 0° and 10°, and grouser angled 40° forward from gravity vertical direction for inclines of 20° and 30°. The rotation speeds for both of the wheels are set to be 1 revolution per minute.

Current consumption was measured using current sensors (U.R.D. Ltd., Yokohama, Japan, HCS-20-50-AS) attached to the wires powering DC voltage to the wheel DC motors (Fig. 4).

4 Results and Discussion

Results for the current measurement are shown below for 0° incline (Fig. 5), 10° incline (Fig. 6), 20° incline (Fig. 7), and 30° incline (Fig. 8).

For the current consumption on 0° incline as shown in Fig. 5, the conventional rover with fixed grousers produced a sharp spike when the wheel started spinning. This could be caused by high starting torque required as a number of the long grousers are already inside the sand when the test run begins, resulting in a large wheel rolling resistance. We can also see that the current fluctuates rapidly as the wheel turns on the flat surface, which shows a slight downward trend as time increases. On the other hand, the wheel motor current consumption when the assistive grousers were attached showed a more consistent current consumption throughout the test run. The current consumption shows an oscillating pattern which can be explained by the periodical difference in wheel rolling resistance when the grousers periodically enter and exit the sand surface as the wheel rotates.

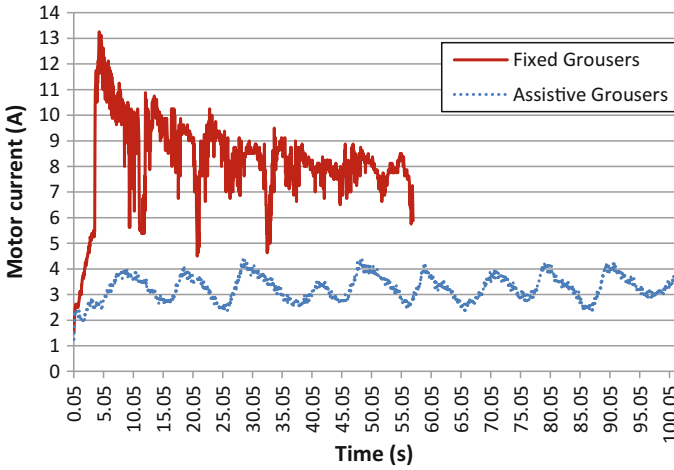


Fig. 5 Wheel motor current consumption for rover with fixed grousers and assistive grousers traversing on 0° incline. Lengths for the fixed grousers are 8 cm while lengths for the assistive grousers are 9 cm with 20° grouser angle

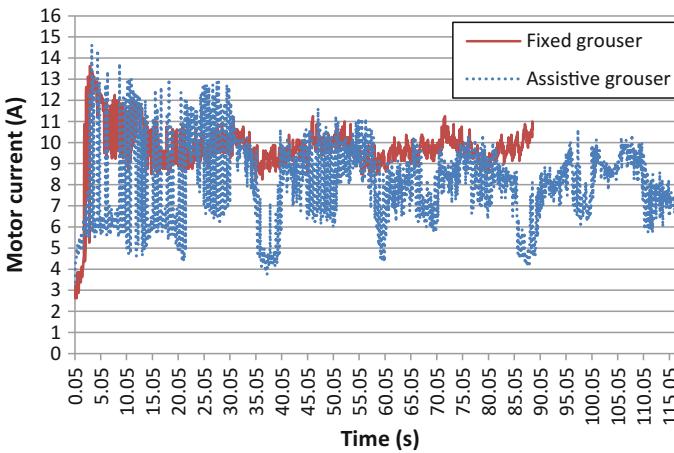


Fig. 6 Wheel motor current consumption for rover with fixed grousers and assistive grousers traversing on 10° incline. Lengths for the fixed grousers are 8 cm while lengths for the assistive grousers are 9 cm with 20° grouser angle

The conventional wheeled rover, however, manages to finish the 1900 mm run in about 57 s, compared to 100 s for the rover with assistive grousers. This shows that on a 0° incline, the conventional wheels are able to provide more forward traction compared to when using the assistive grousers.

For test runs on 10°, the rover with conventional wheels produced an almost similar current consumption trend as when on a 0° incline, with a slight increase in

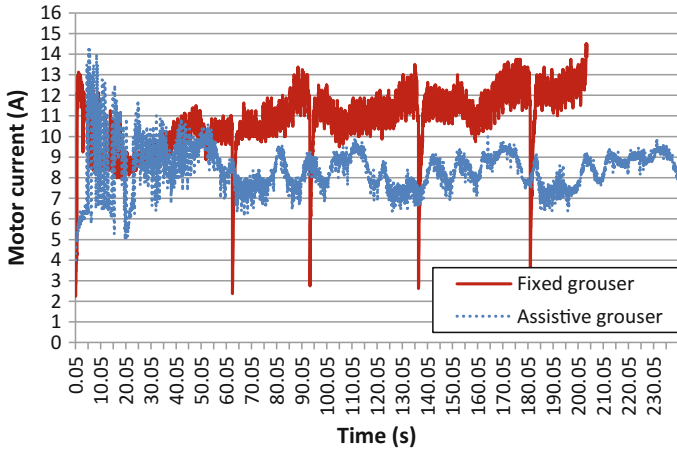


Fig. 7 Wheel motor current consumption for rover with fixed grousers and assistive grousers traversing on 20° incline. Lengths for the fixed grousers are 8 cm while lengths for the assistive grousers are 9 cm with 40° grouser angle

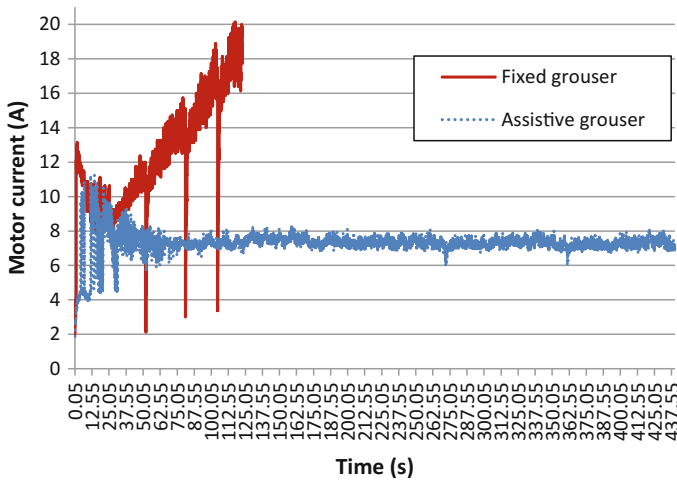


Fig. 8 Wheel motor current consumption for rover with fixed grousers and assistive grousers traversing on 30° incline. Lengths for the fixed grousers are 8 cm while lengths for the assistive grousers are 9 cm with 40° grouser angle. It should be noted that the run for fixed grousers was halted when the current consumption reaches 20 A, meaning the rover did not finish the climb

average current consumption. For the rover with assistive grousers, the current consumption pattern showed large fluctuations throughout the experiments. This could be caused by the increased rolling resistance of the wheel when rolling on a 10° incline, and since the assistive grousers horizontal movement speed does not

match the horizontal speed of the wheel itself translated from its angular speed, the assistive grousers might have acted as an anchor, resisting the wheel from moving forward.

On an incline of 20° , the current consumption patterns show a clear difference between fixed grouser wheels and wheels with assistive grousers. Both wheels show fluctuations at the beginning of the run as the sand surface experiences crumbling due to the wheel rotation, resulting in an inconsistent wheel rolling resistance value. As time continues, the wheels manage to obtain a more constant traction and also experience a more consistent resistance. This is what we refer to as a steady state for the rover locomotion. However we can see that the current consumption of the rover with fixed grousers continue to increase with time, while the rover with assistive grousers is able to maintain a relatively constant current consumption, with a 3 A difference in average current consumption during the steady state. It should also be noted, that the current consumption data also showed sudden dips, which is caused by slipping of the timing belts powering the wheels during the test run.

On the incline of 30° , the rover with fixed grousers did not manage to finish the test run as the current consumption continues to rise to 20 A from the moment the wheels turned, and we interpret this as the wheel unable to recover from sinking into the 30° soft sand slope. The rover with assistive grousers however, is able to finish the climb with a relatively stable current consumption after reaching a steady state. This shows that the assistive grousers are extremely effective on steep slopes, even on slopes of 30° .

5 Conclusion and Future Works

As a conclusion, the results from test runs on 0° and 10° inclines show that although the average current consumption for the fixed grouser wheels are higher than assistive grouser wheels, considerations should be given of the effect of assistive grousers on rover movement speed, as the fixed grousers are able to provide traction with minimal slip on low inclines, resulting in a higher movement speed. On 20° and 30° inclines, however, the rover with assistive grousers had proven that assistive grousers are able to help the rover traverse over steep inclines with a more stable and lower power consumption, which is important for rovers powered by onboard batteries. For future work, we are designing a new rover with a more robust powertrain to circumvent the problem of the timing belt slipping under a large load. We are also interested in investigating the effects of various angles of the assistive grousers on the performance of the rovers. Computer simulations will also be carried out to model the wheel-terrain interaction when assistive grousers are used.

Acknowledgements The authors would like to thank Universiti Malaysia Pahang (UMP) for the financial aid under grant RDU1703191.

References

1. Sutoh, M., Yusa, J., Ito, T., Nagatani, K., Yoshida, K.: Traveling performance evaluation of planetary rovers on loose soil. *J. Field Robot.* **29**, 648–662 (2012)
2. Wakabayashi, S., Sato, H., Nishida, S.-I.: Design and mobility evaluation of tracked lunar vehicle. *J. Terramech.* **46**, 105–114 (2009)
3. Heverly, M., Matthews, J., Lin, J., Fuller, D., Maimone, M., Biesiadecki, J., Leichty, J.: Traverse performance characterization for the Mars Science Laboratory rover. *J. Field Robot.* **30**, 835–846 (2013)
4. Kohanbash, D., Moreland, S., Wettergreen, D.: Plowing for rover control on extreme slopes. In *Field and Service Robotics*, Yoshida, K., Tadokoro, S., (Eds.) Springer Berlin, Heidelberg: Heidelberg, Germany (2014), pp. 399–413
5. Arvidson, R.E., Bell, J.F., Bellutta, P., Cabrol, N.A., Catalano, J.G., Cohen, J., Crumpler, L.S., Des Marais, D.J., Estlin, T.A., Farrand, W.H. et al.: Spirit Mars rover mission: overview and selected results from the northern home plate winter haven to the side of Scamander crater. *J. Geophys. Res.* **115**, E00F03 (2010)
6. Arvidson, R.E., Ashley, J.W., Bell, J.F., Chojnacki, M., Cohen, J., Economou, T.E., Farrand, W.H., Fergason, R., Fleischer, I., Geissler, P. et al.: Opportunity Mars rover mission: overview and selected results from purgatory ripple to traverses to endeavour crater. *J. Geophys. Res.* **116**, E00F15 (2011)
7. Ibrahim, A.N., Aoshima, S., Shiroma, N., Fukuoka, Y.: The effect of assistive anchor-like grousers on wheeled rover performance over unconsolidated sandy dune inclines. *Sensors* **16**(9), 1507 (2016)
8. Nakashima, H., Shioji, Y., Kobayashi, T., Aoki, S., Shimizu, H., Miyasaka, J., Ohdoi, K.: Determining the angle of repose of sand under low-gravity conditions using discrete element method. *J. Terramech.* **48**, 17–26 (2011)

Part III
Artificial Intelligence

Development of Ergonomic Vehicle Model and Decision Support System for Driving Fatigue



Mohammad Firdaus Ani, Seri Rahayu Kamat, Minoru Fukumi, Momoyo Ito, Mohamad Minhat and Nur Syafiqah Rayme

Abstract Driving fatigue has been recognized as one of the significant contributory factors to the road accidents and fatalities in Malaysia. The aim of this study was to develop an ergonomic vehicle model (EVM) and decision support system (DSSfDF) model for improving the driving fatigue problem among the road users. The ergonomic vehicle model uses to capture the user information data and acts as the database storage to store all the input data and information. While the decision support system provides a systematic analysis and solution to minimize the risk and the number of accidents associated with driving fatigue. There are 6 main components as the pillars for the development of EVM and DSSfDF model; ergonomics evaluation tools, graphical user interface (GUI), ergonomics database, working memory, inference engine, and knowledge base. Both models are essential system and reliable advisory tool for providing analysis on risk factors that contribute significantly to driving fatigue and providing solutions and recommendation to the problem related to driving fatigue. Further analysis and validation are required in future to get the reliable system before being commercialized.

Keywords Driving fatigue · Ergonomic vehicle model · Decision support system · Graphical user interface · Inference engine · Working memory

M. F. Ani (✉) · S. R. Kamat · M. Minhat · N. S. Rayme
Faculty of Manufacturing Engineering, Universiti Teknikal Malaysia Melaka,
76100 Durian Tunggal, Melaka
Malaysia
e-mail: mohammad.firdaus.ani@gmail.com

M. F. Ani · S. R. Kamat
Tokushima Malaysia Academic Center (TMAC), Tokushima University,
2-1 Minamijosanjima-Cho, 770-8506 Tokushima, Japan

M. F. Ani · S. R. Kamat · M. Fukumi · M. Ito
Department of Information Science and Intelligent System, Tokushima University,
2-1 Minamijosanjima-Cho, 770-8506 Tokushima, Japan

1 Introduction

Malaysia aspires to be developed the country by 2020 as outlined in the ninth and tenth Malaysia Plan [1, 2]. However, the research study by [3] has made a prediction on fatalities and found that there will be 10,716 fatalities in Malaysia during 2020. In fact, the data revealed by World Health Organization (WHO) shows that the fatality rate in Malaysia is the highest among the Association of Southeast Asian Nations (ASEAN) countries with 25 fatalities per 100,000 individuals [4, 5]. The WHO's data in Figs. 1 and 2 prove that Malaysia has a significant traffic and driving problem based on the high fatality rate.

Based on statistic data, Malaysia has recorded 7,152 road fatalities and 521,466 road accidents in 2016 as shown in Fig. 3 [6–9]. Besides, the in-depth crash

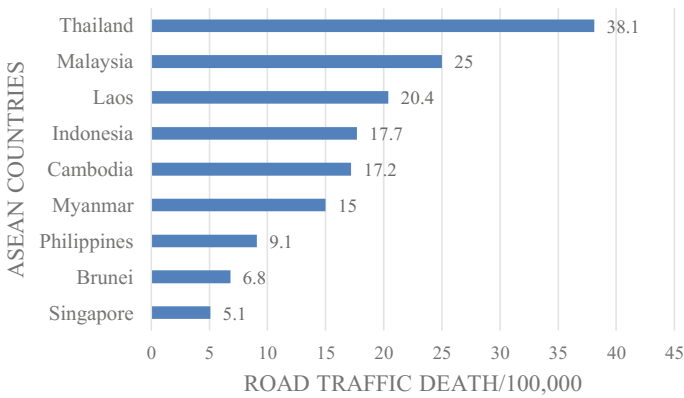


Fig. 1 Road fatality rate among the ASEAN countries [4]

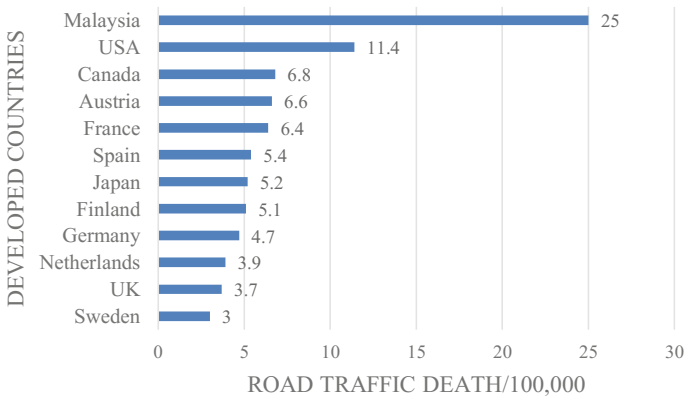


Fig. 2 Road fatality rate among the developed countries [5]

TAHUN Year	JUMLAH REMALANGAN Total Number of Accidents	RECEDERAAN DAN REMATIAN Casualties			
		MATI Death	PARAH Serious	RINGAN Minor	JUMLAH Total
2007	363,319	6,282	9,273	18,444	33,999
2008	373,071	6,527	8,868	16,879	32,274
2009	397,330	6,745	8,849	15,823	31,417
2010	414,421	6,872	7,781	13,616	28,269
2011	449,040	6,877	6,328	12,365	25,570
2012	462,423	6,917	5,868	11,654	24,439
2013	477,204	6,915	4,597	8,388	19,900
2014	476,196	6,674	4,432	8,598	19,704
2015	489,606	6,706	4,120	7,432	18,258
2016	521,466	7,152	4,506	7,415	19,073

Fig. 3 Total number of injuries and fatalities caused by road accident in Malaysia from 2007–2016

investigation on some accident cases by Malaysia Institute of Road Safety Research (MIROS) has found that instead of risky driving and speeding, the driving fatigue is one of the vital contributors to the road accidents in Malaysia from 2007 until 2013 [6]. Driver fatigue is one of the key causes of the road accidents for the driver in transportation [10, 11]. Driver fatigue can be classified as one of the main areas of driver behavior that need to be addressed in order to reduce the number of people killed and seriously injured in road accidents. Based on the previous research, fatigue can be dangerous as other road safety issues such as drink driving and there are no laws regulating driver fatigue. As a driver, fatigue can cause and bring many problems and effects including slowing the driver reactions and decisions, decreasing the driver tolerance for other road users, poor lane tracking, and maintenance of speed and decreasing driver alertness.

According to [12], subjective feeling of fatigue which combined with negative effects on performance due to time spent on cognitively demanding tasks can somehow affect the driving performance due to sleepiness, monotonous driving environment condition and the length of driving period as previous studies proved [13–15]. There are some risk factors that play important roles in the occurrence of fatigued-traffic accidents. The previous work by [16] determined that prolonged driving without rest can increase the fatigue level and deteriorate the driving performance.

In terms of the development of decision support system (DSS) for transportation, there are many previous studies has been done. However, there is no study on the development of decision support system that focuses only on the causes of the road accidents especially driving fatigue. Hence, this study is the new propose decision support system framework in this field. The authors have reviewed some of the previous study on decision support system. The recent study by [17] developed the decision support system for road safety analysis for supporting the public

administration in planning safety intervention on the road network. The system is developed using a multi-criteria method called “Concordance Analysis”. Besides, the study by [18] developed the road safety knowledge-based decision support system. These DSS identify and rank hazardous sites on roadways in order to reduce the number of road accidents. Another recent study is the development of DSS for analysis of vulnerable road users’ safety issues called as SAFE BRAIN [19]. This DSS (Geographic Information System, GIS-based application) developed to select safety measures to reduce the risk of accidents of vulnerable road users.

Hence, this paper was prepared to counter this problem by proposing and developing the ergonomic vehicle model and decision support system for driving fatigue to provide systematic analysis and propose a solution to minimize the number of road accident and fatalities associated with driving fatigue. However, there are some limitations of this study as this study focused on the development of EVM and DSSfDF model, and some of the methodologies are already discussed by the authors in previous studies.

2 Methodology

There are six main components as the pillars for the development decision support system (DSS), which contains two main models, namely, EVM and DSSfDF model. The EVM captures user’s data and information such as user and vehicle profile, and human-machine-environment domain which consists the risk factors data. Meanwhile, the DSSfDF provide the analysis of the data and information that captured by the EVM. In this study, the authors have referred to some of the previous studies [20–22] as the guidelines in developing the decision support system for driving fatigue.

2.1 Ergonomics Evaluation Tools

The purpose of this components is to analyze the risk factors by conducting the real road test experiment. However, the authors have used the regression model as the ergonomics evaluation tools for this study. The users can use the regression model to get their result and data on the risk factors without doing the real road test experiment [23–30]. The six groups of the regression model, which represented six risk factor of driving fatigue were developed in the author’s previous studies. The development of regression models is not been discussed in this paper.

2.2 Graphical User Interface

The GUIs are used as a medium for the user, EVM and DSSfDF model to communicate between them. Python programming language is used to develop the GUI. Python provides various options for developing GUI, and for this study, the authors choose to use Tkinter. Tkinter (Tk) is the standard GUI library for Python that provides a fast and easy way to create GUI applications. Four main GUIs have been designed in this study to perform various functions; user’s profile GUI, vehicle’s profile GUI, risk factor’s GUI, and Result’s GUI. The user provides information such as user’s profile, vehicle’s profile, and the data about risk factors to the ergonomic database in EVM through the GUIs. Figure 4 shows one of the GUI for decision support system of driving fatigue.

2.3 Ergonomics Database

Ergonomics database is the main components of the EVM. This database captured and stored all the data and information of the risk factors associated with the human-machine-environment domain before being retrieved by the DSSfDF model. The six risk factors are identified as the vital factor contributing to the driving fatigue and have been assigned to the human-machine-environment domain as shown in Fig. 5. All the risk factors are selected based on the real road test experiment and a previous study that has proven all these factors give a significant effect on fatigue while driving [23–30]. The whole-body vibration (WBV), muscle activity (MA), heart rate (HR), seat pressure distribution (SPD), hand grip force



Fig. 4 The GUI of the decision support system

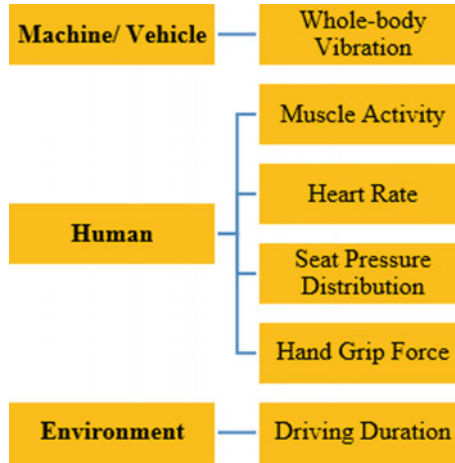


Fig. 5 Human-machine-environment domain

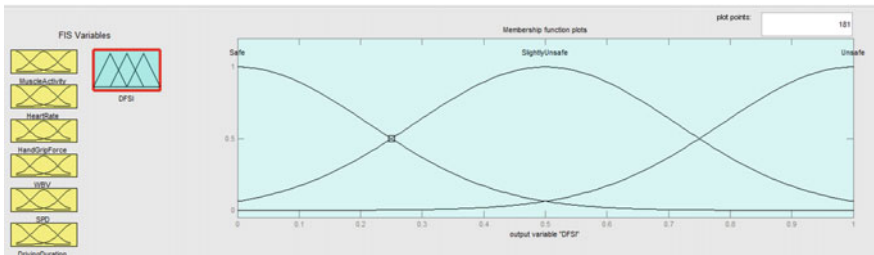


Fig. 6 The FIS displaying the example of a linguistic variable

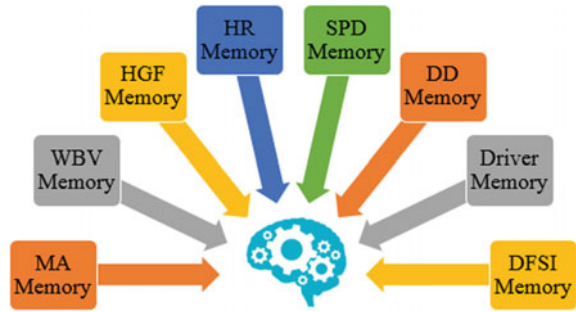
(HGF), and driving duration (DD) have been identified as the significant factors contribute to driver fatigue.

2.4 Working Memory

Working memory temporarily stores the data and the results of the analysis. The DSSfDF is provided with eight working memories for each of the risk factors and a driving fatigue strain index (DFSfI) [31, 32]. DFSfI was developed using the fuzzy inference system (FIS) by MATLAB software capability. The FIS consist of the membership function of inputs, fuzzy linguistic rules, and output memberships function as shown in Fig. 6.

The details study on the development of DFSfI can be found in the author previous study entitled “Development of Driving Fatigue Strain Index using Fuzzy to Analyze the Risk Level of Driving Activity” [32]. The Fig. 7 shows the structure of working memories of the DSSfDF model.

Fig. 7 The structure of working memories of the DSSfDF model



All the working memories consist of the following classes:

1. Driver Memory: Collects data and information on driver's profile; type of vehicle, vehicle category, vehicle model, model year, driver name, age, gender, weight and height, health status, driving experience, and frequency of driving per day.
2. Muscle Activity (MA) Memory: Save data and information, and results of muscle activity analysis
3. Whole-body vibration (WBV) Memory: Save data and information, and results of whole-body vibration analysis.
4. Hand Grip Force (HGF) Memory: Save data and information, and results of hand grip pressure force analysis.
5. Heart Rate (HR) Memory: Save data and information, and results of heart rate analysis.
6. Seat Pressure Distribution (SPD) Memory: Save data and information, and results of seat pressure distribution analysis.
7. Driving Duration (DD) Memory: Save data and information, and results of driving duration analysis.
8. Driving Fatigue Strain Index (DFSI) Memory: Save results of DFSI and solutions.

2.5 Knowledge Base

The knowledge base contains the rule sets for the analysis such as muscle activity rule, hand grip force rule, whole-body vibration rule, heart rate rule, seat pressure rule, driving duration rule and driving fatigue strain index rule as shown in Fig. 8. This is done using fuzzy logic [31, 32].

In this study, the Mamdani-type model [33–36] is used as the inference method, which uses the IF-THEN rules. The rule sets consist of a list of IF statements, and a list of THEN conditions to process any input data and provide a set of alternative

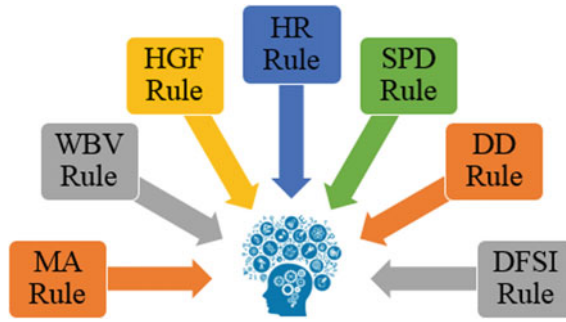


Fig. 8 The rule sets contain in knowledge base of the DSSfDF model

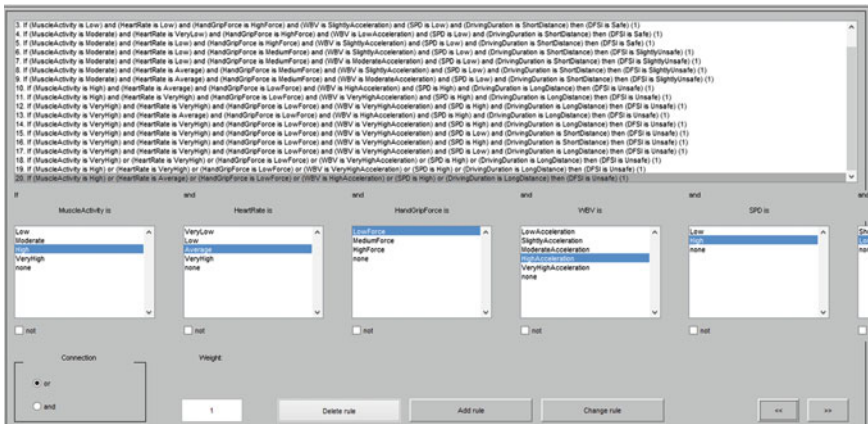


Fig. 9 The rule sets create using the FIS

solutions and conclusions. The FIS by MATLAB is used to create the rule sets as shown in Fig. 9.

2.6 Inference Engine

The inference engine is used to obtain the results and draw the new conclusion by matching the rule sets in the knowledge base and the data available in the working memory. The working process is done using fuzzy logic by applying forward chaining method [31, 32]. The forward chaining works by processing the data first and continuously using the rules in the knowledge base to draw new conclusions given by those data as reflected in Fig. 10 [37, 38]

The forward chaining operates through a top-down approach which takes data available in the working memory before the results being generating based on

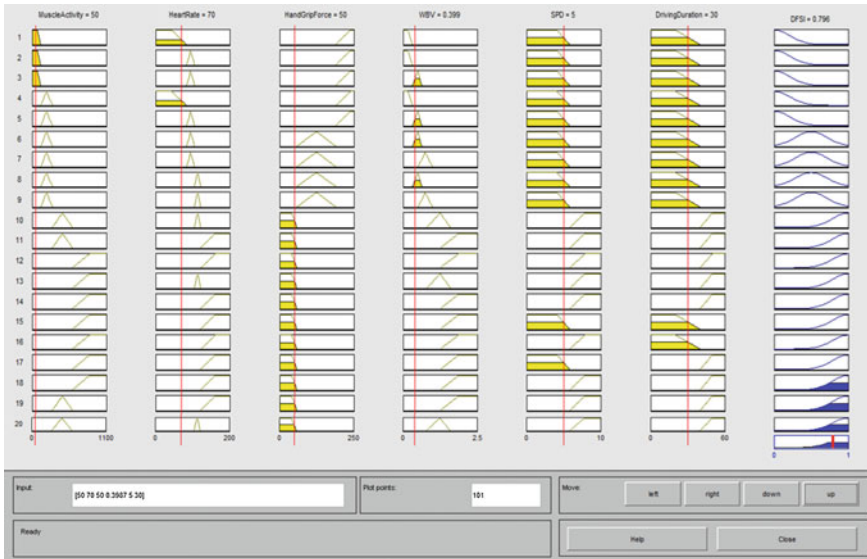


Fig. 10 The FIS’s rule viewer represents the measure of the degree of DFSI

satisfied conditions of rules in the knowledge base. The values of each linguistic variables are entered into the FIS’s rule viewer to get the defuzzification value that shows a measure of the degree of DFSI as reflected in Fig. 10.

This paper does not focus and discuss in details about the FIS and the development of fuzzy logic. However, the readers can find the details about it in the authors’ recent study entitled “Development of Driving Fatigue Strain Index using Fuzzy to Analyze the Risk Level of Driving Activity”.

3 Results and Discussion

This study has developed the EVM and DSSfDF model, which is the main models for the development of decision support system (DSS) model for driving fatigue. Figure 11 shows the DSS model which consist of EVM and DSSfDF model.

Both models have to be integrated into DSS to provide the systematic and rapid analysis of risk factors associated with driving fatigue. In this system, the ergonomics database was created for the EVM and the working memory for the DSSfDF model. The system will obtain the data and information on the user and vehicle profile, and risk factors, which entered by the users through the GUI (see Fig. 4) and stores them into the database in the EVM. In this study, MySQL is used as the database. MySQL is an open-source relational database management system (RDBMS), which is the most popular database and offers the cost-effective delivery of reliable, high performance and scalable Web-based and embedded database

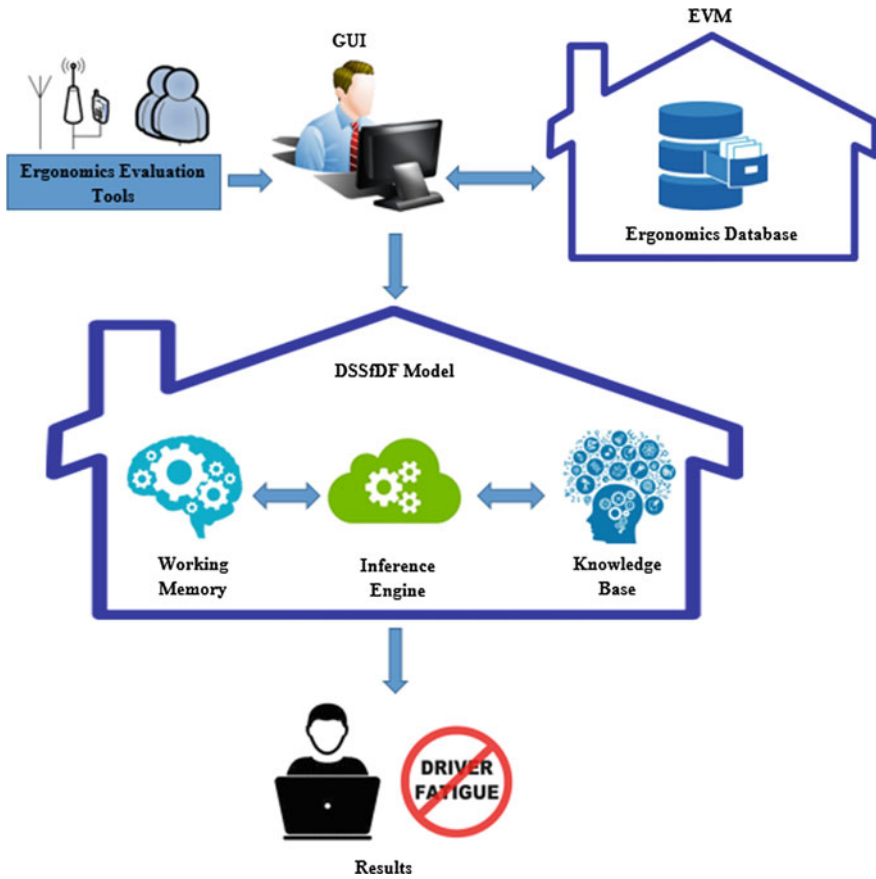
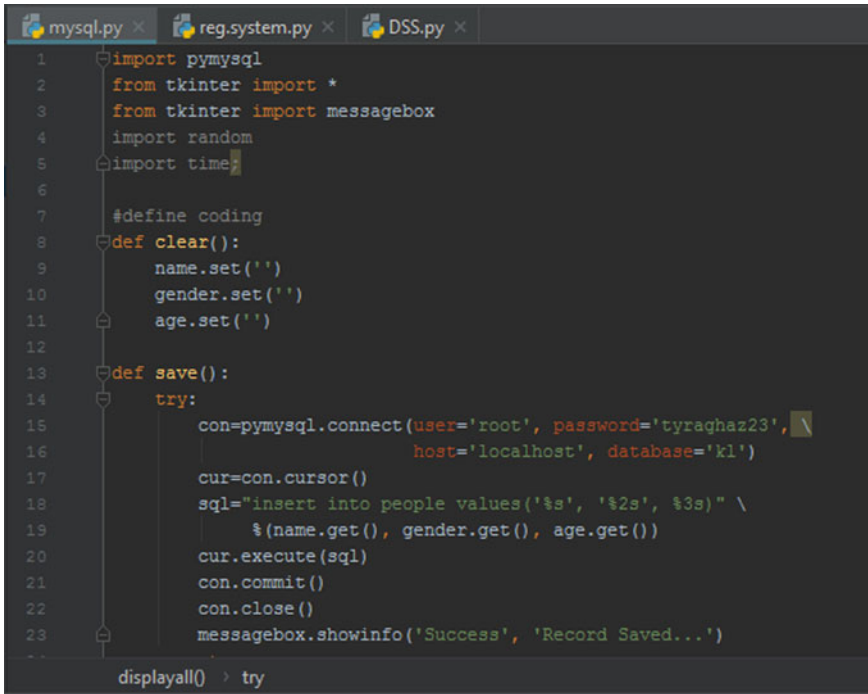


Fig. 11 EVM and DSSfDF in decision support system

applications. The PyMySQL is used as the application program interface (API) to connect the MySQL database server and perform the database operations. PyMySQL is fully written in Python and can be used from Python implementations such as Tkinter. The PyMySQL module is imported into the python program. The database server, database user, password, database name, and encoding is specified to create a connection object using the PyMySQL module as shown in Fig. 12.

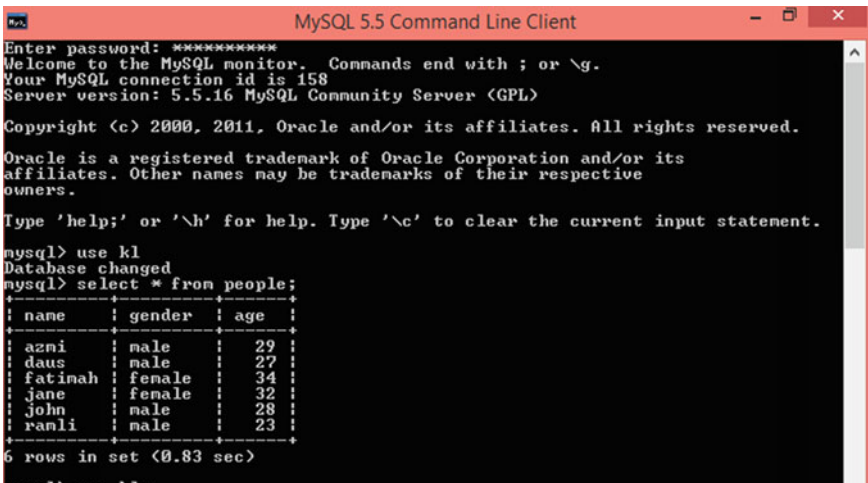
The database can be monitor using the MySQL command line client by entering the database password and calling the database name. Figure 13 shows the MySQL command line client.

This data and information have then been retrieved by the inference engine before it will send to the working memory. Then, the inference engine will examine and matches the data in the working memory with the available rule sets (see Fig. 9) in the knowledge base to generate results and draw a new conclusion and



```
mysql.py x reg.system.py x DSS.py x
1 import pymysql
2 from tkinter import *
3 from tkinter import messagebox
4 import random
5 import time
6
7 #define coding
8 def clear():
9     name.set('')
10    gender.set('')
11    age.set('')
12
13 def save():
14     try:
15         con=pymysql.connect(user='root', password='tyraghaz23',
16                             host='localhost', database='k1')
17         cur=con.cursor()
18         sql="insert into people values('%s', '%2s', %3s)" \
19             %(name.get(), gender.get(), age.get())
20         cur.execute(sql)
21         con.commit()
22         con.close()
23         messagebox.showinfo('Success', 'Record Saved...')
24
25 displayall() > try
```

Fig. 12 Importing PyMySQL and create connection using PyMySQL module



```
MySQL 5.5 Command Line Client
Enter password: *****
Welcome to the MySQL monitor.  Commands end with ; or \g.
Your MySQL connection id is 158
Server version: 5.5.16 MySQL Community Server <GPL>

Copyright (c) 2000, 2011, Oracle and/or its affiliates. All rights reserved.

Oracle is a registered trademark of Oracle Corporation and/or its
affiliates. Other names may be trademarks of their respective
owners.

Type 'help;' or '\h' for help. Type '\c' to clear the current input statement.

mysql> use k1
Database changed
mysql> select * from people;
+----+-----+-----+
| name | gender | age |
+----+-----+-----+
| azni  | male   | 29  |
| daus  | male   | 27  |
| fatinah | female | 34  |
| jane  | female | 32  |
| john  | male   | 28  |
| ramli | male   | 23  |
+----+-----+-----+
6 rows in set (0.83 sec)
```

Fig. 13 The MySQL command line client use to monitor the database

Table 1 The example of data set from the previous studies

Risk Factors	Results
MA	50.0000 μV
HR	70.0000 bpm
HGF	50.0000 N
WBV	0.3987 m/s^2
SPD	5.0000 kPa
DD	30.0000 min

solution. For example, by using the data set available from the previous study [23–30] as shown in Table 1, the data were entered into the FIS.

The Fig. 14 shows the FIS generate the results and draw a new conclusion based on the entered data or input linguistic.

The results obtained will be saved in the working memory or directly displayed to the users through GUI.

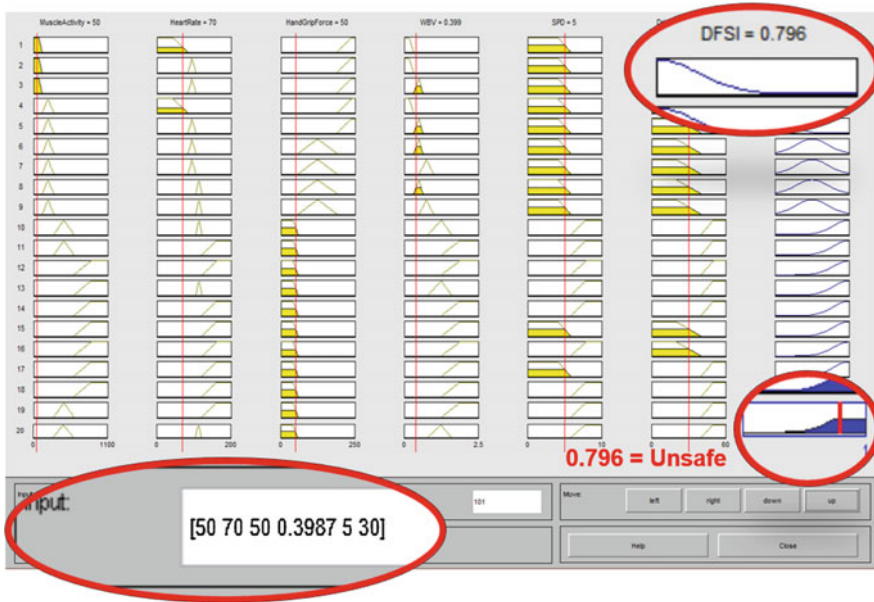


Fig. 14 The FIS generate the result and draw a new conclusion

4 Conclusion

This paper presents the development of EVM and DSSfDF model, which are the vital model in the decision support system. Both models are very important to provide the analysis of the risk factors that contribute significantly to the driving fatigue. The EVM and DSSfDF model will successfully provide the driving condition's risk level for the road users. Besides, the system and models give an early warning and detection of fatigue and give the better solutions and recommendations to the road users while driving. Indirectly, become one of the efforts in order to reduce the number of road accidents and fatalities especially in Malaysia. The main objectives of this study were successfully achieved. However, further testing and validation analysis are required by the authors in future to ensure the system is reliable and effective to be used by the road users. Besides, to prove that the system is capable to reduce the number of road accidents especially in Malaysia.

Acknowledgements The authors would like to acknowledge the Universiti Teknikal Malaysia Melaka (UTeM) and Tokushima University for technical, educational, and financial support through the Tokushima U-UTeM Academic Center (TMAC) and under RAGS/1/2015/SG01/FKP/03/B00107.

References

1. Unit, E.P.: Tenth Malaysia Plan 2011–2015. Economic Planning Unit, Malaysia (2010)
2. Unit, E.P.: Tenth Malaysia Plan 2006–2010. Economic Planning Unit, Malaysia (2006)
3. Rohayu, S., Sharifah Allyana, S.M., Jamilah, M.M., Wong, S.V.: Predicting Malaysian Road Fatalities for Year 2020 (2012)
4. World Health Organization.: Violence, Injury Prevention, World Health Organization. Global status report on road safety 2013: supporting a decade of action. World Health Organization (2013)
5. Abdelfatah, A.: Traffic Fatality Causes and Trends in Malaysia. American University of Sharjah, Massachusetts Institute of Technology (2016)
6. Department of Statistics.: Department of Statistics Malaysia: The Official Website of Malaysia Statistics agency—Statistics of Malaysia. Social Statistic Bulletin, Malaysia 2016. <http://www.statistics.gov.my>, Accessed 29 Sept 2017
7. Ministry of Transport Malaysia: Transport Statistic Malaysia 2016. Ministry of Transport Malaysia, <http://www.mot.gov.my/en/resources/yearly-statistic> (2016). Accessed 31 Oct 2017
8. Malaysia Institute of Road Safety Research: General Road Accident Statistic in Malaysia 2016. <https://www.miros.gov.my/1/page.php?id=364>. Accessed 29 Sept 2017
9. OECD/ITF.: Malaysia in Road Safety Annual Report 2015. OECD Publishing, Paris, <http://dx.doi.org/10.1787/irtad-2015-29-en>. Accessed 15 June 2017
10. San, P.P., Ling, S.H., Chai, R., Tran, Y., Craig, A., Nguyen, H.: August. EEG-based driver fatigue detection using hybrid deep generic model. In Engineering in Medicine and Biology Society (EMBC), 2016 IEEE 38th Annual International Conference of the IEEE pp. 800–803 (2016). <https://doi.org/10.1109/embc.2016.7590822>
11. Desmond, P.A., Neubauer, M.C., Matthews, G., Hancock, P.A. (eds.): The Handbook of Operator Fatigue. Ashgate Publishing, Ltd. (2012)

12. Meletis, C.D., Barker, J.E.: Herbs and Nutrients for the Mind: A Guide to Natural Brain Enhancers, vol. 1. Greenwood Publishing Group (2004)
13. Otmani, S., Pebayle, T., Roge, J., Muzet, A.: Effect of driving duration and partial sleep deprivation on subsequent alertness and performance of car drivers. *Physiol. Behav.* **84**(5), 715–724 (2005). <https://doi.org/10.1016/j.physbeh.2005.02.021>
14. Papadelis, C., Chen, Z., Kourtidou-Papadeli, C., Bamidis, P.D., Chouvarda, I., Bekiaris, E., Maglaveras, N.: Monitoring sleepiness with on-board electrophysiological recordings for preventing sleep-deprived traffic accidents. *Clin. Neurophysiol.* **118**(9), 1906–1922 (2007). <https://doi.org/10.1016/j.clinph.2007.04.031>
15. Seen, K.S., Tamrin, S.B.M., Meng, G.Y.: Driving fatigue and performance among occupational drivers in simulated prolonged driving. *Global J. Health Sci.* **2**(1), 167 (2010)
16. Dobbie, K.: Fatigue-Related Crashes: An Analysis of Fatigue-Related Crashes on Australian Roads Using an Operational Definition of Fatigue. No. OR 23 (2002)
17. Fancello, G., Carta, M., Fadda, P.: A decision support system for road safety analysis. *Transport. Res. Procedia* **5**, 201–210 (2015). <https://doi.org/10.1016/j.trpro.2015.01.009>
18. Dell’Acqua, G., De Luca, M., Mauro, R.: Road safety knowledge-based decision support system. *Procedia Social Behavior. Sci.* **20**, 973–983 (2011). <https://doi.org/10.1016/j.sbspro.2011.08.106>
19. Tripodi, A., Persia, L., Di Mascio, P., Corazza, M.V., Musso, A.: A decision support system for analysis of vulnerable road users safety issues: results of the Saferbrain project. *Procedia Soc. Behav. Sci.* **53**, 841–850 (2012). <https://doi.org/10.1016/j.sbspro.2012.09.933>
20. Angehrn, A.A., Lüthi, H.J.: Intelligent decision support systems: a visual interactive approach. *Interfaces*, **20**(6), pp. 17–28 (1990). <https://doi.org/10.1016/j.inte.20.6.17>
21. Zak, J.: Decision support systems in transportation. In: *Handbook on Decision Making*, pp. 249–294 (2010). <https://doi.org/10.1007/978-3-642-13639-9-11>
22. Halim, I., Arep, H., Kamat, S.R., Abdullah, R., Omar, A.R., Ismail, A.R.: Development of a decision support system for analysis and solutions of prolonged standing in the workplace. *Safety Health Work* **5**(2), 97–105 (2014). <https://doi.org/10.1016/j.shaw.2014.04.002>
23. Kamat, S.K., Ani, M.F., Faiz, M.: A comparison study for the road condition with hand grip force and muscle fatigue. *Malaysia J. Public Health Med.* **16** (Suppl. 1): 7–13 (2016)
24. Ani, M.F., Kamat, S.R., Kushairi, S., Husain, K.: A mathematical modeling of psychophysical factor for driver fatigue. *J Mech. Eng.* in press
25. Ani, M.F., Kamat, S.R., Minhat, M., Fukumi, M., Ito, T.: A study of biomechanical factor for driver fatigue using regression model. In: *International. Design and Concurrent. Engineering 2017 and Manufacturing Systems Conference 2017*, Paper no. 9, JSME, pp. 7–9 September 2017
26. Ani, M.F., Kamat, S.R., Hambali, R.H., Mahmood, W.H.: A study of psychophysical factor (heart rate) for driver fatigue using regression model. *Safety Health Environ.* **38**, 9 (2017)
27. Ani, M.F., Kamat, S.R., Minhat, M., Fukumi, M., Ito, T.: Effect of vibration towards driving fatigue and development of regression model based on vibration. In: *Japan Society of Mechanical Engineers 27th Design Engineering and System Division Lecture 2017*, Paper No. G2506, 13–15 September 2017
28. Kamat, S.R., Ani, M.F., Husain, K.: A Comparison Study between right hand and left hand grip pressure force while driving. *Aust. J. Basic Appl. Sci.* **9**(19), 50–58 (2015)
29. Kamat, S.R., Ani, M.F.: A comparison study between the road condition with pressure distribution on the seat and car vibration. *Int. J. Emerg. Technol. Advanc. Eng.* **5** (2015)
30. Ani, M.F.: Developing Regression Models of Driver Fatigue Using An Ergonomics Approach. Master’s thesis, Universiti Teknikal Malaysia Melaka. <http://eprints.utm.edu.my/id/eprint/18595> (2016)
31. Ani, M.F., Kamat, S.R., Fukumi, M., Minhat, M., Ito, T.: A Construction Framework of Decision Support System for Improving Driving Fatigue (in press)
32. Ani, M.F., Fukumi, M., Kamat, S.R., Minhat, M.: Development of driving fatigue strain index using fuzzy logic to analyze risk levels of driving activity. *IEEJ Trans. Electron. Informat. Syst.* (in press)

33. Tadic, D., Savovic, I., Misita, M., Arsovski, S., Milanovic, D.D.: Development of a fuzzy logic-based inherent safety index for food industries. *Proc. Institut. Mechanic. Eng. Part E J. Process Mechanic. Eng.* **228**(1), 3–13 (2014). <https://doi.org/10.1177/0954408912466368>
34. Azadeh, A., Fam, I.M., Khoshnoud, M., Nikafrouz, M.: Design and implementation of a fuzzy expert system for performance assessment of an integrated health, safety, environment (HSE) and ergonomics system: the case of a gas refinery. *Inf. Sci.* **178**(22), 4280–4300 (2008). <https://doi.org/10.1016/j.ins.2008.06.026>
35. Gentile, M., Rogers, W.J., Mannan, M.S.: Development of a fuzzy logic-based inherent safety index. *Process Safety Environ. Prot.* **81**(6), 444–456 (2003). <https://doi.org/10.1205/095758203770866610>
36. Aluclu, I., Dalgic, A., Toprak, Z.F.: A fuzzy logic-based model for noise control at industrial workplaces. *Appl. Ergonom.* **39**(3), 368–378 (2008). <https://doi.org/10.1016/j.apergo.2007.08.005>
37. Abraham, A.: Rule-Based expert systems. *Handbook of measuring system design*. Wiley Online Library (2005). <https://doi.org/10.1002/0471497398.mm422>
38. Lee, T.Z., Wu, C.H., Wei, H.H.: KBS LUA: A knowledge-based system applied in river land use assessment. *Expert Syst. Appl.* **34**(2), 889–899 (2008). <https://doi.org/10.1016/j.eswa.2006.10.038>

Talent Identification of Potential Archers Through Fitness and Motor Ability Performance Variables by Means of Artificial Neural Network



Zahari Taha, Rabi Muazu Musa, Anwar P. P. Abdul Majeed, Mohamad Razali Abdullah and Mohd Hasnun Arif Hassan

Abstract The utilisation of artificial intelligence for prediction and classification in the sport of archery is still in its infancy. The present study classified and predicted high and low potential archers from a set of fitness and motor ability variables trained on artificial neural network (ANN). 50 youth archers with the mean age and standard deviation of (17.00 ± 0.56) drawn from various archery programmes completed a one end archery shooting score test. Standard fitness and ability measurements of hand grip, vertical jump, standing broad jump, static balance, upper muscle strength and the core muscle were conducted. The cluster analysis was used to cluster the archers based on the performance variables tested to high performing archers (HPA) and low performing archers (LPA), respectively. ANN was used to train the measured performance variables. The five-fold cross-validation technique was utilised in the study. It was established that the ANN model is able to demonstrate a reasonably excellent classification on the evaluated indicators with a classification accuracy of 94% in classifying the HPA and the LPA.

Keywords Archery · Machine learning · Classification · Artificial neural network

Z. Taha · R. M. Musa (✉) · A. P. P. Abdul Majeed · M. H. A. Hassan
Innovative Manufacturing, Mechatronics and Sports Laboratory,
Faculty of Manufacturing Engineering, Universiti Malaysia Pahang,
26600 Pekan, Pahang, Malaysia
e-mail: rabiumazu86@gmail.com

R. M. Musa · M. R. Abdullah
Faculty of Applied Social Sciences, Universiti Sultan Zainal Abidin,
21300 Kuala Terengganu, Terengganu, Malaysia

© Springer Nature Singapore Pte Ltd. 2018
M. H. A. Hassan (ed.), *Intelligent Manufacturing & Mechatronics*,
Lecture Notes in Mechanical Engineering,
https://doi.org/10.1007/978-981-10-8788-2_32

1 Introduction

Performance in archery is observed based on the amount of the scores of the arrows shot by an athlete that hit the board. Archery performance is influenced by numerous elements comprising environmental conditions, fatigue, and the athlete's technique, in addition to the effects of the materials that determine the behaviour of the bow and the arrow [1]. Humaid described that arms muscle strength has a greater contribution to assisting an archer during the execution of archery technique [2]. An archer could deliver a correct archery technique when there is a sufficient arms strength to draw and hold the bow.

Moreover, a number of evidences has demonstrated that certain physical fitness and motor abilities performance variables such as core body strength, upper body strength, handgrip, leg power and static balance play a role in the achievement of higher archery scores [2–5]. The evidence suggested that the aforementioned performance variables are crucial due to the fact that the sport involved several aerobic and anaerobic activities which in turn actuate the main muscle fibres during the stance aiming and releasing the arrow.

Artificial neural network (ANN) has been employed on a number of classification evaluation of physical or fitness performance parameters primarily due to its advantages against conventional methods [6]. Montoye et al. demonstrated that ANN was found to be better in predicting energy expenditure in comparison to linear mixed models and linear regression method [7]. Hagenbuchner et al. also utilised ANN as well as deep learning ensemble network to classify different activity type of preschool children [8].

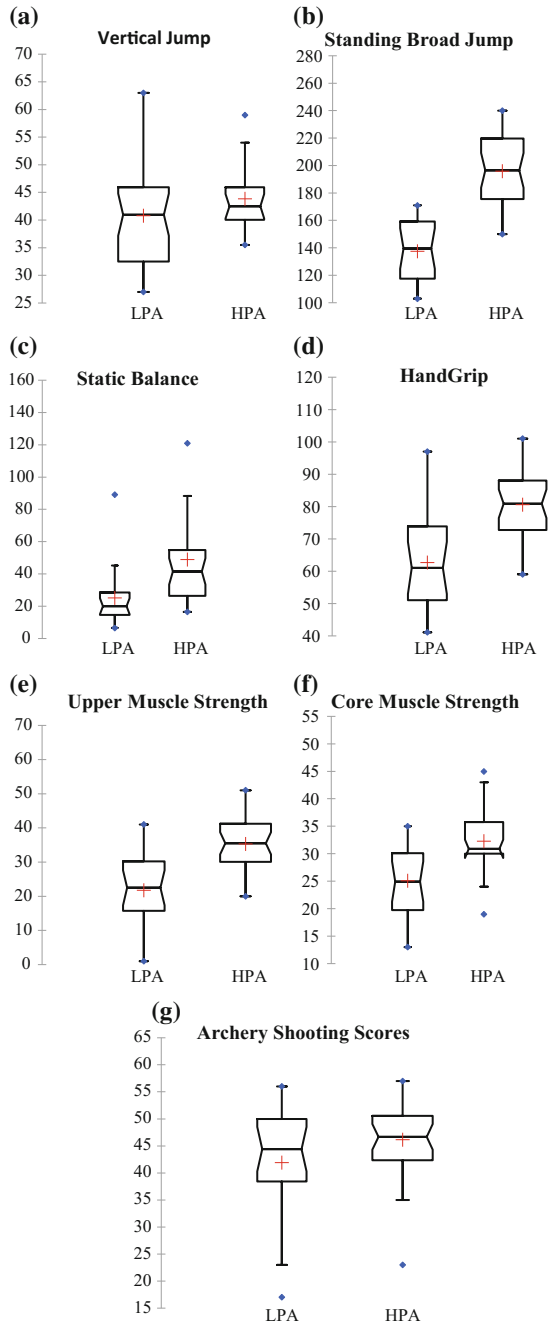
The purpose of the present study is to identify potential athletes in the sport of archery through the selected physical and motor ability performance variables i.e. hand grip, vertical jump, standing broad jump, static balance, upper muscle strength and core muscle strength, respectively in identifying future potential archers using ANN.

2 Methods

2.1 Participants

50 archers were enlisted in this investigation. The archers consisted of 37 male and 13 female youth between the age's range of 13–20 with a mean, and standard deviation of (17.0 ± 0.56) gathered from various archery programmes in Malaysia.

Fig. 1 Evaluations of performance variances of the archers based on the variables evaluated



2.2 *Fitness Assessments*

Standard fitness and motor ability related performance variables of sit up, push up, standing stork test, handgrip test, standing broad jump test and vertical jump test was administered in conformity with ideal physical fitness evaluations [9]. The archers completed a warm-up that composed of a 5–10 min jog and a set of stretches prior to the evaluation sessions. The archery shooting test was completed prior to the previous fitness testing utilizing a simulated competition shooting area of 50 m range. The archers were granted four trials shot before taking the final six arrows scores.

2.3 *Clustering*

The *k*-means clustering technique is employed to cluster the archers based on their performances in the selected variables and their shooting scores in which two classes, i.e. high potential archers (HPA) and low potential archers (LPA) are clustered (Fig. 1). Furthermore, the performance of the ANN in classifying HPA as well as LPA are investigated.

2.4 *Classification*

A single hidden multilayer perceptron ANN model with a single hidden layer utilizing sigmoid activation function was utilised in the study. A sensitivity test was carried out to evaluate the suitable number of neurons that are required to provide reasonable results by varying the number of neurons from 1 to 50 and it was found that 10 neurons are deemed sufficient. Furthermore, a tenfold cross-validation method was used in the study. The performance of the ANN model was evaluated through Orange 2.7 on a number of performance indicators namely classification accuracy (CA), sensitivity (SENS), and specificity (SPEC) and error rate (ER) (Table 1).

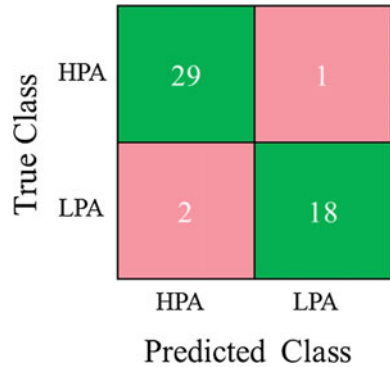
3 *Results and Discussion*

It could be seen from Table 1 that the evaluated ANN model is able to classify well the potential of the archers based on the selected performance variables with a reasonably high CA of 94%. The SENS and SPRC which is essentially the true positive rate or the positive class accuracy as well as the true negative rate or

Table 1 Performance evaluation of the ANN model

Performance indicators	Values (%)
CA	94
SENS	96.67
SPEC	90
ER	6

Fig. 2 ANN confusion matrix



negative class accuracy further suggest the efficacy of the ANN model. Figure 2 illustrates the confusion matrix attained by the model.

The result of the present study has showed that the assembled performance-related components set up in the study can determine or classify the performance of the archers i.e. HPA and LPA in conformity with the archers’ shooting scores. The general discoveries have explained that the named related performance variables under study are central to the archery performance.

It has been emphasized by the preceding investigators that several physical fitness and motor abilities performance variables such as the core body strength, upper body strength, handgrip, leg power and static balance play a role in the achievement of higher archery [6–8]. The capacity of the major muscles to act to the demand set upon them during the performance of the sport serves the archer to shoots the arrows consistently. It has additionally been surmised that muscle power, balance and handgrip capabilities support the archers to withstand the continuation of the sport for a long period of time [9].

Moreover, evidence has demonstrated that leg power and balancing ability or commonly called steadiness is one of the components that impact phases of the accuracies of an archer during aiming process. The stiffer the stability degree of the archer the smaller the resultant angle of the curve angle of the arrow [10]. This will curtail any obstruction from the impact of the external influences which can transform the direction of the arrow.

4 Conclusion

It could be concluded from the present investigation that the ANN model is able to classify well the potential archers based on the aforementioned fitness and motor ability performance variables. This finding are non-trivial as it would allow coaches to identify talented archers.

References

1. Taha, Z., Musa, R.M., Abdullah, M.R., Razman, M.A.M., Lee, C.M., Adnan, F.A., Abdullah, M.A., Haque, M.: The application of inertial measurement units and wearable sensors to measure selected physiological indicators in archery. *Asian J. Pharm. Res. Heal. Care* **9**, 85–92 (2017)
2. Humaid, H.: Influence of arm muscle strength, draw length and archery technique on archery achievement. *Asian Soc. Sci.* **10**, 28 (2014)
3. Bompa, T.O., Haff, G.G.: *Periodization: Theory and Methodology of Training*. Human Kinetics Publishers (2009)
4. Tinazci, C.: Shooting dynamics in archery: a multidimensional analysis from drawing to releasing in male archers. *Procedia Eng.* **13**, 290–296 (2011)
5. Taha, Z., Musa, R.M., Majeed, A.P.P.A., Alim, M.M., Abdullah, M.R.: The identification of high potential archers based on fitness and motor ability variables: a support vector machine approach. *Hum. Mov. Sci.* **57**, 184–193 (2018)
6. Suppiah, P.K., Musa, R.M., Abdullah, M.R., Lee, J.L.F., Maliki, A.B.H.M.: The effectiveness of a core muscles stability program in reducing the postural sway of adolescent archers: a panacea for a better archery performance. *Int. J. Physiother.* **4**, 296–301 (2017)
7. Suppiah, P.K., Musa, R.M., Wong, T., Kiet, K., Abdullah, M.R., Bisyr, A., Maliki, H.M., Kosni, N.A., Haque, M.: Sensitivity prediction analysis of the contribution of physical fitness variables on Terengganu Malaysian youth archers' shooting scores. *Int. J. Pharm. Sci. Rev. Res.* **43**, 133–139
8. Clarys, J.P., Cabri, J., Bollens, E., Smeckx, R., Taeymans, J., Vermeiren, M., Van Reeth, G., Voss, G.: Muscular activity of different shooting distances, different release techniques, and different performance levels, with and without stabilizers, in target archery. *J. Sports Sci.* **8**, 235–57 (1990)
9. Musa, R.M., Abdullah, M.R., Maliki, A.B.H.M., Kosni, N.A., Haque, M.: The application of principal components analysis to recognize essential physical fitness components among youth development archers of Terengganu, Malaysia. *Indian J. Sci. Technol.* **9** (2016)
10. Ertan, H., Kentel, B., Tümer, S.T., Korkusuz, F.: Activation patterns in forearm muscles during archery shooting. *Hum. Mov. Sci.* **22**, 37–45 (2003)

Classification of High Performance Archers by Means of Bio-physiological Performance Variables via k -Nearest Neighbour Classification Model



Zahari Taha, Rabi Muazu Musa, Anwar P. P. Abdul Majeed, Mohamad Razali Abdullah, Ahmad Fakhri Ab. Nasir and Mohd Hasnun Arif Hassan

Abstract The present study classified and predicted high and low potential archers from a set of bio-physiological variables trained via a machine learning technique namely k -Nearest Neighbour (k -NN). 50 youth archers drawn from various archery programmes completed a one end archery shooting score test. Bio-physiological measurements of systolic blood pressure, diastolic blood pressure, resting respiratory rate, resting heart rate and dietary intake were taken. Multiherarchical agglomerative cluster analysis was used to cluster the archers based on the variables tested into low, medium and high potential archers. Three different k -NN models namely fine, medium and coarse were trained based on the measured variables. The five-fold cross-validation technique was utilised in the present investigation. It was shown from the present study, that the utilisation of k -NN is non-trivial in the classification of the performance of the archers.

Keywords Bio-physiological variables • Artificial intelligence Classification • k -Nearest neighbour

1 Introduction

It has been reported that archery sport involves conscious breathing control and its synchronization limb movements [1]. Shooting in archery is the concurrent matching between breathing; gross motor control of body positioning; fine-motor

Z. Taha · R. M. Musa (✉) · A. P. P. Abdul Majeed · A. F. Ab. Nasir
M. H. A. Hassan

Innovative Manufacturing, Mechatronics and Sports Laboratory, Faculty of Manufacturing Engineering, Universiti Malaysia Pahang, 26600 Pekan, Pahang, Malaysia
e-mail: rabiumazu86@gmail.com

R. M. Musa · M. R. Abdullah
Faculty of Applied Social Sciences, Universiti Sultan Zainal Abidin, 21300 Kuala Terengganu, Terengganu, Malaysia

control of the archer's fingers, hands, elbows, legs, feet, and cheek; and the handling of perceptual cues associated with the target, the sights and the peep or string [2].

Moreover, though archery is not considered as physically exhaustive sport compared to other games, such as basketball, rugby, cycling or soccer, nevertheless, there is still a need for the archers to consider their nutritional status. For example, it has been proven a number of times that breakfast is the most essential meal of the day. When an archer is preparing to devote the entire day shooting or during a competition that could take the whole day, he/she will perform well with a healthy breakfast [3]. Evidence has also demonstrated that in the course of archery performance, an archer needs to attain a high level of attention and relaxation, and as such there is need to consider a number of cardiac parameters such as resting heart rate, resting systolic blood pressure, resting diastolic blood pressure as well as the pulmonary parameters which include resting respiratory rate [4]. These set of bio-physiological variables are vital for determining success in the sport of archery.

To date, different types of machine learning methods have been utilised for predicting and classifying a variety of human performance variables due to its inherent advantages against conventional means [5]. For instance, artificial neural networks have been employed to predict energy expenditure [6] as well as to classify activity types [7]. Random forest classifier, on the other hand, has been used also to classify activities from wrist-worn accelerometers [8] as well as categorizing the playing positions of elite junior football players [9] amongst others [10]. Nonetheless, the employment of *k*-NN in classifying potential archers based on a number of bio-physiological performance variables has yet been reported. Therefore, this study aims at evaluating the efficacy of the aforementioned classifier in determining low, medium and high potential archers.

2 Materials and Methods

2.1 Participants

50 archers were enlisted in this investigation. The archers consisted of 37 male and 13 female youth between the age's range of 13–20 with a mean, and standard deviation of (17.0 ± 0.56) gathered from various archery programme in Malaysia. The archery shooting test was completed prior to the previous fitness testing utilizing a simulated competition shooting area of 50 m range. The archers were granted four trials shot before taking the final six arrows scores. Informed consent was obtained in accordance with the procedures of the Ethical Review Board of the University Sultan Zainal Abidin, Malaysia.

2.2 *Nutritional Assessment*

The nutritional status of the archers was evaluated using their three days dietary recall. To achieve this aim, the researcher developed a form containing columns for the dietary of three days and the column for a time the meal is consumed. The form contained the serving size of each meal taken. The archers were enlightened on how to measure the quantity of each meal taken to ensure the accuracy of the actual dietary intake. The researcher instructed the archers to fill the form whenever they take their meals and drinks. The data collected for all their dietary intake of three days (two-week days and a weekend) was assessed using a Nutritionist Pro software to determine their nutritional status.

2.3 *Resting Heart Rate, Diastolic and Systolic Blood Pressure Measurement*

Resting heart rate (RHR), resting systolic blood pressure (RSBP) and resting diastolic blood pressure (RDBP) of the archers were measured using Omron automatic Blood Pressure Monitor Device (HEM-7120) which has been reported as a reliable tool for measuring the related parameters [11]. All the specified cardiac parameters were measured while the archers were in resting condition and sitting comfortably on a chair, the device is placed at the level of chest, and the arm strap was attached securely on the left arm of the archers after which the strap was inflated automatically by the device, and monitor displayed result of Blood pressure, pulse rate measurement was noted. All measurements were completed early in the morning prior to any exercises or warm up.

2.4 *Resting Respiratory Rate Measurement*

The resting respiratory rate (RRR) was measured while the archers were comfortably sitting on a chair in an erect position. The palpating respiratory movements of archer's chest was assessed manually by a specialist therapist for a period of 1 min. A stop watch was used for 1 min time setting to ensure that the reading was collected within 1 min as suggested by the preceding researchers [12]. The assessments were conducted three times, and the maximum value was taken.

2.5 Clustering

The hierarchical agglomerative cluster analysis technique is employed to cluster the archers based on their performances in the selected variables and their shooting scores in which three classes, i.e. high potential archers (HPA), medium potential archers (MPA) and low potential archers (LPA) are clustered. Furthermore, the performance of the k -NN algorithm in classifying HPA, MPA as well as LPA are investigated.

2.6 Classification

The k -NN algorithm is employed in this study to classify the clustered data mentioned earlier, i.e. LPA, MPA and LAP. The algorithm stems by the notion that a sample is assigned to a predefined class per the majority of its k -nearest neighbour in a given data space. The distance matrix is then employed to compute the distance of the individual samples from all the other samples prior to being sorted based on the distance.

In this study, three variations of k -NN i.e., fine, medium and coarse are investigated. The number of neighbours, k for fine, medium and coarse are 1, 10 and 100, respectively. All evaluated variations utilised the equally distanced Euclidean distance metrics. Furthermore, a fivefold cross-validation technique was adopted to mitigate the issue of overfitting. The variations of the k -NN models employed in this study are evaluated by means of classification accuracy (ACC), precision (PREC) as well as recall (REC).

3 Results and Discussion

Figure 1 displays group's profile plot of each cluster of relative performances. The figure describes the performances of the archers based on the variables examined. From the figure, it can be detected that the HPA (green colour), has the highest performance across all the important variables tested (resting respiratory rate, calories intake as well as the archery shooting scores). Similarly, the MPA (red colour) has the medium performance based on the assessed variables. However, the LPA (blue colour) has the lowest scores on the variables examined. These grouping enabled the classification and assignation of the performance-related variables to the athletes and consequently lead us to the further analysis for evaluation and classifying the archers.

It is apparent from Table 1 that the fine k -NN variation provides the best classification accuracy as compared to the medium and coarse variations. Furthermore, it could be seen that the recall, as well as the precision of the coarse variation,

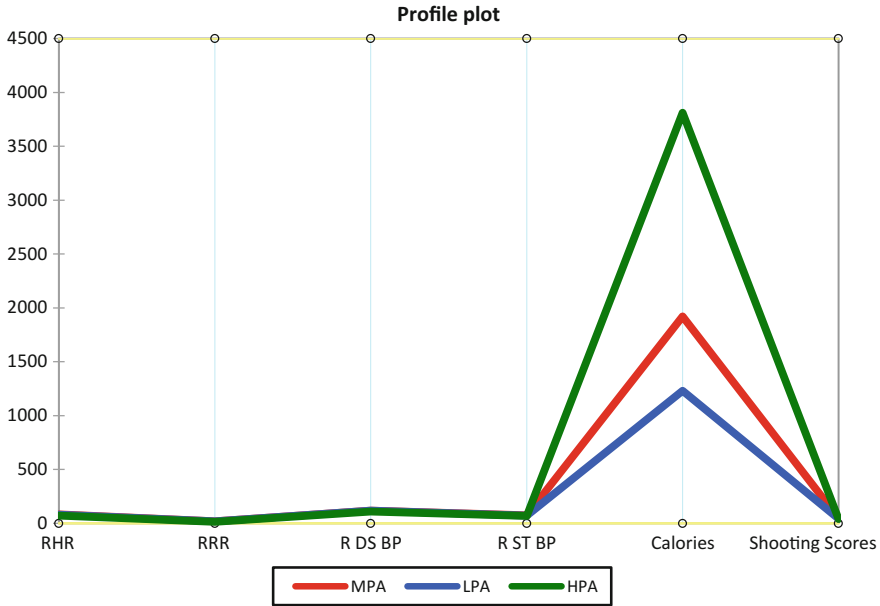


Fig. 1 Profile plot of the two classes in relation to the archers’ performances on the measured variables

Table 1 Model evaluation

k-NN classification	ACC (%)	REC (%)			PREC (%)		
		HPA	MPA	LPA	HPA	MPA	LPA
Fine	84	85.7	80	100	85.7	80	100
Medium	78	74.3	86.7	N/A	92.9	65	0
Coarse	56	56	N/A	N/A	100	0	0

is inconclusive for the classification of both the MPA as well as LPA. This is evident from the confusion matrix depicted in Fig. 2c, in which all the LPA and MPA are totally misclassified.

The findings from the present study have indicated that the capacity of lung function is integral to the archery performance. This discovery is harmonious with the study of [4] who investigated the specific pulmonary parameter in all India inter-university archery competition and found that the capacity of lung function was high on all archers compare to normal men. Moreover, it was inferred that the elite archers’ respiratory frequency is higher as compared to that of novices and as such elite archers have a better and consistent performance during archery competition [13]. The present study shows the high, and medium performance archers have recorded higher levels of resting respiratory rate. The results explained further

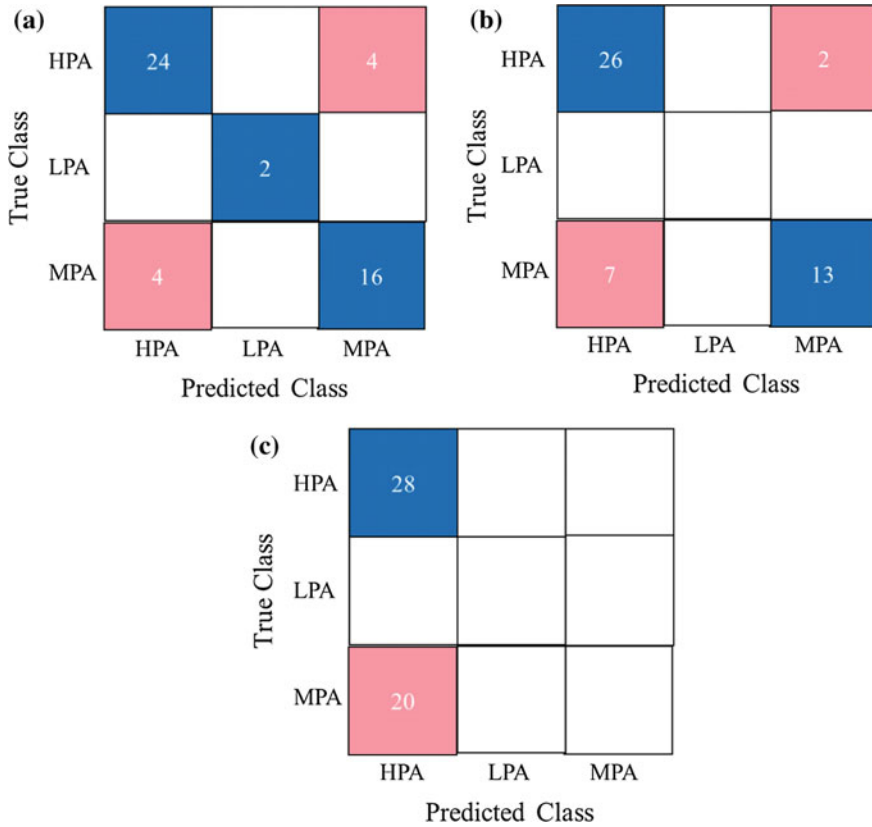


Fig. 2 Confusion matrix of *k*-NN variations **a** fine; **b** medium; **c** coarse

that the HPA and MPA have a good arousal control and autonomic balance help to achieve optimum lung frequency during rest which in turn contribute to gain good breath control and postural stability during the game for a better performance delivery.

It has also been shown from the present study that nutrition is vital for archery performance. Life in the aspect of sport surrounds amid training and competition. To fight for performance progression in sports, components such as skill, strength, power, speed, endurance, as well physical training, good nutrition is very vital to accomplishing this motive [14]. Furthermore, it was reported that an archer has to consider optimum nutrition during both training and competition. If an archer plans on expending more than an hour shooting, it is recommended for him/her to have water, Gatorade and snacks with them [15]. It is equally imperative to keep themselves “fueled” which can give energy to the working muscle amid shooting. An archer may become frail and lose their form during competition as a result of lack of eating enough or properly. Nonetheless, an archer finishes shooting at the

end of a long day; he/she may need to eat a good meal to refuel the body. Similarly, nutrition is also vital in the pre, during, and post of the shooting process. However, there is no adequate evidence from the present study to illustrate that resting heart rate, resting diastolic and systolic blood pressure could differentiate the performance level of the archers (see Fig. 1).

4 Conclusion

The present study has investigated the influence of specific bio-physiological variables in the effective performance of archery sport. It has been identified from the study that a combination of bio-physiological variables specifically resting respiratory rate, calories intake and archery shooting scores could determine the grouping of the archer's performance. The study has also revealed that the utilisation of machine learning algorithms, in particular, the variation of k -NN is able to reasonably predict the class of the archers based on the chosen performance variables. In addition, the finding of this study could be valuable to coaches and sports managers to figure out and to understand the bio-physiological variables that influence the performance of the sport. Subsequent study should consider other related performance variables associated with the sport as well as other non-conventional classification techniques.

References

1. Bartlett, D., Leiter, J.C.: Coordination of breathing with nonrespiratory activities. *Compr. Physiol.* (2012)
2. Chung, G.K.W.K., Delacruz, G.C., de Vries, L.F., Bewley, W.L., Baker, E.L.: New directions in rifle marksmanship research. *Mil. Psychol.* **18**, 161 (2006)
3. Mayén, A.-L., Marques-Vidal, P., Paccaud, F., Bovet, P., Stringhini, S.: Socioeconomic determinants of dietary patterns in low-and middle-income countries: a systematic review. *Am. J. Clin. Nutr.* [AJCN-089029](#) (2014)
4. Thakare, V.: Comparative study of peak expiratory flow rate of archery players participated in all India inter university archery competition. (2015)
5. Robertson, S.: Improving load/injury predictive modelling in sport: the role of data analytics. *J. Sci. Med. Sport.* **18**, e25–e26 (2017)
6. Montoye, A.H.K., Begum, M., Henning, Z., Pfeiffer, K.A.: Comparison of linear and non-linear models for predicting energy expenditure from raw accelerometer data. *Physiol. Meas.* **38**, 343–357 (2017)
7. Hagenbuchner, M., Cliff, D.P., Trost, S.G., Van Tuc, N., Peoples, G.E.: Prediction of activity type in preschool children using machine learning techniques. *J. Sci. Med. Sport.* **18**, 426–431 (2015)
8. Pavey, T.G., Gilson, N.D., Gomersall, S.R., Clark, B., Trost, S.G.: Field evaluation of a random forest activity classifier for wrist-worn accelerometer data. *J. Sci. Med. Sport.* **20**, 75–80 (2017)

9. Woods, C.T., Veale, J., Fransen, J., Robertson, S., Collier, N.F.: Classification of playing position in elite junior Australian football using technical skill indicators. *J. Sports Sci.* 1–7 (2017)
10. Taha, Z., Musa, R.M., Abdul Majeed, A.P.P., Alim, M.M., Abdullah, M.R.: The identification of high potential archers based on fitness and motor ability variables: a support vector machine approach. *Hum. Mov. Sci.* **57**, 184–193 (2018)
11. Abdullah, M.R., Eswaramoorthi, V., Musa, R.M., Maliki, M., Husin, A.B., Kosni, N.A., Haque, M.: The effectiveness of aerobic exercises at difference intensities of managing blood pressure in essential hypertensive information technology officers. *J. Young Pharm.* **8**, (2016)
12. Han, D., Ha, M.: Effect of pelvic floor muscle exercises on pulmonary function. *J. Phys. Ther. Sci.* **27**, 3233–3235 (2015)
13. Neumann, D.L., Thomas, P.R.: The relationship between skill level and patterns in cardiac and respiratory activity during golf putting. *Int. J. Psychophysiol.* **72**, 276–282 (2009)
14. Martorell, M., Capó, X., Sureda, A., Tur, J.A., Pons, A.: Effects of docosahexaenoic acid diet supplementation, training, and acute exercise on oxidative balance in neutrophils. *Appl. Physiol. Nutr. Metab.* **39**, 446–457 (2013)
15. Vargas, A., Parizzi, S.V., Fiamoncini, R.L., Navarro, F.: Utilização da creatina no treinamento de força-revisão sistemática. *Rev. Bras. Nutr. Esportiva.* **4**, 5 (2010)

The Application of Support Vector Machine in Classifying Potential Archers Using Bio-mechanical Indicators



Zahari Taha, Rabi Muazu Musa, Anwar P. P. Abdul Majeed, Mohamad Razali Abdullah, Muhammad Amirul Abdullah and Mohd Hasnun Arif Hassan

Abstract This study classifies potential archers from a set of bio-mechanical indicators trained via different Support Vector Machine (SVM) models. 50 youth archers drawn from a number of archery programmes completed a one end archery shooting score test. Bio-mechanical evaluation of postural sway, bow movement, muscles activation of flexor and extensor as well as static balance were recorded. *k*-means clustering technique was used to cluster the archers based on the indicators tested. Fine, medium and coarse radial basis function kernel-based SVM models were trained based on the measured indicators. The five-fold cross-validation technique was utilised in the present investigation. It was shown from the present study, that the employment of SVM is able to assist coaches in identifying potential athletes in the sport of archery.

Keywords Bio-mechanical indicators • Artificial intelligence • Classification Support vector machine

1 Introduction

Archery is considered as an individual and closed skill-based sport which requires the archer to focus and consider the collaborations of both the physiological and mechanical factors which either straightforwardly or by implication decide the result of performance in the game. It has been shown by the past researchers that the

Z. Taha · R. M. Musa (✉) · A. P. P. Abdul Majeed · M. A. Abdullah · M. H. A. Hassan
Innovative Manufacturing, Mechatronics and Sports Laboratory, Faculty of Manufacturing Engineering, Universiti Malaysia Pahang, 26600 Pekan, Pahang, Malaysia
e-mail: rabiumazu86@gmail.com

R. M. Musa · M. R. Abdullah
Faculty of Applied Social Sciences, Universiti Sultan Zainal Abidin, 21300
Kuala Terengganu, Terengganu, Malaysia

© Springer Nature Singapore Pte Ltd. 2018
M. H. A. Hassan (ed.), *Intelligent Manufacturing & Mechatronics*,
Lecture Notes in Mechanical Engineering,
https://doi.org/10.1007/978-981-10-8788-2_34

capacity of the archer to control his or her postural sway, bow movement, as well as the activations of the pertinent muscles, brought about shooting consistency and thus lead to higher archery shooting scores [1–5].

One of the essential subcomponent in keeping up shooting precision is aiming consistency. Accomplishing a greater state of postural stability is shown to improve shooting consistency [6]. Postural stability is often portrayed as the focal element of achieving shooting accuracy because it helps to ensure constant flight bearing to the target [7]. In another perspective, other researchers explained that during archery performance, an archer pushes the bow with extended arm, which is statically held in the direction of the target, while the other arm applies a dynamic pulling off the bowstring from the initial stage of drawing the bow until the release is dynamically executed [8]. The bowstring is discharged when a detectable sound is gotten from a gadget called “clicker” that is used as a draw length check. It is, therefore, understood that the constriction and relaxation strategy of the forearm muscles are basic for precise and higher scoring in the sport of archery.

Machine learning has recently gained much interest in the field of sports and the ascertainment of physical activity. Different types of machine learning methods have been employed in the aforementioned area namely artificial neural networks [9, 10], Bayesian network [11] and random forest [12, 13] amongst others. Support vector machine (SVM) is also another popular supervised learning method has been demonstrated to provide reasonably good classification and prediction in different fields [14–17]. This study attempts on employing three different SVM models that utilise fine, medium and coarse radial basis function (RBF) kernels in identifying potential archers based on a number of bio-mechanical indicators.

2 Materials and Methods

2.1 *Participants*

A total number of 50 archers were enrolled in this study. The archers comprised of 37 male and 13 female youth between the age’s scope of 13–20 with a mean, and standard deviation of (17.0 ± 0.56) assembled from different archery programs in Malaysia. The archery shooting test was set up to mimic a competition shooting zone of 50 m distance. The archers were permitted four trials shot before taking the last six arrow scores. Prior to any tests, informed consent was obtained in accordance with the procedures of the Ethical Review Board of the University Sultan Zainal Abidin.

2.2 *Biomechanical Measurements*

A sum of 4 IMUs Shimmer sensors was utilized in the present investigation to analyze and recognize the postural sway, balance of the bow, activations of the muscle flexor digitorum and extensor digitorum and the static balance of the archer. To quantify the postural influence, an accelerometer was immovably connected to the pelvic region as proposed by past investigators to be the proper region when a focal point of mass is to be determined [18]. To find out the movement of the bow, a gyroscope sensor inserted into a glove and attached to the hand of the archer. Also, bipolar electrodes were linked with the sensors and attached to the left muscle extensor digitorum and the right muscle flexor digitorum to acquire Electromyography (EMG) signals amid the archery shooting test. All the information was streamed progressively at a sampling amount of 51.2 Hz utilizing an Android telephone and transferred by means of Bluetooth for statistical analysis. Furthermore, the static balance of the archers was assessed using a stork balance test.

2.3 *Clustering*

The k-means clustering technique is employed to cluster the archers based on their performances in the selected variables and their shooting scores in which two classes, i.e. high potential archers (HPA) and low potential archers (LPA) are clustered. Additionally, the performance of the SVM in classifying HPA as well as LPA are investigated.

2.4 *Classification*

SVM is utilised to acquire the optimal hyperplane that could correctly classify the data into two distinct categories that are represented by HPA and LPA in the present study. Three different kernel functions are investigated namely fine, medium and coarse RBF. The scale of the fine, medium and coarse RBF is defined by $0.25 * P^{0.5}$, $P^{0.5}$, $4 * P^{0.5}$, respectively, where P is the number of predictors viz five. The fivefold cross-validation technique was employed in the present investigation. The performance of the SVM models are evaluated through the classification accuracy (CA) of the aforesaid models.

3 Results and Discussion

Figure 1 illustrates the box plot of the selected bio-mechanical indicators employed in the study. It could be seen from the figure that the HPA recorded higher performances in relatively all the performance variables evaluated when compared to LPA.

Table 1 lists the classification accuracy of the evaluated SVM models. It is apparent that the fine RBF based SVM model provides the best classification accuracy in comparison to the other SVM models appraised. It is also noticeable from the CA that both medium and coarse RBF based SVM models perform equally. This is further demonstrated via the confusion matrix of the models shown in Fig. 2b, and Fig. 2c, respectively.

The important findings from the present study have declared that some related biomechanical parameters precisely, muscle activations, bow movement, and postural sway could differentiate high performance and low performance archers and also could influence shooting accuracy in archery sport (see Fig. 1). It has been reported that during the archery shooting technique, muscle extensors serve as the supportive muscle [8]. Therefore, it is expected to be more activated for the achievement of the higher score because it helps to stabilise the bow. Moreover, some authors stressed further that during archery performance, an archer pushes the bow with an extended arm, which is statically held in the bearing of the target, while the other arm applies a dynamic pulling off the bowstring from the earliest starting point of the drawing stage until the discharge is continuously achieved. Hence, The contraction of the muscle extensor during the release of the bowstring is essential for accurate and higher scoring in archery [19].

Furthermore, the findings demonstrated that the HPA is ascribed to lower postural sway as well corresponding lower bow movement compared to LPA as clearly shown in Fig. 1. This finding is consistent with the findings of the precedent investigators who specified that one of the vital subcomponents in keeping up shooting accuracy is aiming stability [7, 19, 20]. Reaching a significant degree of postural stability through aiming intensifies the aiming stability of an archer. Aiming stability is considered as the central form of aiming which guarantees continuous flight direction to the target. The movement of the bow has also shown to hinder shooting archery of the archers such that the higher the sway of the bow the lesser the shooting accuracy is observed [21].

4 Conclusion

It could be concluded from the present study that the fine RBF based SVM model could predict reasonably well the high and low potential archers based on the selected bio-mechanical performance indicators. The results from the present study could be advantageous to coaches and trainers in re-organizing their training

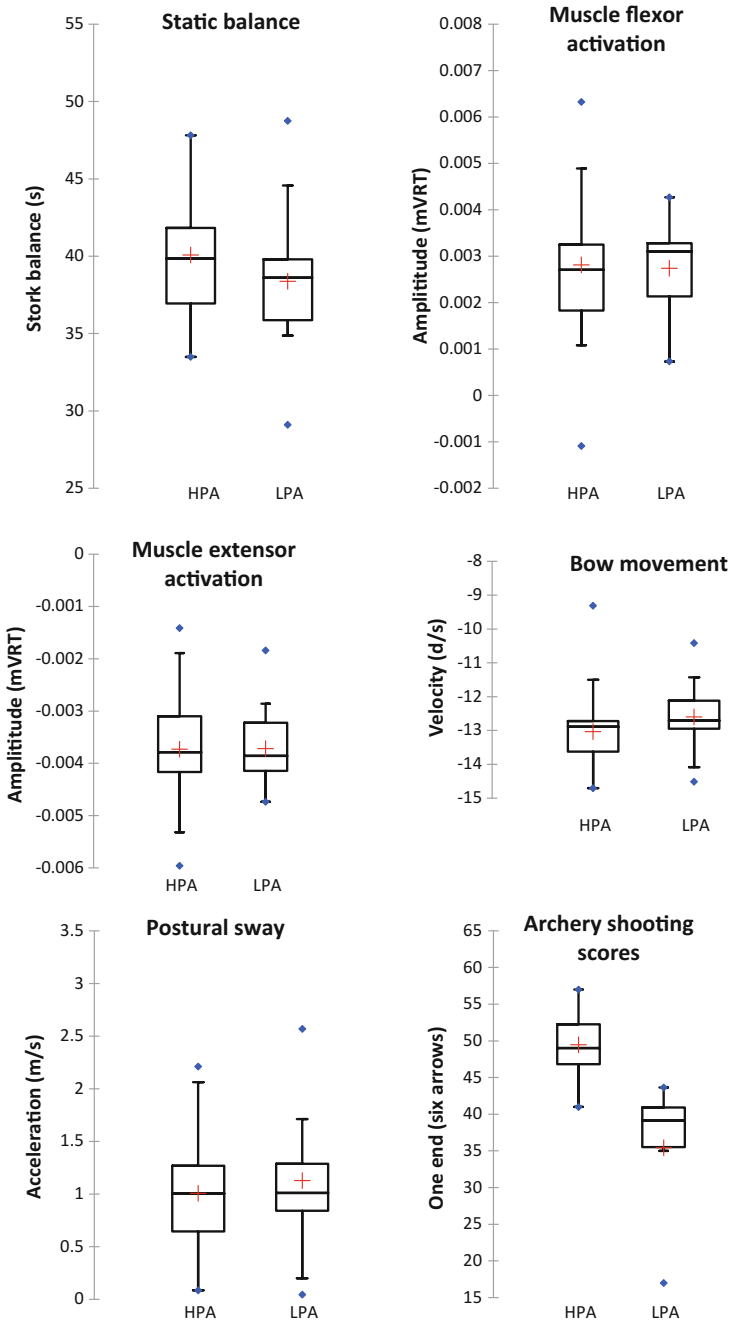


Fig. 1 Box plot of the performance indicators

Table 1 Classification accuracy of the SVM models

Kernel functions	CA (%)
Fine	70
Medium	64
Coarse	64

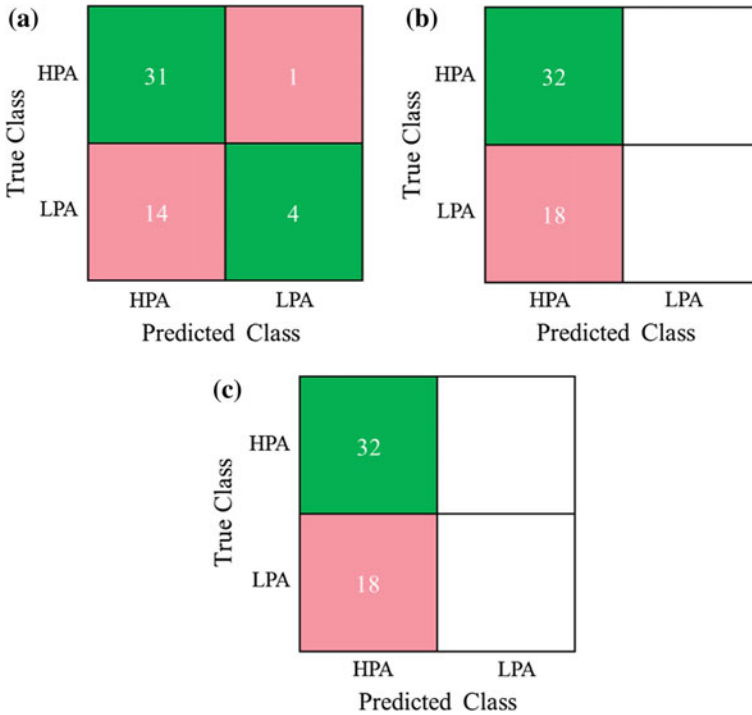


Fig. 2 Confusion matrix of the SVM models evaluated **a** fine; **b** medium; **c** coarse

programme through considering the evaluated performance variables as a model for the optimisation of performance in the sport.

References

1. Martin, P.E., Siler, W.L., Hoffman, D.: Electromyographic analysis of bow string release in highly skilled archers. *J. Sports Sci.* **8**, 215–221 (1990)
2. Ertan, H., Soylu, A.R., Korkusuz, F.: Quantification the relationship between FITA scores and EMG skill indexes in archery. *J. Electromyogr. Kinesiol.* **15**, 222–227 (2005)
3. Ertan, H., Kentel, B., Tümer, S.T., Korkusuz, F.: Activation patterns in forearm muscles during archery shooting. *Hum. Mov. Sci.* **22**, 37–45 (2003)

4. Clarys, J.P., Cabri, J., Bollens, E., Sleenckx, R., Taeymans, J., Vermeiren, M., Van Reeth, G., Voss, G.: Muscular activity of different shooting distances, different release techniques, and different performance levels, with and without stabilizers, in target archery. *J. Sports Sci.* **8**, 235–257 (1990)
5. Keast, D., Elliott, B.: Fine body movements and the cardiac cycle in archery. *J. Sports Sci.* **8**, 203–213 (1990)
6. Pathmanathan, K.S., Wong Kee Kiet, T., Musa, R.M., Abdullah, M.R., Lee, J.L.F., Maliki, A. B.H.M.: The effectiveness of a core muscles stability program in reducing the postural sway of adolescent archers: a panacea for a better archery performance. *Int. J. Physiother.* **4**(5), 296–301 (2017)
7. Kooi, B.W., Sparenberg, J.A.: On the mechanics of the arrow: archer's paradox. *J. Eng. Math.* **31**, 285–303 (1997)
8. Leroyer, P., Van Hoecke, J., Helal, J.N.: Biomechanical study of the final push-pull in archery. *J. Sports Sci.* **11**, 63–69 (1993)
9. Hagenbuchner, M., Cliff, D.P., Trost, S.G., Van Tuc, N., Peoples, G.E.: Prediction of activity type in preschool children using machine learning techniques. *J. Sci. Med. Sport.* **18**, 426–431 (2015)
10. Montoye, A.H.K., Begum, M., Henning, Z., Pfeiffer, K.A.: Comparison of linear and non-linear models for predicting energy expenditure from raw accelerometer data. *Physiol. Meas.* **38**, 343–357 (2017)
11. Fuster-Parra, P., García-Mas, A., Ponseti, F.J., Palou, P., Cruz, J.: A Bayesian network to discover relationships between negative features in sport: a case study of teen players. *Qual. Quant.* **48**, 1473–1491 (2014)
12. Pavey, T.G., Gilson, N.D., Gomersall, S.R., Clark, B., Trost, S.G.: Field evaluation of a random forest activity classifier for wrist-worn accelerometer data. *J. Sci. Med. Sport.* **20**, 75–80 (2017)
13. Ellis, K., Kerr, J., Godbole, S., Lanckriet, G., Wing, D., Marshall, S.: A random forest classifier for the prediction of energy expenditure and type of physical activity from wrist and hip accelerometers. *Physiol. Meas.* **35**, 2191–2203 (2014)
14. Azamathulla, H.M., Wu, F.-C.: Support vector machine approach for longitudinal dispersion coefficients in natural streams. *Appl. Soft Comput. J.* **11** (2011)
15. Guyon, I., Weston, J., Barnhill, S., Vapnik, V.: Gene selection for cancer classification using support vector machines. *Mach. Learn.* **46**, 389–422 (2002)
16. De Yong, D., Bhowmik, S., Magnago, F.: An effective power quality classifier using wavelet transform and support vector machines. *Expert Syst. Appl.* **42**, 6075–6081 (2015)
17. Taha, Z., Musa, R.M., Abdul Majeed, A.P.P., Alim, M.M., Abdullah, M.R.: The identification of high potential archers based on fitness and motor ability variables: a support vector machine approach. *Hum. Mov. Sci.* **57**, 184–193 (2018)
18. Rocchi, L., Chiari, L., Cappello, A., Horak, F.B.: Identification of distinct characteristics of postural sway in Parkinson's disease: a feature selection procedure based on principal component analysis. *Neurosci. Lett.* **394**, 140–145 (2006)
19. Taha, Z., Musa, R.M., Abdullah, M.R., Razman, M.A.M., Lee, C.M., Adnan, F.A., Abdullah, M.A., Haque, M.: The application of inertial measurement units and wearable sensors to measure selected physiological indicators in archery. *Asian J. Pharm. Res. Heal. Care.* **9**, 85–92 (2017)
20. Altini, M., Penders, J., Roebbers, H.: An Android-based body area network gateway for mobile health applications. In: *Wireless Health 2010*. pp. 188–189. ACM (2010)
21. Zulkifli, A., Hasnun, A.H., Mohd Azrul, H., Nasrul, H.J.: Biomechanics measurements in archery. *J. Mech. Eng. Sci.* **6**, 762–771 (2014)

The Identification of Hunger Behaviour of *Lates Calcarifer* Using k -Nearest Neighbour



Zahari Taha, Mohd Azraai Mohd Razman, F. A. Adnan,
Anwar P. P. Abdul Majeed, Rabi Muazu Musa,
Ahmad Shahrizan Abdul Ghani, M. F. Sallehudin and Y. Mukai

Abstract Fish Hunger behaviour is essential in determining the fish feeding routine, particularly for fish farmers. The inability to provide accurate feeding routines (under-feeding or over-feeding) may lead to the death of the fish and consequently inhibits the quantity of the fish produced. Moreover, the excessive food that is not consumed by the fish will be dissolved in the water and accordingly reduce the water quality through the reduction of oxygen quantity. This problem also leads to the death of the fish or even spur fish diseases. In the present study, a correlation of Barramundi fish-school behaviour with hunger condition through the hybrid data integration of image processing technique is established. The behaviour is clustered with respect to the position of the school size as well as the school density of the fish before feeding, during feeding and after feeding. The clustered fish behaviour is then classified through k -Nearest Neighbour (k -NN) learning algorithm. Three different variations of the algorithm namely, fine, medium and coarse are assessed on its ability to classify the aforementioned fish hunger behaviour. It was found from the study that the fine k -NN variation provides the best classification with an accuracy of 88%. Therefore, it could be concluded that the proposed integration technique may assist fish farmers in ascertaining fish feeding routine.

Keywords Fish feeding behaviour • k -Nearest neighbour • *Lates Calcarifer*

Z. Taha · M. A. M. Razman (✉) · F. A. Adnan · A. P. P. Abdul Majeed
R. M. Musa · A. S. Abdul Ghani
Innovative Manufacturing, Mechatronics and Sports Lab (iMAMS),
Faculty of Manufacturing Engineering, Universiti Malaysia Pahang,
Pekan Campus, 26600 Pekan, Pahang, Malaysia
e-mail: azraai@ump.edu.my

M. F. Sallehudin · Y. Mukai
Kulliyah of Science, International Islamic University Malaysia, Jalan Sultan Ahmad Shah,
Bandar Indera Mahkota, 25200, Kuantan Pahang, Malaysia

1 Introduction

Fish farming is considered as one of the most important avenues for a gauging as well as the steady supply of sufficient fish according to the demand and societal needs. The conventional method of fish farming could not address such issue without the application of technology and other multi-disciplinary acts. To ensure the consistent supply of the fish, both methods have to be integrated in order to contribute to the production, reducing the wastages of unsettling results such as dead fish, murky water, overfeeding and so on. The characteristics of the fish must be identified with the parameters that are required to be extracted for the technologist to define their behaviour and this has to comply with marine biology point of view. The most obvious trait that can be highlighted is the movement of the fish or in general term locomotor activity. It was previously suggested that the prediction towards feeding behaviour does correlate with the increasing gestures among the fish and even in a clustered form of higher quantity [1].

Considering this as a major issue, researchers have seen to collaborate with one another intertwining between disciplines to investigate the effects between fishes and their behaviour from different aspects, for example, environmental changes, circadian rhythm patterns, sensory cues and inter-individual reactions. There is an unambiguous relationship between the less fed individual and wandering fish in which the more hungry the fish are, the larger area that it will cover to search for food [2]. The study furthermore found that the movement is less attracted along the walls or the bounding are such as aquarium and fish ponds. This phenomenon can provide a better judgment for assessing the fish behaviour rhythm or in another scientific term *zeitgeber*, thus ensuring an allusive experimental setup can be reliably constructed. Commonly the circadian rhythm is associated with the endogenous rhythms in which the biological act from within a mammal and this nature emulates sleeping anatomy [3]. The free running motion is adjourned throughout the 24 h, and during that time, most major information is vital for measuring the behaviour of the fish.

A frequent question often asked regarding the parameters for quantification of fish hunger behaviour is; to what extent of parameters does one need? The answer to such question all depends on the outcome of findings researchers yearn for, for example, interval times between meals and volume of the foods. Similarly, it has been demonstrated that by altering the frequencies of the meal and timing of feeding, the movement of the fish suggests the behaviour between satiated and unfed state [4]. On the other hand, if the fish were to scavenge in a group, the implication does show a similar pattern where the activity is rather aggressive compared to after feeding mode [5]. Noting the fact that circadian rhythm was initially based on sleeping patterns, the consequent towards feeding behaviour also portray the changes of motion given the light or dark environment onto the collective individuals [6]. The study implements self-demand feeder for the fishes to acquire food on demand. The present study exploits that notion and will be further discussed in the following section.

The operation of the self-demand feeder is how it necessitates the needs of dropping pellets when and only when the fish needs it. Two criteria need to be

predefined such as the moment the fish does when it needs to eat and by how much they require. This is the part where classification methods were calculated to determine the objectives that reflect the findings. An example was shown where fishes were studied on the growth rate for *Lates Calcarifer* or generally known as Asian sea bass [7]. The specimens were placed in net cages, and observation was made throughout the period up until certain growth was achieved. Similarly, Barramundi apart from being term as the Asian sea bass depicts favourable results when they adjust the lights to imitate the night and day situations [8]. Razor fish or *Xyrihchys novacula* the zebrafish or *Danio rerio* were the other common species that has undergone similar practices in identifying the patters where the genders and resting time were evaluated as a part of circadian rhythm studies [9, 10].

There have been findings that suggest using machine learning based classification methods could support the objective of monitoring the fish behaviours [11, 12]. k -Nearest Neighbour (k -NN) has been demonstrated to be able to detect abnormal fish trajectories [11]. Rainbow trout or *Oncorhynchus mykiss* had been the subject of an examination for the activity of muscles whether it has satiated or not by means of support vector machine (SVM) [13].

The approach of displaying a credible hunger behaviour observation is implemented into this current study by using computer vision for tracking the behaviour thus integrate with a machine learning technique namely k -NN that will be discussed in the ensuing sections.

The present study utilises two main parameters to identify the *Lates Calcarifer* fish hunger behaviour which is the school density and the location of the center of gravity. The following subheading explains the organisation of the paper: Sect. 2 depicts the experimental setup on the rig and capturing image for processing along with the classification method used, Sect. 3 presented and discussed the results obtained from the study and lastly draws to the conclusion of the study and will provide some recommendation for future research in Sect. 4.

2 Materials and Methods

To ensure that a reliable extraction of data and all the elements of observing fish behaviour is met, the laboratory setup has to be aligned with the proposed methods. The self-demand feeder procedures, computer vision concept, and methods of classification are discussed in this section.

2.1 Fish

The Asian sea bass species was taken for the experiment since the behaviour demands food as the basis standard complies with the circadian rhythm. The species were taken from Fisheries Research Institute, Gelang Patah Johor, Malaysia, and the laboratory at the International Islamic University Malaysia serve as the centre where the hunger behaviour of 20 juveniles Asian seabass was observed.

2.2 Experiment Setup

The fish tank was filled with 130 L of water with a dimension of 92 cm x 46 cm x 46 cm (Fig. 1). An infrared sensor was employed below the surface water level as a triggering point for the fish to drop them in the form of a 0.5 g volume of pellets and 3 mm diameter for each. Once the feeding process has started, the feeder will constantly drop the pellet until there is not any fish to triggers the sensor. A microcontroller was the one cooperated with the feeder and projects the time stamp of the feeding process with the parameters of the centre of gravity and school size which was taken by a webcam modelled Logitech, C270h being transferred into a computer. The captured files were converted into.avi file and transferred to Roboreal software for evaluation which tracks the Centre of Gravity (CoG) of the school fish and the box size. Hence the parameters of x and y coordinates in pixels were sent for classification methods of Before Feeding (BF), During Feeding (DF) and After feeding (AF). The evaluation was employed using classification method by means from the data acquired of BF, DF and AF for the classification efficacy of k -NN algorithm (Table 1).

2.3 Classification Method

The k -NN classification algorithm is employed in this study to classify the aforementioned clustered data viz. BF, DF and AF. In this study, three different variations of k -NN algorithms namely fine, medium and coarse are investigated. The number of neighbours, k for fine, medium and coarse are 1, 10 and 100, respectively. The equally distanced Euclidean distance metrics are used for all the

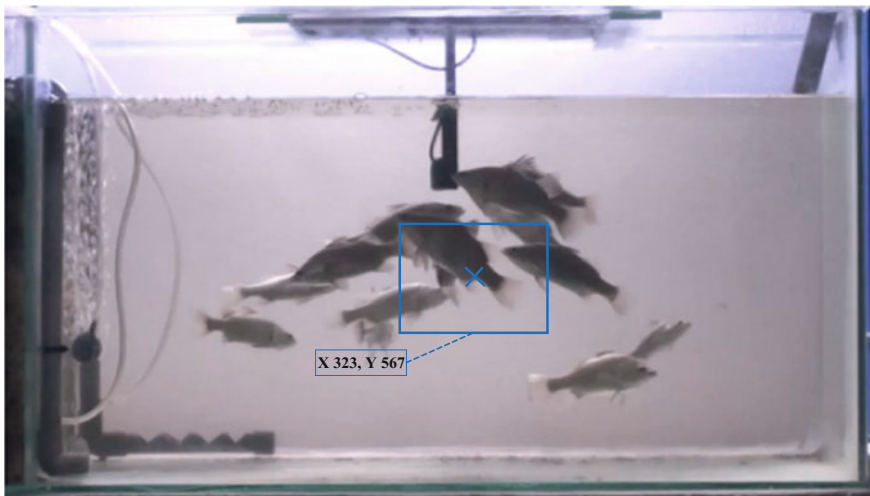


Fig. 1 Screenshot of COG box on the fish behaviour during feeding

evaluated variations. Moreover, a fivefold cross-validation procedure was carried out to mitigate the issue of overfitting. The variations of the k -NN models employed in this study are evaluated by means of classification accuracy (CA).

3 Results and Discussion

It is evident from Table 1 that the fine k -NN variation delivers the best classification accuracy as compared to the medium and coarse variations. It appears that the coarse variation is the worst performing classifier amongst the others. This is

Table 1 Evaluation of the k -NN classifiers

k -NN classification	Fine	Medium	Coarse
CA (%)	88	78.1	66.2

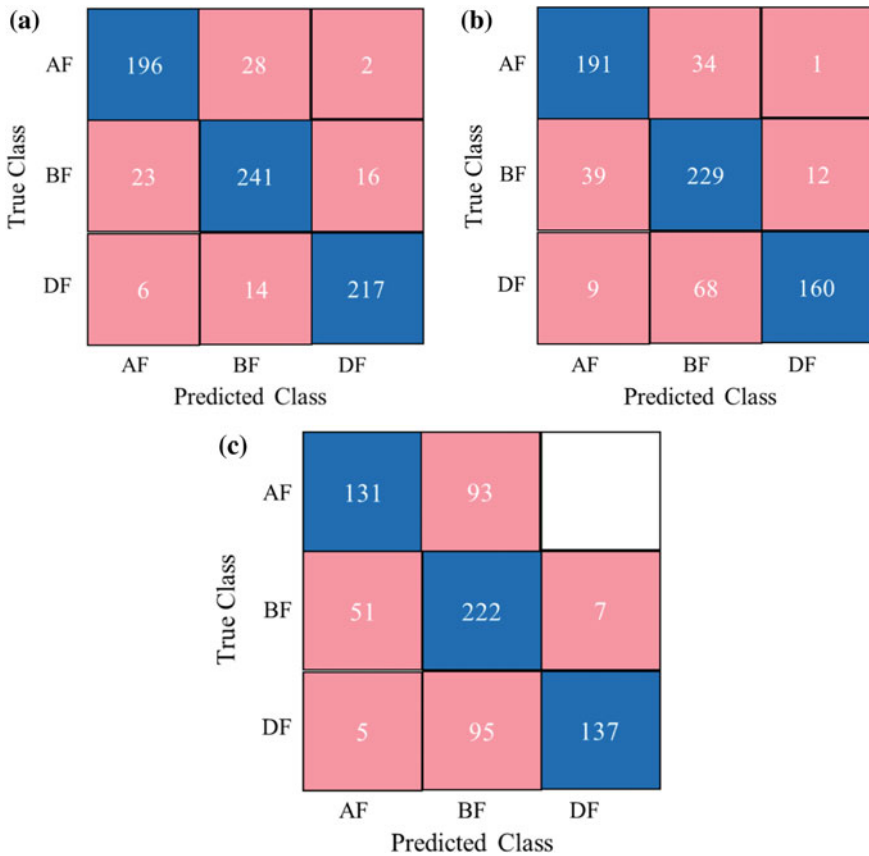


Fig. 2 Confusion matrix of k -NN variations **a** fine; **b** medium; **c** coarse

apparent from the confusion matrix depicted in Fig. 2c, higher misclassification transpires across all clustered feeding duration.

4 Conclusion

It could be concluded from the present investigation that the fine variation of k -NN is able to provide a reasonably accurate classification of fish feeding behaviour with regards to the abovementioned parameters examined, i.e. centre of gravity and school fish density. Further study could be carried out by considering other relevant parameters that may explain the hunger behaviour of *Lates Calcarifer* as well as the effectiveness of other forms of classification techniques.

References

1. Cavallari, N., Frigato, E., Vallone, D., Fröhlich, N., Lopez-Olmeda, J.F., Foà, A., Berti, R., Sánchez-Vázquez, F.J., Bertolucci, C., Foulkes, N.S.: A blind circadian clock in cavefish reveals that opsins mediate peripheral clock photoreception. *PLoS Biol.* **9**, e1001142 (2011)
2. Hansen, M.J., Schaerf, T.M., Ward, A.J.W.: The effect of hunger on the exploratory behaviour of shoals of mosquitofish *Gambusia holbrooki*. *Behaviour* **152**, 1659–1677 (2015)
3. Beale, A., Guibal, C., Tamai, T.K., Klotz, L., Cowen, S., Peyric, E., Reynoso, V.H., Yamamoto, Y., Whitmore, D.: Circadian rhythms in Mexican blind cavefish *Astyanax mexicanus* in the lab and in the field. **4**, 2769 (2013)
4. Priyadarshana, T., Asaeda, T., Manatunge, J.: Hunger-induced foraging behavior of two cyprinid fish: *Pseudorasbora parva* and *Rasbora daniconius*. *Hydrobiologia* **568**, 341–352 (2006)
5. Chapman, B.B., Morrell, L.J., Krause, J.: Unpredictability in food supply during early life influences boldness in fish. *Behav. Ecol.* **21**, 501–506 (2010)
6. Sanchez-Vázquez, F.J., Madrid, J.A., Zamora, S.: Circadian rhythms of feeding activity in sea bass, *Dicentrarchus labrax* L.: dual phasing capacity of diel demand-feeding pattern. *J. Biol. Rhythms* **10**, 256–266 (1995)
7. Biswas, G., Thirunavukkarasu, A.R., Sundaray, J.K., Kailasam, M.: Optimization of feeding frequency of Asian seabass (*Lates calcarifer*) fry reared in net cages under brackishwater environment. *Aquaculture* **305**, 26–31 (2010)
8. Harpaz, S., Hakim, Y., Barki, A., Karplus, I., Slosman, T., Tufan Eroldogan, O.: Effects of different feeding levels during day and/or night on growth and brush-border enzyme activity in juvenile *Lates calcarifer* reared in freshwater re-circulating tanks. *Aquaculture* **248**, 325–335 (2005)
9. Ariyomo, T.O., Watt, P.J.: Effect of hunger level and time of day on boldness and aggression in the zebrafish *Danio rerio*. *J. Fish Biol.* **86**, 1852–1859 (2015)
10. Alós, J., Martorell-Barceló, M., Campos-Candela, A.: Repeatability of circadian behavioural variation revealed in free-ranging marine fish. *R. Soc. Open Sci.* **4**, 160791 (2017)

11. Beyan, C., Fisher, R.B.: Detection of abnormal fish trajectories using a clustering based hierarchical classifier. In: BMVC (2013)
12. Dutta, M.K., Sengar, N., Kamble, N., Banerjee, K., Minhas, N., Sarkar, B.: Image processing based technique for classification of fish quality after cypermethrine exposure. *LWT—Food Sci. Technol.* **68**, 408–417 (2016)
13. Cubitt, K.F., Williams, H.T., Rowsell, D., McFarlane, W.J., Gosine, R.G., Butterworth, K.G., McKinley, R.S.: Development of an intelligent reasoning system to distinguish hunger states in Rainbow trout (*Oncorhynchus mykiss*). *Comput. Electron. Agric.* **62**, 29–34 (2008)

Decision Making Support System Using Intelligence Tools to Select Best Alternative in Design for Remanufacturing (Economy Indicator)



Ahamad Zaki Mohamed Noor, Muhammad Hafidz Fazli Md Fauadi,
Fairul Azni Jafar, Nor Rashidah Mohamad,
Muhammad Winal Zikril Zulkifli, Muhammad Haziq Hasbulah,
Muhammad Azri Othman, Mahasan Mat Ali, Jee Boon Goh
and Rajandran Morthui

Abstract Sustainable practice is needed in every manufacturing industry. To make this practice successfully implemented in manufacturing industry, three indicators must be look into. The three indicators are environmental, economy and social indicator. In this paper, only economy indicator will be looked into for the implementation of intelligence tools. Economy indicator obtained from Design for Remanufacturing (DFREM) consists of several variables where cost will be substituted into the variables. However, industries are unaware that with this practice, an industry can save money and reduce waste from finished part. The industry can implement the economy indicator equation and substitute the cheapest value from several option provided by the supplier. This may cost time but in long term return, DFReM can make an industry to save money. In this paper, three intelligence tools will be used to make the best selection of cost to be substitute in DFReM equation. The intelligence tools are Fuzzy Analytic Hierarchy Process (FAHP), Artificial Neural Network (ANN) and combination of both FAHP and ANN. The objective of this paper is to compare the output result obtained from three intelligence tool. The final result shows FAHP and ANN provides the best solution, followed by ANN and lastly FAHP. Therefore, combination of FAHP and ANN should be used for selecting alternatives from supplier hence applied in DFReM economy indicator equation.

Keywords Design for remanufacturing · Fuzzy analytic hierarchy process
Artificial neural network · Economy indicator

A. Z. Mohamed Noor (✉) · M. H. F. Md Fauadi · F. A. Jafar · N. R. Mohamad
M. W. Z. Zulkifli · M. H. Hasbulah · M. A. Othman · M. Mat Ali · J. B. Goh · R. Morthui
Faculty of Manufacturing Engineering, Universiti Teknikal Malaysia, Durian Tunggal,
Melaka, Malaysia
e-mail: ahamadzaki.mohamednoor@gmail.com

© Springer Nature Singapore Pte Ltd. 2018
M. H. A. Hassan (ed.), *Intelligent Manufacturing & Mechatronics*,
Lecture Notes in Mechanical Engineering,
https://doi.org/10.1007/978-981-10-8788-2_36

1 Introduction

Design for Remanufacturing is a concept of manufacturing environment which are developed currently for future generation of manufacturing and process technology. This system will be easily utilised by other departments. Remanufacturing is also a process of returning used product by rework, reassemble, disassemble reprocess, inspect and testing in order to bring back current appearance to brand new part [1]. There are three indicators in Design for Remanufacturing. The indicators are economic, social and environment. The problem with current situation is that the techniques used are very difficult to apply in the assessment of the remanufacturing process [2]. Total of alternatives can be more than five, could also be twenty and the techniques used are not suitable to the situation. The techniques that are look into are narrowed down to a technique used for cost optimization in manufacturing field.

This research focuses on improving the Design for Remanufacturing by optimizing the steps in term of money and cost. The objective of this paper is to compare output of different AI techniques and propose new technique of decision making for economy indicator in DFReM. This research also will eventually be able to make the decision flexible according to the changes in environment [3]. The weightage is not being placed randomly but consistency and sensitivity analysis will be carried out in order the weightage is suitable for each criterion. Meanwhile, Fuzzy logic algorithm will be utilized to manage the decision maker's subjective preferences. Fuzzy logic is linguistic judgmental whereby is gives decimal value rather than provide binary number one and zero which currently computer does [4]. Therefore, believes that this two method is fused might be able to give a better decision since AHP is being supported by Fuzzy Logic Algorithm. In order to process more than 10 alternative, Fuzzy AHP will be lengthy. Therefore, ANN will be adapted for human—like thinking to happen [5]. The best value will be substituted into DFReM for economy indicator. The final answer will be substituted in Eqs. (1), (2) and (3).

$$C_o = C_W + C_{MR} + C_{DO} + C_{IO} + C_D + C_I \quad (1)$$

where

- C_W Warranty cost
- C_{MR} Maintenance repair cost
- C_{DO} Direct overhead cost
- C_{IO} Indirect overhead cost
- C_D Depreciation cost
- C_I Insurance cost

$$LCC_{RM} = C_{ProdU} + C_{SP} + C_C + C_L + C_T + C_P + C_o \quad (2)$$

where

LCC_{RM}	Life cycle cost after remanufacture
C_{ProdU}	Used product acquisition cost
C_{SP}	New spare parts cost
C_C	Cleaning parts cost
C_L	Labor cost
C_T	Transport cost
C_P	Packaging cost
C_O	Other remanufacturing cost

Next is to calculate new life cycle cost (LCC_n);

$$LCC_n = C_{Prod} + C_{Exp} + C_{DP} \quad (3)$$

where

C_{Prod}	New product acquisition cost
C_{Exp}	Exploitation cost
C_{DP}	Disposal cost

The last step is to calculate cost effective comparison (ΔLCC). This is done by subtracting Eq. (3) with Eq. (2).

$$\Delta LCC = LCC_n - LCC_{RM} \quad (4)$$

2 Methodology

In this section, flow chart is developed to show overall process to carry out this research. The flow chart here is used to analyse, documenting and managing stage of experiment and time spent. This is important to determine the stage in order to complete this research. This flow chart will also provide aid if there is problem occurred during this research carried out.

From Fig. 1, only the red box region will be experimented and documented in this paper. The data obtained will be classify according to its company and categorize according to cost. The types of costs selected are direct overhead, indirect overhead and other remanufacturing costs. Once all the data obtain, the data will be input in Microsoft Excel file and save as “.csv” extension. The purpose of creating this Microsoft Excel file is to observe the data better and for the ease of MATLAB to recall and read the file created in Microsoft Excel If the data received is insufficient or illogical, the data have to be obtained again via industrial visit. The same data from excel file will be used for another two methods. The final answer will select the company giving the best price. This price will be substituted into DFR_eM economy indicator formula.

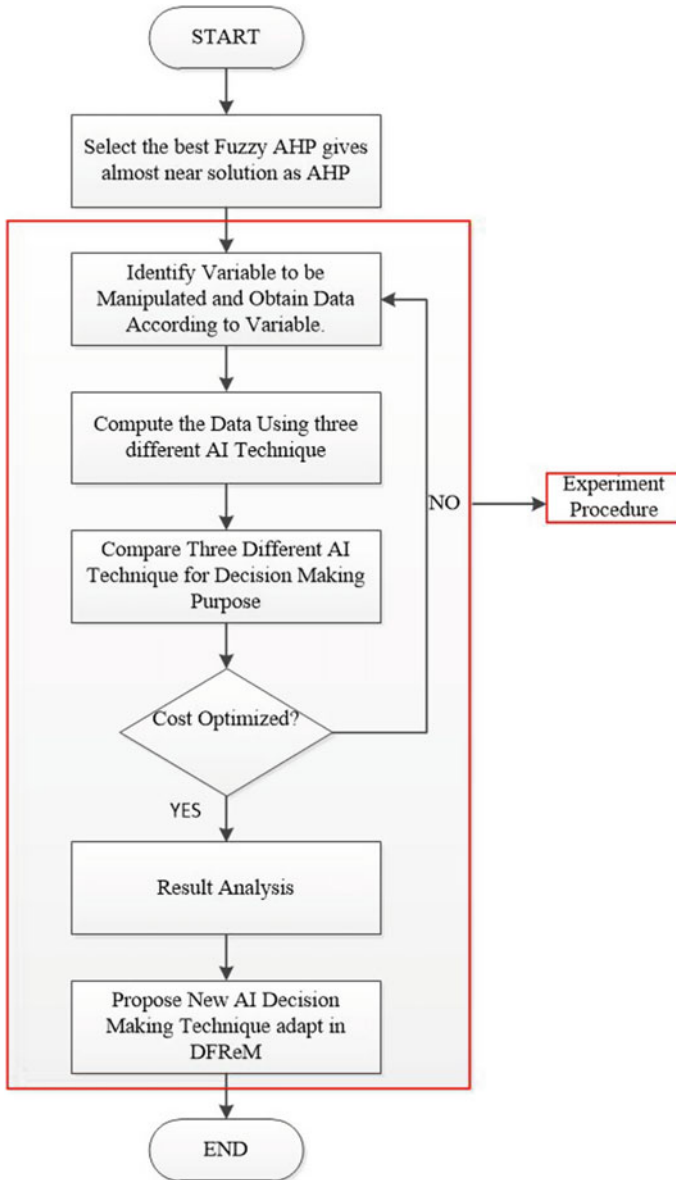


Fig. 1 Overall flow chart

3 Result

Several variables were selected for the computation to select best optimized cost. The cost related and to be manipulated are direct overhead, indirect overhead, spare part cost and packaging cost. Total of 20 companies given the data for computation

purposes. In this result section, three AI methods will be carried out and the results will be analysed.

3.1 DFR_eM Experiment Using Fuzzy AHP

Table 1 shows the result obtained based on Fuzzy AHP. Observed the highlighted box gives the cheapest cost to be selected before substituting in Design for Remanufacturing economy formula.

Discussion for FAHP Technique

In this section, the final answer will be analysed, and the price will be referred from the data sheet obtained from 20 different companies assuming they produce same product. The disposal cost is excluded because some company does not provide such cost. Fuzzy AHP select Company 18 as the best price offered for Direct Overhead cost.

$$Direct\ Overhead = Direct\ Material + Direct\ Labor$$

$$Direct\ Overhead = RM\ 3,200 + RM\ 1,650$$

Table 1 Final result from FAHP technique

	Direct overhead	Indirect overhead	Spare parts	Packaging
Company 1	0.08520582	0.0269	0	0.02360743
Company 2	0.10000982	0.0904	0.08800215	0.10682189
Company 3	0	-0.1499	0.10138067	0.11457565
Company 4	0.05088576	0.0857	0	0.07760683
Company 5	0.10028407	0.0629	0.02099989	0
Company 6	0	0	0	0
Company 7	0.02050642	0.1351	0.06870199	0
Company 8	0	0.0543	0.07944867	0.08979131
Company 9	0.0520706	0.05583	0.03975175	0
Company 10	0.04078344	0	0	0.11194491
Company 11	0.09348515	0.029	0	0.02360743
Company 12	0.10311294	0.1751	0.09452692	0
Company 13	0	0.0454	0	0
Company 14	0	0	0	0
Company 15	0	0	0	0
Company 16	0.01066356	0	0	0
Company 17	0.03914862	0.0728	0	0
Company 18	0.11548255	0.13	0.05554279	0.04486104
Company 19	0.04854726	0.117	0	0
Company 20	0	0.0509	0	0.09948351

$$\text{Direct Overhead} = \text{RM } 4,850$$

Fuzzy AHP select Company 12 as the best price offered for Indirect Overhead cost.

$$\text{Indirect Overhead} = \text{Account} + \text{Admin Salary} + \text{Postage} + \text{Office Expenses}$$

$$\text{Indirect Overhead} = \text{RM } 3,100 + \text{RM } 98,752 + \text{RM } 550 + \text{RM } 1,320$$

$$\text{Indirect Overhead} = \text{RM } 103,722$$

Assuming total exploitation cost and disposal cost are RM 202,000 for every company Therefore to compute Life Cycle Cost Remanufacture Perspective:

$$LCC_{RM} = \text{RM } 1,700 + \text{RM } 300 + \text{RM } 103,722 + \text{RM } 4,850 = \text{RM } 110,572$$

$$LCC_n = \text{RM } 202,000$$

$$\Delta LCC = LCC_n - LCC_{RM}$$

$$\Delta LCC = \text{RM } 202,000 - \text{RM } 110,572 = \text{RM } 91,428$$

3.2 DFR_eM Experiment Using ANN

In this experiment using neural network, two files are introduced. There are input and target files. The input files will be the scaling of Fuzzy AHP. The scaling is changed into single digit number instead of three numbers. As of target files, the weightage are differentiated between companies from 0.05 to 1. Criteria which will undergo neural network fitting in MATLAB are, direct labor, direct material, accounting, admin salary, office expenses, postage printing, spare parts cost and packaging cost. Last step is to identify the life cycle cost after using neural network. Figures shows the output obtained from neural network technique.

From Fig. 2, the highest weightage of 0.8860 is Company 4. Company 4 purchased material with RM 2,400. The price is not the cheapest however can be considered for life cycle cost determination.

From Fig. 3, the highest weightage of 0.9326 is Company 4. Company 4 hires labor with RM 1,030. The price is not the cheapest however can be considered for life cycle cost determination.

From Fig. 4, the highest weightage of 0.7996 is Company 2. Company 2 hire accountant with RM 1,000. The price is the cheapest and can be considered for life cycle cost determination.

Variables - DirectMaterial_outputs																				
DirectMaterial_outputs																				
t120 double																				
	1	2	3	4	5	6	7	8	9	10	11	12	13	14	15	16	17	18	19	20
1	0.6880	0.6884	0.4377	0.8860	0.6298	0.8112	0.6733	0.3047	0.7084	0.6817	0.6313	0.6834	0.3358	0.6245	0.3944	0.5225	0.6397	0.6664	0.3372	0.6813
2																				

Fig. 2 Weightage of 20 companies for direct material

Variables - DirectLabor_outputs																				
DirectLabor_outputs																				
t120 double																				
	1	2	3	4	5	6	7	8	9	10	11	12	13	14	15	16	17	18	19	20
1	0.8125	0.9306	0.7598	0.9326	0.6822	0.6306	0.8052	0.8010	0.9294	0.8895	0.7427	0.8361	0.7422	0.7236	0.7309	0.7329	0.7163	0.8504	0.9315	0.7181
2																				

Fig. 3 Weightage of 20 companies for direct labor

Variables - Accounting_outputs																				
Accounting_outputs																				
t120 double																				
	1	2	3	4	5	6	7	8	9	10	11	12	13	14	15	16	17	18	19	20
1	0.4391	0.7996	0.4400	0.4390	0.4394	0.4074	0.4274	0.4396	0.4361	0.5422	0.4394	0.4434	0.4364	0.4387	0.6326	0.5670	0.4341	0.4389	0.4001	0.4313
2																				

Fig. 4 Weightage of 20 companies for accounting

Variables - AdminSalary_outputs																				
AdminSalary_outputs																				
t120 double																				
	1	2	3	4	5	6	7	8	9	10	11	12	13	14	15	16	17	18	19	20
1	0.4765	0.4765	0.4990	0.8259	0.4765	0.5379	0.4807	0.4765	0.4765	0.5196	0.4765	0.8940	0.4765	0.4785	0.5537	0.4766	0.4772	0.4765	0.4765	0.4766
2																				

Fig. 5 Weightage of 20 companies for admin salary

Variables - PostagePrinting_outputs																				
PostagePrinting_outputs																				
t120 double																				
	1	2	3	4	5	6	7	8	9	10	11	12	13	14	15	16	17	18	19	20
1	0.8185	0.8262	0.8275	0.7854	0.8119	0.7206	0.8241	0.8255	0.8248	0.7305	0.7569	0.8271	0.8177	0.7124	0.7134	0.7449	0.7220	0.8227	0.7502	0.7279
2																				

Fig. 6 Weightage of 20 companies for postage and printing

Variables - OfficeExpenses_outputs																				
OfficeExpenses_outputs																				
t120 double																				
	1	2	3	4	5	6	7	8	9	10	11	12	13	14	15	16	17	18	19	20
1	0.9172	0.1477	0.8622	0.2921	0.1874	0.8001	0.9335	0.3161	0.6469	0.8527	0.4905	0.2718	0.1737	0.8766	0.2968	0.3252	0.2278	0.1503	0.3188	0.1654
2																				

Fig. 7 Weightage of 20 companies for office expenses

From Fig. 5, the highest weightage of 0.8940 is Company 12. Company 12 pays the admin staff with RM 98,752. The price is the cheapest and can be considered for life cycle cost determination.

From Fig. 6, the highest weightage of 0.8275 is Company 3. Company 3 spent for postage and printing with RM 725. The price is not the cheapest however can be considered for life cycle cost determination.

From Fig. 7, the highest weightage of 0.9335 is Company 7. Company 7 spends money for office expenses with RM 900. The price is the cheapest and can be considered for life cycle cost determination.

	1	2	3	4	5	6	7	8	9	10	11	12	13	14	15	16	17	18	19	20
1	0.7777	0.5785	0.5559	0.4090	0.7233	0.4093	0.5355	0.5240	0.6428	0.7423	0.7509	0.5629	0.4226	0.3975	0.4584	0.7166	0.4178	0.5163	0.5606	0.3938
2																				

Fig. 8 Weightage of 20 companies for spare parts cost

	1	2	3	4	5	6	7	8	9	10	11	12	13	14	15	16	17	18	19	20
1	0.3031	0.1640	0.6456	0.2118	0.5824	0.4784	0.4851	0.1964	0.1289	0.1369	0.5933	0.5877	0.4950	0.4273	0.5715	0.5078	0.5091	0.4414	0.5829	0.2051
2																				

Fig. 9 Weightage of 20 companies for packaging cost

From Fig. 8, the highest weightage of 0.7777 is Company 1. Company 1 purchased spare parts with RM 1,800. The price is not the cheapest however can be considered for life cycle cost determination.

From Fig. 9, the highest weightage of 0.6456 is Company 3. Company 3 spent on packaging with RM 300. The price is not the cheapest however can be considered for life cycle cost determination.

Discussion for ANN Technique

In this section, the final answer will be analysed, and the price will be referred from the data sheet obtained from 20 different companies assuming they produce same product. The disposal cost is excluded because some company does not provide such cost. ANN select Company 4 as the best price offered for both variable in Direct Overhead cost.

$$Direct\ Overhead = Direct\ Material + Direct\ Labor$$

$$Direct\ Overhead = RM\ 2,400 + RM\ 1,030$$

$$Direct\ Overhead = RM\ 3,430$$

The next calculation is to determine the Indirect Overhead Cost. For Accounting, Company 2 was selected as cheapest pay. For admin salary, company 12 was selected due to the admin staffs were paid cheapest. Postage and Printing shows Company 3 is selected based on Neural Network training the input and target file. Lastly, for office expenses, Company 7 is selected.

$$Indirect\ Overhead = Account + Admin\ Salary + Postage + Office\ Expenses$$

$$Indirect\ Overhead = RM\ 1,000 + RM\ 98,752 + RM\ 725 + RM\ 900$$

$$Indirect\ Overhead = RM\ 101,377$$

From the experiment also, Neural Network select Company 1 as the best price offered for Spare Parts cost. The cheapest cost for Spare Parts cost detected by Neural Network is RM 1,800. For packaging cost, Fuzzy AHP selects Company 3 deal with cheapest price from packaging supplier. The cheapest cost for packaging is RM 300. Assuming total exploitation cost and disposal cost are RM 202,000 for every company Therefore to compute Life Cycle Cost Remanufacture Perspective:

$$LCC_{RM} = RM\ 1,800 + RM\ 300 + RM\ 101,377 + RM\ 3,430 = RM\ 106,907$$

$$LCC_n = RM\ 202,000$$

$$\Delta LCC = LCC_n - LCC_{RM}$$

$$\Delta LCC = RM\ 202,000 - RM\ 106,907 = RM\ 95,093$$

3.3 DFReM Experiment Using Combination FAHP and ANN

In this experiment using neural network, two files are introduced. There are input and target files. The input files will be the scaling of Fuzzy AHP. The scaling is changed into single digit number instead of three numbers. As of target files, the weightage are differentiated after the computation of Fuzzy AHP using MATLAB. Criteria which will undergo neural network fitting in MATLAB are, direct labor, direct material, accounting, admin salary, office expenses, postage printing, spare parts cost and packaging cost. Last step is to identify the life cycle cost after using combination of Fuzzy AHP and neural network.

From Fig. 10, the highest weightage of 0.1125 is Company 5. Company 5 purchased material with RM 2,010. The price is not the cheapest however can be considered for life cycle cost determination.

From Fig. 11, the highest weightage of 0.1657 is Company 9. Company 4 hires labor with RM 890. The price is not the cheapest however can be considered for life cycle cost determination.

	1	2	3	4	5	6	7	8	9	10	11	12	13	14	15	16	17	18	19	20
1	0.1119	0.0920	0.0068	0.1117	0.1125	0.0975	0.0278	0.0278	0.1119	0.0105	0.0071	0.1085	0.0080	0.0095	0.0063	0.0089	0.0791	0.1113	0.0068	0.0073
2																				

Fig. 10 Weightage of 20 companies for direct material

	1	2	3	4	5	6	7	8	9	10	11	12	13	14	15	16	17	18	19	20
1	0.0730	0.1520	7.2956e-	0.1637	1.3416e-	2.5640e-	1.2413e-	0.0014	0.1657	0.1300	1.9990e-	0.1130	1.4678e-	3.4893e-	4.9525e-	0.0342	1.5392e-	0.0913	0.1555	2.2301e-
2																				

Fig. 11 Weightage of 20 companies for direct labor

From Fig. 12, the highest weightage of 0.1558 is Company 2. Company 2 hire accountant with RM 1,000. The price is the cheapest and can be considered for life cycle cost determination.

From Fig. 13, the highest weightage of 0.1224 is Company 12. Company 12 pays the admin staff with RM 98,752. The price is the cheapest and can be considered for life cycle cost determination.

From Fig. 14, the highest weightage of 0.1658 is Company 18. Company 18 spent for postage and printing with RM 525. The price is not the cheapest however can be considered for life cycle cost determination.

From Fig. 15, the highest weightage of 0.2153 is Company 19. Company 19 spends money for office expenses with RM 1,090. The price is the cheapest and can be considered for life cycle cost determination.

From Fig. 16, the highest weightage of 0.1392 is Company 3. Company 3 purchased spare parts with RM 1,700. The price is not the cheapest however can be considered for life cycle cost determination.

	1	2	3	4	5	6	7	8	9	10	11	12	13	14	15	16	17	18	19	20
1	0.1529	0.1558	1.9025e-04	0.1069	0.0861	6.3930e-04	0.0011	0.1426	5.3201e-04	4.5622e-04	0.1238	5.1016e-04	0.0620	2.1187e-04	2.5457e-04	3.4204e-04	0.0333	0.1553	7.6341e-04	0.0014
2																				

Fig. 12 Weightage of 20 companies for accounting

	1	2	3	4	5	6	7	8	9	10	11	12	13	14	15	16	17	18	19	20
1	0.1151	0.0903	0.0085	0.0095	0.0102	0.0351	0.0083	0.0957	0.0160	0.0080	0.1209	0.1224	0.1223	0.0194	0.0085	0.0087	0.0092	0.1219	0.1184	0.0085
2																				

Fig. 13 Weightage of 20 companies for admin salary

	1	2	3	4	5	6	7	8	9	10	11	12	13	14	15	16	17	18	19	20
1	0.0046	0.1555	0.0394	5.4242e-05	8.5606e-05	2.9184e-05	0.1131	0.1435	0.1308	2.6374e-05	2.8484e-05	0.1637	1.5820e-04	2.5659e-04	2.8193e-05	3.1152e-05	3.4493e-05	0.1658	3.6774e-05	3.0648e-05
2																				

Fig. 14 Weightage of 20 companies for postage and printing

	1	2	3	4	5	6	7	8	9	10	11	12	13	14	15	16	17	18	19	20
1	0.1164	0.0047	-0.4514	0.2100	0.1542	7.2309e-04	0.2141	6.9158e-04	7.1165e-04	7.4215e-04	6.9900e-04	0.1991	7.2048e-04	7.3091e-04	7.7047e-04	7.4254e-04	0.1923	0.0893	0.2153	0.1247
2																				

Fig. 15 Weightage of 20 companies for office expenses

	1	2	3	4	5	6	7	8	9	10	11	12	13	14	15	16	17	18	19	20
1	0.1058	0.1184	0.1392	0.0016	0.0231	0.0015	0.1216	0.1369	0.0729	0.0088	0.0065	0.1029	0.0015	0.0017	0.0021	0.0044	0.0024	0.1057	0.0047	0.0016
2																				

Fig. 16 Weightage of 20 companies for spare parts cost

	1	2	3	4	5	6	7	8	9	10	11	12	13	14	15	16	17	18	19	20
1	0.0583	0.1209	0.1236	0.0833	0.0065	0.0053	0.0113	0.1036	0.0198	0.1225	0.0236	0.0067	0.0429	0.0080	0.0170	0.0190	0.0200	0.0356	0.0743	0.1153
2																				

Fig. 17 Weightage of 20 companies for packaging cost

From Fig. 17, the highest weightage of 0.1236 is Company 3. Company 3 spent on packaging with RM 300. The price is not the cheapest however can be considered for life cycle cost determination.

Discussion for Combination of ANN and FAHP Technique

In this section, the final answer will be analysed, and the price will be referred from the data sheet obtained from 20 different companies assuming they produce same product. The disposal cost is excluded because some company does not provide such cost. Both cost of direct labor with direct material were obtained from Company 5 and Company 9.

$$Direct\ Overhead = Direct\ Material + Direct\ Labor$$

$$Direct\ Overhead = RM\ 2,010 + RM\ 890$$

$$Direct\ Overhead = RM2,900$$

The next calculation is to determine the Indirect Overhead Cost. For Accounting, Company 2 was selected as cheapest pay. For admin salary, company 12 was selected due to the admin staffs were paid cheapest. Postage and Printing shows Company 18 is selected based on Neural Network training the input and target file. Lastly, for office expenses, Company 19 is selected.

$$Indirect\ Overhead = Account + Admin\ Salary + Postage + Office\ Expenses$$

$$Indirect\ Overhead = RM\ 1,000 + RM\ 98,752 + RM\ 525 + RM\ 1,090$$

$$Indirect\ Overhead = RM\ 101,367$$

From the experiment also, Neural Network select Company 1 as the best price offered for Spare Parts cost. The cheapest cost for Spare Parts cost detected by Neural Network is RM 1,700. For packaging cost, Fuzzy AHP selects Company 3 deal with cheapest price from packaging supplier. The cheapest cost for packaging is RM 300. Assuming total exploitation cost and disposal cost are RM 202,000 for every company. Therefore to compute Life Cycle Cost Remanufacture Perspective:

$$LCC_{RM} = RM\ 1,700 + RM\ 300 + RM\ 101,367 + RM\ 2,900 = RM\ 106,367$$

$$LCC_n = RM\ 202,000$$

$$\Delta LCC = LCC_n - LCC_{RM}$$

$$\Delta LCC = RM\ 202,000 - RM\ 106,367 = RM\ 95,633$$

4 Conclusion

Three techniques experimented for DFR_eM are Fuzzy AHP, Neural Network and combination of both Fuzzy AHP and neural network. The computation of Fuzzy AHP for 20 different companies was carried out using MATLAB programming. Proceed to neural network experiment to be compared with Fuzzy AHP. From this objective, the final output having the highest accuracy in selecting lowest cost is combination of Fuzzy AHP and Neural Network Technique. Figure 18 is the illustration in life cycle cost different between three methods. This technique manages a company to save highest cost compared to other two techniques.

The best technique enables a company to save total of RM 95,633 if the exploitation cost of all this companies are RM 200,000. To conclude, combination of Fuzzy AHP and neural network is the most suitable for selecting the best cost before substitute into Design for Remanufacturing. This technique was never introduced by any researcher specifically to solve economy indicator for DFR_eM.

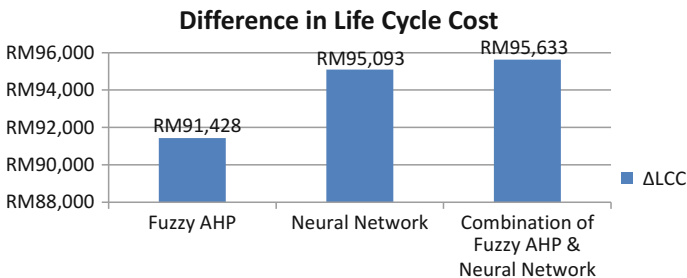


Fig. 18 Illustration of three techniques in design for remanufacturing

References

1. Golinska, P., Kosacka, M., Mierzwiak, R., Werner-Lewandowska, K.: Grey decision making as a tool for the classification of the sustainability level of remanufacturing companies. *J. Clean. Prod.* **105**, 28–40 (2014)
2. Tchertchian, N., Millet, D., El Korchi, A.: Design for remanufacturing: what performances can be expected? *Int. J. Environ. Technol. Manag.* **15**(1), 28 (2012)
3. Prakash, C., Barua, M.K.: Integration of AHP-TOPSIS method for prioritizing the solutions of reverse logistics adoption to overcome its barriers under fuzzy environment. *J. Manuf. Syst.* **37**, 599–615 (2015)
4. Noor, A.Z.M., Fauadi, M.H.F.M., Jafar, F.A., Zainudin, S.F.: Fusion Of Fuzzy AHP in selecting material for drinking water bottle based on customer needs. *ARPN J. Eng. Appl. Sci.* **12**(14), 4243–4249 (2017)
5. Kalogirou, S.A.: Applications of artificial neural-networks for energy systems. *Appl. Energy* **67**(1–2), 17–35 (2000)

Towards EEG-Based Brain-Controlled Modular Robots: Preliminary Framework by Interfacing OpenVIBE, Python and V-REP for Simulate Modular Robot Control



Muhammad Haziq Hasbulah, Fairul Azni Jafar, M. Hisham Nordin and Kazutaka Yokota

Abstract Mostly in natural disaster situations, for example an earthquake, we will face a situation where people get trapped and unable to be found as soon as possible due to the unpredictable terrain. Hence, robot is being seen as scouts that able to adapt and perceive, and usually snake type robot is able to move throughout rubble and small confines. Then, the idea of using modular self-reconfigurable (MSR) robots based on CEBOT in 1988 spark an interest to researchers to fit the search and rescue purpose. Besides that, the idea of controlling robots without manual control but by using “thinking” have fascinated researchers and lead to the development of interfaces between human and machines. In 1970, a Brain Computer Interface (BCI) system has been establish and the BCI system usually is based on the Electroencephalogram (EEG) which is the electrical potentials generated in which the information generated by user and independent of any muscular activities. The implementations of both technologies to each other will frontier for a new alternatives which improves self-reconfigurable modular robot in term of control strategy. As a preliminary framework, a simulation is needed to determine both systems capabilities, and it can be achieved by interfacing the robot simulator,

M. H. Hasbulah (✉)

Centre for Graduate Studies, Universiti Teknikal Malaysia Melaka,
Hang Tuah Jaya, 76100 Durian Tunggal, Melaka, Malaysia
e-mail: m051620001@student.utem.edu.my

F. A. Jafar · M. Hisham Nordin

Faculty of Manufacturing Engineering, Universiti Teknikal Malaysia Melaka,
Hang Tuah Jaya, 76100 Durian Tunggal, Melaka, Malaysia
e-mail: fairul@utem.edu.my

M. Hisham Nordin

e-mail: hisham@utem.edu.my

K. Yokota

Research Division of Design and Engineering for Sustainability, Graduate School
of Engineering, Utsunomiya University, 7-1-2 Yoto, Utsunomiya-shi 321-8585, Japan
e-mail: yokotak@cc.utsunomiya-u.ac.jp

© Springer Nature Singapore Pte Ltd. 2018

M. H. A. Hassan (ed.), *Intelligent Manufacturing & Mechatronics*,
Lecture Notes in Mechanical Engineering,
https://doi.org/10.1007/978-981-10-8788-2_37

OpenVIBE and Virtual Experimentation Platform (V-REP) with the Python programming language. This study presentation will focus on how to control the modular robot in V-REP environment by using Python language which can be used for interfacing with BCI system created in OpenVIBE software and the simulated robot configuration. Each joint handles of modular robot based on V-REP hierarchy being streamed by Python language. There are several methods for establishment of communication between OpenVIBE and other applications. The method purpose in this paper will utilizing Lab Streaming Layer (LSL) and Python script as mediator. The outcome that is expected to be obtained for this study will be the success of communication establish to control virtual modular robot based on data from OpenVIBE. The future work based on this study will involving the BCI system designed using OpenVIBE and implementation to real modular robot might be applied.

Keywords Modular self-reconfigurable robot • Brain computer interface (BCI) EEG

1 Introduction

Nowadays, robots applications has been extended which it not only used widely in industry, but also robot has been entering into human life for assistive purpose especially. Besides that, mostly in natural disaster situations, for example an earthquake, we will face a situation where people get trapped and unable to be found as soon as possible due to the unpredictable terrain. Hence, the idea of modular self-reconfigurable (MSR) robot based on CEBOT in 1988 [1] spark an interest to researchers to fit the search and rescue purpose. Furthermore, robot can be controlled or can be operated with a conventional input device such as keyboard, mouse, or joystick. But these devices however can be used by healthy user, which might be difficult to use for elderly or disabled individuals. Established by Jaques in the 1970s [2], a Brain Computer Interface (BCI) is a direct communication pathway between the human brain and an external device. Nowadays, BCI has been utilized for the usage towards non-disabled individuals in term of applications such as gaming, entertainment, 3D virtual environments and in robotics field. Those two technologies open an opportunity for a new control method for MSR robot which is EEG-based brain controlled. Nowadays, several software tools had been developed and being widely used to process the EEG data such as OpenVIBE etc. OpenVIBE is an open source software platform which being developed for designing, test and using BCI system. OpenVIBE also is a neurosciences tool. It can be used for EEG data acquisition, processing and brain signals visualization in real time.

As a preliminary framework, a simulation is needed to determine both system capabilities. Determination of the system capabilities can be achieved by interfacing the robot simulator, Virtual Experimentation Platform (V-REP) [3] with the OpenVIBE software [4]. V-REP is one of the 3D robotic simulator with

development environment for modelling, programming and simulating robotic system by several provided features and extension mechanics. V-REP also capable with six programming approaches which means V-REP extensions and command can be written in C++ or other languages. It is provided with multiple of functionality for integrating and combined purpose with other applications based on Application Programming Interface (API) and script functionality. This software also capable for several functionalities which are remote monitoring, hardware control, safety checking simulation, algorithm development/parameter adjustment, robotics-related education or factory automation simulation and prototyping and verification [5]. The virtual DTTO modular robot used for this study able to be obtained from a project by Alberto in HACKADAY.IO website [6]. DTTO MSR robot is being designed based on the hybrid architecture MSR robot called M-TRAN. The robot has been minimized as much as possible to have a large free space in half of the robot. Each module consists of two boxes, rounded on one side, connected by a bar.

Based on the OpenVIBE website, a tutorial provided for communication between OpenVIBE to external software are based on utilizing VRPN server and a basic C++ programming as mediator. VRPN protocol is not very convenient for sending multichannel data but it is appropriate for stimulations data. According to Tom Radcliffe [7], even though C/C++ have faster coding runtime, it is difficult to write and frequently unreadable. Hence, another technique besides VRPN and C++ as mediator can be used such as Python language.

Python can be considered as high-level programming language which is widely used for general-purpose programming. This programming language was designed in order to emphasize in term of code syntax and readability. This will allow for the program to be written in fewer lines of code compared to another programming languages such as C++ or Java that might be used by programmers. This study presentation will focus on how to establish communication for control from OpenVibe to V-REP software for controlling DTTO Explorer modular robot [6] by using Python programming language as mediator. The communication will be between OpenVIBE, Python programming and V-REP software.

2 Literature Review

The study focus on communication establish from OpenVIBE to V-REP through Python language as mediator. There are several methods for communication between OpenVIBE to external applications. The common method to transmit information from or to OpenVIBE in real time are VRPN, TCP/IP, LabStreamingLayer (LSL), OpenSoundControl (OSC), Python and MATLAB, Lua and C++ [8].

Streamed matrix data will be sent by OpenVIBE by chunks which containing several values and may have several channels. All the data has to be sent to the VRPN client at the same time so it can be processed in one run. All the data will be

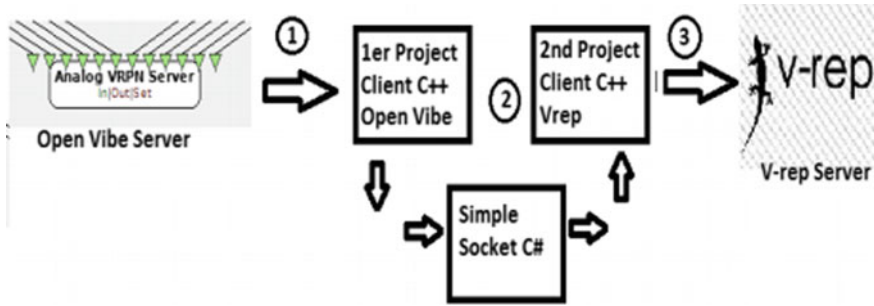


Fig. 1 Establishment of communication from OpenVIBE to V-REP by VRPN server [9]

turned into a one-dimensional array by OpenVIBE and the data will be send over VRPN. A method that utilized VRPN server had been applied in EEG mind guided motion control of robot manipulator by Malki et al. [9]. Analog VRPN server was employed in OpenVIBE for P300 speller online. It only able to receive analogue value and 6 letters corresponding to 6 robot movements from P300 stimulations are sent via VRPN to first client coded in C++. To create a communication to V-REP, a C# socket is established on both first C++ client and second C++ client. The second C++ client is coded and C# server is implemented in order to receive data. According to Antoni, there could be a more efficient way to establish communication between OpenVIBE and V-REP [9] (Fig. 1).

Besides that, there are another research which used MATLAB for transmitting information from OpenVIBE to external communication. OpenVIBE is used to acquires live data only from EEG headset. There are only 3 components in OpenVIBE scenario which are Acquisition client box, Time based epoching box which collects the signals with an epoch duration of 3 s at an interval of 0.5 s, and MATLAB scripting box for sending data to MATLAB to be processed and the output being stored in a file and being read by Arduino micro-controller for robot control [10]. This reference shows that the EEG data is transferred to Arduino but the data is processed by MATLAB software at first and OpenVIBE only being to acquire EEG data. In our opinion, even though this method being considered easy-to-setup, but it require coding knowledge of MATLAB for EEG data processing. The method mentioned before use OpenVIBE for signal acquisition and processing and C++ is only being as mediator to transmit value to external application without being facilitated by file reading.

OSC has provided a standard for communication among computers, sound synthesizers and other multimedia [11]. For OpenVIBE software, there is an OSC Controller box for sending OSC messages to an OSC server. But in the current implementation, OpenVIBE internal timing is not passed to the OSC. Besides that, the sampling rate is ignored if input type is signal. For method that involved

stimulation signal input type, for example in Motor Imagery scenario which right/left hand movement as stimulation input to be send to external applications, OSC is may not be suitable.

Then, there is a system being designed and implemented for study on standard visual feedback and tactile feedback in terms of BCI performance [12]. The method used was by utilizing LSL for communicating OpenVIBE to Arduino. In research experiment, LSL is a system that unified collection of measurement time series which can be used for real-time access besides viewing and recording data [13]. The EEG data is processed in OpenVIBE software where the processed data is transmitted to Python where the data will be streamed and become a stimulation code for Arduino. This method might not be the best but it is easy to be understood for future research and it is accessible. As this method is for establish communication from OpenVIBE to Arduino, it also can be used for communicating with V-REP. Instead of using VRPN and C++, the establishment of communication by LSL and Python as mediator to V-REP might be better and faster compared to method by Antoni as mentioned before.

In addition, there is a tutorial video on interfacing of Python to V-REP which can be found in Youtube webpage entitled “Python Robot Simulation with V-Rep” [14]. In this tutorial, it provide with step by step robot simulation with Python and V-REP. The video shows how to connect Python with V-REP, how to write a simple obstacle avoidance in Python, retrieve object handles, control robot actuators, read proximity sensors and retrieve and display images in Python. This tutorial is easy to understand and extensive for Python-V-REP interface. However, this tutorial is focusing on the communication between Python and V-REP only. Besides that, the robot used in the tutorial is Pioneer 3DX differential drive robot which is difference with modular robot. The paper intended to have control for modular robot based on the brain signals. As OpenVIBE software is needed for brain signals processing, a communication from OpenVIBE to V-REP is needed and Python is act as mediator between two software.

3 Methodology

The proposed method for the establishment of communication to VREP can be done in following sequence based on Fig. 2:

The method for communication establishment from OpenVIBE to V-REP will be divided into two phases which are:

Phase 1: Communication from OpenVIBE to Python through LSL.

Phase 2: Communication from Python to VREP through remote API.

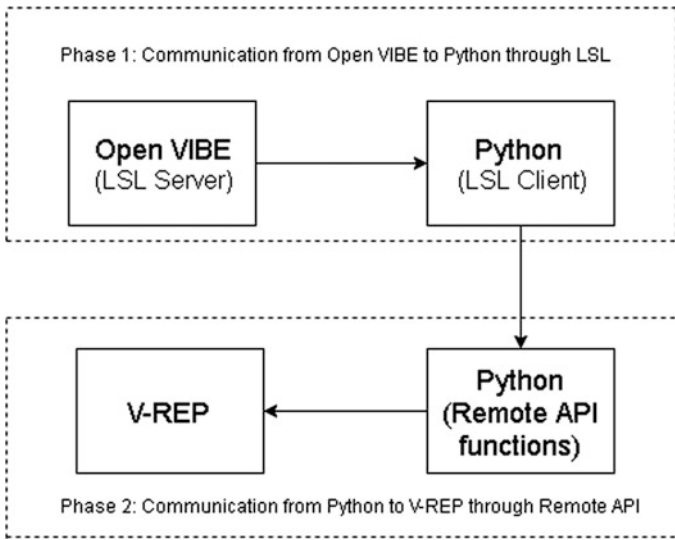


Fig. 2 Communication establishment from OpenVIBE to V-REP by LSL

3.1 Phase 1: Communication from OpenVIBE to Python Through LSL

OpenVIBE (LSL Server)

In order to establish communication with Python, in OpenVIBE online scenario, at the end of the EEG processing, ‘LSL Export (Gipsa)’ box need to be added as in Fig. 3.

Python Script (LSL Client)

From Python script, to load the LSL library, `import pylsl` need to be called (Fig. 4).

Then, the following code is needed to resolve an EEG stream on the lab network and create a new inlet to read from the stream data.

```
streams = resolve_stream('type', 'EEG')
inlet = StreamInlet(streams[0])
```

Fig. 3 LSL server box in OpenVIBE



```
import vrep
from pylsl import StreamInlet, resolve_stream
import sys
import time # used to keep track of time
import numpy as np # array library
```

Fig. 4 Calling LSL library in Python script [13]

OpenViBE stimulation codes

```
1 #define OVTK_StimulationId_ExperimentStart 0x00008001
2 #define OVTK_StimulationId_ExperimentStop 0x00008002
3 #define OVTK_StimulationId_SegmentStart 0x00008003
4 #define OVTK_StimulationId_SegmentStop 0x00008004
5 #define OVTK_StimulationId_TrialStart 0x00008005
6 #define OVTK_StimulationId_TrialStop 0x00008006
7 #define OVTK_StimulationId_BaselineStart 0x00008007
8 #define OVTK_StimulationId_BaselineStop 0x00008008
9 #define OVTK_StimulationId_BaseStart 0x00008009
```

Fig. 5 OpenViBE stimulation code [15]

Then the data can be manipulated in term of stimulation code which has been declared in OpenViBE by default and numeric values. The list of stimulation codes which being provided in OpenViBE website is as shown as in Fig. 5.

The stimulation code is the input command for controlling modular robot in V-REP and its communication establishment is in Phase 2.

3.2 Phase 2: Communication from Python to VREP Through Remote API

To establish communication with V-REP, the V-REP remote API is the best way to use, because it can be easily used in a Python project. The Python coding is designed so that the modular robot is able to change its configurations based on the user input. As V-REP plugin, where a server already being integrated, it only requires launching it on the V-REP installation folder. Several robots are directly accessible once the software is being launched or user can import their designs from Computer Aided Design (CAD) software into V-REP. Remote API functionality allowed for access from various possible external applications or hardwares. Meanwhile, within the simulator, the regular API can be accessed.

Python Script (Remote API functions)

Remote API functionality in Python script can be used and three following files are needed which are vrep.py, vrepConst.py and remoteApi.dll. Those files are located in V-REP's installation directory and those three must be included together with the Python script project so that the directory of those elements are known to Python.

```

import vrep # close any open connections
import sys  vrep.simxFinish(-1)
import time # used to keep track of time         vrep.simxStart('127.0.0.1', 19999, True, True, 500, 5)
import numpy as np # array library
import math

if clientID != -1: # if we connected successfully

```

Fig. 6 Python script to import V-REP library (left) and enabling remote API (right) [3, 14]

From Python script, call ‘import vrep’ code is needed for load vrep library. Remote API on the client side being enabled as code ‘vrep.simxStart’ being called. It is actually one of the remote API functions for Python and all other remote API functions have been also described in Coopeliarobotics websites. V-REP remote API functions can easily be recognized from their “simx”-prefix (Fig. 6).

A Python script is designed as V-REP client and it is used for interfacing with the OpenVIBE software. This communication between Python and V-REP is maintained via a while loop and the configuration of the robot change based on user input in which the robot configuration is being predetermined. The following Fig. 7 is the flowchart for Python script coding which establish communication to V-REP.

As the simulation time step, the value of time steps is specified at 0.001 which considered small value (Fig. 8). The increment of simulation time will be based on each of the simulation time step for each time the simulation is executed. For preventing inaccurate or unstable simulations, 0.001 is a good choice as small value of time steps will lead to more accurate and precise simulations. Large value of time steps will lead for faster simulations but it will be inaccurate and unstable.

The motor movement for modular robot that being simulated is based on the equation of Serpentinoid curve which can be seen in Fig. 7. It was discovered by Professor Hirose in 1976 according to Juan Gonzalez Gomez [16]. The motion of snake-like is needed for the DTTO modular robot so that it has the ability to move as it does not have specific mobility item such as a wheel.

The object that need to be worked on need a reference. It is needed as it being done with handles, that being obtained via various handle retrieving functions that expect an object name as input argument. From a plugin, the joint of the robot which is the object in V-REP, is accessed as Fig. 9.

For this research work, all the virtual DTTO modular robots will be control based on the number of joints. Hence, as the robot have multiple of joints, by using the same name the robot joint will be accessed based on the number. Hence, an array with range based on the number of joint is created so each of the joint object can be accessed.

As the code is running, the code while loop will start as the user enter the letter “Y” which indicate the user want to proceed with the simulation. The robot movement code in the while loop will keep running and the robot can be changed from time to time (Fig. 10).

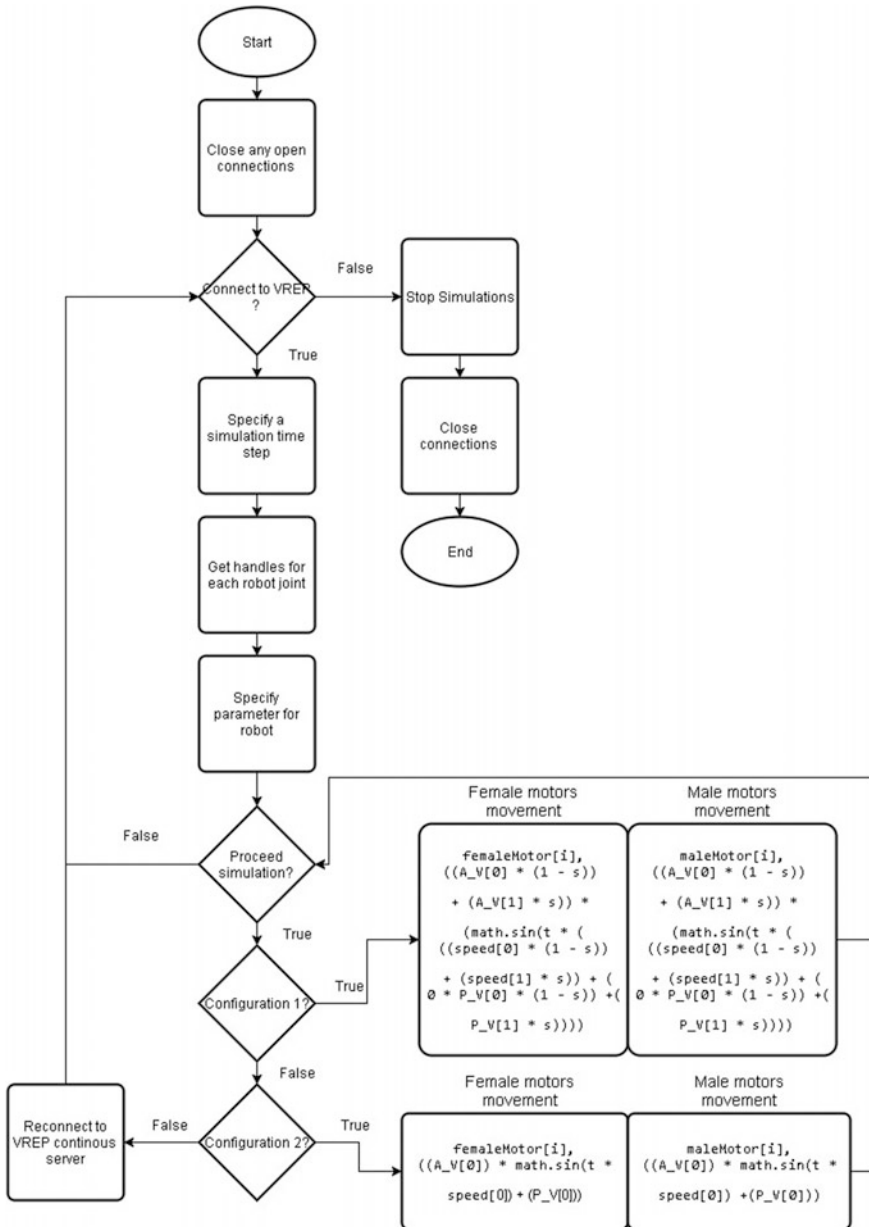


Fig. 7 The flowchart on how Python script work to communicate and control modular robot in V-REP


```

dt=0.001
vrep.simxSetFloatingParameter(clientID,
                              vrep.sim_floatparam_simulation_time_step,
                              dt,
                              vrep.simx_opmode_oneshot)

```

Fig. 8 Simulation time step being specified [3, 14]

```

for i in range(0, number_of_joints):
    errorCode, maleMotor[i] = vrep.simxGetObjectHandle(clientID, 'Male_joint' + str(i + 1),
                                                       vrep.simx_opmode_oneshot_wait)
    errorCode, femaleMotor[i] = vrep.simxGetObjectHandle(clientID, 'Female_joint' + str(i + 1),
                                                         vrep.simx_opmode_oneshot_wait)

```

Fig. 9 Get the handles for each robot joint

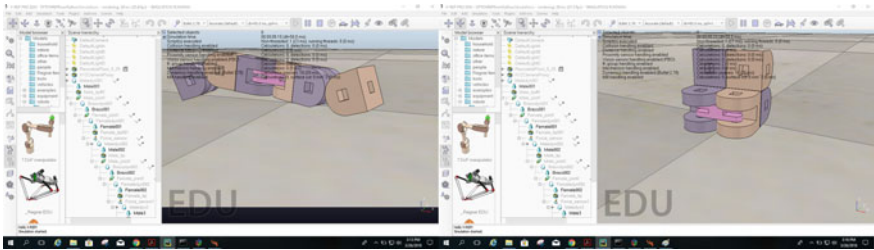


Fig. 10 Configuration 1 where movement for DTTO robot being simulated (left) and configuration 2 where the DTTO robot stop movement and change into box-like shape (right)

4 Expected Outcome

As this paper focusing on easiest and good establishment of communication between OpenVIBE and V-REP, the expected outcome is as the associated command being activated, the virtual robot control can be achieved. Hence, if the robot control is not achieved, it is expected that the error is coming from bad EEG data acquired and not due to the method of communication established. Besides that, it is expected that the data can be transferred efficiently from OpenVIBE to external applications which is V-REP in real time.

As this paper is not discussing on EEG processing in OpenVIBE, this method is expected to be able to be used for transferring processed EEG data whether it is P300 speller, Motor Imagery or SSVEP BCI system for future work. For future work, the BCI system created by OpenVIBE will basically consists of several scenario before running online scenario for real-time EEG control. It will consists of

Signal monitoring, Signal acquisition, Filter training, Classifier training and Real-time Online scenario. Besides that, for future work this method might be applied to real modular robot.

Hence, it is expected that the method framework discussed in this paper can achieve promising successful rate for purpose of real time EEG control using OpenVIBE.

The difference between this paper and the tutorial available throughout internet is that, this paper is focusing on the idea of how to simulate control of the modular robot in V-REP which is based on the output from OpenVIBE. The literature review in the paper is focusing on a comparison how other researcher communicate from OpenVIBE to the external applications. As the tutorial mentioned in Literature Review section focusing on the controlling robot by using Python script which extensive on Python programming. This paper introduced the idea of controlling robot using OpenVIBE which Python script act as mediator from OpenVIBE to external applications. As the tutorial shows the Pioneer 3DX differential drive robot control from Python [14], this paper shows how modular robot in V-REP being control based on the output from OpenVIBE. The multiple configuration simulated by modular robot in V-REP being shown as in flowchart in Fig. 7 where it is intended for the robot to simulate multiple configuration based on the input from user. The input from the user will be change to the input from OpenVIBE. Hence, EEG-Based Brain-Controlled Modular Robots that able to propagate multiple configuration is expected to be achieved.

5 Conclusion

Towards an EEG controlled modular robot, a simulation is needed to determine both system capabilities, and it can be achieved starting by establish communication of EEG processing software tools with external applications. For simulatings the capabilities of EEG processing tools in controlling the robot, a virtual modular robot can be used in V-REP software but the communication need to be established first for EEG processing tools and V-REP.

OpenVIBE is one of the EEG processing tools softwares that is recently used for the purpose of control. There are several studies which utilize this software for control external applications whether for controlling mobile robot, robot manipulator or virtual applications. However, it cannot be directly used for control purpose in real time. There are several ways for communicating with eternal applications and it involves another application as mediator such as C++, Python or MATLAB. Available box algorithm provided for communication is LSL, OSC controller, TCP Writer and VRPN. The communication also able to be achieved even though the EEG processing is not done in OpenVIBE. But, the communication will be executed by file reading of the data. At this point, there is no absolute way for establish the communication which mean there could be other method which can be used to achieve the same goal.

By using LSL server/client and Python script as mediator to external applications, the framework become less complicated and easier to be understand which will however benefits other researcher to understand and apply for different application.

References

1. Fukuda, T., Nakagawa, S.: Dynamically reconfigurable robotic system. In: Proceedings of the IEEE International Conference on Robotics and Automation, 1988, pp. 1581–1586
2. Vidal, J.J.: Toward direct brain-computer communication. *Annu. Rev. Biophys. Bioeng.* **2**, 157–180 (1973)
3. Coppelia Robotics V-REP: Create. Compose. Simulate. Any Robot. Coppelia Robotics (2016). <http://www.coppeliarobotics.com/index.html>. Accessed: 16 Nov 2017
4. Inria: OpenViBE | Software for brain computer interfaces and real time (2015). <http://openvibe.inria.fr/>. Accessed 17 Nov 2017
5. V-REP Robot Simulator. Azo Robotics. <https://www.azorobotics.com/software-details.aspx?SoftwareID=27>. Accessed 16 Nov 2017
6. Alberto: Dttto—Explorer Modular Robot. Hackaday (2016). <https://hackaday.io/project/9976-dtto-explorer-modular-robot>. Accessed 04 Jul 2017
7. Tomr: Python vs. C/C++ in Embedded Systems. In: ActiveState (2016). <https://www.activestate.com/blog/2016/09/python-vs-cc-embedded-systems>. Accessed 16 Nov 2017
8. Lindgren, J.: Overview: Sending data and stimulations to/from OpenViBE. In: OpenViBE | Software for Brain Computer Interfaces and Real Time (2015). <http://openvibe.inria.fr/overview-sending-data-stimulations-out-from-openvibe/>. Accessed 15 Nov 2017
9. Malki, A., Yang, C., Wang, N., Li, Z.: Mind guided motion control of robot manipulator using EEG signals. In: 2015 5th International Conference on Information Science and Technology (ICIST) (2015)
10. Gargava, P., Sindwani, K., Soman, S.: Controlling an Arduino robot using brain computer interface. In: Proceedings of 3rd International Conference on Reliability, Infocom Technologies and Optimization 2014, pp. 3–7
11. Wright, M., Freed, A., Momeni, A.: Open sound control: state of the art 2003. In: Proceedings of the 2013 International Conference on New Instruments for Musical Expression (NIME-2013), 2013, pp. 153–159
12. Jeunet, C., Vi, C., Spelmezan, D., N’Kaoua, B., Lotte, F., Subramanian, S.: Continuous tactile feedback for motor-imagery based brain-computer interaction in a multitasking context. In: Lecture Notes in Computer Science (including Subseries Lecture Notes in Artificial Intelligence Notes Bioinformatics), vol. 9296, no. Mi, pp. 488–505 (2015)
13. LabStreamingLayer: Google Code (2012). <https://code.google.com/archive/p/labstreaminglayer/>. Accessed 19 Nov 2017
14. Nikolai, K.: Python Robot Simulation with V-Rep | V-rep Tutorial. YouTube (2015). <https://www.youtube.com/watch?v=SQont-mTnfM>. Accessed 03 Jan 2018
15. Ibonnet: Stimulation Codes. OpenViBE | Software for Brain Computer Interfaces and Real Time (2011). <http://openvibe.inria.fr/stimulation-codes/>. Accessed 17 Nov 2017
16. Gomez, J.G.: Serpentinoid Curve. *Jupyter nbviewer* (2015). <http://nbviewer.jupyter.org/github/Objuan/My-Ipython-notebooks/blob/master/serpenoid-curve/Serpenoid-Curve-es.ipynb>. Accessed 10 Nov 2017

Genetic Algorithm Optimization of PID Controller for Brushed DC Motor



A. A. M. Zahir, S. S. N. Alhady, W. A. F. W. Othman
and M. F. Ahmad

Abstract PID controller is one of the most common usable controller in controlling the velocity of brushed DC motor due to its reliability and simplicity. Classical design formulas to tune the PID parameter such as Ziegler-Nichols and Skogestad IMC produce less desirable results in terms of performance. In order to improve the performance, PID parameter is optimized by using Genetic Algorithm (GA) method. Integral of Time Multiplied by Absolute Error (ITAE) objective function is modified based on design requirements. The results obtained show that tuning method by using GA produce the best outcome. Rise time, settling time, percentage of overshoot yields from modified fitness function of GA is the fastest compare with Ziegler-Nichols, Skogestad IMC, and unmodified GA fitness function. The modification of ITAE fitness function improve the rise time and settling time by 76.63% and 78.29% respectively. All of the methods produce minimal steady-state error and is acceptable for velocity control application. Embedding the PID optimized by GA into the microcontroller and the comparison between the simulation and real-time application should be done in the future to evaluate the performance in real life application.

Keywords Brushed DC motor · PID controller · PID tuning method
Genetic algorithm

1 Brushed DC Motor

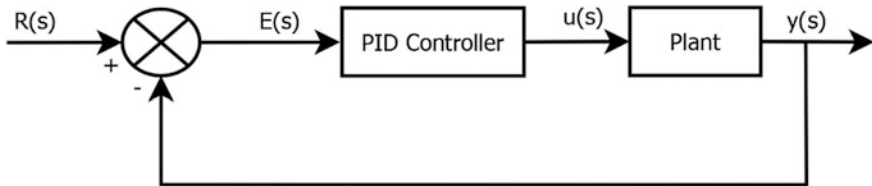
Brushed DC Motor is widely used in industry due to its good performance, low cost and easiness to control [1]. Designing a PID controller to control the velocity of the brushed DC motor is the main objective of this paper. The crucial element in designing a PID controller for the motor is to determine the plant module.

A. A. M. Zahir · S. S. N. Alhady (✉) · W. A. F. W. Othman · M. F. Ahmad
School of Electric and Electronic, Engineering Campus Universiti Sains Malaysia,
14300 Nibong Tebal, Penang, Malaysia
e-mail: sahal@usm.my

© Springer Nature Singapore Pte Ltd. 2018
M. H. A. Hassan (ed.), *Intelligent Manufacturing & Mechatronics*,
Lecture Notes in Mechanical Engineering,
https://doi.org/10.1007/978-981-10-8788-2_38

Table 1 PPSM63L-01 brushed DC motor specification

Parameter	Value
Voltage	24 V
Speed	4700 rpm
Maximum torque	10.95 Nm
Power rate	270 W
Weight	6.8 kg

**Fig. 1** Block diagram of the system with PID controller

A good system identification method is needed to be carried in order to approximate an accurate transfer function of the motor.

The DC motor used is PPSM63L-01 model manufactured by Shanghai Dixi Technical Co. Ltd. The specification of the motor is specified in Table 1. The input voltage is 24 V and produce maximum speed and torque of 4700 rpm and 10.95 Nm respectively.

The bump test is conducted on the motor in order to determine the transfer function of the motor. Constant voltage is applied on the motor and the output velocity is recorded. Based on the datasets, the transfer function of the motor is estimated by using MATLAB. The transfer function of the motor obtained from MATLAB approximation is as follow:

$$G(s) = \frac{104.9}{s^2 + 103.5s + 2617} \quad (1)$$

The block diagram of the system including PID controller could be represented in Fig. 1.

2 PID Tuning Method

Proportional-Integral-Derivative (PID) controller is one of the most common controller that is widely being used in industry to control the velocity of the brushed dc motor. PID yields good control performance and is not complicated to configure. The basic form of PID controller is as follow:

$$C(s) = K_p + \frac{K_p}{T_i s} + T_d K_p s = K_p + \frac{K_i}{s} + K_d s \quad (2)$$

where K_p , K_i and K_d indicate proportional, integral and derivative gain respectively. Determining the best value of gains is crucial in order to design a good performance controller. Classical tuning method and metaheuristic tuning method is widely used in tuning the PID's gains.

There is a lot of classical design formulas for PID tuning such as Ziegler-Nichols [2] and Skogestad IMC [3]. Ziegler Nichols often produce good performance in term of rise time and good disturbance rejection. Disadvantages of Ziegler-Nichols tuning method is it produce oscillatory response and yields large percentage of overshoot. Skogestad IMC usually produce less percentage of overshoot compare with Ziegler-Nichols but have poor disturbance rejection properties.

In [4, 5], it is clearly shown that the most worst performance parameter for Ziegler-Nichols tuning method is it produce large number of overshoot and long settling time compare with metaheuristic method such as GA and PSO. In the application of velocity control where the reference velocity is always varied, the tracking performance especially overshoot percentage, settling time, and steady-state error is important.

Recently metaheuristic approach such as Genetic Algorithm (GA) and Particle Swarm Optimization (PSO) are widely being used to optimize the value of K_p , K_i , and K_d [4–7]. GA and PSO are proven to optimize good PID gains that results in better controller performance. The block diagram of GA with PID controller is presented in Fig. 2 where GA will optimize the value of gain in order to minimize the error between the feedback value and reference value.

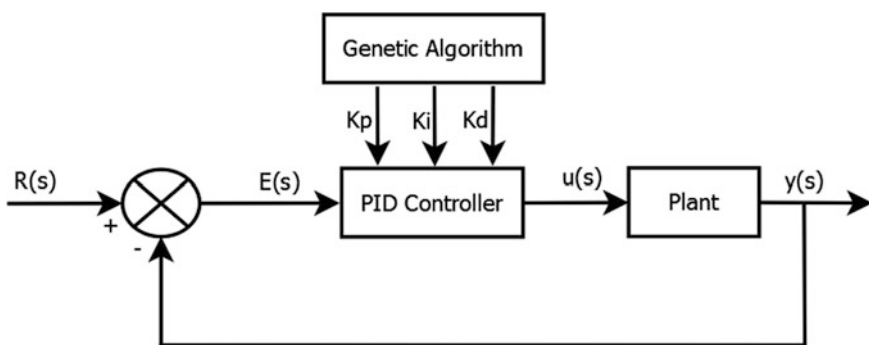


Fig. 2 Block diagram of PID controller optimized by GA

3 Fitness Function

In order to optimize the value of gains by using GA, a good fitness function needed to be determined. Widely used fitness functions are summarized in Table 2 which is Mean of the Squared Error (MSE), Integral of Time Multiplied by Absolute Error (ITAE), Integral of Absolute Magnitude of the Error (IAE), Integral of the Squared Error (ISE), and Integral of Time multiplied by the Squared Error (ITSE) [8–12].

The fitness of the chromosome is decided by the value of the fitness function. The main objective of the fitness function mention in [8–12] are to minimize the error. It can be concluded that the smallest value of fitness function indicates that the fitness function is able to minimize error the best as stated in Eq. 3 [4].

$$Fitness\ Function\ Value = \frac{1}{Performance\ Index} \tag{3}$$

Basic fitness functions as stated in Table 2 are insufficient to design a PID controller that meet the design requirement. Design requirement such as percentage of overshoot, steady state error, settling time, and rise time is included in the fitness function. Results of modified ITAE fitness function shows better response compared with original ITAE function [7]. Weightage is assigned to performance parameters based on design requirements. In this paper ITAE fitness function is selected and modified as in Eq. 4.

$$f_{(modified\ ITAE)}(K_p, K_i, K_d) = \int_0^\tau t|e(t)|dt + \alpha O_v + \beta SS_e + \delta t_s + \gamma t_r \tag{4}$$

where O_v , SS_e , t_s , t_r are overshoot, steady state error, settling time, and rise time respectively. α , β , δ , and γ indicates the weightage assigned on performance parameters based on design requirement. The weightage of α , β , δ , and γ used in this paper are 1.5, 15, 7, and 1 respectively. The weightage value is selected based on the desired output performance based on the brushed DC motor. For this case,

Table 2 Type of fitness function

Fitness function	Equation
MSE	$\frac{1}{\tau} \int_0^\tau [e(t)]^2 dt$
ITAE	$\int_0^\tau t e(t) dt$
IAE	$\int_0^\tau e(t) dt$
ISE	$\int_0^\tau e(t)^2 dt$
ITSE	$\int_0^\tau te(t)^2 dt$

the most desired performance is to achieve the most minimum steady state error and followed by slower settling time. Based on the observation, the weightage value assigned as above produced the best output performance of PID controller.

4 Genetic Algorithm Implementation

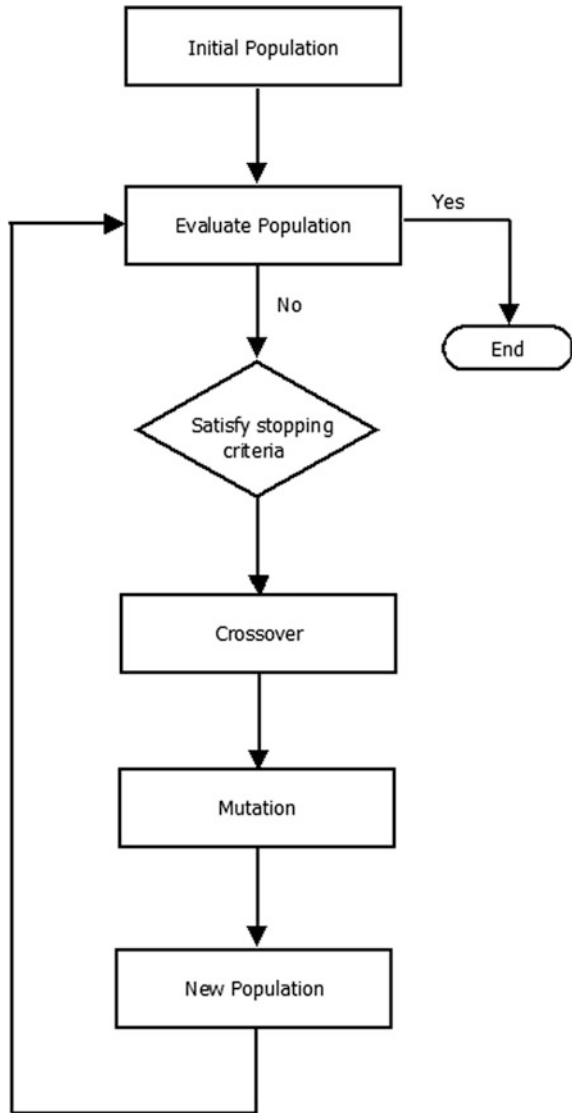
GA optimization is simulated by using optimization tool in MATLAB. The code to define the fitness function is created before inserted into the optimization tool. Modified ITAE function is determined as the fitness function. The unknown output parameter of the fitness function is defined as K_p , K_i , and K_d . Others input parameter is presented in Table 3. The flowchart of genetic algorithm process is as in Fig. 3. General execution procedure for GA is as follow:

1. The fitness function is created. Modified ITAE function is used as the fitness function. Three unknown output is defined as K_p , K_i , and K_d .
2. Initial population of 20 is created. For small number of output parameter, small number of population is sufficient. To improve accuracy, bigger number of population could be selected but will increase simulation time. MATLAB generate new population from the individuals in the generation.
3. Lower bound and upper bound is defined as [0 0 0] and [700 8000 5] respectively as in Table 3. The value is decided based on the gains value obtained from Ziegler-Nichols and Skogestad IMC. The lower and upper bound selection is crucial in order to reduce the iteration time.
4. Each individual is rated based on the fitness function value. A small value indicates the individual is fit. A large value shows that the individual is less fit.
5. The best fit individuals is selected as parent. The best fit parent is selected to be bred by crossover and mutation to produce new population. The value of elite count in this case is 0.1. This indicates that only small amount of low fitness individual is selected to be inherited to new population in new generation.

Table 3 Input GA parameter

Population size	20
Lower bound	[0 0 0]
Upper bound	[700 8000 5]
Initial range	[-10 10]
Selection function	Stochastic uniform
Elite count	0.1
Crossover fraction	0.8
Mutation function	Constraint dependent

Fig. 3 Flowchart of genetic algorithm process



6. Crossover and mutation of parents is done to create new children for new population.
7. Process is repeated until the output satisfy the stopping criteria. For each generation the iteration try to converge zero value of fitness function.
8. The simulation is conducted for 20 times to ensure the accuracy of the results. The simulation is conducted 20 times to observe the variance of output produce by the simulations.

The pseudo-code of the genetic algorithm is as follow:

- (2) Evaluate Population
- (3) For N=3 to all numbers of K_p , K_i , and K_d .
- (4) $K_p = (0,700)$
- (5) $K_i = (0,8000)$
- (6) $K_d = (0,5)$
- (7) evaluate K_p , K_i , and K_d by Eq. 4.
- (8) repeat GA :
- (9) for each K_p , K_i , and K_d .
- (10) $f_i =$ evaluate K_p , K_i , and K_d .by Eq. 4.
- (11) next i
- (12) select 2 parents
- (13) create 2 parents and 2 offspring
- (14) evaluate offsprings by Eq. 4.
- (15) replacement
- (16) until GA stopping criteria is fulfilled.
- (17) end N
- (18) End

5 Results and Discussions

Based on 20 times of simulation conducted, the best fitness simulation produce objective function value of 6.7 while the worst fitness value is 12.29. Figure 4 show the graph of fitness value for each generation for the best fitness value. Blue dot indicates fitness value for each generation and black line represent the mean fitness value. From the graph it shows that the GA try to find the best fitness value by minimizing the error value on each generation based on modified ITAE function.

Table 4 shows the results of K_p , K_i , and K_d obtained from different methods. It shows that modified ITAE fitness function produce the biggest value of proportional, integral and derivative gain compare with other methods.

The final form of controller of modified ITAE fitness function in frequency domain is as follow:

$$C_{(ITAE\text{Modified})}(s) = 549.445 + \frac{7890}{s} + 4.608s \quad (5)$$

Based on K_p , K_i , and K_D value obtained, step response of the system is plotted as shown in Fig. 5. From the response, the graph clearly shows that Ziegler-Nichols tuning method produce oscillatory or overdamped step response. Skogestad IMC tuning produce slowest response among all of the methods but have less percentage of overshoot than Ziegler-Nichols. Both GA tuning method by using modified and

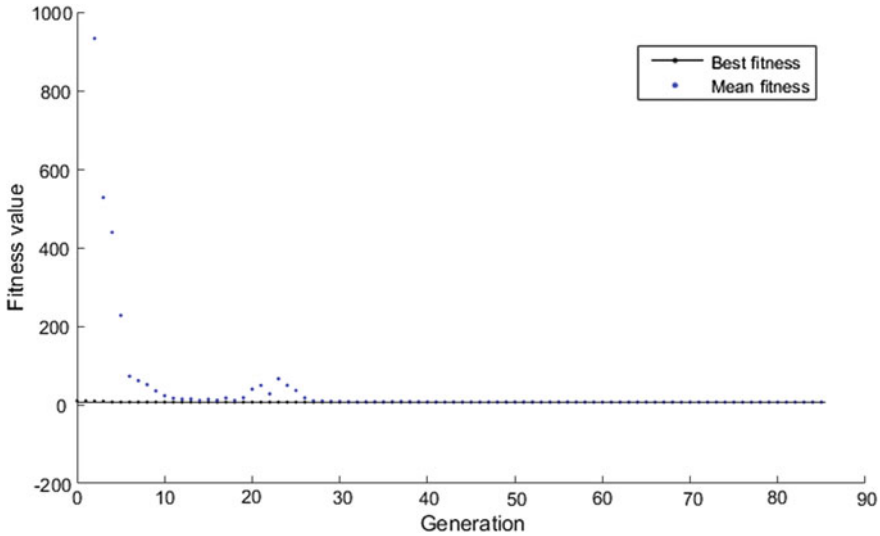


Fig. 4 Fitness value graph for the simulation that produce the lowest fitness value

Table 4 Tabulation of K_p , K_i , and K_d

Methods	K_p	K_i	K_d
Ziegler-Nichols	203.01	18545.0	0.5558
Skogestad IMC	90.870	2102.70	0.2315
Unmodified ITAE fitness function	116.96	2999.40	1.0786
Modified ITAE fitness function	549.45	7890.00	4.6080

unmodified fitness function give better response compare with classical tuning method. The performances of each method is tabulated in Table 5.

In term of overshoot percentage, Ziegler-Nichols tuning produce the worst performance with 47.371% of overshoot among all of the method. Skogestad IMC produce less overshoot percentage compare with Ziegler-Nichols. The best performance in term of overshoot percentage is GA tuning for both modified and unmodified ITAE fitness function that yield 0% overshoot percentage.

GA-Modified ITAE fitness function have the fastest rise time, 0.0043 s while unmodified ITAE fitness function have the slowest rise time compare with all tuning method. Ziegler-Nichols yield second faster rise time after GA-modified ITAE fitness function but is unfavorable due to high percentage of overshoot.

GA-Modified ITAE fitness function clearly produce the fastest settling time compared with all of the methods with 0.0071 s. The slowest settling time is 0.1240 s tuned by Ziegler-Nichols method. Due to overdamped response, Ziegler-Nichols consume the most time to reach steady state. The percentage difference between the fastest settling time (tuned by GA modified ITAE function) and

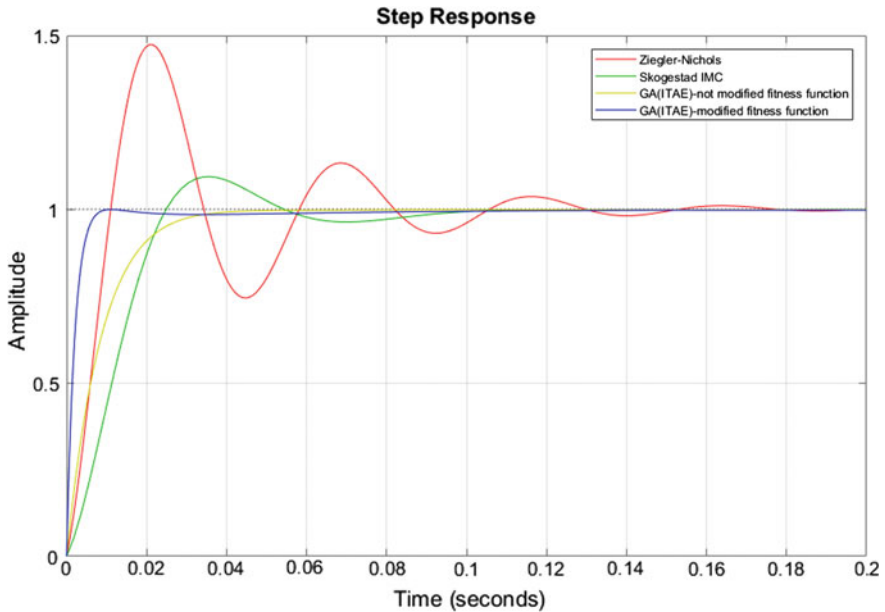


Fig. 5 Step response of different tuning methods

Table 5 Performance of different tuning methods

Tuning method	Overshoot (%)	Rise time (s)	Settling time (s)	Steady-state error
Ziegler-Nichols	47.371	0.0085	0.1240	0.0021
Skogestad IMC	9.3685	0.0180	0.0868	0.0034
Unmodified ITAE fitness function	0.0000	0.0184	0.0327	0.0024
Modified ITAE fitness function	0.0000	0.0043	0.0071	0.0041

the slowest settling time (Ziegler-Nichols) is 94%. Modified ITAE fitness function shows superior performance compared with other methods in term of settling time.

The systems objective is to achieve zero steady state error. All of the methods produce minimal steady state error that is less than 0.01 error. Modified ITAE fitness function produce the biggest steady state error while Ziegler-Nichols produce the smallest error.

The comparison between modified and unmodified ITAE function is needed in order to evaluate the effect of modification on ITAE fitness function. Modified ITAE fitness function have better rise time and settling time by 76.63% and 78.29% respectively. Both fitness function produce 0% of overshoot. GA-Unmodified ITAE fitness function have smaller steady state error by 41.46%.

It can be concluded that GA-modified ITAE fitness function improved the rise time and settling time performance compared with original ITAE function.

From the discussions above it can be concluded that optimization by using GA for both modified and unmodified ITA fitness function improve the performance in terms of percentage of overshoot, rise time, and settling time. As for steady state error, by using GA unmodified ITAE function, the steady state error is improved by 0.0010 compare with Skogestad IMC. By using GA-unmodified ITAE fitness function the performance in terms of steady state error drop by 0.002 in value. It could be seen clearly that by using GA, performances in terms of overshoot, rise time and settling time have significant improvement.

6 Conclusion

This paper objective is to use Genetic Algorithm optimization in order to optimized PID gain and compare the performance with classical tuning methods such as Ziegler-Nichols and Skogestad IMC. The ITAE fitness function is modified by adding specific weightage on performance such as rise time, settling time, overshoot percentage, and steady state error. From the results, it shows that modified ITAE fitness function optimized by using GA can be concluded as the best in term of rise time, settling time, and overshoot. Even though produces the biggest steady state error compares with all methods, the value of error is considered small. Modifying ITAE fitness function by adding weightage to performance parameter is proven to improve the rise time and settling time. Genetic Algorithm optimization of PID produces better performance response compare with classical tuning formulas such as Ziegler-Nichols and Skogestad IMC.

Acknowledgements This paper would like to give appreciation to Universiti Sains Malaysia (USM) for the support of the research under grant no 305/PELECT/6013112.

References

1. Yan, W., Wang, D., Jia, P., Li, W.: The PWM speed regulation of DC motor based on intelligent control. *Syst. Eng. Proc.* **3**, 259–267 (2012)
2. Díaz-Rodríguez, I.D., Han, S., Keel, L.H., Bhattacharyya, S.P.: Advanced tuning for Ziegler-Nichols plants. *IFAC-PapersOnLine* **50**(1), 1805–1810 (2017)
3. Skogestad, S.: Simple analytic rules for model reduction and PID controller tuning. *J. Process Control* **13**(4), 291–309 (2003)
4. Mirzal, A., Yoshii, S., Furukawa, M.: PID parameters optimization by using genetic algorithm (2012). [arXiv:1204.0885](https://arxiv.org/abs/1204.0885)
5. Sunthong, A., Assawinchaichote, W.: Particle swarm optimization based optimal PID parameters for air heater temperature control system. *Proc Comput Sci* **86**, 108–111 (2016)
6. Samakwong, T., Assawinchaichote, W.: PID controller design for electro-hydraulic servo valve system with genetic algorithm. *Proc. Comput. Sci.* **86**, 91–94 (2016)

7. Aly, A.A.: PID parameters optimization using genetic algorithm technique for electrohydraulic servo control system. *Intell Control Autom* **2**(02), 69 (2011)
8. Altintas, G., Aydin, Y.: Optimization of fractional and integer order PID parameters using big bang big crunch and genetic algorithms for a MAGLEV system. *IFAC-PapersOnLine* **50**(1), 4881–4886 (2017)
9. Panigrahi, T.K., Behera, A., Sahoo, A.K.: Novel approach to automatic generation control with various non-linearities using 2-degree-of-freedom PID controller. *Energy Proc.* **138**, 464–469 (2017)
10. Mendes, J., Osório, L., Araújo, R.: Self-tuning PID controllers in pursuit of plug and play capacity. *Control Eng. Pract.* **69**, 73–84 (2017)
11. Lamba, R., Singla, S.K., Sondhi, S.: Fractional order PID controller for power control in perturbed pressurized heavy water reactor. *Nucl. Eng. Des.* **323**, 84–94 (2017)
12. Haroun, A.G., Li, Y.Y.: A novel optimized hybrid fuzzy logic intelligent PID controller for an interconnected multi-area power system with physical constraints and boiler dynamics. *ISA Trans.* **71**, 364–379 (2017)

SKF-Based Image Template Matching for Distance Measurement by Using Stereo Vision



Nurnajmin Qasrina Ann, Dwi Pebrianti, Luhur Bayuaji, Mohd Razali Daud, Rosdiyana Samad, Zuwairie Ibrahim, Rosyati Hamid and Mohammad Syafrullah

Abstract In this paper, a novel image template matching approach to tackle distance measurement problem has been proposed. There are many conventional algorithms to increase the accuracy of distance measurement as reported in the literature such as Semi-global algorithm to produce the disparity map. Meanwhile, in this paper, the reverse engineering technique had been implemented to get the correct depth value by applying the image template matching method as reference for the distance measurement. The traditional algorithm to solve image matching problem take a lot of memory and computational time. Therefore, image matching problem can be considered to optimization problem and can be solved precisely. The search of the image template has been performed exhaustively by using Simulated Kalman Filter (SKF) algorithm. The experiment is conducted with a set of images taken by using stereo vision system. Experimental results show the accuracy of the distance measurement by using stereo camera, after applying (1) the estimate error model, (2) SKF and (3) PSO algorithm are 89.95%, 96.09%, 95.29% and 58.51% respectively. The limitation of estimate error model that it can only be applied into the same setup of the experiment, environment, parameters of the camera and acquired images. Instead, the proposed algorithm which is SKF can be applied to original image and image under the vision problems like illumination and partially occluded. The SKF algorithm shows more robust, more efficient and more accurate to solve the distance measurement problem.

N. Q. Ann · D. Pebrianti (✉) · M. R. Daud · R. Samad · Z. Ibrahim · R. Hamid
Faculty of Electrical and Electronics Engineering, Universiti Malaysia Pahang,
Pekan, Malaysia
e-mail: dwipebrianti@ump.edu.my

N. Q. Ann
e-mail: qasrinaann@gmail.com

L. Bayuaji
Faculty of Computer Science and Software Engineering, Universiti Malaysia Pahang,
Gambang, Malaysia

D. Pebrianti · L. Bayuaji · M. Syafrullah
Magister of Computer Science, Universitas Budi Luhur, South Jakarta, Indonesia

Keywords Distance measurement • Image template matching
Optimization • SKF

1 Introduction

Image matching has been long regarded as a serious stage for object recognition in the fields of digital image processing, vision system and pattern recognition. There are so many image matching algorithms available within these 20 years. Particularly, the traditional algorithm for image matching need very high computational time because the algorithm will compute each pixel of an image, for instance Sum of Absolute Differences (SAD) method. Nowadays, image matching problem already become one of the optimization problem and uses the traditional algorithm as the objective function for the algorithm as reported in [1–3].

Image matching is a fundamental issue in robotics vision. It has been widely used in tracking, image stitching, 3D reconstruction, simultaneous localization and mapping systems, camera calibration, object classification, recognition and so on. The most simple and popular image matching technique is by using template image of the reference image. There are two most reliable algorithms in template matching. Firstly, match via picking up the image's unique point and another one is calculated the similarity value through comparing the matched region.

Indeed, the mathematics behind of the image matching process is very complicated and involving high dimensional of data. It will need a large computational time and memory to handle all the calculations. For the past few years, the image matching problem is already converted to optimization problem that can help to obtain a more accurate and efficient result. Meanwhile, there are seven well-known optimization algorithms [2, 4–12] are already implemented into this problem and slowly, solve the problems better than the conventional methods. It is also reported the algorithm become more robust which can handle different illumination, angles and so on.

Ibrahim et al. [13] introduced a new metaheuristic optimization algorithm named as Simulated Kalman Filter (SKF). This recent algorithm is motivated by the estimation capability of Kalman Filter. Kamil et al. introduced a solving system for identification problem to test the effectiveness of the SKF algorithm in 2015. The overall performance is evaluated based on six study cases. According to the results, SKF shows the better performance compared to another algorithm [14].

The outline of the paper is as follows. Section 2 is about the methodology of the experiment. The details of the experimental setup are described in Sect. 3. Section 4 is the result and discussion. Then followed by conclusion and future works in Sect. 5.

2 Methodology

In this section, there are two parts of the system. The first part explained how the distance can be measure using the proposed algorithm and the next part is about the discussion of the proposed algorithm which is Simulated Kalman Filter.

2.1 Distance Measurement

For the past few decades, sensors are widely used in the distance measurement application. For example, stereo vision sensor. For this sensor, there are conventional ways to obtained the distance measurement and construct the estimate error model has been discussed in [3]. As been reported in the paper, the accuracy of the method used is in doubt which is because the researchers are using a model that can only be implement for the experimental condition only.

Therefore, the new approach to measure the distance for stereo vision system is introduced in this paper. Some part of the conventional method which is produced the disparity map using existing algorithm such as semi-global algorithm had been cut out and replace with image template matching algorithm as shown in the Fig. 1. The dotted rectangle is the new approach for obtaining the distance measurement by using stereo vision that is applying the image matching application.

Image template matching problem is one of the major problem for getting the accurate and precise result. By dealing with images, huge memory and expensive time cost will be consumed to analyze the problem. That is why, Simulated Kalman Filter (SKF) algorithm is implemented in this application to help reduce time consuming and increase accuracy for image matching.

2.2 Simulated Kalman Filter (SKF) Algorithm

SKF was presented by Ibrahim et al. [13, 15] in 2015. SKF is a population-based metaheuristic algorithm introduced for continuous optimization problem and it is inspired by the estimation capability of Kalman Filter. The SKF algorithm is shown in Fig. 2 [14].

The algorithm is started with the initialization of the particles within the search space randomly. In addition, the initial value of error covariance estimate, $P(0)$, the process noise value, Q , and measurement noise value, R are needed during the initialization stage, which is also needed in Kalman Filter process.

After that, the fitness value of each particle needs to be calculated and the best fitness value of each iteration is recorded as $X_{best}(t)$. Image matching is considered as a maximization problem, therefore Eq. (1) is used in this case.

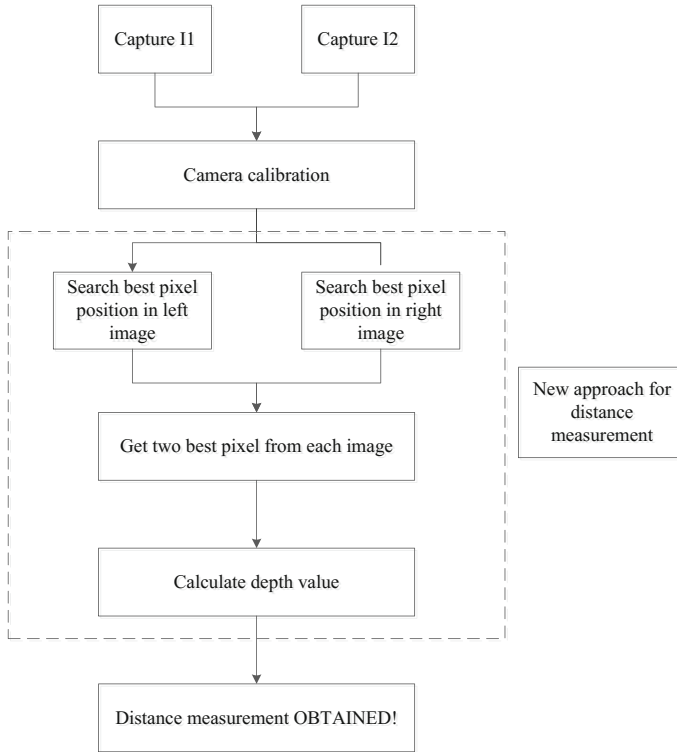


Fig. 1 Proposed approach for distance measurement

$$X_{best} = \max_{i \in 1, \dots, n} fit_i(X(t)) \tag{1}$$

where $X_{best}(t)$ is the maximum value of fitness function in one run within assigned number of iteration. Therefore, the algorithm will produce a best fitness value in one run or one trial.

The updated best in the program known as X_{true} . The X_{true} is updated only if the $X_{best}(t)$ is better than X_{true} which is $X_{best} > X_{true}$ for maximization problem. The next calculations are like Kalman Filter which are prediction, measurement and estimation.

In the prediction stage, the following time-update equations are evaluated as below:

$$X_i(t|t) = X_i(t) \tag{2}$$

$$P(t|t) = P(t) + Q \tag{3}$$

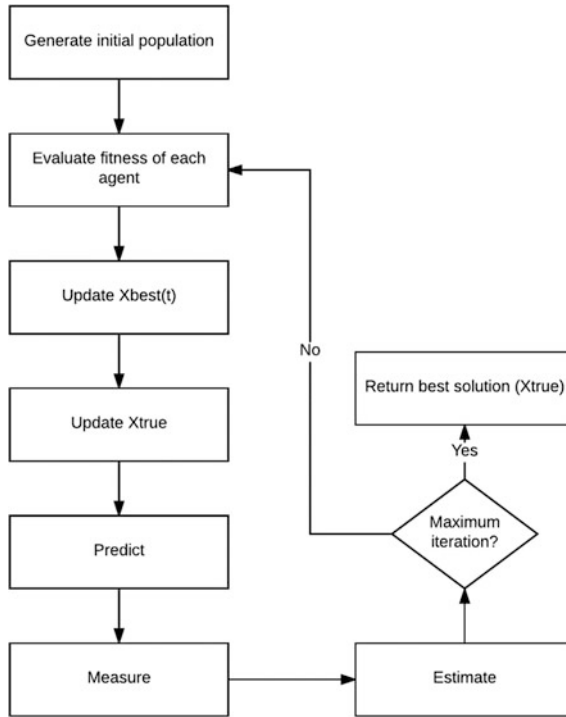


Fig. 2 SKF algorithm

where $X_i(t|t)$ is the predicted state and $X_i(t)$ is the previous state, $P(t|t)$ and $P(t)$ are predicted error covariance estimate and previous error covariance estimate, respectively and Q is the process noise.

The next step is measurement. It acts as feedback to estimation process. Measurement, $Z_i(t)$ of each individual agent is calculated using the Eq. (4).

$$Z_i(t) = X_i(t|t) + \sin(rand \times 2\pi) \times |X_i(t|t) - X_{true}| \tag{4}$$

where $\sin(rand \times 2\pi)$ term gives the stochastic part of SKF and $rand$ gives the random number in 0–1 range.

The last step is the estimation. Kalman gain is needed in this step and calculated as shown below:

$$K(t) = \frac{P(t|t)}{P(t|t) + R} \tag{5}$$

where $K(t)$ is the Kalman filter for each particle, $P(t|t)$ is predicted error covariance estimation value and R is noise value.

The estimation of next state $X_i(t + 1)$, is calculated based on Eq. (6) and the error covariant is updated based on Eq. (7).

$$X_i(t+1) = X_i(t|t) + K(t) \times (Z_i(t) - X_i(t|t)) \quad (6)$$

$$P(t) = (1 - K(t)) \times P(t|t) \quad (7)$$

where $X_i(t+1)$ and $X_i(t|t)$ are the estimation of next state and predicted state, $K(t)$ is the calculated Kalman gain, $Z_i(t)$ value is taken from measurement stage and $P(t)$ and $P(t|t)$ are updates error covariant value and predicted error covariance respectively.

Lastly, the algorithm will continue the searching until meet the stopping condition and in this case, until the maximum iteration reached.

3 Experimental Setup

The experimental setup is by using the Blackfly stereo vision camera system from Point Grey Research is used throughout the experiment. It consists of two different cameras, which are mounted in parallel to get the stationary position. Figure 3 shows the developed stereo vision system. Figure 4a and b is the example of the image taken by using stereo vision system and template of the original image that be used throughout the experiment.

Moreover, a few of pre-processing methods had been added to improve both standard algorithms. Then, the experiment continues with applying Simulated Kalman Filter (SKF) algorithm in image template matching application for distance measurement in robot navigation. The initialization parameters for SKF algorithm are: $P(0) = 1000$, $Q = 0.5$ and $R = 0.5$ while the experimental parameters for both



Fig. 3 Developed stereo vision system

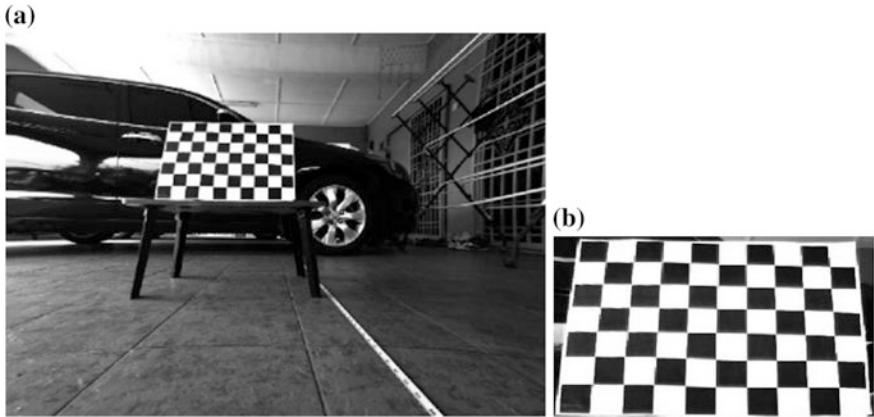


Fig. 4 a Original image b Template image

algorithms are: 20 for number of particles, 2 dimensions and 300 for number of iterations in 25 runs. Those experiments are conducted outdoor under ambient light. The system is robust for analyze the landscape scenery.

4 Result and Discussion

The image used in this experiment is taken from developed stereo vision sensor that had been mentioned earlier. The result images obtained from the sensor will be discussed in this section later.

The distance measurement is conducted in range of 85–190 cm. Total data used in the experiment is 24 images. The ground truth data, the distance viewing by using the stereo camera, the distance after applying the estimate error model, the distance after implementing the proposed algorithm and PSO algorithm are clearly stated in the Fig. 5.

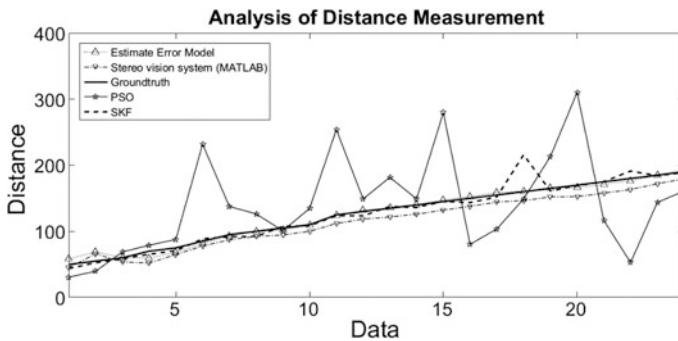


Fig. 5 Analysis of distance measurement

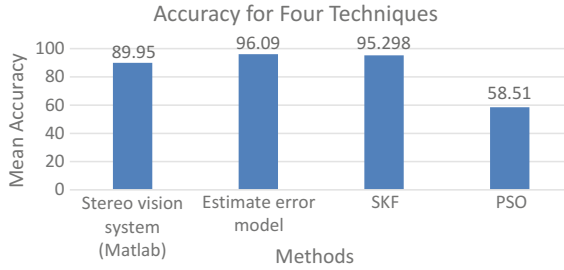


Fig. 6 Mean accuracy for four techniques

The accuracy of the distance measurement by using stereo camera, after applying the estimate error model [3], SKF and PSO algorithm are 89.95%, 96.09%, 95.29% and 58.51% respectively as showed in Fig. 6. The highest accuracy is the distance measurement after applying the estimate error model that had been discussed in [3] among all. However, the limitation of this model is that it only can be applied into the same setup of the experiment, environment, camera parameters and acquired images. Instead, the proposed algorithm which is SKF can be applied to original image and image under the vision problems like illumination and partially occluded. The result shows that the proposed algorithm is more robust, efficient and accurate to solve the distance measurement problem by using image matching techniques.

5 Conclusion

This paper puts SKF algorithm into use in image matching problems for distance measurement and achieve satisfying effects. The accuracy of the distance measurement by using stereo camera, after applying the estimate error model [3], SKF and PSO algorithm are 89.95%, 96.09%, 95.29% and 58.51% respectively. As for improving the SKF algorithm to solve the problem, the parameters setting like $P(0)$, Q and R of the system should be changed to achieve a better performance. The proposed algorithm can be applied to low and medium dimensional image to solve the image template matching problem and will apply to high dimensional image later. However, the proposed algorithm is more accurate proven by the performance analysis as showed in the Sect. 4.

The future works will focus on image matching for more complex image and image matching for real-time application such as live streaming. Lastly, the important part of the system is to increase the percentage of successful image matching by adding image preprocessing techniques to the original image.

References

1. Zhang, J., Wang, G.: Image matching using a bat algorithm with mutation, **203**, 88–93 (2012)
2. Liu, X., Jiang, W., Xie, J.: An image template matching method using particle swarm optimization. In: 2009 Second Asia-Pacific Conference Computational Intelligence and Industrial Applications, pp. 83–86 (2009)
3. Ann, N.Q., Achmad, M.S.H., Bayuaji, L., Daud, M.R., Pebrianti, D.: Study on 3D scene reconstruction in robot navigation using stereo vision. In: 2016 IEEE International Conference on Automatic Control and Intelligent Systems, pp. 72–77 (2016)
4. Cui, W., He, Y.: Tournament selection based fruit fly optimization and its application in template matching, pp. 362–365 (2016)
5. Chidambaram, C., Lopes, H.S.: A new approach for template matching in digital images using an artificial bee colony algorithm. In: 2009 NaBIC 2009. World Congress on Nature and Biologically Inspired Computing, pp. 146–151. IEEE (2009)
6. Banhamsakun, A., Tanathong, S.: Object detection based on template matching through use of best-so-far ABC. *Comput. Intell. Neurosci.* **2014**, 1–8 (2014)
7. Wang, Z.-F., Zheng, Z.-G.: A region based stereo matching algorithm using cooperative optimization. In: 2008 IEEE Conference on Computer Vision and Pattern Recognition, pp. 1–8. IEEE (2008)
8. Gong, M.: Multi-resolution stereo matching using genetic algorithm. In: Proceedings IEEE Workshop on Stereo and Multi-Baseline Vision (SMBV 2001), pp. 21–29. IEEE Computer Society (2001)
9. Das, A., Bhattacharya, M.: Affine-based registration of CT and MR modality images of human brain using multiresolution approaches: comparative study on genetic algorithm and particle swarm optimization. *Neural Comput. Appl.* **20**, 223–237 (2010)
10. Jiang, F., Frater, M.R., Pickering, M.: Threshold-based image segmentation through an improved particle swarm optimisation. In: 2012 International Conference on Digital Image Computing Techniques and Applications (DICTA), pp. 1–5. IEEE (2012)
11. Sharma, A.: Object detection in image using particle swarm optimization. *Int. J. Eng. Technol.* **2**, 419–426 (2010)
12. Yao, L., Duan, H., Shao, S.: Adaptive template matching based on improved ant colony optimization. In: 2009 International Workshop on Intelligent Systems and Applications, pp. 1–4 (2009)
13. Ibrahim, Z., Aziz, N.H.A., Aziz, N.A.A., Razali, S., Shapiai, M.I., Nawawi, S.W., Mohamad, M.S.: A Kalman filter approach for solving unimodal optimization problems. *ICIC Express Lett.* **9**, 3415–3422 (2015)
14. Mohd Azmi, K.Z., Ibrahim, Z., Pebrianti, D.: Simultaneous computation of model order and parameter estimation for ARX model based on multi-swarm particle swarm optimization. *ARPN J. Eng. Appl. Sci.* **10**, 17191–17196 (2015)
15. Ibrahim, Z., Aziz, N.H.A., Aziz, N.A.A., Razali, S., Mohamad, M.S.: Simulated Kalman filter: a novel estimation-based metaheuristic optimization algorithm. *Adv. Sci. Lett.* **22**, 2941–2946 (2016)

Butterfly Species Recognition Using Artificial Neural Network



S. S. N. Alhady and Xin Yong Kai

Abstract In 2017, there are about 20,000 species of butterfly has been discovered all over the world. Butterfly is well known because of its beautiful wings pattern and its benefits to the environment. In this research, butterfly species recognition is automated using artificial intelligence. Pattern on the butterfly wings is used as a parameter to determine the species of the butterfly. The butterfly image is captured and the background of the image is removed to make the recognition process easier. Local binary pattern (LBP) descriptor is then applied to the processed image and a histogram consist of image information is computed. Artificial Neural Network (ANN) is used to classify the image. Two types of butterfly species were selected namely *ideopsis vulgaris* and *hypolimnas bolina*. Both of the species have been correctly identify with accuracy of 90% (for *ideopsis vulgaris*) and 100% (for *hypolimnas bolina*).

Keywords Pattern recognition • Artificial intelligence • Neural network

1 Introduction

Species recognition has been one of the research carried out by researchers in near decades, especially when the conservation of endangered species become more common and urgent nowadays. There are a few methods to carry out species identification for all sorts of living organism on earth. Some methods need the individual to be caught then collect sample and statistics to do further investigation. Individual with distinct size, shape and colour can be recognized effortlessly. When it comes to insects, they are small and they may look similar but are from different species. Locust and grasshopper made a good example in this case. Both have very similar appearance such as features and shape. These two-species behaved very

S. S. N. Alhady (✉) · X. Y. Kai

School of Electrical & Electronic Engineering, Universiti Sains Malaysia,
George Town, Malaysia
e-mail: sahal@usm.my

© Springer Nature Singapore Pte Ltd. 2018

M. H. A. Hassan (ed.), *Intelligent Manufacturing & Mechatronics*,
Lecture Notes in Mechanical Engineering,
https://doi.org/10.1007/978-981-10-8788-2_40

449

differently after study has been carried out. Same goes to butterfly, all the butterflies on earth have similar appearance. They are classified under the category of insects. Scientists have classified the butterfly under different categories based on the butterfly wing shape and behavior. The butterflies have been divided into approximately 135 families [1–3].

Previously, identification of butterfly species was done by first glance observation. The first glance observation found not working properly. The genital characteristics analysis have to be carry out by preparing genital slides of the collected butterflies through some specific processing using various chemicals. This method become less popular due to argument and misinterpretation of butterfly species [2].

This research will focus on the recognition of butterfly species using artificial neural network (ANN). In this research, *ideopsis vulgaris* (commonly known as Blue Glassy Tiger butterfly) and 39 images of *hypolimnas bolina* (commonly known as Bluemoon butterfly) are being chosen. The butterflies that need to be recognise will be captured using any devices. Image processing technique which is local binary pattern (LBP) is used to process the pictures of butterflies [4, 5]. A single layer artificial neural network is used to match the processed data to the database and found the correct species [6].

2 Methodology

This section explains the overall project flow of automatic identification of butterflies' species. The overall project flow will be visualized using flow chart. The process to identify butterfly is separated into five phases. Each phase will be discussed in detail. The five phases are data collection, data pre-processing, feature extraction, classification and performance evaluation.

2.1 Data Collection

The total number of images collected is tabulated according to butterfly species and usage of the images.

2.2 Data Pre-processing

Two butterfly species were selected to be recognized in this project. Hence, images of butterfly are collected to carry out this project. Images collected were taken at the Penang Butterfly Farm (Entopia). After the photo had been taken, volunteer from Penang Butterfly Farm helped to identify the species of the butterfly. This was to ensure the images used in this project are unambiguous. Especially the butterfly

species that have similar wings pattern, extra attention is needed to observe the details on the wings to ensure the butterfly species are the one that was chosen to be studied. The total butterfly images collected were 78 images. These images were made up of 39 images of *ideopsis vulgaris* (commonly known as Blue Glassy Tiger butterfly) and 39 images of *hypolimnas bolina* (commonly known as Bluemoon butterfly).

2.3 Feature Extraction

Local binary pattern (LBP) descriptor was used to do feature extraction in this project [7, 8]. The RGB image was converted to grey scale image and use the with descriptor. In LBP descriptor, the image was divided into cells. Each cell contained R radius and N number of neighbours as shown in Fig. 1.

The centre pixel’s value was compared with each of the neighbour pixel’s value. Below showed the formula of local binary pattern for a pixel:

$$LBP(x) = \sum_{n=0}^p S(G(x_n)G(x))2^{n-1}$$

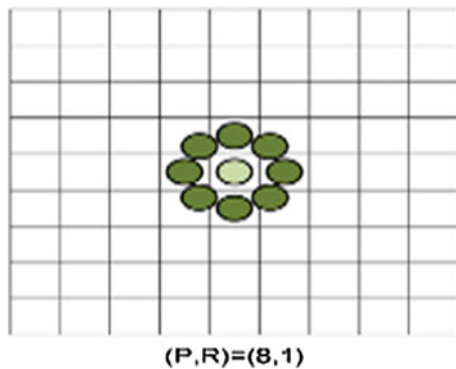
$$S(t) = \begin{cases} 1, t \geq 0 \\ 0, t < 0 \end{cases}$$

where

- x location of centre pixel
- x_i location of ith neighbouring pixel

When the neighbour pixel’s value was smaller than the center pixel’s value, the neighbour pixel’s value was replaced by binary number “0”. When the neighbour pixel’s value was greater than the center pixel’s value, the neighbour pixel’s value

Fig. 1 Example of dividing image into cells using different values of LBP descriptor



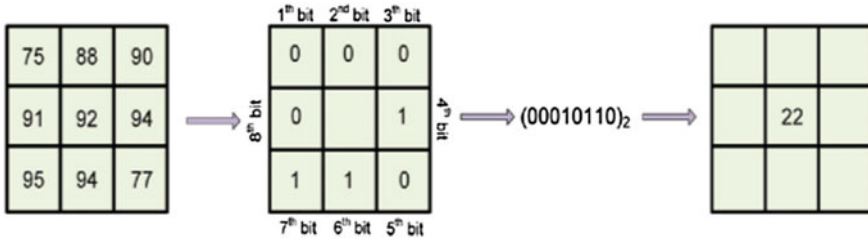


Fig. 2 Process of computing decimal representation of a cell using LBP descriptor

was replaced by binary number “1”. This resulted in a series of binary number representing the cell as shown in Fig. 2.

A histogram containing components equivalent to the number of cells was computed. The average, deviation, energy, entropy and correlation of the histogram was calculated using the following formula.

$$average = \frac{1}{AB} \sum_{x=0}^{A-1} \sum_{y=0}^{B-1} f(x,y)$$

$$deviation = \sqrt{\frac{1}{AB} \sum_{x=0}^{A-1} \sum_{y=0}^{B-1} (f(x,y) - average)^2}$$

$$energy = \frac{1}{AB} \sum_{x=0}^{A-1} \sum_{y=0}^{B-1} f^2(x,y)$$

where

μ mean

σ standard deviation

2.4 Classification

An Artificial neural network was a model that designed based on the structure and functions of the human brain neural networks. Neural network can be trained to perform different tasks such as computer vision, speech recognition and pattern recognition. There were a few advantages in using neural network which are ability to learn based on data given, suitable for real-time application and high fault tolerance using redundant information coding.

In this project, the average, deviation, energy, entropy and correlation of the histogram calculated from previous stage were used as input to the artificial neural

network (ANN). The output of this stage were the butterfly species. In artificial neural network (ANN), there were a few strategies for learning to be carried out which were supervised learning, unsupervised learning and reinforcement learning. The learning strategy used in this project was supervised learning.

In supervised learning, a set of known input data and known output data was taken and the artificial neural network model was trained to give reasonable response of new data. The goal of supervised learning was to use existing data to do prediction for a new data. Since the purpose of this project was to do classification, the responses of the model were categorical variables [9].

There were a few steps involved in supervised learning which were data preparation, choosing algorithm, fitting a model, choosing validation method, examine fitting parameters performance, update fitting parameters and use fitted model for prediction.

2.5 Performance Evaluation

The classification results were tabulated into a confusion matrix. This made the process of analyzing the results easier as it was summarized in a table. The accuracy of the designed system was obtained by calculating the percentage of successful recognized image over the total image selected. The formula is presented as below.

$$Accuracy = \frac{\text{number of successful recognised image}}{\text{total image selected}} \times 100\%$$

3 Results

This section described the outcome of this research. Firstly, the total number of pictures collected is tabulated according to butterfly species and usage of the pictures. Next, the pictures are pre-processed. Feature extraction has been done on the edited pictures to get in formation of the pictures to do further classification of butterfly species. Finally, the classification step carried out using Artificial Neural Network is done and results are recorded.

3.1 Data Collection

Table below shows the number of pictures collected for each chosen species of butterflies. The number of pictures used for training purpose and testing purpose are listed in the Table 1.

Table 1 Number of pictures collected

Species	Species name	Number of pictures for training	Number of pictures for testing
1	<i>Ideopsis vulgaris</i>	29	29
2	<i>Hypolimnas bolina</i>	10	10
	Total	39	39

3.2 Data Pre-processing

Figure 3 shows the coloured image of the butterfly. The back ground of the image will be removed and replaced with white colour background.

3.3 Feature Extraction

Figure 4 shows the grayscale image that has been converted from the white colored background butterfly image. Local Binary Pattern (LBP) descriptor is used to convert the gray scaled image into LBP image. The histogram shows the summed up binary bits of range 0–255.

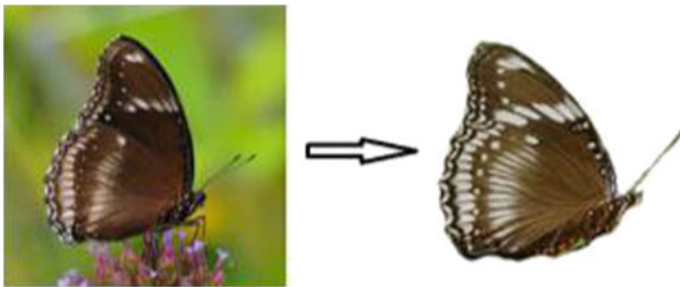


Fig. 3 Original and processed butterfly images



Fig. 4 Gray scaled image being converted to LBP image and LBP histogram

Table 2 ANN architecture and training parameters

Architecture	Training
Number of layers = 3	Performance function, MSE
Number of neuron on layers	Learning rule used
Input = 3	Levenberg-Marquardt
Hidden = 105	
Output = 2	
Initial weight = 0.01	Learning rate 0.7
Initial bias = 0.01	Momentum constant 0.97
Activation function = sigmoid for hidden and output layer	Performance goal = 2E-10

Table 3 Confusion matrix of butterfly species recognition

Butterfly species	Butterfly species 1	Butterfly species 2	Accuracy (%)
Butterfly species 1	9	1	90
Butterfly species 2	0	10	100

3.4 Classification

Table 2 shows the shows the Artificial Neural Network (ANN) architecture and training parameters.

Table 3 summarized the results of the butterfly species recognition results from Table 2. The accuracy of species recognition for *ideopsis vulgaris* butterfly species and *hypolimnas bolina* butterfly species are computed and recorded. It can be observed that recognition of *ideopsis vulgaris* butterfly species has the accuracy of 90% while recognition of *hypolimnas bolina* butterfly species 100% accurate.

4 Discussion

In this research, images of chosen butterfly species are recognized automatically using Artificial Neural Network (ANN). The research has been carried out in five phases which are data collection, image pre-processing, features extraction, classification and performance evaluation.

In data collection phase, the butterfly images are taken at the Penang Butterfly Farm. Two type of butterfly images are taken which are butterfly with opened wings and butterfly with closed wings. There are total of 78 images collected in this phase. The images include 48 images of *Ideopsis vulgaris* butterfly species and 49 images of *hypolimnas bolina* butterfly species. In the 49 images of each butterfly species, 39 images are used for training purpose while 10 images are used for testing. The images for training and testing are selected randomly.

In image pre-processing phase, the images background is removed. Also, the image is resized to same pixels. The images are adjusted so the size of the butterfly is roughly the same. The orientation of the butterfly is not fixed since the orientation will not affect the results of the butterfly species recognition.

In the feature extraction phase, the Local Binary Pattern (LBP) descriptor is used to do feature extraction based on the butterfly wings pattern. The images are divide into cells and each cell contained 9 pixels. A binary number will be computed for each cell. The binary numbers of all the cells are summarized into a histogram. In the histogram, it contains components equivalent to the number of cells was computed. The average, deviation, energy, entropy and correlation of the histogram was calculated. These data represent the pattern of the butterfly.

In classification phase, the average, deviation and energy are used as inputs for the neural network. The neural network consists of 3 layers which are input layer, hidden layer and output layer. There are 3 inputs in input layer and 2 outputs in output layer. The number of neurons in hidden layer is decided by training neural network with different number of neurons. The accuracies of the trained neural networks are recorded. Then, the results are compared to find the suitable number of neuron in hidden layer. After doing comparison among the accuracies of the trained neural network, 105 neurons in hidden layer of the neural network has the best performance. After the number of neurons in hidden layer has been decided, the performance of the neural network has been evaluated by looking at the performance plot and regression plot of the trained network. From the plots, it can be concluded that the training has been carried out correctly and the neural network is well trained. This can be told by the decreasing training mean squared error (MSE) over epochs, similar shape of validation mean squared error (MSE) and testing mean squared error (MSE) and R values that are very close to 1. There is no over fitting parameter occurs in the training. The testing data set is being used to test the trained neural network to identify selected butterfly species based on the average, deviation and energy calculated.

In performance evaluation phase, the results from classification stage is summarized into a confusion matrix. This is to ensure the results can be read easily, the accuracy to recognize each species is calculated accordingly. As conclusion, *ideopsis vulgaris* butterfly species has lower accuracy as compared to *hypolimnas bolina* butterfly species. The accuracies for both the butterfly species are 90% and 100% respectively.

5 Conclusion

This research aimed to recognize butterfly species automatically using Artificial Neural Network. Two different type of butterfly have been chosen in this research. The chosen butterfly species are *ideopsis vulgaris* butterfly species and *hypolimnas bolina* butterfly species. The images of the mentioned butterfly species are collected and edited. Edited images will undergo feature extraction and classification.

The final results are recorded and the performance of butterfly species recognition is evaluated.

The key feature used to recognize the butterfly species in this research is the pattern on the butterfly's wings. The pattern of butterfly wings is digitalized into information using Local Binary Pattern (LBP) descriptor. After LBP descriptor, the pattern that can be visualized by human eyes is transposed to numbers. The values are the average, deviation and energy of the Local Binary Pattern (LBP) histogram. These values will be used as input for the neural network to be used as variables for species recognition.

At the end of this research, it can be concluded that the selected butterfly species can be recognized automatically. The accuracy of both the butterfly species are 90% and 100% respectively.

References

1. Kaya, Y., Kayci, L., Uyar, M.: Automatic identification of butterfly species based on local binary patterns and artificial neural network. *Appl. Soft Comput.* **28**, 132–137 (2015)
2. Kang, S.-H., Cho, J.-H., Lee, S.-H.: Identification of butterfly based on their shapes when viewed from different angles using an artificial neural network. *J. Asia-Pacific Entomol.* **17**, 143–149 (2014)
3. Kang, S.-H., Song, S.-H., Lee, S.-H.: Identification of butterfly species with a single neural network system. *J. Asia-Pacific Entomol.* **15**, 431–435 (2012)
4. Liu, L., Fieguth, P., Zhao, G., Pietikäinen, M., Hu, D.: Extended local binary patterns for face recognition. *Inf. Sci.* **358–359**, 56–72 (2016)
5. Liu, L., Fieguth, P., Guo, Y., Wang, X., Pietikäinen, M.: Local binary features for texture classification: taxonomy and experimental study. *Pattern Recogn.* **62**, 135–160 (2017)
6. Banerjee, A.K., Kiran, K., Murty, U.S.N., Venkateswarlu, C.: Classification and identification of mosquito species using artificial neural networks. *Comput. Biol. Chem.* **32**, 442–447 (2008)
7. Abbasi, S., Tajeripour, F.: Detection of brain tumor in 3D MRI images using local binary patterns and histogram orientation gradient. *Neurocomputing* **219**, 526–535 (2017)
8. Wang, X., Liang, J., Guo, F.: Feature extraction algorithm based on dual-scale decomposition and local binary descriptors for plant leaf recognition. *Digit. Signal Proc.* **34**, 101–107 (2014)
9. Żbikowski, R.: Use of artificial neural networks to identify the origin of green macroalgae. *Estuar. Coast. Shelf Sci.* **94**, 138–143 (2011)

Investigation of Steering Wheel Control of an Electric Buggy Car for Designing Fuzzy Controller



Hafiz Halin, Wan Khairunizam, K. Ikram, Hasri Haris, S. A. Bakar, Z. M. Razlan, I. Zunaidi and H. Desa

Abstract Steering control for path tracking and navigation are important for the autonomous vehicle. A good steering control system can determine the success of autonomous navigation through designed paths. Comfort and safety for the passenger are the main concerns in developing a controller for an autonomous electric vehicle (AEV). Comfort and the safe autonomous system can be achieving by imitating human intelligence and decision-making ability into the controller. A GPS module couple with a fuzzy controller to follow the designed path. Steering is control by using brushless DC motor with certain gear configuration. In order to achieve better drive performance for the autonomous vehicle, the behaviors of human subjects are studied and investigated. Investigation of steering angle on 3 different paths is designed to study the driving patterns by the human subjects, which are straight, turn right and turn left. The results show satisfactory outcomes as the subject navigates through the designed path with the similar patterns. The average value of steering wheel angle for the straight, right and left path are 13° , -151° , and 237° , respectively. The maximum angle to turning to the left and right are 286° (subject #1) and -226° (subject #1). This paper consists of the construction of a Fuzzy logic controller to control steering wheel and experiments set-up to develop the Fuzzy controller for an autonomous vehicle.

Keywords Steering wheel · Human behavior · Electric vehicle Autonomous · Fuzzy

H. Halin · W. Khairunizam (✉) · K. Ikram · H. Haris
S. A. Bakar · Z. M. Razlan · H. Desa
Advanced Computing and Sustainable School of Mechatronics,
Universiti Malaysia Perlis, Perlis, Malaysia
e-mail: khairunizam@unimap.edu.my

H. Halin
e-mail: abdhafiz.halin@gmail.com

I. Zunaidi
Technopreneur at UniMAP Sdn. Bhd, Arau, Malaysia

1 Introduction

The development of electric vehicle technology was a stepping-stone to the development of an autonomous vehicle powered by an electric motor. The main concerns for the development of the autonomous electric vehicle are to reduce the traffic accident and pollution from the internal combustion engine smoke emission [1]. The number of fatal road accidents due to human errors and negligence increasing even with the current law enforcement. The road accident is either cause by driver error [2], road condition, or visibility of the driver.

Research in autonomous vehicle drawn great attention in the automotive related since the past decade. Some researchers focus in specific subsystem, such as steering, braking and throttling, whereas others focus on all elements in designing an autonomous system [3]. The interest in the autonomous vehicle also caught large company like Google [4], Toyota [5], Tesla [6] etc. to develop their own autonomous vehicle. The Tesla autopilot system show a glimpse of the future autonomous vehicle for mass production.

Automatic steering of vehicles is increasing interest as a part of an integrated system of automated highway or drive assistance [7], Defense Advanced Research Project Agency (DARPA) [8], California Partner for advanced Transportation Technology (PATH) project [9] and other related projects showed positive development for autonomous vehicles. The DARPA Grand Challenge are the race sponsored by Defense Advanced Research Projects Agency to show the effectiveness of the autonomous vehicle in terrain path. The races focus on the ability of the autonomous vehicle to reach the target point. The path error in navigation process need to be as small as possible in order to maintain the vehicle on desired path [10, 11]. Complex algorithm like Model Predictive Control (MPC) [12], Multiple Model Adaptive Control (MMAC) [13], Neural Network [14], and others need a lot of data from surrounding environment in order to evaluate/create path planning. Although others algorithm can produce satisfying results, fuzzy serve the right functions for complex sensor integration [15]. A buggy car used to test the Fuzzy controller. The training data are gathered from the human driver behavior in order to create rules-base [16] for fuzzy controller. The fuzzy rules used the driver's behavior as a base in order to imitate human decision-making ability and to make sure the comfort and safety for the passenger of the autonomous vehicle. Pre-determined GPS coordinates used as reference for path planning. There are 5 pre-determined waypoints for the navigation for this project.

This paper organized as follows. Methodologies in Sect. 2 describe the vehicle modelling and proposed methods used in the research. The data collected use for the development of the Fuzzy controller. Result and Discussion in Sect. 3 shows the results and discusses the outcomes of the experiments. Finally, conclusion presents the finding and future works of this research.

2 Research Method

2.1 Development of an Autonomous Vehicle

A buggy car was chosen to develop an autonomous vehicle. The architecture of the buggy car was simple. It makes the buggy car easier to be modified and installed sensors. An Encoder and a GPS module selected to help the navigation of an autonomous vehicle. A brushless DC motor was used to rotate the steering shaft to the desired angle. The GPS module updates the current position of the vehicle. The difference between prior and current positions used to navigate the vehicle through the path.

Figure 1 shows the installation of the encoder B106. The encoder can read up to 500 pulse per rotation. The rotary encoder B106 can measure a minimum of 0.72° for each pulse. The gear ratio between steering and motor gear used to determine the steering angle rotation. The specification of the buggy car used for this experiment is show in Table 1. The buggy car selected as a platform to test and validate the developed autonomous system. The selected electric buggy car used 48 V DC motor. The maximum speed is up to 12 km/h on fully charge battery.

2.2 Vehicular Model

The *two-wheel model* used to visualize the force acting on a vehicle. The *two-wheel model* derives from Ackerman vehicle model. The *two-wheel model* derive by assume the 2 wheels at the front as 1 wheel (Fig. 2). It is the same as rear wheel. The side force $f_f := 2Y_f, f_r := 2Y_r$ are

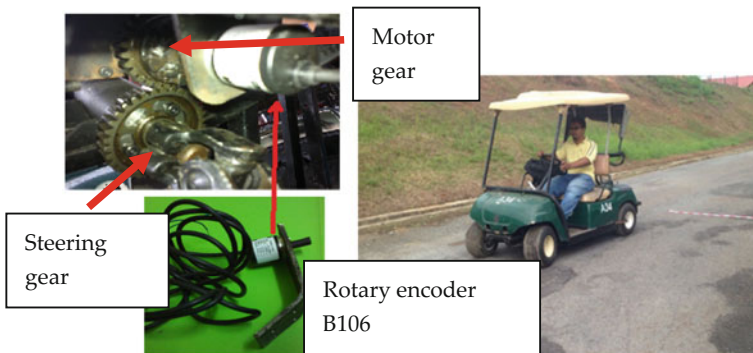


Fig. 1 Installation of the rotary encoder B106 to the steering shaft

Table 1 A buggy car specification

Parameter	Dimension
Length	231 cm
Width	111 cm
Weight	249 kg
Wheel base distance	163 cm
Top speed	30 km/h
Battery	48 V DC
Steering system	Rack and pinion gear
Brake	Mechanical brake cable system to drum brake

$$\begin{bmatrix} f_x \\ f_y \\ m_z \end{bmatrix} = \begin{bmatrix} -\sin \delta & 0 \\ \cos \delta & 1 \\ l_f \cos \delta & -l_r \end{bmatrix} \begin{bmatrix} f_f \\ f_r \end{bmatrix} \quad (1)$$

The variables cause by forces acting on the vehicles. The equation for vehicle three-degree of freedom in the horizontal plane are;

(1) Longitudinal motion

$$-mV(\dot{\beta} + r) \sin \beta + m\dot{V} \cos \beta = f_x \quad (2)$$

(2) Lateral motion

$$mV(\dot{\beta} + r) \cos \beta + m\dot{V} \sin \beta = f_y \quad (3)$$

(3) Yaw motion

$$I\dot{r} = m_z \quad (4)$$

The sideslip angle, β are consider very small and neglected. Equation (5) obtained from Eqs. (2) to (4)

$$\begin{bmatrix} mV(\dot{\beta} + r) \\ m\dot{V} \\ I\dot{r} \end{bmatrix} = \begin{bmatrix} -\sin \beta & \cos \beta & 0 \\ \cos \beta & \sin \beta & 0 \\ 0 & 0 & 1 \end{bmatrix} \quad (5)$$

Fig. 2 Vehicle model diagram

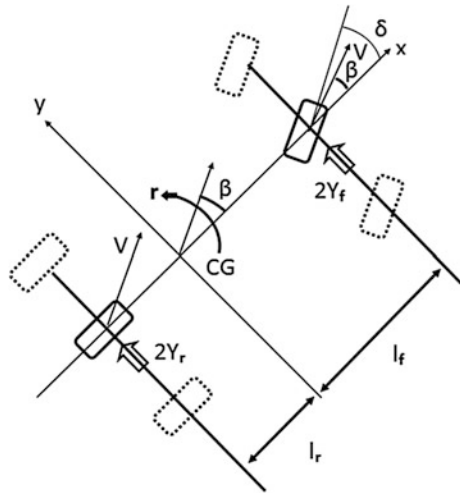


Table 2 The parameter and their symbols

Parameter	Symbol	Parameter	Symbol	Parameter	Symbol
Mass	m	Velocity	V	Radius of turn	r
Sideslip angle	β	Side force at y and x-axis	f_y, f_x	Yaw	m_z
Length from rear wheel to CG	l_r	Length from front wheel to CG	l_f	Inertia	I

The Eq. (5) known as two-wheel model. Table 2 show the parameters and symbols used in the equation above.

2.3 Design of the Experiments-Human Behavior Data Collection

The experiments were conducted to study the driving pattern of each subjects/human when driving on the designed path. The path consists of 3 segments which were a straight path, left turn and right turn. Five subjects selected for the experiments as shown in Fig. 3. The selected subjects own a driving license with driving experience less than 10 years.

The path selected for the experiments were the combination of the straight path, left and right turn. The path selected based from [17–19] research papers. The distance of the full path was approximately 40 m. The experiments start at point A and finish at point B for the straight path as in Fig. 4. The experiments repeated for

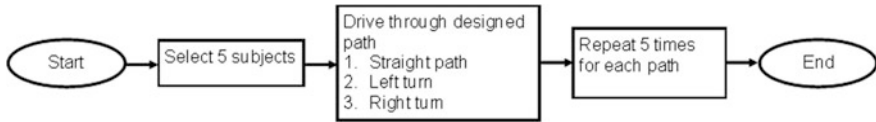


Fig. 3 Flow chart for the experiments

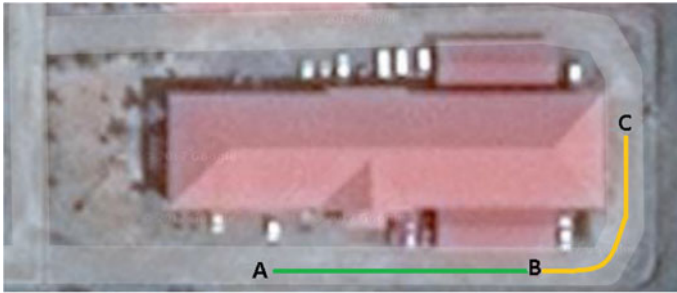


Fig. 4 Path for the experiment

5 times for each test subject. The right turn start at point C and finish at point B. While, left turn start at point B and finish at point C.

3 Result and Discussion

The results for straight, left and right paths are discussing in this section. In the results, a positive sign angle means turning to the left side, while a negative sign angle means turning to the right side.

Figure 5 shows the steering angle results for the paths of the straight line for the subject #3, #4, and #5. The steering angle varies because of the roughness of the road conditions. The steering angle changes between -16° and 15° . The reason for the small changes in steering angle while moving in the straight line is the use of the rack and pinion steering systems on the buggy car. The average for maximum steering angle for all subjects are 13° while moving in a straight line. Maximum steering angle at the straight path is 19° , while the minimum is 12° .

Fig. 5 Steering angle for straight path AB

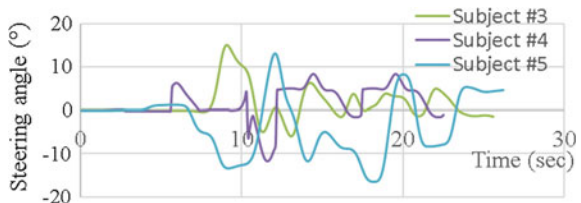


Fig. 6 Steering angle for right turn CB

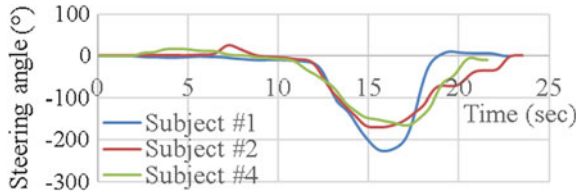
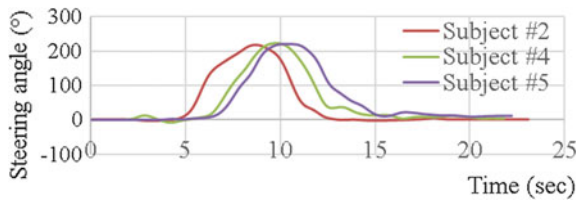


Fig. 7 Steering angle for left turn BC



The maximum steering angles when turning to the right side are -226° , -170° and -165° by subject #1, #2, and #4, respectively as shown in Fig. 6. The pattern of moving steering angle shows similar pattern for all subjects when turning to the right side. At the time 11 s, subject #4 starts to turn right while subject #1 and #2 at the time 11.5 s. The average of maximum steering angle for all subjects are -151° while turning to the right side. The transition from straight to turning seen as the steering angle decrease.

The maximum steering angles when turning to the left side are 219° , 223° and 220° by subject #2, #4, and #5, respectively as shown in Fig. 7. The pattern of moving steering angle shows similar pattern for all subjects when turning to the right side. At the time 4.6 s, subject #2 starts to turn right while subject #1 and #2 at the time 5.9 s. The average of maximum steering angle for all subjects are 237° while turning to the left side. The transition from straight to turning seen as the steering angle decrease.

The characteristic of each subject when taking the corner studied. Each subject show the ability to drive the car for each path. The data used to train the Fuzzy controller. Small change in steering angle while at the straight path are because of uneven road condition. At right turn, the maximum steering angle recorded are almost same for all subjects. This show the consistency of steering angle rotation even for the different subjects. It is same for the left turn. Table 3 show the summary result for human navigation test. The result shows the maximum and minimum steering angle while subject entering the left, right turn and straight path.

Table 3 Summary result for human navigation test

Paths	Minimum angle (°)	Maximum angle (°)
Straight	-16	15
Right turn	-165	-226
Left turn	219	223

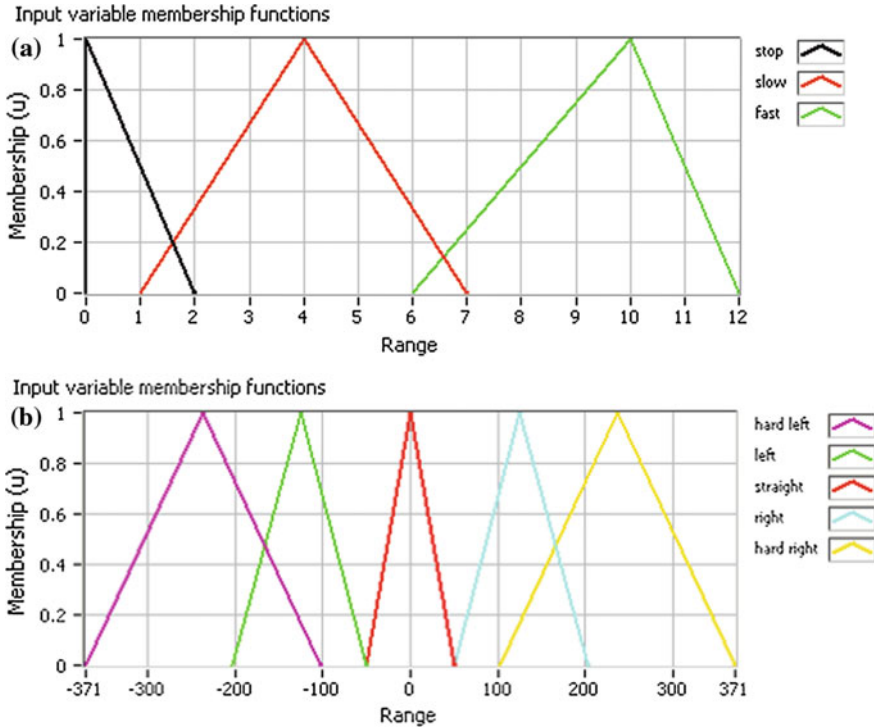


Fig. 8 Fuzzy membership function; a Speed; b Current steering angle

Figure 8 shows the fuzzy membership function used in the controller. A speed membership function as shown in Fig. 8a were designed from the GPS module data was divided into three parts, which were stop, slow, and fast. From the experiments, the maximum speed of the buggy car was 12 km/h on fully charge. The stop was defined when the speed of the buggy was 0–2 km/h. The slow was defined when the speed of the buggy was 1–7 km/h. The fast was defined when the speed of the buggy was 8–12 km/h. A current steering angle membership function as shown in Fig. 8b was designed from the encoder data. It was divided to five parts, which are hard left, left, straight, right, and hard right. The hard left was defined when the steering angle between -371° and -103° . The left was defined when the steering angle between -203° and -51° . The straight was defined when the steering angle between -51° and 51° . The hard right was defined when the steering angle between 51° and 203° . The right was defined when the steering angle between 103° and 371° .

4 Conclusion

The development of the fuzzy controller used human decision-making ability to decide the importance of each action and decision. The driving experiences of the selected subject's drivers produce the same driving pattern for the straight, right and left turns. The rule-base were create based on data from human drive on the designed path. The main reason to create a controller that imitate human behavior is to make an autonomous vehicle passenger feel safer and comfortable. The performance of the fuzzy controller still in testing phase. In the future, the autonomous vehicle will be test on designed path with the developed fuzzy controller.

References

1. EUCAR: The electrification of the vehicle and the urban transport
2. Rasekhipour, Y., Khajepour, A., Chen, S.-K., Litkouhi, B.: A potential field-based model predictive path-planning controller for autonomous road vehicles. *IEEE Trans. Intell. Transp. Syst.*, 1255–1267 (2017)
3. Marr, B.: Rolls-royce and Google partner to create smarter, autonomous ships based on AI and machine learning. <https://www.forbes.com/sites/bernardmarr/2017/10/23/rolls-royce-and-google-partner-to-create-smarter-autonomous-ships-based-on-ai-and-machine-learning/#16a5de066dfe>. Accessed 25 Oct 2017
4. Hawkins, A.J.: Toyota's new self-driving car has two steering wheels to prevent robot joyriding. <https://www.theverge.com/2017/9/27/16373058/toyota-research-institute-self-driving-car-luminar>. Accessed 25 Oct 2017
5. Galeon, D.: Elon Musk Says Tesla's AI will let cars predict your destination. <https://www.nbcnews.com/mach/science/elon-musk-says-tesla-s-ai-will-let-cars-predict-ncna813211>. Accessed 25 Oct 2017
6. Ping, E.P., Swee, S.K.: Simulation and experiment of automatic steering control for lane keeping manoeuvre. In: *Proceeding in 2012 4th International Conference on Intelligent and Advanced System (ICIAS 2012)*, vol. 1, pp. 105–110
7. Mammari, S.: H ∞ robust automatic steering of a vehicle. In: *Proceeding 1996 IEEE Intelligent Vehicles Symposium, Tokyo*, pp. 19–24 (1996)
8. Hoffmann, G.M., Tomlin, C.J., Montemerlo, M., Thrun, S.: Autonomous automobile trajectory tracking for off-road driving controller: controller design, experimental validation and racing. In: *Proceedings of the 2007 American Control Conference, New York*, pp. 2296–2301 (2007)
9. Guldner, J., Sielen, W., Tan, H.-S., Ackermann, J., Patwardhan, S., Bunte, T.: Robust automatic steering control for look down reference systems with front and rear sensor. *Proc. IEEE Trans. Control Syst. Technol.* 7(1), 2–11 (1999)
10. Kahveci, N.E.: Adaptive steering control for uncertain vehicle dynamics with crosswind effects and steering angle constraints. In: *Proceeding of the 2008 IEEE International Conference on Vehicular Electronics and Safety, Ohio*, pp. 162–167 (2008)
11. Bjelonic, M., Homberger, T., Kottege, N., Borges, P., Chli, M., Beckerle, P.: Autonomous navigation of hexapod robots with vision-based controller adaption. In: *IEEE International Conference on Robotics and Automation (ICRA)*, Singapore, pp. 5561–5568 (2017)
12. Shen, C., Guo, H., Liu, F., Chen, H.: MPC-based path tracking design for autonomous ground vehicles. In: *Proceeding of the 36th Chinese Control Conference, Dalian*, pp. 9584–9589 (2017)

13. Aoki, T., Sigumachi, T., Fukuo, T., Kawashima, H.: Autonomous steering control with adaptive mechanism by MMAC. In: SICE Annual Conference 2012, Akita, pp. 203–210 (2012)
14. Yang, S., Wang, W., Liu, C., Deng, W., Hendrick, J.K.: Feature analysis and selection for training an end-to-end autonomous vehicle controller using deep learning approach. In: 2017 Intelligence Vehicles Symposium, California, pp. 1033–1038 (2017)
15. Rasheed, U., Ahmed, M., Afride, M.J., Kunwar, F.: Road trajectory mining and autonomous steering control for vision-based unmanned vehicles. In: 2010 10th International Conference on Intelligent Systems Design and Applications (ISDA), Cairo, pp. 97–202 (2010)
16. Labeye, E., Hugot, M., Brusque, C., Regan, M.A.: The electric vehicle: a new driving experience involving specific skills and rules, Elsevier (2014). www.elsevier.com/locate/trf
17. Bae, I.I., Kim, J.H., Kim, S.: Steering rate controller based on curvature of trajectory for autonomous driving vehicle, Gold Coast, pp. 1381–1386 (2013)
18. Aoki, T., Sugimachi, T., Fukuo, T., Kawashima, H.: Autonomous steering control with adaptive mechanism by MMAC. SICA Annual Conference, Akita, pp. 203–210 (2012)
19. Qu, T., Chen, H., Ji, Y., Guo, H., Cao, D.: Modelling driver steering control based on stochastic model predictive control. In: 2013 IEEE International Conference on System, Man, and Cybernetics, pp. 3704–3709 (2013)

Statistical Pattern Recognition as an After Service for Statistical Process Control



Norazlin Nasir, A. Y. Bani Hashim,
Muhammad Hafidz Fazli Md Fauadi and Teruaki Ito

Abstract Since internet of things has brings a lot of benefits in various fields, the benefits in manufacturing is widely explored. While Industry 4.0 offers an integration concepts between current manufacturing devices with IoT. In I4, all the resources are connected, and information exchange became ease in shortest period. In any manufacturing application, statistical process control seems fit to be implemented because it shows the process trend as a tool. In this paper, consideration of the boundaries condition as SPC features is explained. Based on the five un behavioral trend conditions, engineers are able to make a process change and minimize the risk of losses and accidents. Eventually, the concept of SPR as an after Service is proposed, consisted of the combination of the element of IoT and SPC boundaries condition. The SPR as an after Service is proposed to be used for traceability tools in network environment.

Keywords Statistical process control · Statistical patter recognition
Internet of things

1 Introduction

1.1 Background

Qin et al. [1] explained that the internet of things (IoT) is one of the advanced art technologies within the last decade that able to help in expediting the processes and ease the management activities. IoT offers a bunch of benefits to manufacturing, for

N. Nasir (✉) · A. Y. Bani Hashim · M. H. F. Md Fauadi
Faculty of Manufacturing Engineering, Universiti Teknikal Malaysia Melaka,
Hang Tuah Jaya, 76100 Durian Tunggal, Melaka, Malaysia
e-mail: p051410006@student.utem.edu.my

N. Nasir · T. Ito
Institute of Technology and Science, Tokushima University, Minami-Jyousanjima 2-1,
Tokushima-Shi, Tokushima 770-8506, Japan

© Springer Nature Singapore Pte Ltd. 2018
M. H. A. Hassan (ed.), *Intelligent Manufacturing & Mechatronics*,
Lecture Notes in Mechanical Engineering,
https://doi.org/10.1007/978-981-10-8788-2_42

example, expedite the management process, information exchange, and control the machines and production. Those benefits make the manufacturing assets such machines and production units becomes interoperable in autonomous and intelligent ways [1]. Furthermore, IoT makes easy management to handle the big data and integrates the data with the coordinated disparate process and the sequential process can be carried out in parallel. Thus, the redundant steps can be recognized and eliminated in order to simplify the manufacturing processes [2] exchange, paperless management, etc.

The main idea in statistical process control (SPC) is to trace and make the corrections on the process. To make the SPC become intelligent by combining the element of IoT become necessary but the question is how to make it real. The term “as an after Service” means the graphical view of the statistical pattern recognition function as a service to the user with various applications, for example a graphical user interface (GUI).

By concerning on expedite tracking system, the SPC as an effective tool has been chosen to be integrated with IoT. The aim of this paper is to develop the graphical user interface by emphasizing the statistical process control—control chart and the use of SPC boundaries conditions to trace the manufacturing process before going out of control. In the designed GUI, the control processes’ interface will help the engineer/operator to change the process accordingly before more losses occur.

1.2 Industry 4.0

In product development, the Industry 4.0 (I4) encourages the close collaboration between various disciplines. The close collaboration initiate by integrating the physical components and internet technology (IT) systems as an application of intelligent system in product manufacturing environment [3]. The digitization of the manufacturing enterprise resulting in real time data exchange through the inter-connection between people, objects, as well as systems, is a new concept for I4 [4–6]. To cope with digitization and intelligent manufacturing system, a strategic approach is needed to manage and control the man, machine, and management. Due to the intelligent manufacturing system, the level of complexity will increase and high manpower’s skills are needed. The challenge is to need the accountability on digitization and intelligent manufacturing system in man, machine, and management perspective.

1.3 Internet of Things

An efficient manufacturing layout able to give an impact on costing for time reduction where the movement of worker and transport become faster. Designing a

factory layout requires a well-planned task. Nowadays, Internet of Things (IoT) helps many manufacturers to successfully design efficient cell layouts. Furthermore, an efficient layout helps in improving performance and minimizing total production by nearly 50% [7]. IoT also initiates the I4 that encourages the close collaboration between various disciplines. The close collaboration initiated by integrating the physical components and IT systems as an application for intelligent system in product manufacturing environment [3]. The digitization of the manufacturing enterprise resulting in real-time data exchange through the interconnection between people, objects, as well as systems is a new concept for I4 [4–6].

Online customization and purchasing is a new disruptive purchasing model that affects the manufacturing system and its chain. This model requires an evolution in management while the operational levels become a huge challenge [8]. Big Data application is essential in I4 where the only effective solution to manage and control the complexity and disturbances is by adapting the manufacturing networks [9]. Besides the manufacturing networks, IoT, data exchange, product life cycle management (PLM), business web, social web, computer hardware, and software become the pillars.

2 Statistical Process Control

2.1 Control Chart

In SPC, there are variance charts can be used for monitoring and controlling the production process. In this study, the p -chart is chosen due to its capability in obtaining the number of non-confirming units, rapidly [10]. Furthermore, it is compatible to be used if the sample is more than 30 units. However, the information obtained may not be reliable on the state of control if the sample is less than 30 [11].

The p -chart represented by a ratio of the number of non-confirming units to the total number of units in the sample set. The probability having the non-confirming units in the set of n is known as p and the experimental data can be evaluated from Eq. 1 where in the fraction of the non-confirming units, p_i in i th sample set, k is known as the number of the sample set.

$$p = \frac{1}{k} \sum_{i=1}^k p_i \quad (1)$$

The p -chart can be prepared with constant n and graphically represented the confidence limits with:

$$CL = \bar{p} \quad (2)$$

$$LCL = \bar{p} - 3 \left(\sqrt{\frac{\bar{p}(1-\bar{p})}{n}} \right) \quad (3)$$

$$UCL = \bar{p} + 3 \left(\sqrt{\frac{\bar{p}(1-\bar{p})}{n}} \right) \quad (4)$$

If the size sample n is not constant, the p can be evaluated by using Eq. 4 where the n_i is the size and p_i is the non-confirming fraction units in the i th sample set.

$$\bar{p} = \frac{\sum_{i=1}^k P_i n_i}{\sum_{i=1}^k n_i} \quad (5)$$

2.2 SPC Boundary Condition

The graphical p -chart representation also able to show the lack of control scenarios which may occur under various circumstances that evidenced of un-behavior trend. ASTM International suggested nine conditions of un-behavior trend that can be detected if one or more points for un-behavior trend are violated [11]. However, in this paper, only five conditions are considered for further investigation. The conditions are:

1. Any single point, β or more those beyond 3σ which is upper control limit (UCL), or lower control limit (LCL), $\beta \pm 3\sigma$.
2. Two consecutive points, 2β beyond 2σ from the mean or centreline either above or below, $2(\beta \pm \sigma)$.
3. Four out of five consecutive points, 4β beyond 1σ from the mean or centreline either above or below, $4\beta \pm 1\sigma$.
4. Six or more points, 6β that consecutive higher or lower with no change in direction, $6\beta \pm \bar{x}$.
5. Eight or more points, 8β in a row on one side of the centerline, $8\beta \pm \bar{x}$.

2.3 Statistical Process Control Revolution

The statistical process monitoring (SPM) technology roadmap that proposed by He and Wang [12] may lead to SPC revolution by integrating the SPC with IoT for I4. The SPM roadmap is shown in Fig. 1. The roadmap is divided into three generations and used as a basic for monitoring purpose. In 1st Generation, the behavior of

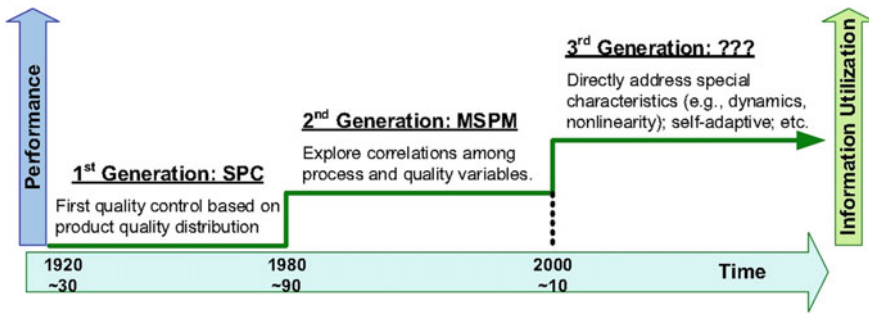


Fig. 1 The statistical process monitoring (SPM) roadmap [12]

SPC and SPC boundaries are recognized and required full attentions for minimizing the risk of losses in production lines. While in 2nd Generation, the correlation between process and quality variables were explored. For the 3rd Generation, the big data and its features were considered for I4. The features or characteristics became a base for monitoring activities for process.

For I4, the integration with IoT is a must. By integrating the IoT with SPC and considering the 1st Generation of SPM technology, the statistical pattern recognition is proposed in this paper as “an after service” of SPC. The statistical pattern recognition (SPR) is a correlation between SPM technology and IoT for I4. This correlation is called as “an after service” because the user or customer may view the statistical process control and statistical pattern recognition by logging in into the SPC-GUI.

3 Statistical Pattern Recognition and Discussion

3.1 The Architecture

In the SPC-GUI, the element of control chart and SPR were considered. Figure 2 shows the architecture framework for the SPC-GUI system work. In this system, only authorized user able to access and view the graphical data present in GUI layer. There are two types of data sources: database and data application. Those data storages were relying each other. The data application is the local data storage for user to upload the real data to be analyzed. After the analyzation process, the control chart and SPR were generated as the output for graphical data. The output generated was categorized as manufacturing report to monitor the production status. The output was stored in database as historical data and for future references. The arrows denoted as the control flows in the SPC-GUI.

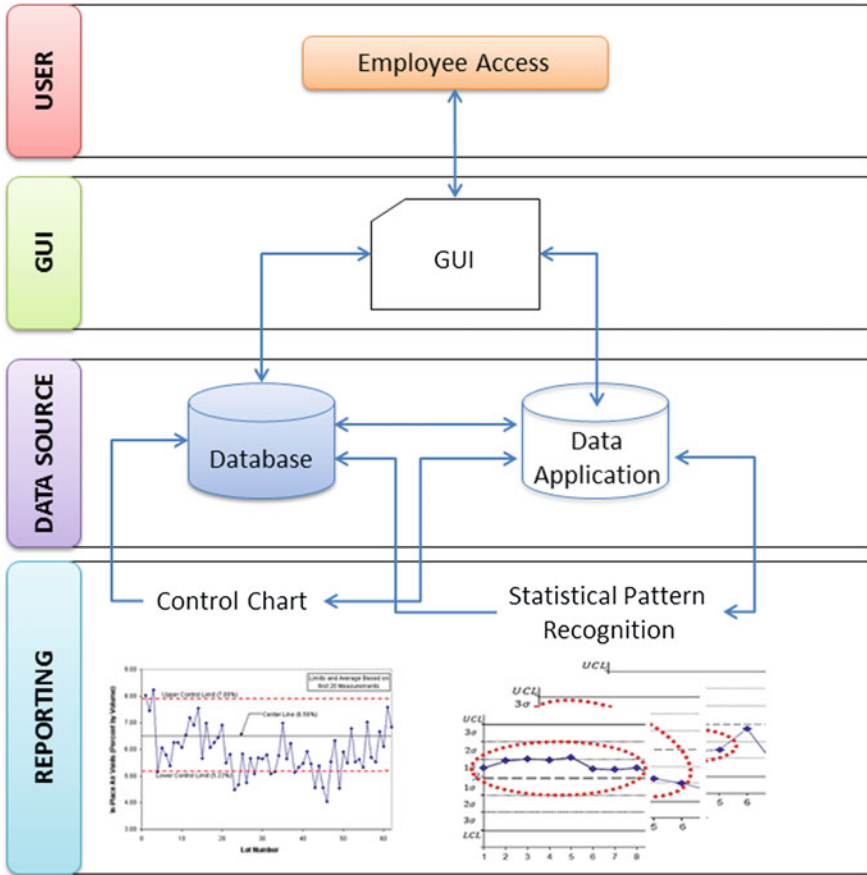
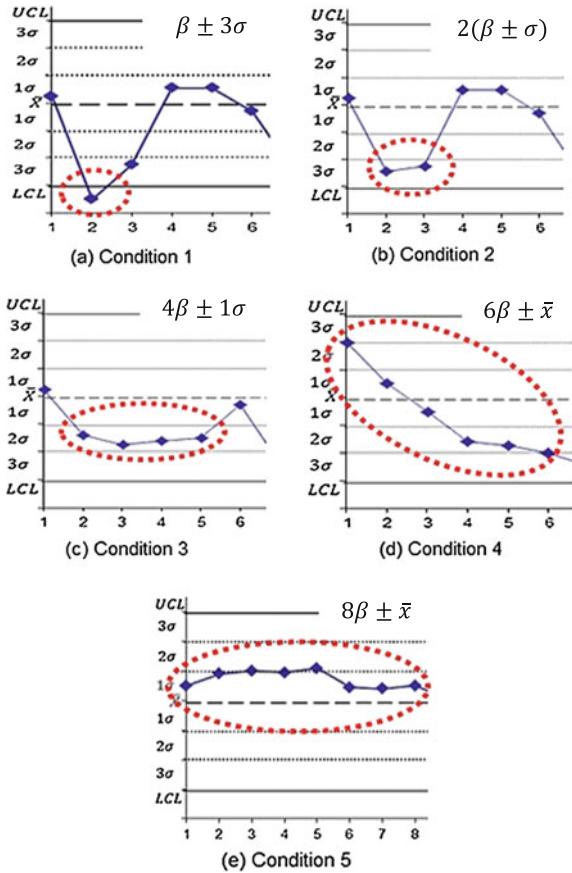


Fig. 2 The architecture framework for statistical process control-graphical user interface

3.2 Statistical Pattern Recognition as an After Service

As per discussed earlier, only five boundaries condition considered in this paper. The boundaries' conditions were features in SPC chart that were faulty to be detected in old SPC. By getting assists from IoT, the faulty samples were easily to be detected just-in-time. The SPR as an after service for SPC is viewed as shown in Fig. 3. The SPR chart is only able to be viewed directly after the SPC data is analyzed and the SPC chart is generated in the same GUI. That is the reason why the SPR called as an after service for SPC in this study.

Fig. 3 The SPR overview in the SPC GUI



3.3 Hidden Markov Model

For pattern recognition, the Hidden Markov Model (HMM) is chosen. HMM as a tremendous approach have the capabilities in process monitoring. To represent the machining signal with statistical parameter has become the strong capabilities for HMM [13]. In SPR using HMM approach, the state of SPR is denoted as $x = \{x_1, x_2, x_3, x_4, x_5\}$ while the possible observation, $o = \{o_1, o_2, o_3, o_4, o_5\}$. The x_1 represents the SPR_1 , x_2 represents SPR_2 , x_3 represents SPR_3 , x_4 represents SPR_4 , and x_5 represents SPR_5 . The possible observations are boundaries condition for SPR where o_1 represents $\beta \pm 3\sigma$, o_2 represents $2(\beta \pm \sigma)$, o_3 represents $4\beta \pm 1\sigma$, o_4 represents $6\beta \pm \bar{x}$, and o_5 represents $8\beta \pm \bar{x}$. In Fig. 4, the conceptual framework for the SPR emphasized the probabilistic parameter of HMM to analyze the all the possible state. The SPR_1 in Fig. 4 represents the variable of $x(t)$ is the hidden state at time t with the probabilistic parameter $x(t) \in \{x_1, x_2, x_3, x_4, x_5\}$. $o(t) \in \{o_1, o_2, o_3, o_4, o_5\}$ is the observation time for variable $o(t)$. The conditional dependencies are represented

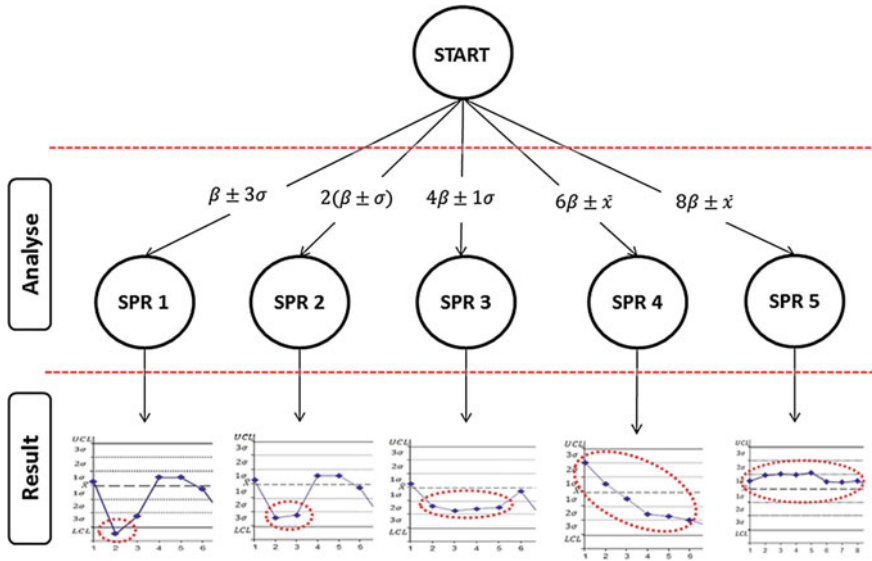


Fig. 4 The conceptual framework for statistical pattern recognition using Hidden Markov Model (HMM)

as arrows in Fig. 4. The result is Fig. 4 is known as next state in HMM. The next state x_t^j is obtained from the transition probabilities matrix, a^{ij} and another current state that contains the first number a specified number of times.

The probability of state x^j at time t , is known as transition state. The transition probability for the a^{ij} is given in the Eq. 6 below. The next state x_t^j is obtained from the transition probabilities matrix, a^{ij} and current state x_{t-1}^i as shown in Eq. 7.

$$a^{ij} = p(x_t^j | x_{t-1}^i) \tag{6}$$

$$[x_t^j] = [a^{ij}] [x_{t-1}^i] \tag{7}$$

3.4 The Pseudocode

The pseudocode as shown in Table 1, is choose as a unify language to share the procedure in SPR chart development. In this pseudocode, $i \leq 100$ as a set of data input for the GUI that needed to be analyzed. The size of data must not more than 100 for optimal evaluation in SPC. β is any single point of data plotted in SPC chart where the value is bigger than mean, \bar{x} and 3σ in order to show the boundaries conditions. If the value of β is similar to \bar{x} means that the process is under control, return $(x, y) = (0, 0)$ and no SPR chart will be displayed.

Table 1 The pseudocode for SPR chart development

Pseudocode: SPR Chart

```

a=  $\beta \pm 3\sigma$ , b=  $2(\beta \pm \sigma)$ , c=  $4\beta \pm 1\sigma$ , d=  $6\beta \pm \bar{x}$ , e=  $8\beta \pm \bar{x}$ 
 $i \leq 100$ ,  $\beta := i > \bar{x}$ ,  $i \geq 3\sigma$ 

if  $\beta = \bar{x}$  then
    return (x,y)=(0,0)
else
    if  $i > 100$  then
        return (x,y)=(0,0)
    end
end

end

```

3.5 Discussion

The SPC-GUI is aimed to ease the production monitoring activities. The SPC-GUI contains the control chart and SPR chart as the reporting result. The artificial neural network (ANN) is another approach to obtain the SPR chart. However, ANN is not compatible enough due to amount of reference data are not always available. Especially for new product development where the reference data is not available for recommendation. These strong reason give more benefits to HMM to be chosen for monitoring based where the ANN is not compatible enough for that. The SPC-GUI is developed by using MATLAB software.

4 Conclusions

The integration between IoT and manufacturing process is widely explored. The implementation on traceability tools between IoT and manufacturing can be questioned. The concept of SPR as an after Service in this study has combination of the element of IoT and SPC boundaries condition. The SPR as an after Service is only generated directly after the set of manufacturing data is analyzed. The SPR as an after Service able to detect the faulty data and recognize the data features based on the boundaries conditions. Based on that, the SPR as an after Service can be used for traceability tools in network environment. The SPR as an after Service is designed to use as monitoring purpose for process control and minimizing the risk of losses and accident. Based on the SPR chart represented, the user able to make any changes in the production lines just in time and avoid more losses.

As a future study, the SPC-GUI development is targeting to assist the user in timely decision making reduction. The different SPC-GUI between other, the SPC-GUI able to view the faulty data based on boundaries condition by offering that as a service to the users.

References

1. Qin, J., Liu, Y., Grosvenor, R.: A categorical framework of manufacturing for Industry 4.0 and beyond. *Proced. CIRP* **52**, 173–178 (2016)
2. Bhatt, G.D.: An empirical examination of the effects of information systems integration on business process improvement. *Int. J. Oper. Prod. Manage.* **20**(11), 1331–1359 (2000)
3. Herter, J., Ovtcharova, J.: A model based visualization framework for cross discipline collaboration in Industry 4.0 scenarios. *Proced. CIRP* **57**, 398–403 (2016)
4. Hecklau, F., Galeitzke, M., Flachs, S., Kohl, H.: Holistic approach for human resource management in Industry 4.0. *Proced. CIRP* **54**, 1–6 (2016)
5. Spath, D., Ganschar, O., Gerlach, S., Hämmerle, M., Krause, T., Schlund, S.: *Produktionsarbeit der Zukunft—Industrie 4.0*. Fraunhofer Verlag, Stuttgart (2013)
6. Wolfgang, D., Gloh, C., Hahn, T., Knafla, F., Loewen, U., Rosen, R., et al.: *Umsetzungsstrategie Industrie 4.0. Ergebnisbericht der Plattform Industrie 4.0*. BITKOM eV, VDMA eV, ZVEI eV Berlin, Frankfurt (2015)
7. Ghosh, T., Doloi, B., Dan, P.K. Applying soft-computing techniques in solving dynamic multi-objective layout problems in cellular manufacturing system. *The Int. J. Adv. Manuf. Technol.* 1–21 (2015)
8. Mourtzis, D.: Challenges and future perspectives for the life cycle of manufacturing networks in the mass customisation era. *Logist. Res.* **9**(1), 1–20 (2016)
9. Mourtzis, D., Doukas, M., Psarommatis, F.: A toolbox for the design, planning and operation of manufacturing networks in a mass customisation environment. *J. Manuf. Syst.* **36**, 274–286 (2015)
10. Özilgen, Mustafa: *Handbook of Food Process Modeling and Statistical Quality Control with Extensio Matlab® Applications*, 2nd edn. CRC Press, Taylor & Francis Group, New York, USA (2011)
11. Committee E-11 on Quality and Statistics. *Manual on Presentation of Data and control Chart Analysis*, 7th edn. ASTM International, West Conshohocken, Pennsylvania, USA. (2002)
12. He, Q.P., Wang, J.: Statistical process monitoring as a big data analytics tool for smart manufacturing. *J. Process Control* (2017)
13. Cho, W., Lee, S.W., Kim, J.H.: Modeling and recognition of cursive words with hidden Markov models. *Pattern Recogn.* **28**(12), 1941–1953 (1995)

Visual Based Distance Recognition Technique by Using Pixy CMUcam5



M. F. Ahmad, S. S. N. Alhady, Wan Rahiman,
W. A. F. W. Othman and A. A. M. Zahir

Abstract This paper presents a robust color code tracking system using low-cost vision sensor Pixy CMUcam5 for cart follower in an indoor environment. The CMUcam5 camera mounted on the front of the cart to have a perfect vision for establishing tracking task. The camera gives an excellent performance that has the ability to identify a various number of targets with color code features. The acquired data in image view than transformed to the real coordinate. The experimental result shows that the proposed technique granted a slight error in average pixels and angle errors. As a conclusion, the project met with the objective of this research.

Keywords Pixy CMUcam · Color tracking technique · Cart following system

1 Introduction

In the development world now, the growth of autonomous mobile following robot increases rapidly. Today's trend evolves with small mobile robots equipped with microcontroller which controls numerous sensors and actuators. The robot platform itself can be controlled via wireless connection without having any physical contact [1].

The interest of having personal mobile robots already spread towards civilian usage in which it affects personal necessities. The mobile robot needs an efficient navigation system that has a lot of similarities like normal human visual perception. It can be programmed so that it can move independently [2].

Problems occurred when camera loss track. This due to the chosen color might be same with the ambient color. Moreover, this might worst the situation if the camera misidentified the target or tracked the wrong target.

M. F. Ahmad · S. S. N. Alhady · W. Rahiman · W. A. F. W. Othman (✉)
A. A. M. Zahir
School of Electrical and Electronic Engineering, Universiti Sains Malaysia,
14300, Nibong Tebal, Penang, Malaysia
e-mail: wafw_othman@usm.my

© Springer Nature Singapore Pte Ltd. 2018
M. H. A. Hassan (ed.), *Intelligent Manufacturing & Mechatronics*,
Lecture Notes in Mechanical Engineering,
https://doi.org/10.1007/978-981-10-8788-2_43

The objective of this work is to obtain the best tracking performance using CMUcam5 with pan-tilt mechanism devices. In addition, special feature of CMUcam5 that has color code ability whereby multiple colors can be tracked in real time and gives a feedback data to calculate the pan-tilt angle variation rates. Finally, the controller will produce new control signal to minimize the tracking error and increase the efficiency of the tracking systems. As a result, the CMUcam5 with pan-tilt mechanism is capable to identify and tracked the image centroid accurately and smoothly. The evaluation regarding performance of the proposed algorithms is evaluated by intensive experiments.

2 Related Works

CMUcam is a steady vision tracking camera and was produced by Carnegie Mellon University. The advantages of CMUcam are handy, low cost and able to follow the changing direction of target centroid, making it a suitable choice for vision tracking camera application. It will keep rotating to lock the centroid inside the tracking box [3].

In recent findings, many researchers found that the usage of CMUcam itself is restricted to the static field of view. A mechanical instrument named pan-tilt mechanism was used to enhance the performance of CMUcam itself [4–6].

There is a related work on cart following robot being investigated using CMUcam3. The experiment was done to obtain the data on Field of View (FOV) of the camera in addition to gather sensors' reading. The sensor used for obstacle avoidance is GP2D120 Infrared sensor. Overall cart system works well but the limitation is that, it is restricted to only a single color for tracking purpose and it is easy for the cart to lose track if the tracked color equal to the color of the environment [7].

A target tracking control of the mobile robot in diversified maneuver modes was established using low technology embedded vision system, CMUcam3 with pan-tilt. A high precision tracking system is the main objective. An error in pan-tilt mechanism was calculated to remain the centroid of the target inside the camera tracking box [8].

Another example of successful task of following using vision-based sensor is by using features of contour and color based detection. The HSI (Hue, Saturation, and Intensity) color model was used. The method of taking difference information between the position of targeted object and center of the camera screen was used for tracking. The camera will always follow the object in order to make sure that the tracked object is always at the center view of the camera screen [9].

3 Implementation Method

CMUcam5 used for tracking is set to have 50 frames per second with maximum 1280×800 pixels resolution. The field of view of the camera gives several aspects like image centroid, size and pixel image value of tracked color. All the gathered data can be converted into the real world position of the landmark. Another special ability of Pixy CMUcam5 is it has color code feature which can track multiple colors at the same time. Other information like image rotating angle, width, height, distance and area can also be obtained [10].

There are two Pixy CMUcam5 being used in this experiment. One is placed in the front part of the cart and mounted at the same level with the tracked color code. It will collect image information and feed it to the microcontroller to obtain such data that being grabbed. Another one is placed on top of the experimental area. The reason for using double camera is to grab the exact coordinate of the targeted object since the Pixy CMUcam5 camera cannot determine the depth of the tracked object. Figure 1 shows the visualization of the experiment environment. However, the real research only used two color patterns which are orange and green. Figure 2 shows all the relevant information of the captured image by CMUcam5.

However, there is an error in obtaining angle value when the wheelchair prototype moved from one point to another. The average between two angle values can be calculated by Eq. (1) to counter this problem.

$$\theta_{avg} = \frac{\theta_i + \theta_f}{N} \tag{1}$$

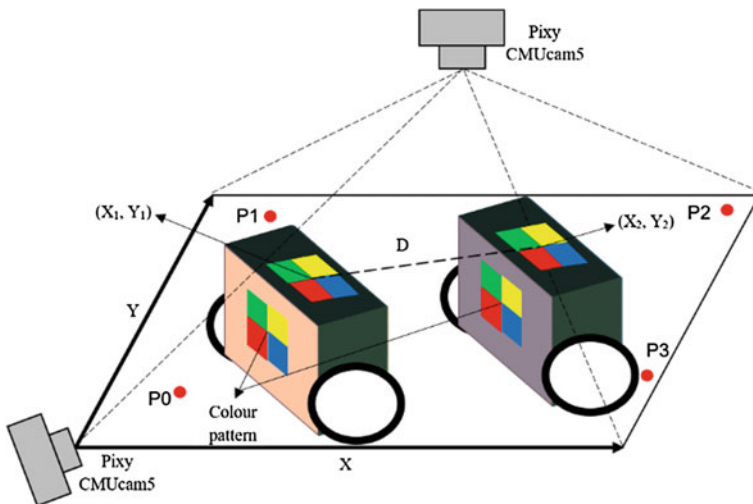


Fig. 1 Experiment environment visualization

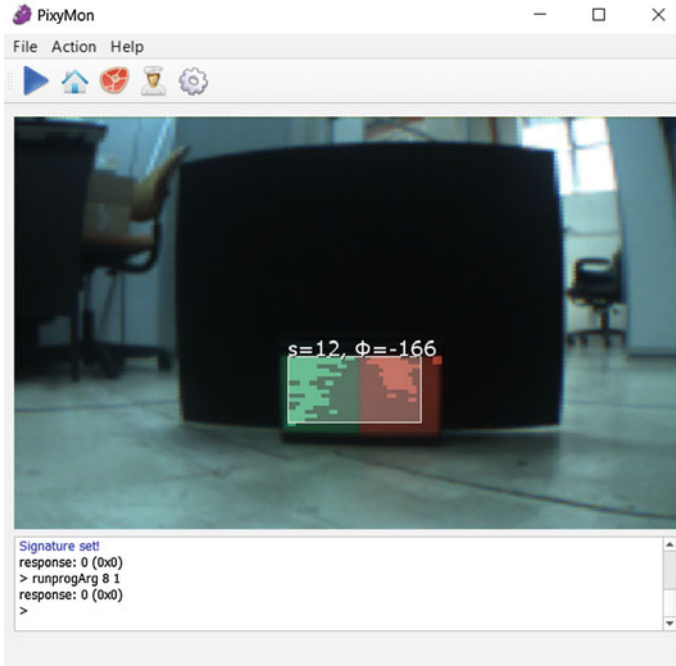


Fig. 2 Captured image by CMUcam5 with relevant information

where θ_i is the initial angle of color code and θ_f is the final angle of the color code.

The changes of θ value lead to the changes of dimension of the color code placard. The value of width and height of the placard can be recalculated by using Eq. (2).

$$\begin{aligned}
 W &= \frac{(M_X X \ W_I)}{D} \\
 H &= \frac{(M_Y X \ H_I)}{D}
 \end{aligned}
 \tag{2}$$

where M_X and M_Y are real range of the wheelchair prototype to the x and y axis respectively.

D in Fig. 1 is the distance between the previous and current position of the wheelchair. The definition yields by Eq. (3).

$$D = \sqrt{(X_2 - X_1)^2 + (Y_2 - Y_1)^2}
 \tag{3}$$

The calculation of current position of the wheelchair prototype can be done by converting the x and y coordinates from image to real domain. Hence, the conversion yields the Eq. (4).

$$X_F = \frac{(X_M \times W_I)}{W} \tag{4}$$

$$Y_F = \frac{(Y_M \times H_I)}{H}$$

where X_M and Y_M are the centroids of the color code in the image frame.

The mean value of the data can be obtained with Eq. (5).

$$\bar{z} = \frac{\sum z}{n} \tag{5}$$

where z is value of data, n is number of data, hence the standard deviation calculation yields Eq. (6).

$$\sigma = \sqrt{\frac{\sum z^2}{n} - (\bar{z})^2} \tag{6}$$

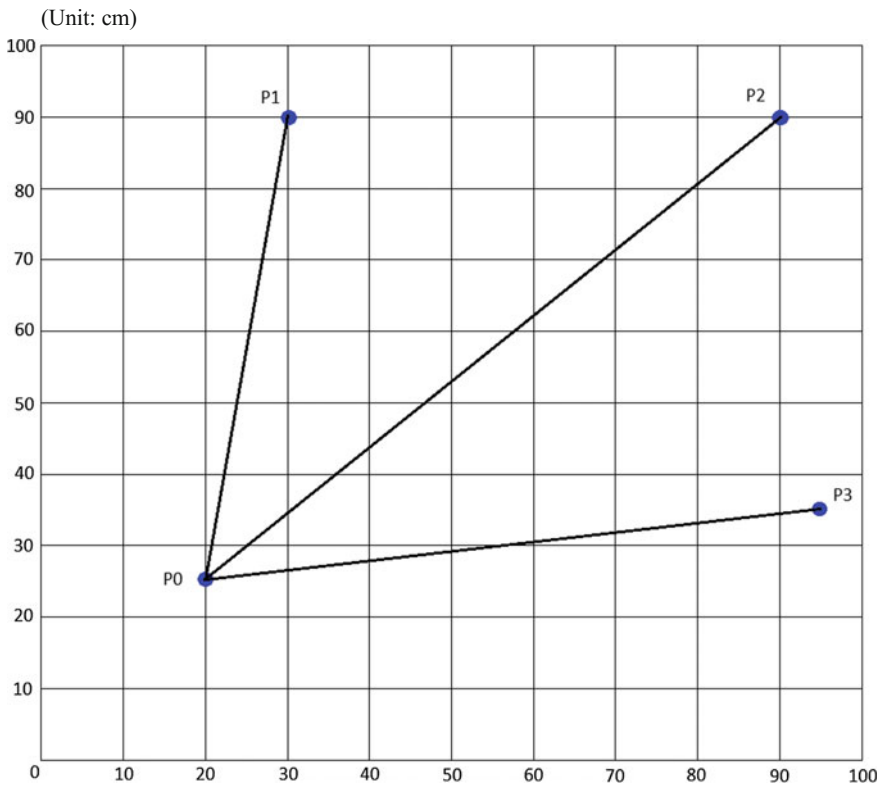


Fig. 3 Experimental trajectory of the wheelchair prototype

Fig. 4 Average tracking pixel error

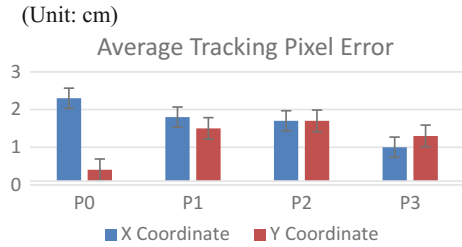
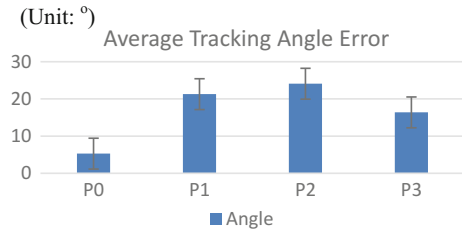


Fig. 5 Average tracking angle error



4 Result

The vision-based localization experiment has been conducted in closed environment. The tested area for Pixy CMUcam5 camera is around 200 cm wide and 250 cm long. The first camera is attached to the cart whereby the second camera is hanging around 200 cm above the experiment area. Figure 3 shows the visualization of the experiment area in top view. The real width and height of each color tag are 5 cm and 5 cm respectively. Hence, the physical dimensions of two color code tags together are 10 and 5 cm in width and height.

The test was repeated for 20 times to obtain better average accuracy result. Figure 4 shows the average errors in each point the wheelchair prototype reached for the *x*, *y* coordinates meanwhile Fig. 5 depicts the difference in angle of the targeted color code. The standard deviation for both results was calculated and marked on the graph to test the robustness of the tracking performance.

5 Conclusion

In this paper, the robust tracking localization method using Pixy CMUcam5 to determine the position of wheelchair prototype has been shown. The usage of color code features is important to differentiate the target with the surrounding hence give smooth tracking visual for the camera. In repeated experimental tests, the proposed method was able to achieve average localization accuracy with errors in the range

0.40–2.30 cm and heading errors in the range 5.30–21.30° from P0 to P1, P2 and P3 locations.

As a conclusion, the proposed color-codes based tracking method using Pixy CMUcam5 is robust after making a standard deviation test and efficient to be used for real-world target localization. In addition to this work in future, a dynamic tracking method can be determined to give more additional features to the project.

Acknowledgements The authors would like to thank The Ministry of Science, Technology and Innovation Malaysia (MOSTI), and Universiti Sains Malaysia (USM) for the support of the research under grant number 305/PELECT/6013112.

References

1. Bräunl, T.: *Embedded Robotics: Mobile Robot Design and Application with Embedded Systems*, pp. 1–7, 3rd edn. Springer, Berlin (2008)
2. Chen, S., Li, Y., Kwok, N.M.: Active vision in robotic systems: a survey of recent developments. *Int. J. Robot. Res.* **30**(11), 1343–1377 (2011)
3. Rowe, A., LeGrand, R., Robinson, A.: Overview—CMUcam5Pixy—CMUcam: Open Source Programmable Embedded Color Vision Sensors. <http://www.cmucam.org> (2017). Accessed 10 Oct 2017
4. Lee, S., Tewolde, G.S., Lim, J., Kwon, J.: Vision based localization for multiple mobile robots using low-cost vision sensor. In: *IEEE International Conference Electro/Information Technology (EIT)*, pp. 280–285 (2015)
5. Ahmad, M.F., Alhady, S.S.N., Kaharuddin, S., Othman, W.A.F.W.: Visual based sensor cart follower for wheelchair by using microcontroller. In: *5th International Conference on Control System, Computing and Engineering (ICCSCE)*, pp. 123–128. IEEE International Conference, Penang, Malaysia (2015)
6. Ahmad, M.F., Rong, H.J., Alhady, S.S.N., Rahiman, W., Othman, W.A.F.W.: Colour tracking technique by using Pixy CMUcam5 for wheelchair luggage follower. In: *7th International Conference on Control System, Computing and Engineering (ICCSCE)*, pp. 187–192. IEEE International Conference, Penang (2017)
7. Sani, N.A., Alhady, S.S.N., Othman, W.A.F.W., Kaharuddin, S.: Cordless cart follower for wheelchair user. *Intelligent Robotics Automation, and Manufacturing*, pp. 252–262. Springer, Berlin, Heidelberg (2012)
8. Xu, H., Shen, Y.P.: Target tracking control of mobile robot in diversified manoeuvre modes with a low cost embedded vision system. In: *Industrial Robot: An International Journal*, vol. 40 Issue 3, pp. 275–287. Emerald Insight, UK (2013)
9. Trang, T.T., Ha, C.: Irregular moving object detecting and tracking based on color and shape in real-time system. In: *Computing, Management and Telecommunications (ComManTel)*, pp. 415–419. IEEE International Conference (2013)
10. CMUcam5 Pixy: <http://cmucam.org/projects/cmucam5> (2017). Accessed 11 Nov 2017

Parallel Guided Image Processing Model for *Ficus Deltoidea* (Jack) Moraceae Varietal Recognition



Ahmad Fakhri Ab. Nasir, Ahmad Shahrizan Abdul Ghani
and M. Nordin A. Rahman

Abstract Nowadays, with the huge number of leaves data, plant species recognition process becomes computationally expensive. Many computer scientists have suggested that the usage of parallel and distributed computing should be strongly considered as mandatory for handling computationally intensive programs. The availability of high performance multi-cores architecture results the complex recognition system to become popular in parallel computing area. This paper emphasizes on the computational flow design to enable the execution of the complex image processing tasks for *Ficus deltoidea* varietal recognition to be processed on parallel computing environment. Multi-cores computer is used whereas one of them acts as a master processor of the process and the other remaining processors act as worker processors. The master processor responsible for controlling the main system operations such as data partitioning, data allocation, and data merging which results from worker processors. Experiments showed that a multi-cores parallel environment is a very appropriate platform for pipeline image processing. From the results, the sequential complex image processing model and computational flow design are significantly improved when executed through parallel model under multi-cores computer system. As the number of cores increases, the computational time taken by the parallel algorithm becomes less.

Keywords *Ficus deltoidea* jack • Plant species recognition • Image processing SPMD architecture • Parallel computing

A. F. Ab. Nasir (✉) • A. S. Abdul Ghani
Innovative Manufacturing, Mechatronics & Sport Labs, Faculty of Manufacturing Engineering, Universiti Malaysia Pahang, 26600 Pekan, Pahang, Malaysia
e-mail: afakhri@ump.edu.my

M. N. A. Rahman
Faculty of Informatics and Computing, Universiti Sultan Zainal Abidin,
Tembila Campus, 22000 Besut, Terengganu, Malaysia

© Springer Nature Singapore Pte Ltd. 2018
M. H. A. Hassan (ed.), *Intelligent Manufacturing & Mechatronics*,
Lecture Notes in Mechanical Engineering,
https://doi.org/10.1007/978-981-10-8788-2_44

1 Introduction

Statistical pattern recognition is widely used in many application areas, including face recognition, speech recognition, character recognition, medical imaging, plant species recognition, etc. [1]. In some of these areas, the size of the images is very large and the processing time has to be very small in which sometimes a real-time processing is required. A large volume of plant species data, a massive size of images, and extensive computing in statistical pattern recognition cause the computational operations to consume long processing time. For instance, authors in [2, 3, 4], have to process 1200 leaf images. On the other report, authors in [5] use 1400 images, whereas [6] use 2170 images and [7] use 1800 images. In addition, it is reported that some researchers use up to 6000 leaf images for the purpose of recognition and classification [8, 9]. The increasing number of plant processing indicates that the requirement of the low power consumption and effective computational processing are necessary.

Looking at this situation, plant species recognition applications have to use parallel computing approach to speed up the process. However, limited literatures on parallel and distributed image processing for plant species recognition complicates the situation [10]. Besides, from the observation, this situation happens due to the enormous area of statistical pattern recognition which is composed of two principal disciplines: image processing (data pre-processing and feature measurement) and data mining (feature representation and classification). When these two fields are searched separately through scientific literature database, many literatures implement parallel computing approach in their researches. The needs for parallel image processing thus can be categorized as following: (i) Large image-bases of high resolution image data existed in the last decade [11] and (ii) Parallel processing can speed up the computational rates to perform within a reasonable time [12].

Previously, the image processing model for *Ficus deltoidea* varietal recognition has been developed. The main processes involved in this model are segmentation of target leaf object, petiole removal, and features measurement [13]. The empirical experiments showed that turnaround time dramatically increased with the increase of database size (Fig. 1). In practice, the size of database is increased when the number of images is increased [11].

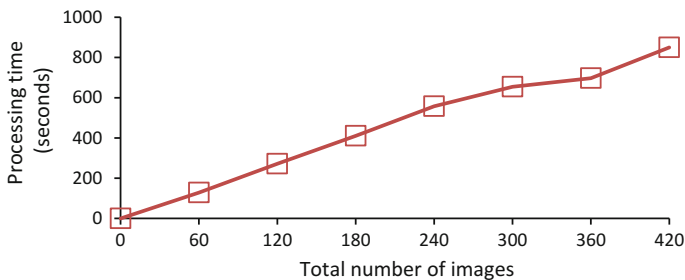


Fig. 1 Processing time for various numbers of leaf images

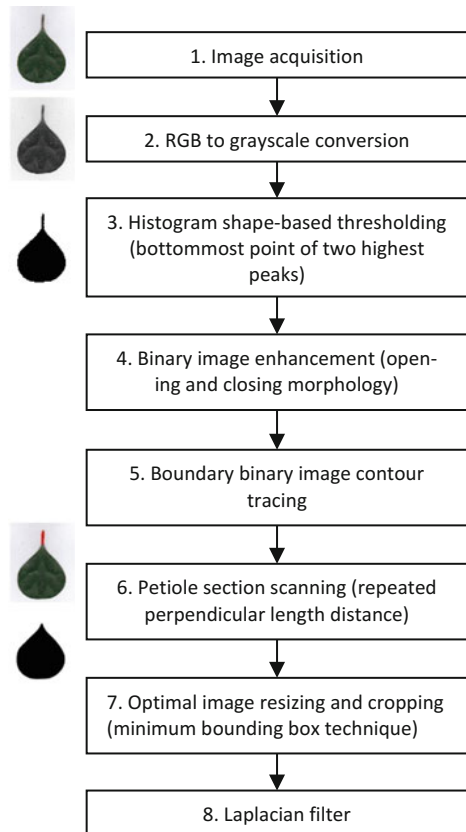
2 Image Processing Model

As mentioned earlier, the main processes involved in image processing model for *Ficus deltoidea* varietal recognition are (i) segmentation of target leaf object, (ii) petiole removal, and (iii) features measurement. Figure 2 shows the general flow of all phases in the developed image processing model for process (i) and (ii).

Four output images are produced from these phases and used for feature measurement in process (iii). These types of images are:

- (i) Grayscale of raw leaf image for calculating texture features. This image is obtained from process number 2 as shown in Fig. 2;
- (ii) Leaf region with elimination of petiole section in binary image for computing leaf shape, and vein. The image is produced by the process number 4 to number 7 based on flow phases in Fig. 2;
- (iii) Leaf apex region, the image is cropped to ~25% on top of image after performing process number 7. The image is used for calculating apex angle, and;

Fig. 2 Illustration of the whole process flow for image recognition and classification



- (iv) Leaf boundary for completing the leaf vein features calculation. The image is produced by the process number 8 as illustrates in Fig. 2.

Feature measurement function provides analysis on leaf image by calculating its special leaf parameters or characteristics. This feature are responsible to discriminate and allow distinguishing between different this plant varieties. In this model, a total of 23 features consist of shape, texture, and vein are extracted from the leaf images that invariant to rotation, scale and translation. Other five features are derived from texture analysis using Gray-Level-Co-Occurrence-Matrix (GLCM). The GLCM is formulated based on grayscale image. In this work, five leaf image texture characteristics namely contrast, correlation, energy, homogeneity, and entropy are used. Furthermore, the model used morphological operation to extract vein features since it is hard to extract the fine details of veins. The morphological opening on grayscale image is computed using disk-shaped structuring element of radius 1, 2, 3, 4 (in separated process) and subtract remained image by the leaf boundary. Area of left pixels is then calculated (same with leaf area (A) calculation) and denoted as $Av1$, $Av2$, $Av3$ and $Av4$ respectively. Then, the five vein features are calculated as $Av1/A$, $Av2/A$, $Av3/A$, $Av4/A$, and $Av4/Av1$, where A is the leaf area. In [13], the definitions shape features used in the implementation has been presented.

3 The Parallel Image Processing Model

The developed image processing model as elaborated in Sect. 2 has been designed in sequential algorithm and only able to run on single processor architecture. The aim of this paper is to reengineer the model to produce a parallel algorithm for processing in multi-cores computer.

3.1 The Parallel Architecture

The parallel image processing model has been mapped onto the Single Program Multiple Data (SPMD) architecture where each processor has read and write access on shared memory. Lets k be the number of processors, the architecture permits for k processors to execute the same program or instruction, I and each of processor has its own private data, $D = \{d_1, \dots, d_k\}$. Each processor then produces its own output which is $O = \{o_1, \dots, o_k\}$.

The parallel processing model using master-worker scheme is one of the most dominant models used in parallel architecture [14]. The master-worker model represents centralized control with distributed execution. A master core is responsible for scheduling various instructions that can be allocated to any available core for processing. It also must deliver any data to the worker cores. The challenge for applications using this model is real-time load balancing because the core

instruction can be random. Individual core execution can have very different throughput requirements. The master must be able to optimize the balance of work across the cores so that optimal parallelism is achieved. An example of a master-slave task allocation model in multi-cores architecture is showed in Fig. 3.

The successful parallel processing systems are always based on communication interface for all processors. In parallel image processing model, the MATLAB's PCT software [15] is used to enable the communication between processors. The MATLAB's PCT provides functions for parallel for-loop execution, creation or manipulation of distributed arrays, as well as message passing functions.

3.2 The Algorithms

In order to run a program on multiple processors, the data should be distributed among the processors. In avoiding a larger communication overhead between the master processor and worker processors, static scheduling is utilized where the schedule of each processor is produced before job execution is started. The job execution will not be modified during execution period. Specifically, the operations allocation scheme in the parallel image processing model can be assigned as: Master = {read images, read number of cores, partitioning images, gathering final features output} and Worker = {segmentation of target leaf object, petiole removal, feature measurements and generate features output}. The master processor executes a single instruction stream, and broadcast each instruction to be executed by all worker processors. If a set of workers is $W = \{w_1, w_2, \dots, w_k\}$, then a divide and conquer approach is applied where leaf images are partitioned into k , thus each worker will have their own dataset. In order to provide a good load balancing for each worker, the partition strategy is done using the total number of image size to be executed in each of partition block. This is due to the size of image is variants. Table 1 shows the empirical experiments on different size of a single leaf image.

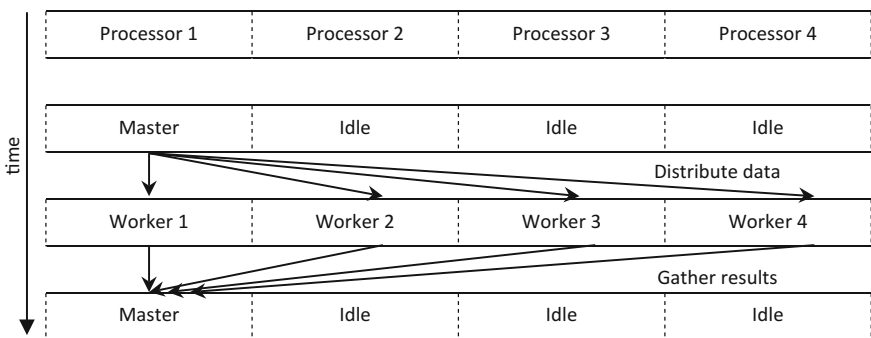


Fig. 3 Master-worker in shared memory

Table 1 Processing time of single leaf image with different image size

Image	Variety	Image dimension	Image size (KB)	Processing time (s)
1.jpg	<i>angustifolia</i>	558 × 948	157	2.85
55.jpg	<i>bilobata</i>	397 × 576	77.7	2.27
8.jpg	<i>trengganuensis</i>	672 × 1242	288	3.57
13.jpg	<i>kunstleri</i>	1404 × 1620	584	6.73
4.jpg	<i>intermedia</i>	947 × 2046	521	5.82
44.jpg	<i>deltoidea</i>	546 × 696	149	2.73

Based on Table 2, image “55.jpg” has the lowest processing time since it has the smallest image size. As the size of image increases, more processing time is needed to compute the image processing tasks. The execution time for images “1.jpg” and “44.jpg” are almost the same because they have nearly similar image size. Therefore, if T is all images size, then each worker processor w_i will received τ_i partition block of image size and denoted as:

$$T = \sum_{i=1}^k \tau_i \quad (1)$$

Theoretically, using this approach, all processors are assumed to work in a balanced execution and well-suited to SPMD architecture. Figure 4 shows the process flow of the parallel image processing model.

The first job of the master processor is to receive the leaf images $Q = \{q_1, q_2, \dots, q_r\}$ from the database or query form users, where r is the maximum number of images. Secondly, the size of all leaf images T in database is calculated. The number of available cores k is read in the next step. Then, the master processor will calculate data partitioning based on τ_i which gives each processor w_k its own private data d_k . Consider the number of available cores are 4, the data partitioned for $w_1, w_2, w_3,$ and w_4 are computed as the following conditions:

- (i) w_1 : if size of image $\{q_1 + q_2 + \dots + q_n\} \leq \tau_1$
: $d_1 = \{q_1 + q_2 + \dots + q_n\}$
- (ii) w_2 : else if $\tau_1 \leq \text{size of image } \{q_{n+1} + q_{n+2} + \dots + q_o\} \leq \tau_2$
: $d_2 = \{q_{n+1} + q_{n+2} + \dots + q_o\}$
- (iii) w_3 : else if $\tau_2 \leq \text{size of image } \{q_{o+1} + q_{o+2} + \dots + q_p\} \leq \tau_3$
: $d_3 = \{q_{o+1} + q_{o+2} + \dots + q_p\}$
- (iv) w_4 : else $\tau_3 \leq \text{size of image } \{q_{p+1} + q_{p+2} + \dots + q_r\} \leq \tau_4$
: $d_4 = \{q_{p+1} + q_{p+2} + \dots + q_r\}$

Table 2 Seven different volumes of dataset for parallel model evaluation

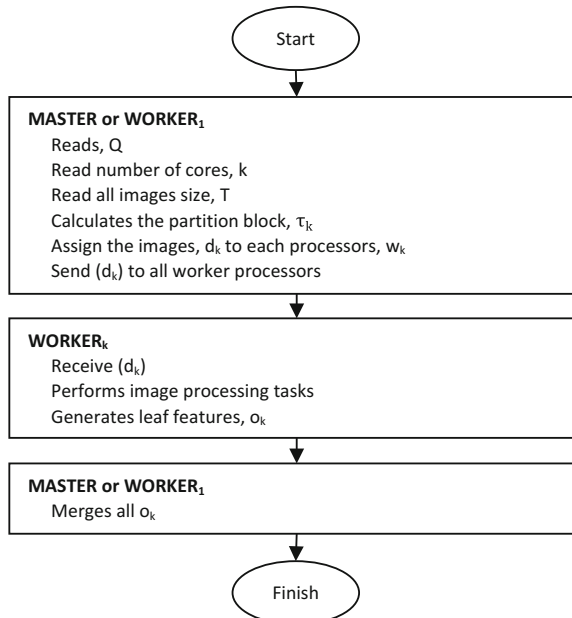
No.	Database volume	Image no.					
		var. <i>angustifolia</i>	var. <i>bilobata</i>	var. <i>deltoidea</i>	var. <i>intermedia</i>	var. <i>kunstleri</i>	var. <i>trengganuensis</i>
1	60	1–10	71–80	141–150	211–220	281–290	351–360
2	120	1–20	71–90	141–160	211–230	281–300	351–370
3	180	1–30	71–100	141–170	211–240	281–310	351–380
4	240	1–40	71–110	141–180	211–250	281–320	351–390
5	300	1–50	71–120	141–190	211–260	281–330	351–400
6	360	1–60	71–130	141–200	211–270	281–340	351–410
7	420	1–70	71–140	141–210	211–280	281–350	351–420

According to data partitioned, each worker processors will have the specific leaf images. For each of leaf image, image processing tasks is executed and all of features are obtained. Finally, all leaf features extracted are gathered by master processor. Lets say B is image processing process and O is a set of leaf features, the computation by each worker can be assigned as $B(\tau_i) = O_i$. After receiving all the leaf features from worker processors, the master processor will combine all these results. The combination process can be viewed as:

$$B(T) = \bigcup_{i=1}^k B(\tau_i) \tag{2}$$

where, \cup denotes a combination operation. Based on the O values, the learning model process will be executed afterwards. The pseudo-code algorithm for parallel image processing model is depicted in Fig. 5.

Fig. 4 The parallel image processing model process flow



```

Algorithm: Parallel image processing model
Input: All images in database
Output: Leaf features for each of image
1. Start
2. Read number of core
3. Step through all images  $q_1$ ...final images  $q_r$ 
   Calculate size of all leaf images, T
4. Step through all number of cores  $k=1$ ...maximum number of cores
   Calculate partition block of image size  $\tau_k$ 
5. Find the image partitioned to each block size
   For each of  $\tau_k$ 
      $d_k = \{\text{size of } q_{\text{first}}+q_{\text{next}}+\dots, q_{\text{final}} \leq \tau_k\}$ 
6. Send image data to each of worker processors  $w_k$ 
7. Compute image processing task and calculate features
   For each of  $w_k$ 
      $o_k = \text{processing of } d_k$ 
8. Gathering leaf features results
   For each of k
     FinalResults =  $o_k+o_{k+1}$ 
9. Stop

```

Fig. 5 Pseudo-code for parallel image processing model algorithm

3.3 Experimental Setup

The algorithm is coded under MATLAB computing language and the implementation of parallel execution is done using MATLAB's PCT. The parallel model is executed under a quad core platform using PCT's single program multiple data (spmd) keyword. The multi-core CPU platform used is an Intel Core 2 Quad CPU Q8200, where it has 4 cores working at 2.33 GHz with 4.00 GB DDR3 memory. As the experiments in [13], the same *Ficus deltoidea* leaf database is used to evaluate the performance of the developed parallel image processing model. The model is evaluated with seven different image volumes of dataset (Table 2): 60 leaf images (10 images of each variety), 120 leaf images (20 images of each variety), 180 leaf images (30 images of each variety), 240 leaf images (40 images of each variety), 300 leaf images (50 images of each variety), 360 leaf images (60 images of each variety), and 420 leaf images (70 images of each variety). Each of *F. deltoidea* variety has different image size, for example var. *kunstleri* has a bigger size of image and var. *angustifolia* and *bilobata* have the smaller size of image. Therefore, to illustrate an almost similar size, each of database volume is divided by considering all varieties. For instance in illustrating 60 leaf images, 10 images from each variety are put together. By considering these partitions, the database volume for each partition is assumed to have the nearly similar size.

4 Experimental Results

A basic performance evaluation of a parallel program is to reduce runtime when the application is executed on more than one processor. The processing time for both serial and parallel executions is recorded. At first, the processing time for each worker processor is showed to illustrate workload balancing received in each processor. Then, the results are organized in tables and graphs to give a clear picture of speed up trends. Finally, by using a standard rule, the overall system efficiency is also discussed.

4.1 The Load Balancing

This section discusses the load balancing, given by the parallel image processing model, on maximum 4 worker processors. Using partitioning by the total images size, the images are distributed based on database of equal size on each of worker processors. For instance, in database size that consists of 60 leaf images (database volume), each worker processor is supposed to have a closely the same images size to ($\tau_i = 16.18 \times 10^6/4 = 4.05 \text{ KB} \times 10^6$) with a different number of leaf images that need to be processed. The distributed work results for each processor on 60 leaf images generated by the developed parallel model are as follows:

- (i) d_1 : 19 leaf images {1.jpg, 10.jpg, 141.jpg, 142.jpg, 143.jpg, 144.jpg, 145.jpg, 146.jpg, 147.jpg, 148.jpg, 149.jpg, 150.jpg, 2.jpg, 211.jpg, 212.jpg, 213.jpg, 214.jpg, 215.jpg, 216.jpg} which are calculated as the cumulative image size that is equal to $4.29 \text{ KB} \times 10^6$.
- (ii) d_2 : 8 leaf images {217.jpg, 218.jpg, 219.jpg, 220.jpg, 281.jpg, 282.jpg, 283.jpg, 284.jpg} which are calculated as the cumulative image size that is equal to $3.80 \text{ KB} \times 10^6$.
- (iii) d_3 : 10 leaf images {285.jpg, 286.jpg, 287.jpg, 288.jpg, 289.jpg, 290.jpg, 3.jpg, 351.jpg, 352.jpg, 353.jpg} are calculated as the cumulative image size that is equal to $4.09 \text{ KB} \times 10^6$.
- (iv) d_4 : 23 leaf images {354.jpg, 355.jpg, 356.jpg, 357.jpg, 358.jpg, 359.jpg, 360.jpg, 4.jpg, 5.jpg, 6.jpg, 7.jpg, 71.jpg, 72.jpg, 73.jpg, 74.jpg, 75.jpg, 76.jpg, 77.jpg, 78.jpg, 79.jpg, 8.jpg, 80.jpg, 9.jpg} are calculated as the cumulative image size that is equal to $3.99 \text{ KB} \times 10^6$.

Table 3 summarizes the number and size of images that is distributed for each worker processor unit. In Table 4, the total number of images and database size for each of worker processor is displayed. By using these partitioned images, execution times for each database volume with 1, 2, 3, and 4 worker processors are showed in Fig. 6. Figure 6 is constructed to illustrate workload balancing between each worker processor using database size partitioning, where three main processes involved are: (i) data partitioning process, (ii) image processing tasks, and (iii) final

Table 3 The partitioned images for each worker processor units

Database volume	Database size (KB × 10 ⁶)	The partitioned images: (i) no. of images (ii) database size τ_i (KB × 10 ⁶)			
		w_1	w_2	w_3	w_4
60	16.18	19 (4.29)	8 (3.80)	10 (4.09)	23 (3.99)
120	34.28	43 (8.78)	16 (8.52)	18 (8.63)	43 (8.35)
180	49.44	61 (12.57)	28 (12.20)	25 (12.35)	66 (12.31)
240	63.03	83 (16.80)	37 (14.74)	33 (15.82)	87 (15.67)
300	75.74	103 (19.22)	48 (18.78)	42 (19.09)	107 (18.65)
360	87.38	123 (21.85)	58 (21.96)	53 (21.88)	126 (21.69)
420	98.21	144 (24.71)	68 (24.42)	61 (24.59)	147 (24.49)

Table 4 Processing times for all of database volume with respective number of worker processors

Worker processors (k)	Database volume						
	60 (s)	120 (s)	180 (s)	240 (s)	300 (s)	360 (s)	420 (s)
1	128.58	271.69	410.17	557.47	654.29	697.27	849.67
2	97.66	192.38	279.33	355.97	443.92	490.49	558.91
3	69.49	137.55	194.48	250.74	294.49	350.95	390.71
4	49.45	103.08	159.00	192.50	243.62	266.23	312.59

data gathering. Theoretically, each of worker processor received almost the same data size block. For example in the database volume 420 (Table 3), the database size to be computed by each processor is 24.71 KB, 24.42 KB, 24.59 KB, and 24.49 KB for worker 1, 2, 3, and 4, respectively. The serial processing for each of database volume is also displayed in Fig. 6. As referred to Fig. 6, the execution time for parallel image processing model is the best for all of database volume.

Considering 60 database volume, executing image processing task in serial mode required for 128.58 s. The processing time is decreased to 49.45 s when the parallel model is executed using 4 worker processors. The w_1 is the last finished worker processor where w_2 solved its jobs in about 5 s faster than w_1 . In w_3 and w_4 , they only took approximately 6 and 12 s earlier to finish their jobs as compared to w_1 , respectively. At this stage, the workload distributed for each worker processor in 60 database volume can be said as “in a good balance” since each processor finished their jobs at nearly similar time. However, the execution times different between the last finished worker processor showed that the execution times differences are slightly increased when the size of database increased. In parallel mode, it takes about 12 s, 14 s, 21 s, 24 s, 43 s, 42 s, and 58 s between the first and last finished jobs times with 60, 120, 180, 240, 300, 360 and 420 database volumes, respectively. Excluding 60 database volume, the last finished worker processor is always w_3 in this four cores environment.

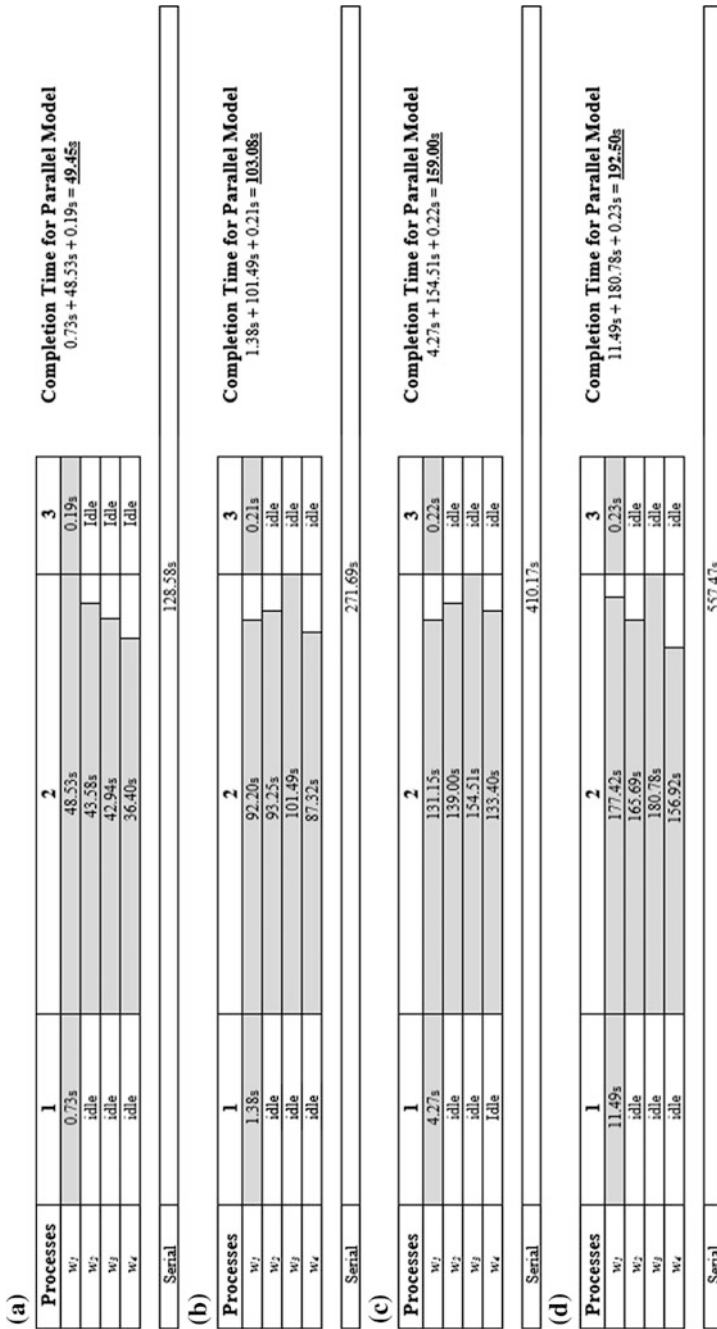


Fig. 6 a Processing time for four worker processors with database volume, **a** 60, **b** 120, **c** 180, and **d** 240. **e** 300, **f** 360, and **g** 420

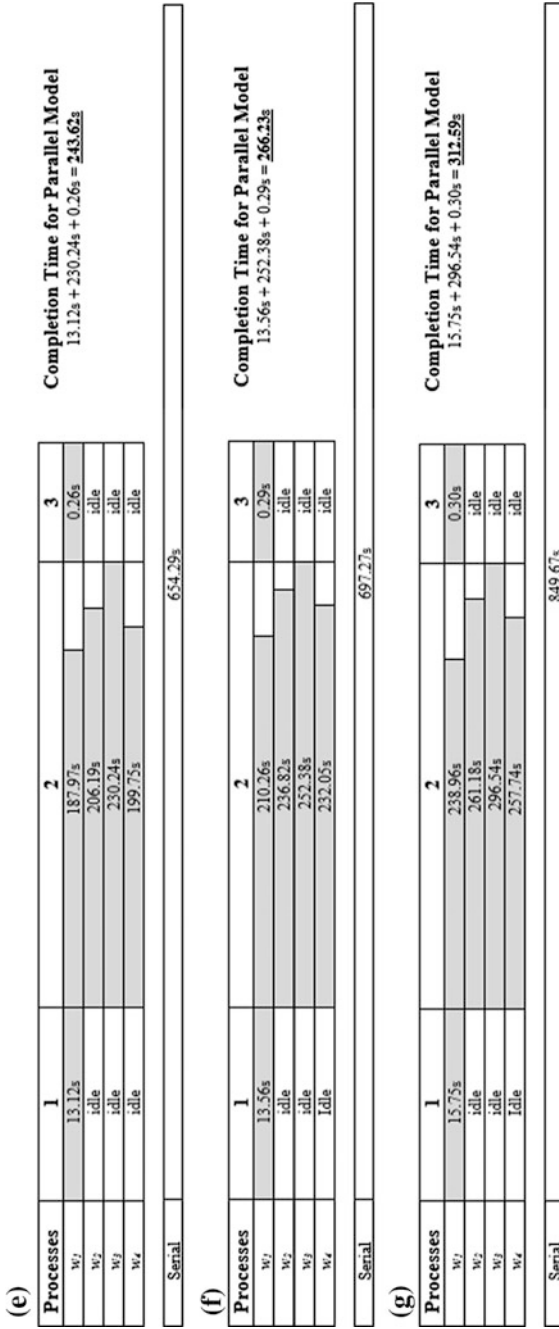


Fig. 6 (continued)

4.2 The Processing Time and Speed Up

This section elaborates the processing time and speed up given by the parallel image processing model. Lets k be the number of processor(s), execution times for each data volume with 1 (serial processing), 2, 3 and 4 worker processors are implemented and showed in Table 4.

The processing time is significantly decreased when the parallel model is executed by using 2 and more processors. For all of database volume, elapsed times seem to exponentially decrease when more worker processors are considered. For instance in 120 database volume, the serial image processing model took 271.69 s to process 120 leaf images. In parallel mode, the model took 69.83 s, 53.74 s and 103.08 s with 2, 3 and 4 worker processors respectively. The same result trend (exponentially decrease) is also observed all in other database volumes.

The performance of parallel computing model can be evaluated by calculating the speed up [16]. Speed up shows how much of an improvement is practically possible in the best case, ignoring overhead and communication costs. Assuming that the speed of the processors and communication are constant, the speed up of the processor(s) is calculated by using the following equation:

$$S(k) = \frac{T_1}{T_k} \quad (3)$$

where, T_1 is the time required to execute an equivalent sequential program on one processor and T_k is the time required to execute the parallel version of the program on k processors. T_1 is obtained by executing sequential algorithm on the same multi-cores platform with parallel algorithm. However, sequential algorithm is executed by ignoring many processors that exist in multi-cores platform. T_1 and T_k are measured by using “tic” and “toc” stopwatch time in MATLAB. Using the experimental results tabulated in Table 4, Fig. 7 shows the speed-ups of different number of processors and database volumes.

The experimental results showed that the parallel image processing model exhibits good speed-up for two and more worker processors. The ideal (best) speed-up is illustrated in black line in Fig. 7. Based on these results, as the database volume (size) is increased, the benefits from parallel model became more noticeable. However, for all of database volume, the speed-up is getting far away from the ideal speed-up when the number of processors is increased. Clearly, referring to Fig. 7, by average, the processing time for parallel model is 1.45, 2.09, and 2.68 times higher than previous sequential model for 2, 3, and 4 processors, respectively.

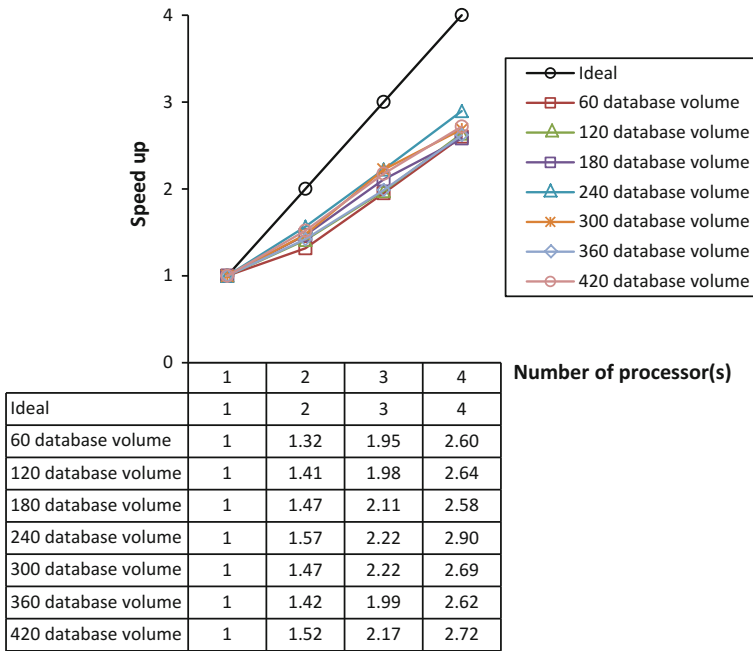


Fig. 7 The speed-up on different number of processors

4.3 The Parallel System Efficiency

The parallel communication efficiency can be calculated using the formula of:

$$E = \frac{T_1}{k \times T_k} \times 100\% \tag{4}$$

where T_k is the processing time for k processors and T_1 denotes the processing time for single processor. The best E is 100% and this occurred when the processors are always being used at all times [16]. Figures 8 and 9 show the parallel model efficiency on different number of worker processors and database size, respectively. From the tabulated results, most of the parallel models efficiency values are above 60%. These indicated that the worker processors are being used only about 60% on the actual computation. This situation occurred because other time involved in the whole processes in parallel image processing are used for calculating data distribution, gathering final result, data accessed efforts in shared memory system, and parallel overhead in starting and stopping the parallel region. With the increasing of k , the efficiency is also decreased due to many cores need to be activated to start parallel region, as well as to deactivate the cores. As mentioned by [17], there always some delay in starting and stopping the parallel region in multi-cores environment using MATLAB whereby more computation is needed to activate and

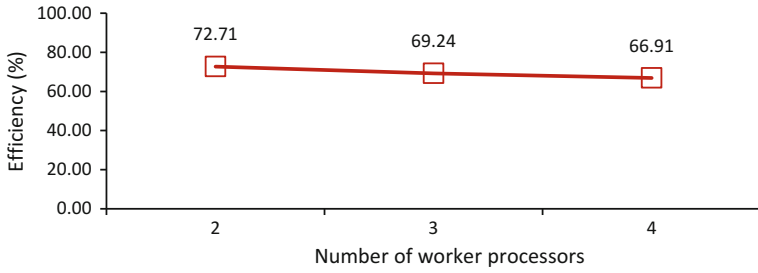


Fig. 8 Model efficiency versus number of worker processors

deactivate more processors. Other than that, the slightly unbalanced work load for each processor can also reduce the efficiency. This data structure is considered as a static memory allocation. Hence, the workload by each core cannot be resized during processing time.

Based on Fig. 9, no significant change in the efficiency is observed when the size of database is increased since the shared memory buffer architecture in multi-cores platform made the data available to each processor at any time. It means that a message buffer is set up in a memory that is accessible by both sender (master processors) and receiver (worker processors), whereby each processor is responsible for its portion of the transaction. The sender sends the message to the shared buffer and notifies the receiver. The receiver retrieves the message by copying the contents from a source of buffer to a destination buffer and notifies the sender that the buffer is free. Although with the bigger size of database, the data access effort is always in constant manner in this multi-cores platform.

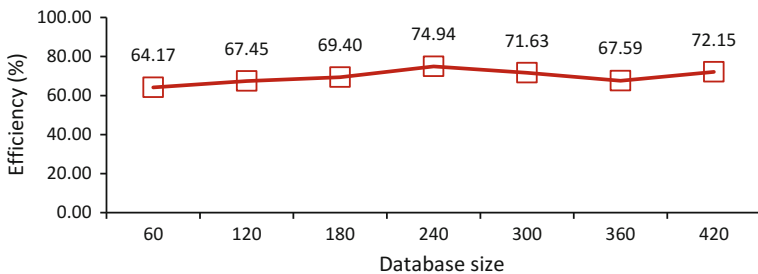


Fig. 9 Model efficiency versus database size

5 Conclusion

The image processing model has been reengineered in order to be executed under parallel computation environment. The main objective of parallel model is to speed-up the image processing phases in the model that involves huge workloads. The processes involved in the image processing phase included image pre-processing tasks and feature measurement tasks. The parallel model is designed to be implemented in the multi-cores computer system. The master-workers paradigm is used to send the balanced images to each of computer processors. The parallelization of the image processing model is done under the Single Program Multiple Data (SPMD) architecture. The MATLAB's Parallel Computing Toolbox is used for completing the activities of sending data and receiving output between processors.

Experiments showed that a multi-cores parallel environment is a very appropriate platform for pipeline image processing. The sequential image processing model is significantly improved when executed in parallel model under multi-cores computer system. The results clearly indicated that as the number of cores increases, the computation time taken by the parallel algorithm is also less. The overall speed-up performance is good enough when run with two and more worker processors. However, the slightly unbalanced load distributions by using the image size caused the efficiency of the parallel image processing model to drop when the number of worker processors is increased. Better modification of load balancing strategy using other parameters such as the image row and column dimensions is believed to improve the whole parallel model performance. The model has been tested on four multi-cores computer hardware and the results showed that at least 2.68 speed-up factors have been achieved when all four cores are used.

Acknowledgement The authors are grateful to the Universiti Malaysia Pahang for providing the funding under internal research grant [RDU1703159] to support this research.

References

1. Szeliski, R.: *Computer Vision: Algorithms and Applications*. Springer Science & Business Media, New York, NY, USA (2010)
2. Wang, X.-F., Huang, D.-S., Du, J.-X., Xu, H., Heutte, L.: Classification of plant leaf images with complicated background. *Appl. Math. Comput.* **205**, 916–926 (2008)
3. Hossain, J., Amin, M.A.: Leaf shape identification based plant biometrics. In: *Proceedings of the 13th International Conference on Computer and Information Technology*, pp. 458–463. IEEE, Dhaka (2010)
4. Shabanzade, M., Zahedi, M., Aghvami, S.A.: Combination of local descriptors and global features for leaf recognition. *Signal Image Process. Int. J.* **2**(3), 23–31 (2011)
5. Wang, Z., Chi, Z., Feng, D.: Shape based leaf image retrieval. *Vis. Image Signal Process.* **150** (1), 34–43 (2003)

6. Du, J.-X., Huang, D.-S., Wang, X.-F., Gu, X.: Computer-aided plant species identification (CAPSI) based on leaf shape matching technique. *Trans. Inst. Meas. Control* **28**(3), 275–284 (2006)
7. Wu, S.G., Bao, F.S., Xu, E.U., Wang, Y.-X., Chang, Y.-F., Xiang, Q.-L.: A leaf recognition algorithm for plant classification using probabilistic neural network. In: *Proceedings of the IEEE International Symposium on Signal Processing and Information Technology*, pp. 11–16. IEEE, Giza (2007)
8. Zhang, S., Wang, H., Huang, W.: Two-stage plant species recognition by local mean clustering and Weighted sparse representation classification. *J. Clust. Comput.* **20**(2), 1517–1525 (2017)
9. Zhang, S., Wu, X., You, Z.: Jaccard distance based weighted sparse representation for coarse-to-fine plant species recognition. *PLoS ONE* **12**(6) (2017)
10. Nasir, A.F.A., Rahman, M.N.A., Mamat, R.: A study of image processing in agriculture application under high performance computing environment. *Int. J. Comput. Sci. Telecommun.* **3**(8), 16–24 (2012)
11. Saxena, S., Sharma, N., Sharma, S.: Parallel image processing techniques, benefits and limitations. *Res. J. Appl. Sci. Eng. Technol.* **12**(2), 223–238 (2016)
12. Saxena, S., Sharma, N., Sharma, S.: Image processing tasks using parallel computing in multi core architecture and its applications in medical imaging. *Int. J. Adv. Res. Comput. Commun. Eng.* **2**(4), 1896–1900 (2013)
13. Nasir, A.F.A., Rahman, M.N.A., Mat, N., Mamat, R., Ghani, A.S.A.: *Ficusdeltoidea* (Jack) *Moraceae* Varietal identification using statistical recognition approach. *World Appl. Sci. J.* **35**, 82–88 (2017)
14. Vega, F.F.D., Pérez, J.I.H., Lanchares, J.: *Parallel Architectures and Bioinspired Algorithms*. Springer, Berlin, Heidelberg, New York, NY, USA (2012)
15. Alyasseri, Z.A.A.: Survey of Parallel Computing with MATLAB. <http://arxiv.org/ftp/arxiv/papers/1407/1407.6878.pdf> (2014). Accessed 21 June 2016
16. Nordin, A.R.M., Yazid, M.S.M., Aziz, A., Osman, M.T.A.: Parallel guided dynamic programming approach for DNA sequence similarity search. *Int. J. Comput. Electr. Eng.* **1**, 402–409 (2009)
17. Tadonki, C., Caruana, P.-L.: Seamless multicore parallelism in MATLAB. In: *Proceedings of the Software Engineering: Parallel and Distributed Computing and Networks: Artificial Intelligent and Applications*, pp. 1–5. ACTA Press, Innsbruck, Austria (2014)

Part IV

Instrumentation

Ontological Framework of Arm Gesture Information for the Human Upper Body



Wan Khairunizam, K. Ikram, S. A. Bakar, Z. M. Razlan
and I. Zunaidi

Abstract In the research of the human motion analysis, the characteristic movements of the human upper body are intensively investigated for many applications such as sign language recognition, robot control and gait analysis. The human upper body consists of many body parts such as both arms including fingers, facials and head movements. Previously, many researches proposed various sensors to record arm movements and the acquired data are used to train the computer understand the behavioral motion of arms movements by using various algorithmic approaches. However, the current challenge is to increase the knowledge level of the computational systems to recognize gestural information containing in arm movements. The objective of this paper is to construct and derive the arm movement's model based on the conceptual of ontology. The gestural information is investigated from characteristic features of arm movements. The knowledge of the computational systems about gestural information is developed by describing the characteristic features of arm movements in the form of the ontological framework. The ontological framework is defined as a structure containing characteristic features placed in mathematical order and has the relationship among them. Based on the mathematical model as proposed in this paper, the ontology framework could be used to describe knowledge of the arm gesture and could recognize it with a higher accuracy.

Keywords Arm gesture · Ontology · Gesture database

W. Khairunizam (✉) · K. Ikram
Advanced Computing and Sustainable Laboratory, Perlis, Malaysia
e-mail: khairunizam@unimap.edu.my

W. Khairunizam · K. Ikram · S. A. Bakar · Z. M. Razlan
School of Mechatronic, Universiti Malaysia Perlis, Perlis, Malaysia

I. Zunaidi
Technopreneur at UniMAP Sdn. Bhd., Perlis, Malaysia

© Springer Nature Singapore Pte Ltd. 2018
M. H. A. Hassan (ed.), *Intelligent Manufacturing & Mechatronics*,
Lecture Notes in Mechanical Engineering,
https://doi.org/10.1007/978-981-10-8788-2_45

1 Introduction

In computer science and information science, an ontology formally represents knowledge as a set of concepts within a domain, and the relationships between those concepts. It can be used to reason about the entities within that domain and may be used to describe the domain. In theory, an ontology is a formal, explicit specification of a shared conceptualisation. An ontology renders shared vocabulary and taxonomy which models a domain with the definition of objects and concepts and their properties and relations. Ontologies are the structural frameworks for organizing information and could be used in artificial intelligence, the Semantic Web, systems engineering, software engineering, biomedical informatics, library science, enterprise bookmarking, and information architecture as a form of knowledge representation about the world or some part of it [1–4]. However, nowadays, many researchers give efforts on the development of Semantic web, especially researches in the fields of computer science. More researches on ontology, which are related to engineering should be done by scientists from the field of engineering. The creation of domain ontologies is also fundamental to the definition and use of an enterprise architecture framework.

Ontology engineering in computer science and information science is a new field, which studies the methods and methodologies for building ontologies. Nowadays, many researchers trying to use the conceptual of ontology in engineering. In the other hand, researchers and engineers work very hard to employ the conceptual of ontology toward engineering [1–4]. Researchers believes ontology could solve occlusion problem in image processing by combining two conceptals, which are mereology and mereotopolog [5–7]. R. Mizoguchi et al. published many results on the application of ontology in engineering such as in power plant, nuclear, biofuel Problems, medical domain and Artificial Intelligence (AI) [8–12].

In this research, the concept of ontology is employed for the purpose of recognizing arm gestures. To investigate the framework, 5 geometrical gesture data are used. In the conventional approaches, all gestures are stored in the database, and each gesture is presented by several features such as arm trajectories, hand shapes and hand motions [13–15], however, the features have no relation among them. By using ontological approach all features are described based on topological relation such as part of relation, boundaries and similarity measures.

The outline of this research paper is as follows. Section 1 describes the background of the research. Section 2 discusses the related researches to the research projects. Section 3 discusses the acquisition of geometrical gesture and Sect. 4 discusses the pre-processing of the signals. Section 5 discusses the proposed ontological framework of the arm gesture and Sect. 6 describes the recognition of arm gesture. The conclusions of this research is discussed in Sect. 6.

2 Related Researches

Previously, several approaches to recognize arm motions were proposed for the implementation in the various digital applications [13–16]. Arm movements contain many physical quantities, and modelling algorithms are required to form mathematical quantities from the available physical data [17, 18]. Furthermore, movements data obtained through the tracking devices are low-level information and it needs to be combined to produce higher-level semantic features information, which can be used to investigate various motion features [19]. Once arm movements data have been collected through tracking devices, it needs to be analyzed for the systems to understand the behavior of the characteristic arm features through various computational approaches. The conventional approach to model arm movements is by using deterministic approach, which is based on artificial intelligence methods [20–23]. However, the performance of the proposed arm movement's model could be improved by using a knowledge-based approach. In this paper, an ontology approach is proposed to model the arm gesture information. Ontology is a structural framework for organizing information as a form of knowledge representation and is used in artificial intelligence, the semantic web, systems engineering, software engineering, bioinformatics, library science and information architecture. At present many researchers employ ontological approach to the development of the semantic web, especially researches in the fields of computer science [1–4]. The concept of ontology could be expanded to the various applications in the engineering field.

Ontology engineering in computer science and information science is a new research field, which studies the methodology for building the ontology's structure. R. Mizoguchi et al. discuss about the applications of ontology in various engineering fields such as in the power plant, nuclear, bio-fuel problems, medical domain and artificial intelligence (AI) [8–12]. As the applications of ontology in engineering, they developed the ontological mapping systems to monitor the power nuclear plant in Japan. R. Mizoguchi introduces the application of ontology not only in engineering domain, but also many applications in medical domain are proposed [12].

Based on the literature search conducted, the arm movements could be modeled by using the conceptual of ontology. A statistical approach could be used to describe a relationship among characteristic features of arm movements. In the conventional approaches to model arm movements are based on the patterns of characteristic features, which are stored in the database as a reference. The characteristic features are extracted and investigated in the random experiments. However, the recognition performance in term of the accuracy is still lower than the expected, and the most crucial is the systems are not sustained when facing with various environments. The reason is some important characteristic features of arm movements have similar characters. Thus, the conceptual of ontology for describing the ontology framework of arm gesture information is seen possible to overcome the sustainability and accuracy problems of the arm gesture recognition systems.

Fig. 1 The environment of the data collection experiment

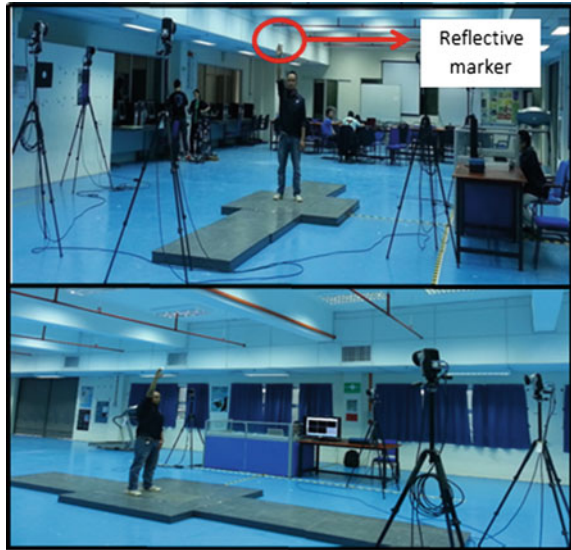


Fig. 2 Five geometrical gestures used in the experiments



3 Acquisition of Geometrical Gesture

Qualisys motion capture (MOCAP) was used to capture the movement of the subject's right arm while performing arm gesture. For the purpose of modelling ontological framework, one subject was involved in the experiments. A reflected marker was attached to the subject's right hand and the subject was instructed to perform five geometrical gestures. Figure 1 shows the environment of the experiment and Fig. 2 shows a set of geometrical gestures used in the experiments $G = \{\text{Round, Square, Diamond, Triangle, Eight}\}$.

The MOCAP consist of 5 Oqus cameras that are able to capture image with resolution 200 fps to track the movements of the reflective marker attached to the subject's right hand. The MOCAP produces three-dimensional position data of the moving reflective marker x, y and z-axes.

4 Pre-processing of Arm Gesture Data

Based on the position of a reflective marker, the characteristic features of the arm motion of a subject were computed. Since motion features were time-interval based data, and difficult to differentiate between them because its change according to the

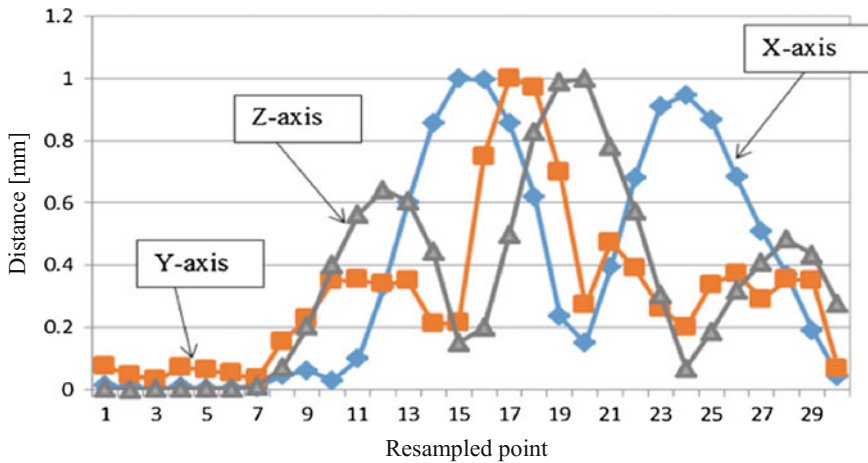


Fig. 3 Resampled point of position data for x, y and z-axes

speed and the size of the motion. To obtain the distance-interval based data, a resampling algorithm was used [24, 25] and by following their approach it is easy to do comparison of data. The resampling result produced 30 resampled points in term of distance, and is also known as reference points of gesture data. The selection of 30 reference points are sufficient for a large amount of data after conducting numerous testing of significant value for resampled points. After the resampling process, these data were normalized in the same scale value. These normalized data were used to design the ontological framework. Figure 3 shows the gesture data after the normalization process with 30 reference points.

5 Ontological Framework of Geometrical Gesture

5.1 Designing Knowledge and Attribute Domains of the Ontology

As discussed in the previous chapter, ontology is the structural frameworks for organizing information, which describes a particular thing or event. Ontology can be described in three domains as mentioned by W. Fang et al. [26]. These domains are knowledge, attribute and process. In this paper, a knowledge domain is defined as a level that contains the extracted features from the raw arm gesture data. In this domain, a raw data produced by MOCAP systems are resampled and normalized. The attribute is a level that contains several sets of feature that each has similar attribute. Each feature is presented in 30 reference points or resampled points. In the research, the attribute domain contains position (P_G), velocity (V_G) and acceleration (A_G) of the moving marker. G is the registered gestures, which are five geometrical

gestures {Round, Square, Diamond, Triangle, Eight}. The attribute P_G , V_G and A_G are shown in Eqs. 1, 2 and 3. $P_{G,x}$, $P_{G,y}$ and $P_{G,z}$ are the positions of the marker. $V_{G,x}$, $V_{G,y}$ and $V_{G,z}$ are the velocities of the marker. $A_{G,x}$, $A_{G,y}$, and $A_{G,z}$ are the accelerations of the marker in the three-dimensional coordinates space. The number of attributes could be increased by adding more reflective markers to the subject's arm or by using multiple sensors. Moreover, the number of elements in each attribute could be increased by combining them each other for example $P_{G,x}$ & $P_{G,y}$, $P_{G,y}$ & $P_{G,z}$, $P_{G,x}$ & $P_{G,z}$ and $P_{G,x}$ & $P_{G,y}$ & $P_{G,z}$. Similarly, the combination could be determined for V_G and A_G .

$$P_G = \{P_{G,x}, P_{G,y}, P_{G,z}\} \quad (1)$$

$$V_G = \{V_{G,x}, V_{G,y}, V_{G,z}\} \quad (2)$$

$$A_G = \{A_{G,x}, A_{G,y}, A_{G,z}\} \quad (3)$$

$$R = \begin{bmatrix} R_{G_m G_n Res_{-1}} & \cdots & R_{G_m G_n Res_{-1}} \\ \vdots & \ddots & \vdots \\ R_{G_m G_n Res_{-30}} & \cdots & R_{G_m G_n Res_{-30}} \end{bmatrix} \quad (4)$$

The process domain is level that contains the relation relationship between elements of the attribute. The relationship R could be expressed by using the distributed resampled points as discussed previously. Moreover, the probability density function (pdf) is used to address the distributed resampled point. The relationship R can be represented in semantic matrix form as denoted in Eq. 4. R describes the relation of the resampled points $Res_n = \{Res_{-1}, Res_{-2}, Res_{-3}, \dots, Res_{-30}\}$. m and n are two registered gestures {Round, Square, Diamond, Triangle, Eight}. Due to Res_n are distributed points, and R can be expressed in several ways like a mereotopology connection, similarity measure distance and fuzzy inference technique. In the mereotopological connection, the conceptual relationship that can be used like a proper part, overlap, underlap, over-crossing, proper overlap and proper underlap. Other than mereotopological connection, the similarity measure distance could be used to express the relationship R among the distributed resampled point of five registered gestures [27]. The combination of information in knowledge, attribute and process domains serves as a database of the five registered gestures. The complexity of the ontological framework could be increased by adding multiple sensors, produces more features and attributes, and creates more relationship R between elements in the attributes.

5.2 Recognition of Unknown Input Gesture

Recognition of the unknown input gesture G_i process is similar with the information retrieval in the ontology-based applications. The information retrieval process

produces the matching and ranking compared with the registered gestures in the ontological framework. The matching process is to compare the query vector $q(G_i)$ against each registered gesture $G_{n(\text{Round, Square, Diamond, Triangle, Eight})}$ could be done by using similarity measure techniques. The paper proposes to use Jaccard similarity measure. It measures the similarity between finite sample sets, and is defined as the size of the intersection divided by the size of the union of the sample sets as given by the Eq. 5. $\text{Jac}(RG_i, RG_n)$ is representation of a Jaccard similarity coefficient. RG_i and RG_n are the possible relationship of the unknown input gesture and the registered gestures. Then, if RG_i and RG_n are both empty, we define $\text{Jac}(RG_i, RG_n) = 1$. Subsequently, a Jaccard similarity coefficient is between $[0, 1]$ as expressed in Eq. 6. Jaccard distance d_J measures dissimilarity between sample sets, which is complementary to the Jaccard coefficient. Jaccard distance d_J is determined by using Eq. 7. The ranking process is conducted based the similarity value obtained from the matching process.

$$\text{Jac}(RG_i, RG_n) = |RG_i \cap RG_n| / |RG_i \cup RG_n| \quad (5)$$

$$0 \leq \text{Jac}(RG_i, RG_n) \leq 1 \quad (6)$$

$$d_J(RG_i, RG_n) = 1 - \text{Jac}(RG_i, RG_n) \quad (7)$$

6 Conclusion and Future Works

Ontological framework for the presentation of five geometrical gestures performed by the arm movements is presented in this paper. A motion capture system (MOCAP) is used to track the reflective marker attached to the subject's right hand. The acquired three-dimensional position signals are resampled to 30 reference points. The proposed ontology framework has three domains, which are knowledge, attribute and process. Knowledge domain contains lower-level data that are pre-processed until achieve the 30 normalized features points. In this domain, all the possible features are gone through resampling and normalization algorithms. The attribute domain contains a collection of features and the relations between them are presented in the form of semantic matrix. The semantic matrix presents the ontology framework of the geometrical gesture information. The process of gesture recognition is similar with the information retrieval of the ontology-based applications. The gesture recognition contains matching and ranking processes. In the matching process, a similarity measure technique is used to determine the distances of the query vector to the registered gestures in the ontology framework. Moreover, the ranking process is to rank the similarity distance between the query vectors with the registered gestures in the ontology framework. In the future, a further investigation will be conducted to evaluate the performance of the ontology framework based on the individual features and the combining features in the knowledge domain.

Acknowledgements This research is supported by the research grant FRGS 9003-00634 and is conducted under Advanced Intelligent Computing and Sustainability Research Lab (AICoS), School of Mechatronic, Universiti Malaysia Perlis.

References

1. Kollia, I., Glimm, B., Horrocks, I.: Query answering over SROIQ knowledge bases with SPARQL. In: Proceedings of the Eighth International Workshop on OWL Experiences and Directions (2011)
2. Horrocks, I.: Tool Support for Ontology Engineering. Foundations for the Web of Information and Services, pp. 103–112. Springer (2011)
3. Mika, P.: Ontologies are us: a unified model of social networks and semantics. *J. Web Semant.* **5**(1), 5–15 (2007)
4. Giri, K.: Role of ontology in semantic web. *J. Libr. Inf. Technol.* **31**(2), 116–120 (2011)
5. Dapoigny, R., Barlatier, P., Foulloy, L., Benoit, E.: Formal goal generation for intelligent control systems. *Lect. Notes Comput. Sci.* **3533**, 712–721 (2005)
6. Dapoigny, R., Barlatier, P., Benoit, E., Foulloy, L.: Deriving behavior from goal structure for the intelligent control of physical systems. *Inf. Control Autom. Robot. II Part 1*, 51–58 (2007)
7. Khairunizam, W., Todo, A., Sawada, H., Passalacqua, O., Benoit, E., Huget, M., Moreaux, P.: Video conference smart room: an information fusion system based on distributed sensors. In: Proceeding of 7th France-Japan Congress on Mecatronics (Mecatronics2008), Version 1, 31 July 2008, Hal-00308562 (2008)
8. Kozaki, K., Hirota, T., Mizoguchi, R.: Understanding ontology through divergent exploration. In: Proceedings of 8th Extended Semantic Web Conference (ESWC2011), pp. 305–320 (2011)
9. Ohtai, M., Kozaki, K., Mizoguchi, R.: A quality assurance framework for ontology construction and refinement. In: Proceedings of 7th Atlantic Web Intelligence Conference (AWIC2011), pp. 207–216 (2011)
10. Masolo, C., Vieu, L., Kitamura, Y., Kozaki, K., Mizoguchi, R.: The counting problem in the light of role kinds. In: Proceedings of Tenth International Symposium on Logical Formalizations of Commonsense Reasoning (Commonsense 2011) (2011)
11. Ohta, M., Kozaki, K., Mizoguchi, R.: An extension of the environment for building using ontologies “Hozo” toward practical ontology engineering—focused on practical issues. *Trans. Jpn. Soc. Artif. Intell.* **26**(2), 403–418 (2011)
12. Saito, O., Kozaki, K., Hirota, T., Mizoguchi, R.: Sustainability Science: A Multidisciplinary Approach. Book, Section 2–4, pp. 69–86. United Nations University Press (2011)
13. Hienz, H., Grobel, K., Offner, G.: Real-time hand-arm motion analysis using a single video camera. *Autom. Face Gesture Recognit.* 323–327 (1996)
14. Bernmark, E., Wiktorin, C.: A triaxial accelerometer for measuring arm movements. *Appl. Ergonom.* **3**(6), 541–547 (2002)
15. Lementec, J., Bajcsy, P.: Recognition of arm gestures using multiple orientation sensor. In: IEEE Intelligent Transportation Conference, USA (2004)
16. Garbarini, F., Rabuffetti, M., Piedimonte, A., et. al.: Bimanual coupling effects during arm immobilization and passive movements. *Hum. Mov. Sci.* 114–126 (2015)
17. Hachaj, T., Ogiela, M.R.: Full body movement’s recognition—unsupervised learning approach with heuristic R-GDL method. *Digit. Signal Proc.* **46**, 239–252 (2015)
18. Samadani, A., Ghodsi, A., Kulić, D.: Discriminative functional analysis of human movement. *Pattern Recogn. Lett.* **34**(15), 1829–1839 (2013)
19. Dahlqvist, C., Hansson, G., Forsman, M.: Validity of a small low-cost triaxial accelerometer with integrated logger for uncomplicated measurements of postures and movements of head, upper back and upper arms. *Appl. Ergon.* **55**, 108–116 (2016)

20. Rubine, D.: Specifying gestures by example. In: Proceedings of SIGGRAPH' 91, pp. 329–337. ACM Press (1991)
21. Nagaya, S., Seki, S., Oka, R.: A proposal of pattern space trajectory for gesture spotting recognition. In: Proceeding of MIRU, pp. 157–162 (1995)
22. Arroyave-Tobón, S., Osorio-Gómez, G., Cardona-McCormick, J.F.: Air-Modelling: a tool for gesture-based solid modelling in context during early design stages in AR environments. *Comput. Ind.* **6**, 73–81 (2015)
23. Vinayak, F., Ramani, K.: A gesture-free geometric approach for mid-air expression of design intent in 3D virtual pottery. *Comput.-Aided Des.* **69**, 11–24 (2015)
24. Wan, K., Aziz, A.A., Shahrman, A.B., Zaaba, S.K., Ibrahim, Z., Yusoff, Z., Ibrahim, I., Mukred, J.A.A., Mokhtar, N.: Probability distribution of arm trajectory for motion estimation and gesture recognition. *Adv. Sci. Lett.* **13**(6), 534–539 (2012)
25. Wan, K., Sawada, H.: 3D measurement of human upper body for gesture recognition. In: Proceeding of International Symposium on Optomechatronics Technologies 2007, (ISOT 2007), vol. 6718, p. 67180 (2007)
26. Fang, W., Guo, Y., Liao, W.: Ontology-based indexing method for engineering documents retrieval. In: IEEE International Conference on Knowledge Engineering and Applications, pp. 172–176 (2016)
27. Irani, J., Pise, N., Phatak, M.: Clustering techniques and the similarity measures used in clustering: *Surv. Int. J. Comput. Appl.* **134**(7), 9–14

RGB Classification Determination with Different Light Intensity Using Pixy CMUcam5



M. F. Ahmad, S. S. N. Alhady, Wan Rahiman, W. A. F. W. Othman
and A. A. M. Zahir

Abstract The surrounding conditions may influence the robustness of tracking performance. The objective of this research is to get the best tracking performance using Pixy CMUcam5 tracking camera while tracking the colour pattern. The RGB values from PixyMon image frame-grabber were extracted from the different light intensity. Each of the information taken from Pixy CMUcam5 was tabulated into the table. The result shows that the most suitable conditions for Pixy CMUcam5 to operates is within 58 to 205 lx of light in a closed environment as it gives a smooth and uniform RGB value. It shows that the camera may have too much of tracking errors if the light is too dim or too high in intensity. Several information such as RGB boundaries and RGB average values were measured with several algorithms using MATLAB. The tracking error rate being computed to get the best conditions for tracking performance. As the conclusion, the determinations of best tracking performance for CMUcam5 is important and it can be applied to other systems like mobile robot tracking.

Keywords Pixy CMUcam5 · RGB · Light intensity · Colour tracking technique · Cart following system

1 Introduction

Previous mobile robots are usually supervised by expensive and heavy computer systems that need to be linked with cable or wireless devices. However, these robots are replaced with smaller robot size that is integrated with a lot of sensors and actuators [1]. There are also several researchers using a vision-based sensor to perform tracking technique with obtaining the data on Field of View (FOV) of the camera with aid of additional data from other sensors. The overall system per-

M. F. Ahmad · S. S. N. Alhady (✉) · W. Rahiman · W. A. F. W. Othman · A. A. M. Zahir
School of Electrical and Electronic Engineering, Engineering Campus, Universiti Sains
Malaysia, 14300 Nibong Tebal, Penang, Malaysia
e-mail: sahal@usm.my

formed well but sometimes the tracking loss may occur due to some insufficient of light in the surrounding [2, 3]. Another target tracking control of the mobile robot in diversified maneuver modes was established using CMUcam3 a low technology embedded vision system [4]. The centroid of the target needs to be remained inside the camera tracking boundary. Otherwise, the camera will detect the different pixel value to ensure the target centroid remain in the tracking box [5].

The objective of this paper is to obtain the best tracking performance for mobile following robot using CMUcam5 by extracting the RGB value from frame-grabber with different light intensity. However, the contribution of this research only focusing on the camera part only. The tracking error rate also being calculated to find the most suitable conditions of light intensity value for the robust tracking system. The findings will give that the CMUcam5 is able to determine the image centroid accurately. Several experiments were carried out with proposed algorithms to get the best result.

2 Colour Tracking Technique

2.1 CMUcam5 Tracking Camera

CMUcam can be said as a well-known open source programmable low technology visual camera that has a visual ability in an embedded system to produce an intelligent visual sensor. The latest version being commercialized is Pixy CMUcam5 and has been used for this project. Pixy calculates the colour (hue) and saturation of each pixel of RGB obtained from the image sensor which acts as a primary filtering parameter [6]. Pixy uses colour-based filtering algorithm method to identify objects due to its system robustness, fast processing speed with 50 fps and higher efficiency. Colour code (CC) is one of the special features where up to seven colour signatures can be placed closely together and present as a special target object [7].

2.2 Tracking Boundary Field of View

Pixy CMUcam5 resolutions are 640×400 pixels. However, the standard tracking library for Pixy CMUcam5 works with 320×200 pixels [7]. Figure 1 shows the CMUcam5 tracking box that contains the threshold of the tracking error. The green square *fghi* constitute the overall image surface area while the yellow square *jklm* constitute the CMUcam5 field of view (FOV). Figure 2 gives the visualization of PixyMon frame-grabber and tracking lock.

Fig. 1 CMUcam5 tracking boundary

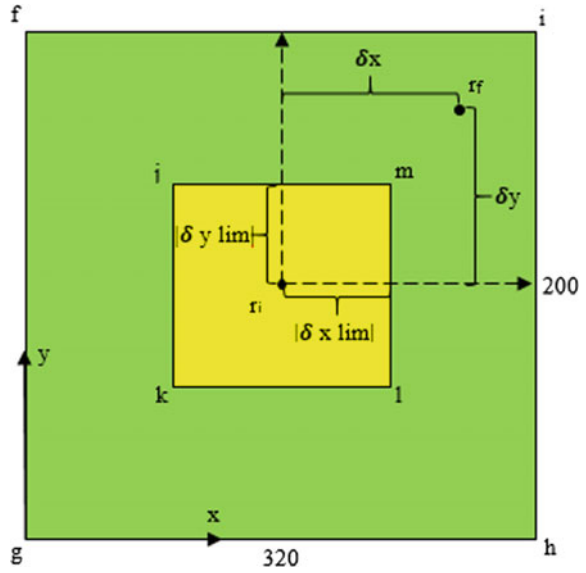


Fig. 2 PixyMon frame-grabber



2.3 Light Intensity Adjustment

The manipulation of light intensity can be controlled by increasing or decreasing of the light source itself inside the closed area to neglect other light source disturbance [8]. The measurement can be obtained using Lux meter. The measurement was taken for 5 times for each different intensity to get the most accurate results. The changes for

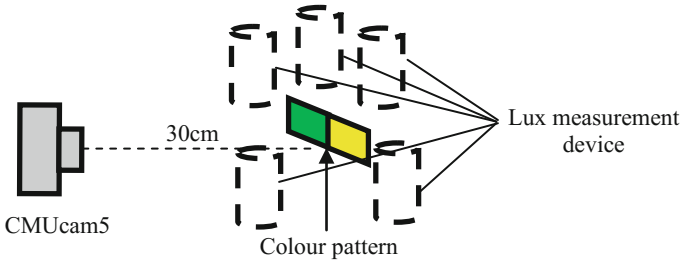


Fig. 3 Visualization for experimental setup

each different intensity being done with adjusting the brightness of the lights in the surrounding. Figure 3 below show the experimental set up for adjusting the brightness of light. The distance from the camera to the colour being fixed to 30 cm.

2.4 RGB Value Determination

The extraction of colour features from each pixel on colour sample chart in term of R, G and B is compulsory to analyze the digital image [8]. Digital images are stored in an array of point (pixels). Each of the pixel represented by three components which are Red, Green, and Blue [9]. There are also researchers used Red, Green, Blue—Distance (RGB-D) method with kinect 3D sensors for tracking purpose [10, 11].

The image taken from CMUcam5 camera being grabbed by using PixyMon software which acts like CMUcam5 frame-grabber. The image then was saved in image.png format. Figure 4 shows the GUI designed in MATLAB software for extracting each of R, G and B component inside the grabbed image.

The determination of RGB value was taken by using MATLAB software with several algorithms. The grabbed image is converted from X, Y and Z to R, G and B value as in Eqs. (1).

$$\begin{bmatrix} R \\ G \\ B \end{bmatrix} = [M]^{-1} \begin{bmatrix} X \\ Y \\ Z \end{bmatrix} \text{ where } [M] = \begin{bmatrix} S_R X_R & S_G X_G & S_B X_B \\ S_R Y_R & S_G Y_G & S_B Y_B \\ S_R Z_R & S_G Z_G & S_B Z_B \end{bmatrix} \quad (1)$$

where R = Red, G = Green and B = Blue. M is the coefficient of conversion. X, Y and Z are standard illuminant colour value. S_R, S_G and S_B stand for Standard Red, Standard Green and Standard Blue value respectively. The determination for X, Y and Z for each R, G and B in Eqs. (2), (3), (4).

$$X_R = \frac{x_R}{y_R}, Y_R = 1, Z_R = \frac{1 - x_R - y_R}{y_R} \quad (2)$$



Fig. 4 GUI for R, G and B classification

$$X_G = \frac{x_G}{y_G}, Y_G = 1, Z_G = \frac{1 - x_G - y_G}{y_G} \tag{3}$$

$$X_B = \frac{x_B}{y_B}, Y_B = 1, Z_B = \frac{1 - x_B - y_B}{y_B} \tag{4}$$

where $(x_R, y_R), (x_G, y_G), (x_B, y_B)$ are chromatically coordinates [8] with (X_W, Y_W, Z_W) as the white reference. The equations were arranged into matrices yields Eq. (5).

$$\begin{bmatrix} S_R \\ S_G \\ S_B \end{bmatrix} = \begin{bmatrix} X_R & X_G & X_B \\ Y_R & Y_G & Y_B \\ Z_R & Z_G & Z_B \end{bmatrix}^{-1} \begin{bmatrix} X \\ Y \\ Z \end{bmatrix} \tag{5}$$

3 Results

3.1 RGB Versus Light Intensity

One experiment has been carried out to relate RGB value with the different light intensities. The sample size of overall data for each measured Lux is 1551. Several information like RGB boundaries of the colour pattern and average RGB values were collected and tabulated in Table 1.

The results obtained for five different light intensities being plotted on a graph. The presented graph shows for 16, 58, 125, 205 and 325 lx value as each of them give the huge value of different. Figure 5, Fig. 6, Fig. 7, Fig. 8 and Fig. 9 present the graph for each different light intensity respectively. The green value was the highest among all the graph followed by blue and red. This is due to the colour pattern being used as sample are green and yellow.

Table 1 RGB boundaries and the average value of colour pattern at different light intensity

Light intensity (lx)	RGB boundaries of colour pattern						Average RGB value		
	Red Min	Red Max	Green Min	Green Max	Blue Min	Blue Max	Red	Green	Blue
16	21	90	57	183	41	150	38.99	88.76	67.74
58	92	164	99	236	102	209	148.14	214.28	189.86
125	93	179	110	236	110	209	147.27	218.37	193.85
205	60	122	108	220	93	181	104.18	205.28	170.80
325	27	101	40	195	33	158	72.64	144.69	115.53

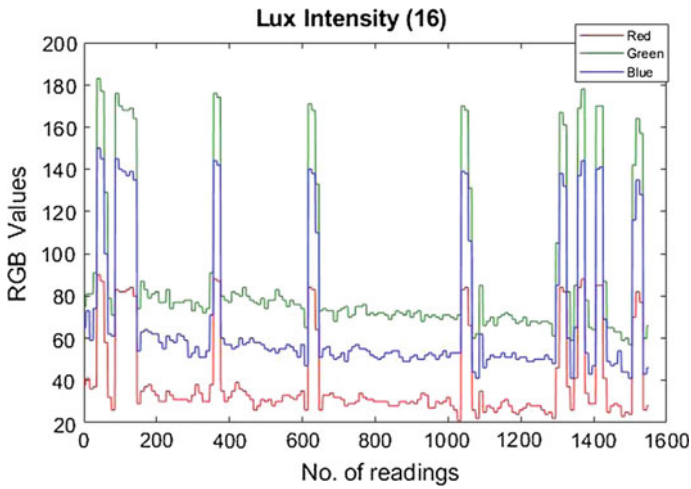


Fig. 5 16 lx

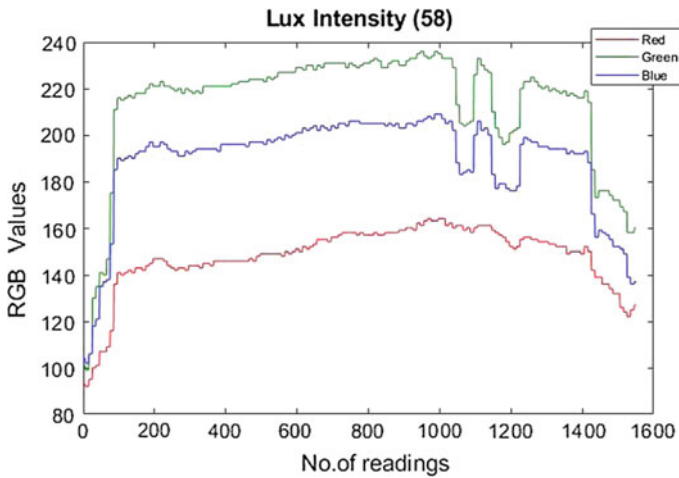


Fig. 6 58 lx

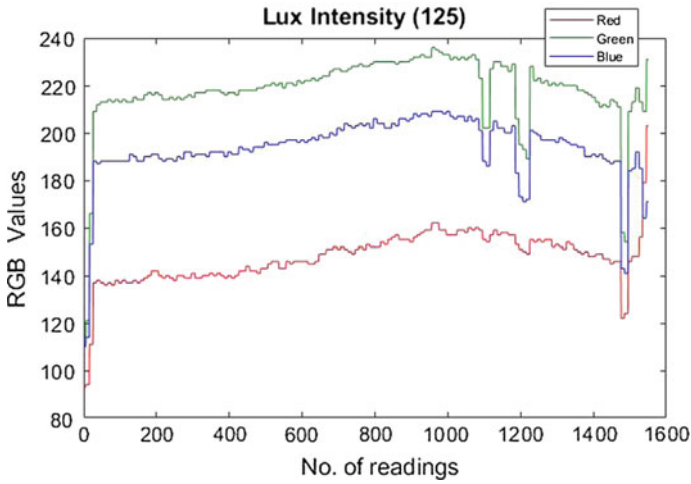


Fig. 7 125 lx

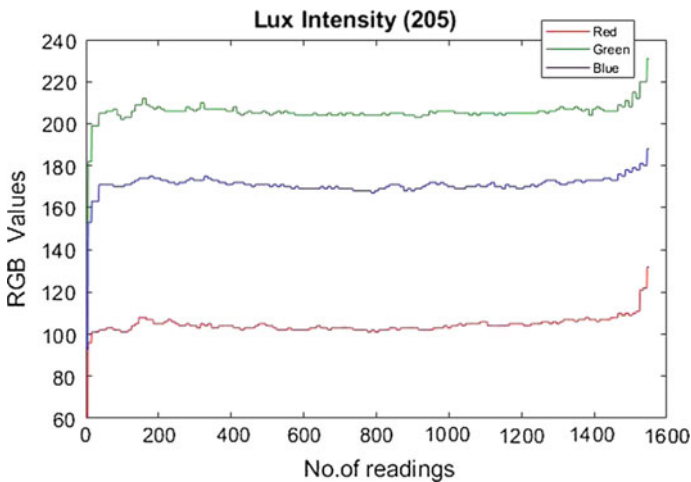


Fig. 8 205 lx

Too many spikes in the graph show the bad tracking conditions while steady graph shows the good tracking conditions. The fluctuating graph for 16 and 325 lx shows that there is a lot of error in tracking pixels. As the value is not stable, thus this can interrupt the tracking process. For the most ideal case is when the light reached 205 lx. This is because at this stage the trend of the graph shows that the RGB value keeps steady at high value. So, the pixel loss less compared to others hence it is the most stable situation.

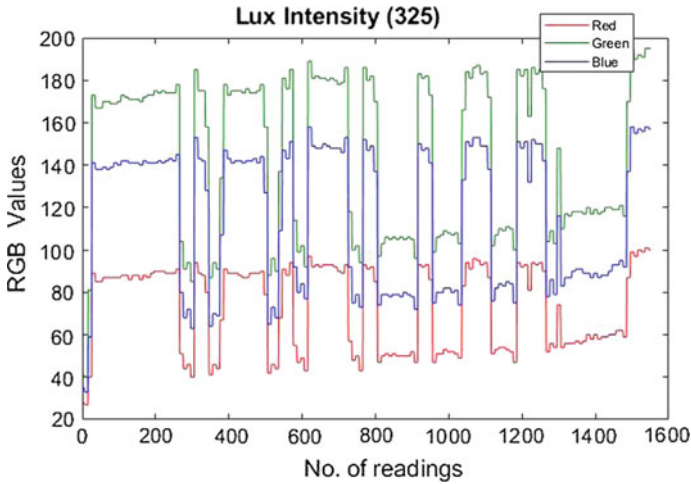


Fig. 9 325 lx

3.2 Tracking Error Rate

A standard deviation test has been made to test the error rate in the tracking system for the sample size of 1551 data for each different Lux as shown in Table 2. The test shows that the most ideal tracking system is for 205 lx since it has the lowest value of disturbance for each of the R, G and B value followed with 125, 58, 16 lx while the worst situation at 325 and 16 lx as too bright or too dim of light intensity decrease the tracked pixel by CMUcam5 hence increasing the tracking error and reducing the tracking performance rate. This type of test is enough for determining the obtained data match with the experimental objective since the main focusing of this paper is RGB behaviour with different light intensities.

Table 2 Variance and standard deviation from the taken data

Light intensity (lx)	Variance			Standard deviation		
	Red	Green	Blue	Red	Green	Blue
16	380.3776	1231.3289	962.5348	19.5033	35.0903	31.0247
58	192.4162	683.3090	460.8475	13.8714	26.1402	21.4674
125	114.0369	238.8818	176.3704	10.6788	15.4558	13.2805
205	17.8235	43.2039	29.1089	4.2218	6.5730	5.3953
325	401.0234	1405.1320	1110.4060	20.0256	37.4851	33.3228

4 Conclusion

As a conclusion, the determination of CMUcam5 tracking performance is important so that tracking loss might be reduced. The main factor that gives the big impact on the performance is the brightness of the light as shown in the results where the disturbance is high when the Lux is less than 58 and more than 205. The most stable tracking rate at 205 lx value as the graph shows RGB value keeps steady at the high value. This informs that tracking error is less thus tracking performance rate is high. This analysis was then confirmed with the statistical test that proven all the taken data are accurate. The standard deviation test shows that the best tracking performance is also at 205 lx as the value is the lowest and bad tracking performance is at 325 lx as the value is the highest thus showing that the data is scattered.

Acknowledgements The authors would like to thank Universiti Sains Malaysia (USM) for the support of the research under grant no 305/PELECT/6013112.

References

1. Bräunl, T.: *Embedded Robotics: Mobile Robot Design and Application with Embedded Systems*, 3rd edn, pp. 1–7. Springer, Berlin (2008)
2. Ahmad, M.F., Alhady, S.S.N., Kaharuddin, S. and Othman, W.A.F.W.: Visual based sensor cart follower for wheelchair by using microcontroller. In: 5th International Conference on Control System, Computing and Engineering (ICCSCE), pp. 123–128. IEEE International Conference, Penang, Malaysia (2015)
3. Ahmad, M.F., Rong, H.J., Alhady, S.S.N., Rahiman, W. and Othman, W.A.F.W.: Colour tracking technique by using Pixy CMUcam5 for wheelchair luggage follower. In: 7th International Conference on Control System, Computing and Engineering (ICCSCE), pp. 187–192. IEEE International Conference, Penang (2017)
4. Sani, N.A., Alhady, S.S.N., Othman, W.A.F.W., Kaharuddin, S.: Cordless cart follower for wheelchair user. *Intelligent Robotics Automation, and Manufacturing*, pp. 252–262. Springer, Berlin, Heidelberg (2012)
5. Xu, H. and Shen, Y.P.: Target tracking control of mobile robot in diversified manoeuvre modes with a low cost embedded vision system. In: *Industrial Robot: An International Journal*, vol. 40 no. 3 pp. 275–287. Emerald Insight, UK (2013)
6. Rowe, A., Goode, A., Goel, D., Nourbakhsh, I.: “CMUcam3: an open programmable embedded vision sensor”, Technical Report RI-TR-07-13. Robotics Institute Carnegie Mellon University, Pittsburgh, PA (2007)
7. CMUcam5 Pixy, <http://cmucam.org/projects/cmucam5>, Accessed 11 Nov 2017
8. Leon, K., Mery, D., Pedreschi, F., Leon, J.: Color measurement in $L^* a^* b^*$ units from RGB digital images. *Food Res. Int. (Elsevier)* **39**(10), 1084–1091 (2006)
9. Gutub, A., Al-Qahtani, A., Tabakh, A.: Triple-A: Secure RGB Image Steganography Based on Randomization. In: *Computer Systems and Applications*, pp. 400–403. IEEE (2009)
10. Endres, F., Hess, J., Engelhard, N., Sturm, J., Cremers, D., Burgard, W.: An evaluation of the RGB-D SLAM system. In: *Robotics and Automation (ICRA)*, pp. 1691–1696. IEEE International Conference (2012)
11. Lai, K., Bo, L., Ren, X., Fox, D.: A large-scale hierarchical multi-view rgb-d object dataset. In: *Robotics and Automation (ICRA)*, pp. 1817–1824. IEEE International Conference (2011)

Detection of Metallic Contaminant in Aluminium Soda Can Using TMR Sensor



Nurul A'in Nadzri, Mohd Mawardi Saari, Saifuddin Razali,
Mohd Rusllim Mohamed and Hamzah Ahmad

Abstract The contaminant is one of the big concerns in food processing industry and metallic objects can be one of the contaminant factors since most of the food processing equipment and tools are composed of metallic parts. Metal detector is used because these contaminant objects might cause injury to the consumers. Moreover, even the smallest particle of metals can lead to machinery failure. In this study, we have developed an inspection system for detecting the magnetic remanence of the contaminants. The system utilizes a Tunnel Magnetoresistance (TMR) Mag3110 magnetometer. An Arduino operating software was developed for data acquisition of Mag3110, and identification of the presence of the contaminant. In order to optimize the position of the magnetometer so that detection sensitivity can be enhanced, we performed a simulation based on magnetic moment dipole. The system performance was evaluated using stainless steel balls. The developed system could detect a stainless steel ball having diameter as small as 0.1 cm. The detected signal is sent to the control panel to analyze the presence of a metal object. The magnetic response with respect to position of the sensor, different size of metal objects and magnetization effect, is studied as well.

Keywords Metal detector · Magnetometer · Magnetic remanence

1 Introduction

Canned foods are one of the processed foods that popular in this age. Due to this, to ensure the safety of the consumers, finding a detector that can detect any foreign bodies in canned products before they are being distributed to market is important [1, 2]. A mixture of metallic contaminants to food is a serious problem not only for

N. A. Nadzri · M. M. Saari (✉) · S. Razali · M. R. Mohamed · H. Ahmad
Faculty of Electrical & Electronic Engineering, Universiti Malaysia Pahang,
26600 Pekan, Pahang, Malaysia
e-mail: mmawardi@ump.edu.my

© Springer Nature Singapore Pte Ltd. 2018
M. H. A. Hassan (ed.), *Intelligent Manufacturing & Mechatronics*,
Lecture Notes in Mechanical Engineering,
https://doi.org/10.1007/978-981-10-8788-2_47

the consumers; it also can affect the mechanism and operation of machines in food processing lines which can cause a high cost to repair the machine.

Metal detection is the most popular metallic detection system method that has been used in food industries [3, 4]. This method can identify large metallic objects and works well in bulk containers of raw materials. Kwan et al. [5] proposed a detection method of foreign object by using an x-ray technique for a dry food manufacturing line. This method is widely used because it is easy to operate and can work efficiently in high production lines. However, detection resolution of this method may not be sufficient for detection of small size or low density foreign objects. Moreover, to generate an x-ray, a high voltage power supply is required and the system is high cost.

According to Tanaka et al. [6–8], they proposed a method using Superconducting Quantum Interference Device (SQUID) system for the detection of small magnetic contaminants. This method has been proposed because the high-sensitivity of the SQUID can overcome the problem where the X-ray system has low detection resolution for thin materials. The SQUID system has a good ability detection for small magnetic materials. This system has already been installed in food industry plant. Moreover, Krause et al. [9] discussed about a detection system of magnetic contaminations in industrial products using High Temperature Superconductor (HTS) SQUIDs. They mentioned that the key requirement of industrial quality control resides in the inspection at the end of the production lines, in which the products need to go through inspection after they are wrapped. The use of SQUID magnetometers allows the realization of excellent sensitivity.

In this paper, a magnetometer of Mag3110 (Freescale) is used to detect metal contaminants in aluminum canned foods. This sensor is selected because it is small, low-power, low-cost and having digital 3-axis detection capability. This sensor is based on Tunnel Magnetoresistance (TMR) and it can detect magnetic field strength as low as 0.1 μT . An Arduino Uno is used as a core platform that featured in the developed system.

2 Methodology

We first study magnetic dipole moment by using a simulation method. Based on the simulation result, we measure signal from steel balls at different conditions.

In the experiment, the sensor was fixed below the conveyer belt to increase detection sensitivity, assuming that metal contaminants are located at the bottom of a can. By using the Mag3110 sensor, a testing technique based on the remanent magnetic field of metallic contaminants is developed. The size of contaminants has also been considered. The magnetic responses are experimentally determined using steel balls with different diameters to test the sensitivity of the developed system.

An analogue-to-digital conversion of the Mag3110 sensor has been achieved by using the Arduino board. The software of the Arduino board is developed to suit the

developed system. All the collected data will be sent to a computer and the result will be displayed on the computer.

2.1 Theoretical Calculation

We first simulate the pattern of magnetic fields produced by a steel ball. From the distribution characteristic of magnetic fields, the optimum configuration for the magnetic sensor can be determined. Using the magnetic dipole law, the response of magnetic field from a magnetic moment dipole m can be expressed as

$$B = \frac{\mu_0}{4\pi} \left(\frac{3\mathbf{m} \cdot \mathbf{r}}{r^5} \mathbf{r} - \frac{\mathbf{m}}{r^3} \right). \quad (1)$$

Using Eq. (1), it is possible to simulate the magnetic field of x -, y - and z -oriented dipoles. Here, μ_0 , \mathbf{m} , and \mathbf{r} are vacuum permeability, magnetic moment vector and distance vector from magnetic moment dipole to observation point. The simulated theoretical data can also be used in order to satisfy the visualization requirements in industrial applications. According to Eq. (1), ferromagnetic objects such as iron that are moving through the detection space, will cause temporary but detectable changes due to the magnetization induced by the Earth's ambient magnetic field.

From the magnetic dipole law, Eq. (1) can be simplified to find the axial magnetic field B_z with different value of distance, r , and it is given by

$$B_z = \frac{\mu m z}{2\pi r^3} = \frac{\mu D^3 M}{12r^3}. \quad (2)$$

Here, M , D , and μ are the magnetization, diameter and magnetic permeability of the steel ball.

Furthermore, the movement of the contaminants will produce an inertia force where they may roll during detection. Due to this reason, we have included in the simulation where the magnetic moment dipole is tilted to different values of angles. Moreover, since the rolling of contaminants will affect the magnetic signal, this requires us to determine the best detection direction of the magnetic field. To study this effect, the inclination of a magnetic moment of the steel ball is simulated from 0 to 90° in x - y , plane. Since metal components have magnetic remanence characteristic that can be represented by magnetic moments, we assume that the magnetic moment is pointing towards z -axis when the tilting angle is 0° from the z -axis. When the sensor senses the magnetic field of the contaminant and it will produce values of magnetic field vectors which are composed of x -, y -, and z -components of magnetic fields, B_x , B_y and B_z , respectively.

3 Result and Discussion

3.1 Simulation of Magnetic Moment Dipole

The results of the calculated signal traces using Eq. (1) are displayed in Fig. 1a and b. Here, we assumed the value of $M = 6000$ A/m, and the diameter D of the steel ball is 0.01 m. From the Fig. 1, we could conclude that if the steel ball is located close to the sensor, the reading of the magnetic field will be high. The distance of the sensor to the contaminants needs to be considered so that the contaminants can be detected efficiently. A particle is detectable if the peak-to-peak signal detected by the sensor is greater than the noise of the environmental and the sensor. From Fig. 1b where we set the diameter from 0.5 cm until 2.5 cm, it was found that the intensity of the magnetic field increased as the size of the steel ball was increased. As we can see from Fig. 1b, the smallest diameter of steel balls gave the intensity of magnetic field near to zero, in which the presence of metal contaminant could be difficult to be determined. In this case, the sensitivity of the sensor is very crucial where a sensitive sensor is capable to detect the presence of small metallic contaminants.

Figure 2 shows the simulation results of the B_z component using Matlab (MathWorks, USA) when the ball is pointing towards z -axis with the angles of 0° and 90° .

From Fig. 2, it was concluded that, the detection response using B_z component showed a higher value when the ball was pointing towards z -axis with the angle of 0° . The magnetic field was strong at z -axis when the angle was 0° but the field intensity gradually became weaker when the magnetic moment of the ball rolled towards 90° . The intensity was higher when the ball was pointing at 0° since the sensor sensed the magnetic field in the z -axis.

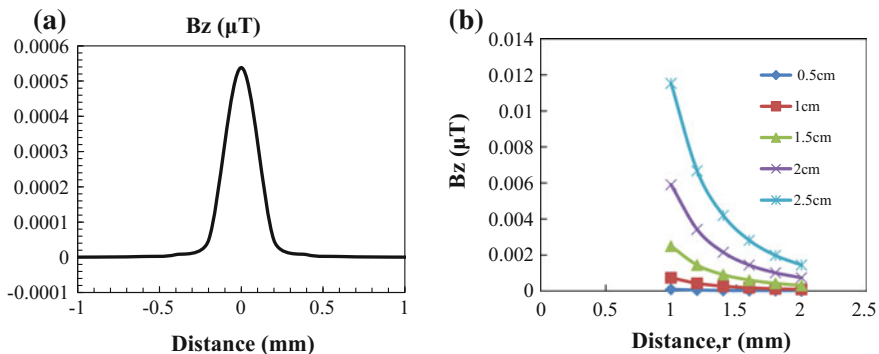


Fig. 1 a Signal of metal particle (diameter 0.01 m), passing the sensor plane at a distance about 10 cm. The solid line shows the trace simulated with the particle alone. b Signal of metal particle with different diameters of the stainless steel balls

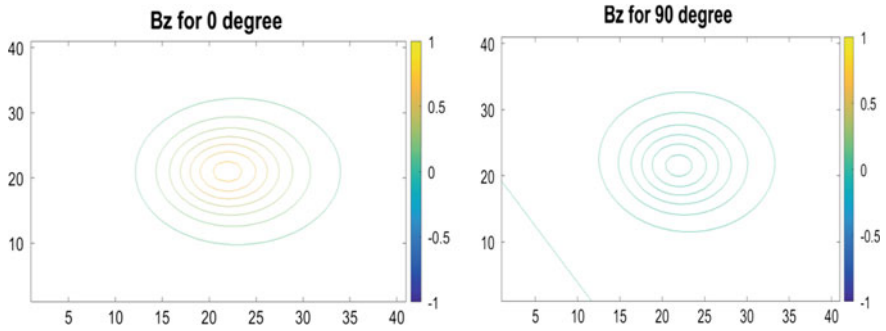


Fig. 2 Graph of B_z magnetic response of a magnetic dipole pointing at 0 and 90° from z -axis, respectively

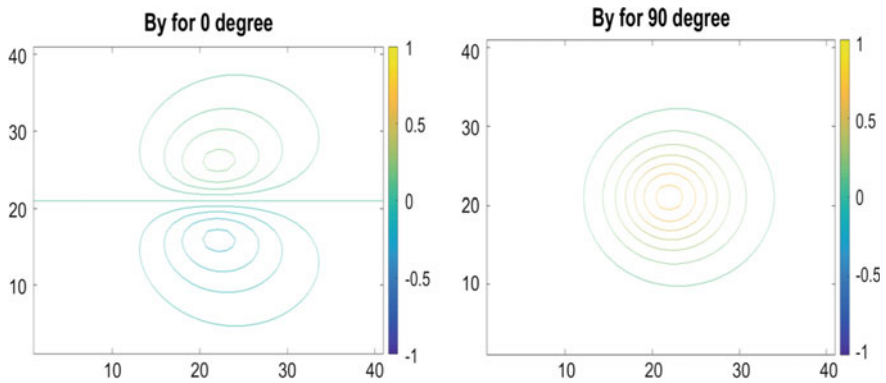


Fig. 3 Graph of B_y magnetic response of a magnetic dipole pointing at 0 and 90° pointing towards z -axis, respectively

Figure 3 shows the results for the B_y component when the ball was pointing towards z -axis with the angles of 0 and 90° . For the magnetic field response in the y -component, it was different with the z -component, where we could see that the magnetic field was weak when the ball was pointing at 0° . However, the strength of magnetic field gradually increased when the value of the angle was increased.

Figure 4 shows the results for x -component of the magnetic field B_x , when the ball was pointing at the angles of 0 and 90° . The results were almost the same with B_y ; however, the position of the contours was changed. When the ball was pointing at 0° , the strength of the magnetic field was weak but it gradually increased when the value of the angle was increased. Furthermore, from the distribution profiles of B_x , B_y and B_z , the magnetic responses were high when the steel ball was near to the sensor, i.e., a sensor with a capability of measuring x -, y -, and z -components of magnetic fields can be placed at the center of production lines such as carrier conveyer belts, to enhance the detection sensitivity.

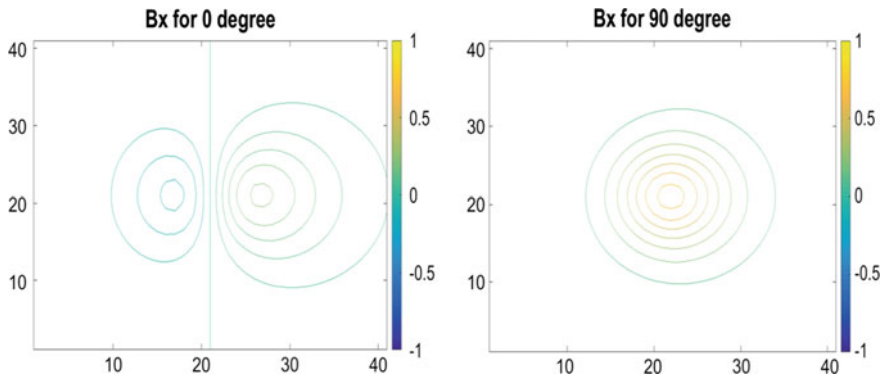


Fig. 4 Graph of B_x magnetic response of a magnetic dipole pointing at 0 and 90° from z -axis, respectively

3.2 Measurement of Steel Balls

In Fig. 5a, the vertical axis shows the signal intensity of an aluminium can and a white steel nail with length of 3 cm, and Fig. 5b shows the signal intensity when the nail was placed inside the aluminium can. By fixing the sensor at a fixed position, we moved the aluminium can and nail separately. From the measured signal, it shows that the signal reached a maximum when the sample was on top of the sensor. For the aluminium can signal, spurious signals were observed. This was thought that the aluminium can might contain other magnetized metal particles and was not made of pure aluminium. For Fig. 5b, it shows that the signal intensity was almost similar to the signal intensity of the nail. The sensor could sense the remanent magnetic field of the nail despite it was placed inside the aluminium can.

Figure 6a shows the results of magnetic field vectors that responded to x -, y - and z -directions of remanent fields from a 0.5 cm steel ball. The intensity of B_x was

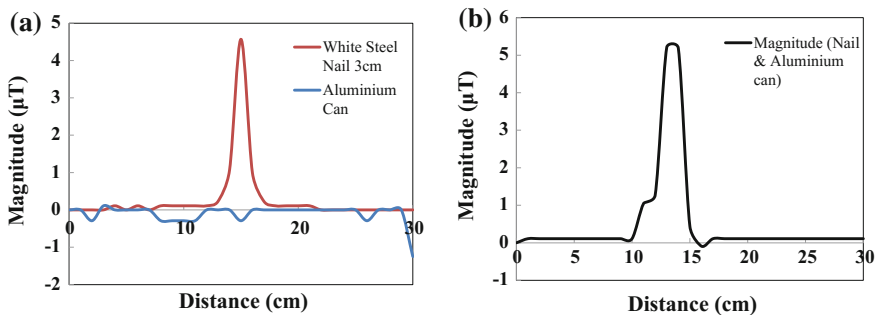


Fig. 5 a Magnitude signal of a nail and aluminium can. **b** Magnitude signal of the nail placed inside the aluminium can

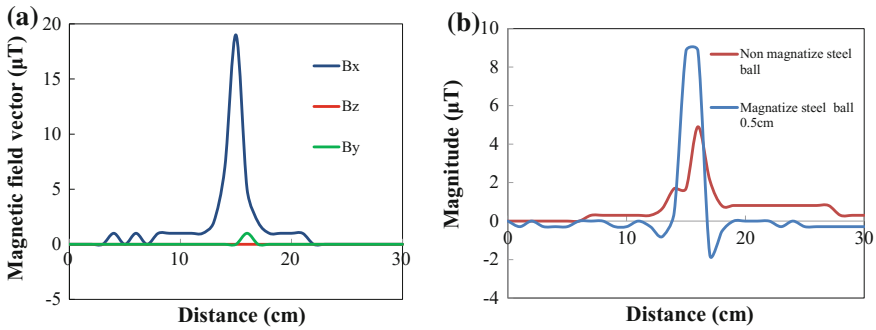


Fig. 6 **a** Magnetic field vector signals that responded to B_x , B_y and B_z , respectively, of a 0.5 cm steel ball. **b** Magnitude signal of the 0.5 cm steel ball before and after magnetization

higher compare to B_y and B_z . This was thought that the magnetic moments in the metal were pointing towards x -axis. Figure 6b shows results of the magnetized and non-magnetize steel balls of 0.5 cm diameter. After the steel ball was magnetized, the magnitude was increased compare to the non-magnetize steel ball. Since this method is based of magnetic remanence measurement, the magnetic remanence in a metal object can be improved temporarily by magnetizing it with external magnetic field such as by using a magnet.

Figure 7a shows the magnitudes of the detected magnetic fields at different positions of the steel ball in an aluminium can. From the differences in the position of magnetic responses, the position of the steel ball could be determined based on the response characteristics. Figure 7b shows the intensity of magnetic response of different sizes of steel balls. In this experiment steel balls with diameter of 0.5, 0.3 and 0.1 cm were used. The peak intensity was not correlated with the size of steel balls. This was thought due to the magnetic properties of the steel balls, which is reflected by the magnetic permeability μ and magnetization M as shown in Eq. (2) [10]. However, the width of the signal reflected the size of the steel balls where the

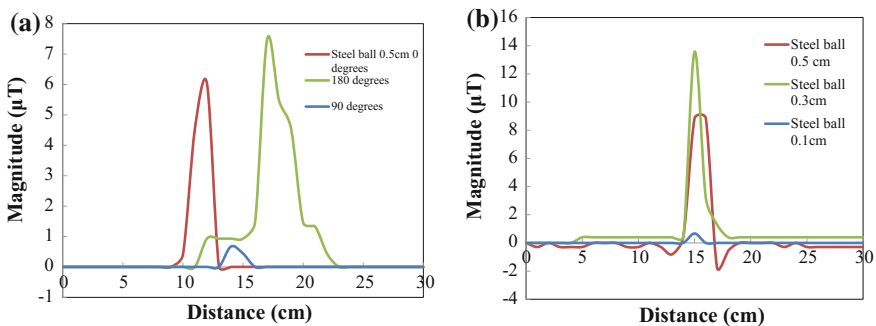


Fig. 7 **a** Magnitude signal of steel ball (0.5 cm) at different location. **b** Magnitude signal of steel ball with different size of steel balls

steel ball of 0.5 cm diameter has a bigger width of signal compared to others. From here, the signal width could be used to estimate the size of the metallic contaminants. The developed system was able to detect the magnetic response from the steel balls as small as 0.1 cm by using the Mag3110 sensor. Although further improvement in detection sensitivity can be expected by using a superior magnetic sensor such as SQUIDs for detection size smaller than 0.1 mm [8], a compact and low-cost system with sufficient sensitivity was shown by the developed system.

4 Conclusion

The fundamental studies on metal detector system have led to the finding of factors that affect the magnetic signal intensity from metallic parts. Based on the theoretical result, a detection system of metallic contaminants was developed based on detection of the remanent magnetic field using the Mag3110 magnetic sensor. The position of the sensor has been optimized to increase the performance of the system on the basis of simulation results. The effectiveness of the metal detection system was experimentally conducted using steel balls with different diameters. A good qualitative agreement with theoretically predicted characteristics was found. The system could detect a steel ball having a diameter as small as 0.1 cm diameter. Thus, the developed metal detection system can be expected to be used for the inspection of wrapped aluminium products.

Acknowledgements This work was supported by Ministry of Higher Education of Malaysia under grant number of RDU160115 and Research Management Center of Universiti Malaysia Pahang under grant number of RDU170377.

References

1. Miyakawa, T., Honjo, K.: Development of instrument detecting nonmetal foreign body in food material. In: 1993 IEEE Instrumentation and Measurement Technology Conference, pp. 519–533. IEEE (1993)
2. Patel, D., Hannah, I., Davies, E.R.: Automatic detection of foreign objects in food products. In: 4th International Conference on Advanced Factory Automation (Factory 2000), pp 517–522. IEE (1994)
3. Zhao, Y., Yin, W., Ktistis, C., et al.: On the low-frequency electromagnetic responses of in-line metal detectors to metal contaminants. *IEEE Trans. Instrum. Meas.* **63**, 3181–3189 (2014)
4. Tanaka, S., Akai, T., Hatsukade, Y., Suzuki, S.: High Tc SQUID detector for magnetic metallic particles in products. *IEICE Trans. Electron.* **E92–C**, 323–326 (2009)
5. Kwon, J.S., Lee, J.M., Kim, W.Y.: Real-time detection of foreign objects using X-ray imaging for dry food manufacturing line. In: Proceedings of the International Symposium on Consumer Electronics ISCE, pp. 1–4 (2008)

6. Nagaiishi, T., Kamitani, F., Ota, H., et al.: First practical high Tc SQUID system for the detection of magnetic contaminants in commercial products. *IEEE Trans. Appl. Supercond.* **17**, 800–803 (2007)
7. Tanaka, S., Kitamura, Y., Uchida, Y., et al: Development of metallic contaminant detection system using eight-channel high-Tc SQUIDs. *IEEE Trans. Appl. Supercond.* **23**, 1600404–1600404 (2013)
8. Tanaka, S., Kitamura, Y., Hatsukade, Y., et al.: Metallic contaminant detection system using multi-channel high Tc SQUIDs. *J. Magn. Magn. Mater.* **324**, 3487–3490 (2012)
9. Krause, H.J., Panaitov, G.I., Wolters, N., et al.: Detection of magnetic contaminations in industrial products using HTS SQUIDs. *IEEE Trans. Appl. Supercond.* **15**, 729–732 (2005)
10. Tsukada, K., Haga, Y., Morita, K., et al.: Detection of inner corrosion of steel construction using magnetic resistance sensor and magnetic spectroscopy analysis. *IEEE Trans. Magn.* **9464**, 1–1 (2016)

Performance Evaluation of Distributed Gain Offered by Raman Amplifier in WDM and EDFA



M. Z. H. Jesmeen, J. Hossen, Thangavel Bhuvaneshwari,
M. A. Hasnayeem, J. Emerson Raja and K. Tawsif

Abstract An analytical approach is presented to estimate the amplified performance of a multichannel wavelength division multiplexing for optical transmission system. In order to gain power amplification with low noise figure, EDFAs are used. Since the gain bandwidth of EDFA is restricted to 35 nm wave-length of pumping, an additional amplifier has to be used as hybrid amplifier. In this paper, a system of multichannel WDM configuration of Erbium-Doped Fiber Amplifiers without using Raman Amplifier and with Raman Amplifier are simulated, compared and analysed. In this investigation Raman amplifiers is being used beside the high-output-power of EDFA, for pumping, to improve performance. The study is based on the amplifier's parameters, pumping wavelength and pumping power. To expand the proportions of light wave transmission, provide high capacity and raise flexibility of optical network technology the features of both amplifiers can perform together. An implementation of nonlinear photonics is illustrated by distributed Raman fiber amplification to enhance by accepting evolutionary change forward in fiber optic communication.

Keywords Wavelength division multiplexing (WDM) • Optical amplifiers
Distributed-Raman amplifier • Erbium doped fiber amplifier (EDFA)

1 Introduction

In this era of web, number of internet users is increasing gradually with increase of new online network system the volume of transferring data through network [1]. Reported by Cisco Inc. (2016) [2] from 2015 to 2020 ventures worldwide IP

M. Z. H. Jesmeen (✉) · J. Hossen · T. Bhuvaneshwari · J. Emerson Raja · K. Tawsif
Faculty of Engineering and Technology, Multimedia University,
Ayer Keroh 75450, Melaka, Malaysia
e-mail: jesmeen.online@gmail.com

M. A. Hasnayeem
International Islamic University Chittagong, Chittagong, Bangladesh

activity is almost triple, as indicated by the Cisco[®] Visual Networking Index (VNI) forecast. VNI analysis that every month general IP motion will grow from 72.5 EB (2015) to 194 Exabytes (EB) by 2020, for each month, a CAGR of 22%. Whereas, report published in 2017, Global mobile data traffic scale drawn up to 7.2 EB per month and around 63% traffic grew in 2016. According to, Cisco Inc. 2017, [3] VNI estimation in next 5 years monthly (by 2021) around there will be 49 EB global mobile data traffic.

Due to the challenges, amplifiers is being used with Wavelength Division Multiplexing (WDM) [4, 5] in optical communication system. WDM allows the spectrum to slice into many channels to different wavelength; each channel is allocated by one wavelength, Erbium-Doped Fiber Amplifiers (EDFAs) is one of the most important technique applied usually to develop efficiency of optical fiber communication system [6, 7]. EDFAs does not need fast electronic integrated circuits and is recognizable to data rate and form, which is relatively easy to build and that their usage is economically beneficial [6]. EDFAs also provide amplification of power and gain with low noise figure [8]. EDFA have one central problem of able to select wavelength of Pumping source. A gain bandwidth of EDFAs is restricted to 35 nm [6]. To overcome the issue multiple numbers of pumps can be used. A Raman Amplifier is able to magnify power to second higher wavelength photon by immersion in the initial-state of particle. Photonic Communication Networks, by increasing on-off Raman gain will causes decrease in noise figure [8]. Therefore, Raman amplifier can combine with EDFA amplifier, [7–10] called hybrid amplifier (HA). Due to amplifiers nature the WDM system, performance usually depends on power level and quality obtained by HA.

To demonstrate the performance evaluation of distributed gain offered by Raman Amplifier, this paper is arranged into four sections. In Sect. 1, outline is stated of the evaluation study. Section 2 discussed the proposed configuration for WDM system EDFA with Raman Amplifier, while Sect. 3 provides the demonstration of the simulated model. Section 4 presents the results and analyze the result comparing the performance selected fiber optical amplifier in terms of the expression of bit-error-rate (BER), Factor of Q-effective and Q, Threshold used, minimum/maximum power and eye spectrums. Finally, the paper is concluded with future aspects.

2 Proposed Configuration

Since EDFA forms the backbone of optical fiber communication systems, a WDM long distance fiber optic transmission system is shown with EDFA in Fig. 1a. WDM's input end is a coupler which used to combine all inputs pass through one output fiber, as WDMs frequently have several inputs. Whereas, Demultiplexing is used to take the combined input fiber and collimate the light into a narrow fiber. An approach to amplify WDM system with EDFA with Raman amplifier is proposed.

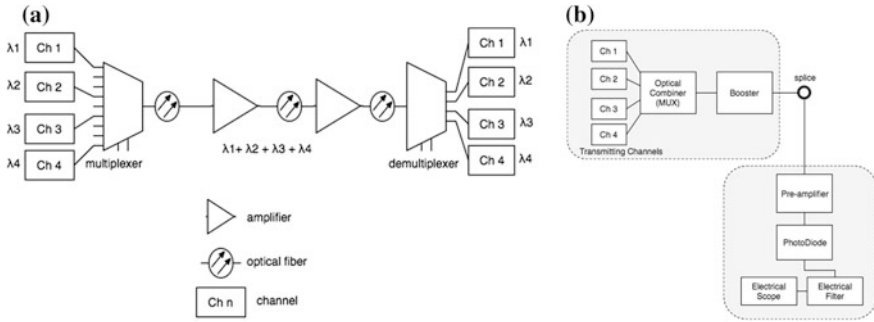


Fig. 1 **a** WDM long distance fiber transmission system with EDFA, **b** an approach to amplify WDM System with EDFA

The proposed system is to amplify WDM transmitted signals using EDFA amplifier, four transmitter channels for parameterizing and modulating, a multiplexer of optical combiner (MUX) and optical fiber of length 175 km. The receiving end of proposed system contains a photodiode, an optical splitter and a visualization device. This system will go through toleration from losing power and the reduction of the amplitude of a signal as the system contains only one EDFA amplifier, as shown in Fig. 1b.

Finally, WDM and EDFA configured with Raman Pumping. Where, EDFA is been used commonly as a Booster, pre amplifier and line amplifier. In the proposed system, EDFA is used, as a Booster, Distributed Raman amplifier is used for pre amplification. This proposed configured in elaborated in following section.

3 Simulation of Proposed Model

The proposed design is simulated using VPI Player simulator developed by VPI Photonics [11]. The results are analyzed with and without Raman Amplifier.

In Fig. 2, 10–40 Gb/s upgraded simulated model using Raman Amplifier with EDFA is shown. The transmitter signal is send by a non-return-to-zero (NRZ) line code, where using one significant condition (positive voltage) ones are represented and by other significant condition (negative voltage) zeros are represented with no other neutral condition. As evaluated by Seraji and Kiaee (2017) [12] NRZ modulation methods minimum Bit Error Rate and high-level of Q-factor for optical transmission network it's prescribed to use for the both 10 and 40 Gb/s single-channel optical networks. This is used to obtain a minimum Bit Error Rate by minimizing errors occurs in a transmission system. A 175 km unrepeated link is shown in the above figure with a EDFA booster amplifier and pre-amp EDFA. Where, Booster amplifier's usage is at the transmitting to amplify optical power end and at the receiver end pre-amplifier is placed to amplify to the required level. The

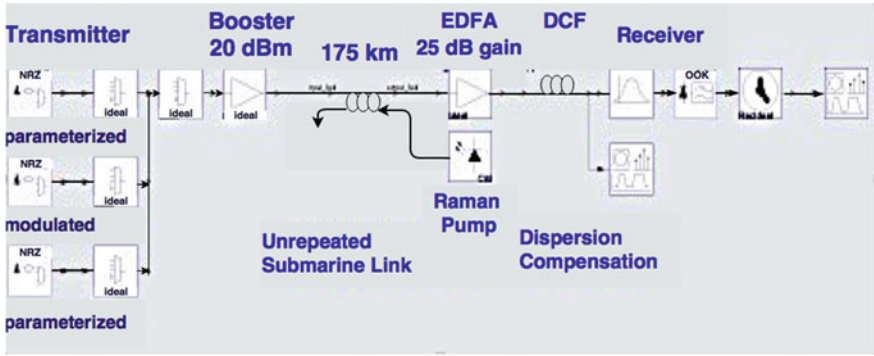


Fig. 2 Demonstration of the WDM + EDFA with Raman amplifier

receiver also consists On Off Keying (OOK). In Optical communication systems, OOK signals used to transfer the data in the intensity, in non-return-to-zero (NRZ) format. The outcomes of the model are analyzed by power inputs and outputs.

4 Results and Discussion

4.1 Simulation with BitRate = 10 Gb/S, Raman Pump Power = 0 W

The simulated graph of optical spectrum and the Eye diagram for bit rate = 10^9 bit/s and Raman pump = 0.0 W is shown in Fig. 3. The peak value in optical spectrum power is -18 dBm which is less than expected, as the system configured experiences power loss due to noise. Sample Band(SB) maximum power is -21.884 dBm, parameterized (PS) is less than -19 and Noise Bins (NB) power is around -43.480 dBm. This noise level is low as WDM and boosters are considered as ideal.

4.2 Simulation with BitRate = 10 Gb/S, Pump Power = 0.5 W

The simulated graph of Optical Spectrum and the Eye diagram for bit rate = 10^9 bit/s and Raman pump = 0.5 W is shown in Fig. 4. The peak value in optical spectrum power is 1 dBm which is absolutely greater value than the output Spectrum power without Raman Pump, as this design tolerates from low-level attenuation and dispersion losses-factor.

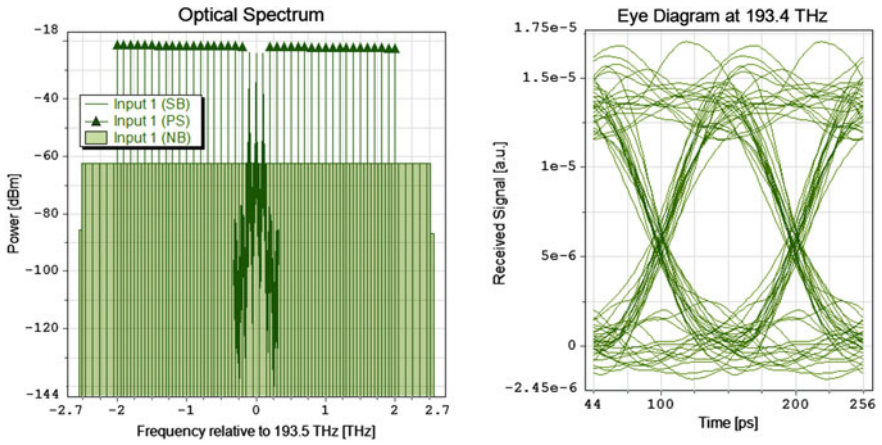


Fig. 3 Optical spectrum and eye diagram of bitrate = 10 Gb/s, pump power = 0.0 W

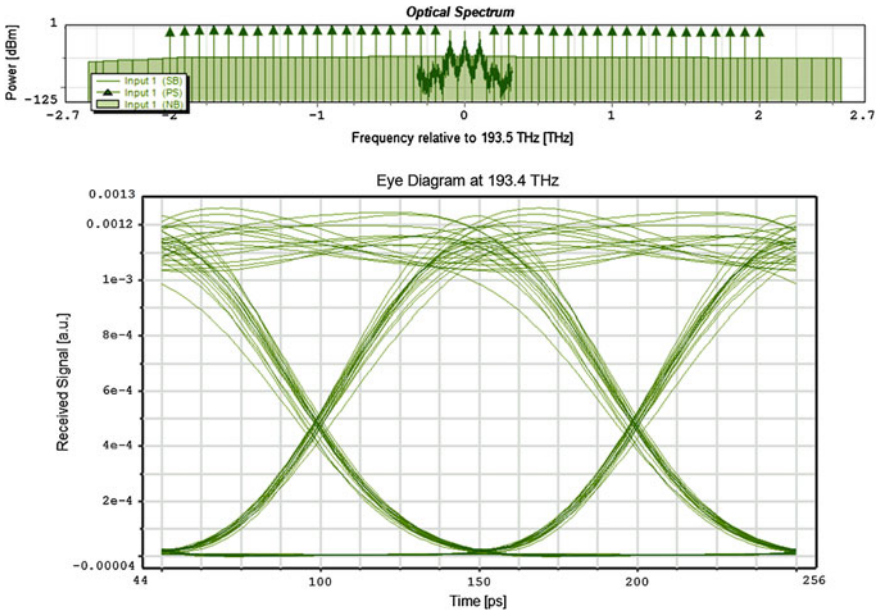


Fig. 4 Optical spectrum and eye diagram of bitrate = 10 Gb/s, pump power = 0.5 W

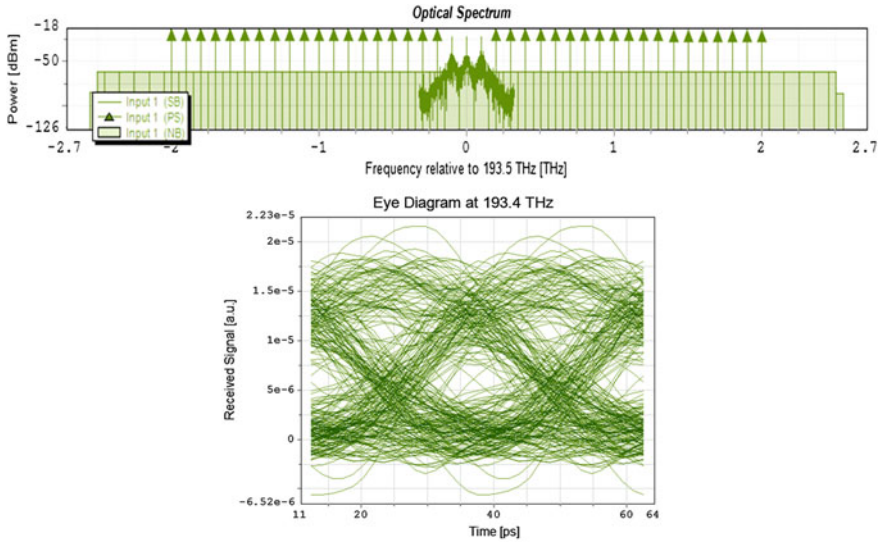


Fig. 5 Optical spectrum and eye diagram of bitrate = 40 Gb/s, pump power = 0.0 W

4.3 Simulation with BitRate = 40 Gb/S, Pump Power = 0.0 W

The simulated graph of optical spectrum and the Eye diagram for bit rate = 40×10^9 bit/s and Raman pump = 0.0 W, is shown in Fig. 5. 40 Gb/s causes 6 dB drop in optical signal-to-noise ratio (OSNR) and -18 dBm is peak value in Spectrum power.

4.4 Simulation with BitRate = 40 Gb/S, Pump Power = 0.5 W

To reduce the attenuation and dispersion seen in Fig. 6, Raman pump is changed to 0.5 W, so the peak value in Optical Spectrum power is 1 dBm which is quite better result. These results obtained from Figs. 3–6 are shown in Tables 1 and 2, for the bit rate of 10 and 40 Gb/s. Optical Spectrum and Eye diagram values are compared for those bit rates. Differentiating Optical Spectrum and eye diagrams in Figs. 3 and 5 in maximum power transmitted is -18 compared to with Raman Pump is very low. When, Raman Pump is set (0.5 W) the higher quantity of Q-factor, higher power, greater received signal and lower BER of received signals showing a better performance of this technique as compared to without Raman Pump.

Without Raman amplification, a 6-dB OSNR degradation occurs due to 6-dB increase in receiver bandwidth. With Raman gain, the OSNR improves at 40 Gbps,

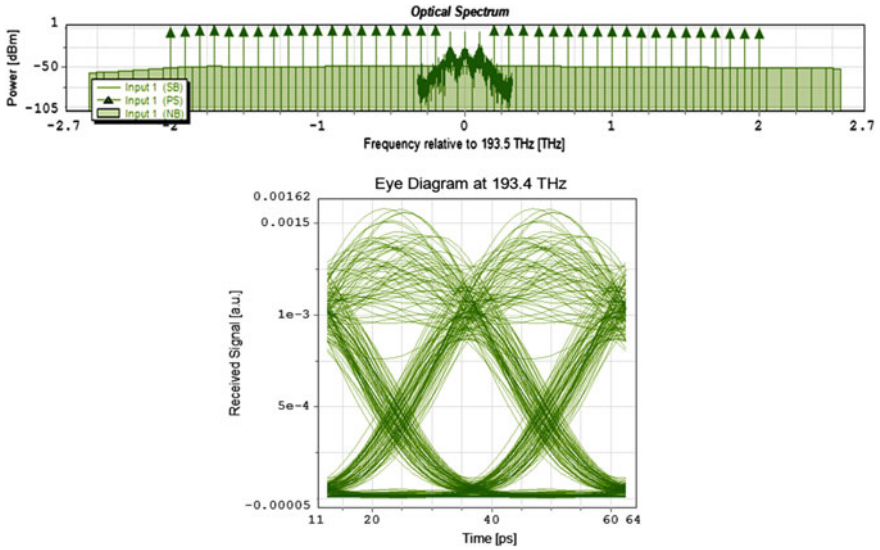


Fig. 6 Optical spectrum and eye diagram of bitrate = 40 Gb/s, pump power = 0.0 W

Table 1 Results of power and received signal

Bit rate (Gb/s)	Raman pump (W)	Power (dBm)		Received signal	
		Minimum	Maximum	Minimum	Maximum
	0	-144	-18	$-2.45e^{-6}$	$1.75e^{-5}$
10	0.5	-125	1	0	1.0013
	0	-126	-18	$-6.52e^{-6}$	$2.23e^{-5}$
40	0.5	-105	1	0	1.0016

Table 2 BER analysis

Bit rate (Gb/s)	Raman pump (W)	BER analysis (Input 1, sample time 0.5)			BER
		Q Effective	Q	Threshold used (a.u)	
	0	6.448	6.444	$5.585e^{-6}$	$5.7e^{-11}$
10	0.5	17.821	17.799	0.0001	2.44
	0	2.913	2.907	$5.691e^{-6}$	0.002
40	0.5	7.626	7.596	0.0002	$1.225e^{-14}$

allowing an upgrade to 40 Gbps. The result and comparison of the simulated system illustrates the benefits of distributed gain offered by Raman amplification.

As shown in Table 2, by analyzing Bit Error Rate (BER), the BER value for Bit rate 10 Gb/s is $5.7e^{-11}$ when Raman pump is set to 0 W and Q-factor is around 6. As concluded by Verma and Meena (2014) [13] a WDM system configured with an

EDFA obtains great uniformed gains and results nearly of 6 Q-factor. By including 0.5 W Raman Amplifier in design, the BERR value for Bit rate 10 Gb/s has reduced to 2.44 with increasing Q-factor around 17. The Q-factor obtained by the proposed method (6 dB) is better than Chang et al. (2006) [14] (1 dB).

5 Conclusion and Future Aspects

The performance of the simulated model of WDM with EDFA and Raman Amplifier are analyzed by demonstrating the system for distributed gain. In fiber optic communication system, WDM enables bidirectional communication as the technology allows multiplexes to more than one carrier signals onto a single fiber only by changing wavelength. The simulated results conclude that the WDM System joined-up with EDFA amplifies to the efficient Output Peak power. However, by using Raman Amplifier, more optimal distributed gain is obtained, since EDFA have restricted bandwidth. When Raman Amplifier is set with 0.5 W, for the Bit rate of 10 and 40 GB/s, the improved Q factors obtained are 17 and 7.5 respectively. For future investigation, comparison with integrating with EDFA-Discrete Raman, EDFA-Distributed Raman and other advanced technologies is required to compete the market requirements of the optical communication system of WDM system.

References

1. Khan, N., Yaqoob, I., Hashem, I.A.T., Inayat, Z., Mahmoud Ali, W.K., Alam, M., Shiraz, M., Gani, A.: Big data: survey, technologies, opportunities, and challenges. *Sci. World J.* **2014**, 1–18 (2014)
2. Cisco Global Cloud Index: Forecast and Methodology, 2015–2020, White Paper, pp. 1–41 (2016)
3. Cisco Visual Networking Index: Global Mobile Data Traffic Forecast, 2016–2021, White Paper (2017)
4. Redyuk, A., Stephens, M.F.C., Doran, N.J.: Characterisation of cascaded Raman-assisted fibre optical parametric amplifiers using WDM QPSK signals. *Opt. Fiber Commun. Conf.* **2**, 37–39 (2016)
5. Radioelektronika, C.: The Four-Channel WDM System Using Semiconductor Optical Amplifier Tomáš Ivaniga, Luboš Ovseník, Ján Turán. Department of Electronics and Multimedia Communications, Faculty of Electrical Engineering and Informatics, University of Technology, Košice. 6–9 (2016)
6. Putrina, J., Olonkins, S., Bobrovs, V.: Investigation of in-line EDFA performance dependence on channel spacing in WDM transmission systems. In: *Proceedings—2016 Advances in Wireless and Optical Communication. RTUWO 2016.* 17–21 (2017)
7. Rashed, A.N.Z.: New trends of forward fiber raman amplification for dense wavelength division multiplexing (DWDM) photonic communication networks. *Int. J. Tech. Phys. Probl. Eng.* **3**, 30–39 (2011)

8. Gaur, A., Rastogi, V.: Gain equalization of six mode groups using trench-assisted annular core EDFA. In: 2015 Workshop on Recent Advances in Photonics, WRAP 2015. pp. 3–6 (2017)
9. Malik, D., Pahwa, K., Wason, A.: Performance optimization of SOA, EDFA, Raman and hybrid optical amplifiers in WDM network with reduced channel spacing of 50 GHz. *Optik (Stuttg)* **127**, 11131–11137 (2016)
10. Mahran, O.: Performance study of macro-bending EDFA/Raman hybrid optical fiber amplifiers. *Opt. Commun.* **353**, 158–164 (2015)
11. VPI Photonics, VPIPlayer simulator. <http://www.vpiphotonics.com/>
12. Seraji, F.E., Kiaee, M.S.: Eye-diagram-based evaluation of RZ and NRZ modulation methods in a 10-Gb/s single-channel and a 160-Gb/s WDM optical networks. *Int. J. Opt. Appl.* **7**, 31–36 (2017)
13. Verma, D., Meena, S.: Gain flatness and bit error rate improvements for an EDFA in WDM system. **3**, 408–412 (2014)
14. Chang, S.H., Han, J.S., Chung, H.S., Kim, K., Ko, J.S.: Characteristics of low noise hybrid fiber amplifier. *Opt. Commun.* **261**, 269–275 (2006)

Vehicle Detection System Using Tunnel Magnetoresistance Sensor



Nurul A'in Nadzri, Chai Kar Hoe, Mohd Mawardi Saari,
Saifuddin Razali, Mohd Razali Daud and Hamzah Ahmad

Abstract Vehicle detectors are useful to provide essential information such as parking occupancy and traffic flow. To create one robust vehicle detector which works not only in controlled environment (i.e. indoor), but it should also work in outdoor environment, a vehicle detection using magnetic approach is proposed. The magnetic signal of a vehicle will be measured based on magnetic remanence technique where it will be processed to a cloud database. To achieve a low-cost and sensitive system, a Tunnel Magnetoresistance (TMR) sensor is employed. With the combinations of software filter and state machine's algorithm, the occupancy of the car park can be identified with high accuracy. After a few series of real field testing, it is shown that a vehicle in a parking lot can be detected by measuring the surrounding magnetic field that is disrupted by the presence of vehicles. The proposed system is tested for forward and reverse parking, and it shows a high accuracy detection for a B-segment sedan car. It can be expected that by using the proposed technique, detection of vehicles using a low-cost system with capability of online monitoring can be realized.

Keywords Tunnel magnetoresistance • Magnetic sensors • Vehicle detectors

1 Introduction

Intelligent transport [1], smart cities [2, 3] and Internet of Things [4] are terms that surround us all the time in this century. With growing population, mobility of people using vehicles will increase rapidly and this will result to severe issues such as parking problem of vehicles. Hence, intelligent and centralized solutions to lessen these problems are highly desired, where specifically in the case of vehicle parking problem, gathering and online monitoring data about traffic flow and

N. A. Nadzri · C. K. Hoe · M. M. Saari (✉) · S. Razali · M. R. Daud · H. Ahmad
Faculty of Electrical & Electronic Engineering, Universiti Malaysia Pahang,
26600 Pekan, Pahang, Malaysia
e-mail: mmawardi@ump.edu.my

absentees of vehicle in a parking slot are important. Based on the real-time data, traffic congestion and the required time to find a vehicle parking slot can be mitigated by efficiently controlling the flow of vehicles.

In conventional ways of vehicle detection, ultra-sonic sensor is used to obtain the information of parking spot due to its low cost, easy installation, and high accuracy. The vehicle detection using the ultrasonic sensor works by emitting radio waves and detecting the reflected radio waves. This method works efficiently in a controlled environment such as inside indoor; however, it is sensitive to the fluctuations of temperature and extreme air turbulence such as in stormy weather, causing unstable measurement with the loss of signal. Besides that, using the ultra-sonic sensor is not preferable for on-street parking where interference of the surrounding traffics may affect the detection of vehicles [5, 6].

Detection of vehicles using laser sensor is one of the popular methods its low cost and easy installation [7, 8]. However, the light of the laser is easily being distorted by weather and light conditions, making it not suitable for all-weather and outdoor vehicle detection usage [9]. In the case of detection using induction loop, this method requires magnetic fields to be generated and the magnetic responses from the metallic body of vehicles, i.e., effect of Eddy's current, are measured. However, this method consumes a higher electricity power to generate the magnetic fields and the system is not compact due to the size of induction loops [10].

In this paper, a magnetic remanence based detection technique is proposed using a low-cost and sensitive magnetometer with combination of an Arduino board and a Motorola M-WICOM platform of Beagle Bone Black (ARM microprocessor). The used platform has sufficient computing power and its functions can be extended for connectivity with cloud database and online monitoring. The magnetometer MAG3110 (Freescale) is used because it is small, low-power, and has digital 3-axis of detection fields. This sensor utilized next generation magnetic tunnel junction (MTJ) technology which enable itself to have high sensitivity under a very low magnetic field strength condition. MAG3110 is capable of detecting small changes in magnetic field with the sensitivity of $0.10 \mu\text{T}$. Furthermore, the size of Mag3110 is small, enabling a compact system, while having immunity to environment noises such as temperature, wind and rain water.

2 Methodology

2.1 Hardware Setup

As for hardware setup, it can be separated into two parts namely a wireless sensor node and a control terminal.

On the wireless sensor node side, the magnetometer MAG3110 is connected to the Arduino board and the x -, y -, and z -axis magnetic field data will be transferred over the air via a 2.4 Ghz RF module.

On the control terminal side, another RF module is connected directly with M-Wicom Platform of Beagle Bone Black for data logging, data processing and decision-making purposes via UART serial protocol. As for the positions of the wireless sensor node, it is placed in the middle of a parking space, having a 5 m length and 2.5 m width.

2.2 Parking Occupancy Detection Algorithm

The occupancy of a parking space can be categorized under binary recognition problem, which possess two states; vacant and occupied conditions.

During parking process of a vehicle, it will undergo entering- and parking-stop stages. Initially, the parking space is vacant. During this vacant condition, the sensor will obtain the background magnetic field of x -, y -, and z -components for background references. For the next phase, when the vehicle is entering the car park regardless of forward or reverse position, it will create a disturbance and causing the surrounding magnetic fields to fluctuate. Next, the parking space is now occupied, and the vehicle will create a stable disturbance on the background magnetic fields. The magnetic fields would also have fluctuated when the vehicle is leaving the parking space. Finally, the parking space is vacant when the vehicle left and the sensor will obtain the background magnetic field again.

As for vehicle detection, it is preferable to use magnitude instead of individual magnetic components. The vehicle detection algorithm based on vector magnitude will be more accurate compared individual x -, y -, and z -axis magnetic fields. The intensity of the magnetic field vectors would be

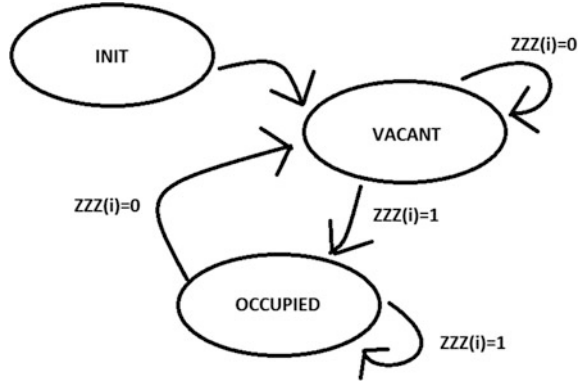
$$G(i) = \sqrt{X_i^2 + Y_i^2 + Z_i^2}, \tag{1}$$

where X_i , Y_i and Z_i is the magnetic fields of x -, y - and z -axis, respectively.

All signals obtained via sensor will include noises. Hence, moving average filter is introduced to reduce the effect due to random variation. The equation of moving average is given by

$$A(i) = \begin{cases} \frac{G(i) + G(i - 1) + \dots + G(1)}{i} & \text{for } i < Z \\ \frac{G(i) + G(i - 1) + \dots + G(i - Z + 1)}{Z} & \text{for } i \geq Z \end{cases} \tag{2}$$

Fig. 1 Algorithm's state machine



$G(i)$ is the magnetic vector magnitude obtained earlier and Z is the averaging filter buffer size. Note that the higher the buffer size, the smoother the graph will be.

Based on all above criteria, the proposed algorithm for the detection system state is shown in Fig. 1. The system state will consist of State: {INIT, VACANT, OCCUPIED}, Input: [ZZZ(i)]: {0, 1}, and Output: [DD(i)]: {0, 1}. The objective of this system state is to detect the occupancy of parking space, whenever there is a vacancy in the spot, the output would yield $DD(i) = 0$, which indicates no car. Otherwise $DD(i) = 1$ indicates it is occupied.

For initialization state $S1$: {INIT}, before the program begins, the parking lot must be ensured vacant as this is the pre-requisite for the detection algorithm to work. When the initialization finishes, the sensor will obtain the surrounding magnetic field data and calculate the desired threshold. When the initializing time passes a pre-defined value, it will jump to state $S2$: {VACANT} where it starts to detect changes in magnetic fields. When the obtained magnetic field data has exceeded certain the pre-determined threshold (i.e., obtained data exceed of G from calibrated value) for a certain count (i.e. parameter H), it will go for the next state. Otherwise, if it stays between the predefined value, it will yield $ZZZ(i) = 0$ and continue to monitor for major changes in magnetic fields. During the state $S2$: {VACANT}, the system will output $DD(i) = 0$ to indicate there is no car in the parking space. A reset count system (i.e. parameter I) has been added to act as a failsafe mechanism in the case of variable H is being triggered by false alert. When the parking space is occupied by a vehicle, the system state will turn to $S3$: {OCCUPIED}. The sensor will continue to obtain changes in magnetic fields. During this state, the system will yield $DD(i) = 1$ to indicate that the parking space is being occupied. Occupancy of parking space is determined by the flow chart as shown in Fig. 2.

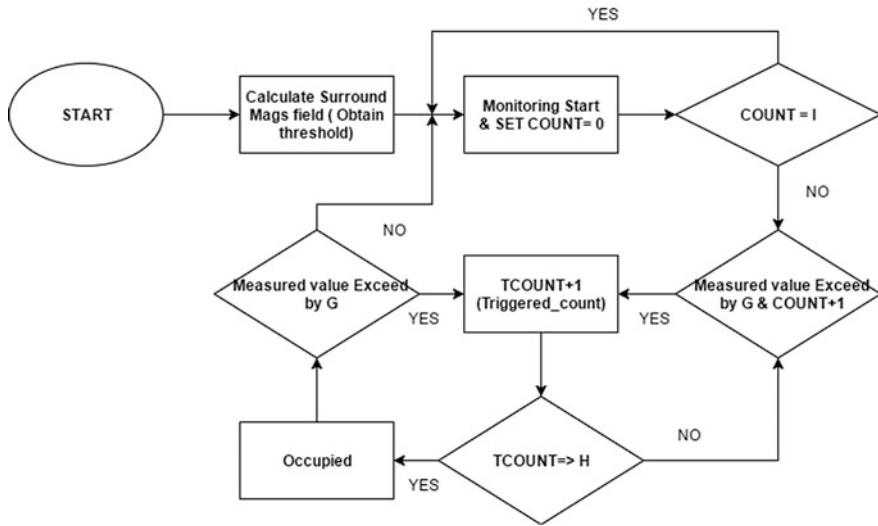


Fig. 2 Flow chart of the proposed algorithm

3 Results and Discussion

3.1 Initial Field Testing Magnetic Response

In this preliminary study, the size of car was fixed as a constant variable since the difference in size of car will yield different waveform. Figure 3a shows the magnetic responses for a B-segment sedan car parked on a parking space using forward parking method, i.e., the front part of the car including its engine will first pass through the magnetic sensor located in the middle of the parking space. Note that the sampling rate of data obtained was fixed at 15 Hz or 1 sample every 0.067 s.

From Fig. 3a, that magnetic signals fluctuated when the car was entering or leaving the sensor. When the car completely stopped, or left, the signal became stable.

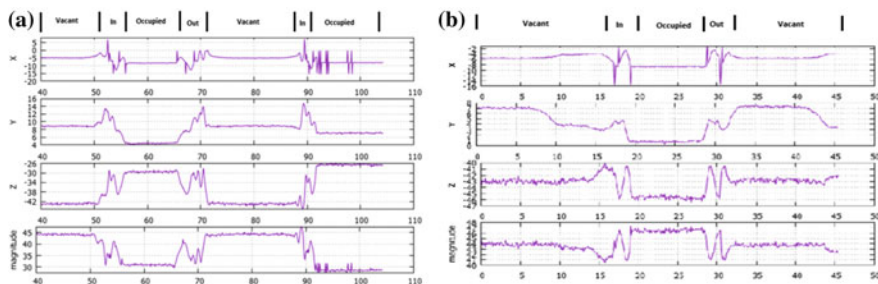


Fig. 3 a Magnetic response for forward parking. b Magnetic response for reverse parking

However, when the vehicle was in the parking slot and completely stopped, the signal fluctuation of the x -axis magnetic field was observed. This was due to the magnetization and demagnetization of the car air conditional compressor's clutch. Furthermore, loose metallic parts under vehicles will vibrate and this can contribute to the spikes in the detected magnetic signal. Nevertheless, the spikes can be eliminated by using a filter and this enhances the precision in car detection. The disturbance of environmental magnetic field can be verified by comparing the magnitude between a vacant and an occupied parking slot. When the parking space was occupied, the sensor detected a significantly lower magnitude as the car acted as a magnetic shield between the sensor and earth's magnetic field. Based on the measured magnetic responses, the magnitude of the magnetic field was reduced when the car entered the parking space. Moreover, the magnitude of the detected magnetic field showed a positive gradient when the car was leaving the parking space.

Figure 3b shows the magnetic response for a vehicle parking using reverse parking method, i.e., the boot of the car will first pass the magnetic sensor. The magnitude of an occupied parking space using reverse parking method showed a higher value compared to the magnitude when the parking space was vacant. The difference in the signal characteristics between occupied states of forward and reverse parking methods was thought to be due to the different metallic parts of the car detected by the sensor. Nevertheless, the disturbance of magnetic signal can be used as an indicator for the presence of vehicles.

To increase detection sensitivity and eliminating the noises in the measured data, a digital moving average filter was used. In Fig. 4, the dotted line is the initially obtained data containing noises. While the solid line represents the filtered data with buffer size of $Z = 20$, where the output was smoothed.

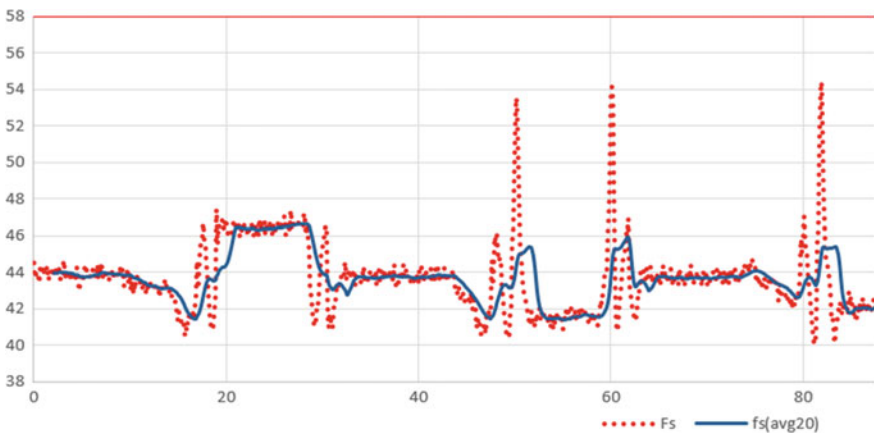


Fig. 4 Unfiltered versus filtered data

3.2 Real-Field Testing with Working Detection Algorithm

The coefficients of the proposed algorithm were set as follows: $G = 1$, $H = 30$ (where if H has been triggered for more than 30 times, it will determine that a vehicle is exist in the parking space) and $I = 450$ (where the counter of H will be reset after a half minute as the system gathers 15 data in one second, i.e., 15 Hz).

The Parameter $G = 1$ is chosen based on initial field testing magnetic response, whenever the instantaneous magnetic field are larger or smaller by $1 \mu\text{T}$, it will increase counter H by 1. On the initial field testing, whenever the vehicle is parked using forward parking, the magnitude of magnetic field would be lower by $10 \mu\text{T}$ compared to initial value when there exists no vehicle. As for reverse parking, the magnitude of occupied car park is higher by 1.5 times compared to vacant car park. Thus, this made $G = 1$ is a very good threshold value for vehicle detection purposes.

The parameter H is introduced to prevent false detection and acts as a failsafe system. In real world scenario, the magnetometer will also pick up noisy spikes from surrounding environment, hence the parameter $H = 30$ was introduced. Whenever the system pick-up changes in the magnetic field compared to initial value for 30 times, it will classify as a vehicle is present in the parking space. In the proposed algorithm, every second the magnetometer will read 15 sampling data, thus continuous changes in magnetic field for two consecutive seconds, it will indicate a vehicle exists.

Parameter I was introduced to complement the existence of parameter H . The purpose of parameter I was to reset H counter every 30 s in the case counter H had been increased previously due to false alert. In the proposed algorithm, the data sampling rate was fixed at 15 Hz, thus parameter I was set to 450 for reset process in every half minute.

Using above parameters, the experiment result is shown in Table 1. From the tabulated results in Table 1, the vehicle detection rate was 95% for the current system and its detection algorithm. In the 20 times of parking attempts, 10 of the samples were using B-segment sedan cars and another 10 of samples were using A-segment mini cars.

In the 10 attempts of B-segment sedan and A-segment mini cars, respectively, 5 attempts were reverse parking and another 5 were forward parking. The proposed remanence magnetic based detection system with the threshold algorithm could identify all the presence of the B-segment sedan cars in the parking space. On the other hand, in the case of A-segment mini cars, only 5 attempts of forward parking and 4 attempts of reverse parking could be detected by the proposed system. One of the reverse parking was not detected due to less soft and hard metallic parts appear

Table 1 Result of real field testing using proposed algorithm

Number of parking attempts	Number of vehicle detected in the car park	Accuracy of the threshold-based algorithm
20	19	0.95

in the bonnet area of the vehicle bodies, resulting in a false detection by the algorithm. Fundamentally, different shape and size of vehicles will produce different magnetic responses; however, the disturbance of environmental magnetic field due to the vehicle can be accurately detected by using a sensitive sensor and a superior algorithm. Further improvement of detection rate could be expected by optimizing the algorithm and the position of the magnetic sensor.

4 Conclusion

In this paper, vehicle detection in parking space using magnetic remanence technique for real-time monitoring system is presented. The disturbance of surrounding magnetic fields caused by the hard and soft metallic parts of vehicle bodies could be detected by using a Tunnel Magnetoresistance sensor. The detected signals were transmitted to the M-Wicom Platform of Beagle Bone Black using the RF modules. Based on the analysis, the proposed threshold-based vehicle detection algorithm showed a high detection accuracy of 95%. For future works, the experiment can be extended with more sample of vehicle including C-, D-, and E-segment cars as well as the optimization of the detection algorithm. This vehicle parking detection system can be extended to support certain additional features such as the direction of vehicle entering the car park, and the size of vehicle.

Acknowledgements This work was supported by Ministry of Higher Education of Malaysia under grant number of RDU 160115 and Research Management Center of Universiti Malaysia Pahang under grant number of RDU 170377.

References

1. Schulz, W., Geis, I.: Future role of cost-benefit analysis in intelligent transport system-research. *IET Intell. Transp. Syst.* **9**, 626–632 (2015)
2. Mone, G.: The new smart cities. *Commun. ACM.* **58**, 20–21 (2015)
3. Glasmeier, A., Christopherson, S.: Thinking about smart cities. *Camb. J. Reg. Econ. Soc.* **8**, 3–12 (2015)
4. Lee, I., Lee, K.: The internet of things (IoT): applications, investments, and challenges for enterprises. *Bus. Horiz.* **58**, 431–440 (2015)
5. Mimbela, L.E.Y., Klein, L.A.: A summary of vehicle detection and surveillance technologies used in intelligent transportation systems. <http://www.nmsu.edu/~traffic/> (November, 2000)
6. Gorden, R.L., Reiss, R.A., Haenel, H., Case, E.R., French, R.L., Mohaddes, A., Wolcott, R.: Traffic control systems handbook, FHWA-SA-95-032, Washington, D.C., Federal Highway Administration, U.S. Department of Transportation, February, 1996A
7. Texas Transportation Institute. Alternative vehicle detection technologies for traffic signal systems. Technical Report. Austin. 2008.A
8. US Department of Transportation, Federal Highway Administration: A new look at sensors. *Public Roads.* **71**(3), 32–39 (2007)

9. Abdelbaki, H.M., Hussain, K., Gelenbe, E.: A laser intensity image based automatic vehicle classification system. In: 2001 Proceedings of the IEEE Conference on Intelligent Transportation Systems, pp. 460–465
10. Mishra, D.P., Asutkar, G.M.: Vehicle detection and classification using wireless sensor network. *IJAREEIE* 2(10) (2013)

Ergonomic Study on Wrist Rehabilitation Therapy (WRist-T) Device



Nurul Ain Abdul Shukor, Idris Mat Sahat
and Mohd Azrul Hisham Mohd Adib

Abstract The emerging issue in complex joints such as human wrist is usually the disability to be precisely coordinated with a traditional mechanical joint. In such cases, mechanical differences between human and robotic joints could lead to musculoskeletal disorder (MSD) and overconstraint due to the device over rotation, misalignment of the rotation axis and also the design of the device. This paper focuses on ergonomic comparison studies between the previous and present WRist-T devices. The result of the ergonomic study especially on anthropometry and ergonomic evaluation shows that the present model is better than the previous one.

Keywords Wrist rehabilitation device • Musculoskeletal diseases
Ergonomic modification

1 Introduction

Traumatic brain injury or stroke is a common non-communicating disease in Malaysia. This is because of the poor lifestyle particularly bad dietary pattern and stress from work. There are two types of strokes which are ischemic and hemorrhagic. In an ischemic stroke, a blood vessel becomes blocked, usually by a blood clot, causing a portion of the brain to be deprived of oxygen and ultimately stop functioning. Ischemic strokes account for 80% of all strokes. A hemorrhagic stroke occurs when a blood vessel that carries oxygen and nutrients to the brain, bursts and spills blood into the brain region. This causes a portion of the brain to be deprived of oxygen and will stop functioning eventually. Hemorrhagic stroke accounts for about 20% of strokes. The casualty rate is high yet it is not the current issue for this product

N. A. Abdul Shukor · I. Mat Sahat · M. A. H. Mohd Adib (✉)
Medical Engineering & Health Intervention Team (MedEHiT),
Human Engineering Group, Faculty of Mechanical Engineering,
Universiti Malaysia Pahang, 26600 Pekan, Pahang, Malaysia
e-mail: azrul@ump.edu.my

© Springer Nature Singapore Pte Ltd. 2018
M. H. A. Hassan (ed.), *Intelligent Manufacturing & Mechatronics*,
Lecture Notes in Mechanical Engineering,
https://doi.org/10.1007/978-981-10-8788-2_50

development. The project is developed for stroke survivors. Stroke is one of the major factors leading to a decreased motor function of the human upper limbs. One of the important parts affected by strokes is the wrist. The patients are significantly restricted in their daily social and household activities. It is known that an appropriate post-traumatic care and rehabilitation therapy is required for recovering patient's lost abilities and disturbed daily activities [1–3]. Normally, this can be achieved through repetitive and long-term rehabilitation process. Though these are helpful for improving hand strength and preventing future injuries, conventional rehabilitation exercise is quite dreary and tough to regularly perform the exercise, thus delaying full recovery [4].

Presently, two WRist-T designs have been developed. Both designs have two modes of exercises: flexion/extension and radial/ulnar deviation [5, 6]. According to physiotherapist specialist, the most important exercise for the wrist is flexion and extension. This device is not trying to replace the role of PT 100% but more for the purpose of providing easy physiotherapy session to the patients with minor supervision from the PT at the hospitals or rehabilitation centers. The session can be conducted at patient's home especially for patients having transportation problem and patients living distantly from the hospitals.

In this study, the aim was to observe and compare the effectiveness between Prototype A and B of WRist-T devices based on ergonomic study.

2 Procedure

2.1 Anthropometry

Anthropometry refers to the study of human physical measures such as the size, form and functional capacities and their interactions with the engaged tasks, tools, machines, vehicles and other equipments to ensure that the equipments are safe and comfortable to be used [7]. In this case, the focus is the distance between the center of grasp until the wrist length and the distance between the elbow to the wrist length while sitting. Figure 1 shows the center of grasp to the wrist length and elbow to the wrist length while sitting. The scope for anthropometric data involves older

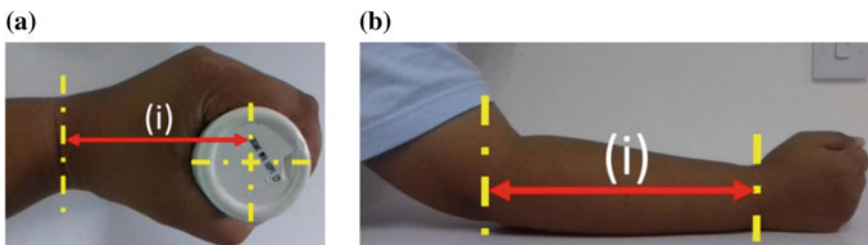


Fig. 1 a(i) Center of grasp to wrist length; and b(i) wrist to elbow length

Table 1 Anthropometric data for older Malaysian males and females aged 60 and above

Dimensions	Male	Female
Center of grasp to wrist length (cm)	8.9	8.6
Wrist to elbow length (cm)	27.7	25.8

Malaysian males and females aged 60 years old and above [8] as shown in Table 1. These two anthropometry measures are the major considerations in the device development.

2.2 Development of Prototype A and Prototype B of WRist-T

In wrist rehabilitation, there is a limited range of movements: flexion/extension and radial/ulnar deviation. The main challenge is to perform the overall movements by a single rehabilitation device without any help from rehabilitation professionals. Figure 2 shows the previous WRist-T device of Prototype A and the current WRist-T device of Prototype B, consisting of the control system and screen, detachable hand grip, palm rest, fixed arm rest for Prototype A and detachable arm rest for Prototype B. The devices provide the capability of performing rehabilitation exercises at home or at any places instead of in a rehabilitation clinic. Figure 3 shows the perspective side view of the WRist-T device in use for wrist flexion/extension and radial/ulnar of Prototype A and Prototype B.

The designs are devised using SolidWorks 3D CAD software that allows direct prototyping with 3D printing technology. Prototype B design is almost similar to Prototype A but with several improvements on the control system, screen positioning and detachable arm rest. Figure 4 shows the dimension of Prototype A and Prototype B. Specification for both prototypes dimension is shown in Table 2. Prototype A and B differ in term of arm rest length. The length of Prototype A and Prototype B is 15 cm and 35 cm respectively. The total cost for Prototype B is lower than A.

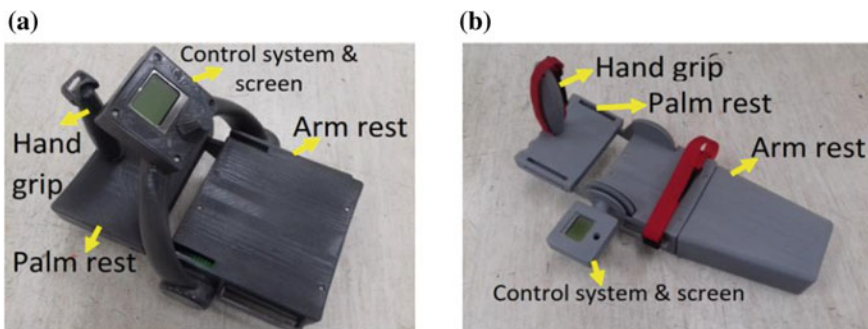


Fig. 2 WRist-T device **a** Prototype A; and **b** Prototype B

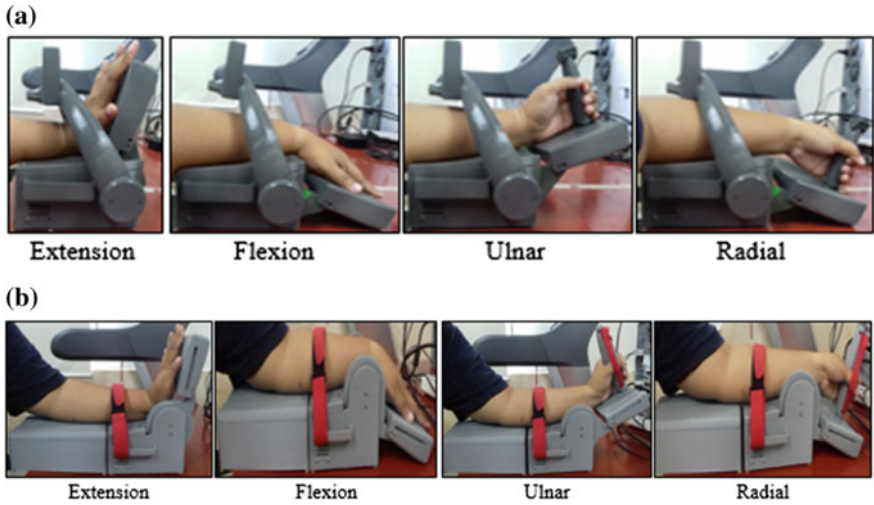


Fig. 3 Perspective views of **a** Prototype A; and **b** Prototype B in an embodiment to give flexion/extension and radial/ulnar deviation of the wrist

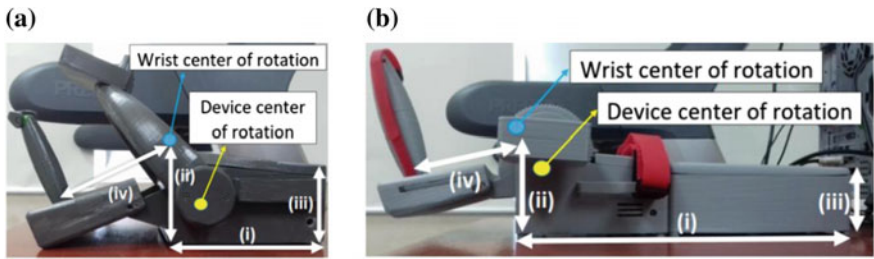


Fig. 4 **a** Prototype A; and **b** Prototype B dimensions where (i) arm rest length; (ii) wrist height; (iii) elbow height; and (iv) wrist to hand grip length

Table 2 WRist-T prototype measurement

Dimensions	Prototype A	Prototype B
Arm rest length (cm)	15	35
Wrist height (cm)	8	8
Elbow height (cm)	7	7
Wrist to hand grip length (cm)	10.5	10.5

3 Result and Discussion

3.1 Function

Both prototypes are compared from ergonomic perspective based on their functions, cost, design, safety, advantages and disadvantages. Based on functionality, both prototypes have flexion, extension, radial deviation, ulnar deviation, active rehabilitation and non-active rehabilitation.

3.2 Design

An efficient rehabilitation device will give good results on patient recovery. For that purpose, having a good alignment of the wrist center of rotation and device center of rotation is important. As shown in Fig. 4 both prototypes are not well aligned. This result in the changes in the wrist center of rotation position as the palm rest pushes the wrist backward during extension. The distance of the center of grasp to wrist length also contributes in the wrist center of rotation position. Therefore, the length between the hand grip and wrist must be around 9 cm to make the wrist stay in its axis as shown in Table 1. Prototype A and B specification in Table 2 shows that both Prototype A and B have wrist to hand grip length of 10.5 cm which is 1.5 cm longer than the suitable length, resulting in changes of wrist position.

Secondly, Prototype B's control system and screen are in suitable position on the left side of the platform arm. Unlike Prototype B, the control system and screen in Prototype A are not in suitable position where they are placed above the arm. This constricts hand movement during extension as shown in Fig. 3a. Prototype A also has more parts than Prototype B, resulting in longer time to fabricate using 3D printing technique.

3.3 Safety

For a safe and comfortable product, the arm rest must possess suitable height and length. A good armrest will protect the patient from having musculoskeletal disorder. Armrests that are too high can cause 'raised shoulders', which is harmful in the long run. Armrests that are too low can cause leaning. The armrest should be long enough to provide adequate coverage of support. A suitable armrest length for this device should be from the wrist until the elbow. Based on Table 1 the mean wrist to elbow length for male and female are 27.7 cm and 25.8 cm respectively, which means a suitable length should be around 28 cm. Prototype A and B specification in Table 2 shows that Prototype A wrist to elbow length is 13 cm shorter, and Prototype B is 7 cm longer than the suitable length. The device is designed to

Table 3 Ergonomic evaluation^a

Traits	Prototype A	Prototype B
Sufficient arm rest length	1	2
Suitable arm rest height	2	2
Suitable wrist to hand grip length	1	1
Center of rotation alignment	2	3
Degree of rotation	4	4
Net	10	12
Rank	2	1

^aResponses are indicated as, 1 = Poor, 2 = Satisfactory, 3 = Good, 4 = Very Good

be placed on the table or bed for bed-ridden patients, with adjustable heights while conforming to the differences in patient anthropometry. Both prototypes have non-adjustable wrist height and elbow height of 8 cm and 7 cm respectively. Both prototypes have a good degree of rotation. Table 3 shows ergonomic evaluation.

3.4 *Advantages and Disadvantages*

Prototype A advantage is having a good degree of rotation, while the disadvantages are higher cost, longer fabrication time, no active rehabilitation, insufficient arm rest length, unsuitable control system and screen position and bad alignment of gear and wrist axis of rotation. Prototype B advantages are lower cost, shorter fabrication time, good degree of rotation, suitable control system and screen position, and sufficient arm rest length, while the disadvantages are higher cost, no active rehabilitation, and bad alignment of gear and wrist axis of rotation.

3.5 *Discussions*

Prototype B ranked as 1 followed by Prototype A as shown in Table 3. Prototype B also has closer alignment than Prototype A as shown in Fig. 4. As a result, Prototype B is chosen over Prototype A as it has more advantages, shorter fabrication time, low cost and safer. It is highly recommended to make an adjustable arm rest and decrease the wrist to hand grip length. The design needs several adjustments by decreasing the arm rest length to a suitable length and by correcting the alignment.

4 Conclusion

This paper presents the ergonomic studies of wrist rehabilitation therapy (WRist-T) device for a stroke patient. Overall, Prototype B is chosen over Prototype A as its design meets the required ergonomic condition, safety, design and function.

References

1. Bayona, N., Bitensky, J., Salter, K., Teasell, R.: The role of task-specific training in rehabilitation therapies. *Top. Stroke Rehabil.* **12**(3), 58–65 (2005). <https://doi.org/10.1310/BQM5-6YGB-MVJ5-WVCR>
2. Bonita, R., Beaglehole, R.: Recovery of motor function after stroke. *Stroke* **19**, 1497–1500 (1988). <https://doi.org/10.1161/01.STR.19.12.1497>
3. Cramer, S.C., Riley, J.: Neuroplasticity and brain repair after stroke. *Curr. Opin. Neurol.* **21**(1), 76–82 (2008). <https://doi.org/10.1097/WCO.0b013e3282f36cb6>
4. Hsieh, W.M., Hwang, Y.S., Chen, S.C., Tan, S.Y., Chen, C.C., Chen, Y.L.: Application of the Blobo bluetooth ball in wrist rehabilitation training. *J. Phys. Ther. Sci.* **28**, 27–32 (2016)
5. Adib, M.A.H.M., Sahat, I.M., Ahmad@Manap, Z., Ghani, S.A.C., Hasni, N.H.M., Daud, N.: Development of the wrist rehabilitation therapy (WRist-T) device based on automatic control for traumatic brain injury patient. In: *International Medical Device and Technology Conference*, pp. 152–155 (2017)
6. Adib, M.A.H.M., Sahat, I.M., Ahmad@Manap, Z., Ghani, S.A.C., Hasni, N.H.M., Daud, N.: Automatic control of wrist rehabilitation therapy (WRist-T) device for Post-Ischemic stroke patient. In: *International Conference on Biomedical Engineering* (2017)
7. The National Institute for Occupational Safety and Health (NIOSH). Centers for Disease Control and Prevention. <https://www.cdc.gov/niosh/topics/anthropometry/default.html>
8. Rosnah, M.Y., Sharifah Norazizan, S.A.R.: Anthropometry dimensions of older Malaysians: comparison of age, gender and ethnicity. *Asian Soc. Sci.* **5**(6), 133–140 (2009)

Pressure Transient Characteristic in Fluid Condition During Opened and Closed Water Line Based on Experimental Method



Syarizal Bakri, Ihsan Ismail, Ahmad Anas Yusof and Suhaimi Misha

Abstract This paper describes the pressure characteristic of fluid in a water line. There are many factors that influences pressure surge in a pipeline system such as fluid velocity, length, diameter and material of pipe. In this study, experimental data will be analysed for pressure transient study by using different water velocity. The relationship between fluid velocity and pressure will be explained throughout the paper. An experiment has been conducted in two different kinds of water line, which are known as open and close line. To study close water line system certain graph will be analyse to study pressure reaction when changing of the velocity of water. The result of this experiment is the change of fluid velocity may affect the rising or falling of the water pressure. The change of fluid velocity when closing the valve is related to water hammer phenomenon. Water hammer is happening when a fluid in motion is forced to stop or change in flow direction. Experimental data of this study proved that velocity is one of the factor that affects the fluid pressure in the piping system.

Keywords Fluid system · Water line · Pressure transient

1 Introduction

The definition of fluid is a substance that can flow easily. Liquid and gases are both refer to the fluid. The pressure in fluid applies in all direction since it has no definite shape. Fluid pressure does not depend on the shape and size of the container. Pressure transient is the analysis of pressure changes over time, especially those associated with small variations in the volume of fluid. In most piping system tests,

S. Bakri (✉) · I. Ismail · A. A. Yusof · S. Misha
Faculty of Mechanical Engineering, Universiti Teknikal Malaysia Melaka,
Hang Tuah Jaya, Durian Tunggal, 76100 Alor Gajah, Melaka, Malaysia
e-mail: syarizalbakri@yahoo.com

A. A. Yusof
e-mail: anas@utem.edu.my

© Springer Nature Singapore Pte Ltd. 2018
M. H. A. Hassan (ed.), *Intelligent Manufacturing & Mechatronics*,
Lecture Notes in Mechanical Engineering,
https://doi.org/10.1007/978-981-10-8788-2_51

a limited amount of fluid is allowed to flow from the formation being tested and the pressure at the formation monitored over time. Then, the flow is closed by a valve and the pressure monitored while the fluid within the formation equilibrates.

There are many parameters that effect the pressure characteristic behaviors in the circuit such as pressure source, pump type, type of pipeline etc. All these parameters can affect the pressure behaviors because the change of the properties of the water in the system such as flowrate and resistance of water to the wall. The pressure surge from the circuit will determine the occurrence of the water hammer in the system. The result shows that water hammer can occur during certain pressure range in a rigid pipeline.

Fluid pressure can occur either in open system or closed system. Closed fluid system is when the fluid is contained in the system which it retained and recirculated through the system [1]. Examples of closed systems are blood circulating in the body, brake system in car, and hydraulic jacks. The fluid can be either static when the system is not moving or dynamic when the system is running. The advantages of this system are the direction can be reversed without the use of valve and system can run at higher pressure with less fluid flow. While the disadvantages are it is difficult to repair if damage and may involve the usage of expensive components [2].

2 Methodology

In this system, the pump, motor, and valve are connected to the reservoir. The fluid flows from the pressure source to perform certain tasks and return to the reservoir. A valve will be used to control the flow of the fluid. The pressure of the fluid in the piping system is constant if the fluid travels at the same velocity. There will be a pressure difference when the valve is closed. This is because the fluid pressure from the pump is continuously supplied to the piping system. The system is designed so that it is easily maintained at the lowest cost possible. However, such design might create a disadvantage where it could create excessive pressure when the pump is still pumping with a valve closed. The large reservoir is used to prevent fluid getting an excessive heat. Pump inlet creates a vacuum condition that allowing atmospheric pressure from surrounding to force the liquid from the reservoir into the pump line. Then this liquid will be transferred to the pump outlet before being delivered to the pipe. The water flow through the pipe, pressure sensor, valve, and back to the reservoir. The pressure of the water flow can be obtained from the pressure sensor. The valve will be closed to observe if there is pressure difference during the water flow being stopped. This step is repeated by different pump speed input. Figure 1 shows the test rig setup of the water line.

Tables 1 and 2 describe the characteristic of pump and pressure sensor. The pump has a three-speed setting, which is based on power input of 35, 45 and 50 W. Current in all three sets are 0.16 A, 0.2 A, and 0.23 A respectively. A centrifugal pump is used in the experiment.

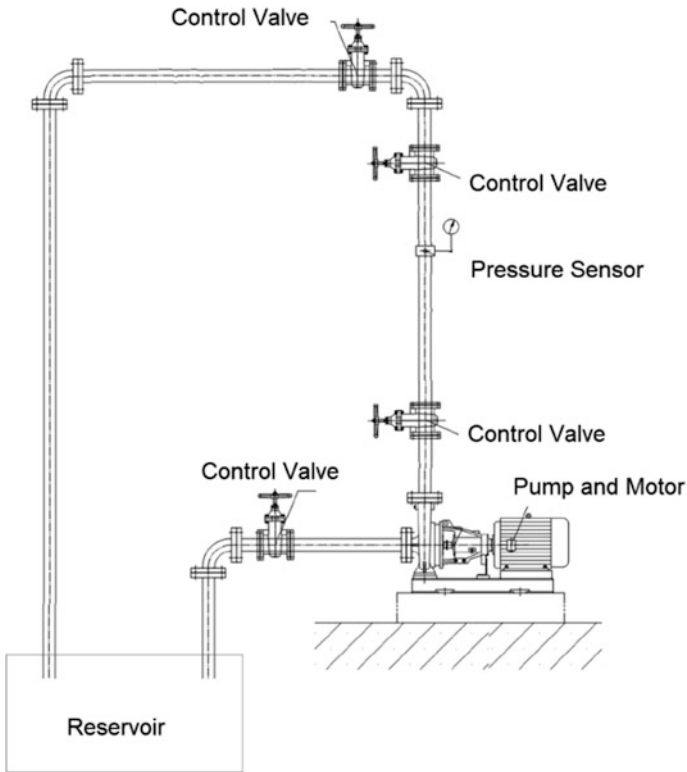


Fig. 1 Schematic diagram of the experiment

Table 1 Pump characteristic

<i>Specification</i>	
Product name	UPS 15-50 130
<i>Technical</i>	
Speed input	3
Head max	50 dm
<i>Liquid</i>	
Pumped liquid	Water
Liquid temperature range	2–110 °C
Liquid temperature during operation	60 °C
Density	983.2 kg/m ³
<i>Electrical data</i>	
Power input in speed 1	35 W
Power input in speed 2	45 W
Max. power input	50 W
Current in speed 1	0.16 A
Current in speed 2	0.2 A
Current in speed 3	0.23 A

Table 2 Pressure sensor characteristic

Product specification	
Measuring principle	Piezo-resistive (poly-crystalline silicon thin film structure on high-grade steel membrane)
Pressure type	Relative pressure
Output signal	0–20 mA
Electrical measuring connector	6 pole device connector, M16 × 0.75

3 Result and Discussion

3.1 Opened Valve Condition

The results show the pressure reading that were obtained by the pressure sensor. In Fig. 2, the pump was turned on for input speed number 1 that produces 35 W of power and, input speed number 2 that produce 45 W of power.

From Table 3 the highest pressure recorded during input speed number 1 is 0.1449 bar when $t = 15.50$ s and the lowest pressure is 0.0946 when $t = 8.10$ s. Meanwhile, for input speed number 2, the highest pressure recorded is 0.2256 bar when $t = 29.70$ s and lowest pressure is 0.1753 bar when $t = 5.40$ s.

Table 3 shows that the pressure characteristic with input speed number 1 is higher than input speed number 2. This result shows that when there is an increasing of water velocity, there will be a decreasing value of pressure. The result shows pressure reading that was obtained by the pressure sensor.

Fluid velocity will change if the internal flow area changes. For example, if the pipe size is reduced, the velocity will increase and act to decrease the static pressure. If the flow area increases through an expansion or diffuser, the velocity will decrease and result in an increase in the static pressure. The application of this

Fig. 2 Pressure transient during opened valve condition of fluid for two different speed pump: 35 W power input speed no 1 and 45 W power input speed no 2

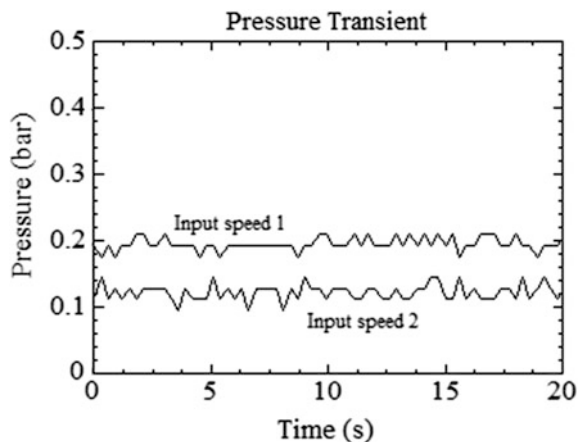


Table 3 Numerical data for opened valve condition

35 W power input speed no 1		45 W power input speed no 2	
Highest pressure	Lowest pressure	Highest pressure	Lowest pressure
0.1449 bar at (15.60 s)	0.0946 bar at (8.10 s)	0.2256 bar at (29.70 s)	0.1753 bar at (5.40 s)

situation can be applied to the water spray system. But in this experiment, the diameter of the pipe is constant, the change of velocity was controlled by pump’s speed.

3.2 Closed Valve Condition

The value of pressure surge is obtained by calculating the difference of pressure during closed valve condition and opened valve condition. From Fig. 3 the sudden increasing of pressure in water flow happens when the valve was turning off. Referring to Table 4 that shows a numerical value of pressure surge where 0.251 bar and 0.5336 bar for pump’s speed number 1 and 2 respectively. It is confirmed that higher velocity of the water will give a higher value of pressure surge of fluid in the piping system.

Fig. 3 Pressure transient of fluid during closed valve condition for two different speed pump: 35 W power input speed no 1 and 45 W power input speed no 2

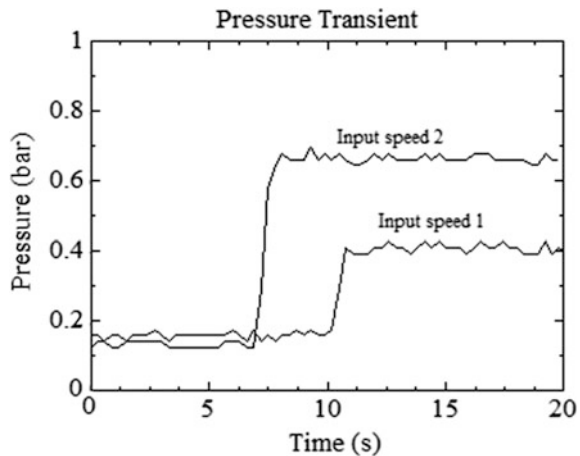


Table 4 Numerical data for closed valve condition

Value of pressure surge (bar)	
35 W power input speed no 1	45 W power input speed no 2
0.2515	0.5336

Pressure surge incident that occurred in pipe show that water hammer phenomenon happened in the pipeline after the valve closed. This phenomenon occurred because the momentum of the fluid abruptly stopping creates a pressure wave that travels through the media within the pipe system, subjecting everything in that closed system to significant forces. The changes in direction of the fluid cause massive forces back through the pipe. Therefore, when the power of pump increase, the value of pressure surge when the valve closed is higher.

To make some improvement of this experiment, the reading of flowrate should be recorded. This parameter will help in giving the exact value of fluid velocity when the increasing or decreasing of pressure occurred in the pipeline.

4 Conclusion

Basic pressure characteristic of water line has been studied by using two different speed sets. The velocity of water that flow in piping system was controlled by the pump's speed. Based on the result, it was shown that the velocity of fluid may affect the rising and falling of the pressure. For an open valve water system, higher velocity gives less pressure compared to the lower value of velocity. The highest pressure recorded for speed number 1 is 0.1449 bar while the highest pressure for speed number 2 is higher which is 0.2256 bar. Meanwhile, when the water system is being stopped by the valve, pressure rises when velocity increases. The pressure surge recorded using speed number 1 is 0.2515 bar while for speed number 2 is 0.5336 bar. Thus, pressure surge can be minimised by controlling the velocity of the water. Pressure surge control had been applied in many industries to protect the equipment from damage. In a further study, a simulation for pressure transient will be conducted by using the same schematic diagram.

Acknowledgements This work was funded by Ministry of Higher Education (MOHE) of Malaysia, under the Fundamental Research Grant Scheme (FRGS). FRGS/1/2016/TK03/FKM-CARE-F00317. The authors wish to thank Ministry of Higher Education and Universiti Teknikal Malaysia Melaka for their support.

References

1. Science and technology. Retrieved from <http://www.encyclopedia.com/science-and-technology/physics/physics/pressure>. 6 December 2017
2. The history of pressure measurement. Retrieved from <http://www.sensorland.com/HowPage059.html>, 6 December 2017
3. Thavamani, J.P.: Bernoulli equation in fluid flow. *Journal* **8**(10), 40459–40461 (2016)
4. Wachter, W., Trimmel, G., Buchner, R., Glatter, O.: Dynamics of water confined in self-assembled monoglyceride–water–oil phases. *Soft Matter* **7**(4), 1409 (2011)

5. Yusof, A.A., Zaili, Z.S., Hassan, S.N., Tuan, T.B., Saadun, M.N., Ibrahim, M.Q.: Promoting water hydraulics in Malaysia: a green educational approach. In: AIP Conference Proceedings, vol. 1621, p. 297 (2014)
6. Pham, N.P.: Improvement of energy and control performance in water hydraulic transmissions. Functional control systems (2014)
7. Elbashir, M.A.M., Oduro, S., Amoah, K.: Using computer model to calculate and simulate transient. Master thesis (2007)

Electronic Water Balancing Tool



Cheow Kah Chun, Ahmad Shahrizan Abdul Ghani, Ker Shao Jiun, Nur Syazwani Abdul Gani, Muhamad Izdhar Zaki and Ahmad Fakhri Ab. Nasir

Abstract This document consists detail of project report, in which the title is electronic water balancing tool. The concept and background knowledge of the title has been studied and objectives has been set to investigate the interaction between the SN-IMU5D-LC gyro sensor with accelerometer and the Arduino UNO with servo motor as output. For that purposed, the gyroscope which produces analogue signals is connected to the Arduino through the analogue pins. The signals from the sensor will be processed by the Arduino and interpreted into the motion of two servo motors that are connected to the digital outputs of the Arduino. Thus, the movement of the device (specifically gyroscope) produces the motion effects of both servo motor either to right or left. The directions (angle) of servo motors could be negative or positive in x- and y-directions. Throughout the project, the group members have gained knowledge in creating developing an application for the SN-IMU5D-LC gyro sensor with accelerometer using Arduino IDE software and the wiring the circuit diagram of the product.

Keywords Water balancing tool · SN-IMU5D-LC · Gyro sensor Accelerator

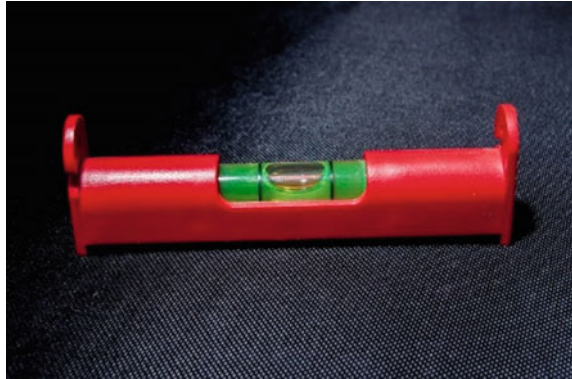
1 Introduction

Water balancing tool or spirit level is a type of instrument to measure the steepness of a surface. The water balancing tool is used to check whether the surface of a product is horizontal [1] or parallel with respect to earth [2] and has any angle of

C. K. Chun · K. S. Jiun · N. S. Abdul Gani · M. I. Zaki
Faculty of Manufacturing Engineering, Universiti Malaysia Pahang,
Gambang, Pahang, Malaysia

A. S. Abdul Ghani (✉) · A. F. Ab. Nasir
Innovative Manufacturing, Mechatronics, and Sports Lab (IMAMS), Faculty of
Manufacturing Engineering, Universiti Malaysia Pahang, Gambang, Pahang, Malaysia
e-mail: shahrizan@ump.edu.my

Fig. 1 Traditional water balancing tool or spirit level



inclination or not. The instrument usually consists of a rectangular plastic with cylinder tube in the middle, covered with fluid and a bubble is spotted in the middle of the cylinder tube, indicating the surface is at horizontal, as shown in Fig. 1.

Although the instrument is very useful for wood crafting workers, metal workers and even housewives in their daily routine, but there exist weaknesses that can be found in the traditional water balancing tool or spirit level, which is lack of precision. There is tolerance found in the traditional water balancing tool, which is the two black lines found at the cylinder tube. There is also no value displayed in the traditional water balancing tool, thus cannot indicate whether the surface is at smooth or there exist inclination angle or not. Based on this weaknesses, the group chose to be electronic water balancing tool to modify and improve the traditional water balancing tool to be more accurate and precise.

The electronic water balancing tool is an instrument similar to that of the traditional balancing tool, but it uses electronic components and peripherals and coding to display whether the surface has any angle of inclination. The electronic water balancing tool consist of an Arduino UNO board interfacing with SN-IMU5D-LC gyro sensor with accelerometer and two servo motors enclosed in a small box. The interaction between SN-IMU5D-LC and Arduino UNO board is used to read and determine the steepness of the surface and the two servo motors are used to indicate the inclination at x-axis and y-axis respectively. The figure below shows the product of electronic water balancing tool (Fig. 2):

There are several objectives set to be achieved in this project and they are listed as below:

1. To understand basic knowledge and technical specification of the SN-IMU5D-LC gyro sensor with accelerometer.
2. To analyze the interaction between the Arduino UNO and the SN-IMU5D-LC with servo motor.
3. To conduct a project using SN-IMU5D-LC gyrometer and investigate the output of the gyrometer.

Fig. 2 Electronic water balancing tool



2 Background Knowledge

2.1 *SN-IMU5D-LC Gyro Sensor with Accelerometer*

The sensor that is used in this project is a SN-IMU5D-LC gyro sensor with accelerometer, which is also known as the 5 V 5 DOF Gyro Accelerometer IMU. It is a type of low cost 5 degree of freedom Inertial Measurement Unit (IMU) which incorporates two gyro sensor and a three-axis accelerometer. This sensor is designed to keep the cost as low as possible without sacrificing the performance. It also consists of a low-noise amplifier to increase the sensitivity of the gyro sensor. This sensor consists of main two components, which are the accelerometer and gyro sensor. The accelerometer is used to measure the static acceleration of gravity in tilt-sensing applications, as well as dynamic acceleration resulting from vibration, shock, or motion while the gyro sensor is an angular rate sensor that uses the Coriolis force theory, which is generated when a rotational angular rate is applied to the vibrator [3].

2.2 Technical Description

The following Fig. 3 shows the technical properties of the implemented gyro sensor for this project [4].

Technical details of ENC-03R which refers to angular rate sensor used in gyro sensor SN-IMUD5D-LC is shown in Fig. 4.

Figure 5 shows the circuit diagram and connectivity of the sub-components of SN-IMU5D-LC which consists of power supply connection, gyro, and accelerometer sensors.

Parameter	Conditions	Min	Typ	Max	Unit
SENSOR INPUT					
Measurement Range	Each axis	±3	±3.6		g
Nonlinearity	% of full scale		±0.3		%
Package Alignment Error			±1		Degrees
Interaxis Alignment Error			±0.1		Degrees
Cross-Axis Sensitivity ¹			±1		%
SENSITIVITY (RATIOMETRIC)²					
Sensitivity at $X_{out}, Y_{out}, Z_{out}$	Each axis $V_s = 3V$	270	300	330	mV/g
Sensitivity Change Due to Temperature ³	$V_s = 3V$		±0.01		%/°C
ZERO g BIAS LEVEL (RATIOMETRIC)					
0 g Voltage at X_{out}, Y_{out}	$V_s = 3V$	1.35	1.5	1.65	V
0 g Voltage at Z_{out}	$V_s = 3V$	1.2	1.5	1.8	V
0 g Offset vs. Temperature			±1		mg/°C
NOISE PERFORMANCE					
Noise Density X_{out}, Y_{out}			150		$\mu\text{g}/\sqrt{\text{Hz}}$ rms
Noise Density Z_{out}			300		$\mu\text{g}/\sqrt{\text{Hz}}$ rms
FREQUENCY RESPONSE⁴					
Bandwidth X_{out}, Y_{out} ⁵	No external filter		1600		Hz
Bandwidth Z_{out} ⁵	No external filter		550		Hz
R_{RLZ} Tolerance			32 ± 15%		k Ω
Sensor Resonant Frequency			5.5		kHz
SELF-TEST⁶					
Logic Input Low			+0.6		V
Logic Input High			+2.4		V
ST Actuation Current			+60		μA
Output Change at X_{out}	Self-Test 0 to Self-Test 1	-150	-325	-600	mV
Output Change at Y_{out}	Self-Test 0 to Self-Test 1	+150	+325	+600	mV
Output Change at Z_{out}	Self-Test 0 to Self-Test 1	+150	+550	+1000	mV
OUTPUT AMPLIFIER					
Output Swing Low	No load		0.1		V
Output Swing High	No load		2.8		V
POWER SUPPLY					
Operating Voltage Range		1.8		3.6	V
Supply Current	$V_s = 3V$		350		μA
Turn-On Time ⁷	No external filter		1		ms
TEMPERATURE					
Operating Temperature Range		-40		+85	°C

¹ Defined as coupling between any two axes.

² Sensitivity is essentially ratiometric to V_s .

³ Defined as the output change from ambient-to-maximum temperature or ambient-to-minimum temperature.

⁴ Actual frequency response controlled by user-supplied external filter capacitors (C_x, C_y, C_z).

⁵ Bandwidth with external capacitors = $1/(2 \times \pi \times 32 \text{ k}\Omega \times C)$. For $C_x, C_y = 0.003 \mu\text{F}$, bandwidth = 1.6 kHz. For $C_z = 0.01 \mu\text{F}$, bandwidth = 500 Hz. For $C_x, C_y = 10 \mu\text{F}$,

bandwidth = 0.5 Hz.

⁶ Self-test response changes cubically with V_s .

⁷ Turn-on time is dependent on C_x, C_y, C_z and is approximately $160 \times C_x$ or C_y or $C_z + 1$ ms, where C_x, C_y, C_z are in microfarads (μF).

Fig. 3 Technical specification of ADXL335 accelerometer in SN-IMU5D-LC

Part Number	Resonance Frequency (kHz)	Supply Voltage	Maximum Angular Velocity (deg./sec.)	Output (at Angular Velocity=0)	Scale Factor	Linearity (%FS)	Response (Hz)	Weight (g)
ENC-03RC-R	30.8	2.7-5.25V	±300	1.35Vdc	0.67mV/deg./sec.	±5	50	0.2
ENC-03RD-R	32.2	2.7-5.25V	±300	1.35Vdc	0.67mV/deg./sec.	±5	50	0.2

Operating Temperature Range: -5°C to 75°C Storage Temp. Range: -30°C to 85°C

Fig. 4 Technical description of ENC-03R angular rate sensor in SN-IMU5D-LC

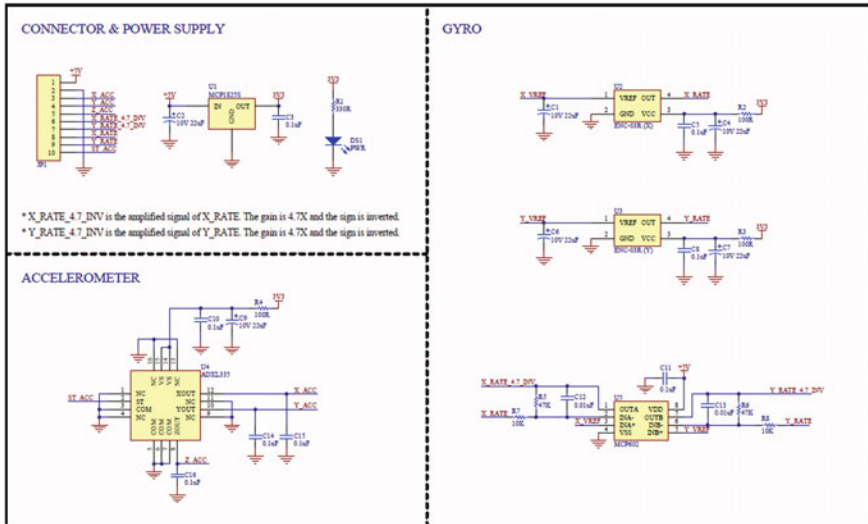


Fig. 5 Circuit diagram of SN-IMU5D-LC gyrometer with accelerometer from datasheet

By reading the data sheet and some information shared on internet, we know the value for voltage and some capacitor values inside this sensor. Figure 5 shows clearly the power supply and connector circuit, accelerometer circuit and also the gyro connection which placed together on one chip.

2.3 Working Principle

This SN-IMU5D-LC sensor works by identifying linear acceleration and rotational rate using one or more accelerometers and gyroscopes respectively. Typical configurations contain one accelerometer, gyro, and magnetometer per axis for each of the three vehicle axes: pitch, roll and yaw.

2.4 Application of SN-IMU5D-LC Gyro Sensor with Accelerometer

Nowadays, the IMU gyrometer [5, 6] sensor is very important in the aspect of navigating application and widely use in the electronic devices such as smart-phones, GPS navigating system and also land vehicles. This type of sensor is also applicable in the navigation and the control of vehicles and machines, from aircraft to ships, submarines, and even satellites that are located above the atmosphere of Earth. For instance, the IMU gyrometer sensor is installed in an airplane, which is capable of moving along a certain direction with high speed, to measure a plane’s acceleration value. According to experts, the SN-IMU5D-LC gyrometer with accelerometer sensor is implemented to provide analog inputs of the related information, which will help in calculating movement and position of the object [7]. This helps in the medical field to detect a patient physical condition and state. For example, experts had used the gyrometer with accelerometer sensor to detect Alzheimer disease in patients.

3 Circuit Diagram

Circuit diagram for the project is shown in the following figures—Figs. 6 and 7. Based on the Fig. 6, analogue signals from gyroscope are connected with Arduino [8] to the analogue pin which are A0 to A4. Power supply and GND of the gyroscope are connected to the supply and ground from the Arduino. On the other hand, the same power supply and ground pins of Arduino are connected to the

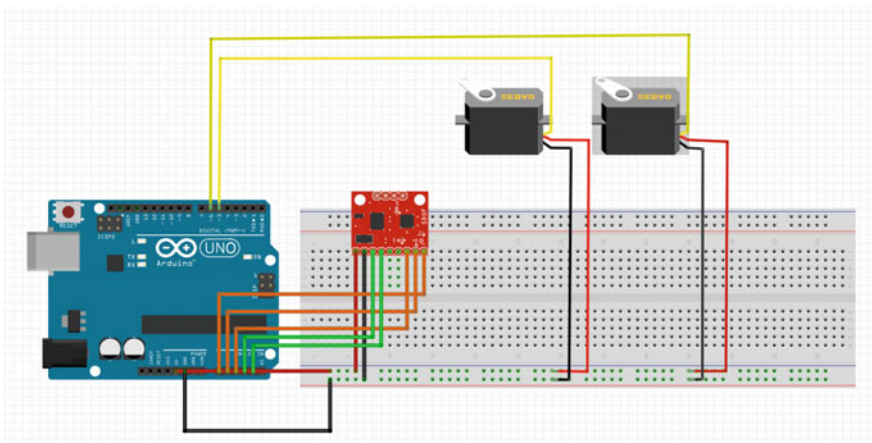


Fig. 6 Circuit diagram of electronic water balancing tool

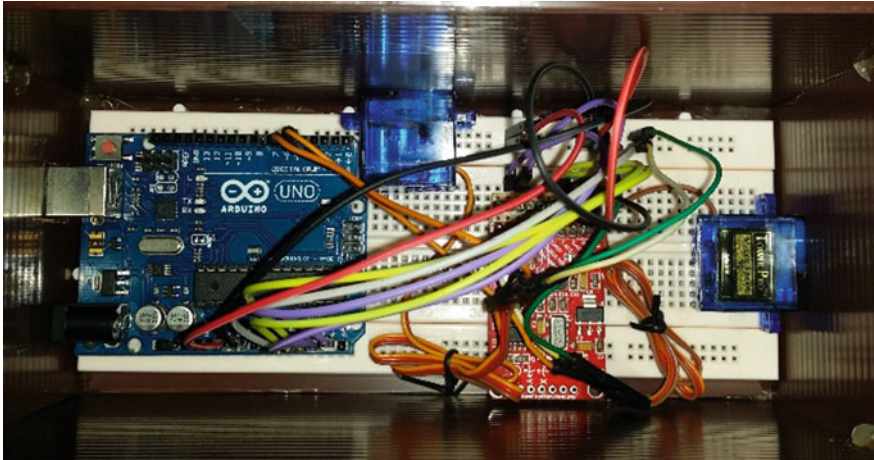


Fig. 7 Actual circuit diagram of electronic water balancing tool product

V+ and GND of the servo motors [9]. Input pins of both servo motors are connected to the digital output of Arduino which are pins 5 and 6.

Based on the Figs. 6 and 7, we know that the wiring connection of the diagram is as follow:

- The +5 V and GND of the SN-IMU5D-LC is connected to the 5 V and GND of the Arduino UNO respectively.
- The X-ACC, Y-ACC, Z-ACC, X-RATE and Y-RATE of the SN-IMU5D-LC is connected to the A0, A1, A2, A3 and A4 of the Arduino UNO respectively.
- The +5 V (red wire) and GND (brown wire) of the two servo motors are connected to the 5 V and GND of the Arduino UNO respectively.
- The two outputs (orange wire) of the servo motors are connected to the 5 and 6 digital pin of the Arduino UNO board respectively.

4 Programming Code

The coding is programmed to detect any change in positioning and acceleration of the SN-IMU5D-LC gyro sensor with accelerometer sensor and causes the servo motor to rotate according to the angle of inclination experience by the sensor. First of all, we have to include the servo motor library into the coding by writing `#include<Servo.h>`. We then have to define the number of analog inputs and the reference voltages of the analog pins by writing `#define INPUT_COUNT 5` and `#define VDD 5000.0f` respectively. Next, we created the two servo motor coding at the digital pin by writing `Servo myservo1;` and `Servo myservo2;` that acts as the output indicator for the sensor.

```

#include<Servo.h>
#define INPUT_COUNT 5           //number of analog inputs
#define VDD 5000.0f           //Analog reference voltage in positive7
#define PI 3.14159265358979f

int an[INPUT_COUNT];
char firstSample;
Servo myservo1;
Servo myservo2;
int servoPin1 = 5;
int servoPin2 = 6;

```

In the *void* setup, we have to set the parameters of the accelerometer and gyro sensor according to the datasheet of the SN-IMU5D-LC. For example, we configure the accelerometer at zero level and its sensitivity by writing ‘config.zeroLevel[i] = 1650;’ and ‘config.inpSens[i] = 300;’ respectively. Then, we attach the servo motors to the digital pin 5 and 6 of the Arduino UNO by writing ‘myservo1.attach(5);’ and ‘myservo1.attach(6);’ respectively.

```

//Setup parameters for Acc_Gyro board
for(i=0;i<=2;i++){
  config.zeroLevel[i] = 1650;    // Accelerometer zero level (Mv) @ 0 G
  config.inpSens[i] = 300;      // Accelerometer Sensitivity Mv/g
}
for(i=3;i<=4;i++){
  config.inpSens[i] = 2000;      // Gyro Sensitivity Mv/deg/ms
  config.zeroLevel[i] = 1230;    // Gyro Zero Level (Mv) @ 0 deg/s
}

```

Then we will print the output, which is the angle of inclination of the sensor, to the servo motor. We have hide the inclination angle of the accelerometer and also the estimated inclination angle to prevent reader from getting confused when reading the output at the serial monitor of the Arduino IDE software.

Next, we will have calculations to calculate the inclination angle of the accelerometer and the estimated inclination in the void loop of ‘getEstimatedInclination’. For example, the code ‘for(w=0;w<=2;w++) RwAcc[w] = getInput(w);’ is used to get accelerometer readings from pin analog pin A0 to A2 while ‘Awz[w] = atan2(RwEst[w],RwEst [2]) * 180 / PI;’ is used to get angles of gyro sensor and converting it to degree. If the angle of gyro sensor is much smaller, then the gyro data is ignored and previous estimated data is taken.


```

//get accelerometer readings in g, gives us RwAcc vector
for(w=0;w<=2;w++)
RwAcc[w] = getInput(w);
normalize3Dvector(RwAcc);

    if (firstSample){
for(w=0;w<=2;w++) RwEst[w] = RwAcc[w];  }
    else{

if(abs(RwEst[2]) < 0.1){
    for(w=0;w<=2;w++) RwGyro[w] = RwEst[w];
}
else{
    for(w=0;w<=1;w++){
tmpf = getInput(3 + w);           //get current gyro rate in deg/ms
tmpf *= interval / 1000.0f;      //get angle change in deg
Awz[w] = atan2(RwEst[w],RwEst[2]) * 180 / PI;
Awz[w] += tmpf;
    }
}
}

```

5 Results

The SN-IMU5D-LC gyro sensor with accelerometer sensor will detect and identify the inclination angle when the sensor is tilted. The results below show the angle of inclination and position of servo motor when the sensor is tilted or at rest.

Figures 8 and 9 shows the angle of inclination and position of servo motor when the SN-IMU5D-LC sensor is horizontal to the ground. We have set the angle of inclination in the Arduino coding to be at 90° in both x-axis and y-axis when the sensor is horizontal to the ground.

Based on Figs. 10 and 11, we can clearly see that the angle of inclination and position of servo motor at x-axis has changed when the SN-IMU5D-LC sensor is tilted to the right. The angle of x-axis is 0° when it is tilted to the right and the position of the servo motor is shifted to the right side, indicating the angle is 0° .

Based on Figs. 12 and 13, we can clearly see that the angle of inclination and position of servo motor at y-axis has changed when the SN-IMU5D-LC sensor is tilted to the front. The angle of y-axis is almost 0° when it is tilted to the front and the position of the servo motor is shifted to the right side, indicating the angle is almost 0° .

Based on Figs. 14 and 15, we can clearly see that the angle of inclination and position of servo motor at y-axis has changed when the SN-IMU5D-LC sensor is tilted to the back. The angle of y-axis is almost 180° when it is tilted to the back and

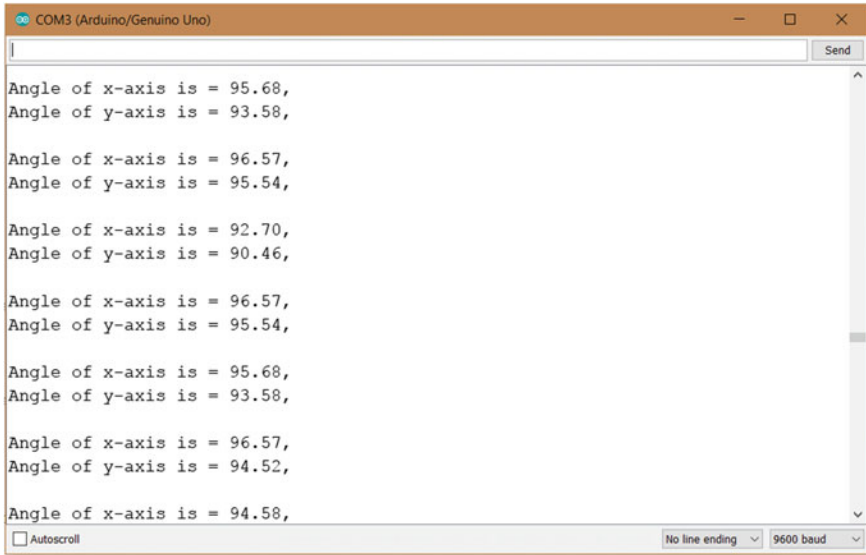


Fig. 8 Angle of inclination of servo motor when SN-IMU5D-LC is horizontal to the ground



Fig. 9 Position of servo motor when SN-IMU5D-LC is horizontal to the ground

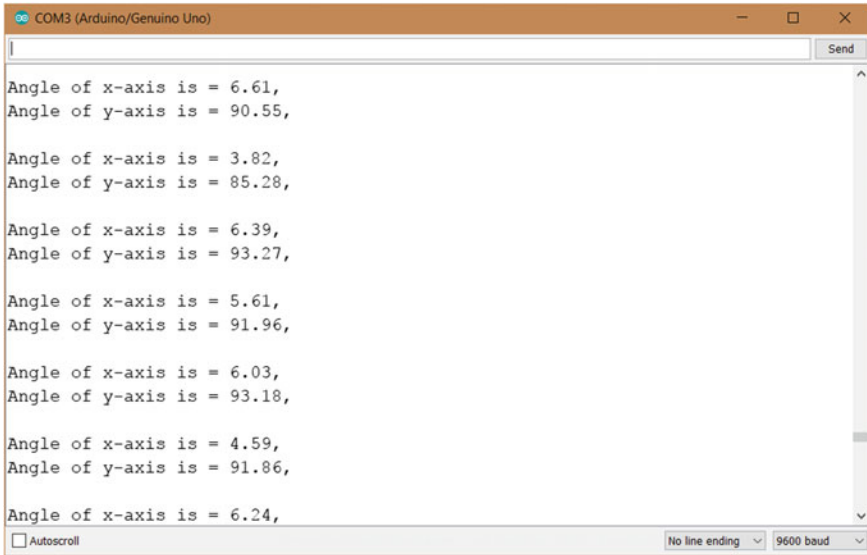


Fig. 10 Angle of inclination of servo motor when SN-IMU5D-LC is tilted to the right

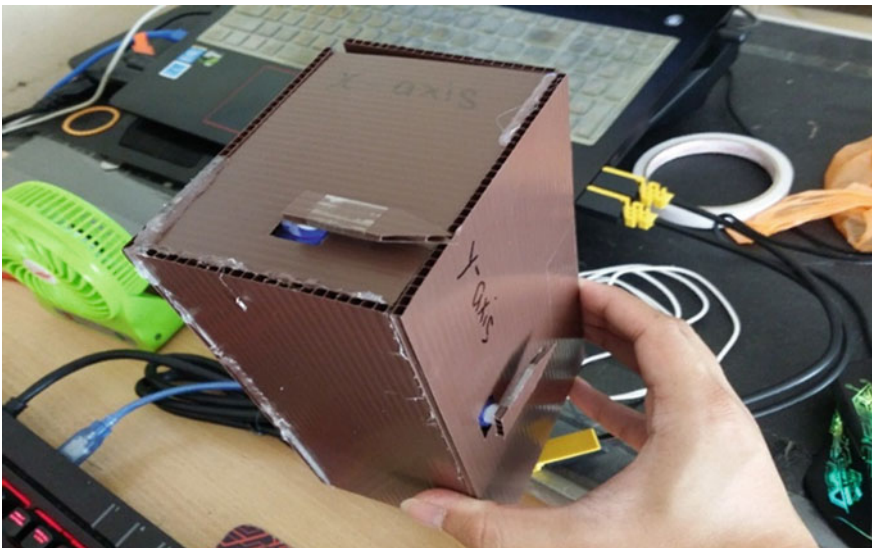


Fig. 11 Position of servo motor when SN-IMU5D-LC is tilted to the right

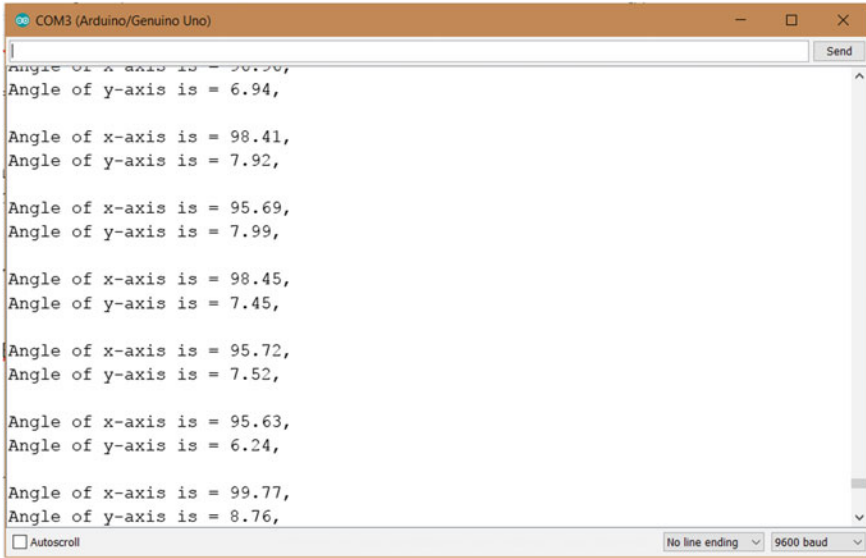


Fig. 12 Angle of inclination of servo motor when SN-IMU5D-LC is tilted to the front



Fig. 13 Position of servo motor when SN-IMU5D-LC is tilted to the front

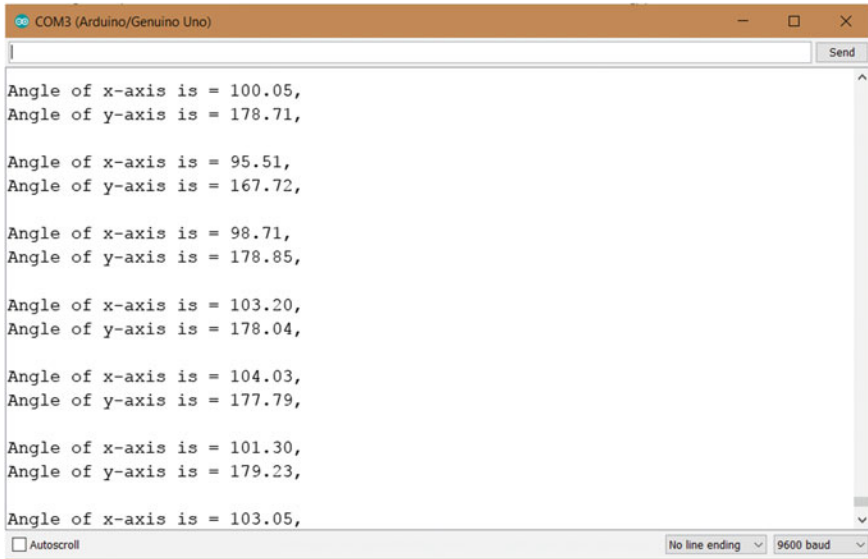


Fig. 14 Angle of inclination of servo motor when SN-IMU5D-LC is tilted to the back



Fig. 15 Position of servo motor when SN-IMU5D-LC is tilted to the back

the position of the servo motor is shifted to the left side, indicating the angle is almost 180°.

Based on Figs. 16 and 17, we can clearly see that the angle of inclination and position of servo motor at x-axis has changed when the SN-IMU5D-LC sensor is

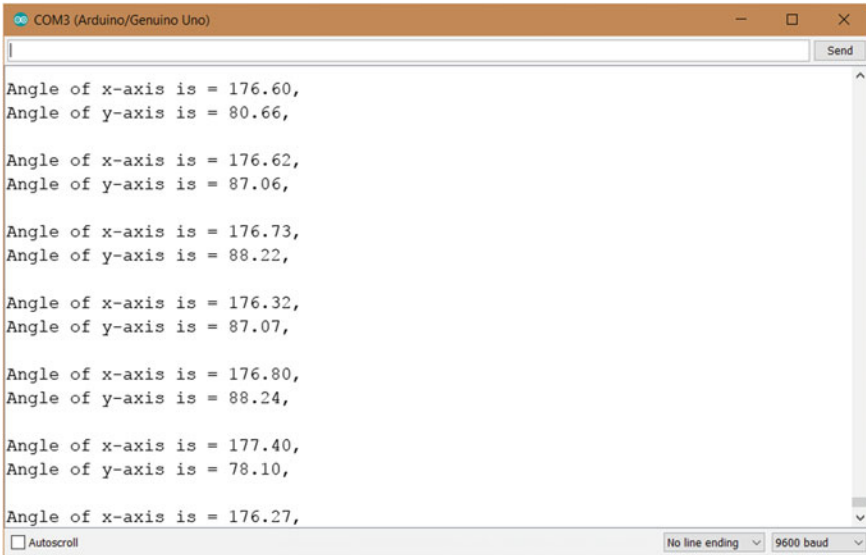


Fig. 16 Angle of inclination of servo motor when SN-IMU5D-LC is tilted to the left

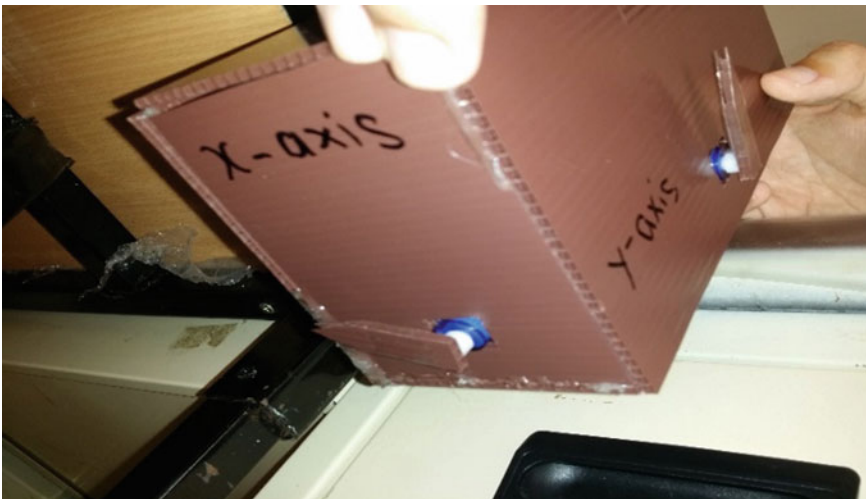


Fig. 17 Position of servo motor when SN-IMU5D-LC is tilted to the left

tilted to the left. The angle of x-axis is almost 180° when it is tilted to the left and the position of the servo motor is shifted to the left side, indicating the angle is almost 180° .

6 Discussion

There are several problems and obstacles that we had encountered during the project. First of all, we found out that the serial monitor value of the Arduino IDE software did not change even after testing the sensor several times. We checked the connector and power supply of +5 V did not experience any problem, so we checked the components embedded in the sensor and we found out that the problem is the MCP1825S output which supposed to be 3.3 V did not show the exact value. After the MCP1825S being tested by the multimeter, we confirmed that the reading of output only has 0.7 V, which is very much lower than the exact value. This is also the main reason that causes the sensitivity of the SN-IMU5D-LC sensor to be weak and not precise, resulting in the serial monitor value shown did not change in a much obvious way. After trying to attach the jumper wire directly to the output and input of the MCP1825S, the reading of the SN-IMU5D-LC sensor and the serial monitor value will change according to the movement and degree of turning of the sensor. After consulting the lecturer, we knew that the sensor is a defect product. We are then able to get a new SN-IMU5D-LC sensor, and it work quite well after being tested (Fig. 18).

Next, there is not enough analog pins for the LCD display. When we first start our project, we are told to use a LCD display to show or indicate the output of the SN-IMU5D-LC sensor. However, the SN-IMU5D-LC sensor uses up five analog pins, which is from A0 to A4, leaving on A5 unconnected. In general, SDA and SCL of the LCD display is required to connect to the A4 and A5 analog pin of the

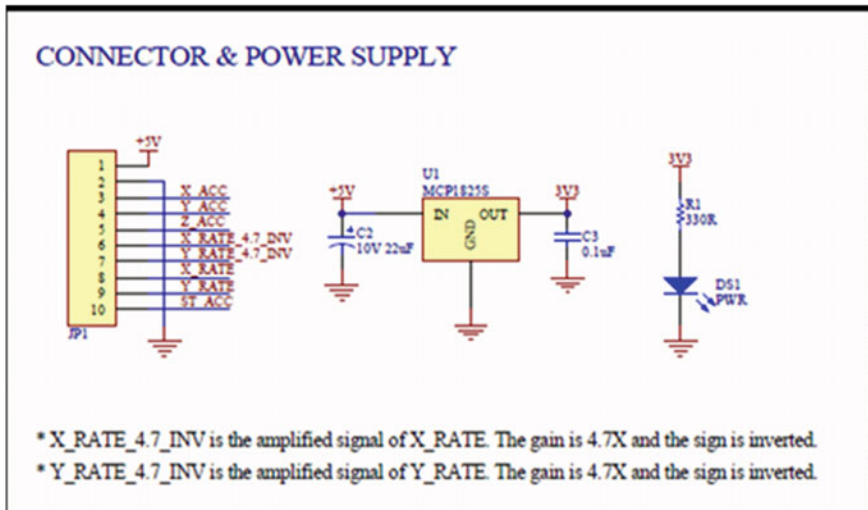


Fig. 18 Circuit diagram of the SN-IMU5D-LC gyro sensor with accelerometer part that shows the output of MCP1825S to be 3.3 V

Arduino UNO board respectively, but the A4 pin has already been occupied. We use servo motors as our output to indicate the inclination angle of the sensor.

When performing coding, we faced the problem to make the servo turn according to the tilt and inclination of the sensor that is attached to the breadboard. After several times of trial and error in changing the code in Arduino UNO, we are able to found out what is missing in the code, which is the calculation of the servo motor according to the inclination of the sensor. We found out that we need to multiple 90° with the projection of the normalized force vector on x and y axes respectively to let the servo to turn exceed 90° without using the increment method. With this modification code, we are able to give output servo motor to turn right or left based on the inclination and angular tilt of the sensor. Beside, we include two servo motors as outputs to indicate the inclination of the x-axis and y-axis. After compiling the code and upload to Arduino UNO board, we can successfully get the correct output from the serial monitor and the servo motors are able to turn according to the coding and inclination.

7 Conclusion

In conclusion, we had successfully implemented the SN-IMU5D-LC gyro sensor and accelerator sensor to the Arduino with output as servo motor. We also learnt that the sensor has the capability and ability to detect change in position and movement of an object. Despite the numerous difficulties faced regarding the sensor, we able to overcome the difficulties and obstacles and able to understand the working principle and function of this sensor. Even though the concept of the balancing sensor instrument is nothing new and revolutionary, and has been implemented successfully throughout history, but we felt successful that able to complete the project with inexpensive equipment and within the deadline. In short, we had achieved our objectives and able to grab hold of the concept of the sensor.


References

1. Wikipedia (n.d.) Spirit Level. Retrieved from https://en.wikipedia.org/wiki/Spirit_level
2. Johnson Level (n.d.) Spirit level information. Retrieved from <http://www.johnsonlevel.com/News/SpiritLevelInformation>
3. Cytron Marketplace (n.d.) 5 DOF IMU. Retrieved from <https://www.cytron.com.my/p-sn-imu5d-lc?search=Imu>
4. Github (n.d.) Cytron_SN-IMU5D-LC. Retrieved from https://github.com/CytronTechnologies/Cytron_SN-IMU5D-LC
5. I2Cdevlib Forums (n.d.) How to decide gyro and accelerometer offset. Retrieved from <https://www.i2cdevlib.com/forums/topic/91-how-to-decide-gyro-and-accelerometer-offset/>
6. Instructables (n.d.) Guide to gyro and accelerometer with Arduino including kalman filtering. Retrieved from <http://www.instructables.com/id/Guide-to-gyro-and-accelerometer-with-Arduino-inclu/>

7. Instructables (n.d.) Accelerator and gyro tutorial. Retrieved from <http://www.instructables.com/id/Accelerometer-Gyro-Tutorial/>
8. Arduino (n.d.) Arduino UNO. Retrieved from <http://www.arduino.org/products/boards/arduino-uno>
9. Jameco (n.d.) How do servo motor works. Retrieved from <http://www.jameco.com/jameco/workshop/howitworks/how-servo-motors-work.html>

Development of a Soccer Ball Launching Device



Mohd Hasnun Arif Hassan , Zahari Taha,
Mohd Ali Hanafiah Shaharudin, Lim Kok Wee and Zulfika Anuar

Abstract Soccer players are allowed to use their heads to direct the ball to the teammates during the game. Studies have shown that purposeful heading of the ball in soccer might cause long-term traumatic brain injury. In order to analyze the impact of soccer heading on the brain in the laboratory, a device that can launch the ball at constant speed is required. This project aims to develop a device, which can launch the ball towards a target such as an instrumented dummy headform at desired speeds. Two counter-rotating wheels that are rotated by two AC motors were used as the launching mechanism. The use of AC motors is economical, but their speeds cannot be easily controlled. Thus, a release mechanism that automates the switching of the motor as well as feeding the ball was developed. Testing shows that the device is capable of launching the ball up to a maximum speed of 18 m/s. This corresponds to the reported maximum heading speed in soccer. The use of the release mechanism allows the ball speed to be varied. A soccer ball launching device was successfully developed. The device is not only economical, but also capable of launching the ball at desired speeds.

Keywords Soccer ball launcher · Ball shooter

M. H. A. Hassan (✉) · Z. Taha · M. A. H. Shaharudin · L. K. Wee
Innovative Manufacturing, Mechatronics and Sports Lab (iMAMS),
Faculty of Manufacturing Engineering, Universiti Malaysia Pahang, 26600 Pekan,
Pahang, Malaysia
e-mail: mhasnun@ump.edu.my

Z. Anuar
Faculty of Mechanical Engineering, Universiti Malaysia Pahang, 26600 Pekan,
Pahang, Malaysia

© Springer Nature Singapore Pte Ltd. 2018
M. H. A. Hassan (ed.), *Intelligent Manufacturing & Mechatronics*,
Lecture Notes in Mechanical Engineering,
https://doi.org/10.1007/978-981-10-8788-2_53

1 Introduction

Soccer is the most popular sport in the world with an active involvement of more than 265 million people worldwide. The uniqueness of this game is that it permits the purposeful use of the head in directing the ball to the teammates or even scoring goals. This manoeuvre is termed 'heading'. A soccer player could be subjected to six to seven occasions of heading in a game [1] with an estimation of approximately 800 headings a year [2]. This purposeful use of the head in soccer has raised concerns as to whether it could lead to brain trauma injury.

Many studies have linked purposeful heading in soccer to brain trauma injury, similar to that found in mild traumatic brain injury (mTBI). Both amateur and professional soccer players were evaluated in the past decades. This was done through a series of neuropsychological tests [3–7], as well as magnetic resonance imaging (MRI) technique [8–10]. These studies demonstrated that heading in soccer might be harmful to the brain. Although the cognitive impairment might also be caused by other head impact cases such as head-to-head or head-to-elbow impacts, the detrimental effects of head-to-ball impact cannot be simply ruled out. A single heading might not be dangerous, but the cumulative effects of the repeated blows are the main concerns.

To study the impact of soccer heading on the brain, experimental studies of soccer heading have been conducted. The experiments were performed on human subjects [11–15] and head dummy such as the Hybrid III crash test dummy [14, 16, 17]. These experiments attempted to measure the linear and angular head accelerations induced by the soccer heading manoeuvre. Most of the experiments focused on the frontal heading, i.e. the ball impacts the forehead of the subjects.

To conduct the dynamic impact tests on the soccer ball and the soccer heading experiment, a device capable of launching a soccer ball at different speeds is required. Due to the high cost of such device and its unavailability in Malaysia during the time this project was conducted, the aim of this work is to develop a cost-effective soccer ball launching device that can propel a soccer ball at various speeds for the purpose of conducting soccer heading experiment. The subsequent sections describe the development of the device and its testing.

2 Method

2.1 Theoretical Calculation

The aim is to develop an economical device that is capable of consistently launching a soccer ball up to a maximum velocity of 18 m/s. The chosen speed is slightly larger than the typical maximum speed of soccer heading of 18 m/s reported in high school soccer games [18]. The launch velocity of the ball is determined using the velocity equation of the uniform circular motion, as follows:

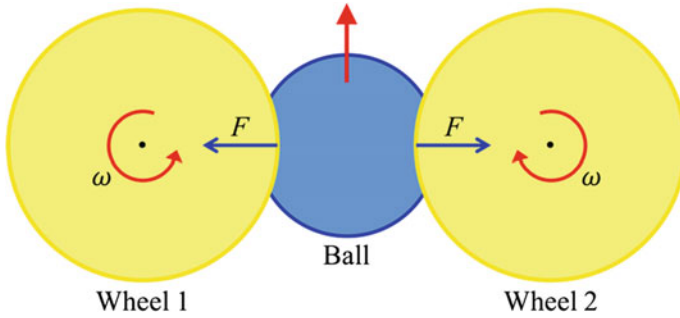


Fig. 1 Force exerted on the wheel during the soccer ball launching

$$v = \omega r_w \tag{1}$$

where v is the ball’s launch velocity, r_w is the radius of the wheel and ω is the angular velocity of the wheel.

Two AC motors were obtained, having a power of 150 W, 1.15 Nm torque and a speed of 1245.56 rpm. The reason behind using the AC motor instead of DC is the fact that it is more economical. The wheel has a radius of 173.5 mm and weighs 1.464 kg. From Eq. (1), the theoretical maximum launch speed is 22.62 m/s; this fulfils the requirement of the device.

The launching is achieved through the counter-rotation of the wheels and the compression of the ball. This results in a force being exerted on each wheel; the direction of the forces points towards the axis of rotation as shown in Fig. 1. The force exerted on each wheel is the summation of the centripetal force and the force exerted by the deformed soccer ball:

$$F = F_c + F_b \tag{2}$$

$$F = m_w r_w \omega^2 + k_b x_b \tag{3}$$

where F_c is the centripetal force, F_b is the force exerted by the deformed soccer ball, m_w is the mass of the wheel, k_b is the ball’s stiffness and x_b is the maximum deformation of the ball. The stiffness, k_b was taken as 36,833 N/m as reported by a previous study [19]; the ball is assumed to undergo a 15% maximum deformation. The maximum force exerted on each wheel, calculated using Eqs. (2) and (3) is then equivalent to 4,926 N.

2.2 Fabrication of the Device

To prevent structural failures due to the aforementioned forces, a ball bearing was incorporated in the design, installed at each wheel. A deep groove ball bearing

(model 61907, SKF) was chosen. This ball bearing has a dynamic load rating of 9.56 kN and a static load rating of 6.8 kN. These are larger than the force calculated previously using the Eqs. (2) and (3); this ball bearing is suitable in this case. The bearing is placed at the centre of mass of a 15 mm-thick aluminium bar. Each end of the bar is fixed to an aluminium profile as shown in Fig. 2.

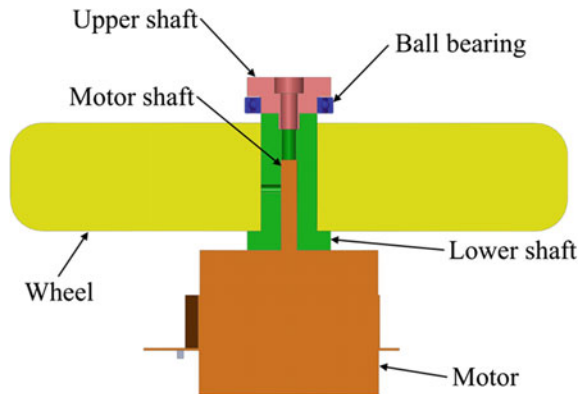
A shaft was manufactured according to the diameter of the opening at the centre of the wheel. The shaft has 2 parts; upper and lower. The upper part clamps the ball bearing to the wheel, preventing it from sliding or moving. The lower part is attached to the motor shaft using an M2.5 screw. Figure 3 depicts the shaft.

The device employs a gravity-feed mechanism. The ball is placed on a pair of angled aluminium profile. A 3-mm thick aluminium sheet attached to a servo motor holds the ball from rolling down. The drawback of using AC motor is the difficulty to control its speed, making the device incapable of launching the ball at various speeds. This problem was overcome by switching off the motor and varying the delay time of which the ball is fed to the device. This is achieved by means of a

Fig. 2 Proposed design of the soccer ball launching device



Fig. 3 Cross-section of the shaft



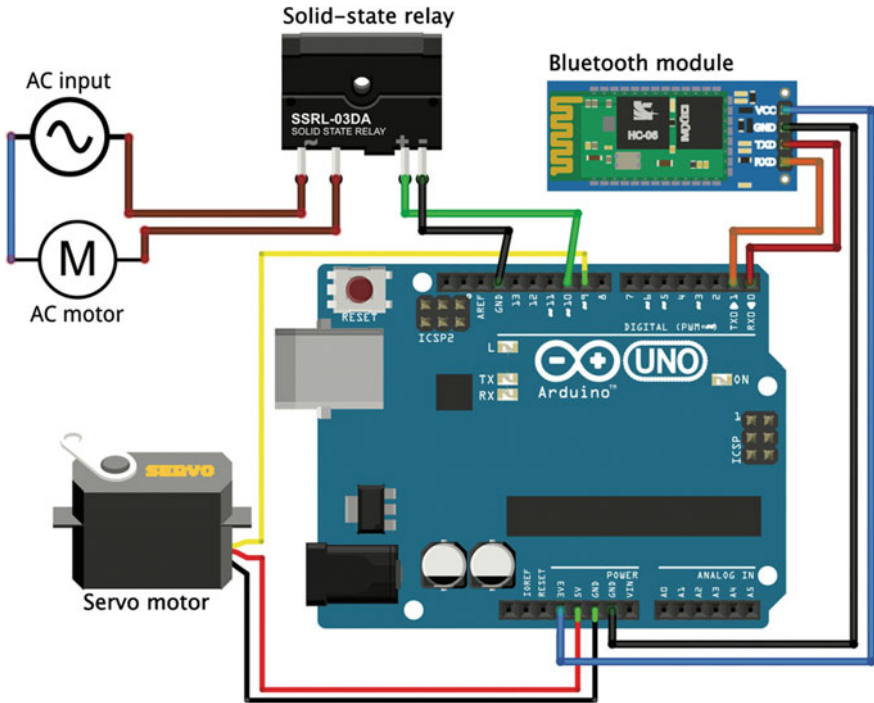


Fig. 4 Wiring diagram of the soccer ball launching device

solid-state relay, a servo motor and a micro-controller (Arduino Uno, Arduino, Italy).

The micro-controller board was programmed to switch on the AC motor, switch it off and release the ball by turning the servo motor. Figure 4 shows the wiring of the electronics parts to the Arduino Uno micro-controller board. A Bluetooth module was used to allow for the wireless operation of the device. An android-based device paired with the aforementioned Bluetooth module was used to operate the device. Figure 5 shows the developed soccer ball launching device.

3 Results and Discussion

The device was successfully developed. But it needs to be tested to ensure the requirements set are fulfilled. An experiment was conducted to measure the velocity of the propelled ball. A high-speed camera (model SV643C, Epix Inc.) was used to capture the motion of the soccer ball propelled by the device. The feeding delay was set to 0, 5 and 10 s.

The ball was launched for at least three times for each delay. The recorded high-speed videos were analysed using the XCAP software (version 3.7, EPIX, Inc.) and the launch velocity was measured.

Figure 6 shows the propelled ball speed plotted against the launch delay. It is apparent that when launched at full speed without delay, the ball was ejected at almost 18 m/s as per requirement. The variation of ball speed was achieved through varying the launch delay. A launch delay of 5 s provides a ball speed of about 12.5 m/s, meanwhile a launch delay of 10 s produced a ball speed of about 8 m/s.

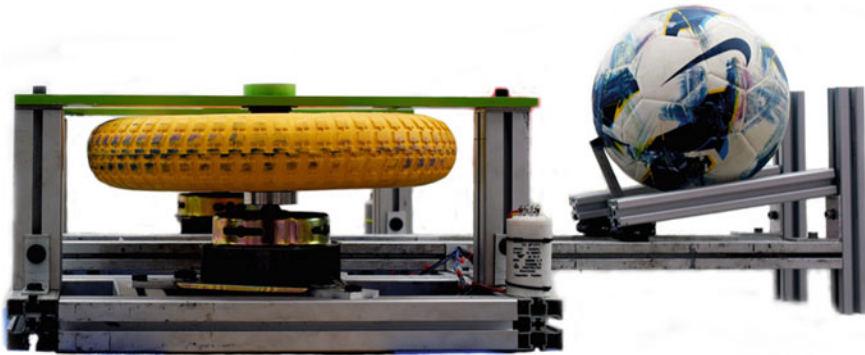


Fig. 5 The developed soccer ball launching device

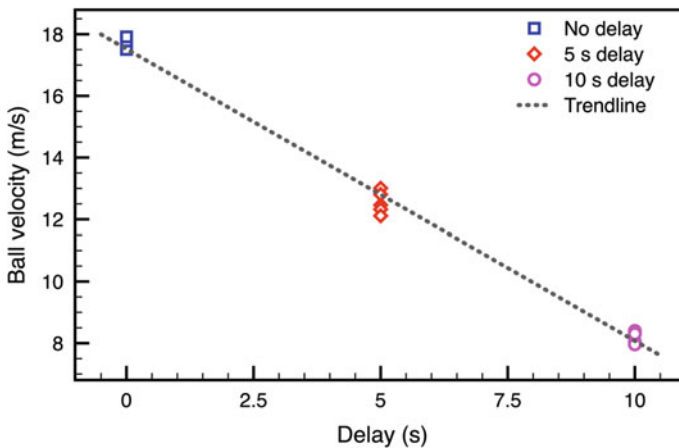


Fig. 6 Propelled ball velocity against launch delay

4 Conclusion

A soccer ball launching device was successfully developed. It utilizes two counter-rotating wheels mechanism. Two identical AC motors were used to drive both wheels in different directions. The variation of launching speed was achieved through delaying the time at which the ball is fed to the device due to the limitation of the AC motor. This method has been proven to work in our experimental testing. The maximum propelled ball speed achieved is 18 m/s as per requirement. This shows that the motor used and the design itself is adequate to fulfil the requirements. The fabricated device only cost around MYR 500, which is more economical than the commercial device which cost around MYR 10,000.

Acknowledgements The authors would like to thanks the Research and Innovation Department of Universiti Malaysia Pahang for funding this study under the internal grant RDU1603106.

References

1. Tysvaer, A.T., Storli, O.: Association football injuries to the brain. A preliminary report. *Br. J. Sports Med.* **15**, 163–166 (1981)
2. Matser, J.T., Kessels, A.G.H., Jordan, B.D., Lezak, M.D., Troost, J.: Chronic traumatic brain injury in professional soccer players. *Neurology* **51**, 791–796 (1998)
3. Tysvaer, A.T., Løchen, E.A.: Soccer injuries to the brain: a neuropsychologic study of former soccer players. *Am. J. Sports Med.* **19**, 56–60 (1991)
4. Matser, E.J.T., Kessels, A.G., Lezak, M.D., Jordan, B.D., Troost, J.: Neuropsychological Impairment in amateur soccer players. *JAMA J. Am. Med. Assoc.* **282**, 971–973 (1999)
5. Matser, J.T., Kessels, A.G., Lezak, M.D., Troost, J.: A dose-response relation of headers and concussions with cognitive impairment in professional soccer players. *J. Clin. Exp. Neuropsychol.* **23**, 770–774 (2001)
6. Webbe, F.M., Ochs, S.R.: Recency and frequency of soccer heading interact to decrease neurocognitive performance. *Appl. Neuropsychol.* **10**, 31–41 (2003)
7. Witol, A.D., Webbe, F.M.: Soccer heading frequency predicts neuropsychological deficits. *Arch. Clin. Neuropsychol.* **18**, 397–417 (2003)
8. Lipton, M.L., Kim, N., Zimmerman, M.E.: Soccer heading is associated with white matter microstructural and cognitive abnormalities. *Radiology* **268** (2013)
9. Koerte, I.K., Lin, A.P., Muehlmann, M., Merugumala, S., Liao, H., Starr, T., Kaufmann, D., Mayinger, M., Steffinger, D., Fisch, B., Karch, S., Heinen, F., Ertl-Wagner, B., Reiser, M., Stern, R., Zafonte, R.D., Shenton, M.E.: Altered neurochemistry in former professional soccer players without a history of concussion. *J. Neurotrauma* (2015). <https://doi.org/10.1089/neu.2014.3715>
10. Koerte, I.K., Ertl-Wagner, B.: White matter integrity in the brains of professional soccer players without a symptomatic concussion. *JAMA J. Am. Med. Assoc.* **308**, 2006–2008 (2012)
11. Naunheim, R., Ryden, A., Standeven, J., Genin, G., Lewis, L., Thompson, P., Bayly, P.: Does soccer headgear attenuate the impact when heading a soccer ball? *Acad. Emerg. Med.* **10**, 85–90 (2003). <https://doi.org/10.1197/aemj.10.1.85>
12. Shewchenko, N., Withnall, C., Keown, M., Gittens, R., Dvorak, J.: Heading in football. Part 1: development of biomechanical methods to investigate head response. *Br. J. Sports Med.* **39** Suppl. **1**, 10–25 (2005) <https://doi.org/10.1136/bjism.2005.019034>

13. Self, B., Beck, J., Schill, D., Eames, C., Knox, T., Plaga, J.: Head accelerations during soccer heading. In: *Engineering of Sport 6 SE—15*, pp. 81–86. Springer, New York (2006)
14. Funk, J.R., Cormier, J.M., Bain, C.E., Guzman, H., Bonugli, E.: Validation and application of a methodology to calculate head accelerations and neck loading in soccer ball impacts. SAE Technical Paper 1 (2009)
15. Gutierrez, G.M., Conte, C., Lightbourne, K.: The relationship between impact force, neck strength, and neurocognitive performance in soccer heading in adolescent females. *Pediatr. Exerc. Sci.* **26**, 33–40 (2014). <https://doi.org/10.1123/pes.2013-0102>
16. Naunheim, R., Bayly, P., Standeven, J., Neubauer, J., Lewis, L., Genin, G.: Linear and angular head accelerations during heading of a soccer ball. *Med. Sci. Sports Exerc.* **35**, 1406–1412 (2003)
17. Hanlon, E., Bir, C.: Validation of a wireless head acceleration measurement system for use in soccer play. *J. Appl. Biomech.* **26**, 424–431 (2010)
18. Jordan, S.E., Green, G.A., Galanty, H.L., Mandelbaum, B.R., Jabour, B.A.: Acute and chronic brain injury in United States National Team soccer players. *Am. J. Sports Med.* **24**, 205–210 (1996)
19. Taha, Z., Hassan, M.H.A., Hasanuddin, I.: Analytical modelling of soccer heading. *Sadhana* **40**, 1567–1578 (2015). <https://doi.org/10.1007/s12046-015-0383-5>

Part V
Modelling and Simulation

A Study on the Exposure of Vertical Vibration Towards the Brain on Seated Human Driver Model



Nurul Afiqah Zainal, Muhammad Aizzat Zakaria and K. Baarath

Abstract Human experiences low-frequency excitation through driving which affect the human's health. Research had been conducted over the years by using biodynamic model of seated human body to analyze and observe the effect of vehicle vertical vibration towards the subject. However, previous study only focuses on the effect of vertical vibration up to head segment without taking the brain effect into account. In this study, biodynamic model is modelled including the brain to study the impact of vibration on the brain. Spring-mass-damper system are used in this model to represent the biodynamic model of seated human body and compared with previous study. From the model, it shows that the proposed model able to show the significant impact that happen on the skull and brain when vibration is exerted to the human body.

Keywords Vibration · Vehicle · Biodynamic model

1 Introduction

Human drivers are exposed to vibration as the traveling increases due to the road condition. Katu et al. [1] had proved that the vibration exposure had cause bad effects towards human health such as back problem, increase in heart rate and effects on digestive system and female reproductive organs. Besides that, human alertness level also decreases which this leads to road accidents [2].

Biodynamic model is the representative of few aspects in human body as to create a hypothesis in predicting the accurate model of human body [3]. There are two methods that are usually used in the study of biodynamic model which are analytical and experimental method. Analytical model can be described as mathematical model that used as to represent the human body which is simple and easy

N. A. Zainal · M. A. Zakaria (✉) · K. Baarath
Faculty of Manufacturing Engineering, Universiti Malaysia Pahang,
26600 Pekan, Pahang, Malaysia
e-mail: maizzat@ump.edu.my

© Springer Nature Singapore Pte Ltd. 2018
M. H. A. Hassan (ed.), *Intelligent Manufacturing & Mechatronics*,
Lecture Notes in Mechanical Engineering,
https://doi.org/10.1007/978-981-10-8788-2_54

601

to analyze which also be validate with experimental work. While for experimental method, this method uses living human, human corpses and dummies as a test subjects in order to performed the experimental [4]. Generally, recent studies on biodynamic models only focus on the model of human body without the present of vehicle model. The biodynamic model is modeled as lumped massed that are connected by springs and dampers which represent the body joints and muscles. Then, these models consist of vibration as input directly to the biodynamic model.

In this paper, previous biodynamic model is improved with the addition of brain part as to observe the effect of vibration on the brain. Studies recently had proved that there are significant response on brain due to an impact towards it [5]. Furthermore, human body are exposed to wide range of vibration with range of frequency from 1 to 80 Hz for whole body vibration and from 80 to 1250 Hz for vibration on the steering wheel [6].

In order to verify the vibration exposed on seated human, vibration data was collected on a road to observe its characteristics when the vehicle hit a bump or a hole with a constant speed at 80 km/h in 1 min travel time. Figure 1 shows that there is significant increase on the amplitude when the vehicle collides on the disturbance every 10 s due to uneven road profile. The data was taken by using iPhone 6 accelerometer due to its accuracy in data measurement [7, 8] which contains 2 types of accelerometer; Bosch BMA280 and InvenSense MPU 6700 sensors. Both sensors come with ± 2 g to ± 16 g 3-axis accelerometer, 3-axis gyroscope with 2000 Hz and 4000 Hz sampling rate respectively.

Besides that, Fig. 2 shows the quarter-car model with mass of 250 kg had been used as to observe the force acting on the tire of the quarter car model that occurred when the car is moving. The model consists of the sprung mass, m_s which represent the car equivalent of the vehicle body mass and unsprung mass, m_u represents the equivalent mass due to axle and tire. Then, the suspension consists of spring k_s , damper, b_s and active force actuator, F_a which can be set to zero in passive suspension. Spring, k_t represent the vertical stiffness of the tire while the z_s , z_u , and z_r

Fig. 1 Vibration on vehicle

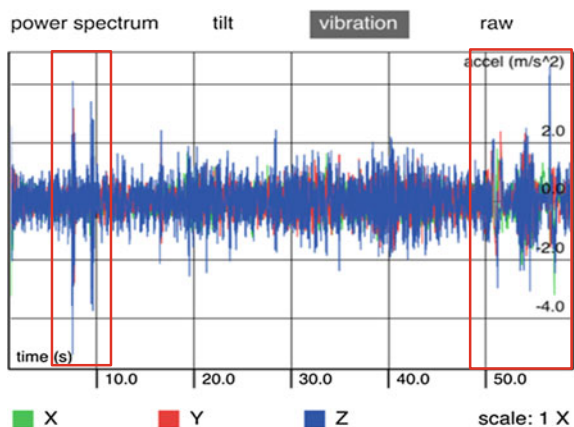
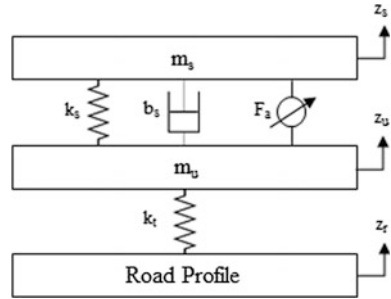


Fig. 2 Quarter-car model [9]



represent the vertical displacement of static equilibrium of the sprung mass, unsprung mass and the road respectively [9].

This two (2) degree of freedom (DOF) model represents the automotive system at any of the four wheel of the vehicle as it present the motion of the axle and the vehicle body [9]. Thus, below are the equations of motion that represent the quarter-car suspension.

$$F_a = m_s \ddot{z}_s + b_s (\dot{z}_s - \dot{z}_u) + k_s (z_s - z_u) \tag{1}$$

$$-F_a = m_u \ddot{z}_u + b_1 (\dot{z}_u - \dot{z}_r) + k_t (z_u - z_r) - b_s (\dot{z}_s - \dot{z}_u) - k_s (z_s - z_u) \tag{2}$$

The force output acting on the tire of the quarter-car model were on z-axis (F_z). Figure 3 and 4 shows the quarter-car model used and the F_z output obtained from the model. From Fig. 4, the result shows high force acting on the tire when constant speed was given. This output may result high vibration exerted on human body coming from the vehicle.

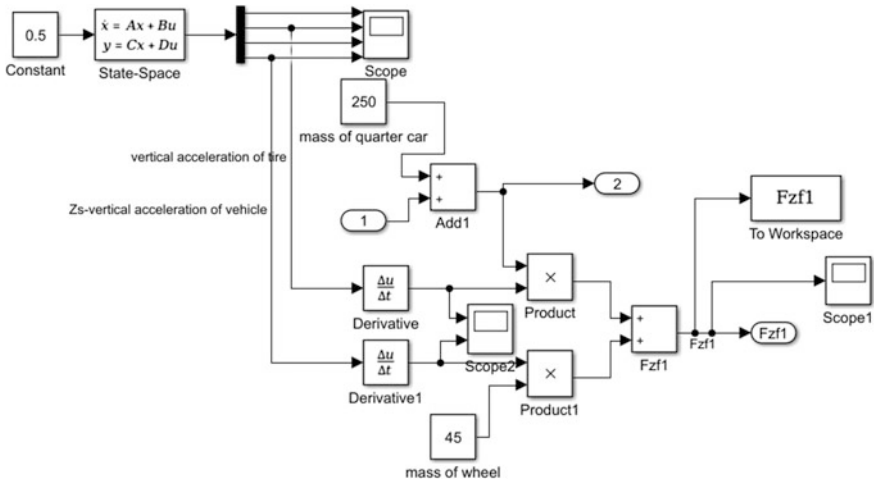


Fig. 3 Quarter-car model

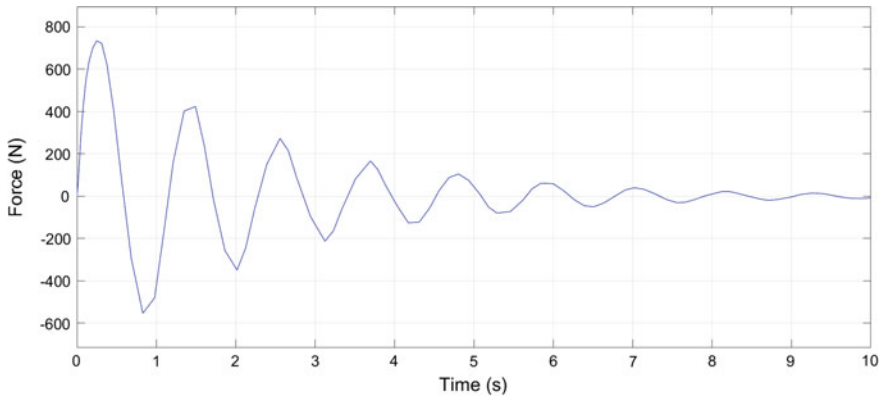


Fig. 4 Force on z-axis (F_z)

2 Biodynamic Model of Seated Human and Mathematical Model

Two biodynamic models with brain parameters were used to investigate the respond towards the vibration. Seven (7) and eleven (11) DOF model [4] which commonly used were used and brain model were added to the models respectively by using the proposed parameters [5] which represent eight (8) and twelve (12) DOF as the new model. These models were linear model which were the composition of lumped mass model connected with springs and dampers which represents the joints and muscles in the human body. This model is simple and easy for analysis.

The schematic of 8 DOF and 12 DOF model of seated human body as shown in Fig. 5 respectively. The lumped model consists of masses, m_i attached with dampers, c_i and springs, k_i which represents the joints and muscles on the human body for each degree of freedom. Table 1 shows lists of biodynamic model parameters for 8 DOF and 12 DOF model respectively.

The set of equation representing the vertical seated human model in 8 DOF is presented as equation below.

$$m_1\ddot{z}_1 = -k_1(z_1 - z_0) - c_1(\dot{z}_1 - \dot{z}_0) + k_2(z_2 - z_1) + c_2(\dot{z}_2 - \dot{z}_1) + k_6(z_6 - z_1) + c_6(\dot{z}_6 - \dot{z}_1) \quad (3)$$

$$m_2\ddot{z}_2 = -k_2(z_2 - z_1) - c_2(\dot{z}_2 - \dot{z}_1) + k_3(z_3 - z_2) + c_3(\dot{z}_3 - \dot{z}_2) \quad (4)$$

$$m_3\ddot{z}_3 = -k_3(z_3 - z_2) - c_3(\dot{z}_3 - \dot{z}_2) + k_4(z_4 - z_3) + c_4(\dot{z}_4 - \dot{z}_3) \quad (5)$$

$$m_4\ddot{z}_4 = -k_4(z_4 - z_3) - c_4(\dot{z}_4 - \dot{z}_3) + k_5(z_5 - z_4) + c_5(\dot{z}_5 - \dot{z}_4) \quad (6)$$

Table 1 8 DOF and 12 DOF biodynamic model parameter [4, 5]

Model	Mass (kg)	Damping (Ns/m)	Stiffness (N/m)
8 DOF	$m_1 = 27.230, m_2 = 5.291$ $m_3 = 0.455, m_4 = 1.362$ $m_5 = 32.762, m_6 = 6.820$ $m_7 = 3.500, m_8 = 1.500$	$c_1 = 371.0, c_2 = 292.0$ $c_3 = 292.0, c_4 = 292.0$ $c_5 = 292.0, c_{56} = 3\ 580.0$ $c_6 = 3\ 580.0$ $c_7 = 450.0$ $c_8 = 340.0$	$k_1 = 25\ 500.0, k_2 = 877.0$ $k_3 = 877.0, k_4 = 877.0$ $k_5 = 877.0, k_{56} = 52\ 600.0$ $k_6 = 52\ 600.0$ $k_7 = 800\ 000.0$ $k_8 = 156\ 000.0$
12 DOF	$m_1 = 27.230, m_2 = 5.906$ $m_3 = 0.454, m_4 = 1.362$ $m_5 = 32.697, m_6 = 5.470$ $m_7 = 5.297, m_8 = 2.002$ $m_9 = 4.806, m_{10} = 1.084$ $m_{11} = 3.500, m_{12} = 1.500$	$c_1 = 370.8, c_2 = 292.3$ $c_3 = 292.3, c_4 = 292.3$ $c_{54} = 292.3, c_{59} = 3\ 581.6$ $c_6 = 3\ 581.6, c_7 = 3\ 581.6$ $c_8 = 3\ 581.6, c_9 = 3\ 581.6$ $c_{10} = 3\ 581.6$ $c_{11} = 450.0$ $c_{12} = 340.0$	$k_1 = 25\ 016.0, k_2 = 877.0$ $k_3 = 877.0, k_4 = 877.0$ $k_5 = 877.0, k_{59} = 52\ 621.0$ $k_6 = 67\ 542.0$ $k_7 = 67\ 542.0$ $k_8 = 52\ 621.0$ $k_9 = 52\ 621.0$ $k_{10} = 52\ 621.0,$ $k_{11} = 1\ 800\ 000.0$ $k_{12} = 156\ 000.0$

$$m_5\ddot{z}_5 = -k_5(z_5 - z_4) - c_5(\dot{z}_5 - \dot{z}_4) - k_{56}(z_5 - z_6) - c_{56}(\dot{z}_5 - \dot{z}_6) \tag{7}$$

$$m_6\ddot{z}_6 = -k_6(z_6 - z_1) - c_6(\dot{z}_6 - \dot{z}_1) + k_{56}(z_5 - z_6) + c_{56}(\dot{z}_5 - \dot{z}_6) + k_7(z_7 - z_6) + c_7(\dot{z}_7 - \dot{z}_6) \tag{8}$$

$$m_7\ddot{z}_7 = -k_7(z_7 - z_6) - c_7(\dot{z}_7 - \dot{z}_6) + k_8(z_8 - z_7) + c_8(\dot{z}_8 - \dot{z}_7) \tag{9}$$

$$m_8\ddot{z}_8 = -k_8(z_8 - z_7) - c_8(\dot{z}_8 - \dot{z}_7) \tag{10}$$

While for 12 DOF, it also can be modelled same as 8 DOF equation of motion derivation.

3 Result and Discussions

Simulation based by using MATLAB[®] Simulink was used to investigate the vibration impact on brain. By using the developed equation of motion as shown in Eqs. (1)–(8), time-domain analysis was done as shown in Fig. 6.

Sine wave input was used as the input of vibration with amplitude value was one (1) and frequency value was 5 Hz [6]. These values were chosen as human body was subjected to vibration ranging from 5 to 500 Hz [10]. As for the output, both output from brain and skull were observed in one scope to observe the relationship

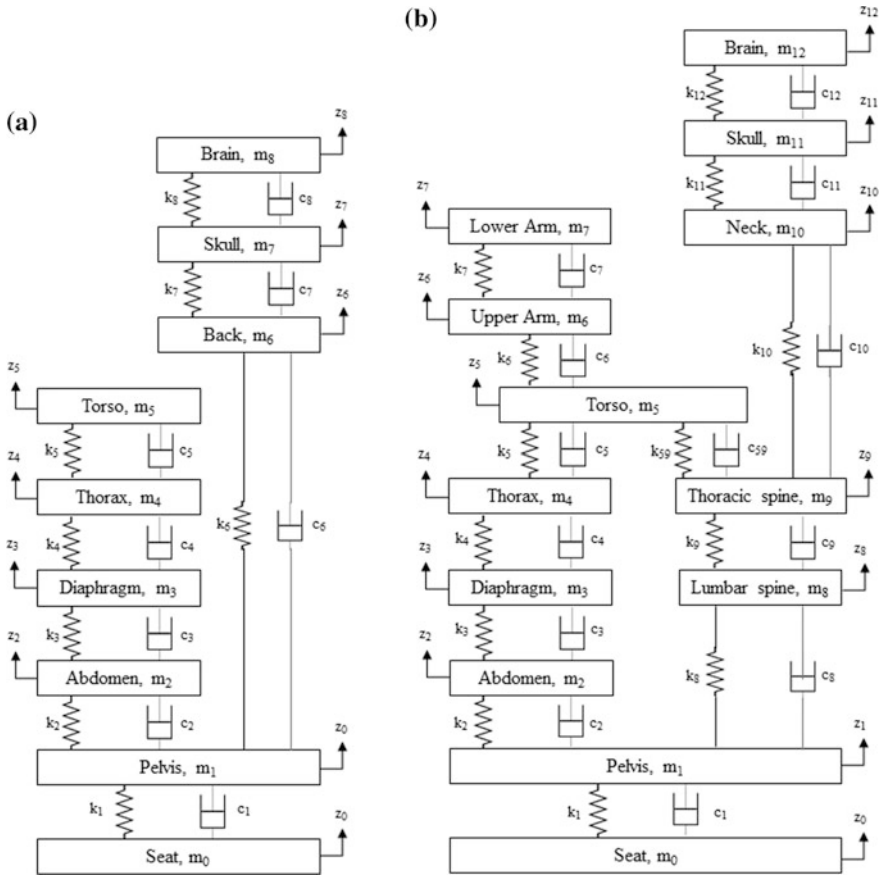


Fig. 5 Schematic of a 8 DOF and b 12 DOF [4, 5]

of both output. Figure 7 and 8 show the simulation results for both 8 DOF and 12 DOF biodynamic model respectively.

Both figures show an impact on skull and brain when a force applied to the model. From the figures, the displacement happens when a force was acting on the model and oscillate before it comes to its steady state. Besides that, from the closeup figures, there were intersection point occurred between the signals from skull and brain on the peak of oscillation where 0.1122 s for 8 DOF and 0.1176 s for 12 DOF. The signal of skull begins to accelerate follow by the brain's signal with a gap of time of milliseconds before both signals reach the peak of acceleration and collide with each other. Besides that, it shows that the amplitude of brain's signals higher after the impact on both signals. Then, the brain takes the leads when decelerate followed by the skull before it reaches to its steady state. These results show there were significant displacement recorded on the brain and the skull before a collision happen between these two parameters. This shows the vibration exerted

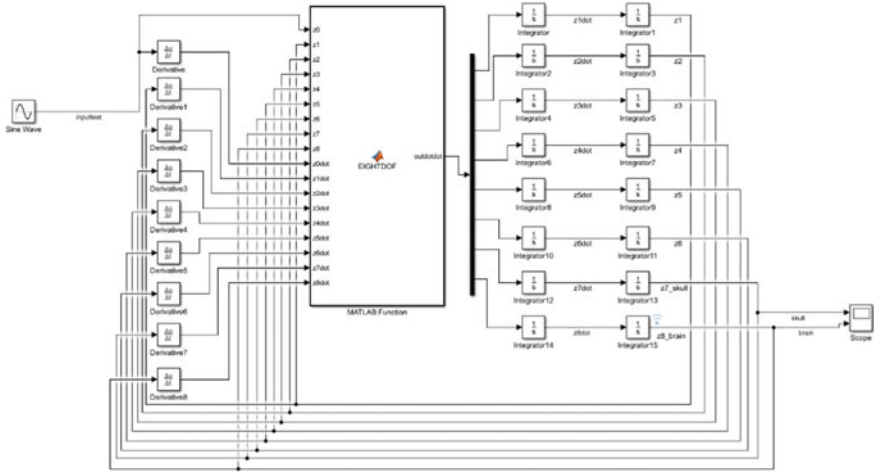


Fig. 6 8 DOF Simulink

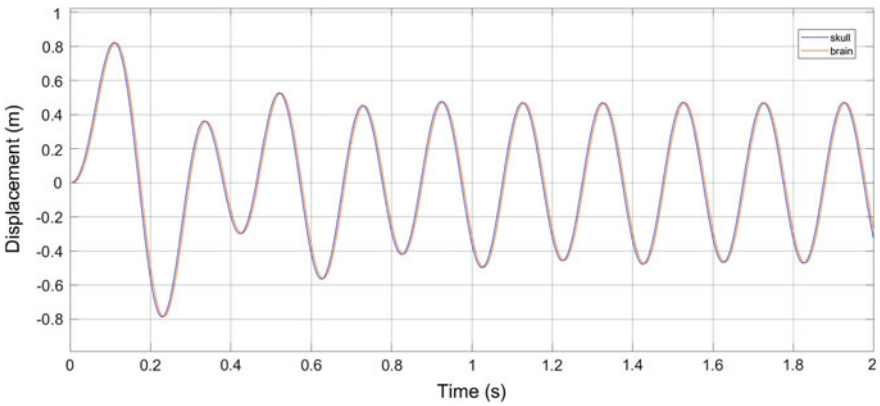


Fig. 7 Skull and brain displacement for 8 DOF model

on human body due to uneven road profile (Fig. 1) will cause higher amplitude on brain compared to skull. From this result, the impact could lead to brain injury or trauma [5].

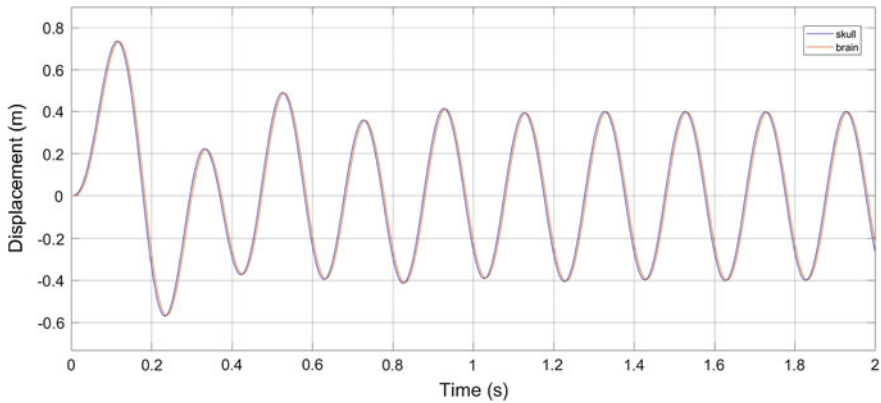


Fig. 8 Skull and brain displacement for 12 DOF model

4 Conclusion

8 DOF and 12 DOF biodynamic model had been developed to investigate the relationship of skull and brain towards the vertical vibration exerted on human body during driving based on the parameters obtained from the literature. The results show there were significant impact on skull and brain during the peak of acceleration and deceleration which could leads to brain injury or trauma before its reach to the steady state. Furthermore, it clearly shows the relationship of vibration and the impact towards brain where the higher the vibration could lead to higher impact on skull and brain.

Acknowledgements The authors would like to thank Universiti Malaysia Pahang (UMP) for the financial aid for this research under grant RDU170371.

References

1. Katu, U.S., Desavale, R.G., Kanai, R.A.: Effect of vehicle vibration on human body—RIT experience. In: Proceedings of the 11th National Conference on Machines and Mechanisms, pp. 1–9 (2003)
2. Azizan, A., et al.: The influence of vibration on seated human drowsiness. *Ind. Health* **54**(4), 296–307 (2016)
3. Griffin, M.J.: The validation of biodynamic models. *Clin. Biomech.* **16**(1), S81–S92 (2001)
4. Liang, C.C., Chiang, C.F.: A study on biodynamic models of seated human subjects exposed to vertical vibration. *Int. J. Ind. Ergon.* **36**(10), 869–890 (2006)
5. Taha, Z., Arif Hassan, M.H., Hasanuddin, I.: Analytical modelling of soccer heading. *Sadhana Acad. Proc. Eng. Sci.* **40**(5), 1567–1578 (2015)
6. Brammer, A.J.: Chapter 10 vibration, mechanical shock, and impact. In: Source : Standard Handbook of Biomedical Engineering and Design. Library (Lond), pp. 1–28 (2004)

7. Yang, L., Grooten, W.J.A., Forsman, M.: An iPhone application for upper arm posture and movement measurements. *Appl. Ergon.* **65**, 492–500 (2017)
8. McNab, T., James, D.A., Rowlands, D.: iPhone sensor platforms: Applications to sports monitoring. *Procedia Eng.* **13**, 507–512 (2011)
9. Rajamani, R.: *Vehicle Dynamics and Control* (2006)
10. Qassem, W., Othman, M.O., Abdul-Majeed, S.: The effects of vertical and horizontal vibrations on the human body. *Med. Eng. Phys.* **16**(2), 151–161 (1994)

An Investigation on the Effect of Lateral Motion on Normal Forces Acting on Each Tires for Nonholonomic Vehicle



K. Baarath, Muhammad Aizzat Zakaria and Nurul Afiqah Zainal

Abstract Stability of vehicle has been the topic of interest among researchers for decades. Research conducted on vehicle stability relies on the vehicle's lateral and longitudinal dynamics. In order to determine the longitudinal and lateral force acting on tires, the normal force that acts on the tire is required. Furthermore, the forces generated to move the vehicle are dependent on the vehicle's mass. Smaller force is generated if the mass is low and vice versa. Therefore, in this paper, the vehicle modelling is conducted to determine the effect of lateral motion on the normal force generated. Dugoff's tire model and combined vehicle dynamics are used to determine the characteristic of the vehicle. The lateral and longitudinal acceleration generated is used to calculate the normal force generated on each tire. Based on the result, a significant change in normal forces can be observed on each tire when a steering input of 0.05 rad is given. This shows a significant correlation between the lateral motion and normal tire force. Results obtained shows that normal force acting on the left and right side of the tires is affected by the direction of the lateral motion of the vehicle.

Keywords Combined vehicle dynamics · Dugoff's model · Vehicle stability

Nomenclature

α_f	front tire slip angle
α_r	rear tire slip angle
\ddot{x}	longitudinal acceleration
\ddot{y}	lateral acceleration
δ	steering angle
$\dot{\psi}$	vehicle yaw rate

K. Baarath · M. A. Zakaria (✉) · N. A. Zainal
Faculty of Manufacturing Engineering, Universiti Malaysia Pahang, 26600 Pekan,
Pahang, Malaysia
e-mail: maizzat@ump.edu.my

© Springer Nature Singapore Pte Ltd. 2018
M. H. A. Hassan (ed.), *Intelligent Manufacturing & Mechatronics*,
Lecture Notes in Mechanical Engineering,
https://doi.org/10.1007/978-981-10-8788-2_55

ρ	tire slip ratio
C_σ	tire stiffness parameter
C_{α_f}	cornering stiffness of front wheel
C_{α_r}	cornering stiffness of rear wheel
F_{xfl}	longitudinal tire force on the front left tire
F_{xfr}	longitudinal tire force on the front right tire
F_{xrl}	longitudinal tire force on the rear left tire
F_{xrr}	longitudinal tire force on the rear right tire
F_{yfl}	lateral tire force on the front left tire
F_{yfr}	lateral tire force on the front right tire
F_{yrl}	lateral tire force on the rear left tire
F_{yrr}	lateral tire force on the rear right tire
F_{zfl}	normal force acting on the front left wheel
F_{zfr}	normal force acting on the front right wheel
F_{zrl}	normal force acting on the rear left wheel
F_{zrr}	normal force acting on the rear right wheel
g	gravitational acceleration
h_c	height of the vehicle from the centre of gravity
I_w	yaw inertia moment of vehicle at the centre of gravity
I_z	Inertia moment of vehicle
m	total mass of the vehicle
m_f	mass of the vehicle at front
m_r	mass of the vehicle at rear
r_{eff}	effective tire radius
V_w	Velocity of the wheel
V_x	Velocity of the vehicle

1 Introduction

Vehicle stability has always been the focus of many researchers for decades [1, 2]. Longitudinal and lateral motion is the major contributing factor in the development of traction and stability control system [2]. Generally, a vehicle is affected by the tire-road friction, tire-vehicle slip ratio, and tire slip angle during driving or braking [3]. Furthermore, tire models and tire-road friction forces are used in lateral dynamics to analyse the vehicle stability [1]. There is two major tire model used which are Magic Formula and Dugoff's. Development of active vehicle dynamics control system usually focuses on either longitudinal or lateral tire dynamics [4]. Researchers, Ishak et al. in [5] and Piee et al. [6] used the combined dynamic model where both lateral and longitudinal dynamics are considered in their system. Both Dugoff's model and Magic Formula requires the normal force acting on the tire to determine the lateral and longitudinal force. The normal force that acts on a tire is usually used to identify the rollover threshold of a vehicle [7]. The tendency of a vehicle to undergo rollover is called rollover indices. A vehicle experiencing high rollover indices than

its rollover threshold, the vehicle is likely to roll and crash. For instance, a standard sedan has a rollover threshold of 1.0–1.2g of lateral acceleration [8]. Vehicle acceleration in lateral and longitudinal affects the normal force that is exerted on the tires. Furthermore, M. A. Zakaria stated that stability of the vehicle decreases with the road curvature at high velocity [9]. A vehicle at high velocity experiences instability at high curvature road which causes the weight of the vehicle to shift more towards the direction of turning. Therefore, this research will focus on the effect of lateral acceleration on the normal force that acts on the tires.

2 Model Development

In this section, the vehicle model development is discussed. Vehicle dynamic model can be classified into two separate model which is lateral and longitudinal. However, the combined lateral and longitudinal model will be used in this paper since the weight shift effect is considered. In order to calculate the longitudinal and lateral force acting on the tires, Dugoff’s tire model is used. Further up, the wheel load transfer equation is used to calculate the normal force acting on each wheel.

2.1 Vehicle Model

The vehicle model used is the combined lateral and longitudinal model. Usually, the lateral and longitudinal model is used independently. However, using both models together requires consideration of the wheel orientation. Initially, the longitudinal force on each tire is in the direction of the vehicle, however when steering input is given the orientation of the tire changes causing the force to be shifted with the steering angle. This is the same for the lateral force acting on the tire. Figure 1 shows the lateral and longitudinal forces acting on the vehicle when steering input is given.

The equation of motion derived from Fig. 1 is as below.

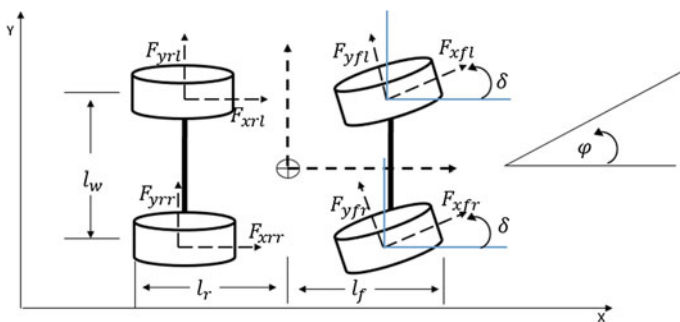


Fig. 1 Longitudinal and lateral forces acting on the vehicle

$$m\ddot{x} = (F_{xfl} + F_{xfr})\cos(\delta) + (F_{xrl} + F_{xrr}) - (F_{yfl} + F_{yfr})\sin(\delta) + m\dot{\psi}\dot{y} \quad (1)$$

$$m\ddot{y} = (F_{yrl} + F_{yrr}) + (F_{xfl} + F_{xfr})\sin(\delta) + (F_{yfl} + F_{yfr})\cos(\delta) - m\dot{\psi}\dot{x} \quad (2)$$

$$\begin{aligned} I_z\ddot{\psi} &= l_f(F_{xfl} + F_{xfr})\sin(\delta) + l_f(F_{yfl} + F_{yfr})\cos(\delta) - l_r(F_{yrl} + F_{yrr}) \\ &\quad + \frac{l_w}{2}(F_{xfr} - F_{xfl})\cos(\delta) + \frac{l_w}{2}(F_{xrr} - F_{xrl}) + \frac{l_w}{2}(F_{yfl} - F_{yfr})\sin(\delta) \end{aligned} \quad (3)$$

Equations 1, 2 and 3 shows the motion in longitudinal and lateral directions and yaw motion respectively. The longitudinal distance from the centre of gravity c.g. to the front wheels and longitudinal distance from the c.g. to the rear wheels are represented by l_f and l_r . Meanwhile, l_w represents the track width.

2.2 Development of Tire Model

The major forces that act on the vehicle generated by the forces and moments from the road that act on each tire of the vehicle. The tires used in vehicles are not rigid, thus they are easily deformable due to the vertical load on it. The forces that act on the vehicle is shown in Fig. 2a. The lateral and longitudinal force is calculated using the Dugoff's model. Dugoff's tire model is advantageous since it considers the independent value of tire stiffness in lateral and longitudinal direction. Moreover, the Dugoff's model is developed from force balance equation which is analytically derived.

The longitudinal and lateral force equation are given as

$$F_x = C_\sigma \frac{\rho}{1 + \rho} f(\lambda) \quad (4)$$

$$F_y = C_\alpha \frac{\tan\alpha}{1 + \rho} f(\lambda) \quad (5)$$

where λ is given by

$$\lambda = \frac{\mu F_z (1 + \rho)}{2[(C_\sigma \rho)^2 + (C_\alpha \tan(\alpha))^2]^{\frac{1}{2}}} \quad (6)$$

and

$$\begin{aligned} f(\lambda) &= (2 - \lambda)\lambda \quad \text{if } \lambda < 1 \\ f(\lambda) &= 1 \quad \text{if } \lambda > 1 \end{aligned}$$

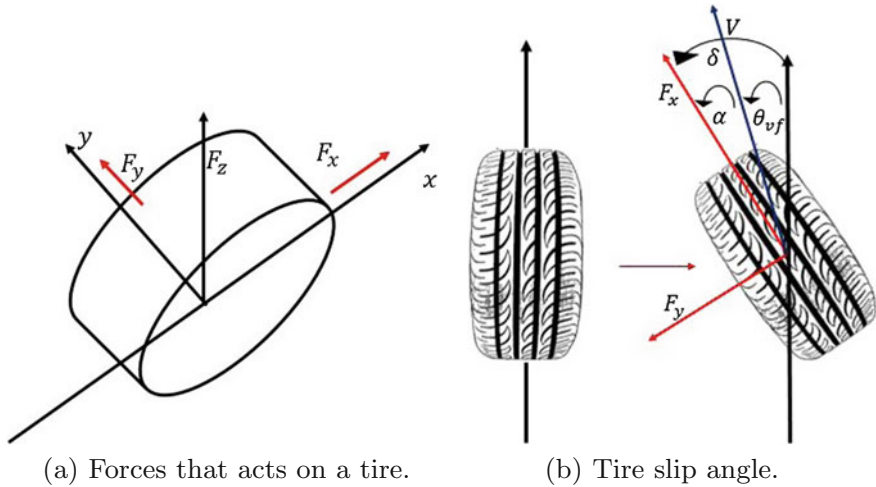


Fig. 2 Forces acting on a tire and its corresponding slip angle given steering input, δ

Based on Fig. 2b, α is given by;

$$\alpha_f = \delta - \theta_{vf} \tag{7}$$

$$\alpha_r = -\theta_{vr} \tag{8}$$

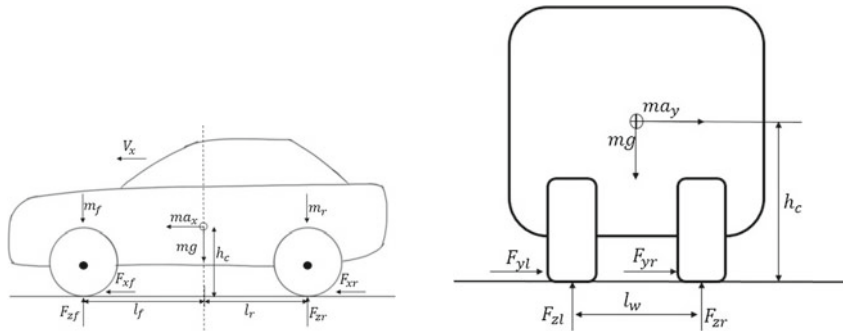
where

$$\theta_{vf} = \tanh \left(\frac{V_y + l_f \dot{\psi}}{V_x} \right) \tag{9}$$

$$\theta_{vr} = \tanh \left(\frac{V_y - l_r \dot{\psi}}{V_x} \right) \tag{10}$$

2.3 Load Transfer

The total mass m , of a vehicle, can be divided into two segments of masses m_r and m_f . The distribution of rear and front vehicle mass is depicted in Fig. 3a. On the other hand, the lateral load transfer is depicted in Fig. 3b. The normal force and load transfer acting on the vehicle is derived based on Fig. 3. Based on the Eq. (11)–(14), the direction of vehicle lateral and longitudinal acceleration determines the vehicle mass shift.



(a) Representation of mass distribution and forces acting on the vehicle. (b) Load transfer in lateral motion.

Fig. 3 Normal Force, F_z acting on the vehicle

$$F_{zfr} = mg \frac{l_r}{2l} + \frac{m_f a_y}{l_w} - ma_x \frac{h_c}{2l} \quad (11)$$

$$F_{zfl} = mg \frac{l_r}{2l} - \frac{m_f a_y}{l_w} - ma_x \frac{h_c}{2l} \quad (12)$$

$$F_{zrr} = mg \frac{l_f}{2l} + \frac{m_r a_y}{l_w} + ma_x \frac{h_c}{2l} \quad (13)$$

$$F_{zrl} = mg \frac{l_f}{2l} - \frac{m_r a_y}{l_w} + ma_x \frac{h_c}{2l} \quad (14)$$

where, $l = l_f + l_r$.

2.4 Simulation Setup

The simulation is conducted using MATLAB Simulink software. The block diagram is arranged as shown in Fig. 4. An initial value of wheel rotational speed ω is given as an input. On the other hand, the normal force is calculated using Eqs. 11–14 for each tire respectively. The calculated force is used in the Dugoffs tire model with the coefficient of road tire friction μ , slip ratio ρ , slip angle α , lateral and longitudinal tire stiffness parameter C_σ and front and rear wheel cornering stiffness (C_{af} , C_{ar}). The output from Dugoffs tire model is the lateral and longitudinal tire force, which is used in vehicle dynamics to calculate the longitudinal and lateral acceleration, velocity and vehicle yaw rate. The value of parameters shown in Table 1 is referred from Ishak [5].

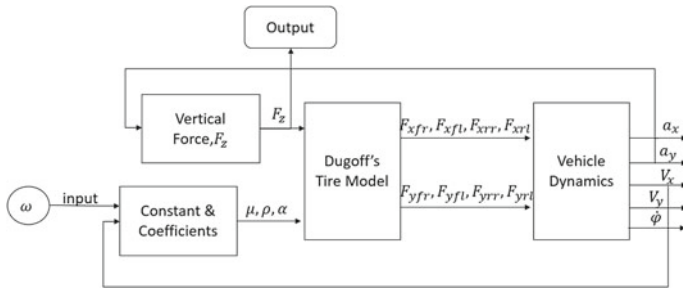


Fig. 4 Representation of simulation block arrangement

Table 1 Value of parameters used [5]

Symbol	Value	Units
l_f	1.4	m
l_r	1.4	m
C_{af}	2000	N/rad
C_{ar}	2612.62	N/rad
C_σ	3000	N/m ³
k	1 = dry asphalt	-
r_{eff}	0.23	m
g	9.81	m/s ²
h_c	0.75	m
l_w	0.9	m
m_f	650	kg
m_r	980	kg
I_w	1.53	kgm ²
I_z	1470	kgm ²

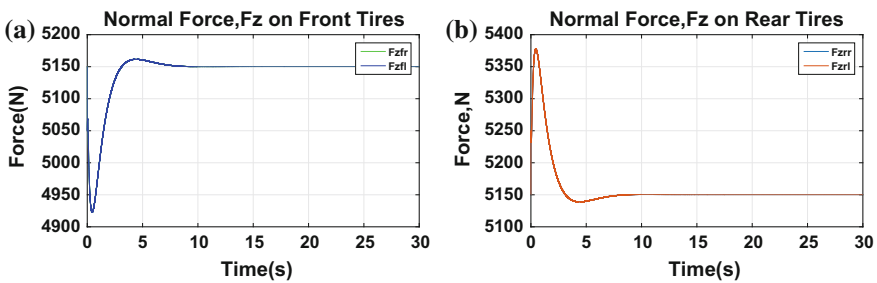
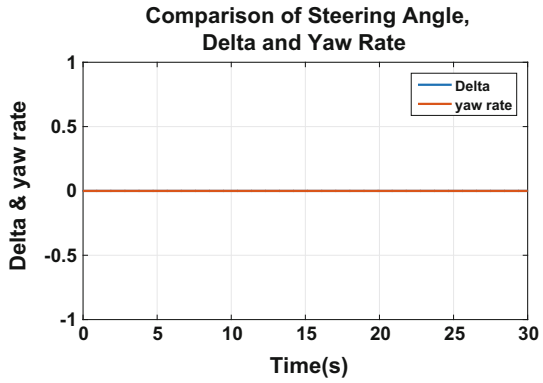
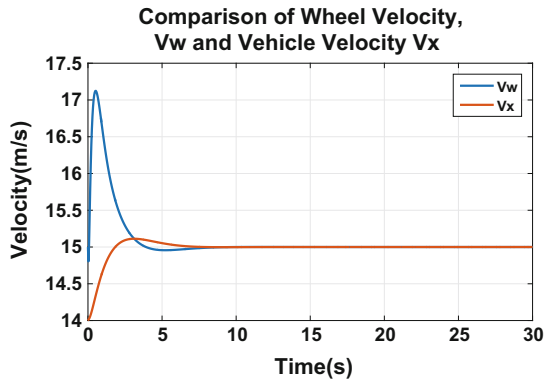


Fig. 5 Velocity and vehicle trajectory given steering input, $\delta = 0$ rad

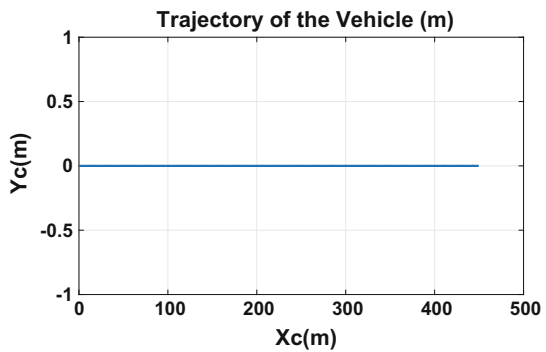
Fig. 6 Normal Force, F_z acting on the tires for $\delta = 0$ rad



(a) Steering input, δ and vehicle heading, $\dot{\psi}$.



(b) Comparison of wheel speed and vehicle speed.



(c) Trajectory of the Vehicle.

The coefficient of friction between road and tire is [10]

$$\mu = -1.05k[(\exp^{-45\rho}) - (\exp^{-0.45\rho})] \quad \text{driving} \tag{15}$$

$$\mu = 1.1k[(\exp^{35\rho}) - (\exp^{0.35\rho})] \quad \text{braking} \tag{16}$$

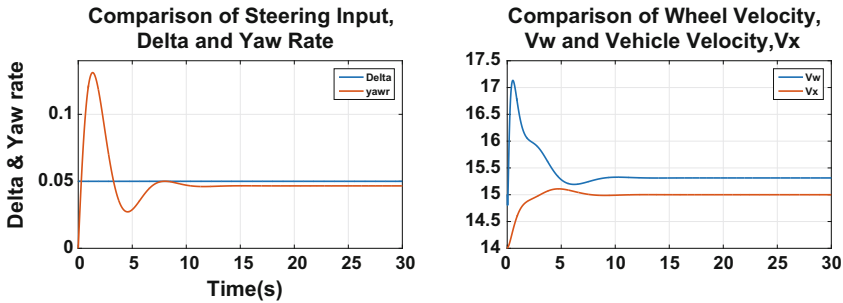
and slip ratio is given by

$$\rho = \frac{V_w - V_x}{V_w} \quad \text{driving} \tag{17}$$

$$\rho = \frac{V_w - V_x}{V_x} \quad \text{braking} \tag{18}$$

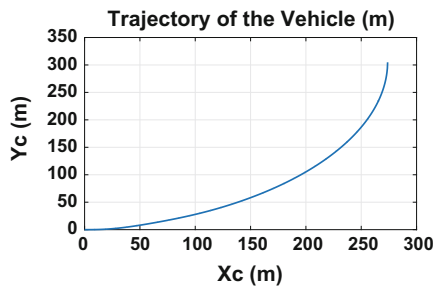
3 Simulation Analysis

A vehicle travelling at 14 m/s is given zero steering input. Figure 5 shows the characteristic of the vehicle. The initial wheel velocity is higher than the vehicle velocity because the vehicle is accelerating, however, both the velocities stabilize at 15 m/s



(a) Steering input, δ and vehicle heading, ψ .

(b) Comparison of wheel speed and vehicle speed.



(c) Trajectory of the Vehicle.

Fig. 7 Velocity and vehicle trajectory given steering input, $\delta = 0.05$ rad

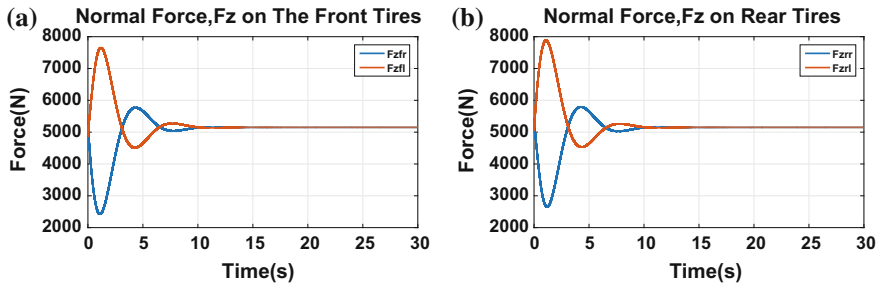


Fig. 8 Normal Force, F_z acting on the tires for $\delta = 0.05$ rad

as depicted in Fig. 5b. Moreover, the motion of the vehicle can be seen in Fig. 5c. In Fig. 6 the normal force acting on the vehicle is shown. The forces that act on front tires are in the same direction and magnitude and this is the same for the rear tires.

For the second case study, an input signal of 0.05 rad (2.8°) is given to the vehicle. The lateral motion of the vehicle changes the motion characteristic of the vehicle which is shown in Fig. 7. A large change of normal force can be detected on the left side of the vehicle as shown in Fig. 8. Initially, the force on right and left of the front and rear tires are in the same direction respectively. However, when there is a lateral motion to the left, the normal force acting on the left tires increases and are in opposite direction of their counterparts.

When there is a high normal force acting in the opposing direction on either side of the vehicle, the stability of the car is affected. For example, as the vehicle turns left, the normal force acting on the left side is high and downwards whereas the normal force acting on the right side is upwards, thus the vehicle could experience rollover if the imbalance in force is too high.

4 Conclusion

The vehicle load transfer model has been developed to investigate the effect of lateral motion on normal forces acting on the tires based on parameters obtained from the literature. A vehicle subjected to normal longitudinal motion only produces normal forces of same magnitude and direction on the front and rear tires respectively. On the contrary, when the vehicle is subjected to lateral motion, the normal forces produced on the left and right tire changes depending on the direction of lateral motion. A vehicle subjected to the lateral motion to the left produces a normal force acting on the left tires to have higher magnitude and opposing direction to the right tires. This could adversely affect the rollover of the vehicle since the roll of the vehicle relies on the normal force acting on the tire. A very high normal force on either side of the vehicle could cause rollover to occur. The modelling presented in this paper could

help identify the normal force generated due to lateral motion, thus enabling us to determine the stability criterion of the vehicle.

Acknowledgements The authors would like to thank Universiti Malaysia Pahang (UMP) for the financial aid for the research under grant RDU170371 and RDU160343.

References

1. Hashemi, E., Pirani, M., Khajepour, A., Kasaiezadeh, A.: A comprehensive study on the stability analysis of vehicle dynamics with pure/combined-slip tyre models. *Veh. Syst. Dyn.* **54**(12), 1736–1761 (2016)
2. Hashemi, E., Pirani, M., Khajepour, A., Kasaiezadeh, A., Chen, S.K., Litkouhi, B.: Corner-based estimation of tire forces and vehicle velocities robust to road conditions. *Control Eng. Pract.* **61**(February), 28–40 (2017)
3. Zhang, B., Du, H., Lam, J., Zhang, N., Li, W.: A novel observer design for simultaneous estimation of vehicle steering angle and sideslip angle. *IEEE Trans. Ind. Electron.* **63**(7), 4357–4366 (2016)
4. Kunnappillil Madhusudhanan, A., Corno, M., Arat, M.A., Holweg, E.: Load sensing bearing based road-tyre friction estimation considering combined tyre slip. *Mechatronics* **39**, 136–146 (2016)
5. Ishak, M.I., Ogino, H., Yamamoto, Y.: Numerical simulation analysis of an oversteer in-wheel small electric vehicle integrated with four-wheel drive and independent steering. *Int. J. Veh. Technol.* **2016**, (2016)
6. Peeie, M.H.B., Ogino, H., Oshinoya, Y.: Skid control of a small electric vehicle with two in-wheel motors: simulation model of ABS and regenerative brake control. *Int. J. Crashworthiness* **21**(5), 396–406 (2016)
7. Ma, Z., Ji, X., Zhang, Y., Yang, J.: State estimation in roll dynamics for commercial vehicles. *Veh. Syst. Dyn.* **55**(3), 313–337 (2017)
8. Mashadi, B., Mostaghimi, H.: Vehicle lift-off modelling and a new rollover detection criterion. *Veh. Syst. Dyn.* **55**(5), 704–724 (2017)
9. Zakaria, M.A., Zamzuri, H., Mazlan, S.A.: Dynamic curvature steering control for autonomous vehicle: performance analysis. In: *IOP Conference Series: Materials Science and Engineering*, vol. 114, no. 1 (2016)
10. Kodama, S., Hori, Y., Li, L.: Skid prevention for EVs based on the emulation of torque characteristics of separately-wound DC motor. In: *The 8th IEEE International Workshop on Advanced Motion Control, 2004. AMC '04*, no. 6, pp. 75–80 (2004)

Numerical Analysis of Fuzzy Logic Temperature and Humidity Control System in Pharmaceutical Warehouse Using MATLAB Fuzzy Toolbox



Nurainaa Elias, Nafrizuan Mat Yahya and Er Hong Sing

Abstract This paper describes the simulation for performance evaluation of fuzzy logic controller in pharmaceutical warehouse's temperature and humidity control system by using MATLAB Fuzzy Logic Toolbox and MATLAB Simulink. MATLAB fuzzy toolbox is used where a fuzzy logic controller is designed to simulate the control system based on control input such as user desired temperature, user desired humidity and deviation from desired parameters. The output control will be the cool fan speed, operation speed of ventilation fan (humidifier) and exhaust fan (dehumidifier). The result will be described in terms of the speed of output actuators changing with the difference in input temperature and humidity. The results of the Simulink model with optimized efficient and good performance are presented. The main aim is to achieve the output actuators with good performance, stable and smooth as the desired set point temperature and humidity and also develop fuzzy inference control system to simulate and monitor the desired temperature and ventilation system in pharmaceutical warehouse area.

Keywords Fuzzy logic controller • MATLAB simulink • MATLAB toolbox

1 Introduction

The control system for temperature and ventilation play an important role in pharmaceutical industry especially in warehouse area. All of the medical products should be stored under the recommended temperature and ventilation conditions at all times, as permitted by the medicine manufacturer. Heating, Ventilation and Air-Conditioning (HVAC) system plays a very important role in supporting the quality of pharmaceutical products and also some medical's chemical reaction process [1]. The components of HVAC systems generally include exhaust fans,

N. Elias (✉) · N. M. Yahya · E. H. Sing
Faculty of Manufacturing Engineering, University Malaysia Pahang (UMP),
26600 Pekan, Malaysia
e-mail: nurainaa_elias@yahoo.com

© Springer Nature Singapore Pte Ltd. 2018
M. H. A. Hassan (ed.), *Intelligent Manufacturing & Mechatronics*,
Lecture Notes in Mechanical Engineering,
https://doi.org/10.1007/978-981-10-8788-2_56

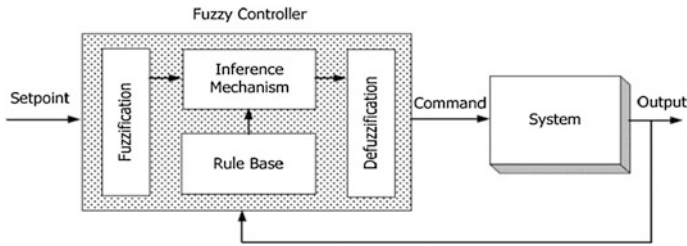


Fig. 1 Basic configuration of fuzzy logic controller

filters, humidifiers, dehumidifiers, heating and cooling coils, ducts, and various sensors [2]. The reason for developing concepts of fuzzy logic control on previous control theory is that the previous classical control theory usually requires a mathematical model. The inaccuracy of mathematical modelling of the plants will affect the performance of the controller, especially for non-linear and complex control problems [3]. Fuzzy logic control do not require mathematical models of the plants information and expert knowledge into control. Fuzzy logic is easier to develop since fuzzy logic is based on natural language as human communication [4]. Fuzzy logic has been proposed as the model for humans' sense of words, decision making and common sense, it is leading to more human intelligent machines [4]. A system that takes uses fuzzy membership functions to make a decision based on the processing of reasoning in fuzzy logic is called a fuzzy inference system (FIS). Fuzzy Logic controller consists of four basic components: fuzzification, a rule base, inference engine, and a defuzzification interface as shown in Fig. 1.

2 Method

2.1 MATLAB Fuzzy Logic Toolbox

The Fuzzy Logic Toolbox is a collection of functions built on the MATLAB software. MATLAB provides graphical user interface (GUI) tools inside the fuzzy logic toolbox for users to create and edit fuzzy inference systems. There are five primary GUI tools for building, editing, and observing fuzzy inference systems in the Fuzzy Logic Toolbox which shown in Fig. 2. These five primary GUI tools are the Fuzzy Inference System or FIS Editor, the Membership Function Editor, the Rule Editor, the Rule Viewer, and the Surface Viewer.

Temperature and humidity fuzzy logic controllers was developed in MATLAB Fuzzy Logic Toolbox. The fuzzy rule was set or evaluated by the rule antecedent (the IF part of the rule) and applying the result to the consequent (the THEN part of the rule). The Rule Editor is the text field for editing the list of rules that defines the behavior of the system. There are 15 fuzzy rules that set respectively for each

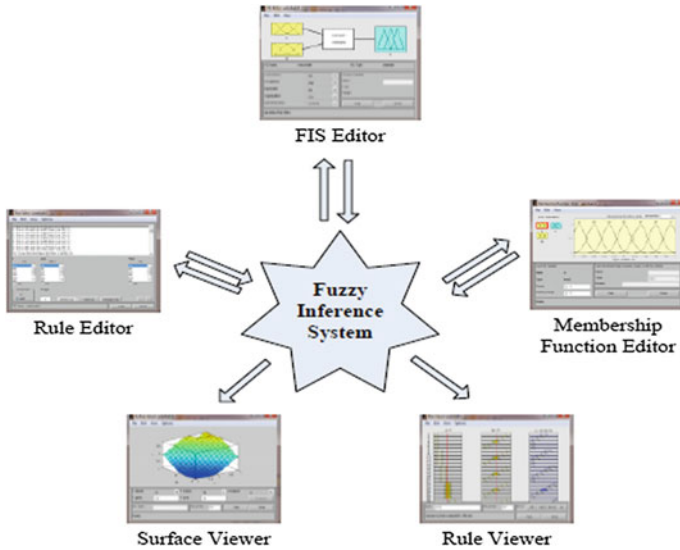


Fig. 2 MATLAB fuzzy logic toolbox

temperature and humidity fuzzy logic controllers. The last two GUIs (Rule Viewer and Surface Viewer) are used for looking and analyze the results.

2.2 MATLAB Simulink

After the fuzzy logic controller (FLC) was developed completely and also the results obtained by Surface Viewer, the MATLAB Simulink model was developed for fuzzy logic controller to simulate and evaluate the performance of the system. The output actuator in the Simulink model was used was the DC motor. The transfer function of DC motor was used inside the Simulink model to represent the output actuators. The performance of the system was simulate throughout the output scope of Simulink model. The Simulink model for temperature and humidity fuzzy logic controller was developed as shown in Figs. 3 and 4. The Simulink model that shown in Figs. 3 and 4 consists mainly of the fuzzy logic controller block and the DC motor block. The output of the DC motor block which is the motor speed is monitored using a scope to examine its response. Similarity for Simulink model of Fig. 4, two output signals of the DC motor block which is the motor speed for humidifier (ventilation fan) and dehumidifier (exhaust fan) are monitored by using a scope to examine their response. The values used in the gains of scale have been selected through an adaptive method based on the results of successive simulations.

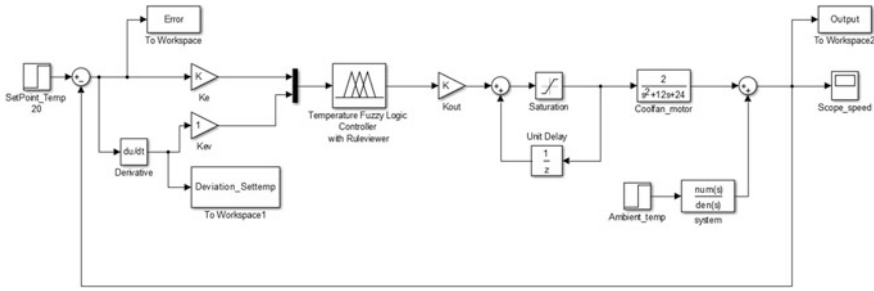


Fig. 3 Simulink model for temperature fuzzy logic controller

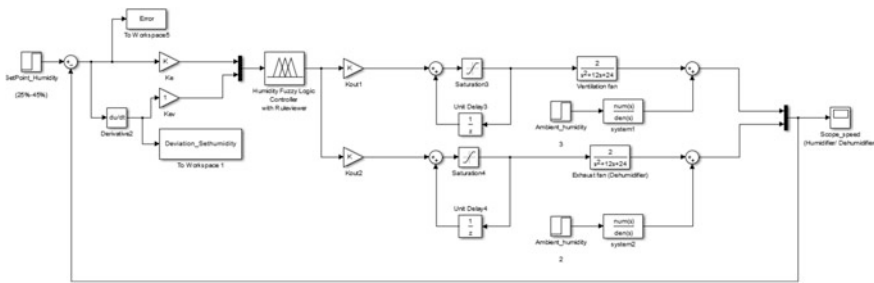


Fig. 4 Simulink model for humidity fuzzy logic controller

3 Result

The tuning of fuzzy logic controller can be achieved by adjusting the range of the universe of discourse for the linguistic variables and positions of the membership function used [5]. The performance of the system was simulate throughout the output Scope of Simulink model. The output of the DC motor block which motor speed is monitored to examine its response. The time response of output actuators (motor speed) for temperature and humidity fuzzy controller was shown in Tables 1 and 2.

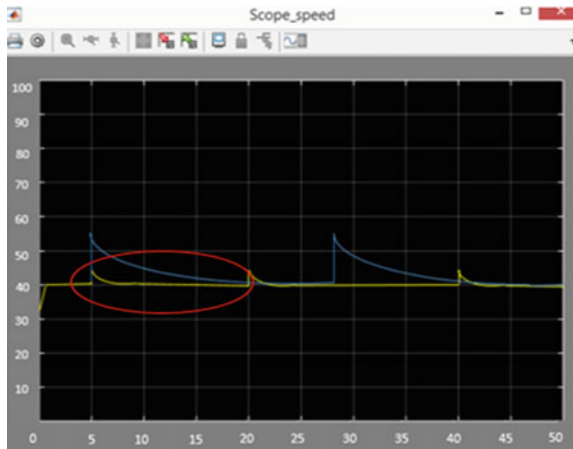
Table 1 Time response for different temperature

Current temperature (°C)	Deviation from set temperature (°C)	Cool fan speed (rpm)	Time response (ms)
7	+13	8	30
12	+8	20	14
20	0	40	4
28	-8	62	17
35	-15	90	22.5

Table 2 Time response for different humidity

Current relative humidity (%)	Speed (rpm)		Time response (ms)	
	Ventilation fan	Exhaust fan	Ventilation fan	Exhaust fan
15	72	5	18	13
20	50	20	10	6
35	30	38	4	4
50	20	56	8	12
80	5	64	10	14

Fig. 5 Disturbance signal for the temperature control system from simulink scope



Beside analysis the performance of the fuzzy logic system, the disturbance factors also consider to analysis the system response (Fig. 5).

Disturbance means the interruption of the system. For the temperature control system, the outdoor air or temperature will affect the room or indoor condition. For example, when the door of warehouse was opened for a long time, the indoor temperature might have slightly effect. This means the disturbance or interruption of the system. Similarity, for humidity control system, the air flow level or air movement from the outdoor might cause the slightly changing or effect to the system. For disturbance analysis, the disturbance block was included in the Simulink model to analysis the changed performance of the system.

4 Discussion

From the results above, the tuning of fuzzy logic controller was successfully control by the fuzzy rules. The performances of the output actuator (motor) are changing as the input variables by the manipulated of fuzzy logic controller. The result

described in terms of the speed of output actuators changing with the difference input temperature and humidity. The results of the Simulink model with optimized efficient and good performance are presented. The output actuators (motor speed) was achieved with good performance, stable and smooth as the desired set point temperature and humidity at specified time period. In fact, the performance result was analysis based on two parts which first part is the simulation performance on temperature and humidity fuzzy logic controller respectively on Simulink model and the second part is the disturbance analysis on the performance of system. It can be seen that the results are acceptable since fuzzy logic controller (FLC) is operated efficiency and delivered the result depend on the requirement of user (fuzzy rules). So, the result is good performance and the best efficiency by using fuzzy logic controller and Gaussian membership function for this system.

For second part, the disturbance analysis on the performance of system shown that the consideration of disturbance factor from outside had caused the effect to the performance of system. The disturbance factor that considered into the system such as the outdoor temperature and air flow had affect the performance of the output motor speed. For example, in temperature fuzzy control system the disturbance motor speed signal appear bigger noise than the system that without disturbance. However, the fuzzy logic controller overcome the disturbance factor in the short time. The motor speed only taken around 11 ms to stabilize the cool fan speed. In other hand, for humidity fuzzy controller taken around 15 ms to overcome the disturbance factor and stabilize the motor speed. All of the result can be seen that the fuzzy logic controller was operated in good performance and efficiency.

5 Conclusion

The objective of this project was successfully accomplished since fuzzy logic controller (FLC) is operated efficiency and delivered the result depend on the requirement of user (fuzzy rules). The output actuators of motor speed are achieved with good performance, stable and smooth as the desired set point temperature and humidity. Besides, in disturbance analysis part, fuzzy logic controller overcome the disturbance factor in short time and stabilize desired motor speed with good efficiency. Although the objectives of this present research had been successfully accomplished as discussed in the conclusion, but there are still have many improvements can be made to achieve better outcomes. Therefore, there are some recommendations for the future work to achieve the better outcomes and improve their further studies.

1. Compare the results with other controllers such as PID controller although the fuzzy logic controller method in this project achieved the good performance. The comparison between both methods can made the better proven for the results and enhance the credibility of this study.

2. Develop the experimental work or controller's prototype in the real condition for pharmaceutical warehouse. This is because the limitation for this project is we don't have the real data analysis for the temperature and humidity condition in pharmaceutical warehouse.

References

1. Authority, H.S.: Guidance notes on heating, ventilation and air-conditioning (HVAC) systems for manufacturers of oral solid dosage forms. *Eng. Manuf. Med. Appl.* **49**, 865–873 (2013)
2. Om Prakash Verma, H.G.: Fuzzy logic based water bath temperature control system. *IEEE Control Syst. J.* **22**(3), 56–67 (2012)
3. Addison-Wesley: artificial intelligence-a guide to intelligent systems. *Eng. Appl. Artif. Intel.* New York **20**(1), 89–99 (2005)
4. Parkson, S., Nickel, David: Temperature control using fuzzy logic. *Int. J. Instrum. Control Syst.* **4**(1), 1–10 (2014)
5. Nise, N.S.: *Control Syst. Eng.* Mc Graw Hill, United State, **6**(2), 329-345 (2006)

Parameter Properties of a Sliding Mode Controller Design in Friction Compensation



N. A. Rafan, Zamberi Jamaludin, Tsung Heng Chiew
and N. A. Mulop

Abstract An optimized controller provides consistent performance with high accuracy and precision even in the presence of disturbance forces. Disturbance forces can be a cutting force or friction force or both. Tracking performance of a drive system is critically influenced by the mechanical structure, disturbance forces and work piece mass. Sliding mode controller is designed to compensate disturbance forces especially friction. This paper presents parameter tuning strategies in designing a sliding mode controller in compensating a nonlinear friction behaviour occurred in machine tools application. The main parameter properties of a sliding mode controller are identified and analyzed. The proposed methods are analytically designed and numerically validated by variability index performance. The result analysis is presented by comparison of tracking position errors of linear motion using proposed methods with lower variability index. The result shows that method a with approach b has lower tracking position error and lower variability index, hence a better chattering effect and tracking position error performance.

Keywords Friction compensation · Sliding mode controller · Chattering

1 Introduction

Friction compensation models can be applied in a feedforward configuration. The effectiveness of feedforward depends on the accuracy of the applied friction model [1]. Tracking performance in case of motion systems is enhanced by the feedforward controller. The feedforward controller as a part of a two degree of freedom controller structure is usually designed based on the closed-loop transfer function. If the closed-loop transfer function is depending on the plant model, like in traditional controllers, no robustness property can be expected in the feedforward controller.

N. A. Rafan (✉) · Z. Jamaludin · T. H. Chiew · N. A. Mulop
Faculty of Manufacturing Engineering, Universiti Teknikal Malaysia Melaka,
76100 Durian Tunggal, Melaka, Malaysia
e-mail: aidawaty@utem.edu.my

© Springer Nature Singapore Pte Ltd. 2018
M. H. A. Hassan (ed.), *Intelligent Manufacturing & Mechatronics*,
Lecture Notes in Mechanical Engineering,
https://doi.org/10.1007/978-981-10-8788-2_57

This problem can be partly solved by applying the Sliding Mode Controller (SMC) technique in the closed-loop [2]. It has been proven that the closed-loop system designed with SMC may have a characteristic equation independent of the plant model. However, the main drawback of SMC method is chattering effect due to fast switching within trajectory [3–5].

This paper describes the study of parameter tuning strategies for Sliding Mode Control (SMC) and to analyze the effectiveness of tuning strategies selected. SMC design is modelled by control law and defined sliding surface. However, Baeza and Garcia [6] demonstrated numerically in parameter tuning of SMC design and compared the variability of controllers design by using variability index. The authors conducted performance analysis of valve design by using SMC controllers and PID controllers, and have shown that low variability index managed to obtained best tracking performance. Since, tuning methods that have been studied previously are the best methods for tuning PID controller [7], this paper explores parameter tuning strategies as proposed in [6] and validated by variability index to compare the performance theoretically.

This paper is organized as follows. Section 2 provides controller design and parameters of Sliding Mode Controller that affect tracking position error. The design simulation requirement for good performance of SMC is also presented in this section. Section 3 discusses results analysis of selected parameters to the performance of SMC in tracking position error by tracking error and variability index. Section 4 concludes the finding and recommendation of future works.

2 Parameter Estimation of SMC Controller

2.1 Controller Design

In sliding mode controller (SMC), tracking error input signal is a difference between measured position signals with reference input signal. Tracking position error is affected by lambda (λ), delta (δ) and gain (k) [6]. Trajectories of motion are driven to reach sliding surface designed which is called reaching phase. Ideal sliding motion is to ensure trajectories maintain on sliding surface causes fast switching function.

The general form of the sliding surface:

$$s(e, \dot{e}) = \left(\frac{d}{dt} + \lambda \right)^{n-1} e \quad \text{where } \lambda > 0 \quad (1)$$

$$\text{Position error, } e(t) = y(t) - r(t) \quad (2)$$

where, $y(t) = z(t)$ is actual position and $r(t) = z_{ref}(t)$ is reference position.

The plant transfer function for the table relating the amplifier voltage to the encoder position is given as follow:

$$\frac{y(s)}{u(s)} = \frac{69380}{s^2 + 144.8s + 166.3} \tag{3}$$

where, $y(s)$ is encoder position in mm and $u(s)$ is voltage input in volts.

At the moment of ideal sliding motion, the followings are true:

$$n = 2; \text{ order of SMC} \tag{4}$$

$$s(e, \dot{e}) = \dot{e} + \lambda e \quad \text{where } \dot{e} = \dot{y} - \dot{r} \tag{5}$$

$$s(\dot{e}, \ddot{e}) = \ddot{e} + \lambda \dot{e} = 0 \quad \text{where } \ddot{e} = \ddot{y} - \ddot{r} \tag{6}$$

$$\text{Thus, } \ddot{e} = -\lambda \dot{e} \tag{7}$$

$$\text{where, } \dot{y} = \ddot{e} + \dot{r} \tag{8}$$

In most cases the friction is bounded over a certain known limit. Thus, only approximate control input, u can be obtained [8]. The approximate control input, u is therefore,

$$u_{equivalent} = \frac{-\lambda \dot{e} + \dot{r} + 144.8\dot{y} + 166.3y}{69380} \tag{9}$$

Thus, sliding motion is follows,

$$u = \frac{1}{69380} (-\lambda \dot{e} + \dot{r} + 144.8\dot{y} + 166.3y) - k \cdot \text{sgn}(s) \tag{10}$$

where $\text{sgn}(s)$ is signum function represents the discontinuous control across sliding surface. The discontinuous control associated with the signum function often resulted in noisy control input signal. It was reported by Edwards and Spurgeon [7] that replacing the signum function with sigmoid function has reduced the noise content of the control input signal. An example of the sigmoid function is as follow:

$$V_\delta(s) = \frac{s}{(|s| + \delta)} \tag{11}$$

where

- s sliding surface tension,
- δ positive scalar

2.2 Methodology

The parameter that will be tuned is lambda (λ), gain (k), and delta (δ) based on Baeza and Garcia [6]. A simulation test will be performed for the performance of reducing friction in y-axis using SMC controller. The simulation test is performed with velocity of motion, 2 m/s with friction compensation model in ball screw positioning milling table with sample time 50 s. A schematic block diagram of simulation test is shown in Fig. 1 where delta (δ) is included in sigmoid function.

During tuning, there will be two approaches to choose the best tuning strategies for SMC controller. The simulation requirement for two different approaches as in Table 1. Approach A is based on experimental parameter estimation of SMC design. The parameter of SMC design is simulated and selected when output voltage of system is not exceed than 0.7 V since stability effect occurred beyond the stated voltage. In addition, the output voltage of system simulated has minimal noise in frequency and minimal tracking error. Whereas, approach B is based on criterion mentioned by Baeza and Garcia [6]. The simulation requirement for approach B as in Table 1 state that parameter is selected when the system simulated has 0.3% of maximum error, reach time less than 1 s and maximum error of 10%.

The performance of the approach A will be compared with the approach B. For tracking position error, friction compensation performance of the approach A will be analyzed and compared to the approach B in terms of the tracking position error and variability index. By investigating approach B, two proposed methods namely method a and method b is analyzed. In order to compare the variability for proposed methods, Eq. (12) presents the variability index [6]:

$$VI = \frac{2 \cdot \sigma(y)}{\bar{y}} \cdot 100\% \tag{12}$$

where:

- $\sigma(y)$ Standard deviation of output signal
- \bar{y} Mean of output signal

Variability index illustrate the theoretical performance of controllers based on the ratio of standard deviation of output signal of system and mean of output

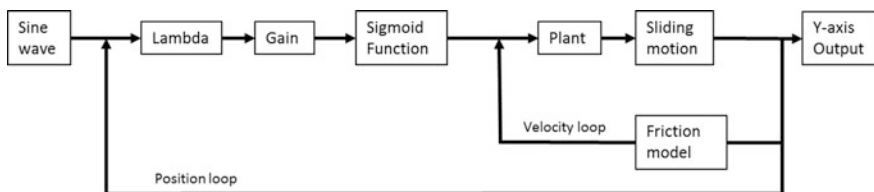


Fig. 1 Schematic block diagram of simulation test

Table 1 Simulation requirement for approach A and approach B

Approach A	Approach B [6]
The output voltage should not exceed than 0.7 V	0.3% of maximum error
The output voltage has minimal noise in frequency	Reach time less than 1 s
The maximum error is minimal	Maximum error in the parameters of 10%

system. According to Baeza and Garcia [6], controllers with low variability index present the best tracking performance.

3 Results and Discussions

In order to select the best parameters for gain, k , lambda, λ and delta, δ for each proposed method, the tracking position error for y-axis linear motion is obtained and the parameters are chosen according to the design requirements of approach B (see Table 1). The best parameters for each proposed method are shown in Table 2.

Figure 2 is tracking position error of approach A where no method applied. Figure 3 is the tracking position error for method a and Fig. 4 is the tracking

Table 2 Parameters according to the simulation requirement for method a and method b

Parameter	Method a	Method b
k	0.1	0.1
λ	2.6	2.1
δ	1.6	1.1

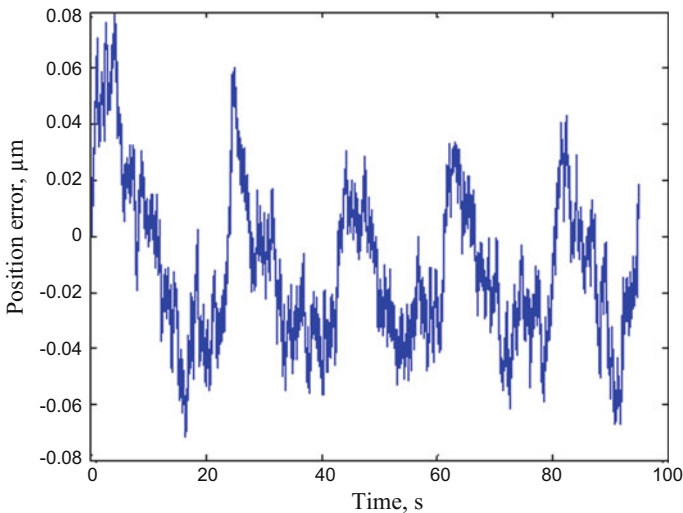


Fig. 2 Tracking position error with approach A

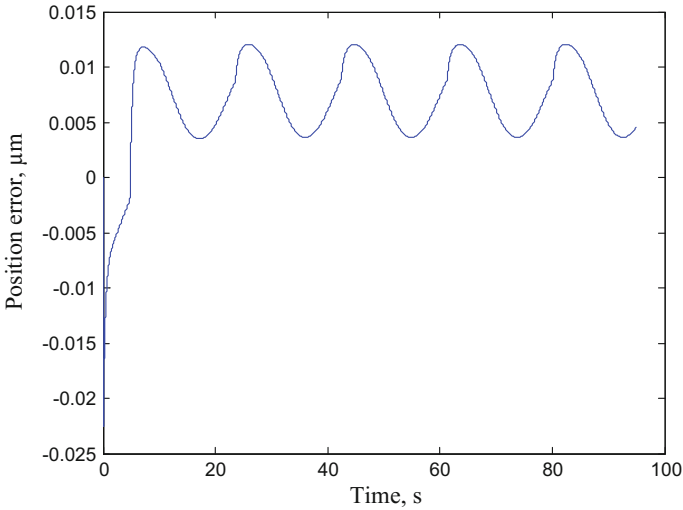


Fig. 3 Tracking position error for method a

positions error for method b. Tracking position error is evaluated by root-mean-square-error (RMSE). The results demonstrate that tracking position error with method applied provides better tracking error performance.

Table 3 shows the results for variability index of method a and method b. From Table 3, method a shows a lower RMSE and lower variability index value

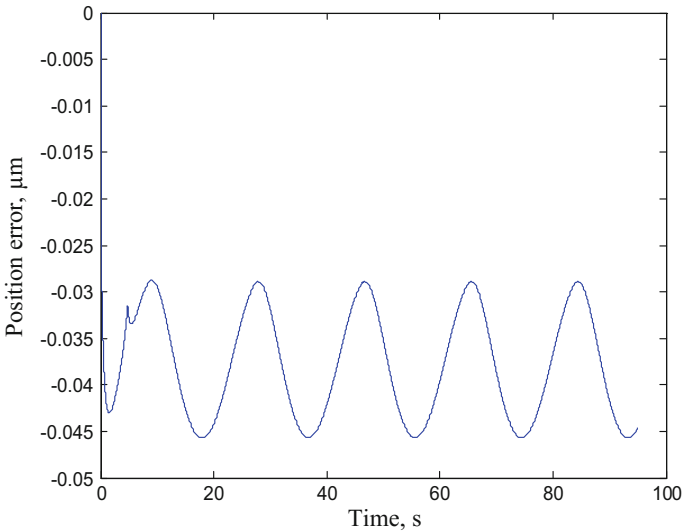


Fig. 4 Tracking position error for method b

Table 3 Variability index of method a and method b

Method	RMSE	VI (%)
a	0.0084	1.462
b	0.0374	1.481

compared to method b. According to Baeza and Garcia [6], controllers with low variability index present the best tracking performance. Therefore, method a is selected as the best parameter tuning method for SMC controller. Furthermore, good parameter tuning strategies lead to better friction compensation in terms of decreasing tracking position error.

4 Conclusion

This paper has evaluated and presented the parameter tuning strategies for Sliding Mode Control (SMC) position controller. There are two methods analysed in order to determine the best parameter and tuning strategies in reducing friction through Sliding Mode Control (SMC) controller. In order to analyze the effectiveness of tuning strategies for Sliding Mode Control (SMC), the variability index value of method a and b are compared. The results show that method a has the best parameter tuning as method a has lower RMSE and variability index value than method b. Further research will be conducted experimentally by using parameter selected for SMC design with defined control law and sliding surface to investigate the tracking position error and quadrant glitches compensation.

Acknowledgements This research was supported by Universiti Teknikal Malaysia Melaka (UTeM) and Advanced Manufacturing Centre (AMC).

References

1. Jamaludin, Z., Van Brussel, H., Swevers, J.: Friction compensation of an XY feed table using friction-model-based feedforward and an inverse-model based disturbance observer. *IEEE Trans. Industr. Electron.* **56**(10), 3848–3853 (2009)
2. Wang, J., Hendrik, V.B., Swevers, J.: Positioning and tracking control of an X-Y table with sliding mode control. In: 4th IFAC Symposium on Robust Control Design, vol. 36, Issue 11, pp. 157–162. Milan, Italy, 25–27 June 2003
3. Tjahjowidodo, T., Jamaludin, Z., Shara, S.: Sliding mode control for a frictional system. *Int. Conf. Design Concur. Eng. iDecon* **2010**, 100–104 (2010)
4. Rafan, N.A., Jamaludin, T.T., Chey, L., Chiew, T.: Theoretical analysis of friction compensation using sliding mode control. *Appl. Mech. Mat.* **231**, 2385–2388 (2012)
5. Nakashima, A., Ooka, Y., Hayakawa, Y.: Contact transition modelling on planar manipulation system with LuGre friction model. In: 10th International Workshop on Robot Motion and Control, pp. 300–307 (2015)

6. Baeza, J.R., Garcia, C.: Friction compensation for control valves through sliding mode control. In: Memoria XV Congreso Latino Americano De Control Automatico. Lima, Peru (2012)
7. Astrom, K., Huggland, T.: The future of PID control. *Control Eng. Pract.* **9**(11), 1163–1175 (2001)
8. Edwards, C., Spurgeon, S.K.: *Sliding Mode Control: Theory and Applications*, 1st edn. Taylor & Francis Ltd, London (1998)

System Interface Design for CAD/ CAM-Simulink Data Exchange System Using MATLAB[®]



N. Mat Seman, Zamberi Jamaludin and Mohamad Minhat

Abstract Integration between advanced control system theory and automation tools and technology brings about advancement in machining technology in tandem with requirement for smart and flexible manufacturing system. The integration takes in the form of seamless and automatic data communication between a CAD/CAM system and the more advanced control systems technology. This paper presents an interface design of a novel CAD/CAM-Simulink Data Exchange System (CS-DES) which links part geometry design using CAD/CAM technology with position controller scheme and algorithm designed in Matlab/Simulink environment. The proposed CS-DES system enhances data automation through formation of the graphical user input reference interface of the machine tools control system using NC manufacturing codes data as the reference input signal. The framework and role of CS-DES are elaborated and described in detail including pseudocodes generation for the CAD drawing graphical data integrated with the controller scheme designed in Simulink. The CS-DES interface was designed using MATLAB graphical user interactive development platform. Functions related to the user interface design are discussed in this paper. Finally, the system interface design of the data exchange system is expected to further enhance versatility of existing control system performance of a machine tool via creation of flexible input reference forms hence improving system accuracy, efficiency and productivity.

Keywords GUI • MATLAB/Simulink • CAD/CAM

N. Mat Seman · Z. Jamaludin (✉) · M. Minhat
Fakulti Kejuruteraan Pembuatan, Universiti Teknikal Malaysia Melaka, Hang Tuah Jaya,
76100 Durian Tunggal, Melaka, Malaysia
e-mail: zamberi@utem.edu.my

© Springer Nature Singapore Pte Ltd. 2018
M. H. A. Hassan (ed.), *Intelligent Manufacturing & Mechatronics*,
Lecture Notes in Mechanical Engineering,
https://doi.org/10.1007/978-981-10-8788-2_58

1 Introduction CIM-CAD/CAM-CS

In production systems, automation tools and advanced technologies flourished and evolved with the introduction of Computer Numerical Control (CNC) machines, Computer Aided Manufacturing (CAM) and later Computer Integrated Manufacturing (CIM). Theoretically, computer integrated manufacturing refers to the utilization of computer-controlled machineries and automation systems in manufacturing of products. It involves the CAD/CAM processes and business functions such as cost accounting, employee time records and payroll, order entry, and customer billing [1].

Researchers in [2] have proposed elements of Computer Integrated Manufacturing (CIM) that consisted of Computer Aided Design/Engineering (CAD/CAE), Computer Aided Manufacturing (CAM), Computer Aided Production Planning (CAPP) and Computer Aided Quality (CAQ). Figure 1 shows these elements of CIM systems [2]. These elements of CIM systems are used in applications of automated machines, storage systems, material handling systems, and control systems. However, this study only focuses on CAD and CAM elements as an implementation in control systems for machine tools application as highlighted in Fig. 1.

CAD/CAM plays an important role in manufacturing of discreet products. CAD/CAM system is a complex preparation in the process of manufacturing production. Integration between a CAD/CAM system and position controller of a machine servo drive system creates the possibility for automatic generation of position input data of the designed parts and products [3]. An example of application in virtual environment was proposed by [4]. It incorporates CAD/CAM environment and the control system for robot-based machining application. Also, an intention for applying STEP-NC in CNC machine systems application using LabVIEW was proposed by [5, 6]. In this paper, the system exchanges CAD/CAM data format to

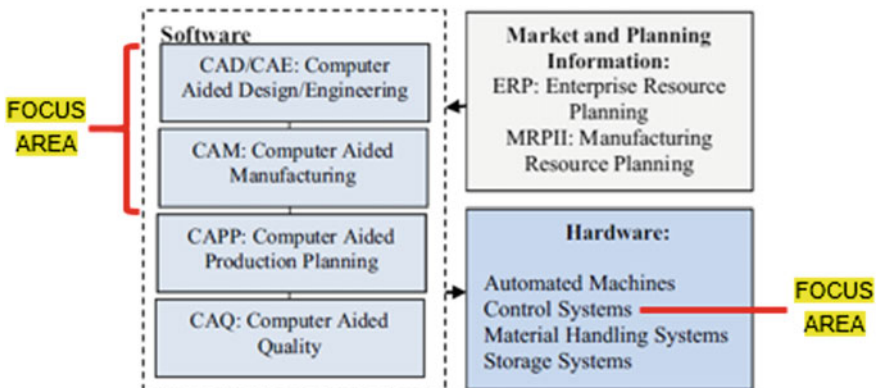


Fig. 1 Elements of computer integrated manufacturing systems [2]

raw position data for milling process using system designed in LabVIEW environment.

Various independent researches have been conducted to develop position controllers for machine tools applications with the objective of delivering a control system that is accurate and effective. For example, [7–9] have designed cascade and sliding mode controllers for position control of an XY milling table that produced excellent performance in reference tracking and disturbance rejection. Besides dictating the geometry of the part to be machined, the reference input signal was also used to observe tracking errors of the positioning system. A system that effectively combines both the controller and the CAD software would add flexibility to the overall control system thus expanding the quality of parts and products that are produced. An effective integration of controllers with a CAD/CAM system would benefit practitioners of machine tools.

Modern control systems apply concept of integration to cooperate with CAD/CAM technology requirements. The demands for better precision and accuracy of parts and products have boosted the advancement of machine tool technologies. Presently, a prototype XYZ milling table positioning system is controlled using self-critically-designed advanced position controller that applies predefined reference trajectory as its reference input signal. It can effectively control positions of the XY milling table based on the input reference points. However, the application of this position control system is limited by the signal input forms that are currently only available via the Simulink reference input signal library. Figure 2 shows a common block scheme of a control system with highlighted reference input as the focus of study in this paper.

Therefore, the main aim of this study is to design a user-interface system that integrates a CAD/CAM geometrical data software with an advanced controller built using MATLAB/Simulink for an effective and flexible control system of an XY ball-screw driven milling table. The system interfaced the CAD/CAM component of the part manufacturing with the drives system controller for both x -axis and y -axis of the positioning table. This paper presents a novel interface system design for a CAD/CAM–Simulink Data Exchange System for a prototype XYZ milling machine. The paper is organized as follows. Section 2 explains the methodology applied in design of the user-interface while Sect. 3 presents the interface systems with discussions. Finally, Sect. 4 concludes the findings of this study.

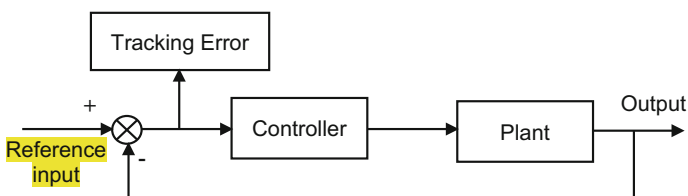


Fig. 2 Common control systems block scheme

2 Methodology

In this study, elements of computer integrated manufacturing used were CAD and CAM embedded with a graphical user interface (GUI) for control systems application. This is shown in Fig. 3. The GUI of the CAD/CAM-Simulink Data Exchange System (CS-DES) was designed in order to establish seamless data connection between CAD/CAM part of the product design with the controller scheme and algorithms. The NC manufacturing codes obtained from CAD and CAM consists of both the x and y axes coordinates data. The data are necessary as the input reference position signal for the control systems of the milling machine feed table. In designing the CS-DES interface, the function *Load File* serves as interface between the CAD/CAM and the GUI, and function for reference input signal becomes the interface between the GUI and the position controller scheme and algorithms. These interfaces ensure seamless interconnectivity in data flow between CAD/CAM, GUI and the controller scheme.

Essentially, there are three ways to establish communication with the computer via MATLAB: (i) through utilization of functions and scripts, (ii) through the Command Window, and (iii) through GUIs. A GUI provides an impulsive interface between the user and the programming language. It allows user to execute programming routines with a simple keypress or mouse click [10]. In this study, MATLAB GUIDE (Graphical User Interface Development Environment) was selected as the software tool for the interface development. MATLAB GUIDE enables user to execute interactive tasks without writing a script in the Editor or manual typing commands in the Command Window [11]. CS-DES is an interface system providing data exchange functionality from CAD/CAM to the control systems.

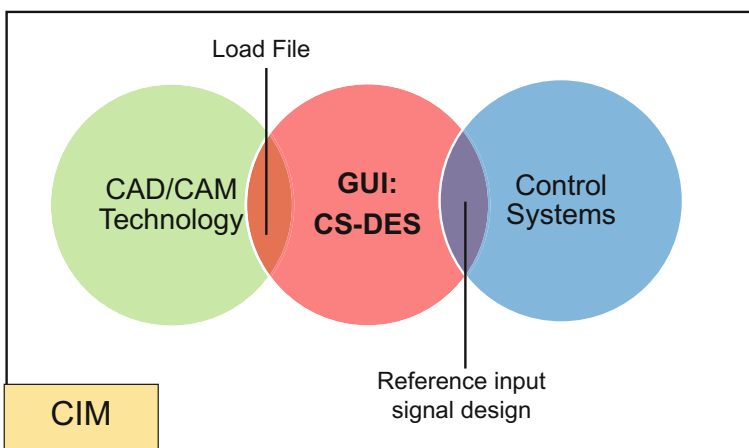


Fig. 3 Framework of CS-DES in computer integrated manufacturing concept

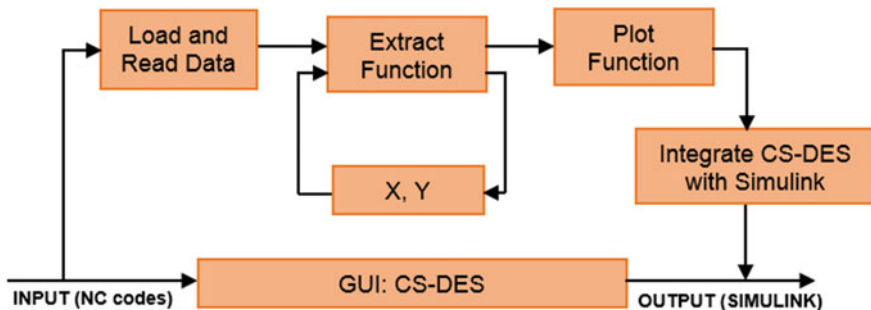


Fig. 4 The role of CS-DES

Figure 4 shows schematic diagram of CS-DES. The input to the CS-DES interface system is the NC manufacturing codes obtained from the CAD/CAM software which are automatically saved as text file (*.txt). The output of the GUI consists of the x and y positions data and a graph illustrating the path and trajectory of the respective product design. The data then became the reference input signal to the control scheme and algorithm located in the Simulink platform.

However, since both the GUI and Simulink are in different interface format, a programming function is designed in order to integrate the two components to become the overall system. Table 1 lists the algorithm in the form of pseudocode commands for the respective data integration. User needs to click a pushbutton as the input for this pseudocode function and the output is displayed in the form of controller scheme in Simulink platform. This pseudocode shows the steps required to integrate data in MATLAB Workspace with reference input signal for controller in Simulink. The pseudocode begins with initialization of the controller’s filename. The filename must be in *.mdl format. However, only defined controller’s filename will execute the Simulink controller scheme. Next, the filename is opened. There is

Table 1 Pseudocode for algorithm of data integration

Algorithm 1: Data Integration with Simulink Input Controller
Input: User click the pushbutton
Process: Integrate the data in workspace with Simulink Input Controller
Output: Display the Simulink controller scheme
Procedure:
Begin
Initialize filename//name of controller scheme file must be in *.mdl format
Open filename
IF final_x and final_y is not available, THEN
Message error dialog ('Please locate final_x and final_y value')
ELSE
Continue run system
End

a loop selection used in this function. If final_x and final_y are not available in the MATLAB Workspace, then there would be a message error dialog displayed “Please locate final_x and final_y value”. Else, the system continues its programming sequences.

3 Results and Discussions

The objective of the CS-DES interface is to extract the x and y axes positioning data from NC manufacturing codes so that these data could be forwarded as input reference position data for the feed table of the servo drive system of the XYZ milling machine. Figure 5 shows the start-up window that consists of three main section: (i) data extraction, (ii) positioning movement, and (iii) Simulink control scheme.

In the first section, user is prompted to load and read the NC manufacturing codes. Full path name of the file is displayed in a string text box. The content of NC manufacturing codes is displayed in a multi-line edit box. MATLAB GUIDE enables scrolling of the vertical scrollbar for multi-line edit boxes. Multiple lines are allowed when max – min is set at >1 [12]. Figure 6 shows the property inspector for uicontrol edit box.

Next, user needs to click extract pushbutton to extract both the x and y axes data. Here, str2double function is used to convert the string text to float number value. The extracted x and y values are later saved as *.mat file. The x and y values are also saved in MATLAB workspace as final_x and final_y. Then, the saved position data are simulated and previewed in order to analyse the reference

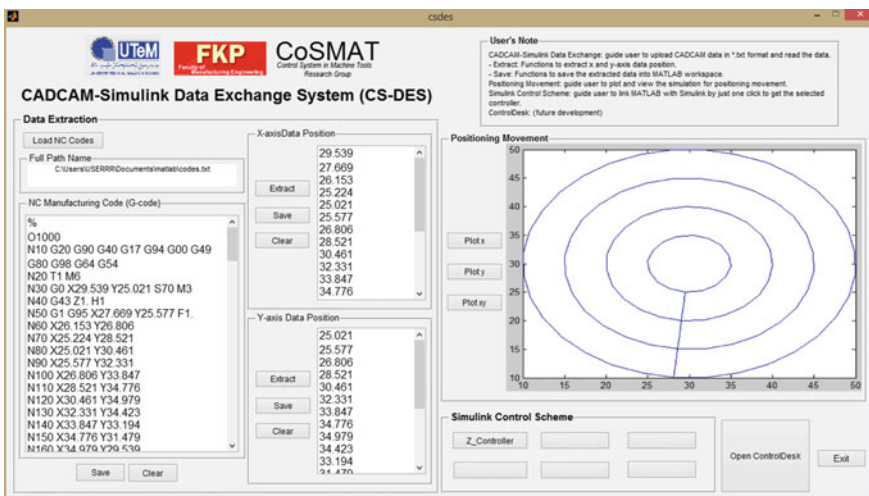


Fig. 5 Interface of CAD/CAM-Simulink data exchange system with preliminary results

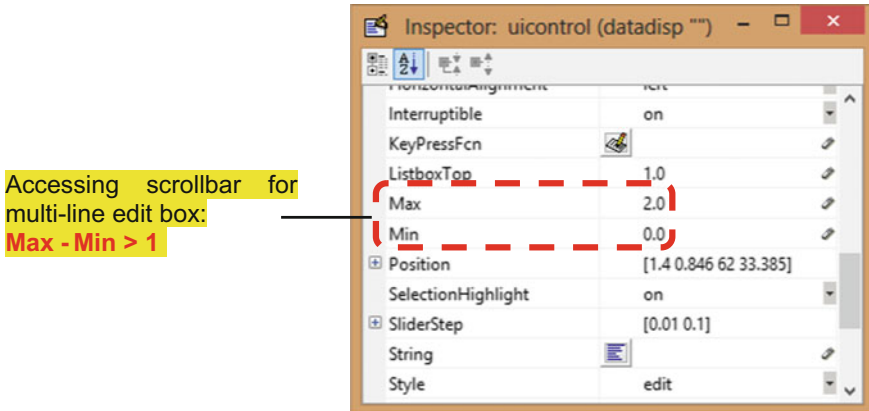


Fig. 6 Property inspector for uicontrol edit box

trajectory before being uploaded to the control scheme of choice in the Simulink platform for machining purpose. The plot function was designed to simulate position of the table as confirmation before any experimental work is performed so as to ensure safety and efficiency of the machining process. Figure 5 shows the preliminary results, which are the extracted x and y data positions, and the plotted graph of x and y data positions, displayed in the GUI.

Finally, a pushbutton was designed to integrate the CS-DES interface with the controller of choice in the Simulink platform. Figure 7 shows an example of Simulink control scheme menu section located in CS-DES interface. By implementing pseudocodes presented in Algorithm 1, user has the freedom to apply any controller schemes previously designed in MATLAB/Simulink environment, with condition that the controller scheme's filename is defined in *.mdl format. Some examples of position controllers that could be applied are classical controllers such as proportional-integral-derivative (PID) controller and cascade P/PI controller, including even more advanced controllers such as sliding mode controller and the H-infinity controller.

Figure 8 shows an overview of Simulink scheme where `final_x` and `final_y` are implemented as input reference positions for the x and y axes controlled by



Fig. 7 Example of Simulink control scheme section in CS-DES interface

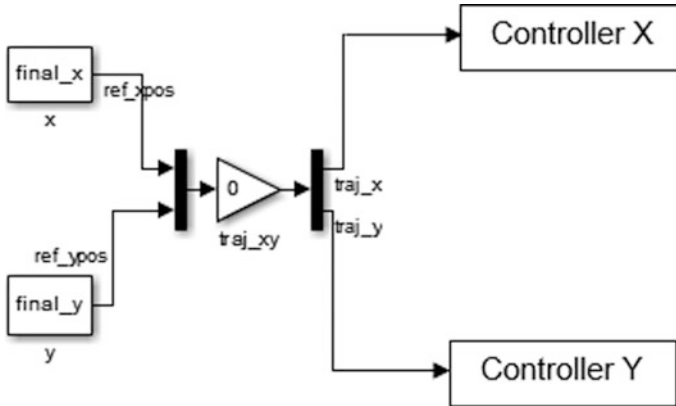


Fig. 8 Overview of Simulink blocks implemented in current controller scheme

Controller X and Controller Y respectively. The x and y position data are read from the MATLAB Workspace environment. The name of the block must be specified as `final_x` and `final_y` position reference; similar variable names located in MATLAB workspace. In the future, the system is to be linked to a digital signal processing unit user interface panel named ControlDesk for better management of the control system.

4 Conclusions and Future Works

In this paper, a graphical user interface (GUI) was developed and presented to serve as a platform that would extract input reference data for a dedicated machine tool position controller based on CAD/CAM particulars of an intended part and product. This interface was devised to add convenient, flexibility and adaptability features to current advanced position control system previously developed for a prototype milling machine. The implementation of CS-DES provides alternative input reference signal approachable by CAD/CAM environment. A control block was illustrated to describe the role of CS-DES. A pseudocode was presented to explain the functionality of integrating CS-DES with the Simulink controller scheme. Then, the ability of the GUI to extract and integrate the x and y axes position data with the Simulink-based position controller was presented. This novel data exchange system, once fully developed is expected to simplify current control system development process thus providing greater flexibility that could then be translated into improved control performance of the machine tools drives system.

As for future work, CS-DES will be implemented in conventional XY milling machine positioning table utilizing classical and advanced position controllers such as cascade P/PI, proportional-integral-derivatives (PID) controller and sliding mode

controller (SMC). The input signal for the selected controller will have CS-DES as the platform that retrieved position data of the geometrical drawing for the part manufacture. The operability and adaptability of the interface will be justified and verified.

Acknowledgements This research work is supported by the Malaysia Ministry of Higher Education (MoHE) through research grant FRGS/1/2015/TK03/FKP/02/F00281. The authors would also like to acknowledge Faculty of Manufacturing Engineering, Universiti Teknikal Malaysia Melaka (UTeM) for the support provided.

References

1. Automation-CIM. <https://www.britannica.com/technology/automation/Computer-integrated-manufacturing>. Accessed 21 Nov 2017
2. Esmaeilian, B., Behdad, S., Wang, B.: The evolution and future of manufacturing: a review. *J. Manuf. Syst.* **39**, 80–95 (2016)
3. Dubovska, R., Jambor, J., Majerik, J.: Implementation of CAD/CAM system CATIA V5 in simulation of CNC machining process. In: 24th DAAAM International Symposium on Intelligent Manufacturing and Automation, 2013, pp. 638–645. Elsevier Ltd., Czech Republic (2014)
4. Dimic, Z., Milutinovic, D., Zivanovic, S., Kvirgic, V.: Virtual environment in control and programming system for reconfigurable machining robot. *Tehnicki Vjesnik* **23**(6), 1821–1829 (2016)
5. Yusof, Y., Minhat, M.: An Open STEP-NC controller via LABVIEW platform. *Appl. Mech. Mater.* **660**, 873–877 (2014)
6. Elias, D.M., Yusof, Y., Minhat, M.: CNC machine system via STEP-NC data model and LABVIEW platform for milling operation. In: IEEE Conference on Open Systems, December, pp. 27–31 (2013)
7. Jamaludin, Z., Van Brussel, H., Swevers, J.: Tracking performances of cascade and sliding mode controllers with application to a XY milling table. In: Proceedings of ISMA2006 81 (May 2014), pp. 81–92 (2006)
8. Jamaludin, Z., Van Brussel, H., Swevers, J.: Classical cascade and sliding mode control tracking performances for a XY feed table of a high-speed machine tool. *Int. J. Precis. Technol.* **1**(1), 65 (2007)
9. Chiew, T.H., Jamaludin, Z., Bani Hashim, A.Y., Leo, K.J., Abdullah, L., Rafan, N.A.: Analysis of tracking performance in machine tools for disturbance forces compensation using sliding mode control and PID controller. *Int. J. Mechatron. Eng.* **12**, 34–40 (2012)
10. Harley, E.M., Loftus, G.R.: MATLAB and graphical user interfaces: tools for experimental management. *Behav. Res. Methods Instrum. Comput.* **32**(2), 290–296 (2000)
11. Trauth, M.H.: Introduction to MATLAB. In: MATLAB® Recipes for Earth Sciences. Springer, Heidelberg (2015)
12. Multiple lines in “Edit Text” box in GUIDE-MATLAB Answers™. <https://www.mathworks.com/matlabcentral/answers/11851-multiple-lines-in-edit-text-box-in-guide>. Accessed 23 Nov 2017

Single-Solution Simulated Kalman Filter Algorithm for Routing in Printed Circuit Board Drilling Process



Nor Hidayati Abdul Aziz, Zuwairie Ibrahim, Nor Azlina Ab Aziz, Zulkiffi Md. Yusof and Mohd Saberi Mohamad

Abstract Optimal drilling path for printed circuit board is crucial in increasing productivity and reduce production costs. Single-solution Simulated Kalman Filter (ssSKF) is a new optimizer inspired by the Kalman filtering process. It uses only a single agent to solve optimization process by finding the estimate of the optimal solution. Principally, ssSKF algorithm uses the standard Kalman filter framework, aided by a local neighborhood technique during its prediction step. This paper reveals the potential of ssSKF as a good routing method in printed circuit board (PCB) drilling process. Experimental results indicate that the ssSKF algorithm outperforms the existing methods in searching a good route to speed up a PCB drilling process.

Keywords Simulated Kalman filter · Printed circuit board · Routing

1 Introduction

Simulated Kalman Filter (SKF) [1, 2] is a population-based optimizer inspired by the Kalman filtering process. Recently, it is found that the SKF optimizer can also operates using only a single agent. This optimizer is called single-solution SKF (ssSKF) [3]. An advantage of the ssSKF is that it only requires one parameter

N. H. Abdul Aziz · N. A. Ab Aziz

Faculty of Engineering and Technology, Multimedia University, Melaka, Malaysia

N. H. Abdul Aziz · Z. Ibrahim (✉)

Faculty of Electrical and Electronics Engineering, Universiti Malaysia Pahang, Pekan, Malaysia

e-mail: zuwairie@ump.edu.my

Z. Ibrahim · Z. Md.Yusof

Faculty of Manufacturing Engineering, Universiti Malaysia Pahang, Pekan, Malaysia

M. S. Mohamad

Faculty of Creative Technology and Heritage, Universiti Malaysia Kelantan, Pengkalan Chepa, Malaysia

© Springer Nature Singapore Pte Ltd. 2018

M. H. A. Hassan (ed.), *Intelligent Manufacturing & Mechatronics*,

Lecture Notes in Mechanical Engineering,

https://doi.org/10.1007/978-981-10-8788-2_59

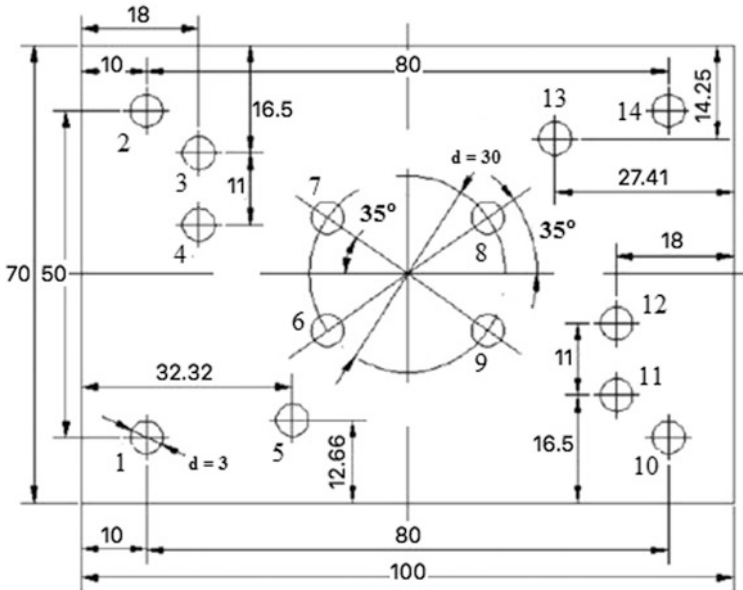


Fig. 1 A printed circuit board with 14-holes

tuning, whereas in SKF, determination of initial value, error covariance, and noise statistic should be done properly to get good results.

Routing is a process to find the best path. A lot of applications involve routing. In this paper, routing in printed circuit board (PCB) drilling process is studied. Consider a 14-hole PCB workpiece 100 mm in length and 70 mm in width as shown in Fig. 1 [4]. The optimal length to drill all the 14 holes is 280 mm. These sequences and their reverse sequences lead to the optimal length: 2-3-4-7-8-13-14-10-11-12-9-6-5-1 and 10-11-12-9-6-5-1-2-3-4-7-8-13-14). However, there are $14!/2 = 43\ 589\ 000\ 000$ possible sequences are available. Thus, finding the optimal route is a challenging task. While brute force approach requires computation of all possible paths, optimization-based approaches which require less computation are preferred. Up to date, a number of optimizers have been studied to solve this problem, such as global convergence particle swarm optimization (PSO) [4], global convergence PSO with decreasing inertia weight [5], ant colony system (ACS) [6], cuckoo search (CS) [7], and population-based SKF algorithm [8].

2 Single-Solution Simulated Kalman Filter Algorithm (SsSKF)

The flowchart of ssSKF algorithm is shown in Fig. 2. The algorithm begins with random initial solution, $\mathbf{X}(0)$. Initial error covariance, $P(0)$, is set to a normally distributed random number. Then, fitness is calculated. After that, according to the type of problem, the best-so-far solution, \mathbf{X}_{best} , is updated. The \mathbf{X}_{best} is updated only if the solution at current iteration, $\mathbf{X}(t)$, is better. For minimization problem, \mathbf{X}_{best} is updated if the fitness of $\mathbf{X}(t)$ is less than the fitness of \mathbf{X}_{best} . On the other hand, for maximization problem, \mathbf{X}_{best} is updated if the fitness of $\mathbf{X}(t)$ is greater than the fitness of \mathbf{X}_{best} .

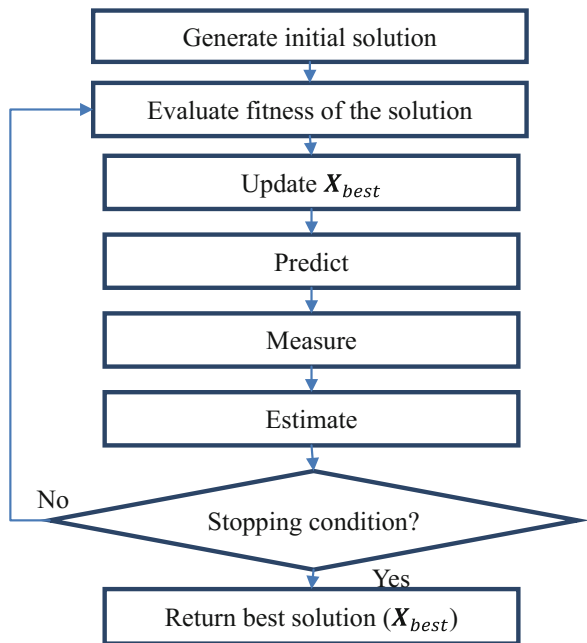
The search strategy in ssSKF mimics the predict-measure-estimate cycle in Kalman filtering. During prediction, the following equations are used to predict the optimum solution.

$$\mathbf{X}^d(t|t+1) \sim U[\mathbf{X}_{best}^d - \delta, \mathbf{X}_{best}^d + \delta] \tag{1}$$

$$P^d(t|t+1) = P^d(t) + randn^d \tag{2}$$

where $randn^d$ is a normally distributed random number and is used whenever the parameter value is needed for each dimension in every iteration.

Fig. 2 The flowchart of single-solution simulated Kalman filter algorithm



Equation 1 indicates that the prediction is carried out in a local neighbourhood surrounding the best-so-far solution, \mathbf{X}_{best}^d . The size of the local neighbourhood is determined by the adaptively decreasing step-size δ .

$$\delta = \exp^{-5t/tMax} \times \delta_0 \tag{3}$$

where $tMax$ is the maximum number of iteration. The initial neighbourhood limit, δ_0 , is determined using $\delta_0 = \max(\text{lowerlimit}, \text{lupperlimit})$ to ensure maximum coverage of the search space during the first iteration.

The next step is measurement. In this step, the best-so-far solution, \mathbf{X}_{best}^d , steered the agent’s simulated measurement value, $\mathbf{Z}^d(t)$, as follows:

$$\mathbf{Z}^d(t) = \mathbf{X}^d(t|t+1) + \sin(\text{rand}^d \times 2\pi) \times |\mathbf{X}^d(t|t+1) - \mathbf{X}_{best}^d| \tag{4}$$

The purpose of the measurement is to give feedback to the estimation process. The measurement is simulated in such a way that the measured value of the agent may take any random value surrounding the predicted value, $\mathbf{X}^d(t|t+1)$, either approaching to or moving away from the best-so-far solution, \mathbf{X}_{best}^d , balancing between exploration and exploitation. The exploration and exploitation mechanism is further compromised as the distance between the predicted value and the best-so-far solution decreases with the increase of the number of iteration.

Finally, during the estimation step, the solution and error covariance estimates for the next iteration are calculated using the estimate equations right after the calculation of the Kalman gain.

$$K^d(t) = \frac{P^d(t|t+1)}{P^d(t|t+1) + \text{rand}^d} \tag{5}$$

$$\mathbf{X}^d(t+1) = \mathbf{X}^d(t|t+1) + K^d(t) \times (\mathbf{Z}^d(t) - \mathbf{X}^d(t|t+1)) \tag{6}$$

$$P^d(t+1) = (1 - K^d(t)) \times P^d(t|t+1) \tag{7}$$

At the end of the estimation step, a better solution for the next iteration that lies between the predicted and the measured value is produced. This process continues until the maximum number of iteration.

3 Routing in PCB Drilling Process

The PCB drill path optimization aims to reduce the time taken in drilling a group of holes a PCB. Referring to the PCB layout in Fig. 1, the optimal paths are 2-3-4-7-8-13-14-10-11-12-9-6-5-1, 10-11-12-9-6-5-1-2-3-4-7-8-13-14, and their reverse sequences. Different sequence of hole will increase the total time required to

Table 1 The PCB data

Hole No.	Coordinate (x, y)	Hole No.	Coordinate (x, y)	Hole No.	Coordinate (x, y)	Hole No.	Coordinate (x, y)
1	(10, 10)	5	(32.32, 12.66)	9	(62.3, 26.4)	13	(72.59, 55.75)
2	(10, 60)	6	(37.7, 26.4)	10	(90, 10)	14	(90, 600)
3	(18, 53.5)	7	(37.7, 43.6)	11	(82, 16.5)		
4	(18, 42.5)	8	(62.3, 43.6)	12	(82, 27.5)		

complete a drilling process. By assuming the speed is constant, total drilling time is correlated with the total routing distance. Thus, the fitness function can be formulated as Eq. 8.

$$\min \sum_{i=1}^n \sum_{j=1}^n (|x_i - x_j| + |y_i - y_j|) \times p_{ij} \quad (8)$$

where (x_i, y_i) is the coordinate of a source hole, (x_j, y_j) is the coordinate of a destination hole, n is the number of holes, and p_{ij} acts as the decision variable that decides whether or not to move from hole i to hole j . A movement is indicated by $p_{ij} = 1$. By taking the lower left hand corner of the PCB as coordinate $(0, 0)$, the coordinate of all 14 holes of PCB shown in Fig. 1 is tabulated in Table 1.

4 Experiment, Result, and Discussion

Since routing problem is a combinatorial optimization problem, the solution is encoded as a vector of n numbers, each in the range of $[-1, 1]$. To determine a sequence, the encoded solution is sorted in ascending order. The hole with the smallest number will be drilled first. This sorted sequence represent the drilling sequence. Thus, in ssSKF, the lowerlimit and upperlimit are -1 and 1 , respectively. During the search process, if a value is outside this boundary, the value will be reinitialized within $[-1, 1]$.

The search using ssSKF algorithm was implemented in MATLAB R2016a. The maximum number of iterations and the number of computation (number of trial) are 5000 and 100, respectively. Figure 3 shows an example of convergence curve. This graph shows that the optimal path was obtained at iteration 2136. The performance of the ssSKF is compared with global convergence particle swarm optimization (PSO) [4], global convergence PSO with decreasing inertia weight (IW PSO) [5], ant colony system (ACS) [6], cuckoo search (CS) [7], and population-based SKF algorithm [8]. The results are tabulated in Table 2.

Due to 14 number of holes, which is relatively small, all algorithms able to find the optimal path. Hence, further analysis is required.

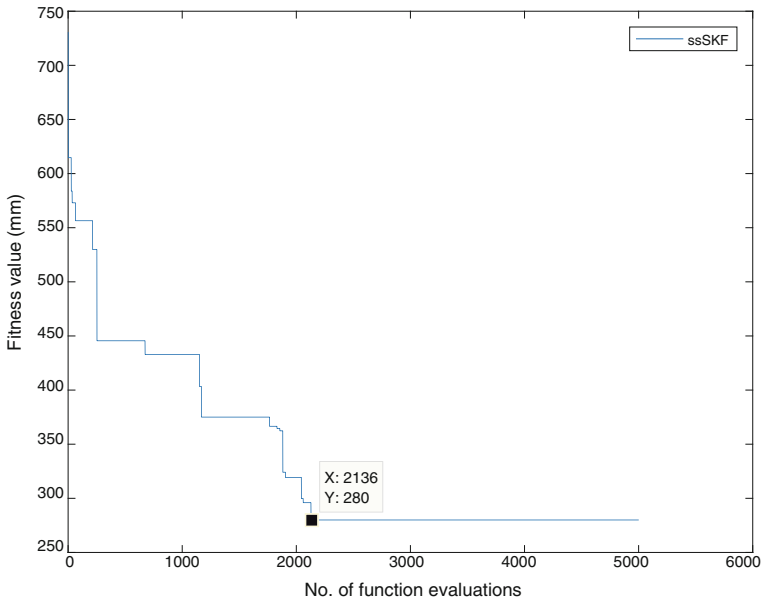


Fig. 3 ssSKF convergence curve in solving 14-hole PCB drill path optimization problem

Table 2 Performance comparison of ssSKF with PSO variants, ACO, CS, and SKF

Performance indicator (during global convergence)	PSO	IW PSO	ACS	CS	SKF	ssSKF
Least no. of solution searched	1500	350	4825	2300	2700	2136
Average no. of solution searched	243,000	17,650	25,925	42,900	7300	2357
Least search ratio	3.4×10^{-6}	8.0×10^{-7}	1.1×10^{-5}	5.2×10^{-6}	6.1×10^{-6}	4.9×10^{-8}
Average search ratio	5.5×10^{-4}	4.0×10^{-5}	5.9×10^{-5}	9.8×10^{-5}	1.6×10^{-5}	5.4×10^{-8}

The search ratio is used to compare the performances of ssSKF algorithm with the published results. The search ratio can be obtained by multiplying the total number of function evaluations required to reach the solution divide by the total number of possible solutions in the solution space. Results in Table 2 show that the average search ratio of ssSKF is the smallest compared to other algorithms. This finding indicates that the ssSKF able to find the optimal path faster than the other algorithms.

5 Conclusion

The ssSKF is a newly introduced optimizer, which operates by a single agent following the Kalman filtering process. This paper presents the first practical industrial application of ssSKF algorithm in PCB hole drilling process. The performance of the ssSKF is compared with others based on a case study. The results suggest that the ssSKF algorithm has a huge potential as routing method in PCB hole drilling process. The performance of ssSKF will be further investigated in other routing-based applications.

References

1. Ibrahim, Z., Abdul Aziz, N.H., Ab Aziz, N.A., Razali, S., Shapiai, M.I.: A Kalman filter approach for solving unimodal optimization problem. *ICIC Express Lett.* **9**(12), 3415–3422 (2015)
2. Ibrahim, Z., Abdul Aziz, N.H., Ab Aziz, N.A., Razali, S., Mohamad, M.S.: Simulated Kalman filter: a novel estimation-based metaheuristic optimization algorithm. *Adv. Sci. Lett.* **22**, 2941–2946 (2016)
3. Abdul Aziz, N.H., Ibrahim, Z., Ab Aziz, N.A., Mohamad, M.S., Watada, J.: Single-solution simulated Kalman filter algorithm for global optimisation problems. *Sadhana* (accepted)
4. Zhu, G.-Y.: Drilling path optimization based on swarm intelligent algorithm. In: *IEEE International Conference on Robotics and Biomimetics*, pp. 193–196 (2008)
5. Adam, A., Zainal Abidin, A.F., Ibrahim, Z., Husain, R., Md Yusof, Z., Ibrahim, I.: A particle swarm optimization approach to robotic drill route optimization. In: *The 4th Asia International Conference on Mathematical/Analytical Modelling and Computer Simulation*, pp. 60–64 (2010)
6. Saealal, M. S., Abidin, A.F., Adam, A., Mukred, J., Khalil, K., Md. Yusof, Z., Ibrahim, Z., Nordin, N.A.: An ant colony system for routing in PCB holes drilling process. *Int. J. Innov. Manag. Inf. Prod.* **4**(1), 50–56 (2013)
7. Lim, W.C.E., Kanagaraj, G., Ponnambalam, S.G.: PCB drill path optimization by combinatorial cuckoo search algorithm. *Sci. World J.* **2014**(264518) (2014)
8. Abdul Aziz, N.H., Ab Aziz, N.A., Ibrahim, Z., Razali, S., Abas, K.H., Mohamad, M.S.: A Kalman filter approach to PCB drill path optimization problem. In: *IEEE International Conference on Systems, Process, and Control*, pp. 33–36 (2016)

Performance Evaluation of Random Search Based Methods on Model-Free Wind Farm Control



Mok Ren Hao, Mohd Ashraf Ahmad, Raja Mohd Taufika Raja Ismail
and Ahmad Nor Kasruddin Nasir

Abstract This paper investigates the performance of Sequential Random Search (SRS), Fixed Step Size Random search (FSSRS), Optimized Relative Step Size Random Search (ORSSRS) and Adaptive Step Size Random Search (ASSRS) methods on maximizing offshore wind farms power production. The RS based methods are used to tune the control parameter of each turbine to its optimum until the wind farm total power production is maximized. The validation of this investigation is performed using the Horns Rev wind farm model with turbulence interaction between turbines. Simulation results show that Optimized Relative Step Size Random Search (ORSSRS) produces higher total power production as compared to other types of RS based methods.

Keywords Random search · Model-free · Wind farm optimization
Power production · Stochastic search · Renewable energy

1 Introduction

Among the sources of renewable energy, wind power is considered as one of the cheapest and easiest to be installed. Due to the expanding demand of electrical power in recent year, the recent trend is to increase wind farm efficiency by reducing power cost and increase the power production of the existing wind farm. However, there are still many unsolved challenges in harnessing wind power due to the ineffective wind farm control design. Therefore, wind farm control problem is actively studied in control community.

M. R. Hao (✉) · M. A. Ahmad · R. M. T. Raja Ismail · A. N. K. Nasir
Instrumentation & Control Engineering Research Group (ICE),
Faculty of Electrical Engineering, Universiti Malaysia Pahang,
Pekan, Pahang, Malaysia
e-mail: mel16011@stdmail.ump.edu.my

M. A. Ahmad
e-mail: mashraf@ump.edu.my

There are 432.4 GW of wind power installed in the end of year 2016 [1]. These wind farms could be optimized to extract more power from the wind. Instead of building new wind farms, optimizing the existing wind farm could be more cost effective. Many efforts had been done by researchers to improve the performance of existing wind farm by modeling the wind farm. However, the complexity of wake interaction between turbines is very difficult until it is almost impossible to model due to the chaotic nature of wind. Therefore, model-free approach could help to avoid this problem as modelling of wind farm is not required in this approach.

There are several studies on model-free approach to maximize total power production of wind farm. These include game theoretic (GT) and cooperative control based [2–4], maximum power tracking [5], multi-resolution simultaneous perturbation stochastic approximation [6], Bayesian ascent [7], Spiral Dynamic [8] and Sequential Random Search [9] based approaches. In our previous study [9], Sequential Random Search (SRS) method is a promising tool to outperform other optimization methods on optimizing total power production of wind farm. RS based methods are a type of stochastic numerical optimization methods that is not rely on the gradient of optimization function. Therefore, they are suitable to solve discrete or differentiable function, which is also known as direct-search method [10]. For example, the optimization problem is treated as a black-box where the output is optimized only based on inputs. So far, there are a various types of RS methods such as Fixed Step Size Random Search (FSSRS) [11], Adaptive Step Size Random Search (ASSRS) [12], Sequential Random Search (SRS) [9] and Optimized Relative Step Size Random Search (ORSSRS) [13]. These RS variants have been applied to various optimization problem. However, there are very few applications of these methods on wind farm optimization problem. Therefore, this paper discusses the performance impact of SRS, FSSRS, ASSRS and ORSSRS on optimizing total power production of wind farm to maximum.

FSSRS is the fundamental random search algorithm which uses random vectors with uniform distribution on the hypersphere for selection as search direction throughout iterations. It is proposed by Rastrigin in year 1963 [11]. He has compared FSSRS with a fixed step size gradient method and the result shows FSSRS could perform very well under certain condition [11, 12]. The key performance of FSSRS is the search step size. If the search step size is small, it could increase the chance of improvement, but longer time is required to obtain optimum improvement. On the other hand, if the search step is large, it could shorten the time required to obtain optimum improvement but reduce the chance of improvement. Therefore, ASSRS is introduced to overcome this problem [13].

ASSRS evaluates the effectiveness of improvement from two random step sizes which are randomly selected according to a nominal step size. The step size with higher improvement is updated and stored as nominal step size for next iteration and repeat the step until maximum iteration is achieved. In this way, maximum convergence is guaranteed in every iteration. Hence, increase the convergence rate and reduce time required to obtain optimum. However, ASSRS is expensive to execute as it requires more than one sample in each iteration in order to carry out the evaluation [13–15].

Moreover, Sequential Random Search (SRS) is reducing its step size relative to the number of iterations [9]. This would allow the step size to reduce sequentially rather than fixed in every iteration. Therefore, it could overcome the difficulty in optimum step size selection of FSSRS. Besides that, SRS is more cost effective to execute than ASSRS as it is a single loop optimization method. However, step size in SRS may be not optimum for the next iteration as the step size is always reducing regardless the successful or failure during the previous iteration which may cause insignificant improvement to the next iteration as the step size is over reduced to smaller value.

In the other hand, Optimized Relative Step Size Random Search (ORSSRS) is like SRS which reduces step size relative to the number of iterations, but in more optimum way. Unlike the other RS based algorithm, ORSSRS always investigate the number of success and failure of the process, which is also known as Random Search with reversal. This method is first proposed by Lawrence and Stieglitz in year 1972 [16]. If the process is a success, the step size is reduced in the next iteration. However, if the process is a failure, the step size is maintained for the next iteration. Meanwhile, if continuous failure happened, the step size is cumulatively maintained for the next iteration. This procedure is used to ensure the successful step size is sufficient to counter the step size of failure hence, maintain convergence rate [10, 14, 15, 17]. Without the procedure, more iteration is required to achieve optimum result.

The organization of this paper is described as follows. Section 2 explains the problem formulation. Meanwhile, the step-by-step procedure of each of the RS based methods is discussed in Sect. 3. Next, Sect. 4 discusses the model-free design in this study. In Sect. 5, the RS based approach is validated to the Horns Rev wind farm model. The comparative study between each variation of the RS based methods are also discussed in the same section. Finally, Sect. 6 provides some concluding remarks.

2 Problem Formulation

In this study, we assume the wind farm has n turbines which are located randomly. Let the axial induction factor, $a_i (i = 1, 2, \dots, n)$ to be the control parameter of turbine i , which is a general form of the turbine controllers, such as, pitch angle of the blade and speed of turbine rotor [18]. Next, define the power production of turbine i as $J_i(a_1, a_2, \dots, a_n) (i = 1, 2, \dots, n)$. This study is considering the incoming wind speed with random direction and time varying. Therefore, we can assume that the control parameters except for turbine i , which are $a_1, a_2, \dots, a_{i-1}, a_{i+1}, \dots, a_n$, would also affect the turbine i power production J_i because of the turbulence interaction between turbines. Similarly, any variations of control parameter a_i not only affect J_i but also $J_1, J_2, \dots, J_{i-1}, J_{i+1}, \dots, J_n$. Therefore, the total power production of turbine i J_i highly depends on a_i and weakly depends on other control parameters $a_1, a_2, \dots, a_{i-1}, a_{i+1}, \dots, a_n$. Since the turbines dynamics and the

turbulence interactions amongst turbines are very complex, it is difficult to obtain an accurate model of the wind farm, which accurately provides the relation between J_i and a_1, a_2, \dots, a_n . However, we assume that the total power production of the wind farm is measurable and can be represented as:

$$\bar{J}(a_1, a_2, \dots, a_n) = \sum_{i=1}^n J_i(a_1, a_2, \dots, a_n). \quad (1)$$

Then, we describe the problem as:

Problem 2.1 Let the wind farm total power production $\bar{J}(a_1, a_2, \dots, a_n)$ is given in (1) and the function $J_i(a_1, a_2, \dots, a_n)$ are unknown. Then, find control parameters $a_i (i=1, 2, \dots, n)$ such that $\bar{J}(a_1, a_2, \dots, a_n)$ is maximized.

3 Random Search Methods

This section presents the method to solve Problem 2.1. Here, the SRS, FSSRS, ASSRS and ORSSRS algorithms introduced in [11–13, 19] are explained.

Consider the optimization problem given by

$$\max_{\alpha \in \mathbb{R}^n} f(\alpha), \quad (2)$$

where $f: \mathbb{R}^n \rightarrow \mathbb{R}$ is the objective function and $\alpha \in \mathbb{R}^n$ are the design parameters. Then, the step-by step procedure of each RS algorithm is explained as follows:

3.1 Fixed Step Size Random Search

The FSSRS algorithm updates α iteratively by performing the neighborhood search as follow. For $t=0, 1, \dots$,

$$\alpha_{Nt} = \alpha_t + \varepsilon(Sr_{t-1}) - Sr_t, \quad (3)$$

where S is a constant step size and r_t is a random vector correspond to iteration t with n dimension size, which is in form of gradient:

$$r_t = \sin \theta_t, (0 < \theta_t \leq \pi/2). \quad (4)$$

Meanwhile, the coefficient ε is given by:

$$\varepsilon = \begin{cases} 0, & \text{if } f(\alpha_t) \geq f(\alpha_{t-1}), \\ 1, & \text{if } f(\alpha_t) < f(\alpha_{t-1}). \end{cases} \quad (5)$$

Then, the FSSRS algorithm process is accordingly illustrated as follow:

- (i) Preset the maximum iteration t_{\max} . Select the constant step size S and initial conditions α_0 . Set $t = 1$, $\varepsilon = 0$ and $f_{\text{best}} = f(\alpha_0)$.
- (ii) Generate random vector r_t .
- (iii) Perform the neighborhood search in (3) and obtain α_{Nt} .
- (iv) Compute the objective function $f(\alpha_{Nt})$.
- (v) If $f(\alpha_{Nt}) \geq f_{\text{best}}$, update the design parameter $\alpha_{t+1} = \alpha_{Nt}$, set $f_{\text{best}} = f(\alpha_{Nt})$ and $\varepsilon = 0$. Otherwise, set $\alpha_{t+1} = \alpha_t$ and $\varepsilon = 1$.
- (vi) Set $t = t + 1$ and repeat (ii) if $t < t_{\max}$. However, if $t = t_{\max}$ the algorithm ends with the optimal design parameter $\alpha^* := \arg \max_{\alpha \in \{\alpha_0, \alpha_1, \dots, \alpha_{t+1}\}} f(\alpha)$.

Note: t_{\max} is the maximum iteration where the algorithm stops after a preset number of iteration t_{\max} .

3.2 Adaptive Step Size Random Search

The ASSRS algorithm requires to compare results of two design parameters β and γ , where β and γ are the independent control parameter for objective function f to update α iteratively by performing two neighborhood searches as follow. For $t = 1, 2, \dots$,

$$\beta_{Nt} = \alpha_t + \varepsilon^\beta \left(S^\beta r_{t-1}^\beta \right) - S^\beta r_t^\beta, \quad (6)$$

$$\gamma_{Nt} = \alpha_t + \varepsilon^\gamma \left(S^\gamma r_{t-1}^\gamma \right) - S^\gamma r_t^\gamma. \quad (7)$$

The S^β and S^γ are random step size which are randomly selected based on a nominal step size S^* such that $0 < S^{\beta, \gamma} \leq S^*$ and $S^\beta \neq S^\gamma$. Meanwhile, r_t^β and r_t^γ are random vectors correspond to iteration t with n dimension size, which are in form of gradient:

$$r_t^{\beta, \gamma} = \sin \theta_t, \quad (0 < \theta_t \leq \pi/2) \quad (8)$$

and the coefficient ε^β and ε^γ are given by:

$$\varepsilon^\beta = \begin{cases} 0, & \text{if } f(\beta_t) \geq f(\beta_{t-1}), \\ 1, & \text{if } f(\beta_t) < f(\beta_{t-1}), \end{cases} \tag{9}$$

$$\varepsilon^\gamma = \begin{cases} 0, & \text{if } f(\gamma_t) \geq f(\gamma_{t-1}), \\ 1, & \text{if } f(\gamma_t) < f(\gamma_{t-1}). \end{cases} \tag{10}$$

Then, the ASSRS algorithm procedure is illustrated as follow:

- (i) Preset the maximum iteration t_{\max} . Select the nominal step size S^* and initial conditions α_0 . Set $t = 1$, $\varepsilon = 0$ and $f_{\text{best}} = f(\alpha_0)$.
- (ii) Generate random step sizes S^β and S^γ . Meanwhile, generate random vectors r_t^β and r_t^γ .
- (iii) Perform the neighborhood search in (6) and (7) then, obtain β_{Nt} and γ_{Nt} respectively.
- (iv) Compute and compare the sub objective functions $f(\beta_{Nt})$ and $f(\gamma_{Nt})$.
- (v) For $f(\beta_{Nt}) \geq f(\gamma_{Nt})$:
 - If $f(\beta_{Nt}) \geq f_{\text{best}}$, update the design parameters $\beta_{t+1} = \beta_{Nt}$ and $\gamma_{t+1} = \beta_{Nt}$ then, set $f_{\text{best}} = f(\beta_{Nt})$, $\varepsilon^\beta = 0$ and $\varepsilon^\gamma = 1$. Otherwise, set $\beta_{t+1} = \alpha_t$, $\gamma_{t+1} = \alpha_t$, $\varepsilon^\beta = 1$ and $\varepsilon^\gamma = 1$.

For $f(\beta_{Nt}) < f(\gamma_{Nt})$:

- If $f(\gamma_{Nt}) \geq f_{\text{best}}$, update the design parameter $\beta_{t+1} = \gamma_{Nt}$ and $\gamma_{t+1} = \gamma_{Nt}$ then, set $f_{\text{best}} = f(\gamma_{Nt})$, $\varepsilon^\beta = 1$ and $\varepsilon^\gamma = 0$. Otherwise, set $\beta_{t+1} = \alpha_t$, $\gamma_{t+1} = \alpha_t$, $\varepsilon^\beta = 1$ and $\varepsilon^\gamma = 1$.

For none of above:

- If continuous happened after several iterations, decrease the nominal step size S^* such that:

$$S^{**} = \beta S^*, \tag{11}$$

where S^{**} is temporarily nominal the step size by multiplying the nominal step size S^* with a gain constant β ($0 < \beta < 1$) and store back to S^* for next iteration as given by:

$$S^* = S^{**}. \tag{12}$$

- (vi) Set $t = t + 1$ and repeat (ii) if $t < t_{\max}$. However, if $t = t_{\max}$ the algorithm ends with the optimal design parameter $\alpha^* := \arg \max_{\alpha \in \{\alpha_0, \alpha_1, \dots, \alpha_{t+1}\}} f(\alpha)$.

3.3 Sequential Random Search

The SRS algorithm updates α iteratively by performing the neighborhood search as follow. For $t=0, 1, \dots$,

$$\alpha_{Nt} = \alpha_t + \delta_t r_t \tag{13}$$

From (13), δ_t is the sequence gain and r_t is the random vector with n dimensional size, which is obtained from the elementwise Bernoulli distribution

$$\begin{cases} \mathbb{P}(r_{ii} = -1) = 0.5, \\ \mathbb{P}(r_{ii} = 1) = 0.5. \end{cases} \tag{14}$$

where r_{ii} is the i th element of the random vector r_t . Then, the SRS algorithm procedure is illustrated as follow:

- (i) Identify the sequence gain δ_t and preset the maximum iteration t_{\max} . Select the initial conditions α_0 , set $t = 1$ and $f_{best} = f(\alpha_0)$.
- (ii) Generate random vector r_t .
- (iii) Perform the neighborhood search in (13) and obtain α_{Nt} .
- (iv) Compute the objective function $f(\alpha_{Nt})$.
- (v) If $f(\alpha_{Nt}) > f_{best}$, update the design parameter $\alpha_{t+1} = \alpha_{Nt}$ and set $f_{best} = f(\alpha_{Nt})$. Otherwise, set $\alpha_{t+1} = \alpha_t$.
- (vi) Set $t = t + 1$ and repeat (ii) if $t < t_{\max}$. However, if $t = t_{\max}$ the algorithm ends with the optimal design parameter $\alpha^* := \arg \max_{\alpha \in \{\alpha_0, \alpha_1, \dots, \alpha_{t+1}\}} f(\alpha)$.

3.4 Optimized Relative Step Size Random Search

The ORSSRS algorithm updates α iteratively by performing the neighborhood search as follow. For $t=0, 1, \dots$,

$$\alpha_{Nt} = \alpha_t + \varepsilon(S_{t-1} \Delta r_{t-1}) - S_t r_t. \tag{15}$$

where S_t is a step size correspond to iteration t with an update sequence given by:

$$\overline{S}_t = K\overline{S}_{t-1}, (0 < K < 1), \quad (16)$$

$$S_t = \overline{S}_t. \quad (17)$$

Here, K is a gain constant and \overline{S}_t is a step size memory. Meanwhile, r_t is a random vector correspond to iteration t with n dimension size, which is in form of gradient as given in (4) and coefficient ε is as (5). Then, the ORSSRS algorithm process is accordingly illustrated as follow:

- (i) Preset the maximum iteration t_{\max} . Select the step size memory \overline{S}_0 and gain constant K then, initial conditions α_0 . Set $t=1$, $S_{t-1} = \overline{S}_0$, $\varepsilon=0$, and $f_{best} = f(\alpha_0)$.
- (ii) Generate random vector r_t , set $S_t = \overline{S}_t$.
- (iii) Perform the neighborhood search in (15) and obtain α_{N_t} .
- (iv) Compute the objective function $f(\alpha_{N_t})$.
- (v) If $f(\alpha_{N_t}) \geq f_{best}$, update the design parameter $\alpha_{t+1} = \alpha_{N_t}$ and step size memory $\overline{S}_{t+1} = K\overline{S}_t$ then, set $f_{best} = f(\alpha_{N_t})$ and $\varepsilon=0$. Otherwise, set $\alpha_{t+1} = \alpha_t$, $\overline{S}_{t+1} = K\overline{S}_t$ and $\varepsilon=1$.
- (vi) Set $t=t+1$ and repeat (ii) if $t < t_{\max}$. However, if $t = t_{\max}$ the algorithm ends with the optimal design parameter $\alpha^* := \arg \max_{\alpha \in \{\alpha_0, \alpha_1, \dots, \alpha_{t+1}\}} f(\alpha)$.

As in (v), the step size memory \overline{S}_t only update if the process is a success, for example, $f(\alpha_{N_t}) \geq f_{best}$. Otherwise, \overline{S}_t is remain for the next iteration until next successful process.

4 Model-Free Design

Applying the RS based algorithms in Sect. 3, the model-free RS based methods for maximizing wind farm power production is explained:

- (i) Preset the maximum iteration number t_{\max} .
- (ii) Perform the RS based algorithm in Sect. 3 by setting \overline{J} as f and a as α .
- (iii) After t_{\max} iteration, the algorithm stops with the optimal solution $\alpha^* := a^*$ and the total power production \overline{J} is recorded.

The flow of the model-free wind farm control synthesizes based on Random Search based algorithms is illustrated in Fig. 1.

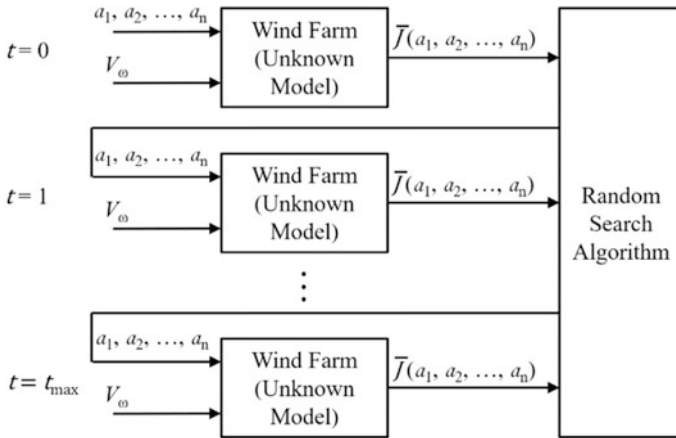


Fig. 1 The structure of model-free wind farm control based on Random Search based algorithms [9]

5 Simulation Result

This section demonstrate the RS based methods for maximizing wind farm power production. A wind farm model, which replicates a real commercial wind farm, is considered to evaluate the proposed method. Firstly, the model of wind farm proposed in [18] is described. Next, the RS based methods are validated to the model of Horns Rev wind farm.

5.1 Numerical Model of Wind Farm

Consider the wind farm has n wind turbines and represented by the set $s = 1, 2, \dots, n$, the wind speed is assigned as V_ω , the turbine rotor diameter is defined by D_i , the swept area of turbine i is represented by A_i . The symbol ϕ is a roughness parameter that describes the gradient of turbulence propagation, $A_{i \rightarrow j}^{ov}$ is defined as the overlap region between the upstream turbine i turbulence and turbine j rotor swept region. The expression (z, r) is defined as a point in the turbulence of the turbine, where z is the distance to the turbine rotor disk plane and r is the distance to the center of the turbine rotor axis. Then, the aggregate wind speed is represented as:

$$\bar{V}_j = V_\omega \left(1 - 2 \sqrt{\sum_{u \in S: z_i < z_j} \left(V_i \left(\frac{D_i}{D_i + 2\phi(z_j - z_i)} \right)^2 \frac{A_{i \rightarrow j}^{ov}}{A_j} \right)^2} \right). \quad (18)$$

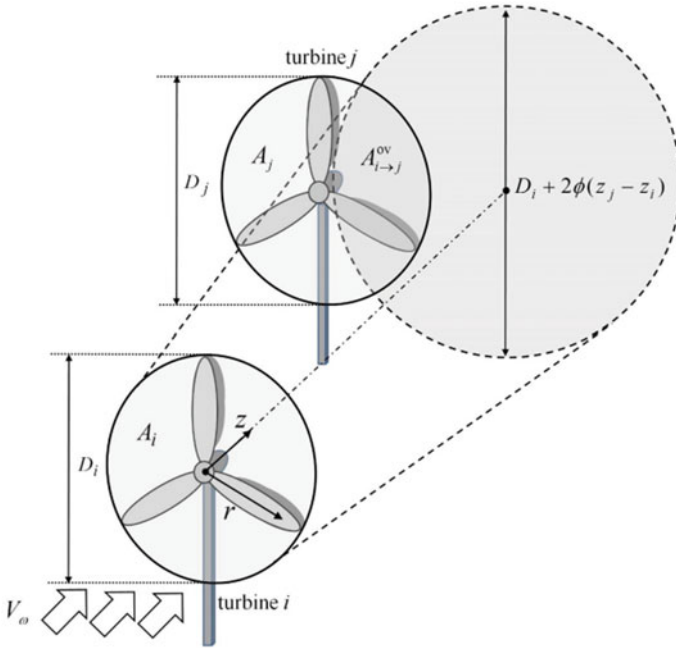


Fig. 2 The illustration of wake expansion [9]

where z_i is the distance to the turbine i rotor disk plane, while z_j is the distance to the turbine j rotor disk plane. Figure 2 shows the illustration of turbulence interaction between the two turbines. For $j \in s$, the wind speed \bar{V}_j is calculated using the wind speed aggregation deficit produced by each upstream turbine. It is assumed that the turbulence expands proportionally to the distance z and its diameter has a circular cross-section. Moreover, the power of each turbine is given as:

$$J_j = 2\rho A_j a_j (1 - a_j)^2 \bar{V}_j^3. \tag{19}$$

where ρ is the density of air.

5.2 Horns Rev Example

This section evaluates the effectiveness of the RS based method based on the Horns Rev wind farm model in Sect. 5.1. The Horns Rev wind farm consists of 80 turbines with 80 m diameter. It is in North Sea off the coast of Denmark. The layout

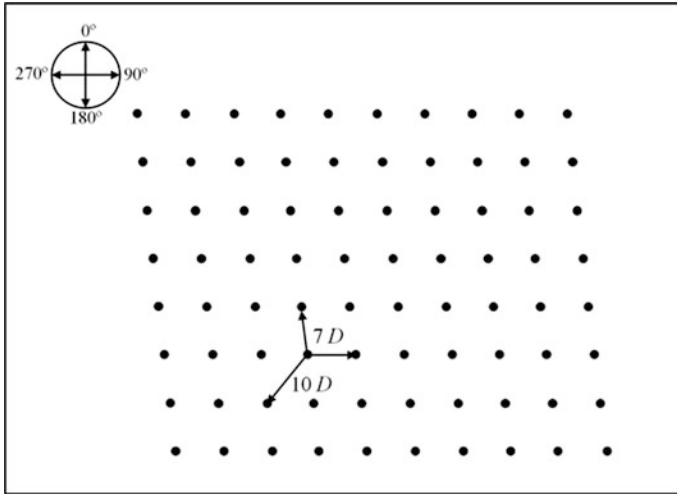


Fig. 3 Horns Rev wind farm layout [9]

of the wind farm is shown in Fig. 3. Note that, each turbine is positioned in an oblique rectangle, where the distance between each turbine is equal to seven turbines diameters, for example, 560 m, in both x and y directions. The value of air density and the roughness parameter are $\rho = 1.225 \text{ kg/m}^3$ and $\phi = 0.04$, respectively. In this study, the performance comparison of the variation of RS based methods is presented for specific wind direction only. In particular, we select the case when wind direction is 270° since a much larger wake effect is generated amongst turbines [20].

Firstly, it is assumed that the incoming wind speed is constant at $V_\omega = 8 \text{ m/s}$. Next, the gain sequences of SRS are set as $\delta_i = 0.01 / (t + 18)^{1/5}$, the step size constant of FSSRS is set as $S = 0.003$, the nominal step size of ASSRS is initialized as $S^* = 0.009$ and the step size memory of ORSSRS is initialized as $\bar{S}_0 = 0.003$. The initial control parameter of each turbine is set to the optimal control parameter of standalone turbine, which is given by $\alpha_{0i} = 1/3$ for these algorithms. In order to see the effect random parameter in all methods, 100 independent trials are executed for these algorithms.

Figure 4 shows the wind farm total power production responses $\bar{J}(a_1, a_2, \dots, a_n)$ of each approach after 2500 number of objective function evaluations. Here, the responses of the SRS, ASSRS, FSSRS and ORSSRS methods are represented by the black, blue, green and magenta lines respectively. It shows that the convergence curve of SRS, FSSRS, ASSRS and ORSSRS are comparable. However, FSSRS, ASSRS and ORSSRS can achieve very fast convergence rate. Meanwhile, SRS and ORSSRS can obtain the highest output. Moreover, if we looked into detail as shown in Fig. 5 and refer to the statistical analysis of the total power production at 2500 number of evaluations as shown in Table 1, the ORSSRS approach produces highest power production (38.114113936 MW) compared to SRS (38.109070950 MW),

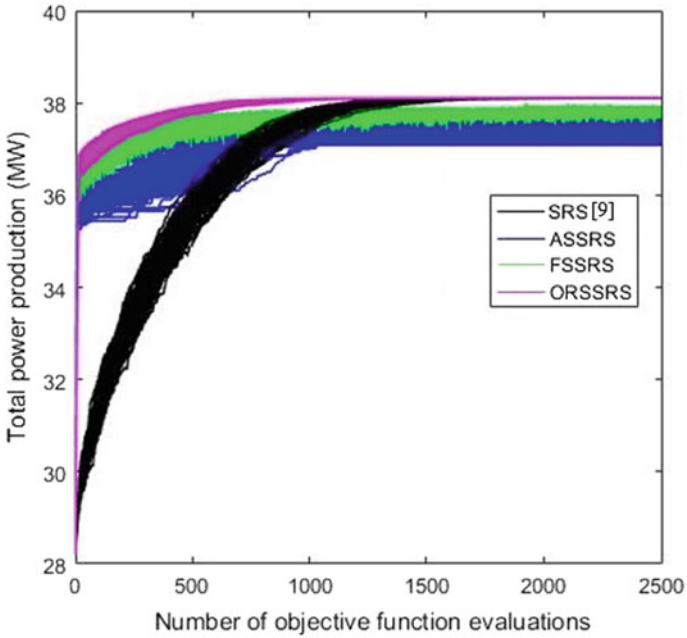


Fig. 4 The total power production $\bar{J}(a_1, a_2, \dots, a_n)$ convergence responses

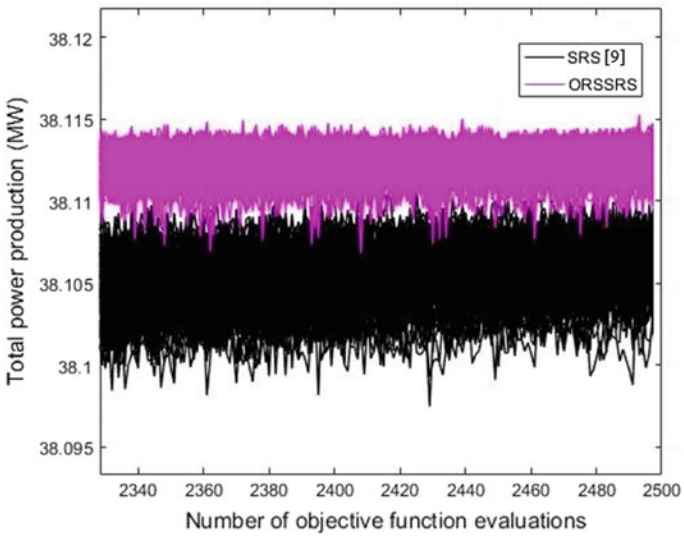


Fig. 5 Magnified view of the highest total power production of SRS and ORSSRS

Table 1 Performance comparison of the total power production (MW) of the FSSRS, ASSRS, SRS and ORSSRS methods

Statistical analysis	FSSRS	ASSRS	SRS [9]	ORSSRS
Mean	37.811343625	37.436745748	38.106292730	38.112608096
Best	37.930451437	37.844105469	38.109070950	38.114113936
Worst	37.712495620	37.086143841	38.101570162	38.110629775
Std. deviation ($\times 10^{-3}$)	37.316361434	180.29620188	1.5554057002	0.7765571572

ASSRS (37.861633677 MW) and FSSRS (37.930451437 MW). We also can observe a similar pattern for the values of mean and worst of the total power production. In terms of the obtained optimal control parameter, it is expected that these values are same for all turbines in the same row are the same, since the generated turbulence is propagated symmetrically. Particularly, the turbines in the first row receive the incoming wind speed V_w , the best optimal control parameters of the ORSSRS approach are as row $\{1; 2; 3; 4; 5; 6; 7; 8; 9; 10\} = \{0.2074; 0.1602; 0.1675; 0.1659; 0.1714; 0.1192; 0.2242; 0.1848; 0.1863; 0.3311\}$. The optimal control parameters value in the first row is higher than the intermediate row, while the values in the final row are remained as the initial control parameters. This pattern is like recent investigation on the wind farm control [3, 9].

6 Conclusion

In this paper, a study of a model-free method based on variations random search methods which are Sequential Random Search, Fixed Step Size Random Search, Adaptive Step Size Random Search and Optimized Relative Step Size Random Search for wind farm control have been investigate. The proposed method is simulated on Horns Rev wind farm layout. The results show ORSSRS is the most suitable to apply in our future study. Because of its fast convergence rate and the ability to obtain highest total power production. In the future study, we will add multi-resolution function to the ORSSRS to further increase convergence rate without losses the potential to get high total power production.

References

1. Global Wind Energy Council: Global Wind Statistics. J. Chem. Inf. Model. **53**(9), 1689–1699 (2016)
2. Marden, J.R., Ruben, S.D., Pao, L.Y.: Surveying game theoretic approaches for wind farm optimization. In: 50th AIAA Aerospace Sciences Meeting Including the New Horizons Forum and Aerospace Exposition, pp. 1–10 (2012)

3. Marden, J.R., Ruben, S.D., Pao, L.Y.: A model-free approach to wind farm control using game theoretic methods. *IEEE Trans. Control Syst. Technol.* **21**(4), 1207–1214 (2013)
4. Park, J., Kwon, S., Law, K.H.: Wind farm power maximization based on a cooperative static game approach. *SPIE Smart Struct. Conf.* **8688**, 1–15 (2013)
5. Kim, C., Member, S., Gui, Y., Member, S.: Maximum Power Point Tracking of a Wind Power Plant With Predictive Gradient Ascent Method **8**(2), 685–694 (2017)
6. Ahmad, M.A., Azuma, S.I., Sugie, T.: A model-free approach for maximizing power production of wind farm using multi-resolution simultaneous perturbation stochastic approximation. *Energies* **7**(9), 5624–5646 (2014)
7. Park, J., Law, K.H.: A data-driven, cooperative wind farm control to maximize the total power production. *Appl. Energy* **165**, 151–165 (2016)
8. Hao, M.R., Ismail, R.M.T.R., Ahmad, M.A.: Using spiral dynamic algorithm for maximizing power production of wind farm. In: 2017 International Conference on Applied System Innovation (ICASI), pp. 1706–1709 (2017)
9. Ahmad, M.A., Hao, M.R., Ismail, R.M.T.R., Nasir, A.N.K.: Model-free wind farm control based on random search. In: 2016 IEEE International Conference on Automatic Control and Intelligent Systems (I2CACIS), pp. 131–134 (2016)
10. Zabinsky, Z.: Random search algorithms. *Wiley Encycl. Oper. Res. Manag. Sci.* 1–16 (2011)
11. Rastrigin, L.A.: Convergence of random search method in extremal control of multi-parameter systems. *Avtom. i Telemekhanika* **24**(11), 1467–1473 (1963)
12. Schumer, M.A., Steiglitz, K.: Adaptive step size random search. *IEEE Trans. Automat. Control* **13**(3), 270–276 (1968)
13. Schrack, G., Choit, M.: Optimized relative step size random searches. *Math. Program.* **10**(1), 230–244 (1976)
14. Zabinsky, Z.B., Smith, R.L., McDonald, J.F., Romeijn, H.E., Kaufman, D.E.: Improving hit-and-run for global optimization. *J. Glob. Optim.* **3**(2), 171–192 (1993)
15. Zabinsky, Z.B.: Stochastic Adaptive Search for Global Optimization, p. 224 (2003)
16. Lawrence, J.P., Steiglitz, K.: Randomized pattern search. *IEEE Trans. Comput.* **C-21**(4), 382–385 (1972)
17. Solis, F.J., Wets, R.J.-B.: Minimization by random search techniques. *Math. Oper. Res.* **6**(1), 19–30 (1981)
18. Scholbrock, A.K.: Optimizing Wind Farm Control Strategies to Minimize Wake Loss Effects (2011)
19. Karnopp, D.C.: Random search techniques for optimization problems. *Automatica* **1**(2–3), 111–121 (1963)
20. Porté-Agel, F., Wu, Y.-T., Chen, C.-H.: A numerical study of the effects of wind direction on turbine wakes and power losses in a large wind farm. *Energies* **6**(10), 5297–5313 (2013)

The Development of Graphical Overall Equipment Effectiveness Interface



Norazlin Nasir, Teruaki Ito, A. Y. Bani Hashim
and Muhammad Hafidz Fazli Md Fauadi

Abstract Internet of things emphasized on integration the process and management with the network by providing all the data on-board. To cope with the new era of management becomes a challenge to manufacturer especially to handle the manufacturing asset such as man, machine and management. Web-based management is an option to manage the manufacturing asset well. However, present web-based management oriented was independent furthermore there is a chance to integrate the web-based management with the existing manufacturing concept can be implemented. Based on the current manufacturing issues, the key characteristic and critical success factors for future manufacturing are identified in this paper. Skill gap, leadership, and traceability are critical success factor that needs to be strengthened before embedded the IoT into manufacturing. To develop the web-based management, the entity relationship diagram and sequence diagram are emphasized in this paper for graphical overall equipment effectiveness interface. The graphical overall equipment effectiveness interface represent the manufacturing data graphically in order to make the monitoring and operation verification process become ease by showing the data graphically.

Keywords Internet of thing · Overall equipment effectiveness
Graphical user interface

N. Nasir (✉) · A. Y. Bani Hashim · M. H. F. Md Fauadi
Institute of Technology and Science, Tokushima University,
Minami-Jyousanjima 2-1, Tokushima-shi, Tokushima 770-8506, Japan
e-mail: c51442007@tokushima-u.ac.jp

N. Nasir · T. Ito
Faculty of Manufacturing Engineering, Universiti Teknikal Malaysia Melaka,
Hang Tuah Jaya, 76100 Durian Tunggal, Melaka, Malaysia

© Springer Nature Singapore Pte Ltd. 2018
M. H. A. Hassan (ed.), *Intelligent Manufacturing & Mechatronics*,
Lecture Notes in Mechanical Engineering,
https://doi.org/10.1007/978-981-10-8788-2_61

1 Introduction

1.1 Background

The integration between manufacturing process and internet of thing (IoT) favors the optimization in any activities. The real-time monitoring and control the manufacturing process able to reduce the timely decision making for production. The term IoT was introduced by Kevin Ashton which refers to uniquely identifiable objects (Things) and the information is represented virtually in a structure alike Internet. The communication and information network technologies have brought the IoT into a new era [1, 2].

One of the benefits of IoT is the capacity to be integrated with other manufacturing tools or approach such as overall equipment effectiveness (OEE) for process optimization. OEE also known as performance indicator can be applied in product lifecycle management (PLM) to detect problems and initiate the optimum process changes. It should be noted that PLM is a crucial approach to improve the information management in the manufacturing enterprise. The information caters in PLM begin in pre-production phase until the user phase. The pre-production phase is a critical phase where the design and material selection required the complete and precise information for the optimum manufacturing process.

1.2 Motivations

Two worst case scenarios occurred in 2009 where Toyota made massive vehicles call for 11 major models and over 9 million vehicles due to car complexity specifically pedal entrapment. The recalls cost more than \$2 billion in repair and lost deals. The recall resulted in 5% loss of its market share in the United State of America and further drops were foreseen [3]. A380, a superjumbo model developed by Airbus company was reported as missing their target in new production, causing delayed market entry due to their weak PLM [4]. These two cases give the signal to all industries to possess and optimize the facilities for better traceability in the shortest time period. Those real cases faced by A380 model and the lost cost of repair, deals and market share by the Toyota massive call have become the motivation for this study. Company reputations are at stake. The sustainable PLM should be started with a strong foundation where IoT utilization should be considered.

1.3 Our Works and Contributions

Motivated by these real cases happened and observations done for this study, this paper will address the challenges for Industry 4.0 (I4) that become a part of future manufacturing. More specifically, the challenges are explained based on three main views: man, machine, and management. Concisely, people tend to relate man, machine, and method in all manufacturing process but management also plays important roles in order to make all the manufacturing process become efficient and optimal. To utilize all the resources and optimize the manufacturing efficiencies may lead to complex management. The assist from IoT able to make the monitoring and management process become easier. In this paper the development of web-based monitoring system is discuss where the graphical OEE representation is emphasized.

2 Preliminary Knowledge

2.1 Manufacturing Challenges

The challenges of future manufacturing can be elucidated based on three main views: man, machine, and management. In three main view the leadership, skill gap and traceability become a main point to be discussed further. Concretely, people tend to relate man, machine, and method in all manufacturing process however IoT is more capable to assist the management process to control and monitor the manufacturing process to become more efficient and optimal. To cope with digitization and intelligent manufacturing system, the skill gap, leadership and traceability are challenges that contribute to manufacturing issues.

Skill gap bond the man and machines where the high skill is extremely required to operate and control the intelligent manufacturing system. The more intelligent devices in production floor, the level of complexity become high. Skill is defined as the ability to complete the well-defined task and to apply the knowledge including know-how [5]. Skills can drive the improvement in productivity and enable the man/operator to accomplish the complex task, the high-value product produced in an effective manner [6]. Necessary the high skill talent may require once the technology change. To be high comparative industry, to manage the intelligent and digitization manufacturing devices, it is postulated.

Between man and management, the high leadership capabilities become an issue in I4. The leadership challenge is to need the accountability on digitization and intelligent manufacturing system in man, machine, and management perspective when the real-time data is on-board. Leadership is specified as a process of the social effect that finds the subordinates voluntary participation to carry out each task given and meet the organizational targets. An effective leader is able to successfully influence the subordinate participation to achieve the targets in the desired manner

[7]. In advance, comparative industry such as intelligent and digitization manufacturing, the effective leadership is required to minimize the attrition rate among employee.

In IoT environment, trust is a best practice to overcome the data leakage issues. From internet provider that maintaining the track record on cloud services, features have developed the trust over the particular time. The trackback of file-centric approached has increased the data traceability, real-time record, accountability as well as transparency in IoT environment [8]. Traceability is an information path between two different domain/addressed platform that allows changes, decision and eases the maintenance. Traceability also a transformation model for round-trip development that enables to keep track the information evolvement and its original source by providing the trackback record in different-time [9]. The real-time source obtained makes the man/operator able to trace back the information sent and expedite the decision-making without any delay. To provide the track information record, round trip time experiment is defined as path length in time unit to measure the data transmission to different platforms. Traceability for example for the residential user may not be a concerned instead of the high-quality timing source. However, when manufacturing required automation process that worked under internet network to transmit the information between synchronized distinct and devices that correlate with time, the real-time source is necessary [10].

2.2 Overall Equipment Effectiveness

OEE is a performance efficiency metric that primarily used to recognize and evaluate the manufacturing assets: individual equipment by taking the accessibility, performance and quality rate [11–15]. En-Nhaili, Meddaoui, and Bouami believed the OEE is linked directly to 5S and total preventive maintenance (TPM), also OEE is a proven methodology approach to enhance the overall performance [16].

It is significant to connect the OEE into cloud network with help from IoT devices. From that, less planned and unexpected downtime will become more efficient. In addition, machines capacities and benefits in manufacturing process can be increased by adopting OEE [17]. As an efficiency metric for manufacturing, the OEE can be evaluated based on Eq. 1, where A is defined as availability, P is a term for performance and quality rate is known as Q . Term of availability used in OEE is referring to the existing and accessible the information for authorized user and services. Availability also related to data persistence where the data must always be available with no failure to be accessed [18].

The previous or conventional OEE required complex calculation. In real application, daily basis data is needed for performance measure and improvement. This complex calculation required substantial time and effort to obtain optimum OEE.

The use of information system in manufacturing is able to increase the productivity and performance measure. The use of IoT has enabled the manufacturing

execution system interaction, smarter manufacturing, and large communication and computation capabilities for big data. Besides IoT enables the large computation on OEE KPIs, process accomplishment and investigates the relationship between planned scheduled and real production operation [19]. Previous application of OEE was timely evaluation making. By integrating the OEE and IoT, it enables the evaluation process is done rapidly.

$$OEE = A \times P \times Q \quad (1)$$

$$\text{Availability Rate (A)} = \frac{\text{Operating Time (hrs)}}{\text{Loading Time (hrs)}} \times 100 \quad (2)$$

$$\text{Performance Efficiency (P)} = \frac{\text{Theoretical Cycle Time (hrs)} \times \text{Actual Output (units)}}{\text{Operating Time (hrs)}} \quad (3)$$

$$\text{Quality Rate (Q)} = \frac{\text{Total Production} - \text{Defect Amount}}{\text{Total Production (units)}} \times 100 \quad (4)$$

3 Critical Success Factors for Industry 4.0

3.1 Man, Machine, and Management

Manpower or employee is an asset to the organization that makes the product development run smoothly. Mentally aspect such temperament, personality as well as emotions may limit the human capabilities and influence the human perception, response speed, strength and etc. [20]. In IoT environment, the aptitude to control the mental aspect is needed when they dealing with intelligent machinery in order to avoid any accident and lost. To enable the real-time data communications in IoT environment, the communication can be executed with the dedicated network or existing wireless networks telemetry transmission. The core concept of the intelligent machine in IoT environment are; to remote the machines by enhancing the remote devices for the user, to monitor the generated data onboard and rapid data transmission from man to machine or machine to machine [21]. The IoT is help to improve and manage the performance of the management system in the manufacturing process by eliminating the manual management that too relies on human intervention. Management can be defined as a set of activities to configure, monitor and manage the network elements, resources, applications and services for the system. Management with embedded IoT, resulted in benefits real-time data collection, data exchange interoperability, minimize the system cost as well as maximize the computer and network device utilization in an integrated mode [22].

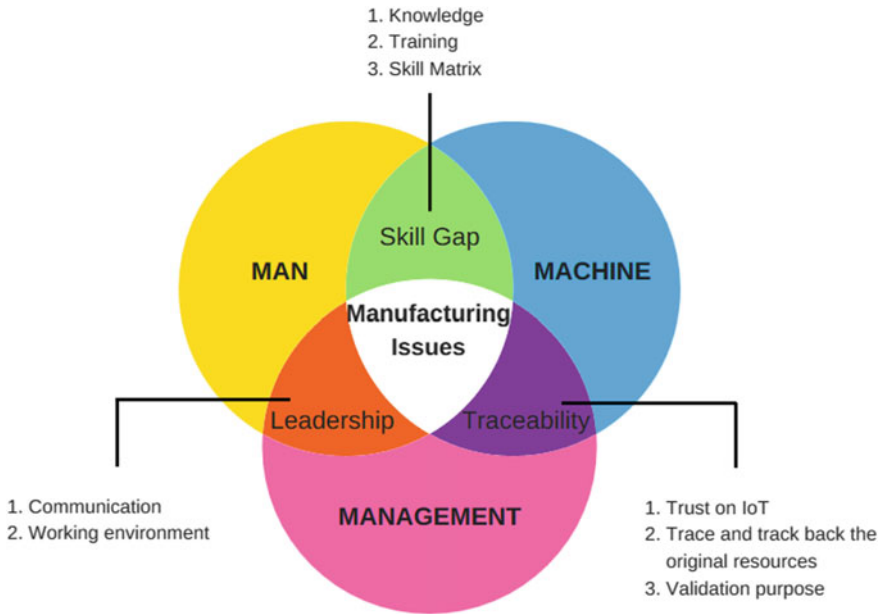


Fig. 1 The elements of key characteristic and success factors for industry 4.0 based on manufacturing perspective

The manufacturing issues are view form man, machine, and management perspective. The IoT give more impact to man, machine, and management instead of method perspective even people or industrial generally always make the relation between man, machine, and method. It is undeniable that the man, machine, and method have eased the management and optimize the manufacturing processes but the IoT also have the capabilities to make those become excellent. That was a reason to ignore the method perspective in this study. Figure 1 shows the elements of key characteristic and success factor that contribute to the success of I4.

3.2 Critical Success Factors

3.2.1 Skill Gap

Knowledge and training are most important factors for a man/operator to operate the intelligent machines and devices. Skill is developed from knowledge gain and training given. Skill is believed as manufacturing resources by Pullan et al. [23] and in fact, skill is an asset for intelligent manufacturing. The existing skills possess by any man/operator to complete the task given is not enough for skill achievement determination. The skill matrix is proposed for validating the skill developed to

operate certain processes and machines. It is agreed by Kulkarni et al. [24] in the employability skill matrix required the skilled man to demonstrate the technical knowledge gain. The main purposed of skill matrix to choose the competent man/operator to operate the intelligent machine and devices without any losses and failure.

3.2.2 Leadership

In this study, the success factors for leadership are determined by communication/social skill and working environment. A group of man/operator needs to be lead which the leader must have a good communication skill to influence or order them to accomplish the task given. Kalinga et al. [25] explained that the role of leadership is to simplify the result, mentor the man/operator and encourage them to be more effective and efficient workers. The working environment is another factor for leadership achievement. A leader must possess the ability to create and control the good environment and conducive. The ability helps to avoid the chaos and manage the man/operator behavior. The competence leadership able to enrich the working environment with variety skilled man/operator and optimized the organizational performance. To eliminate the social gap among subordinate, leader may keep frequent spend casual time. The casual time may ease the discussion and planning activities in order to meet the organization requirement.

3.2.3 Traceability

Traceability is a method proposed based on machine and management relationship. To provide the track information record, round trip time experiment is defined as path length in time unit to measure the data transmits to different platforms. The trace and track back the information gained able to expedite the decision making or changes to any issues to be solved. In digitization manufacturing, the original resources are important to be known and trust in order to make a worth decision. Furthermore, the ability to be tracked and traced back the original resources become necessary. The method to know the original resources is through round-trip time where the information is permitted to be transferred from one location to another. In round trip time, the less time different resulted in influencing just-in-time decision making without any delay. In addition, the validation purpose is important for traceability achievement. Data and process need to be validated in order to ensure the process done comply with standard operation procedure (SOP). In addition, the system performance needs to be evaluated to ensure the system is optimized. The ability to trace the system history/previous record required secure data storage in the server to be stolen, misused or being manipulated by non-authorized man/operator. Eventually, the traceability purpose is to increase the trust level on IoT.

4 Overall Equipment Effectiveness Dashboard and Discussion

4.1 The Architecture

To develop the product lifecycle management dashboard, the JAVA software was used. Figure 2 shows the architecture for PLM dashboard. There are two types of the user which are IoT user and application service's user. The IoT user able to use the visualization application of web user interface (UI), to load and view the report of manufacturing operation as well self-service directory. In self-directory, the IoT user able to save the file and print the manufacturing report. In the application service, the user also able to visualize the web UI, choose the user directories and file repositories. Additionally, the user can upload the manufacturing data through file repositories application service.

Notably, the webs UI is an interface connect the users with the database layer. In the data store service, there are two groups of data; enterprise application and enterprise data. The enterprise application consists of data from customer experience and manufacturing operation. Instead of that, the application data, historical data and reference data are grouped into enterprise data. The application data consist of the PLM data, start from pre-production, production, distribution, use and recycle data. The OEE data also grouped into application data. Basically, the

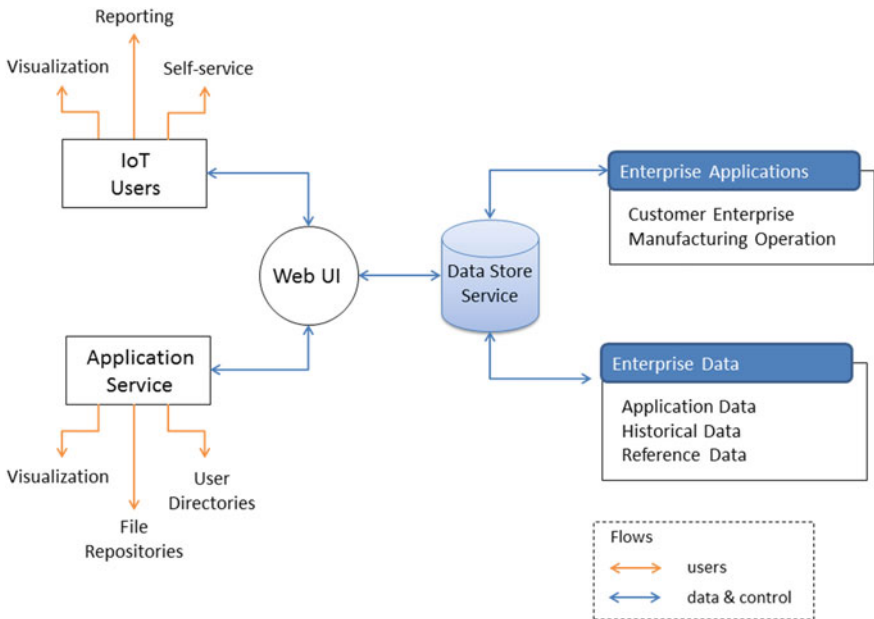


Fig. 2 The architecture for product lifecycle management dashboard

enterprise application is targeted to verify the application service user and manufacturing operation. Different with enterprise data where it's has designed for user to analyze the application data.

The authorized user is required to upload the manufacturing operation data through file repositories in application service in order to use this dashboard. From that, the uploaded data is analyzed for IoT user visualization, reporting, and self-service.

4.2 The Entity Relationship Diagram and Sequence Diagram

The entity relationship diagram (ERD) was used to represent the enterprise data view [26]. In this study, the ERD has an aim to represent the data for the OEE dashboard. In Fig. 3, the ERD represents the detail of OEE data that the user able to view. The OEE data comprise operating time, planned production time, cycle time, total output and finished good quantity. Besides that, the downtime and rejection units also can be reviewed in the OEE dashboard. Only the authorized users only can assess the OEE dashboard. As shown in ERD below, the user details like user identification and password is required to view the OEE dashboard.

The sequence diagram is used to view the login operation for the user as shown in Fig. 4. The login operation showed has interaction between the various classes and the graphical user interface (GUI). In the sequence diagram below the authorized user will enter his/her user identification (ID) and password and click on login button the login interface. The Database class gets the user ID and user details from

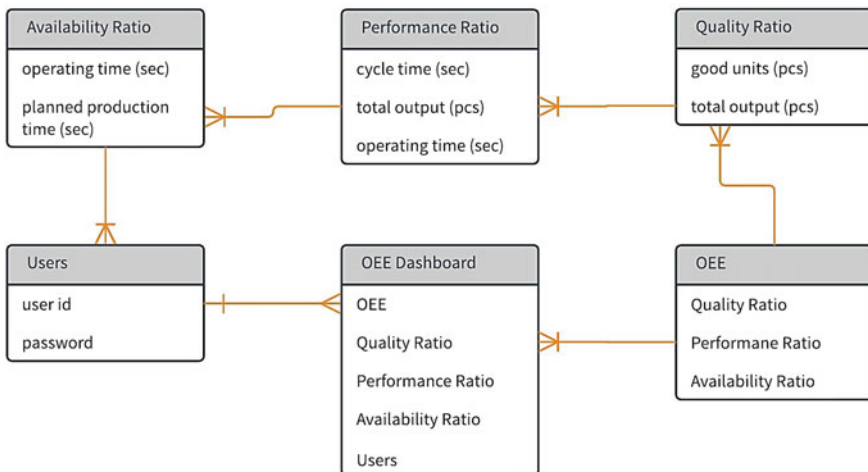


Fig. 3 The entity relationship diagram for overall equipment effectiveness dashboard



Fig. 5 GUI overview for OEE dashboard

good units is show based on daily basis. The database will keep the data for OEE evaluation purpose. The OEE evaluation is done by adopting the general equations in (1), (2), (3), (4) as shown previously.

4.4 Discussion

The OEE dashboard is one of six dashboards for PLM web-based monitoring system. The web-based monitoring system as a support system for manufacturing is targeted to assist in monitoring activities for the manufacturing enterprise. The architecture of PLM dashboard represents the entire system, while the sequence diagram represents user to be the authorized user in application service. Only an authorized user is allowed to upload the manufacturing data. Both users, IoT user and service user are able to use the web-based monitoring system with a different task. The IoT user cannot upload the manufacturing operation data into web-based monitoring system while application service user able to do so. Web-based is chosen for this study because web-based make the onboard data become possible. Furthermore, this benefit allows any IoT users to surf and analyzed the data in anywhere. The decision-making process can be done just in time without any delay.

5 Conclusions

To minimize the risk in production lines, a lot of study and suggestion are proposed for manufacturing improvement. Recently, IoT showed its capability that able to expedite the decision-making process and the simulation of manufacturing process helps in reducing losses. Furthermore, the production lines optimization can be monitored by integrating the IoT and OEE.

The graphical OEE interface is able to ease the monitoring activities by integrating the elements of IoT and manufacturing data. The used of ERD and sequence diagram in this study may help in better understanding in the graphical user interface development process for OEE dashboard. The monitoring activities for production lines become much easier since the OEE dashboard shows the historical data for four weeks.

As a future study, the development of PLM dashboard becomes a target since PLM offer the best monitoring approach by correlating the various manufacturing phase starting pre-production until user. The PLM has a similar target with OEE where it's designed to monitor the production process and its optimization.

References

1. Zhang, Y., Tao, F.: Optimization of manufacturing systems using the Internet of Things. In: Chapter 2: Overview of IoT-Enabled Manufacturing System. Academic Press (2016)
2. Ashton, K.: That 'Internet of Things' thing. *RFID J.* **22**(7), 97–114 (2009)
3. Xiaoyuan, G.: Toyota recalls: revealing the value of secure supply chain. Dissertation. Massachusetts Institute of Technology (2010)
4. Drummer, T.: Case Study: IBM & Airbus: Tech Drummer (2008)
5. European Parliament and Council of the European Union: Recommendation of the European parliament and the council of the European union on the establishment of the European qualifications framework for lifelong learning. *Off. J. Euro. Union* (2008)
6. Chryssolouris, G., Mavrikios, D., Mourtzis, D.: Manufacturing systems: skills and competencies for the future. *Procedia CIRp* **7**, 17–24 (2013)
7. Nanjundeswaraswamy, T.S., Swamy, D.R.: Leader. *Styles. Adv. Manag.* **7**(2), 57 (2014)
8. Zaigham, M., Saeed, S. (eds.): Software engineering frameworks for the cloud computing paradigm. Springer (2013)
9. Cheung, M.Y.S.: Round-trip business process driven SOA modelling between ARIS and Cordys. In: Web Information Systems Group, Department of Software Technology, Faculty EEMCS, Delft University of Technology Delft, The Netherlands (2010)
10. Chapman, J.T., Chopra, R., Montini, L.: The DOCSIS timing protocol (DTP) generating precision timing services from a DOCSIS system. In: Proceedings of the Spring Technical Forum (2011)
11. Nakajima, S.: Introduction to TPM Total Productive Maintenance. Productivity Press, Oregon, USA (1988)
12. Atkinson, A.: Fixed factor fine tuning. *CMA Manag.* **81**(7), 42–46 (2007)
13. SEMI E79-0200: Standard for definition and measurement of equipment productivity. *Semicond. Equip. Mat. Int. CA* (2000)
14. SEMI EI0-0701: Specification for definition and measurement of equipment reliability, availability, and maintainability (RAM). *Semicond. Equip. Mat. Int. CA* (2000)

15. Malli, S., Vijayalakshmi, S., Balaji, V.: Real time big data analytics to derive actionable intelligence in enterprise applications. In: *Internet of Things and Big Data Analytics Toward Next-Generation Intelligence*, pp. 99–121. Springer, Cham (2018)
16. En-Nhaili, A., Meddaoui, A., Bouami, D.: Effectiveness improvement approach basing on OEE and lean maintenance tools. *Int. J. Process Manag. Benchmark.* **6**(2), 147–169 (2016)
17. Balaji, V., Venkumar, P., Sabitha, M., Vijayalakshmi, S., Sre, R.R.: Smart manufacturing through sensor based efficiency monitoring system (SBEMS). In: *International Conference on Soft Computing and Pattern Recognition*, pp. 34–43. Springer, Cham (2016)
18. Ulltveit-Moe, N., Nergaard, H., Erdödi, L., Gjørøseter, T., Kolstad, E., Berg, P.: Secure Information Sharing in an Industrial Internet of Things. [arXiv:1601.04301](https://arxiv.org/abs/1601.04301) (2016)
19. Gyusun, H., Jeongcheol, L., Jinwoo, P., Tai-Woo, C.: Developing performance measurement system for Internet of Things and smart factory environment. *Int. J. Prod. Res.* (2016)
20. Xiaoyan, S., Zhongpeng, X.: Application of man-machine-environment system engineering in coal mines safety management. *Procedia Eng.* **84**, 87–92 (2014)
21. Tuna, G., Kogias, D.G., Gungor, V.C., Gezer, C., Taşkın, E., Ayday, E.: A survey on information security threats and solutions for machine to machine (M2M) communications. *J. Parallel Distr. Comput.* **109**, 142–154 (2017)
22. Sheng, Z., Mahapatra, C., Zhu, C., Leung, V.C.: Recent advances in industrial wireless sensor networks toward efficient management in IoT. *IEEE Access* **3**, 622–637 (2015)
23. Pullan, T.T., Bhasi, M., Madhu, G.: Decision support tool for lean product and process development. *Prod. Plan. Control* **24**(6), 449–464 (2013)
24. Kulkarni, V.A., Bewoor, A.K., Malathi, P., Balapgol, B.S.: Employability skill matrix for engineering graduates of tier-II institutes. *J. Eng. Educ. Trans.* **30**(3), 71–76 (2017)
25. Kalinga, J., Robert, L., Adam, L.: A bottom-up approach for productivity measurement and improvement. *Int. J. Prod. Perf. Manage.* **62**(4), 387–406 (2013)
26. Chen, P.P.S.: The entity-relationship model: a basis for the enterprise view of data. In: *Proceedings of the June 13–16, National Computer Conference*, pp. 77–84. ACM (1977)

Effect of Length on Pressure Characteristic in the Water Hydraulic Main Line Circuit Using Simulink-Simscape



Ihsan Ismail, Syarizal Bakri, Ahmad Anas Yusof and Suhaimi Misha

Abstract This study focus on the water hammer pressure characteristic in water hydraulic system. Water hammer shock can cause negative impact to the water hydraulic system by damaging pipeline system, valve and pump. This will increase the maintenance cost of the system. There are many parameters that effect the pressure characteristic behaviours in the circuit such as pressure source, pump type and type of pipeline. All these parameters can affect the pressure behaviours due to change of the properties such as flowrate and resistance of water to the wall. Pressure water surge during water hammer mainly effected by pipeline length of the system. This paper shows that the pipeline length can give the impact to the pressure characteristic of low and high-pressure source from the pump. Result shows that water hammer can occur when the condition meet that long rigid pipeline length. Increasing length of the pipeline can make the flowrate of water increase and gives higher maximum pressure surge with continues isolate wave to the water hydraulic system. Water hammer will occur when 15.0 mm pipe-diameter of 10.0 m length is used in simulation. Model the water hydraulic circuit and simulate the system to study the behaviour using Simulink-Simscape from the MATLAB software as a virtual representation of a real-world system.

Keywords Water hammer · Pressure surge · Flow rate · Pressure characteristic · Simulink

1 Introduction

70% of the Earth is covered by water. Thus, water hydraulic is suitable in industries which operate in environmentally sensitive surrounding. This include food processing industries for the food processing industry, pharmaceutical industry,

I. Ismail · S. Bakri · A. A. Yusof (✉) · S. Misha
Faculty of Mechanical Engineering, Universiti Teknikal Malaysia Melaka,
Hang Tuah Jaya, 76100 Durian Tunggal, Melaka, Malaysia
e-mail: anas@utem.edu.my

© Springer Nature Singapore Pte Ltd. 2018
M. H. A. Hassan (ed.), *Intelligent Manufacturing & Mechatronics*,
Lecture Notes in Mechanical Engineering,
https://doi.org/10.1007/978-981-10-8788-2_62

humidification operations, firefighting, high water pressure cleaners, wood processing, lumber drying, mining, steel and cobber industry, nuclear industry, and mobile machines. Today's progress in water hydraulics includes electro water hydraulic proportional valves and servo valves for design of motion control solutions for machines and robots. Many new technologies and products having been developed including water hydraulics technology that has been in existence for just over 200 years and is now beginning to be fully exploited [1–5].

Environmental friendly and renewable resource is the main advantages for using water hydraulic [6]. Apart from that, other advantages are the overall low cost allocated in setting up this system, the easy-to-get-substances and simple storage system. The water-based hydraulic systems can run on various type of water such as tap water, salt water, and various other low viscous mediums, which make it the ideal solution for many applications where oil contamination is the main risk contributor to the environment.

Other than that, low operational and disposal costs are one of the advantages of using water hydraulics systems. The disposal cost for water is much cheaper and the operational are easier to dispose instead of mineral oil which require proper treatment. Non-flammable quality is also the advantage of water compares to hydraulic fluid. Mineral oils are flammable due to its nature. Hence, such systems which have high fire risk areas often require expensive and specialized fluids to counter. Using water as a medium eliminates the risk and offers a much cheaper and manageable solution. Lastly, the efficiency of the water can be improved by individual components that offer the same solution compared to a similar oil hydraulics component. The almost incompressible nature of water results in higher transmission efficiencies which will reduce the size of both components and plumbing. According to International Standard Organization, ISO 6743-4, water-based hydraulics can generally be described into four HFA, HFB, HFC, and HFD [7]. These fluids are distinguished according to its composition. Among these fluids, only HFA fluids can be regarded as non-combustible since they contain 80–95% of water.

In a compressible fluid, hydraulic transient is influenced by the pressure in the pipe, ΔP , velocity flow in pipe, Δv and sudden change of velocity flow. This is represented by Joukowsky's equation:

$$\Delta P = \rho c \Delta v \quad (1)$$

where ρ is the fluid mass density and c is the speed of sound. The equation expresses that the magnitude of water hammer is directly proportional to the velocity of the wave propagation. Wave propagation velocity depends on the elasticity of the pipe walls and the compressibility of the fluid. Korteweg's (1878) equation characterizes or defines c for liquid contained in round and hollow channels of roundabout cross-segment:

$$c = \sqrt{\frac{K^*}{\rho}} \quad (2)$$

and

$$K^* = \frac{K}{\left[1 + \frac{DK}{eE}\right]} \quad (3)$$

where K is the bulk modulus of the contained fluid, E is the modulus of elasticity for the wall, D the diameter of the pipe, and e the thickness of the wall [8].

In the case where the fluid is incompressible, then hydraulic transient can be analysed by different approaches, which is known as the rigid column theory, which ignores compressibility of the fluid and elasticity of the walls of the pipe. Column separation is a phenomenon that can occur during a water-hammer event, and can be represented by:

$$P = \rho vL / t \quad (4)$$

where P is the pressure inside the pipe, ρ is the fluid density, L is the pipe length, v is the velocity flow in pipe and T_c is the valve closure time. Hydraulic transients can cause a pipe network to fail if the transient pressures are too much high. When the pressure is too big than the pressure limits of the pipeline, failure through joints, curves or pipe elbows movement may happen. On the other hand, over the top low pressure/negative pressure can bring about buckling, implosion and leakage at pipe joints during sub-atmospheric stages. Low pressure transients are ordinarily experienced on the downstream side of a closing valve [9].

2 Methodology

The water hammer occurs when the flow is suddenly stop or change direction at high velocity. As shown in the Fig. 1, when sudden close of valve at high flowrate at certain are pressure can cause water hammer phenomenon. This simulation is conducted to see the characteristic of the pressure surge in the hydraulic system. Difference lengths used as the variable to obtain the data and determine how much the factor of length effects the pressure characteristic in water hydraulic system.

The circuit for the simulation of the system is conducted by using Simulink-Simscape from the MATLAB. The input from the initial condition is computed in the system model. The parameter is set for each component based from the initial condition. The result from the simulation will be used to analyse the pressure surge characteristic in the water hydraulic system with different length and diameter of the pipeline. This will determine if the factor of length and diameter

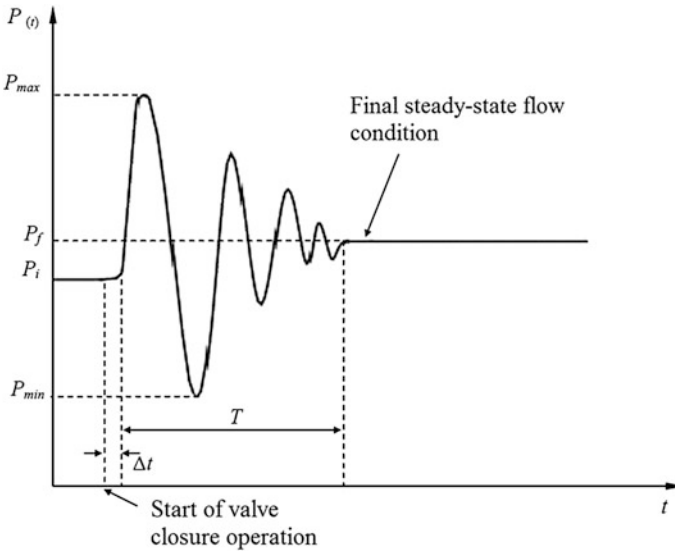


Fig. 1 Pressure characteristic for water hammer condition

effects the pressure characteristic in water hydraulic system. In this paper, the simulation will be conducted of 2 different pressure sources for low pressure and high-pressure condition, which is from 1.0 bar and 10.0 bar pressure source.

The circuit is constructed by using Simulink interface in MATLAB software for the main line circuit. Pipeline with difference parameter, pressure source as water pump shown in the Figure with constant value 10, orifice and hydraulic reference or known as water tank in practical.

2.1 Pressure Sensor (P) and Flow Rate Sensor (Q)

Pressure sensor is used to measure pressure change. Figure 2 shows the location of the sensor, which is located in between pipeline 1 segments and the orifice. The circuit is shown in Fig. 2, consists of pressure sensor (P) to record the pressure change, flowrate sensor (Q) to record for flowrate of water in the system. As shown in Fig. 3, the pressure sensor in block 'P' will record change of water pressure in the system when open and close circuit. The flow rate sensor in block 'Q' will be recorded actual flow in the circuit and used to compare with the behaviour of the pressure during closure of the valve.

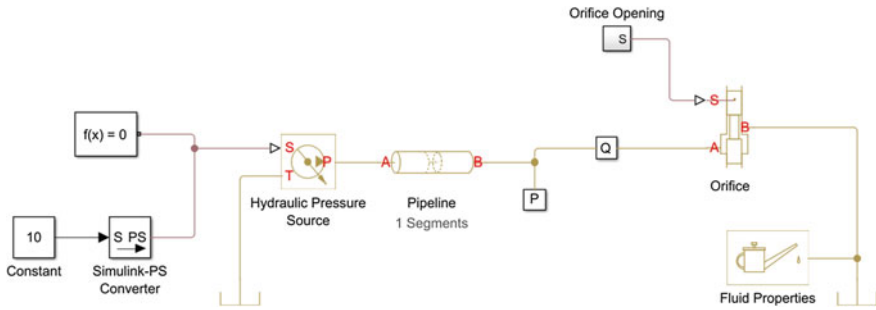


Fig. 2 Schematic diagram main line circuit

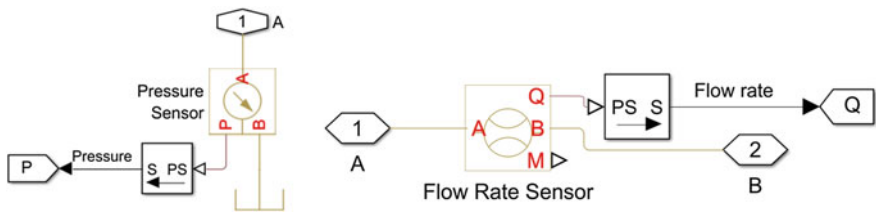


Fig. 3 Sub-element in the main circuit for pressure sensor and flow rate sensor

2.2 Pipeline 1 Segments

Hydraulic circuit is connected from one part to another using pipeline to complete the hydraulic circuit. Length is the main factor that cause the difference value of the pressure in hydraulic circuit. In this simulation, it is to be observe the pressure surge. In this simulation, the pipeline is designed with difference length of pipeline from 2.0, 4.0, 6.0, 8.0 and 10.0 m.

2.3 Hydraulic Pressure Source

The simulation conducted using constant pressure source or pump, type of pipeline. with 2 fixed pressure source which is 1.0 bar and 50.0 bar.

2.4 Type of Pipeline

Rigid pipe wall type selected with internal surface roughness and fit value for modulus of elasticity, $E = 2 \times 10^{11} \text{ Nm}^{-2}$.

2.5 Fluid Properties

Water is selected as the fluid that is used in this water hydraulic system with normal temperature, T at 28 °C.

2.6 Diameter of Pipeline

Diameter of the pipeline value is parameter that are keep constant in this simulation. Diameter of pipe, d is 15.0 mm internal diameter.

2.7 Orifice

Orifice Opening block will control the timing for closure and opening the orifice valve.

The obtain data is based on the result value for using difference length for each testing on low pressure which is 1.0 bar and high pressure at 10.0 bar pressure source. The pressure behaviour in the system will be recorded from the simulator Data Inspector to translate into graph.

3 Result and Discussion

Pressure characteristic simulation is conducted and the data is recorded. All the data is shown in Figs. 4, 5, 6 and 7. From the graph, Figs. 4 and 6 show the pressure characteristic of pipeline length from 2.0, 4.0 and 6.0 m with the low-pressure sources, of 1.0 bar. The result graph shows that the water pressures show more high pressure isolated when used 10.0 m pipeline compare to other pipelines.

3.1 Low Pressure (1.0 Bar)

Figure 4 show full graph for closure and opening operations and Fig. 5 shows more specific with bigger image during valve closure operation that water hammer occurs clearly when the flow of the fluid suddenly closed, and the pressure of that space will automatically increase. In this system, the maximum pressure P_{max} for 10.0 m pipeline is 1.185 bar at $t = 0.6$ s. Unsteady state occurs continuously until valve start open at 1.880 s. For 2.0 m length, the maximum pressure P_{max} is at 1.030 bar and unsteady state occurs 0.164 s before it reaches steady state condition at

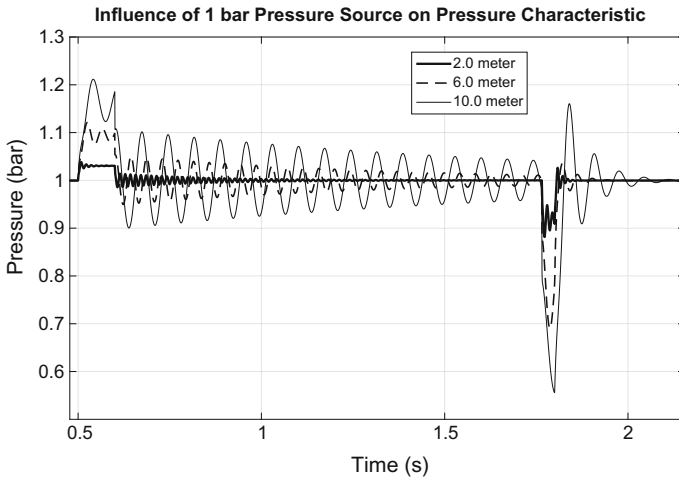


Fig. 4 Pressure behaviour for 1.0 bar pressure source during closure and opening valve

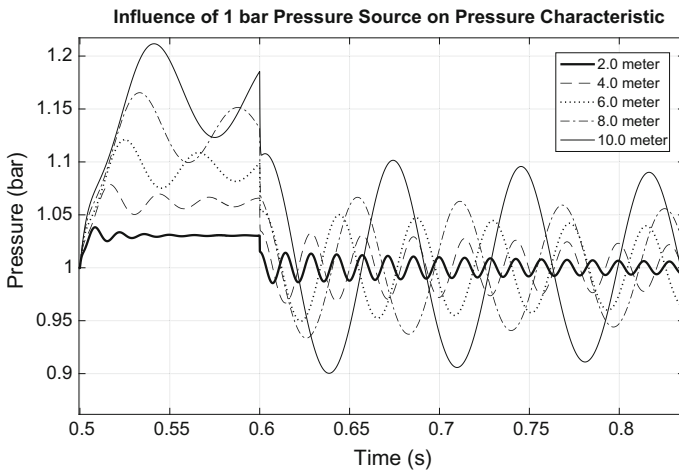


Fig. 5 Pressure behaviour for 1.0 bar pressure source during valve closure

$t = 0.764$ s. Figure 4 show the increasing length of pipeline used, the peak of pressure wave increasing. From the data obtained and graph, the conclusion can be made that at 10.0 m pipeline and 1.0 bar pressure source will produce larger pressure surge effect to the system and the vibration to the pipeline will continuously occur in the system.

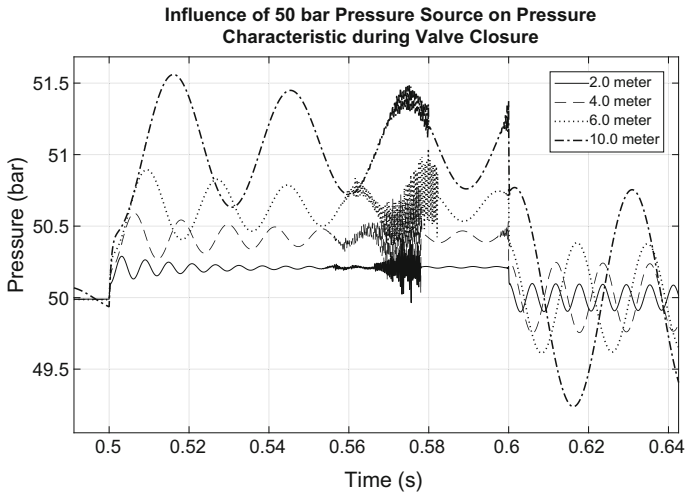


Fig. 6 Pressure behaviour for 50.0 bar pressure sources before valve closure operation

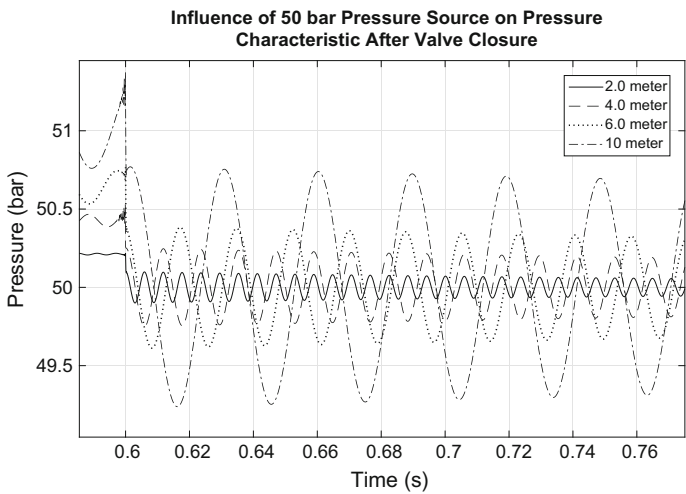


Fig. 7 Pressure behaviour for 50.0 bar pressure sources after valve closure operation

3.2 High Pressure (50 Bar)

In Fig. 6, the graph result show that the unsteady water wave or water hammer suddenly occurs at 0.558 s after the pump start before the valve is close. The sudden effect of water hammer occurs in all 4-tested pipeline length as shown. Figure 7 show the influence of length at 50.0 bar pressure sources to the system. The pressure characteristic as shown in the figure higher than using 1.0 bar as the

pressure source. The maximum pressure P_{max} is 51.231 bar at length 10.0 m at 0.60 s during valve closure operation. The unsteady state or known as water hammer occurs continuously with very low decreasing of the amplitude until the valve is open again. For length 2.0 m with same pressure, maximum pressure P_{max} is only 0.4% higher than pressure source that only 50.208 bar and the unsteady state occurs continuously until valve open.

4 Conclusion

This paper has successfully demonstrated the behaviour and characteristic of the water pressure under various length. It is concluded that each 2.0 m extension of pipeline will increase the maximum pressure head to 2.9–4.5% for each 2.0 m length increasing when pressure is at 1.0 bar. During high pressure source of 50.0 bar, the pressure head during valve closure increasing only increased 0.1–1.0% for each addition of 2.0 m length. From the graph, water hammer is critical when using high pressure source in long pipeline. The best water hydraulic circuit system should be fabricated with shorted line possible, and by using pressure diffuser or absorber to reduce the water hammer phenomena from occurring.

Acknowledgements This work was funded by Ministry of Higher Education (MOHE) of Malaysia, under the Fundamental Research Grant Scheme (FRGS). **FRGS/1/2016/TK03/FKM-CARE-F00317**. The authors wish to thank Ministry of Higher Education and Universiti Teknikal Malaysia Melaka for their support.

References

1. Yusof, A.A., Wasbari, F., Ibrahim, M.Q.: Research development of energy efficient water hydraulics manipulator for underwater application. *Appl. Mech. Mater.* **393**, 723–728 (2013)
2. Systems, F.C. Improvement of Energy and Control Performance in Water Hydraulic Transmissions by PHAM, Ngoc Pha (2014)
3. Hitchcox, A.: *Water Hydraulics: Benefits and Limitations*, 1 Jan (2012)
4. Yusof, A.A., Zaili, Z.S., Hassan, S.N., Tuan, T.B., Saadun, M.N., Ibrahim, M.Q: Promoting water hydraulics in Malaysia: a green educational approach (2014)
5. Krutz, G., Chua, P.: *Water hydraulics—theory and applications 2004*. Workshop on Water Hydraulics (2004)
6. Koskinen, K.T., Leino, T., Riipinen, H.: Sustainable Development with Water Hydraulics—Possibilities and Challenges. *Toyama, s.n.*, pp. 11–18 (2008)
7. Wachter, W., Trimmel, G., Buchner, R., Glatter, O.: Dynamics of water confined in self-assembled monoglyceride–water–oil phases. *Soft Matter* **7**(4), 1409 (2011)
8. Tijsseling, A.S., Anderson, A.: The Joukowski equation for fluids and solids, pp. 1–11 (n.d.)
9. Elbashir, M.A.M., Oduro, S., Amoah, K.: Using Computer Model to Calculate and Simulate Transient Master Thesis Mosab A. Magzoub Elbashir (Jan 2007)

An Enhancement in Control Laws of Super Twisting Sliding Mode Servo Drive Controller Using Hyperbolic Tangent Function and Arc Tangent Smoothing Function



Zamberi Jamaludin, Tsung Heng Chiew, A. Y. Bani Hashim, Lokman Abdullah and N. A. Rafan

Abstract Super Twisting Sliding Mode (ST-SMC) controller belongs to a class of controller known as Sliding Mode Control (SMC). SMC is widely known as a robust controller and has been shown in literature to be an effective medium for excellent control performance especially regarding disturbance force rejection. However, the control performance of SMC is often affected by chattering phenomenon thus reducing the applicability of SMC as position controller of choice in machine tools application where chattering induced vibration cannot be tolerated. ST-SMC is constituted as a higher order SMC. This paper explores control performances of ST-SMC in term of chattering reduction by introducing two types of switching functions in the control laws of the controller; namely, a hyperbolic tangent function (HST-SMC) and an arc tangent function (Arc-ST-SMC). The control performances are analysed based on reduction in magnitude of the tracking error (RMSE) and reduction in magnitude component of the chattering elements observed in frequency domain. The optimized ST-SMC produced the best tracking performance but chattering effect is still persistent. In comparison, HST-SMC produced a comparable tracking performance to ST-SMC with minimal difference of only 12.5% (RMSE). HST-SMC offers a fair trade-off between tracking accuracy and chattering attenuation. On the other hand, arc-ST-SMC produced the most reduction in chattering.

Keywords Sliding mode controller (SMC) • Chattering • Disturbance rejection

Z. Jamaludin (✉) · T. H. Chiew · A. Y. Bani Hashim · L. Abdullah · N. A. Rafan
Fakulti Kejuruteraan Pembuatan, Universiti Teknikal Malaysia Melaka, Hang Tuah Jaya,
Durian Tunggal, 76100 Durian Tunggal, Melaka, Malaysia
e-mail: zamberi@utem.edu.my

© Springer Nature Singapore Pte Ltd. 2018
M. H. A. Hassan (ed.), *Intelligent Manufacturing & Mechatronics*,
Lecture Notes in Mechanical Engineering,
https://doi.org/10.1007/978-981-10-8788-2_63

1 Introduction

In mechatronics system, the accuracy and precision of motions that are generated depend highly on the effectiveness of the servo drives system applied. In turn, the effectiveness of the servo drives system is characterized by the type of motion controllers that were designed and applied. In machine positioning system, especially that applied in manufacturing of parts and products, the ability of these controllers to perform at the highest possible standard in challenging environment is desired. Motion controllers of the various parts and components of the machine mechatronics elements must be able to sustain input disturbance and varying load conditions to produce motions that are accurate (lowest possible tracking error) and vibration-free. Therefore, various control techniques have been proposed, applied, and validated in literatures with varying degree of success.

Most machine tools applied classical control techniques for the simple structures and ease of tuning. Furthermore, it is more practical to apply classical control strategies as typical users with basic knowledge in control theory are able to operate and troubleshoots the machines with limited problems and difficulties. PID and cascade controllers [1] are two most common classical control strategies applied as servo drive controllers. However the success and effective applications of these classical controllers are limited. For this reason, many advanced control strategies have been developed where high robustness and disturbance rejection are desired even though the design process are sometimes challenging. Their remarkable performance on robustness and disturbance rejection serves as good motivation to the many researchers.

SMC is an advanced controller known for its robustness and disturbance rejection properties [2]. SMC maintains its performance even in the presence of disturbances or uncertainties [3]. SMC algorithm was first introduced and popularized by [4] and it created strong interest on many researchers and engineers due to its remarkable performances and suitability for real-time systems that are normally nonlinear in nature. Second order sliding mode controller (SOSMC) is an extension of traditional SMC as stated in [5]. The popularity arises from its chattering attenuation properties while inheriting the traditional advantages of SMC. Even though SOSMC was claimed to be chattering free by [6], this issue is still a debatable discussion as stated in a recent publication by [7]. There exist three popular types of SOSMC, namely; twisting (TA), super twisting (ST) and sub-optimal algorithms (SOA). The advantages of ST-SMC in terms of robustness, chattering attenuation, and disturbance rejection have been presented and documented numerically in [8, 9].

This paper presents design of ST-SMC for application on a single axis directly driven servo drive system. A novel approach using one at a time a hyperbolic function (ST-SMC) and an arc tangent function (Arc-ST-SMC) as the switching function in ST-SMC is proposed. Next, the system setup is introduced followed by introduction to the controller design, experimental validation, discussion and conclusions on the main findings.

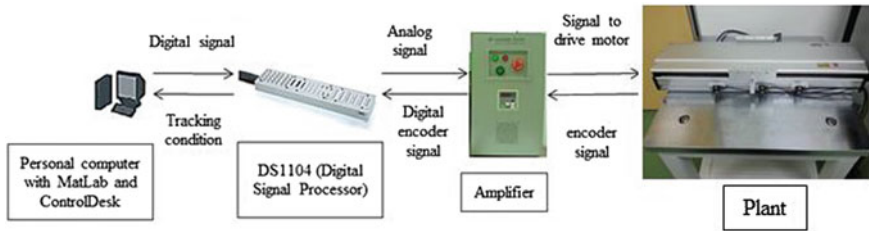


Fig. 1 Overall schematic representation of the experimental test setup

2 System Setup

This section introduces through Fig. 1 the test setup that consists of a single axis direct driven servo motor system. The dynamics of the system is described as a single-output-single-input (SISO) model using frequency domain identification method. The frequency response function (FRF) was estimated based on the measured input voltage and output position using band-limited white noise excitation signal and an H1 estimator [10] at sampling frequency of 5000 Hz. The system transfer function, based on a parametric model fitted on the measured FRF is described in Eq. (1).

$$\frac{Z(s)}{U(s)} = \frac{7.510 \times 10^8}{s^2 + 3622s} e^{-0.00045s} \tag{1}$$

$Z(s)$ and $U(s)$ represent the actual output position in micrometer and input voltage in volt, respectively. A dSPACE DS1104 control board is applied as the data acquisition unit (DAQ) that interfaced the host computer and the single axis positioning system through the servo amplifier. The DAQ supports the analog and digital signals conversion while the host computer is for command control and real-time data monitoring. A personal computer, equipped with MATLAB/SIMULINK and ControlDesk software connects the DSP board and applies the controller design and manages the data communication and collection.

3 Controller Design

Three variants of ST-SMC controller were designed. The three design variations are: (i) classical ST-SMC with optimally design parameters, (ii) ST-SMC with hyperbolic switching function (HT-STC), and (iii) ST-SMC with an arc tangent smoothing function (Arc-ST-SMC).

3.1 ST-SMC

The controller consists of two main components, namely the switching function, $s(t)$, and the control laws [11]. Equations (2) and (3) show the general formula for a typical sliding surface that relates the tracking error, $e(t)$ and first-time derivative of tracking error, $\dot{e}(t)$ with a positive constant, λ and n that represents the order of the uncontrolled system.

$$s(t) = \left(\lambda + \frac{d}{dt} \right)^{-1} \cdot e(t) \tag{2}$$

$$e(t) = y(t) - r(t) \tag{3}$$

The control laws of ST-SMC consist of three parts, namely; (i) equivalent control, (ii) the continuous state function, and (iii) the discontinuous input with integrator. These are shown in Eqs. (4) and (5).

$$u(t) = u_{eq} - L|s(t)|^{0.5} \text{sign}(s(t)) + u_1 t \tag{4}$$

$$\dot{u}_1(t) = -W \cdot \text{sign}(s(t)) \tag{5}$$

L and W are positive gains [12]. The equivalent control, u_{eq} is obtained when $\dot{s}(t) = 0$. The control block diagram of ST-SMC is shown in the following Fig. 2.

3.2 HT-SMC

A hyperbolic tangent function was considered as replacement for the signum function in the previous control law design of ST-SMC. The hyperbolic tangent function has a characteristic that is very similar to the signum function but with smoother transition at near zero regions of s -functions. Equations (4) and (5) were modified with the signum function replaced by the hyperbolic tangent function:

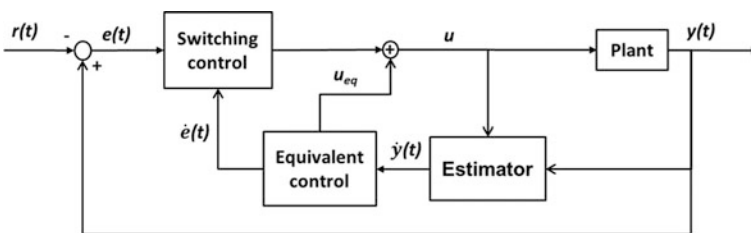


Fig. 2 General block diagram of ST-SMC controller

$$u(t) = u_{eq}(t) - L|s(t)|^{0.5} \cdot \tanh(s(t)) - W \cdot \int \tanh(s(t)) \quad (6)$$

3.3 Arc-ST-SMC

Similar to HT-SMC design, here, an arc-tangent function replaces the signum function in the control laws of ST-SMC. This modification is inspired from the works of [13, 14] in friction forces modeling where the arc-tangent smoothing function was proposed and validated numerically and experimentally to smoothen the transition during pre-sliding and sliding regimes in friction near zero velocity region. Equations (4) and (5) were modified with the signum function replaced by the arc tangent function:

$$u(t) = u_{eq}(t) - L|s(t)|^{0.5} \cdot \frac{a \tan(s(t))}{(0.5 + \pi)} - W \cdot \int \frac{a \tan(s(t))}{(0.5 + \pi)} \quad (7)$$

4 Result and Discussion

Control performances of the three variants of ST-SMC controllers were validated on the test setup. The control performances were compared on the basis of tracking error, and chattering reduction. The performance index related to the tracking error is the maximum tracking error, and the root mean square value of the tracking error (RMSE). The respective control command input signals were measured, analyzed, and evaluated in order to investigate the degree of chattering associated with each controller as sliding mode controller is well known for its chattering effect. Spectrum analyses using method of Fast Fourier Transform (FFT) were performed on the control command input signals in order to produce clear indication on the magnitudes of chattering at respective chattering frequencies.

4.1 Maximum Tracking Errors

For the validation, the system was excited with sinusoidal input reference signals of amplitude 20 mm and frequencies of 0.5 Hz. Figure 3 shows the measured tracking errors of the three controllers. Table 1 summarizes the maximum tracking errors and the RMSE values of the three different control strategies.

The ST-SMC controller produced the smallest tracking error compared to other SMC-based controllers; with largest tracking error observed in the case of Arc-ST-SMC.

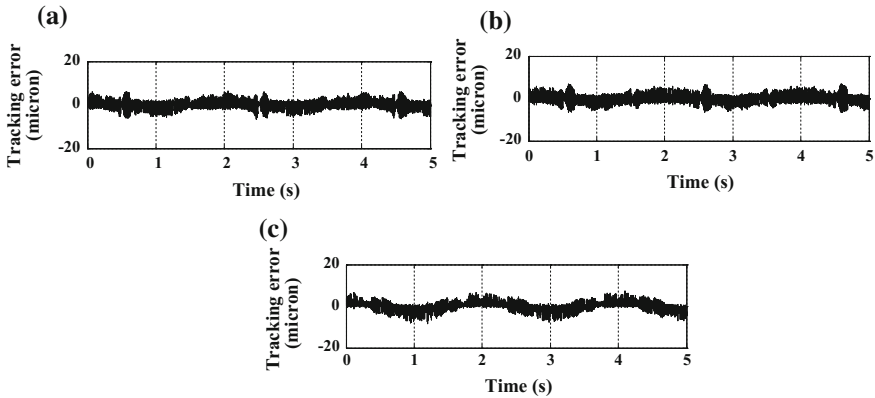


Fig. 3 Measured tracking errors of **a** ST-SMC, **b** HST-SMC, and **c** Arc-ST-SMC

Table 1 Maximum tracking errors and RMSE values of five different controllers for input reference signal of 20 mm amplitude and 0.5 Hz frequency

Controllers	Maximum tracking error (μm)	RMSE (μm)
ST-SMC	6.00	2.00
HST-SMC	6.75	2.19
Arc-ST-SMC	7.30	2.25

4.2 Chattering Effect

Control command input signal refers to voltage generated by the controller to the direct linear drive system in order to compensate for the tracking errors. Analyses of the control command input signals then identified the degree of chattering imposed on the system from the application of the controllers. Figure 4 displays the control command input signals related to input reference amplitude of 20 mm and 0.5 Hz measured using ST-SMC, HST-SMC, and Arc-ST-SMC.

Based on Fig. 4, noises were observed (red rectangular) in each the control command input signals. The presence of noise in these measurements suggests chattering [15]. The presence of noise was significantly obvious in regions corresponding to zero velocity motions. The most reduced effect of noise was observed for Arc-ST-SMC. Effect of chattering could be analyzed quantitatively using frequency domain approach. Figure 5 presents results of Fast Fourier Transform (FFT) performed on the control command input signals of ST-SMC, HST-SMC, and Arc-ST-SMC. Two significant peaks were observed at frequencies of 1000 and 2000 Hz. The presence of peaks at high frequencies confirmed the findings by [8] who stated that chattering is the product of high frequency switching. Therefore, it is concluded that reduction in amplitude of the FFT value at these high frequencies represents attenuation of chattering itself. Results showed that the most significant reduction in amplitude of the FFT peak values was recorded in the case of Arc-ST-SMC. The peak amplitudes were reduced by as much as 39.7% and 71.3%

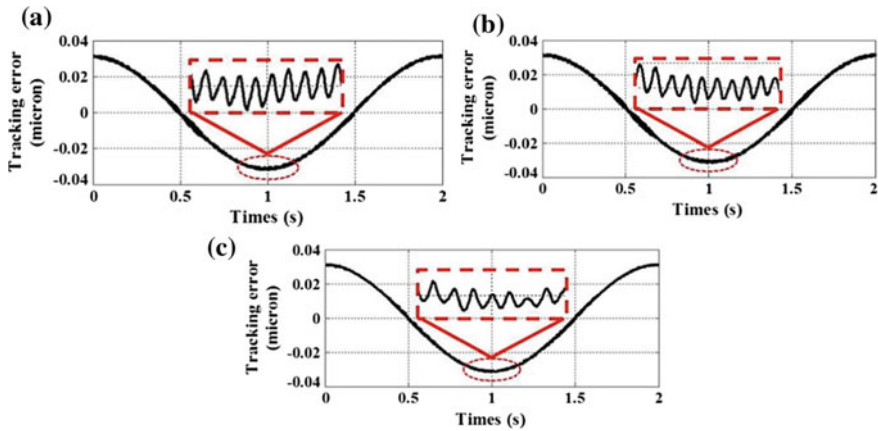


Fig. 4 Control command input signals of a ST-SMC, b HST-SMC, and c Arc-ST-SMC

at 1000 Hz and 2000 Hz frequencies respectively. As for HST-SMC, the peak amplitude reductions observed was only 0.5% and 26.8% at the respective frequencies.

Replacement of the signum function by the hyperbolic function and arc-tangent function was able to reduce chattering to some extent as the two functions smoothen the transition effect at near zero regions. However, the effect of hyperbolic function in chattering reduction was only moderate when compared to the arc-tangent function. The arc-tangent function managed to reduce chattering by a factor of two in comparison to the hyperbolic function.

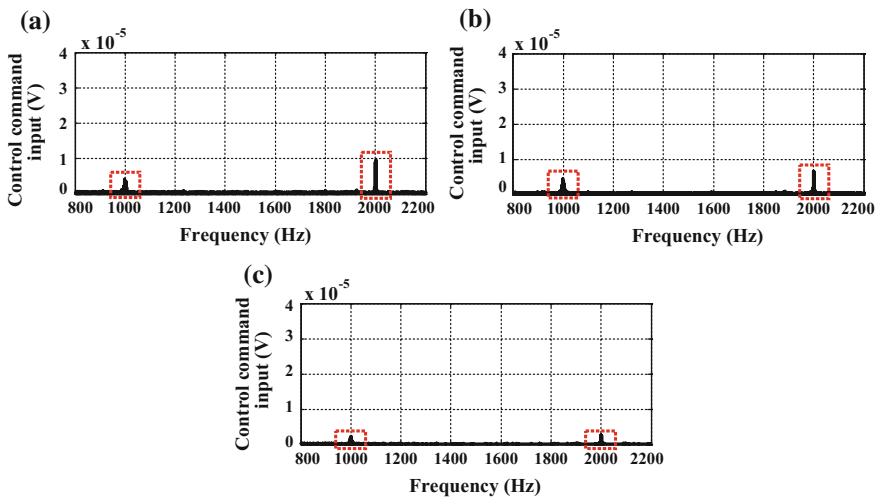


Fig. 5 FFTs of control command input signals at high frequency regions for a ST-SMC, b HST-SMC, and c Arc-ST-SMC

5 Conclusions

As conclusion, this paper has presented results on control performances of Super Twisting Sliding Mode Controller (ST-SMC) whereby the control laws of the controller were enhanced using a hyperbolic tangent function (ST-SMC) and an arc tangent smoothing function (Arc-ST-SMC). The objective was to analyse the effect of this novel addition to the control laws with respect to the degree of chattering that most often associated with application of sliding mode controllers. In addition, the tracking performance of the two variants of ST-SMC were also studied and analysed. Results presented showed the advantage of Arc-ST-SMC in dampening the effect of chattering. In term of tracking error, both the optimally design ST-SMC and HT-ST-SMC performed comparably and superior than the ARC-ST-SMC controller. Hence, the compromise has to be made between requirements for precise tracking performance and reduction in machine vibration through dampening effect of chattering.

Acknowledgements The authors would like to thank the Ministry of Higher Education for the funding of this research with the reference number FRGS/1/2015/TK03/FKP/02/F00281 and the Faculty of Manufacturing Engineering, Universiti Teknikal Malaysia Melaka for the facilities provided.

References

1. Abdullah, L., Jamaludin, Z., Qumrul, A., Rafan, N.A., Yusof, M., Jamaludin, J., Chiew, T.H.: Evaluation on tracking performance of PID, gain scheduling and classical cascade P/PI controller on XY table ball screw drive system. *World Appl. Sci. J.* **21**(1), 1–10 (2013)
2. Utkin, V., Guldner, J., Shi, J.: *Sliding Mode Control In Electro-Mechanical Systems*, vol. 34. CRC Press (2009)
3. Young, K.D., Utkin, V.I., Özgüner, Ü.: A control engineer's guide to sliding mode control. *IEEE Trans. Control Syst. Technol.* **7**(3), 328–342 (1999)
4. Utkin, V.: Variable structure systems with sliding modes. *IEEE Trans. Autom. Control* **22**(2), 212–222 (1977)
5. Fridman, L., Moreno, J., Iriarte, R.: *Sliding Modes After the First Decade of the 21st Century: State of the Art*. Springer, Berlin (2011)
6. Levant, A.: Sliding order and sliding accuracy in sliding mode control. *Int. J. Control* **58**(6), 1247–1263 (1993)
7. Utkin, V.: Discussion aspects of high-order sliding mode control. *IEEE Trans. Autom. Control* **61**(3), 829–833 (2016)
8. Utkin, V.: On convergence time and disturbance rejection of super-twisting control. *IEEE Trans. Autom. Control* **58**(8), 2013–2017 (2013)
9. Rafiq, M., Rehman, S., Rehman, F., Butt, R.Q., Awan, I.: A second order sliding mode control design of a switched reluctance motor using super twisting algorithm. *Simul. Model. Pract. Theory* **25**, 106–117 (2012)
10. Pintelon, R., Schoukens, J.: *System Identification: A Frequency Domain Approach*. Wiley (2012)

11. Chalanga, A., Kamal, S., Fridman, L., Bandyopadhyay, B., Moreno, J.A.: Implementation of super-twisting control: super-twisting and higher order sliding-mode observer-based approaches. *IEEE Trans. Industr. Electron.* **63**(6), 3677–3685 (2016)
12. Chiew, T.H., Jamaludin, Z., Bani Hashim, A.Y., Abdullah, L., Rafan, N.A.: Design of super twisting algorithm for chattering suppression in machine tools. *Int. J. Control Autom. Syst.* **15** (3), 1259–1266 (2017)
13. Piatkowski, T.: GMS friction model approximation. *Mech. Mach. Theory* **75**, 1–11 (2014)
14. Rafan, N.A.: Stick slip friction models control system design approach for friction compensation in machine tools application. Ph.D. Dissertation, Universiti Teknikal Malaysia Melaka, Malaysia (2017)
15. Fossard, A.J., Floquet, T.: An overview of classical sliding mode control. *Sliding Mode Control in Engineering*, pp. 20–46. Marcel Dekker Inc., New York (2002)

Finite Element Analysis of Strand Burner



M. Hafizi, M. M. Noor, R. Mamat, A. Aziz and A. T. Termizi

Abstract The burning rate is a crucial element in the performance of a solid propellant rocket. Strand burner is a device used to measure the propellant burning rate at elevated pressure. Solidworks Simulation is one of the software that is capable of performing finite element analysis that widely used to estimate the mechanical behavior of materials and structures in engineering applications. The objective of this paper is to analyze stresses in developing safe strand burner by using Solidworks Simulation. The strand burner is designed and analyzed using Solidworks 2016 software. Solid standard mesh meshing element is selected for purpose. The withstand loads and stresses on strand burner physically structure is measured by both simulation analysis and hand calculation. The result show the safety factor on developing strand burner is obtained by both method is 2.31. Based on safety factor generated, the strand burner can be test until 60.61 bars (6.061 MPa). In conclusion, the burning test inside the strand burner chamber can be test up to 126 bars. The design is safe for operating conditions.

Keywords Strand burner · Solid propellant · Finite element analysis

1 Introduction

The composite solid rocket propellant is kind of propulsion that usually used as booster for launch vehicles for sending satellite to the outer space [1]. Solid propellant also widely used in a military tactical operation and strategic missiles [2]. The burning rate data plays a vital role in order to build a solid propellant rocket successfully which influenced the ballistic behaviour of a composite solid propellant [3]. The basic combustion processes within a composite solid propellant

M. Hafizi · M. M. Noor (✉) · R. Mamat · A. Aziz · A. T. Termizi
Faculty of Mechanical Engineering, Universiti Malaysia Pahang, Pekan, Malaysia
e-mail: muhamad@ump.edu.my

M. Hafizi
e-mail: hafiziaero@yahoo.com

are much complex and cannot fully understood [4–6]. Several mathematical models have been developed to study the burning behavior of solid propellant at complexity level [7]. The burning rate is defined as the linear rate of regression of the propellant which in parallel layers, in a direction perpendicular to the surface itself [8] as shown in (1). There are various method in determining burning rate reported by Gupta [9]. Strand burner is an apparatus used to measure the solid propellant burning rate at elevated pressure in a closed system which is very quick, simple, and economic compared to subscale and full scale motor [10]. Strand burner method is suitable to explore new propellant compositions to determine characterization of a composite solid propellant over a defined pressure and temperature range, or performing quality control of established compositions. This method can determine burning behaviour at defined pressure range inside the chamber by using Vieille's law expressed by St. Robert [11] as shown (2).

$$r = \frac{\text{Length of propellant strand to be test, } L}{\text{Burning duration, } t} \quad (1)$$

$$r = a \cdot P^n \quad (2)$$

where: r is the burning rate; n is the pressure exponent; P is the pressure; a is dimensionless empirical constant.

The values of a and n are determined experimentally for each propellant formulation at least five tests using propellant strands at constant pressure and the burning test has to be performed at minimum three different pressures. Value of a is influenced by ambient grain temperature while value of n influence the chamber pressure on the burning rate. The operation is said to be stable if the value of n is in the range from 0 to 1. A rapid change of burning rate by pressure may occur due to high values of n . The propellant sample being tested, is referred as a strand which takes the form of a pencil-like stick [12]. The strand burner commonly mounts the strand either horizontally [13, 14] or vertically [15–17] and connected with ignition system and data collection system. Inert gases such as helium, carbon dioxide, argon or nitrogen were used to pressurize the strand burner. Crawford [18] mentioned in an earlier test that there was not much difference in the burning rate when applying those gases. Ni-chrome wire was used as the ignition wire by Nelson and other researches [19–24] in their study while Kirk et al. used 30 S.W.G tin/lead (63/37) for the timing wire [25]. The duration for the strand to burn along its length (cigarette fashion) was measured. The length of the strand is important parameter compared to the size and shape which is less significant to measure propellant burning rate [26, 27]. Mathew [28] reported that the size would not affect burning rate so much except for the smallest size tested, which is 3.2 mm. Nelson et al. [19] used strands that have a circular cross sectional area in their research compared to other researchers who preferred to use the square shape [29, 30].

The effects of loads on physical structures of strand burner is determined by structural analysis. The method that widely used to estimate the mechanical behaviours of materials and structures in engineering applications is by using finite

element method (FEM) [31]. Solid work Simulation is the software that capable to do FEM. The software enables to scrutinize stress on the strand burner. Therefore, this paper strives to analyze stresses on the developing strand burner. The meshing element used was solid standard mesh meshing element that simply selected with the element size is 16.80484 mm and tolerance 0.8402422 mm. The stresses were compared and analyze based on simulation and hand calculation.

2 Design of the Strand Burner

Strand burner is designed and analyzed. The entire strand burner parts including main body and end caps were made by AISI 316 stainless steel. AISI 316 stainless steel has mass density of 8000 kg/m^3 and thermal expansion coefficient of $1.6 \times 10^{-5}/\text{K}$. The yield strength, tensile strength and elastic modulus for AISI 316 stainless steel are 290 MPa, 580 MPa and 1.93×10^5 MPa respectively. The Poisson's ratio for AISI 316 stainless steel is 0.27. The shape of strand burner is designed similar to horizontal pressure vessel developed by previous research [14, 32]. The materials used for each part of the strand burner is tabulated in Table 1.

Figure 1 shows schematic diagram of test system including strand burner assembly and strand holder. The length of cylinder body (main part) acted as combustion chamber was 304.80 mm (12.00 in) while the outer diameter was 152.40 mm (6.00 in) and the inner diameter was 93.98 mm (3.70 in). The internal 4.0–4 UNC with 5.08 mm (2.00 in) deep on each extremity were made at the both sides of the main body to accept end-caps. All strand burner dimension was tabulated in Table 2. Both ends of the cylinder body were two hexagonal. The ends name as forward end cap and aft end cap respectively, were diametrically opposed with the same dimension that was 9.50 mm (0.375 in). The forward end cap had hole to flow in the gas where the exhaust gases flow out from the cylinder through the aft end cap. The thread design inside the end caps provided strength, and enable quick assembly and disassembly. The strand holder was put like a plug at the middle of forward end cap. Window end cap was positioned above the main body and served to investigate the flame condition when the strand is burnt inside the burner. The strand burner was clamped to the table by using two aluminums made stand.

Table 1 Material for each part of the strand burner

Strand burner part	Material
Cylinder body (main part)	AISI 316 stainless steel
Aft end cap	AISI 316 stainless steel
Forward end cap	AISI 316 stainless steel
Window end cap	AISI 316 stainless steel
Strand holder	AISI 316 stainless steel
Stand	Aluminum

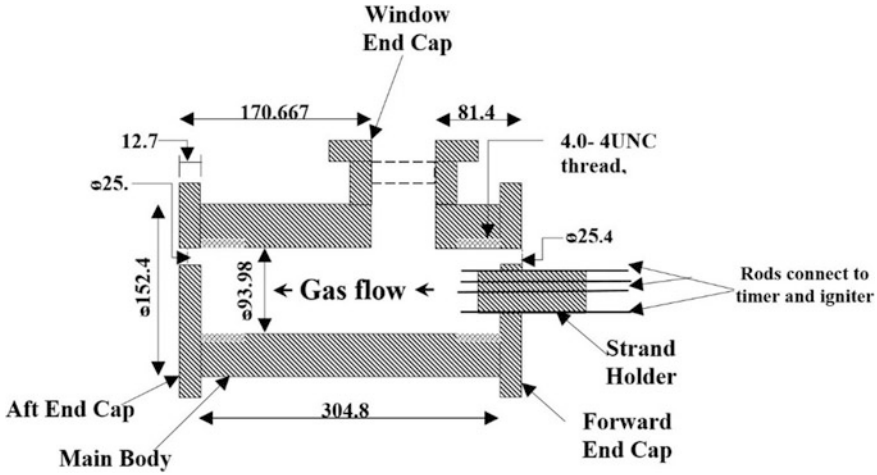


Fig. 1 Test system design including strand burner assembly and strand holder in mm

Table 2 Major dimension of strand burner

Dimension	Millimeter (mm)	Inches (in.)
Inner diameter	93.98	3.70
Outer diameter	152.40	6.00
Wall thickness	29.21	1.15
Outer length	304.80	12.00
Inner length	165.10	6.50
Maximum width	248.92	9.80
Volume	0.001258 m ³	76.76 in. ³
No of end caps	3	

The most common application of the finite element method is structural analysis [33]. Structural analysis of strand burner was performed by using a simulation module from commercial software. Thus, the maximum stress and strand burner safety factor can be determined. The analysis type for the simulation was static analysis. The gas flow in strand burner through forward end cap is set as pressure-inlet while the gas flow out the strand burner through aft end cap is set as pressure outlet. The solver used in the calculation was FFE plus. Zero strain temperature is set as 298 K where thermal effect is on and temperature loads is included. The load is set to 14 MPa (140 bar) that normal to face of the stand burner.

The meshing was conducted with the solid standard mesh meshing element which is shown in Fig. 2. The mesh have four Jacobian points. The mesh element size selected is 16.80484 mm with tolerance 0.8402422 mm. The mesh quality is high consisted the total nodes of 20415 and the total mesh elements about 12262. The maximum aspect ratio recorded was 12.664. The elements recorded for aspect

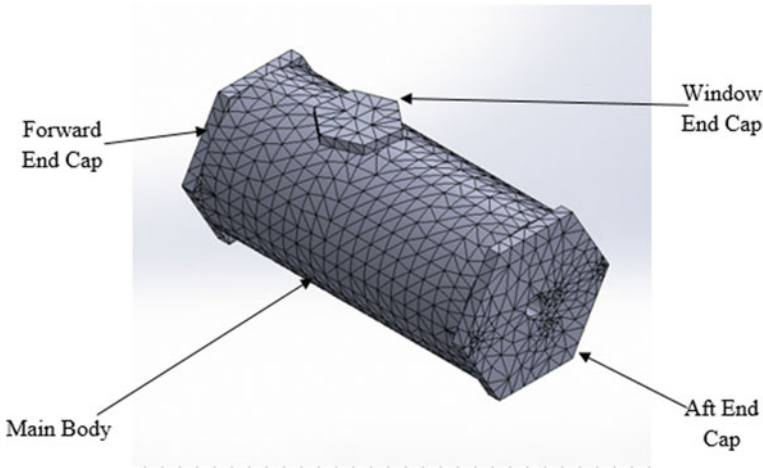


Fig. 2 Standard solid mesh of the strand burner

ratio lower than 3 were 84.5% while 0.4% elements were recorded for aspect ratio greater than 10. From the meshing, there are no distorted elements. Complete meshing all elements take 4 s. The strand burner was clamped to the table by using two aluminums made stand.

3 Structural Analysis on the Strand Burner

Stress distribution for the whole part of the strand burner is shown in Fig. 3 while the strand burner safety factor generated is shown in Fig. 4 by Solidworks software. The stress distributed in the range between minimum stress 0.03223 MPa (0.3223 bar) to maximum stress 74.63050 MPa (746.305 bar). The yield strength of the strand burner is 172.4 MPa (1724 bar). The minimum safety factor was 2.30963 and the maximum was 5347.68.

The safety factor of the strand burner is 2.31. The safety factor is acceptable when comparing to aerospace standard factor of safety of 1.5 for ultimate strength and 1.15 on the yield strength [34]. The stress is concentrated most at the middle part of the strand burner and at the strand burner end cap where the structure supporting internal pressure load from gas pressure flow in and out and generated gas pressure from combustion.

The testing or operating pressure should be lower 10% than the design pressure or even lesser for safety purpose [35, 36]. Bandarupalli [37] using 1.3 times design pressure to obtain hydrostatic test pressure in his research. The safety factor play vital roles on how much stronger the strand burner to withstand with the load or operating pressure. The highest operating pressure or testing pressure for the strand burner is obtained by dividing the design pressure with 2.31.

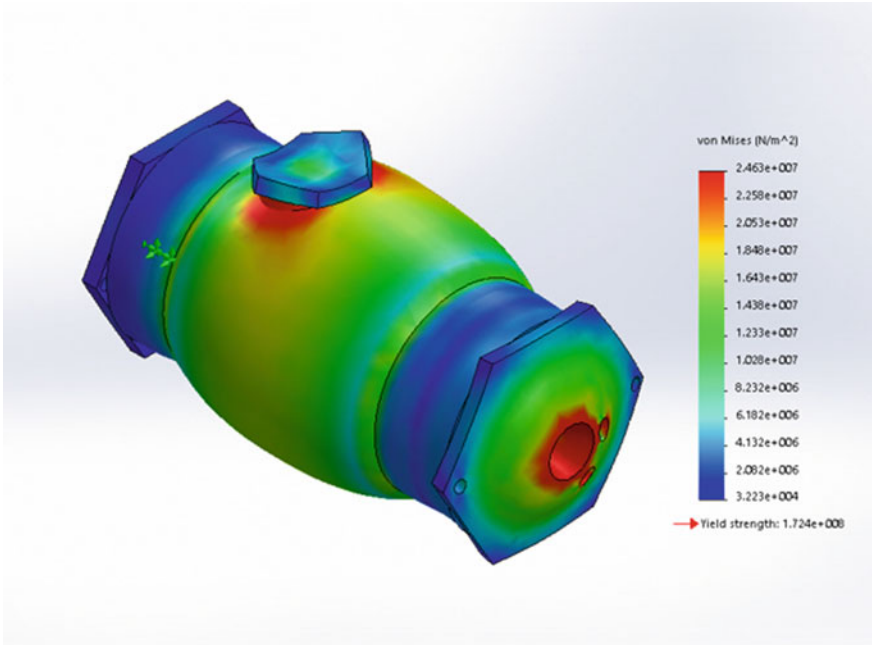


Fig. 3 Stress distribution of strand burner

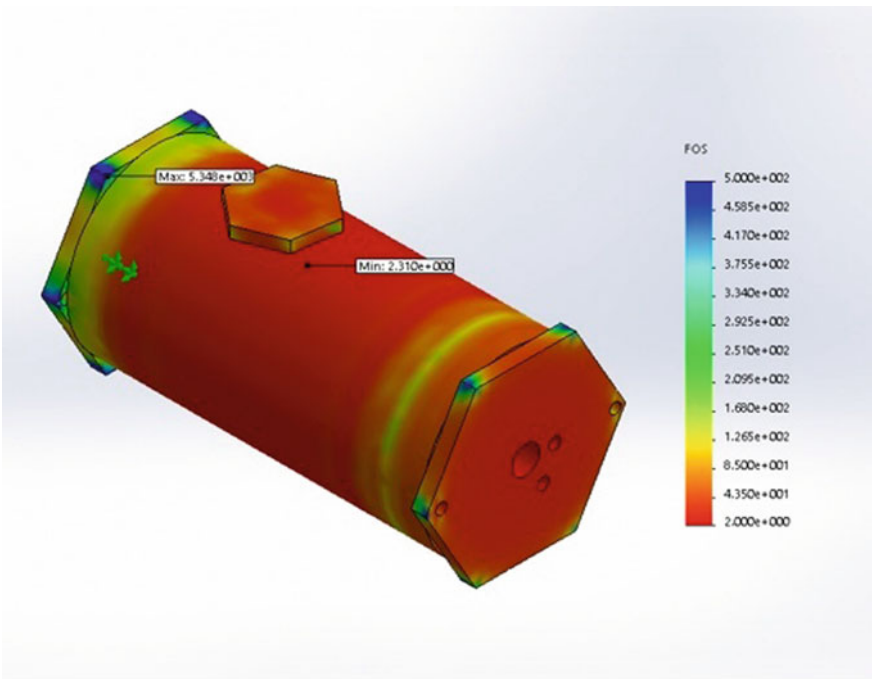


Fig. 4 Strand burner safety factor

Operating pressure (10% lower than design pressure),

$$\begin{aligned} P_O &= 140 - 0.1(140) \\ &= 126 \text{ bars} \end{aligned} \quad (3)$$

Operating pressure based on safety factor generated,

$$\begin{aligned} P_O &= \frac{140}{2.31} \text{ bars} \\ &= 60.67 \text{ bars} \end{aligned} \quad (4)$$

Thus, the strand burner can be tested until 60 bars according to safety factor which is 57% lower than the design pressure. The maximum test pressure must not exceed 126 bars with safety factor 1.11. Margin of safety for both conditions are calculated (5), (6).

$$\begin{aligned} \text{Margin of safety}_{10\% \text{ lower}} &= \text{Safety factor}_{10\% \text{ lower}} - 1 \\ &= 1.11 - 1 \\ &= 0.11 \end{aligned} \quad (5)$$

$$\begin{aligned} \text{Margin of safety}_{\text{simulation}} &= \text{Safety factor}_{\text{simulation}} - 1 \\ &= 2.31 - 1 \\ &= 1.31 \end{aligned} \quad (6)$$

Margin of safety is lie on the range 0.11–1.31 which are greater than 0. Thus, design requirement had been met. The maximum pressure developed in the vessel can be calculated (7) by using maximum stress generated based on simulation which is 746.305 bar (74.6305 MPa).

$$t = R_i \left[\sqrt{\frac{SJ + P}{SJ - P}} - 1 \right] \quad (7)$$

where,

t Wall thickness

R_i Inner radius

J Joint efficiency = 1

Thus, the maximum pressure, $P_{max} = 335.078$ bar. The strand burner which operated 126 bar will lower 37.5% than the maximum allowable pressure. The stress developed (280.63 bar) is less than maximum stress value (746.305 bar).

Hydrostatic pressure is 1.3 times design pressure.

$$\begin{aligned}
 P_H &= 1.3 \times \text{Design pressure} \\
 &= 1.3 \times 140 \\
 &= 182 \text{ bars}
 \end{aligned}
 \tag{8}$$

The bursting pressure is calculated by using Lamé's method Ultimate tensile strength of material = 580 MPa (5800 bars).

$$\begin{aligned}
 K &= \frac{\text{Outer diameter}}{\text{Inner diameter}} \\
 &= \frac{152.4}{93.98} \\
 &= 1.622
 \end{aligned}
 \tag{9}$$

$$\begin{aligned}
 P_B &= U.T.S \times \frac{K^2 - 1}{K^2 + 1} \\
 &= 2605.185 \text{ bars}
 \end{aligned}
 \tag{10}$$

Stress developed during bursting test as,

$$\begin{aligned}
 S_B &= \frac{P_B R_i + 0.2 P_B t}{2t} \\
 &= \frac{2605.185(46.99) + 0.2(2605.185)(29.21)}{2(29.21)} \\
 &= 2355.993 \text{ bars}
 \end{aligned}
 \tag{11}$$

Stress developed (2355.993 bars) is less than yield stress of material (allowable stress) which is 2900 bar (290 MPa). Thus, design is safe.

4 Conclusion

The value of empirical constant, a and pressure exponent, n were important values which determine the burning performance of solid propellant. The strand burner is functioned to study new propellant composition that give quickly and simply value of empirical constant and pressure exponent. The strand burner was designed and analyzed using commercial Solidworks software. The design pressure was set to 140 bars (14 MPa). Safety factor generated from simulation was 2.31 which is good enough for the strand burner design. The burning test inside the strand burner chamber can be done safely until 126 bars which is 10% lower than design pressure. The operating pressure can also be done until 60.67 bars (6.067 MPa) to maintain the safety factor generated from analysis. However both operating pressure values

were accepted as the margin of safety lie in the range 0.11–1.31 that higher than zero which mean the design safety requirement was met.

The hydrostatic pressure calculated was 182 bars (18.2 MPa). The strand burner can be withstand until 2605.185 bars before it burst. The stress developed during burst was 2355.993 bars which is much lower than the strand burner yield stress of stainless steel AISI 316 material. The result show that the developing strand burner is designed much lower than allowable load. Thus, the design was safe to use for operating conditions.

Acknowledgements The financial and laboratory support by University Malaysia Pahang (www.ump.edu.my) to the authors are gratefully acknowledged.

References

1. Fishell, K.R.: Space shuttle solid rocket booster dewatering system. In: AIAA/SAE/ASME 17th Joint Propulsion Conference, Colorado (1982)
2. Biblarz, O., Sutton, G.P.: Rocket Propulsion Elements, 7th edn. Willey, Canada (2001)
3. Sutton, G.P.: Rocket Propulsion Elements. Wiley, New York (1992)
4. Yaman, H., Çelik, V., Deg'irmenci, E.: Experimental investigation of the factors affecting the burning rate of solid rocket propellants. *Fuel* **115** (2014)
5. Davenas, A.: Development of modern solid propellant. *J. Propuls. Power* **19**(6) (2003)
6. Hafizi, M., Mamat, R., Aziz, A., Noor, M.M., Tamimi, A.: Development of strand burner test by using aluminized AP/HTPB. *Mater. Sci. Forum* **880**, 99–104 (2017)
7. Florio, L.A.: Direct particle motion and interaction modeling method applied to simulate propellant burn. *Appl. Math. Model.* **37** (2013)
8. Selected Combustion Problems (1954)
9. Gupta, G., Jawale, L., Mehilal, Battacharya, B.: Various methods for the determination of the burning rates of solid propellants—an overview. *Cent. Eur. J. Energ. Mater.* **12**(3) (2015)
10. Solid Propellant Test Motor Scaling (2001)
11. Gossant, B., Davenas, A.: Solid propellant combustion and internal ballistics of motors. *Solid Rocket Propulsion Technology* (1993)
12. Nakka, R.: Solid propellant rocket motor: design & testing. B.Sc thesis, Faculty of Engineering, University of Manitoba, Canada (1980)
13. Rizalman, M.: Ciri-ciri propelan roket pepejal berasaskan kalium. Master of Engineering, Faculty of Mechanical Engineering, Universiti Teknologi Malaysia, Malaysia (2001)
14. Carro, R.V.: High pressure testing of composite solid rocket propellant mixtures: burner facility characterization. Master of Science, Department of Mechanical Material and Aerospace Engineering, University of Central Florida, USA (2001)
15. Aziz, A.: Combustion characteristics of Ammonium Perchlorate based solid rocket propellant. Master of Science, Universiti Teknologi Malaysia, Malaysia (2011)
16. Kubota: Propellants and Explosive. Willey-VCH Verlag GmbH & Co.KGa.A (2007)
17. Gilbert, P.D.: Multifunctional additives for composite solid propellant. Master of Science, Mechanical Engineering, Purdue University, West Lafayette, Indiana (2008)
18. Crawford, B.L., Huggett, C., Farrington, D., Wilfong, R.E.: Direct determination of burning rates of propellant powders. *Anal. Chem.* **19**(9) (1947)
19. Nelson, D.P., Bresnahan, D.L.: Ejector nozzle test results at simulated flight conditions for an advanced supersonic transport propulsion system. In: 19th Joint Propulsion Conference (1983)

20. Grollman, B.B., Nelson, C.W.: Burning rates of standard army propellants in strand burner and close chamber tests (1977)
21. Kohga, M., Yoshida, S.: Burning rate characteristics of AP-based composite propellant using bimodal AP. In: 42nd AIAA/ASME/SAE/ASEE Joint Propulsion Conference & Exhibit (2006)
22. Cookson, R.A., Fenn, J.B.: Strand size and low-pressure deflagration limit in a composite propellant. *AIAA J* **8**(5) (1969)
23. Description of the W.R.E. Strand Burning Facilities and Instructions for Use (1977)
24. Meda, L., Marra, G., Galfetti, L., Severini, F., Luca, L.D.: Nano-aluminum as energetic material for rocket propellants. *J. Mater. Sci. Eng.* **27** (2007)
25. Kirk, D.R., Creviston, D.O., Waitz, I.A.: Aeroacoustic measurement of transient hot nozzle flows. *J. Propuls. Power* **17**(4) (1990)
26. Carro, R., Stephens, M., Arvanetes, J., Powell, A., Petersen, E., Smith, C.: High-pressure testing of composite solid propellant mixtures: burner facility characterization. In: 41st AIAA/ASME/SAE/ASEE Joint Propulsion Conference & Exhibit, Tucson, Arizona (2005)
27. Steinz, J.A., Stang, P.L., Surmerfield, M.: The burning mechanism of ammonium perchlorate based composite solid propellants. Princeton University, New Jersey (1969)
28. Matthew, S., Radolphe, C., Steven, W., Thomas S.: Performance of AP based composite propellant containing nanoscale of aluminium. In: 41st AIAA/ASME/SAE/ASEE Joint Propulsion Conference & Exhibit (2005)
29. Australian Government: Improved strand burn rate reproducibility using a new preparation methodology for paint-based inhibitors (2003)
30. Kubota, N., Kimura, J.: Oscillatory burning of high pressure exponent double-base propellants. In: AIAA/SAE 12th Propulsion Conference, Palo Alto, California (1976)
31. Reddy, J.N.: An Introduction to the Finite Element Method, 3rd edn. McGrawhill, New York (2005)
32. Bedner, H.H.: Pressure Vessel Design Hand Book. CBS Publisher and Distributors, Delhi, India (1980)
33. Kumawat, M.S., Kalurkar, L.G.: Analysis and design of multistory building using composite structure. *J. Struct. Civil Eng.* **3**(2) (2014)
34. Cowless, D.K.: Design of a tomahawk cruise missile booster rocket motor. Master of Engineering, Rensselaer Polytechnic Institute, Hartford, Connecticut (2012)
35. Pendbhaje, A.R., Gaikwad M., Deskhmukh, N., Patil, R.: Design and analysis of pressure vessel. *Int. J. Innovative Res. Technol. Sci.* **2**(3) (2013)
36. Thakkar, B.S.: Design of pressure vessel using ASME code. *Int. J. Adv. Eng. Res. Stud.* **1**(2) (2012)
37. Praneeth, B., Rao, T.B.S.: Finite element analysis of pressure vessel and piping design. *Int. J. Eng. Trends Technol.* **3**(5) (2012)

High Precision Estimation on Physical Behavior for Cutting with Various Tool Rake Angle by Finite Element Method



Ahmad Shahir Jamaludin, Hosokawa Akira, Tatsuaki Furumoto, Tomohiro Koyano and Yohei Hashimoto

Abstract In metal cutting process, cutting force holds significant information of the cutting tool performance and material machinability. However, it still remains unclear regarding to the relationship between cutting forces and other cutting parameters, such as cutting speed and contact friction coefficient. The main objective of this paper is to design a feasible Finite Element model to estimate cutting behavior with high accuracy. Several FEM models are designed reflecting the process of orthogonal cutting. In the meantime, actual orthogonal cutting tests of mild steel AISI 1045 with TiCN-coated cermet tool are executed in order to observe the real life behavior. There are two significant phenomena can be observed from the simulation: chip thickness and contact length. It is proven that, combination of chip thickness and contact length plays major role in estimating cutting behavior with high accuracy.

Keywords Orthogonal cutting · Finite element method · Chip thickness
Contact length

1 Introduction

Conventional wet cutting method has tended to shift to dry or semi-dry cutting as large amount of cutting fluid not only leads to the increment of power consumption and processing cost, but also environmental pollution [1]. Recently, the development of higher efficiency Minimum Quantity Lubrication (MQL) system for machining has been emphasized to solve or control these matters [1–3].

A. S. Jamaludin (✉)
Faculty of Manufacturing Engineering, Universiti Malaysia Pahang,
26600 Pekan, Pahang, Malaysia
e-mail: shahir@ump.edu.my

H. Akira · T. Furumoto · T. Koyano · Y. Hashimoto
Institute of Science and Technology, Kanazawa University, Kakuma-Machi,
920-1192 Kanazawa, Ishikawa, Japan

In MQL system, a very small amount of cutting fluid is turned into fine oil mist and supplied onto tool-chip contact zone and tool-machined workpiece surface contact zone. The system leads to cleaner working environment and reduction of waste liquid, which leads to lesser processing cost. It is believed that, MQL is capable to decrease the frictional contact between cutting chip and tool surface and lowering the cutting tool temperature [1–3]. However, due to the complex tribological behavior, the mechanism of MQL application is difficult to be explained. In addition, friction can be caused by any means of contact condition (contact pressure, geometry etc.) or defect (wear, foreign contamination etc.). Several studies on cutting simulation have been done by FEM analysis in order to estimate the cutting force and/or cutting temperature, in which appropriate model is assumed in nearly analogous to the actual cutting process [4–9].

The objective of this paper is to propose higher accuracy model in simulating the metal cutting behavior, as well as to study the effect of various cutting condition to relate with the application of Minimum Quantity Lubrication (MQL). In this study, several FEM models of orthogonal cutting are designed with various tool rake angle, and each model's accuracy will be analyzed.

2 Finite Element Model

In this study, FEM simulation model in orthogonal cutting of mild steel, AISI 1045 is designed with the application of DEFORM-3D, whereby the workpiece and cutting tool geometries are designed and simplified with the application of Computer Aided Design (CAD), as shown in Fig. 1. In the simulation, the FEM cutting tool is designed to resemble the actual cutting tool geometry, with 0° or 5° rake angle with 10° clearance angle. In the analysis, the cutting tool is modeled as rigid, and the workpiece is modeled as plastic. Figure 2 shows the models meshing and the main deformation boundary conditions to ensure the workpiece to deform in two-dimensional direction. The cutting condition and material properties for FEM

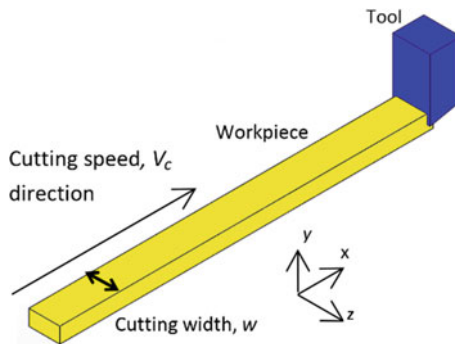


Fig. 1 Simplified orthogonal cutting

Fig. 2 Model meshing and boundary

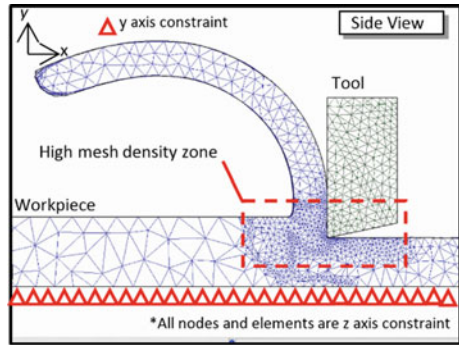


Table 1 Cutting conditions

Cutting tool	TiCN-coated cermet
Workpiece	AISI 1045
Cutting width, w (mm)	1.0
Depth of cut a (Feed f) (mm)	0.3
Cutting speed V_c (m/min)	25, 100, 200

Table 2 Material properties

Material	S45C
Young modulus, E (GPa)	212
Density, ρ (kg/m ³)	7850
Vickers hardness, HV _{0.3} (GPa)	1.96

application is shown in Tables 1 and 2, respectively. The applied FEM models in the study are explained as following:-

2.1 Conventional Average Coulomb Friction Coefficient Input <MODEL A>

In MODEL A, Coulomb friction coefficient, μ_{avg} , obtained from experimental data through Eq. (1), is input into the FEM model along with the pre-designed rake angle (in the case of this study, $\alpha = 0$ and 5°) (Fig. 3). The assumption of constant Coulomb friction coefficient, μ occurs on the whole tool rake face, regardless the length of sticking and sliding zones (Fig. 3).

2.2 Predetermined FEM Chip Thickness Through Deformation Limitation <MODEL B>

In MODEL B, an Eulerian boundary is added to optimize the chip deformation, called as Arbitrary Lagrangian-Eulerian (ALE) method. It is assumed that chip

Fig. 3 Model A

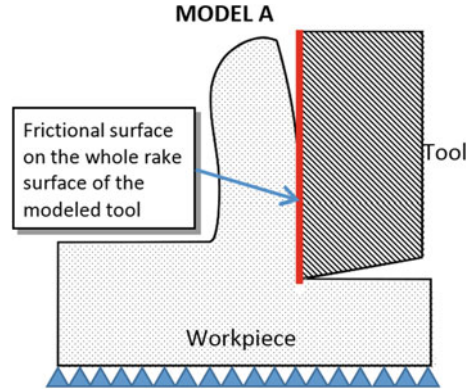
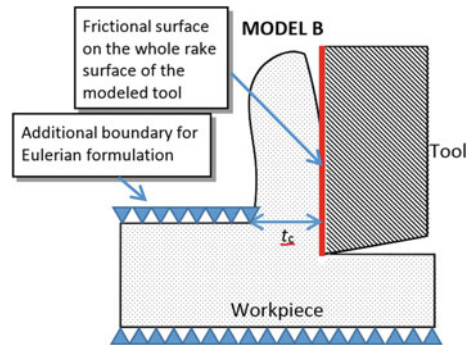


Fig. 4 Model B



thickness, t_c has a direct relationship with the magnitude of the principal force, F_p , thus affected the thrust force, F_t under the frictional condition (Fig. 4).

3 Actual Cutting Test

In this study, pseudo two-dimensional orthogonal cutting test of mild steel, AISI 1045 is carried out using the NC turning center OKUMA Macturn-30, where the tool is fed in the z -axis direction to the thin cylindrical shape of workpiece, as shown in Fig. 5. There are two types of inserts, 0° rake angle and 5° with both have 10° clearance angle. In the orthogonal cutting tests, cutting speed range of 25–100 and 200 m/min and depth of cut of 0.3 mm (feed rate in y -direction is 0.3 mm/rev) are applied. The orthogonal cutting conditions are the same with that shown in Table 2. The cutting forces are measured by a strain gauge type dynamometer. Chip thickness t_c and contact length l_c between chip and tool are also measured, where average chip thickness for 5 most stable measured values and length of scratch mark on the rake face are taken for each cutting condition. Based on the measured

cutting force, average Coulomb friction coefficient μ_{avg} for each cutting condition is calculated from Eq. (1).

$$\mu_{avg} = F/N = (F_t + F_p \tan \alpha) / (F_p - F_t \tan \alpha) \tag{1}$$

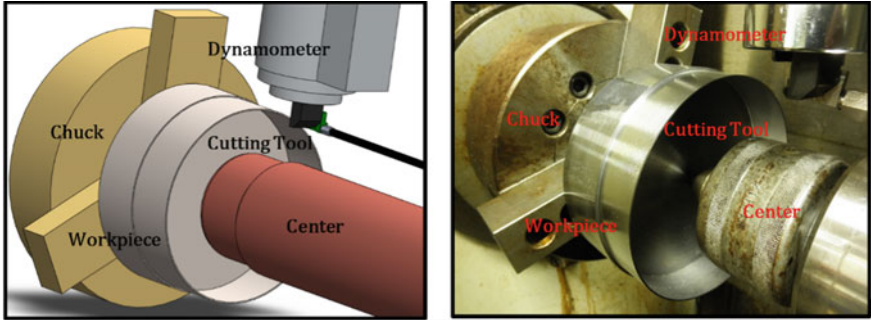


Fig. 5 Schematic illustration and experimental arrangement of orthogonal cutting experiment

Fig. 6 (left): Cutting force and friction coefficient comparison for 0° and 5° rake angle cutting tool

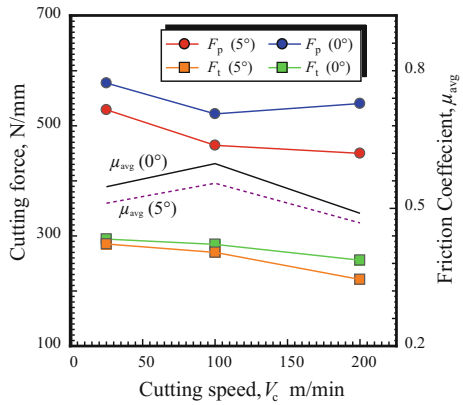


Fig. 7 (right): Contact length and chip compression ratio comparison for 0° and 5° rake angle cutting tool

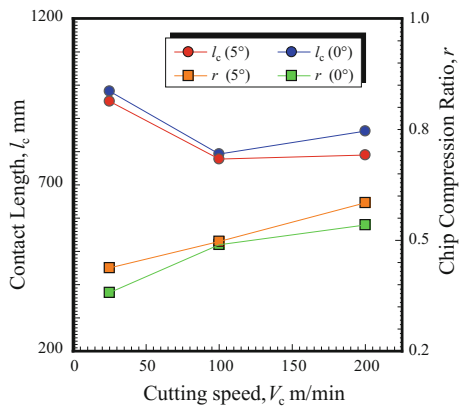


Table 3 Parameters estimation error (%) comparison onto all FEM models involved in the study for 0° rake angle

Cutting speed (m/min)	Model A (μ_{avg})						Model B (μ_{avg})							
	Principal force, F_p (N/mm)	Error (%)	Thrust force, F_t (N/mm)	Error (%)	Contact length, l_c (μ m)	Error (%)	Cutting ratio, r	Error (%)	Principal force, F_p (N/mm)	Error (%)	Thrust force, F_t (N/mm)	Error (%)	Contact length, l_c (μ m)	Error (%)
25	677	17	287	2	947	4	0.37	3	579	0	264	7.5	825	13
100	679	30	259	9	776	2	0.42	15	568	9	251	7.1	705	9
200	667	23	229	11	714	17	0.46	14	565	5	233	5.5	617	22

Table 4 Parameters estimation error (%) comparison onto all FEM models involved in the study for 5° rake angle

Cutting speed (m/min)	Model A (μ_{avg})						Model B (μ_{avg})							
	Principal force, F_p (N/mm)	Error (%)	Thrust force, F_t (N/mm)	Error (%)	Contact length, l_c (μ m)	Error (%)	Cutting ratio, r	Error (%)	Principal force, F_p (N/mm)	Error (%)	Thrust force, F_t (N/mm)	Error (%)	Contact length, l_c (μ m)	Error (%)
25	606	15	282	1	837	12	0.39	10	486	8	244	14	762	11
100	610	31	254	6	695	11	0.44	12	530	14	263	3	702	16
200	598	33	215	3	637	19	0.48	19	506	12	217	2	580	13

4 Results and Discussions

4.1 FEM Models Accuracy and Precision Analysis

Figures 6 and 7 shows the measured parameters obtained from the cutting test, while Tables 3 and 4 shows the accuracy of results estimated by FEM models involved in the study for 0° and 5° rake angle respectively. It can be observed that in some particular cases, MODEL A with average Coulomb friction coefficient, μ_{avg} , is able to estimate thrust force, F_t , accurately ($\sim 15\%$ error), while MODEL A with optimized average Coulomb friction coefficient, μ_{opt} , is able to estimate principal force, F_p , although overall mean estimation errors are significantly large similarly observed by previous researchers. Meanwhile, Model B is the best FEM model in estimating the cutting process as low mean estimating error obtained from cutting process simulation results (Tables 3 and 4).

It can be justified that the accuracy of the FEM estimation relies mainly on capability of the FEM to estimate chip formation accurately, which is related to material flow stress model, along with contact frictional coefficient input. The chip formation estimated in this study is assumed to have a relationship to the chosen flow stress model of the cutting material. However, it can be considered as difficult to obtain high accuracy flow stress model, thus MODEL B is feasible to optimize chip deformation in SFTC DEFORM-3D. The study shows that, it is possible to simulate the cutting process in various orthogonal cutting condition with DEFORM-3D, including MQL assisted cutting.

5 Conclusions

In this study, orthogonal cutting process of mild steel, AISI 1045 with 0° and 5° rake angle tools had been done experimentally and two Finite Element models had been presented to simulate the cutting behavior with the application of SFTC DEFORM-3D. It is conclude that, machining capability of larger rake angle is higher than smaller rake angle, where lower cutting force is obtained during cutting process with larger rake angle. Additionally, simulation and assessment of the cutting process for various cutting process involving dry cutting, Minimum Quantity Lubrication (MQL) cutting, cutting process with different kind of tool geometry are possible by utilizing the parameters such as the average Coulomb friction coefficient, μ_{avg} ; contact length, l_c and chip thickness, t_c obtained from the experimental results. The proposed model can estimate both principal force, F_p and thrust force, F_t with a good degree of accuracy.

Acknowledgements The author would like to acknowledge University Malaysia Pahang in funding the research under Research and Development Grant, RDU 1703252. In addition, the author would like to express deeply gratitude to OKUMA Co. Ltd in providing NC turning machine.

References

1. Arrazola, P.J., Özel, T.: Investigations on the effects of friction modeling in finite element simulation of machining. *Int. J. Mech. Sci.* **52**(1), 31–42 (2010)
2. Bonnet, C., Valiorgue, F., Rech, J., Hamdi, H.: Improvement of the numerical modeling in orthogonal dry cutting of an AISI 316L stainless steel by the introduction of a new friction model. *CIRP J. Manufact. Sci. Technol.* **1**, 114–118 (2008)
3. Childs, T.H.C.: Friction modeling in metal cutting. *Wear* **260**, 310–318 (2006)
4. DEFORM™-3D V10.2: Scientific Forming Technologies Corporation (Computer Software) (2011)
5. Filice, L., Micari, F., Rizutti, S., Umbrello, D.: A critical analysis of the friction modeling in orthogonal machining. *Int. J. Mach. Tools Manuf* **47**, 709–714 (2007)
6. Molinari, A., Cherguene, R., Miguelez, H.: Contact variables and thermal effects at the tool–chip interface in orthogonal cutting. *Int. J. Solids Struct.* **49**, 3774–3796 (2012)
7. Ozel, T.: The Influence of friction model on finite element simulations of machining. *Int. J. Mach. Tools Manuf* **46**, 518–530 (2006)
8. Rech, J., Arrazola, P.J., Claudin, C., Courbon, C., Pusavec, F., Kopac, J.: Characterisation of friction and heat partition coefficients at the tool-work material interface in cutting. *CIRP Ann. Manufact. Technol.* **62**, 79–82 (2013)
9. Yoon, E-S., Singh, R. A., Oh, H-J., Kong, H.: The effect of contact area on nano/micro-scale friction. *Wear* **259**, 1424–1431 (2005)